Dissertation

Measurement of the Higgs-Boson Production Cross-Section and Test of CP Invariance in Vector-Boson Fusion Production with $H \to \tau^+\tau^-$ Decays in the Fully-Leptonic Final State with the ATLAS Detector at the LHC

Alena Lösle

Fakultät für Mathematik und Physik
Albert-Ludwigs-Universität Freiburg

Measurement of the Higgs-Boson Production Cross-Section and Test of CP Invariance in Vector-Boson Fusion Production with $H \to \tau^+\tau^-$ Decays in the Fully-Leptonic Final State with the ATLAS Detector at the LHC

Dissertation

zur Erlangung des Doktorgrades der
Fakultät für Mathematik und Physik der
Albert-Ludwigs-Universität
Freiburg im Breisgau

vorgelegt von
Alena Lösle

Mai 2020

Dekan:	Prof. Dr. Wolfgang Soergel
Betreuer der Arbeit:	Prof. Dr. Markus Schumacher
Koreferent:	Prof. Dr. Gregor Herten
Prüfer:	Prof. Dr. Harald Ita
	Dr. Christian Weiser
	Prof. Dr. Markus Schumacher

Datum der mündlichen Prüfung: 29.07.2020

Abstract

The discovery of the Higgs boson in 2012 marks the start of a new era in particle physics, which is dedicated to the precise measurement of its properties. Currently, the decay of the Higgs-boson into τ-leptons, $H \rightarrow \tau\tau$, is the only accessible process to study the Yukawa coupling to leptons directly and allows to test the Standard Model (SM) predictions.

This thesis presents the measurement of the Higgs-boson production cross-section in the $H \rightarrow \tau\tau$ fully-leptonic final state based on data taken with the ATLAS detector at $\sqrt{s} = 13\,\text{TeV}$ with an integrated luminosity of $36.1\,\text{fb}^{-1}$. The analysis is based on the classification of events into categories, which target the dominant gluon-fusion (ggF) and vector-boson fusion (VBF) production modes, and the $H \rightarrow \tau\tau$ signal is extracted by performing a maximum likelihood fit in the reconstructed di-τ mass. In the fully-leptonic final state, an excess of $H \rightarrow \tau\tau$ signal events over the background-only hypothesis is observed with a significance of 2.2 standard deviations, while 1.2 standard deviations are expected. The obtained Higgs-boson production cross-section times branching ratio is $6.76^{+2.80}_{-2.78}\,\text{pb}$, which is consistent with the SM prediction within two standard deviations. The combined analysis with the semi-leptonic and fully-hadronic final states yields a Higgs-boson production cross-section times branching ratio of $3.77^{+1.06}_{-0.95}\,\text{pb}$. This result is consistent with the SM prediction within the uncertainties. The observed signal excess over the background-only hypothesis corresponds to a significance of 4.4 standard deviations, while 4.14 standard deviations are expected. In combination with the analysis of the data taken at $\sqrt{s} = 7\,\text{TeV}$ and $8\,\text{TeV}$ with integrated luminosities of $4.5\,\text{fb}^{-1}$ and $20.3\,\text{fb}^{-1}$, respectively, the observed significance amounts to 6.4 standard deviations, while 5.4 standard deviations are expected. This result allows to establish the discovery of $H \rightarrow \tau\tau$ decays with the ATLAS experiment.

Furthermore, this thesis presents a search for CP-violating interactions of the Higgs boson with weak gauge-bosons HVV in the VBF production mode with subsequent $H \rightarrow \tau\tau$ decays. Additional CP-odd contributions to the CP-even HVV coupling stucture are described by the parameter $\tilde{d}$ in the framework of an effective field theory with $\tilde{d} = 0$ corresponding to the SM prediction. The VBF Higgs-boson signal is separated from the background processes, where no CP violation is expected, by exploiting a multivariate approach. The CP-odd Optimal Observable is used in order to determine the $\tilde{d}$-parameter and construct its central confidence level (CL) intervals. In the fully-leptonic final state, the obtained $\tilde{d}$-parameter is -0.03 and no CL intervals for $\tilde{d}$ can be derived. The combined analysis with the semi-leptonic and fully-hadronic final states measures $\tilde{d}$ to be -0.01 and obtains a 68 % CL interval of $[-0.090, 0.035]$ compared to the expected 68 % CL interval for the SM hypothesis of $[-0.035, 0.033]$. No 95 % CL interval for $\tilde{d}$ is observed, while the expected 95 % CL interval for the SM hypothesis is $[-0.21, 0.15]$. These results are consistent with the SM prediction of a CP-even Higgs boson and show no sign of CP-violating HVV interactions.

Contents

1 Introduction

The Standard Model (SM) of particle physics provides a theoretical description for the smallest constituents of matter and their fundamental interactions. It predicts the existence of spin-1/2 particles, called *fermions*, and the integer-spin *bosons* as the mediators of the fundamental forces. In its early formulation, the SM did not allow for massive fermions and bosons, which would lead to the violation of local gauge invariance. However, various experimental measurements observed non-zero particle masses, for example the $W^{\pm}$-boson mass of $m_{W^{\pm}} = 80.4$ GeV or the Z^0-boson mass of $m_{Z^0} = 91.2\,\text{GeV}$ [1–3]. This conflict was solved in 1964 by the introduction of the Brout-Englert-Higgs (BEH) mechanism [4–8] based on the principle of spontaneous symmetry breaking, where fermions and bosons aquire their mass through the interaction with a scalar field, the so-called Higgs field. This mechanism results in the existence of a new spin-0 particle, which couples to fermions and bosons proportionally to their respective masses. In the last decades, the quest for discovering this Higgs boson has lead to great efforts on the experimental side and motivated the construction of the Large Hadron Collider (LHC) at CERN[1].

In 2012, the ATLAS[2] and CMS[3] experiments at the LHC announced the observation of a new particle with a mass of about 125 GeV [9,10]. A variety of subsequent measurements of its properties confirmed that this new particle is consistent with the Higgs boson as predicted by the SM and no deviations from these predictions have been observed until today. While the discovery of the Higgs boson was based on the bosonic decay channels, $H \to \gamma\gamma$, $H \to ZZ^*$ and $H \to WW^*$, its interaction with the fermionic sector, which is described by the Yukawa coupling, was only included via loop-induced contributions in the Higgs-boson coupling to gluons and photons. Recently, the observation of the Higgs-boson production in association with top-quarks ttH [11, 12] and its decay into bottom-quarks $H \to bb$ [13, 14] confirmed that the Higgs boson also couples to quarks. In the leptonic sector, only upper limits exist for the occurance of Higgs-boson decays to muons $H \to \mu\mu$ [15,16] and the decay into electrons $H \to ee$ is currently also not accessible. Hence, the decay of the Higgs boson into τ-leptons $H \to \tau\tau$ provides an important process to study the Higgs-boson coupling to leptons directly. First evidence for this decay mode was obtained by the ATLAS experiment based on data taken during Run 1 of the LHC in 2011 and 2012 at center-of-mass energies of $\sqrt{s} = 7\,\text{TeV}$ and $\sqrt{s} = 8\,\text{TeV}$ [17]. The combination with the results obtained by the CMS experiment lead to the observation of $H \to \tau\tau$ decays with a significance of 5.5 standard deviations [18].

[1]**C**onseil **E**uropéen pour la **R**echerche **N**ucléaire
[2]**A** **T**oroidal **L**HC **A**pparatu**S**
[3]**C**ompact **M**uon **S**olenoid

With the upgrade of the LHC between 2013 and 2015 to a center-of-mass energy of $\sqrt{s} = 13\,\text{TeV}$, the ATLAS detector underwent significant improvements, which were crucial in order to cope with the increased event rates while further enhancing the reconstruction efficiencies. As the cross-section for Higgs-boson production at $\sqrt{s} = 13\,\text{TeV}$ increases by about a factor of two compared to $\sqrt{s} = 7\,\text{TeV}$, the dataset collected during Run 2 of the LHC provides a unique opportunity to study the Higgs-boson properties in more detail. The work presented in this thesis is based on data taken with the ATLAS detector during 2015 and 2016 at $\sqrt{s} = 13\,\text{TeV}$ corresponding to an integrated luminosity of $36.1\,\text{fb}^{-1}$.

The first part of this thesis presents the cross-section measurement of Higgs-boson production with subsequent $H \to \tau\tau$ decays. The analysis is based on the classification of events into categories, which target the dominant Higgs-boson production modes in gluon-fusion (ggF) and vector-boson fusion (VBF). Since the τ-lepton decays either leptonically or hadronically, the $H \to \tau\tau$ channel can be classified into the fully-leptonic, the semi-leptonic and the fully-hadronic final states. The analyses presented in thesis focus on the fully-leptonic final state $H \to \tau\tau \to 2\ell 4\nu$, which occurs with the smallest branching ratio, but also profits from highly-efficient lepton triggers and lower contributions from QCD multi-jet production compared to the hadronic decay channels.

The predictions of the SM are further tested in the second part of this thesis, which investigates the behaviour of the Higgs boson under charge conjugation and parity transformation (CP transformation). In general, if all fundamental interactions of a particle are found to be invariant under such CP transformations, this is called CP invariance and the particle is an eigenstate of the CP operation with even (+1) or odd (−1) eigenvalue. On the other hand, CP invariance is violated if the particle does not correspond to an eigenstate of this CP operation. According to the Sakharov conditions [19], CP violating processes are one of the necessary conditions in order to explain the observed asymmetry between matter and antimatter in our universe (baryogenesis). In the SM, the Higgs boson is a CP-even particle and the only source of CP violation arises from the mixing of the quark flavour eigenstates [20, 21], which is not sufficient in order to explain the amount of observed baryon asymmetry [22–26]. While recent measurements by the ATLAS and CMS experiments are in agreement with the SM predictions of a pure CP-even Higgs boson [27–29], the possibility of small CP-odd contributions in addition to the SM interaction is still not excluded. This new source of CP violation would be a direct sign for physics beyond the SM.

The analysis presented in this thesis focuses on CP-violating interactions of the Higgs boson with electroweak gauge bosons HVV with $V = W^{\pm}, Z^0, \gamma$. While the structure of this coupling is often studied in the bosonic decays, $H \to ZZ^*$ and $H \to \gamma\gamma$, the Higgs-boson production in the VBF channel provides a higher sensitivity to possible CP-odd contributions. These CP-violating interactions are described by the parameter $\tilde{d}$ in the framework of an effective field theory, where $\tilde{d} = 0$ yields the SM prediction. Hence, any non-vanishing value of $\tilde{d}$ directly corresponds to the admixture of CP-even and CP-odd eigenstates and therefore implies the violation of CP invariance in HVV interactions. In this thesis, the CP-odd Optimal Observable is exploited to measure $\tilde{d}$ in the VBF Higgs-boson production mode with subsequent $H \to \tau\tau$ decays in the fully-leptonic final state.

The analysis follows a multivariate approach, which allows to efficiently separate the VBF Higgs-boson signal from the background processes, where no CP violation is expected. While previous results with the Run 1 dataset at $\sqrt{s} = 8\,\text{TeV}$ of $20.3\,\text{fb}^{-1}$ are consistent with the SM prediction of $\tilde{d} = 0$ at the 68 % confidence level [30], the enlarged dataset analyzed in this thesis allows to investigate the HVV coupling structure with even higher accuracy.

The thesis is structured as follows. Chapter 2 gives an introduction to the theoretical concepts of the SM and summarizes the results of current measurements of the Higgs-boson properties. In addition, CP-violating HVV interactions are described in the framework of an effective field theory and the Optimal Observable, which is used to search for CP violation, is introduced. Then, Chapter 3 gives an overview of the experimental setup of the ATLAS detector and the LHC. The signal and background processes, which are relevant in the fully-leptonic $H \to \tau\tau$ final state, are described in Chapter 4 along with the reweighting procedure for signal predictions with CP-violating HVV couplings. This is followed by an overview of the reconstruction and identification techniques for the relevant physics objects in Chapter 5. The measurement of the $H \to \tau\tau$ cross-section in the fully-leptonic final state and the combined result with the semi-leptonic and fully-hadronic channels are then presented in Chapter 6. The analysis of testing CP invariance in the VBF Higgs-boson production in the fully-leptonic final state and the combined result with the semi-leptonic and fully-hadronic channels is described in Chapter 7. In addition, Chapter 8 presents a sensitivity study of the Optimal Observable to different CP-odd operators in the VBF Higgs-boson production mode. The thesis concludes in Chapter 9 with a summary of the obtained results and an outlook for future studies.

Personal Contributions

The analyses presented in Chapter 6 ($H \to \tau\tau$ cross-section measurement) and Chapter 7 (VBF CP analysis) were performed within the ATLAS collaboration and rely on the joint effort of about 3000 members. The $H \to \tau\tau$ cross-section measurement is published in Ref. [31] and the VBF CP analysis is published in Ref. [32]. The following list summarizes the personal contributions by the author of this thesis:

- Validation of simulated samples for Higgs-boson production
- Configuration and validation of simulated samples for Higgs-boson production in gluon fusion with two jets at NLO precision
- Optimization of preselection and signal region definition for the $H \to \tau\tau$ cross-section measurement in the $\tau_{lep}\tau_{lep}$ channel
- Derivation of inputs for statistical analysis in the $H \to \tau\tau$ cross-section measurement for the $\tau_{lep}\tau_{lep}$ channel
- Studies on the development of an alternative approach to validate the data-driven fake-lepton background estimate for the $H \to \tau\tau$ cross-section measurement in the $\tau_{lep}\tau_{lep}$ channel
- Complete VBF CP analysis in the $\tau_{lep}\tau_{lep}$ channel:
  - Validation of technical implementation of Optimal Observable, comparison of Optimal Observable on parton level and reconstruction level
  - Event selection, signal region optimization, derivation of systematic uncertainties and studies on their impact in the statistical analysis
  - Studies on the binning of the Optimal Observable
  - BDT training and validation, investigation of BDT performance
- Construction and validation of the Z+jets region for the $\tau_{lep}\tau_{lep}$, $\tau_{lep}\tau_{had}$ and $\tau_{had}\tau_{had}$ channels in the VBF CP analysis
- Construction of modified BDT classifiers in the Z+jets region for the $\tau_{lep}\tau_{lep}$, $\tau_{lep}\tau_{had}$ and $\tau_{had}\tau_{had}$ channels in the VBF CP analysis
- Derivation of Z+jets reweighting for the $\tau_{lep}\tau_{lep}$, $\tau_{lep}\tau_{had}$ and $\tau_{had}\tau_{had}$ channels in the VBF CP analysis
- Implementation and validation of the statistical model in the VBF CP analysis
- Derivation of $\tau_{lep}\tau_{lep}$ standalone and combined results with the $\tau_{lep}\tau_{had}$ and $\tau_{had}\tau_{had}$ channels in the VBF CP analysis

The phenomenology study presented in Chapter 8 is not connected to the ATLAS collaboration, but has been designed and performed by the author of this thesis.

2 Theoretical Background

This chapter describes the theoretical concepts to study the elementary particles and their interactions. The first section gives an overview of the Standard Model (SM) of particle physics and describes the principle of spontaneous symmetry breaking in the electroweak sector. In addition, the theoretical concepts, which lead to CP-violating processes in the SM, are discussed. The next section describes the Higgs-boson production mechanisms in proton-proton (pp) collisions together with the dominant decay channels and gives an overview of the Higgs-boson discovery and the current status of experimental measurements of its properties. The last part of this chapter focuses on CP-violating Higgs-boson interactions within the framework of an effective field theory and introduces the CP-sensitive observables, which are used in this thesis to test CP invariance in the Higgs-boson interaction with weak vector-bosons in the vector-boson fusion production mode.

2.1. The Standard Model

The SM of particle physics, developed in the 1960s and 1970s, provides a theoretical description of all known particles and their fundamental interactions within the framework of a quantum field theory (QFT). The SM contains the internal symmetries of a unitary group and is based on the principle of local gauge invariance, which assures that the QFTs formulating the SM are invariant under local transformations of the respective symmetry groups. Within the SM, the elementary particles forming the matter around us correspond to quantizations of fermion fields with half-integer spins. Their interactions are described by the exchange of gauge fields, which appear as a consequence from the preservation of local gauge invariance. This results in the existence of spin-1 bosons, the so-called gauge bosons. The SM successfully provides a theoretical description for three out of the four fundamental forces: the electromagnetic force, the weak force and the strong force. Only the gravitational force, which can be neglected for energy scales accessible at current collider experiments, can not be formulated within the SM QFTs. The unified description of the electromagnetic and weak interactions is also referred to as the electroweak theory. While the principle of spontaneous symmetry breaking needs to be incorporated in the SM in order to allow for massive fermions and electroweak gauge bosons, it also predicts the existence of an additional spin-0 boson, the Higgs boson.

The validity of the SM was demonstrated multiple times by the experimental confirmation of predicted, previously unknown, particles, like the discovery of the $W^{\pm}$-boson and the Z^0-boson [1–3], the top-quark [33] and recently the Higgs boson [9, 10]. Furthermore, a variety of precision measurements show no significant deviation from the SM as of today.

The following sections give an overview of the particle content and describe the SM QFTs based on Ref. [34–36] and other references given in the text.

2.1.1. Elementary Particles

The particle content of the SM can be grouped into fermions, which carry half-integer spin, and bosons with full-integer spin. Within the group of fermions, particles, which only interact via the electroweak force are called *leptons*, while *quarks* participate in both the electroweak and strong interactions. As shown in Table 2.1, leptons and quarks are arranged in three generations corresponding to different *flavours*, where the fermion masses increase from the first to the third generation. Each generation contains two leptons or two quarks of the same flavour. For the lepton generations, electrons (e), muons (μ) or τ-leptons carrying an electric charge of -1[1] are combined with the electrically neutral neutrinos of the same flavour ν_e, ν_μ, ν_τ. While neutrinos were initially considered to be massless, the observation of neutrino oscillations shows, that they instead have different non-zero masses [37–39]. However, at present, experimental measurements only allow to determine the squared mass differences and provide upper limits on the neutrino masses. As these masses are expected to be very small, neutrinos are treated as massless in the context of this thesis. For quarks, each generation contains one up-type quark with a fractional electric charge of $2/3$ (u, c, t) and one down-type quark with $-1/3$ (d, s, b). While the matter around us consists of electrons, neutrons and protons and is therefore composed of first-generation fermions, particles of the second and third generations are only produced in high-energy processes, like cosmic rays or accelerator experiments. For each charged particle f an anti-particle $\bar{f}$ exists, which carries identical properties, like mass, lifetime and spin, but has opposite electric charge and internal quantum numbers. Since the neutrinos are electrically neutral, the question remains whether they correspond to their own anti-particles (Majorana particle), which would be a sign for physics beyond the SM.

The fundamental interactions between fermions are mediated by spin-1 vector bosons and are summarized in Table 2.2. The photon γ is the mediator of the electromagnetic force and couples to the electric charge Q. Since photons are massless, the range of the electromagnetic interaction is infinite, but gets weaker at large distances. The weak interaction is mediated by three massive vector bosons, the $W^{\pm}$-bosons and the Z^0-boson, which couple to the weak isospin I_w. Due to their large masses of $m_{W^{\pm}} = 80.4$ GeV and $m_{Z^0} = 91.2\,\text{GeV}$ [1–3] the weak interaction has a short range of approximately $10^{-17}\,\text{m}$ at low energies. The strong force describes the interaction between color-charged particles and is mediated by the gluon g. This color charge can take three states, which are commonly referred to as *red* (r), *blue* (b) and *green* (g).

In addition to these spin-1 bosons, the SM also contains a massive spin-0 particle, the Higgs boson. The existence of the Higgs boson appears as a consequence of the spontaneously broken symmetry in the electroweak sector, which is discussed in detail in Section 2.2.

[1] The electric charge is given in units of the elementary charge $e = 1.602177 \cdot 10^{-19}\,\text{C}$.

	Generation	Fermion		Q [e]	Mass [GeV]
Leptons	1^{st}	e	Electron	-1	$\approx 0.5 \times 10^{-3}$
		ν_e	Electron neutrino	0	$< 2 \times 10^{-9}$
	2^{nd}	μ	Muon	-1	$\approx 105 \times 10^{-3}$
		ν_μ	Muon neutrino	0	$< 0.17 \times 10^{-3}$
	3^{rd}	τ	τ-lepton	-1	≈ 1.7
		ν_τ	τ-lepton neutrino	0	$< 15 \times 10^{-3}$
Quarks	1^{st}	u	Up	$\frac{2}{3}$	$\approx 2.3 \times 10^{-3}$
		d	Down	$-\frac{1}{3}$	$\approx 4.8 \times 10^{-3}$
	2^{nd}	c	Charm	$\frac{2}{3}$	≈ 1.3
		s	Strange	$-\frac{1}{3}$	≈ 0.1
	3^{rd}	t	Top	$\frac{2}{3}$	≈ 173.0
		b	Bottom	$-\frac{1}{3}$	≈ 4.2

Table 2.1.: Leptons and quarks in the SM grouped in three generations with their electric charge Q and approximate mass [40].

Gauge boson		Force	Q [e]	Mass [GeV]
γ	Photon	Electromagnetic	0	0
$W^\pm$	W-boson	Weak	± 1	80.385
Z^0	Z-boson	Weak	0	91.188
g	Gluon	Strong	0	0

Table 2.2.: Gauge bosons in the SM with their corresponding fundamental interaction, electric charge Q and approximate mass [40].

2.1.2. Fundamental Interactions

Quantum Electrodynamics

The theory of quantum electrodynamics (QED) describes the electromagnetic interaction and is based on the symmetry of the abelian unitary group $U(1)_Q$ with the electric charge Q. The Lagrangian density for a free fermion field with Dirac spinor $\psi = \psi(x)$ and space-time coordinates $x = x^\mu$ is given by

$$\mathcal{L} = \bar{\psi}\left(i\gamma^\mu \partial_\mu - m_f\right)\psi \tag{2.1}$$

with the fermion mass m_f, the Dirac matrices γ^μ and the partial derivative $\partial_\mu = \frac{\partial}{\partial x^\mu}$. Under the $U(1)_Q$ symmetry, the fermion fields transform according to

$$\psi \mapsto \mathrm{e}^{-iQ\alpha(x)}\psi, \tag{2.2}$$

where $\alpha(x)$ corresponds to the local phase. Due to the space-time dependence of the local phase, the first term in Equation 2.1 transforms as

$$\partial_\mu \psi \mapsto \partial_\mu \left(\mathrm{e}^{-iQ\alpha(x)}\psi\right) = \mathrm{e}^{-iQ\alpha(x)}\partial_\mu \psi - iQ\mathrm{e}^{-iQ\alpha(x)}\partial_\mu \alpha(x)\psi \tag{2.3}$$

and the resulting Lagrangian is not invariant under local $U(1)_Q$ transformations. In order to restore local gauge invariance, an additional interaction between the fermion field and a new vector field A_μ, which transforms as

$$A_\mu \mapsto A_\mu + \partial_\mu \alpha(x) \tag{2.4}$$

has to be introduced. This vector field interacts with the fermion field with the coupling strength q, which is expressed in units of the elementary electric charge, and can be identified with the physical photon γ. In order to account for this vector field, the partial derivative in Equation 2.1 is replaced by the covariant derivative

$$D_\mu = \partial_\mu + iqA_\mu \tag{2.5}$$

and leads to the following QED Lagrangian density

$$\mathcal{L}_{QED} = \bar{\psi}\left(i\gamma^\mu\left(\partial_\mu - iqA_\mu\right) - m_f\right)\psi - \frac{1}{4}F^{\mu\nu}F_{\mu\nu}, \tag{2.6}$$

which is invariant under local gauge transformations. Here, the last term corresponds to an additional kinematic term for the photon $\frac{1}{4}F^{\mu\nu}F_{\mu\nu}$ and contains the field-strength tensor $F_{\mu\nu} = \partial_\mu A_\nu - \partial_\nu A_\mu$. The equation of motion for a free fermion field is then given by applying the Euler-Lagrange equation:

$$(i\gamma^\mu\partial_\mu - m_f)\psi = -q\gamma^\mu A_\mu\psi. \tag{2.7}$$

Since any additional term of the form $\frac{1}{2}m_\gamma A_\mu A^\mu$ in Equation 2.6 violates local gauge invariance, the formalism of QED requires a massless photon. This is in agreement with experimental observations, which provide upper limits on the photon mass of $m_\gamma < 3 \times 10^{-27}\,\text{eV}$ [41].

The coupling strength of QED can also be written in the form $\alpha_{QED} = q^2/4\pi$. The principle of renormalization, which is discussed in Section 4.3.1, results in a dependency of the coupling strength on the energy scale of the process and leads to the introduction of the so-called *running* coupling strength. In particular, the running coupling strength of QED decreases with increasing interaction distances.

Quantum Chromodynamics

The strong interaction between quarks and gluons is described by quantum chromodynamics (QCD) based on the $SU(3)_C$ symmetry group and couples to the color charge C. This color charge can take three values, which are typically referred to as $red,\ blue, green$ [42]. Since quarks and anti-quarks carry one color or anti-color, respectively, they can exist in three differently charged states. The four-component Dirac spinor of a quark field $\psi(x)$ is therefore replaced by a vector of spinors for the three color degrees of freedom:

$$\Psi(x) = (\psi_{red}(x),\ \psi_{blue}(x),\ \psi_{green}(x)). \tag{2.8}$$

This vector transforms under the symmetry of $SU(3)_C$ as

$$\Psi \mapsto \mathrm{e}^{i\frac{g_s}{2}\sum_{a=1}^{8}\lambda_a\beta_a(x)}\Psi \tag{2.9}$$

with the strong coupling strength g_s, the local transformation functions $\beta_a(x)$ and the Gell-Mann matrices λ_a as the generators of $SU(3)_C$ [43], which, in contrast to QED, do not commute. This non-abelian structure of $SU(3)_C$ leads to specific properties of the strong interaction, which are further discussed below. In order to preserve local gauge invariance, eight gauge fields G_a^μ are introduced, which transform under $SU(3)_C$ as

$$G_a^\mu \mapsto G_a^\mu + \frac{1}{g_s}\partial^\mu \beta_a(x) + f_{abc}\beta_b(x)G_c^\mu \tag{2.10}$$

with the anti-symmetric structure constants f_{abc}. These gauge fields can be identified with the eight color states of the gluon, which carries a combination of color and anti-color charge. The covariant derivative is then defined as

$$D^\mu = \partial^\mu + ig_s \sum_{a=1}^{8} \frac{\lambda_a}{2} G_a^\mu \tag{2.11}$$

with the gluon field-strength tensor

$$G_a^{\mu\nu} = \partial^\mu G_a^\nu - \partial^\nu G_a^\mu - g_s f_{abc} G_b^\nu G_c^\mu. \tag{2.12}$$

Here, the last term appears as a consequence of the non-abelian structure of $SU(3)_C$ and describes the gluon self-coupling in terms of three and four gluon interactions. With this, the Lagrangian density of QCD for a specific quark flavour with mass m_q is given by

$$\mathcal{L}_{QCD} = \bar{\Psi}(i\gamma_\mu D^\mu - m_q)\Psi - \frac{1}{4}\sum_{a=1}^{8} G_{a,\mu\nu}G_a^{\mu\nu} \tag{2.13}$$

and preserves local gauge invariance for massless gluons. According to Equation 2.13, quark masses do not differ between the three color states, but only change with the quark flavour. In addition, quarks of different flavour and color states couple to the gauge fields with the same strength. The coupling strength of QCD can also be written as $\alpha_s = g_s/4\pi$. In contrast to QED, the running of the strong coupling strength corresponds to an increase of the strong force with decreasing energy scales. Hence, at small distances quarks and gluons act as free particles, which is also called *asympotic freedom* [44, 45]. On the other hand, as their spatial distance gets larger, the interacting particles experience an increasing confining potential. This principle of *confinement* leads to the spontaneous formation of quark anti-quark pairs out of the vacuum, which then combine with the initially interacting quarks and form color-neutral states. These bound multi-quark states are called *hadrons* and consist of quark and anti-quark pairs (*mesons*) or three (anti-) quarks (*baryons*), which can be experimentally measured. Recently, the LHCb exeriment at CERN also announced the observation of bound states with four quarks (*tetraquarks*) and five quarks (*pentaquarks*) [46, 47].

Electroweak Unification

The electroweak theory, formulated in 1967 by Glashow, Salam and Weingberg [48–50], provides a unified description of the electromagnetic and weak interaction within the symmetry group of $SU(2)_{I_w} \times U(1)_Y$. The charge of the weak interaction under $SU(2)_{I_w}$ corresponds to the weak isospin I_w, while for $U(1)_Y$ the electric charge Q is replaced by the hypercharge Y according to the Gell-Mann-Nishijima relation [51, 52]

$$Q = I_{w,3} + \frac{Y}{2} \tag{2.14}$$

with the third component of the isospin $I_{w,3}$. The electroweak theory comprises fermion fields with left-chiral and right-chiral components

$$\psi = \psi_L + \psi_R = \frac{1}{2}(1-\gamma^5)\psi + \frac{1}{2}(1+\gamma^5)\psi, \tag{2.15}$$

where $\gamma^5 = i\gamma^0\gamma^1\gamma^2\gamma^3$. As shown in Table 2.3, the left-chiral and right-chiral fields are ordered according to their isospin and hypercharge. Left-chiral fermions are grouped into doublets with $I_{w,3} = \pm\frac{1}{2}$ and same hypercharge, while right-chiral fermions form singlets under $SU(2)_{I_w}$ and carry $I_{w,3} = 0$. Hence, only left-chiral fermions and right-chiral anti-fermions participate in the weak interaction, while right-chiral fermions remain invariant under $SU(2)_{I_w}$. In the leptonic sector, each isospin doublet combines the charged leptons with neutrinos of the respective flavour, while quark doublets are built from pairs of up-type and down-type quarks of the same generation. Since neutrinos are assumed to be massless in the context of this thesis, they are only listed in left-chiral doublet states. Under the $SU(2)_{I_w}$ symmetry, local transformations of the left-chiral fermion fields are given by

$$\psi_L \mapsto \mathrm{e}^{i\frac{g}{2}\sum_{a=1}^{3}\tau_a\alpha_a(x)}\psi_L \tag{2.16}$$

with the coupling strength of the weak interaction g and the local phases $\alpha_a(x)$. The generators τ_a correspond to the (2×2) Pauli matrices. Under the $U(1)_Y$ symmetry, left-chiral and right-chiral fermion fields transform as

$$\begin{aligned} \psi_L &\mapsto \mathrm{e}^{i\frac{g'}{2}Y\beta(x)}\psi_L \\ \psi_R &\mapsto \mathrm{e}^{i\frac{g'}{2}Y\beta(x)}\psi_R \end{aligned} \tag{2.17}$$

with another coupling strength g', the local phase $\beta(x)$ and the hypercharge operator Y as the generator of $U(1)_Y$. The requirement of local gauge invariance results in the introduction of three $SU(2)_{I_w}$ gauge fields, W_a^μ with $a = (1, 2, 3)$, which couple to the isospin, and one $U(1)_Y$ gauge field, B_μ, which couples to the hypercharge. The covariant derivatives are then defined as

$$\begin{aligned} D_L^\mu &= \partial^\mu + i\frac{g}{2}\sum_{a=1}^{3}\tau_a W_a^\mu + i\frac{g'}{2}YB^\mu \\ D_R^\mu &= \partial^\mu + i\frac{g'}{2}YB^\mu \end{aligned} \tag{2.18}$$

and replace the derivative in Equation 2.1. This results in the following Lagrangian density:

$$\mathcal{L}_{EW} = \bar{\psi}_L(i\gamma_\mu D_L^\mu)\psi_L + \bar{\psi}_R(i\gamma_\mu D_R^\mu)\psi_R - \frac{1}{4}\sum_{a=1}^{3} W_{a,\mu\nu}W_a^{\mu\nu} - \frac{1}{4}B_{\mu\nu}B^{\mu\nu}. \tag{2.19}$$

Here, the kinetic terms of the gauge bosons contain the field-strength tensors

$$\begin{aligned} W_a^{\mu\nu} &= \partial^\mu W_a^\nu - \partial^\nu W_a^\mu - g\epsilon_{abc}W_b^\mu W_c^\nu \\ B^{\mu\nu} &= \partial^\mu B^\nu - \partial^\nu B^\mu \end{aligned} \tag{2.20}$$

with the anti-symmetric tensor ϵ_{abc} giving the structure constants of the non-abelian $SU(2)_{I_w}$ group. The physical fields Z^μ and A^μ can then be constructed from linear combinations of the neutral $SU(2)_{I_w} \times U(1)_Y$ gauge fields as

$$\begin{pmatrix} Z^\mu \\ A^\mu \end{pmatrix} = \begin{pmatrix} \cos(\theta_w) & -\sin(\theta_w) \\ \sin(\theta_w) & \cos(\theta_w) \end{pmatrix} \begin{pmatrix} W_3^\mu \\ B^\mu \end{pmatrix}, \tag{2.21}$$

where the weak mixing angle

$$\cos(\theta_w) = \frac{g}{\sqrt{g^2 + g'^2}} \tag{2.22}$$

is introduced in order to ensure orthogonality between the Z^0-boson and the photon. This rotation of the gauge fields in Equation 2.21 provide a photon field, which interacts with left-chiral and right-chiral particles with the same coupling strength, but does not couple to neutrinos. Furthermore, the charged fields of the $W^\pm$-bosons are given by:

$$W_\mu^\pm = \frac{1}{\sqrt{2}}\left(W_\mu^1 \mp iW_\mu^2\right). \tag{2.23}$$

As shown in Equation 2.20, the non-abelian structure of $SU(2)_{I_w}$ leads to self-interacting W_a^μ fields and provides cubic and quartic couplings of the electroweak gauge bosons. Due to its preferred coupling to left-chiral states, the electroweak interaction is found to maximally violate the symmetries under parity transformation (P) and charge conjugation (C) [53, 54]. Moreover, the invariance under the combination of charge conjugation and parity transformation (CP) is violated as well. In particular, the left-chiral (right-chiral) isospin doublets of quarks (anti-quarks) allow for charged current interactions via the exchange of a $W^\pm$-boson, which modify the flavour of the participating quarks and lead to CP-violating interactions. On the other hand, flavour-changing neutral currents via Z^0/γ-exchanges are not allowed. The violation of CP invariance in the electroweak interaction is discussed in detail in Section 2.1.4.

As for QED and QCD, the requirement of local gauge invariance forbids the existence of massive electroweak gauge bosons, which is in conflict with experimental measurements of the $W^\pm$-boson and Z^0-boson masses given in Table 2.2. Another conflict appears for the incorporation of mass terms for fermions in the electroweak Lagrangian density. In particular, such mass terms of the form $-m\bar{\psi}\psi = -m(\bar{\psi}_R\psi_L + \bar{\psi}_L\psi_R)$ are not invariant under the symmetry of $SU(2)_{I_w}$. These conflicts can be solved by the introduction of an additional scalar field, which spontaneously breaks the symmetry in the electroweak sector.

	Generation			Quantum numbers			
	1st	2nd	3rd	I_w	$I_{w,3}$	Y	Q [e]
Leptons	$\begin{pmatrix}\nu_e \\ e\end{pmatrix}_L$	$\begin{pmatrix}\nu_\mu \\ \mu\end{pmatrix}_L$	$\begin{pmatrix}\nu_\tau \\ \tau\end{pmatrix}_L$	$\frac{1}{2}$ $\frac{1}{2}$	$\frac{1}{2}$ -$\frac{1}{2}$	-1 -1	0 -1
	e_R	μ_R	τ_R	0	0	-2	-1
Quarks	$\begin{pmatrix}u \\ d'\end{pmatrix}_L$	$\begin{pmatrix}c \\ s'\end{pmatrix}_L$	$\begin{pmatrix}t \\ b'\end{pmatrix}_L$	$\frac{1}{2}$ $\frac{1}{2}$	$\frac{1}{2}$ -$\frac{1}{2}$	$\frac{1}{3}$ $\frac{1}{3}$	$\frac{2}{3}$ -$\frac{1}{3}$
	u_R	c_R	t_R	0	0	$\frac{4}{3}$	$\frac{2}{3}$
	d_R	s_R	b_R	0	0	-$\frac{2}{3}$	-$\frac{1}{3}$

Table 2.3.: Summary of fermions in the electroweak model grouped in three generations with their quantum numbers. Quarks are given in their electroweak eigenstates, which are related to the mass eigenstates according to the CKM matrix (see Section 2.1.4).

2.1.3. Electroweak Symmetry Breaking

The SM requires the spontaneous breaking of the $SU(2)_{I_w} \times U(1)_Y$ symmetry to $U(1)_Q$ in order to introduce mass terms for bosons and fermions while preserving local gauge invariance. This so-called *Higgs mechanism*[2] was proposed in 1964 by Englert, Brout, Higgs, Guralnik, Hagen and Kibble [4–8] and is based on the introduction of an additional isospin doublet of complex scalar fields with hypercharge $Y = 1$ and isospin $I_w = \frac{1}{2}$ [43]:

$$\phi = \begin{pmatrix}\phi^+ \\ \phi^0\end{pmatrix} = \begin{pmatrix}\phi_1 + i\phi_2 \\ \phi_3 + i\phi_4\end{pmatrix}. \tag{2.24}$$

The $SU(2)_{I_w} \times U(1)_Y$ invariant Lagrangian density for this Higgs field is constructed with the covariant derivatives defined in Equation 2.18:

$$\mathcal{L}_{Higgs} = (D_\mu\phi)^\dagger(D^\mu\phi) - V(\phi) + \frac{1}{4}\sum_{i=1}^{a} W_{a,\mu\nu}W_a^{\mu\nu} - \frac{1}{4}B_{\mu\nu}B^{\mu\nu}, \tag{2.25}$$

where the Higgs potential $V(\phi)$ can be written in the following form:

$$V(\phi) = \mu^2\phi^\dagger\phi + \lambda(\phi^\dagger\phi)^2,\ \lambda > 0. \tag{2.26}$$

For $\mu^2 > 0$, the minimum of this potential corresponds to a ground state of $\phi_0 = 0$, while choosing $\mu^2 < 0$ results in a degenerated set of non-zero ground states with

$$\phi_0^\dagger\phi_0 = \frac{-\mu^2}{2\lambda} = \frac{v^2}{2}. \tag{2.27}$$

[2] more precise: Englert-Brout-Higgs-Guralnik-Hagen-Kibble mechanism.

Here, $v \equiv \sqrt{\frac{-\mu^2}{\lambda}}$ is defined as the vacuum expectation value of the Higgs field. Figure 2.1 shows a simplified example of such a potential depending on two out of the four degrees of freedom in ϕ. The symmetry of $SU(2)_{I_w} \times U(1)_Y$ is spontaneously broken by choosing a particular ground state as

$$\phi_0(x) = \frac{1}{\sqrt{2}} \begin{pmatrix} 0 \\ v \end{pmatrix}. \tag{2.28}$$

Here, the choice of $\phi_1 = \phi_2 = \phi_4 = 0$ provides an electrically neutral ground state, which preserves $U(1)_Q$ symmetry and therefore satisfies the requirement of massless photons. The parametrization around the vacuum expectation value leads to a ground state of

$$\phi_0(x) = \frac{1}{\sqrt{2}} \exp\left(i \sum_{a=1}^{3} \frac{\tau_a G_a(x)}{v} \right) \begin{pmatrix} 0 \\ v + H(x) \end{pmatrix} \tag{2.29}$$

and introduces four real field: $G_1(x), G_2(x), G_3(x)$ and $H(x)$. The fields $G_1(x), G_2(x), G_3(x)$ refer to three massless *Nambu-Goldstone* bosons [55, 56], which can be eliminated from the Lagrangian density by making an appropriate unitary gauge choice of

$$\phi_0(x) \mapsto \exp\left(-i \sum_{a=1}^{3} \frac{\tau_a G_a(x)}{v} \right) \phi_0(x). \tag{2.30}$$

The degrees of freedom, which become available with this transformation, are then absorbed into additional longitudinal polarizations of the massive $W^{\pm}$-bosons and the Z^0-boson. The remaining field $H(x)$ can be considered as an excitation from the ground state and results in the existence of a scalar particle, the Higgs boson. The Lagrangian density after electroweak symmetry breaking is then given by [35]

$$\begin{aligned} \mathcal{L}_{Higgs} =& \frac{1}{2} \left(\partial_\mu H\right) \left(\partial^\mu H\right) - \lambda v^2 H^2 - \lambda v H^3 - \frac{1}{4} \lambda H^4 \\ &+ \frac{1}{2} \left(\frac{1}{2} v g\right)^2 W^{\mu,+} W^-_\mu + \frac{1}{2} \left(\frac{vg}{2\cos(\theta_w)}\right)^2 Z^\mu Z_\mu \\ &+ g \left(\frac{vg}{2}\right) H W^{\mu,+} W^-_\mu + g \frac{vg}{4\cos^2(\theta_w)} H Z^\mu Z_\mu \\ &+ \frac{g^2}{4} H^2 W^{\mu,+} W^-_\mu + \frac{g^2}{4\cos^2(\theta_w)} H^2 Z^\mu Z_\mu + \text{const.} \end{aligned} \tag{2.31}$$

and contains mass terms for the $W^{\pm}$-bosons and the Z^0-boson

$$m_{W^\pm} = \frac{1}{2} v g \qquad m_{Z^0} = \frac{m_{W^\pm}}{\cos(\theta_w)}, \tag{2.32}$$

as well as for the Higgs boson

$$m_H = \sqrt{2\lambda v^2} = \sqrt{-2\mu^2}. \tag{2.33}$$

While the relation between the masses of the weak gauge-bosons is determined via the weak mixing angle θ_w, the mass of the Higgs boson can not be derived from Equation 2.33. Measurements of the Fermi constant of the electroweak interaction $G_F = (\sqrt{2} v^2)^{-1}$ allow to derive a vacuum expectation value of $v \approx 246$ GeV [40], while λ remains unconstraint and has to be determined experimentally with the measurement of the Higgs-boson mass.

As shown in Equation 2.31, the strength of the interactions between the Higgs field and the vector fields HVV and H^2VV are proportional to m_V^2/v and m_V^2/v^2, respectively, where m_V refers to the mass of the respective vector boson $V = W^\pm, Z^0$. The Higgs field also couples to itself in terms of cubic (H^3) and quartic (H^4) self-interactions, where the coupling strengths are proportional to m_H^2/v and m_H^2/v^2, respectively.

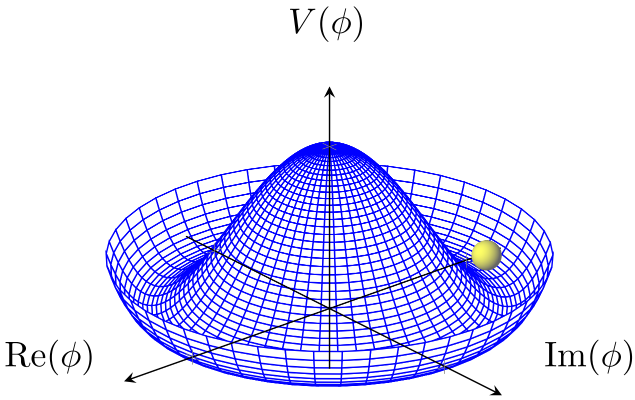

Figure 2.1.: Illustration of the Higgs potential $V(\phi)$ with $\mu^2 < 0$ for two out of four degrees of freedom. The yellow sphere corresponds to a ground state, for which the symmetry is spontaneously broken.

In order to introduce mass terms for fermions, the so-called *Yukawa coupling* proposed by Weinberg [49] describes the interaction between the Higgs doublet, the left-chiral $SU(2)_{I_w}$ doublets and the right-chiral singlets. For leptons of the first generation, the corresponding Yukawa interaction is given by

$$\mathcal{L}^{lep}_{Yukawa} = -g_e \left(\bar{\nu}_e, \bar{e}\right)_L \phi \, e_R + h.c. \tag{2.34}$$

with the coupling strength g_e, the Higgs doublet ϕ as defined in Equation 2.29 and $h.c.$ referring to the respective hermitian conjugate term. In order to provide mass terms for up-type quarks, the charge conjugate Higgs doublet is introduced:

$$\phi_c(x) = \frac{1}{\sqrt{2}} \begin{pmatrix} v + H(x) \\ 0 \end{pmatrix}. \tag{2.35}$$

Then, the Yukawa interaction with first generation quarks reads

$$\mathcal{L}^{quark}_{Yukawa} = -g_d \left(\bar{u}, \bar{d}\right)_L \phi \, d_R - g_u \left(\bar{u}, \bar{d}\right)_L \phi_c \, u_R + h.c, \tag{2.36}$$

where g_d and g_u refer to the strength of the Higgs-boson coupling to up-quarks and down-quarks, respectively. The Yukawa couplings for second and third generation fermions can be constructed analogously. Expanding these Yukawa terms in ϕ around the vacuum expectation value results in the following Lagrangian density:

$$\mathcal{L}_{Yukawa} = -\frac{g_f}{\sqrt{2}} H \bar{\psi}^f \psi^f - \frac{v}{\sqrt{2}} g_f \bar{\psi}^f \psi^f. \tag{2.37}$$

Here, the first term describes the coupling of the Higgs field to fermions f with the coupling strength g_f, while the second term provides the corresponding fermion masses:

$$m_f = \frac{v}{\sqrt{2}} g_f. \tag{2.38}$$

Hence, the coupling strength between the Higgs field and fermions is proportional to their respective masses, which results in favoured interaction with heavier particles. While in general, the Yukawa interaction between the Higgs field and the fermion fields is represented by complex (3×3) Yukawa matrices, the diagonalization of these matrices can be identified with a redefinition of the fermion fields. This redefinition corresponds to a basis change from the eigenstates of the weak interaction to the mass eigenstates and leads to fermion masses as given in Equation 2.38. While for leptons the basis-changing matrix can be chosen as the identity matrix due to the massless neutrinos[3], the transition from the weak interaction basis to the mass basis for quarks results in a mixing between the quark flavours and leads to CP-violating charged-current interactions, which are discussed in more detail in the next section.

Finally, the full Langrangian density of the SM is given by

$$\mathcal{L} = \mathcal{L}_{Higgs} + \mathcal{L}_{EW} + \mathcal{L}_{QCD} + \mathcal{L}_{Yukawa}. \tag{2.39}$$

While the strength of the Higgs-boson coupling to fermions and bosons is predicted by the SM, the Higgs-boson mass remains unknown and has to be determined experimentally. The observation of the Higgs boson and recent measurements of its mass are discussed in Section 2.2.

2.1.4. CP Violation in the SM

There are three fundamental discrete symmetries in nature. First, the parity transformation (P) corresponds to the transformation of a system into its mirrored version by inverting the spatial coordinates $\vec{x} \to -\vec{x}$. Here, a scalar complex field $\phi(t, \vec{x})$ transforms under parity operation as

$$P\phi(t, \vec{x})P^{-1} = \eta_P \phi(t, -\vec{x}), \tag{2.40}$$

where the intrinsic phase of the field η_P can take values of $+1$ (even parity) or -1 (odd parity). For $\eta_P = -1$, the field is also called a *pseudo-scalar*. The application of the parity operation to the spatial components of a vector field $V(t, \vec{x}) = (V_x(t, \vec{x}), V_y(t, \vec{x}), V_z(t, \vec{x}))$ is given by

$$P\,V(t, \vec{x})P^{-1} = \eta_P V(t, -\vec{x}) \tag{2.41}$$

[3]The SM can be extended to include massive neutrinos, where the mixing between the neutrino mass and flavour eigenstates is described by the Pontecorvo-Maki-Nakagawa-Sakata (PMNS) matrix.

and corresponds to phases of $\eta_p = 1$ for *pseudo-vectors* and $\eta_p = -1$ for vectors.

The operation under charge conjugation (C) leads to the reversal of all internal quantum numbers and transforms the field into its complex conjugate:

$$C\phi(t,\vec{x})C^{-1} = \eta_C \phi^*(t,\vec{x}) \tag{2.42}$$

$$C\,V(t,\vec{x})C^{-1} = \eta_C V^*(t,\vec{x}) \tag{2.43}$$

In particular, this corresponds to the transformation of a particle into its anti-particle up to a phase η_C.

Last, the operation of time reversal (T) is given by

$$T\phi(t,\vec{x})T^{-1} = \eta_T \phi(-t,\vec{x}), \tag{2.44}$$

where usually a phase of $\eta_T = 1$ is chosen. For a single particle state $|\phi(p,s)\rangle$ with four momentum p and spin s, the time reversal operation corresponds to an exchange of initial and final states with

$$T|\phi(p,s)\rangle = \langle\phi(-p,-s)|. \tag{2.45}$$

In addition, the so-called naive time reversal $\hat{T}$ [57–59] can be defined as

$$\hat{T}|\phi(p,s)\rangle = |\phi(-p,-s)\rangle, \tag{2.46}$$

where the exchange of initial and final state is omitted, but only spin and momentum directions are inverted. This naive time reversal is exploited in order to search for CP-violating interactions as discussed in Section 2.4. Since the CPT theorem states, that any Lorentz-invariant local quantum field theory has to be invariant under the combined CPT operation, the presence of CP violation in nature implies the non-invariance under T transformation as well.

The observation of a clear asymmetry between matter and anti-matter in our universe, raises the question, which fundamental processes lead to the evolution from an initially symmetric system to an excess of baryons over anti-baryons. This asymmetry can be expressed through the ratio of baryon and anti-baryon densities, n_B and $n_{\bar{B}}$, respectively, to the density of photons n_γ. By using the latest measurements of the Planck satellite for the average energy density of baryons in our universe [60], the asymmetry parameter is found to be

$$\eta = \frac{n_B - n_{\bar{B}}}{n_\gamma} \approx 6 \cdot 10^{-10}. \tag{2.47}$$

In 1967 Sakharov formulated three conditions, which need to be fulfilled in order to explain this asymmetry [19]: The presence of baryon number violating processes, the violation of C and CP invariance and the departure from the thermal equilibrium.

Until today, no experimental sign for the violation of C,P or CP symmetries is observed in the electromagnetic and strong interactions. The weak force, however, maximally violates C and P symmetries due to its preferred coupling to left-chiral fermions. This was first observed in the β-decay of ${}^{60}_{27}\mathrm{Co} \rightarrow {}^{60}\mathrm{Ni}^* e^- \nu_e$, where the electron is preferably emitted in opposite direction to the spin of the nuclei [54]. The measurement of neutral kaon decays in 1964 [61] provided the first experimental evidence, that the weak interaction also violates the combined CP symmetry. This CP violation appears as a consequence of the discrepancy between the quark eigenstates, which participate in the weak interaction, and their mass eigenstates. This allows for the transition of quark flavours via charged-current interactions. The mixing between the weak eigenstates (d',s',b') and the mass eigenstates (d,s,b) is described by the Cabibbo-Kobayashi-Maskawa (CKM) matrix V_{CKM} [20,21] with

$$\begin{pmatrix} d' \\ s' \\ b' \end{pmatrix} = \begin{pmatrix} V_{ud} & V_{us} & V_{ub} \\ V_{cd} & V_{cs} & V_{cb} \\ V_{td} & V_{ts} & V_{tb} \end{pmatrix} \begin{pmatrix} d \\ s \\ b \end{pmatrix}, \tag{2.48}$$

where $|V_{ij}^2|$ corresponds to the probability for a quark flavour transition $i \to j$ in the interaction with a $W^{\pm}$-boson. The CKM matrix is a (3×3) complex and unitary matrix and is therefore described by three mixing angles $\theta_{12}, \theta_{23}, \theta_{13}$ and one complex phase δ_{13}. With these parameters, the CKM matrix can also be written in the following form

$$V_{CKM} = \begin{pmatrix} c_{12}c_{13} & s_{12}c_{13} & s_{13}e^{-i\delta_{13}} \\ -s_{12}c_{23} - c_{12}s_{23}s_{13}e^{i\delta_{13}} & c_{12}c_{23} - s_{12}2_{23}s_{13}e^{i\delta_{13}} & s_{23}c_{13} \\ s_{12}s_{23} - c_{12}c_{23}s_{13_{e^{i\delta_{13}}}} & -c_{12}s_{23} - s_{12}c_{23}s_{13}e^{i\delta_{13}} & c_{23}c_{13} \end{pmatrix} \tag{2.49}$$

with $c_{ij} = \cos(\theta_{ij})$ and $s_{ij} = \sin(\theta_{ij})$ for $i, j \in [1, 2, 3]$. Due to the complex phase δ_{13}, the CKM matrix is not invariant under CP transformation and leads to the violation of CP invariance in the weak interaction. As the CKM matrix is found to have an approximately diagonal structure [40], quark-flavour transitions within one generation are favoured, while the mixing between different generations is suppressed.

Following the first experimental evidence for CP violation in the neutral kaon system, additional contributions were found in the mixing and decay of mesons containing b-quarks and s-quarks [62–65]. Recently, the LHCb collaboration at CERN also observed the violation of CP invariance related to c-quarks in the mixing of neutral D^0-mesons [66]. However, the total amount of CP violation in the weak interaction measured so far is still insufficient to explain the amount of baryon asymmetry we see, but can only account for about $\eta \sim 10^{-19}$ [22, 67, 68]. This requires the existence of additional sources of CP violation beyond the predictions of the SM in order to explain the observed η-value. The recent discovery of the Higgs boson therefore provides a new possibility to search for new sources of CP-violating interactions and is one of the topics of this thesis.

2.2. The Higgs Boson

The Higgs boson of the SM is electrically neutral with a spin of zero and even eigenvalue under CP transformation $J^{CP} = 0^{+}$. As discussed in Section 2.1.3, its interactions with fermions and bosons provide a coupling strength, that is predicted to be proportional to their masses and hence determines the occurance of the various Higgs-boson production and decay processes.

The experimental search for the Higgs boson was one of the main motivations for the construction of the LHC at CERN. However, as shown in Figure 2.2, the total cross section for Higgs-boson production in proton-proton (pp) collisions is found to be many orders of magnitude smaller compared to a multitude of other SM processes and therefore requires advanced detector performance and sophisticated analysis strategies.

The following section gives an overview of the Higgs-boson production modes at the LHC and describes the most important decay channels. In addition, the experimental discovery and the current knowledge of the properties of the Higgs boson are summarized. The last section provides a theoretical description of CP-violating interactions of the Higgs boson in the framework of an effective field theory.

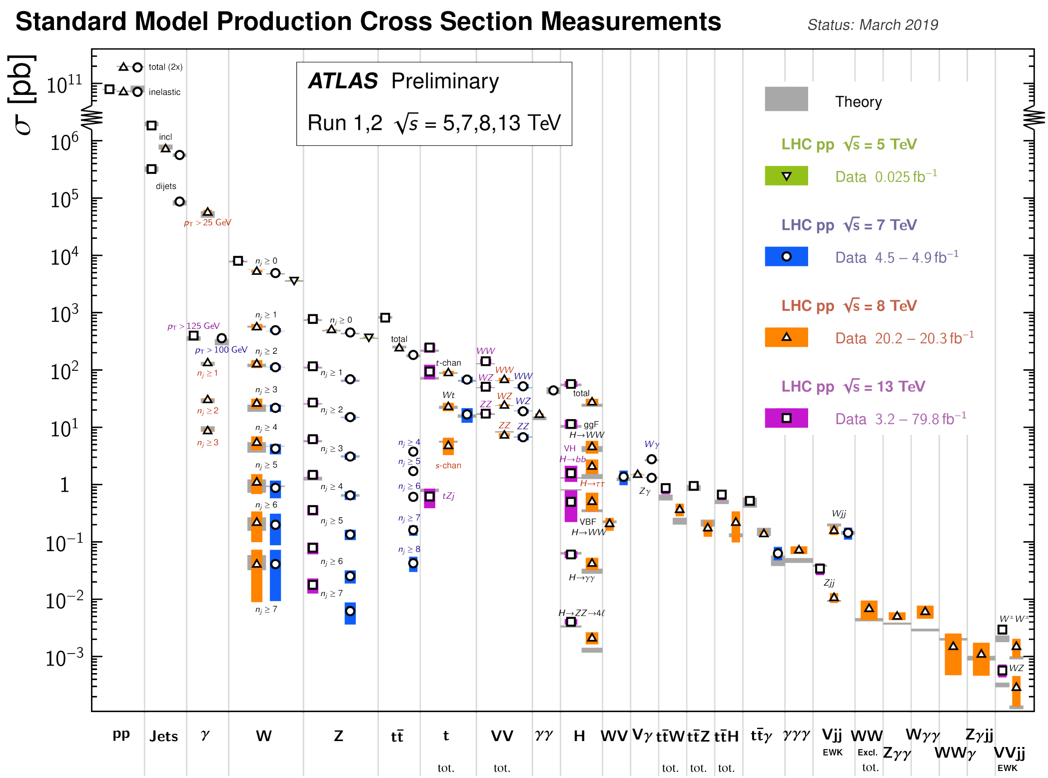

Figure 2.2.: Summary of cross-section measurements by the ATLAS experiment for different center-of-mass energies in pp collisions at the LHC compared to the theoretical predictions [69].

2.2.1. Higgs-Boson Production and Decay Modes

The Higgs-boson production in pp collisions occurs through the interaction of initial-state quarks and gluons and can be classified depending on its couplings to fermions or vector bosons. Exemplary Feynman diagrams for the four most important production mechanisms at the LHC are shown in Figure 2.3: the gluon fusion (ggF) production, the vector-boson fusion (VBF) production, the associated production with a vector boson (VH) and the associated production with a top-quark pair (ttH). A detailed description of the phenomenology of the various production modes can be found in Section 4.1. Figure 2.4 (a) shows the production cross-sections as a function of the Higgs-boson mass for $\sqrt{s} = 13\,\text{TeV}$. These cross-sections are calculated according to the procedure described in Section 4.3 and are subject to various theoretical uncertainties.

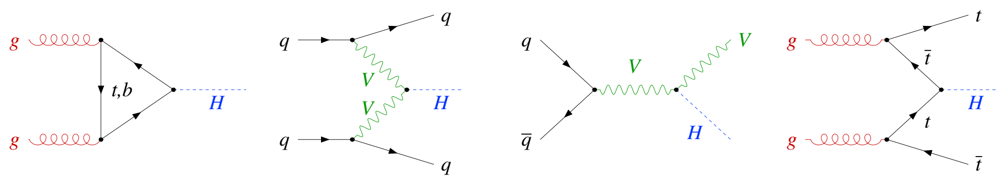

(a) (b) (c) (d)

Figure 2.3.: Feynman diagrams of the most important Higgs-boson production modes at the LHC. The largest cross section is provided by the gluon-fusion production (a), followed by the vector-boson fusion production (b), the associated production with vector bosons (c) and the associated production with top-quark pairs (d).

The favoured Higgs-boson production occurs via the ggF mode due to the abundant production of low-momentum gluons and constitutes about 87 % of the total production cross-section for a mass of about 125 GeV. Here, the Higgs-boson coupling to the massless gluons takes place via a heavy-fermion loop, which is dominated by top-quark contributions. The ggF cross-section is calculated at N3LO[4] with included electroweak (EW) corrections at NLO accuracy as $\sigma_{\text{ggF}} = 48.5^{+4.6\,\%}_{-6.7\,\%}\,\text{pb}$ [70–72].

The second most abundant Higgs-boson production process corresponds to the VBF channel. Here, the cross section is already about one order of magnitude smaller compared to the ggF production with $\sigma_{\text{VBF}} = 3.78^{+2.1\,\%}_{-2.1\,\%}\,\text{pb}$ [73–75], which corresponds to about 7 % of the total Higgs-boson production. The cross section is calculated at approximate NNLO accuracy in QCD with NLO EW corrections. In the VBF channel, the Higgs boson is produced through the fusion of $W^\pm$-bosons or Z^0-bosons, which are radiated off from the incoming quarks.

Next, the associated production with massive vector bosons VH occurs with an even smaller cross section and constitutes only 5 % of the total Higgs-boson production. In this channel, the annihilation of incoming quarks results in the production of a $W^\pm$-

[4] Corresponds to next-to-next-to-next-to leading order accuracy in the strong coupling strength referring to the orders of included perturbative expansions in the cross-section calculation.

boson or Z^0-boson, which then radiates off the Higgs boson. For WH and ZH production, the cross sections are calculated at NNLO in QCD with NLO EW corrections to be $\sigma_{\mathrm{WH}} = 1.37^{+1.9\,\%}_{-2.0\,\%}$ pb and $\sigma_{\mathrm{ZH}} = 0.88^{+4.1\,\%}_{-3.5\,\%}$ pb [76–78], respectively.

Last, the Higgs boson can also be produced in association with two top-quarks, which is however highly suppressed due the limited available phase space from the large top-quark mass and only contributes with less than 1 % to the total Higgs-boson production. The cross section of $\sigma_{\mathrm{ttH}} = 0.51^{+6.8\,\%}_{-9.9\,\%}$ pb is calculated at NLO accuracy in QCD and contains NLO EW corrections [79–84].

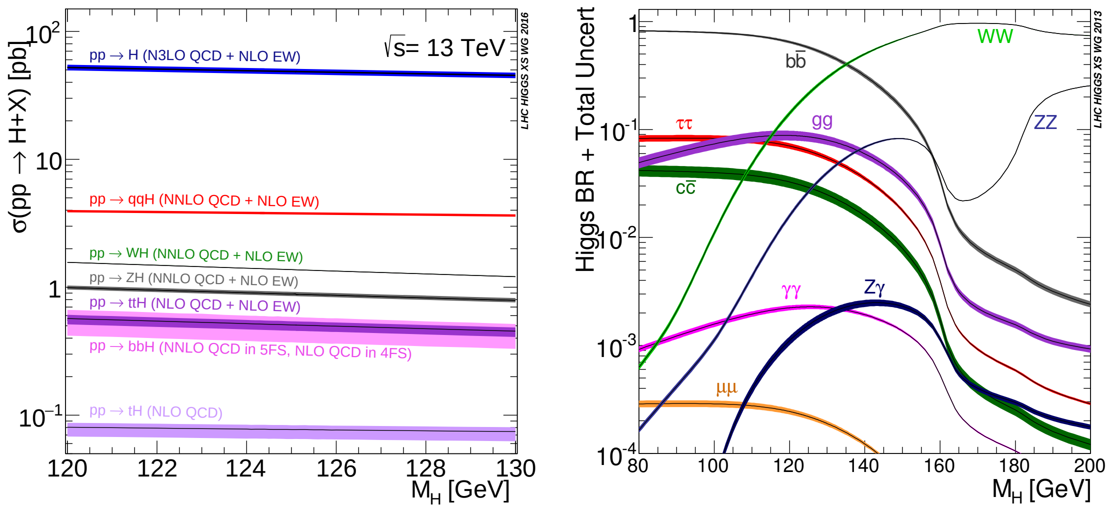

(a) (b)

Figure 2.4.: The Higgs-boson production cross-sections at $\sqrt{s} = 13$ TeV (a) and its branching ratios (b) with uncertainties as a function of the Higgs-boson mass [85].

The Higgs boson decays into massive fermions and bosons as well as into massless photons and gluons. Similar to the ggF production, the decay into massless bosons occurs via heavy-particle loops. Here, the main contribution in the $H \to gg$ channel arises from top-quark and bottom-quark loops, while the $H \to \gamma\gamma$ decay is dominated by top-quark and $W^{\pm}$-boson contributions. Further possible bosonic final states are $H \to WW^*$, $H \to ZZ^*$ and $H \to Z\gamma^*$, where the production of virtual vector bosons V^* is allowed due to their intrinsic width. Fermionic final states are given by $H \to bb$, $H \to cc$, $H \to \tau\tau$ and $H \to \mu\mu$ decays. Figure 2.4 (b) shows the Higgs-boson decay branching ratios [5] as a function of its mass. In the low mass range, the Higgs boson decays predominantly into fermions, while larger masses favour bosonic final states. For a mass of about 125 GeV, the decay $H \to bb$ has the largest branching ratio of $0.58 \pm 0.65\,\%$, followed by $H \to WW^*$ decays with a branching ratio of $0.22 \pm 0.99\,\%$. The decay into gluons $H \to gg$ occurs with a branching ratio of $0.081^{+3.40\,\%}_{-3.41\,\%}$. In addition, the Higgs boson decays into τ-leptons with

[5] The branching ratio for a decay $H \to X$ is defined as the ratio of the corresponding partial width to the total width $\Gamma_{H\to X}/\Gamma_H$.

a branching ratio of $0.063^{+1.17\,\%}_{-1.16\,\%}$ and into c-quarks $H \to cc$ with a branching ratio of $0.029 \pm 1.20\,\%$. Further bosonic final states from $H \to ZZ^*$ decays occur with a branching ratio of $0.026 \pm 0.99\,\%$, while for $H \to \gamma\gamma$ decays the branching ratio is already one order of magnitude smaller with only $0.0023^{+1.73\,\%}_{-1.72\,\%}$. The decays $H \to Z\gamma^*$ and $H \to \mu\mu$ with branching ratios of $0.0015 \pm 5.71\,\%$ and $0.00022 \pm 1.23\,\%$, respectively, are highly suppressed and still not observed.

On the experimental side, the sensitivity and resolution of the Higgs-boson mass vary between the individual decay channels and depend on the subsequent decays of the $W^{\pm}$-boson, the Z^0-boson and the τ-lepton. In particular, since the energy and momentum of *light* leptons $\ell = e, \mu$ and photons can be measured very precisely in the detector, the best mass resolution of about 1-2 % is obtained in the bosonic final states with $H \to ZZ^* \to 4\ell$ and $H \to \gamma\gamma$ decays. Leptonic decays of the $W^{\pm}$-bosons $H \to WW^* \to 2\ell 2\nu$ result in final-state neutrinos with transverse momenta, that cannot be measured in the detector but result in missing transverse energy in the event (see Section 5.5). This decay channel therefore does not allow for a direct reconstruction of the Higgs-boson mass. The dominant $H \to bb$ decay and the decay into gluons $H \to gg$ provide only partons in the final state and therefore have to cope with large background contributions from the abundant QCD production of jets. In particular, the Higgs-boson mass resolution in the $H \to bb$ channel of about 10 % is limited by the achieved measurement precision of the jet energy. In the $H \to \tau\tau$ decay channel, which is the focus of this thesis, subsequent leptonic and hadronic decays of the τ-leptons lead to final-state neutrinos with transverse momenta, that are not measurable in the detector. Hence, the reconstruction of the Higgs-boson mass in this decay channel requires the application of several approximations, which are discussed in detail in Section 6.1.1.

2.2.2. Experimental Knowledge of the Higgs Boson

Pre-LHC Limits on the Higgs-Boson Mass

Although the mass of the Higgs boson is a free parameter in the SM and can not be calculated from first principles, theoretical arguments and experimental constraints have limited the allowed mass range already before the experimental discovery.

On the theoretical side, an upper bound is derived from perturbation theory, where divergencies in the cross section for the scattering of longitudinally polarized $W^{\pm}$-bosons require a Higgs-boson mass of $m_H < 1\,\mathrm{TeV}$ [86]. Further constraints depend on the energy scale Λ up to which no new physics phenomena are expected. These limits are a consequence of the energy dependency of the quartic Higgs-boson self-coupling due to quantum fluctuations [87]. In particular, upper bounds are obtained by requiring a finite quartic Higgs-boson self-coupling in order to ensure the perturbativity of the theory, while lower bounds are necessary in order to avoid negative quartic self-couplings, which would imply the instability of the electroweak vacuum. With this, the Higgs-boson mass is limited to a range of $120 \leq m_H \leq 170\,\mathrm{GeV}$, if the SM is assumed to be valid up to the Planck scale $\Lambda \approx 10^{19}\,\mathrm{GeV}$, while $\Lambda < 1\,\mathrm{TeV}$ results in looser constraints of $50 \leq m_H \leq 800\,\mathrm{GeV}$ [88–91].

Prior to the LHC area, direct searches for the Higgs boson at the Large Electron Positron Collider (LEP) and the Tevatron allowed to derive limits on its mass as well. Measurements by the ALEPH, DELPHI, L3 and OPAL exeriments at center-of-mass energies between 189 GeV and 209 GeV result in a lower mass bound of $m_H > 114.4$ GeV at the 95 % confidence level (CL) [92], while the CDF and DØ experiments constrain the mass to $147 < m_H < 180$ GeV at the 95 % CL based on data taken at $\sqrt{s} = 1.96$ TeV [93, 94]. The combined exclusion limits from these measurements are shown in Figure 2.5.

Complementary to the direct limits, indirect constraints are obtained from electroweak precision measurements at LEP and Tevatron. In particular, the theoretical predictions of various electroweak observables contain higher-order corrections, which depend on the mass of the Higgs-boson. The combination of measurements of the $W^{\pm}$-boson mass and decay width as well as the top-quark mass results in a a best-fit value of $m_H = 94^{+29}_{-24}$ GeV, while masses of $m_H > 155$ GeV are excluded at the 95 % CL [95].

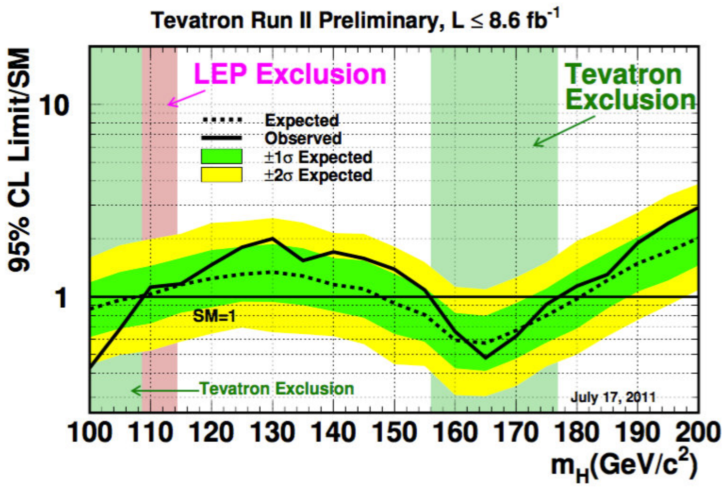

Figure 2.5.: Expected and observed limits on the Higgs-boson mass at the 95 % CL from searches by the CDF and DØ experiments at the Tevatron. The combined LEP exclusion range is shown as well [93].

Discovery of the Higgs Boson and Measurement of its Mass

In 2012, the ATLAS and CMS experiments at the LHC announced the observation of a new particle with a mass of about 125 GeV and consistent with the SM Higgs boson based on data taken at $\sqrt{s} = 7$ TeV and $\sqrt{s} = 8$ TeV [9, 10]. As shown in Figure 2.6, the discovery was achieved with significances of $5.9\,\sigma$ and $5.0\,\sigma$ with respect to the background-only hypothesis for the ATLAS experiment and the CMS experiment, respectively. Hence, both experiments independently exceeded the required threshold of $5\,\sigma$ in order to claim an observation. The discovery was based on the bosonic final states $H \to ZZ^* \to 4\ell$, $H \to \gamma\gamma$ and $H \to WW^* \to 2\ell 2\nu$, which profit from the precise energy and momentum reconstruction of leptons and photons in the detector.

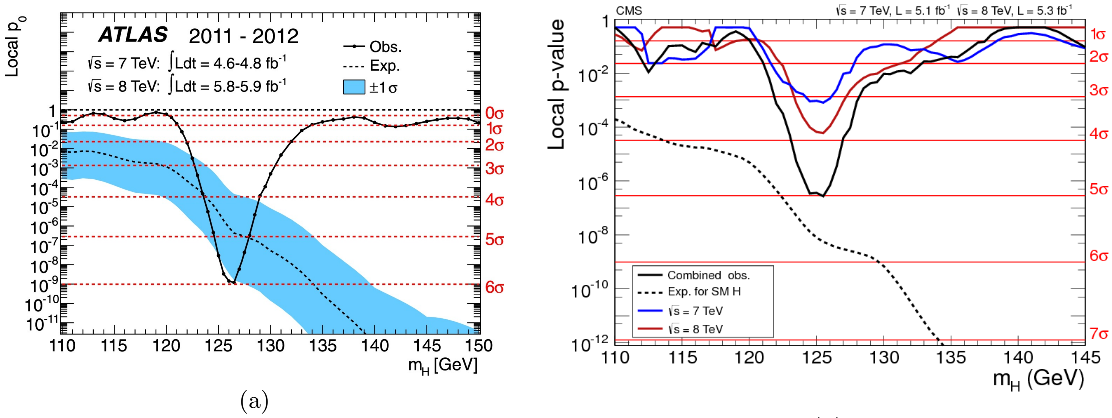

(a) (b)

Figure 2.6.: The observed (solid) and expected (dashed) local p-value as a function of m_H in the low mass range for the ATLAS [9] (a) and CMS [10] (b) experiments.

The subsequent measurement of the Higgs-boson mass in the $H \to ZZ^* \to 4\ell$ and $H \to \gamma\gamma$ channels with the full Run 1 dataset of 25 fb^{-1} yields the combined ATLAS and CMS result of $m_H = 125.09 \pm 0.21\,(\text{stat.}) + 0.11\,(\text{sys.})$ GeV [96]. This result is consistent with the theoretical and experimental limits discussed in the previous section. The measurements of the Higgs-boson mass based on the Run 2 dataset of 36.1 fb^{-1} by the ATLAS experiment are shown in Figure 2.7 and are found to be consistent with the results obtained in Run 1. In the $H \to ZZ^* \to 4\ell$ channel, the precision of the result is limited by the available dataset size, while the measurement in the $H \to \gamma\gamma$ channel is dominated by systematic uncertainties. The combination of these results with the Run 1 measurement by the ATLAS experiment yields a Higgs-boson mass of $m_H = 124.97 \pm 0.16\,(\text{stat.}) \pm 0.18\,(\text{sys.})$ GeV [97].

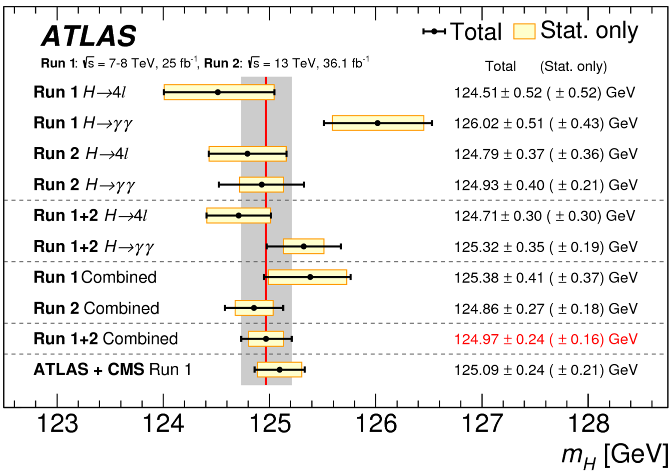

Figure 2.7.: Summary of measurements of the Higgs-boson mass in the $H \to ZZ^* \to 4\ell$ and $H \to \gamma\gamma$ decay channels based on the Run 1 and Run 2 datasets by the ATLAS and CMS experiments.

Higgs-Boson Couplings

Once the Higgs-boson mass is known, its coupling strength to other particles can be calculated according to the predictions of the SM (see Section 2.2). As shown in Figure 2.8, the measurements of the cross section times branching ratio in the dominant Higgs-boson production and decay modes based on data taken in Run 2 by the ATLAS experiment are in good agreement with the SM prediction. The inclusive cross-sections in the ggF, VBF, VH and ttH production modes, which are obtained by fixing the decay branching-fractions to their SM values, show no deviation from the SM as well. While the dominant ggF and VBF production modes were already established with the Run 1 measurements, the analysis of Run 2 data recently allowed to also confirm the Higgs-boson production in the VH [13,14] and ttH channels [11,12]. In particular, the ttH production mode provides the only possibility to directly measure the coupling of the Higgs boson to top-quarks. The structure of the Yukawa coupling can also be investigated on the decay side. In Run 1, the ATLAS experiment achieved evidence for the Higgs-boson coupling to third generation leptons in the $H \to \tau\tau$ decay channel, where the measured signal strength of $\mu = \sigma_{meas}/\sigma_{SM} = 1.43 \pm 0.3\,(\text{stat.})^{+0.3}_{-0.2}\,(\text{sys.}) \pm 0.1\,(\text{theo.})$ is in agreement with the SM prediction of one [17]. The combination with the Run 1 measurement by the CMS experiment lead to the observation of $H \to \tau\tau$ decays with a significance of $5.5\,\sigma$ [18]. Recently, the $H \to bb$ decay channel was also established in the combination of the Run 1 and Run 2 analyses [13,14]. The measurement of the Higgs-boson production cross-section with $H \to \tau\tau$ decays based on data taken in Run 2 by the ATLAS experiment is one of the topic of this thesis and presented in Chapter 6.

Higgs-Boson Spin and Parity

The SM predicts a scalar Higgs boson with even behaviour under CP transformation: $J^{CP} = 0^+$. From the theoretical side, the decay of a spin-1 particle into two massless vector bosons is forbidden according to the Landau-Yang theorem [98,99], which allows to already exclude the spin-1 hypothesis with the observation of $H \to \gamma\gamma$ decays. This is in agreement with experimental measurements, which found strong evidence for the spin-0 nature of the Higgs boson [27]. Moreover, several combinations of spin and CP hypotheses are investigated by both the ATLAS and CMS experiments by mainly exploiting the bosonic decay channels. As shown in Figure 2.9, tests of alternative spin-CP combinations performed by the ATLAS experiment strongly favour the SM hypothesis, where a pure CP-odd Higgs boson $J^{CP} = 0^-$ is excluded at a CL of more than 99.9 % [28]. However, it is still possible that small CP-odd contributions in addition to the CP-even nature of the Higgs boson exist, which would lead to an additional source of CP violation beyond the SM prediction. Figure 2.10 shows the results of searches for such CP-violating contributions in the Higgs-boson coupling to weak vector-bosons HVV based on the Run 1 dataset by the ATLAS experiment, where no deviation from the SM prediction of a pure CP-even Higgs boson is observed. Additional measurements in the bosonic decay channels are summarized in Section 7.5.2 and show no sign of CP violation as well. The analysis presented in this thesis further improves the existing constraints on CP-violating HVV interactions based on the Run 2 dataset of $36.1\,\text{fb}^{-1}$ and is described in Chapter 7.

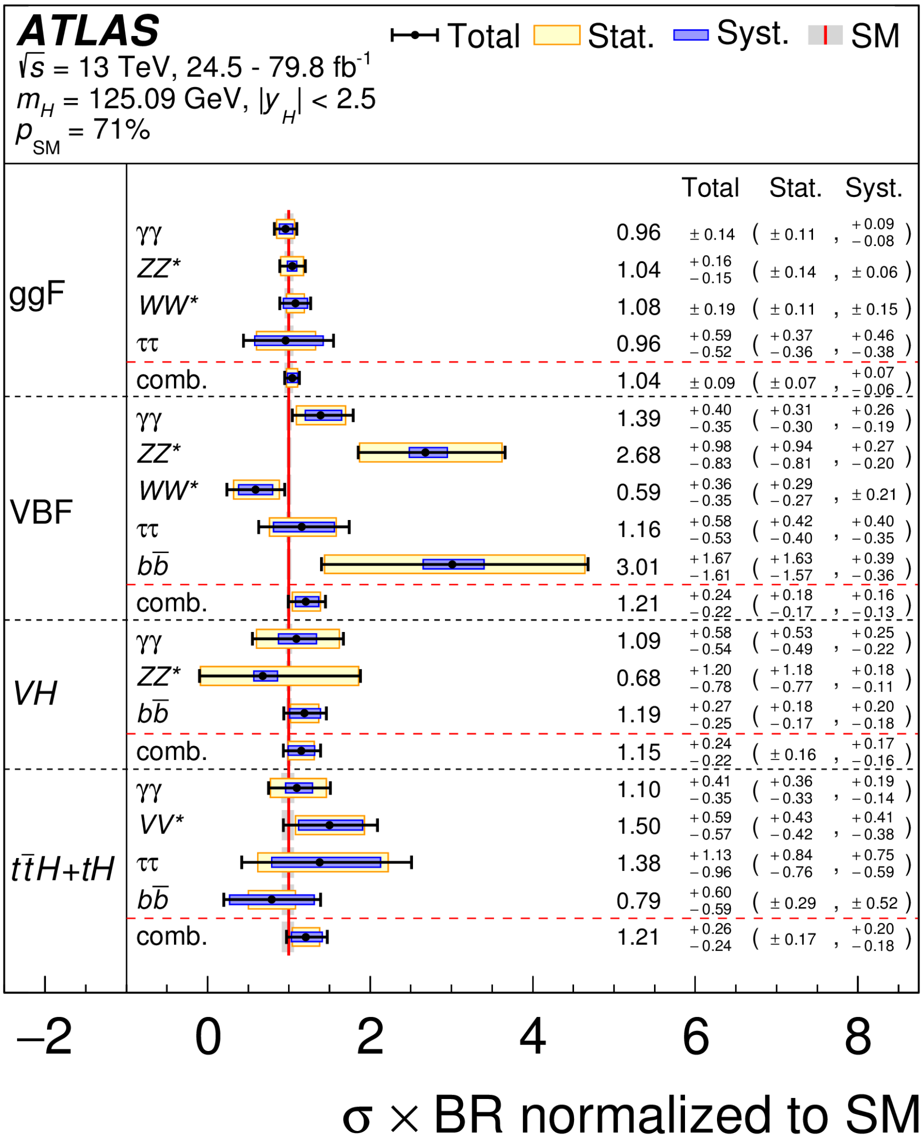

Figure 2.8.: Cross sections times branching fractions for the ggF, VBF, VH and ttH+tH Higgs-boson production channels in several decay modes normalized to their SM predictions. The values are obtained from a simultaneous fit to all channels, where the cross sections of the ggF $H \to bb$, VH $H \to WW^*$ and VH $H \to \tau\tau$ processes are fixed to their SM predictions. Combined results for each production mode are also shown, assuming SM values for the branching fractions into each decay mode. The black error bars, blue boxes and yellow boxes show the total, systematic, and statistical uncertainties in the measurements, respectively. The gray bands show the theory uncertainties in the predictions [100].

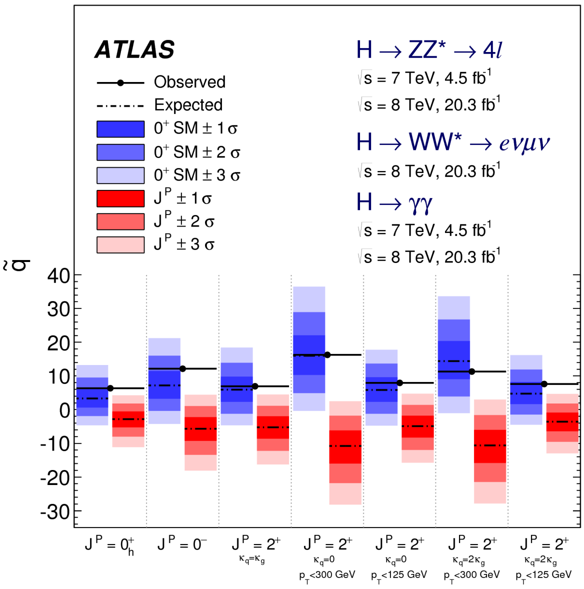

Figure 2.9.: Distributions of the test statistics for probing alternative spin and CP hypotheses against the SM prediction in the bosonic decay channels based on the ATLAS Run 1 dataset. The distribution for the SM hypothesis is shown in blue, while red corresponds to the alternative hypotheses [28].

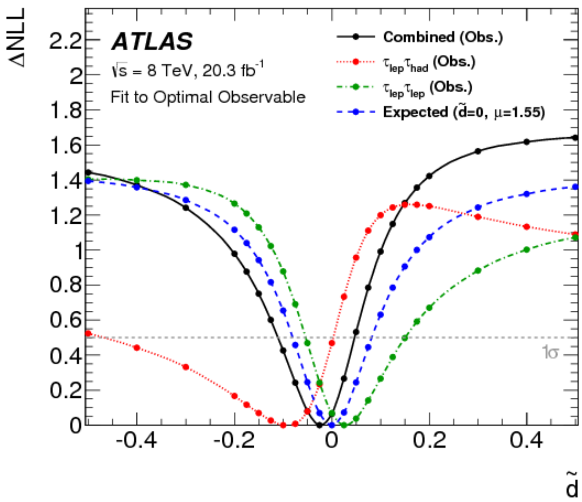

Figure 2.10.: Observed and expected ΔNLL-curve as a function of the parameter $\tilde{d}$, which describes additional CP-odd contributions to the SM CP-even ($\tilde{d} = 0$) coupling structure of the Higgs boson to weak gauge-bosons in the VBF production channel with subsequent $H \to \tau\tau$ decays. The obtained results are shown for the $\tau_{lep}\tau_{lep}$ (green) and $\tau_{lep}\tau_{had}$ (red) final states as well as for their combination (black). The expected sensitivty from the $\tau_{lep}\tau_{lep}$ and $\tau_{lep}\tau_{had}$ combination is given by the blue dashed line [30].

2.3. CP Violation in Higgs-Boson Interactions

As explained in Section 2.1.4, the amount of CP violation in the SM is not sufficient to explain the observed baryon asymmetry in our universe [22–26]. With the discovery of the Higgs boson the question is raised, whether new sources of CP violation may appear from its interaction with other particles. In particular, these CP-violating interactions can occur via additional CP-odd contributions to the CP-even coupling structure of the Higgs boson to fermions or bosons as predicted in the SM. The analysis presented in this thesis focuses on investigating the coupling of the Higgs boson to electroweak gauge bosons HVV in the VBF production channel in the framework of an effective field theory (EFT). The interactions of the Higgs boson with other particles are assumed to agree with the SM prediction. The effective $SU(2)_{I_w} \times U(1)_Y$ invariant Lagrangian density for CP-violating HVV interactions can be constructed in a model-independent way by augmenting the CP-conserving SM Lagrangian with higher dimensional CP-odd operators [101, 102]:

$$\mathcal{L}_{eff} = \mathcal{L}_{SM} + \sum_i \frac{f_i^{(5)}}{\Lambda}\mathcal{O}_i^{(5)} + \sum_i \frac{f_i^{(6)}}{\Lambda^2}\mathcal{O}_i^{(6)} + \mathrm{O}\left(\frac{1}{\Lambda^3}\right). \tag{2.50}$$

Here, Λ corresponds to the scale of new physics and the dimensionless coefficients f_i are called Wilson coefficients. While the only CP-odd dimension-five operator is related to the violation of lepton number and can be neglected for analyses at the electroweak scale, five CP-odd operators arise from the dimension-six contributions [103]. Out of these, three operators are linearly independent and the effective Lagrangian density can then be written as

$$\mathcal{L}_{eff} = \mathcal{L}_{SM} + \frac{f_{B\widetilde{B}}}{\Lambda^2}\mathcal{O}_{B\widetilde{B}} + \frac{f_{W\widetilde{W}}}{\Lambda^2}\mathcal{O}_{W\widetilde{W}} + \frac{f_{\widetilde{B}}}{\Lambda^2}\mathcal{O}_{\widetilde{B}} \tag{2.51}$$

with the following operators:

$$\begin{aligned} \mathcal{O}_{B\widetilde{B}} &= \Phi^\dagger \hat{\widetilde{B}}_{\mu\nu}\hat{B}^{\mu\nu}\Phi \\ \mathcal{O}_{W\widetilde{W}} &= \Phi^\dagger \hat{\widetilde{W}}_{\mu\nu}\hat{W}^{\mu\nu}\Phi \\ \mathcal{O}_{\widetilde{B}} &= (D_\mu\Phi)^\dagger \hat{\widetilde{B}}^{\mu\nu} D_\nu\Phi. \end{aligned} \tag{2.52}$$

Here, the covariant derivative defined in Equation 2.18 is used. The field-strength tensors are given by $\hat{V}_{\mu\nu}$ $(V = B, W^a)$ and the dual field-strength tesnors correspond to $\widetilde{V}_{\mu\nu} = \frac{1}{2}\epsilon_{\mu\nu\rho\sigma}V^{\rho\sigma}$ with $\hat{B}_{\mu\nu} + \hat{W}_{\mu\nu} = i\frac{g'}{2}B_{\mu\nu} + i\frac{g}{2}\sigma^a W^a_{\mu\nu}$. Since previous measurements by the ALEPH and OPAL experiments allow to highly constrain CP-violating charged triple-gauge couplings with $\tilde{\kappa}_\gamma = \cot^2(\theta_W)$ and $\tilde{\kappa}_Z = -\frac{m_W^2}{2\Lambda^2}f_{\widetilde{B}}$ [104–106], the operator $\mathcal{O}_{\widetilde{B}}$ is neglected and only $\mathcal{O}_{B\widetilde{B}}$ and $\mathcal{O}_{W\widetilde{W}}$ are considered in this analysis. The EFT approach is based on the assumption that no new particles with masses below the scale of new physics exist and the Lagrangian density in Equation 2.51 therefore only contains real Wilson coefficients f_i. However, if new particles are present in loop-induced contributions to the HVV vertex, also referred to as *rescattering* in the following, these coefficients can contain imaginary parts as well. Since no new particles are observed until today, the impact from these rescattering effects is assumed to be small and the Wilson coefficients are therefore considered to be real.

After electroweak symmetry breaking the Lagrangian density can be written in terms of the mass eigenstates of the Higgs boson, the $W^{\pm}$-boson, the Z^0-boson and the photon A [107]:

$$\begin{aligned}\mathcal{L}_{eff} = \mathcal{L}_{SM} &+ \tilde{g}_{HAA} H \widetilde{A}_{\mu\nu} A^{\mu\nu} + \tilde{g}_{HAZ} H \widetilde{A}_{\mu\nu} Z^{\mu\nu} \\ &+ g_{HZZ} H \widetilde{Z}_{\mu\nu} Z^{\mu\nu} + \tilde{g}_{HWW} H \widetilde{W}^{+}_{\mu\nu} W^{-,\mu\nu}.\end{aligned} \tag{2.53}$$

While the VBF Higgs-boson production in the SM only includes HWW or HZZ interactions, additional $HZ\gamma$ and $H\gamma\gamma$ interactions can appear with the CP-odd contributions. By requiring $SU(2)_{I_w} \times U(1)_Y$ invariance, the coupling strengths multiplying the corresponding CP-odd operators can be written as

$$\begin{aligned}\tilde{g}_{HAA} &= \frac{g}{2m_W}(\tilde{d}\sin^2(\theta_W) + \tilde{d}_B\cos^2(\theta_W)) \\ \tilde{g}_{HAZ} &= \frac{g}{2m_W}\sin(2\theta_W)(\tilde{d} - \tilde{d}_B) \\ \tilde{g}_{HZZ} &= \frac{g}{2m_W}(\tilde{d}\cos^2(\theta_W) + \tilde{d}_B\sin^2(\theta_W)) \\ \tilde{g}_{HWW} &= \frac{g}{m_W}\tilde{d}.\end{aligned} \tag{2.54}$$

Here, the dimensionless parameters $\tilde{d}$ and $\tilde{d}_B$ describe the amount of CP-odd contribution to the SM HVV coupling and are related to the Wilson coefficients in Equation 2.51 in the following way:

$$\begin{aligned}\tilde{d} &= -\frac{m_W^2}{\Lambda^2} f_{W\widetilde{W}} \\ \tilde{d}_B &= -\frac{m_W^2}{\Lambda^2}\tan^2(\theta_W) f_{B\widetilde{B}}\ .\end{aligned} \tag{2.55}$$

Since the different HVV coupling contributions in Equation 2.53 can not be distinguished experimentally in the VBF production mode, the analysis presented in this thesis uses the arbitrary choice $\tilde{d} = \tilde{d}_B$. This leads to the following CP-odd coupling strengths

$$\begin{aligned}&\tilde{g}_{HAA} = \tilde{g}_{HZZ} = \frac{1}{2}\tilde{g}_{HWW} = \frac{g}{2m_W}\tilde{d} \\ &\tilde{g}_{HAZ} = 0\end{aligned} \tag{2.56}$$

and hence allows to describe the CP-violating HVV interactions in terms of one parameter, $\tilde{d}$. Deriving the tensor structure for CP-violating interactions of the Higgs boson to two vector bosons with momenta p_1 and p_2 from the effective Lagrangian density yields

$$T^{\mu\nu}(p_1, p_2) = \sum_{V=W,Z} \frac{2m_V^2}{v} g^{\mu\nu} + \sum_{V=W,Z,\gamma} \tilde{d}\frac{2g}{m_W}\epsilon^{\mu\nu\rho\sigma} p_{1\rho} p_{2\sigma}. \tag{2.57}$$

Here, the first term describes the SM HVV coupling and the second term contains the CP-odd contributions from dimension-six operators. Analogously, the matrix element for

CP-violating HVV interactions can be written in terms of the SM matrix element and an additional CP-odd contribution multiplied by $\tilde{d}$:

$$\mathcal{M} = \mathcal{M}_{\text{SM}} + \tilde{d} \cdot \mathcal{M}_{\text{CP-odd}}. \tag{2.58}$$

Hence, the squared matrix element and the differential cross section have three contributions:

$$\begin{aligned} |\mathcal{M}|^2 &= |\mathcal{M}_{\text{SM}}|^2 + 2\tilde{d} \cdot \text{Re}(\mathcal{M}^*_{\text{SM}} \mathcal{M}_{\text{CP-odd}}) + \tilde{d}^2 \cdot |\mathcal{M}_{\text{CP-odd}}|^2 \\ d\sigma &= d\sigma_{\text{SM}} + \tilde{d} \cdot d\sigma_{\text{CP-odd}} + \tilde{d}^2 \cdot d\sigma_{\text{CP-even}} \end{aligned} \tag{2.59}$$

While the first and third terms are CP even and hence do not violate CP invariance, the second interference term is odd under CP transformation and provides a possible new source of CP violation. Since this interference term vanishes by the integration over a CP-symmetric phase-space when only CP-symmetric selection criteria are applied, it does not contribute to the total cross section. On the other hand, the third CP-even term leads to a quadratic dependency of the total cross section on $\tilde{d}$ and therefore provides additional information on coupling scenarios beyond the SM. However, as such increased event yields can also originate from higher-dimension CP-even operators, which do not lead to a violation of CP invariance, the analysis presented in this thesis does not rely on the event yield dependency on $\tilde{d}$ but only exploits differences in the shape of CP-odd observables in order to test CP invariance.

Recent measurements by the ATLAS and CMS experiments investigate various Higgs-boson production and decay modes to set limits on Wilson coefficients in the framework of an EFT. While most of these measurements are based on the Higgs-boson decay into vector bosons $H \to VV$, the VBF Higgs-boson production mode provides a higher sensitivity to CP-violating effects. This can be seen in Equation 2.57, where the amount of CP-odd contributions scales with the momenta of the vector bosons $p_{1,2}$. In $H \to VV$ decays, these momenta are restricted to the Higgs-boson mass with $m_H^2 = (p_1 + p_2)^2$ due to the exclusive selection of on-shell Higgs bosons and hence limit the sensitivity to CP-violating contributions. The VBF Higgs-boson production mode is not affected by such restrictions of the vector-boson momenta.

The analyses of the $H \to \gamma\gamma$ [108] and $H \to ZZ$ [109] final states as well as a combined measurement in the VH and VBF Higgs-boson production modes with subsequent $H \to VV$ decays [110] exploit various CP-even observables and event yield information in different phase-space regions to look for deviations from the SM. While these measurements are consistent with the SM prediction so far, they do not directly probe CP invariance in the Higgs-boson interactions, but can also include effects from higher-dimension CP-even contributions. An overview of current experimental results for CP-violating HVV interactions and a comparison to the results obtained in this thesis can be found in Section 7.5.2.

2.4. Testing CP Invariance in HVV Interactions

2.4.1. Model-Independent Test of CP Invariance

The construction of observables, which are sensitive to the CP nature of the Higgs boson, relies on a careful investigation of their transformation properties under C, P and T operation, which are introduced in Section 2.1.4. In particular, it is also important to identify possible assumptions, which are connected to these observables, in order to directly search for CP violation. The following section gives an overview of testing CP invariance in a model-independent way and discusses the application of this approach in the VBF Higgs-boson production mode based on Ref. [111].

In general, an observable, which is called odd under a certain transformation U=C,P,T or their combination corresponds to an eigenstate of the operation with an eigenvalue of -1. Moreover, if the expectation value of such a U-odd observable A in a U-symmetric theory with $\mathcal{L} = \mathrm{U}\mathcal{L}\mathrm{U}^{-1}$ vanishes,

$$\langle A \rangle_{\mathcal{L}=\mathrm{U}\mathcal{L}\mathrm{U}^{-1}} = 0, \tag{2.60}$$

the observable is also called *genuine* U-odd. A more general requirement can be derived for processes with U-symmetric initial states, where any U-odd observable is also found to be genuinely U-odd. Hence, the expectation value of a genuine CP-odd observable can be used to test for CP invariance in a model-independent way, since no assumption about the underlying structure of the interaction is required. In particular, a CP-symmetric theory leads to an expectation value of a genuine CP-odd observable of zero, while non-vanishing values imply the violation of CP invariance.

As it is not always possible to construct genuine CP-odd observables, the transformation property under the naive time reversal $\hat{\mathrm{T}}$ [57–59] comes in handy. This operation acts on a single-particle state ϕ with momentum p and spin s in the following way:

$$\hat{\mathrm{T}}|\phi(p,s)\rangle = |\phi(-p,-s)\rangle. \tag{2.61}$$

In particular, compared to the time reversal defined in Equation 2.45, this operation explicitly omits the exchange of initial and final states. Hence, for processes, where information about the particle spin is not relevant or not directly accessible, the transformation properties under $\hat{\mathrm{T}}$ correspond to the properties under parity transformation

$$\mathrm{P}|\phi(p,s)\rangle = \eta_\phi|\phi(-p,s)\rangle \tag{2.62}$$

with the intrinsic phase η_ϕ. Since it is not possible to construct genuine CP-odd observables for processes, where the initial state is not a CP eigenstate, the expectation value of a genuine $\hat{\mathrm{T}}$-odd observable can be used instead to test CP invariance [112]. However, in this case, non-vanishing expectation values can only be identified with CP violation under the following assumptions [111]:

- CPT invariance
- $\hat{\mathrm{T}}$-symmetric phase-space
- initial state is a $\hat{\mathrm{T}}$ eigenstate
- no rescattering

For initial states, which are symmetric under CP and $\hat{\mathrm{T}}$ transformation, one can construct CP-odd observables, which are either $\hat{\mathrm{T}}$-odd or $\hat{\mathrm{T}}$-even. Since in this case, a CP-odd and $\hat{\mathrm{T}}$-odd observable is also genuinely CP-odd and $\hat{\mathrm{T}}$-odd, a non-vanishing expectation value directly implies CP violation without any assumption on the occurance of rescattering. On the other hand, CP-odd and $\hat{\mathrm{T}}$-even observables, which are genuinely CP-odd but not genuinely $\hat{\mathrm{T}}$-odd, only yield non-vanishing expectation values in the presence of a CP-violating theory and rescattering.

The Higgs-boson production in the VBF channel contains qq'-pairs in the initial state, which is not a C eigenstate and hence not CP symmetric. Testing CP invariance based on a genuine CP-odd observable is therefore not possible in this production mode. However, since the VBF initial-state probability distribution is $\hat{\mathrm{T}}$-symmetric in pp collisions, genuine $\hat{\mathrm{T}}$-odd observables can be exploited instead. The observation of finite expectation values for these genuine $\hat{\mathrm{T}}$-odd observables then either corresponds to the presence of rescattering effects in the HVV vertex or indicates the violation of CP invariance in the absence of rescattering. Both possibilities would be a direct sign for physics beyond the SM. Throughout this thesis, genuine $\hat{\mathrm{T}}$-odd observables are referred to as CP-odd observables and the next section introduces the Optimal Observable, which is exploited to search for CP violation in the VBF Higgs-boson production mode.

2.4.2. The Optimal Observable

The Optimal Observable method [113–115] was first exploited in measurements of the τ-polarisation and the weak dipole-moment of the τ-lepton in $Z \to \tau\tau$ events [116, 117] as well as in sensitivity studies for CP violation in the Higgsstrahlung at a future e^+e^- collider [118]. The analysis presented in this thesis uses the Optimal Observable to search for CP-odd contributions to the SM-like HVV coupling structure in the VBF Higgs-boson production mode. As discussed in the previous section, the expectation value of the Optimal Observables provides a model-independet way to test CP invariance in the VBF mode under the assumption that rescattering effects can be neglected. The analysis also measures the parameter $\tilde{d}$ based on maximum likelihood fits in the Optimal Observable distribution for different HVV coupling scenarios.

The VBF production mode is described by seven independent variables, when assuming a Higgs-boson mass of 125 GeV, neglecting jet masses and exploiting momentum conservation in the transverse plane of the beam pipe. The Optimal Observable allows to combine the information of this seven-dimensional phase in one scalar variable and provides the highest sensitivity to CP violation for small deviations from the SM. It is defined as the ratio of the CP-odd interference term in the squared matrix element given in Equation 2.59

to the squared SM matrix element:

$$OO = \frac{2\mathrm{Re}(\mathcal{M}^*_{\mathrm{SM}}\mathcal{M}_{\text{CP-odd}})}{|\mathcal{M}_{\mathrm{SM}}|^2}. \tag{2.63}$$

In this analysis, the matrix elements are calculated at leading order with HAWK [119,120] and depend on the kinematics of the initial and final-state constituents:

$$\mathcal{M}^{ij\to klH} = \mathcal{M}(p^\mu_i, p^\mu_j, p^\mu_k, p^\mu_l, p^\mu_H). \tag{2.64}$$

Here, $p^\mu_{i,j}$ and $p^\mu_{k,l}$ correspond to the four momenta of the incoming and outgoing partons, respectively, while p^μ_H refers to the four momentum of the Higgs boson. On the experimental side, the outgoing partons correspond to the two *tagging* jets with the highest transverse momenta, while the four momentum of the Higgs boson needs to be reconstructed from its decay products. The analysis in this thesis focuses on the $H \to \tau\tau$ decay channel, which allows to efficiently select events from Higgs-boson production in the VBF channel. The four momentum of the Higgs boson is then reconstructed by using the Missing Mass Calculator method, which is described in Section 6.1. In general, the kinematics of the initial-state partons are not directly acccesible in the experiment either. However, their four momenta can be derived from the momentum fraction of the initial-state partons $x_{1,2}$:

$$p^\mu_{i(j)} = x_{1(2)}\frac{\sqrt{s}}{2}(1, 0, 0, +(-)1). \tag{2.65}$$

These momentum fractions depend on the invariant mass and rapidity of the final-state constituents given by the tagging jets and the reconstructed Higgs boson:

$$x_{1(2)} = \frac{M_{final}}{\sqrt{s}}e^{+(-)y_{final}}. \tag{2.66}$$

The matrix element also depends on the flavour combination of the incoming and outgoing partons, which is experimentally not accessible. Instead, this analysis uses the sum over all possible flavour configurations $ij \to klH$ weighted by the corresponding parton distribution functions (PDF) $f_{i,j}$ from the leading-order CT10 PDF set [121]:

$$\begin{aligned} 2\mathrm{Re}(\mathcal{M}^*_{\mathrm{SM}}\mathcal{M}_{\text{CP-odd}}) &\to \sum_{i,j,k,l} f_i(x_1)f_j(x_2)2\mathrm{Re}((\mathcal{M}^{ij\to klH}_{\mathrm{SM}})^*\mathcal{M}^{ij\to klH}_{\text{CP-odd}}) \\ |\mathcal{M}_{\mathrm{SM}}|^2 &\to \sum_{i,j,k,l} f_i(x_1)f_j(x_2)|\mathcal{M}^{ij\to klH}_{\mathrm{SM}}|^2. \end{aligned} \tag{2.67}$$

Figure 2.11 shows the Optimal Observable distribution in VBF $H \to \tau\tau$ events in the fully-leptonic final state for the SM coupling and for two CP-violating scenarios with $\tilde{d} = 0.04$ and $\tilde{d} = -0.20$. The predictions for non-vanishing $\tilde{d}$-values are derived with the matrix-element based reweighting technique described in Section 4.4. For the SM coupling, a symmetric Optimal Observable distribution is obtained, while the CP-violating scenarios correspond to asymmetric distributions. In particular, positive (negative) $\tilde{d}$-values lead to a skew of the distribution towards positive (negative) Optimal Observable values.

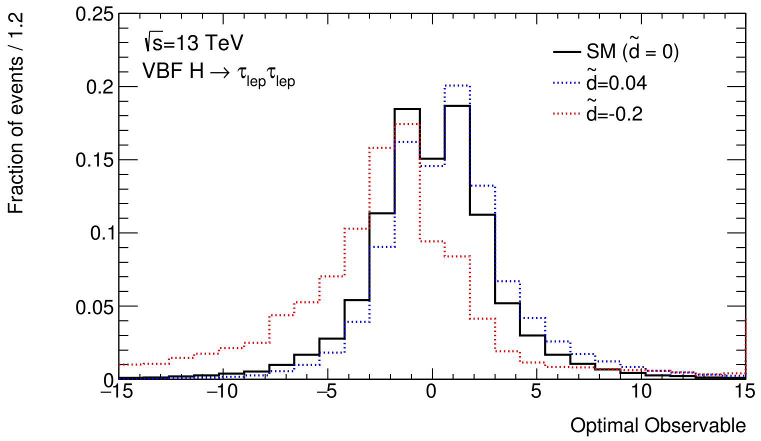

Figure 2.11.: Normalized distributions of the Optimal Observable for the SM coupling and two CP-violating scenarios for VBF $H \to \tau\tau$ events in the fully-leptonic final state. The events are generated at next-to-leading order with PowHeg+Pythia and the VBF event selection requirements described in Section 7.1.1 are applied.

The impact of non-vanishing $\tilde{d}$-values in the underlying coupling hypothesis on the Optimal Observable can also be quantified with its expectation value:

$$\langle OO \rangle = \frac{\int OO(d\sigma_{\mathrm{SM}} + \tilde{d}\, d\sigma_{\text{CP-odd}} + \tilde{d}^2 d\sigma_{\text{CP-even}})}{\int d\sigma_{\mathrm{SM}} + \tilde{d}\, d\sigma_{\text{CP-odd}} + \tilde{d}^2 d\sigma_{\text{CP-even}}}. \tag{2.68}$$

Since the expectation value of a CP-odd observable is zero for CP-even cross-section terms and the integral over the CP-odd cross-section term in the denominator vanishes as well, Equation 2.68 simplifies to

$$\langle OO \rangle = \frac{\tilde{d} \int OO d\sigma_{\text{CP-odd}}}{\int d\sigma_{\mathrm{SM}} + \tilde{d}^2 \int d\sigma_{\text{CP-even}}}. \tag{2.69}$$

The dependency of the Optimal Observable expectation value on $\tilde{d}$ is shown in Figure 2.12 for VBF $H \to \tau\tau$ events in the fully-leptonic final state. The expectation value is consistent with zero within statistical uncertainties for the SM coupling, while CP-violating models correspond to non-vanishing expectation values. For $\tilde{d}$-values close to the SM, a linear dependency of the expectation value on $\tilde{d}$ is found since in this case the denominator term quadratic in $\tilde{d}$ in Equation 2.69 is small compared to the the SM contribution. On the other hand, this term becomes dominant for larger $\tilde{d}$-values and the expectation value first scales approximately with $1/\tilde{d}$ before eventually approaching the SM value of zero again.

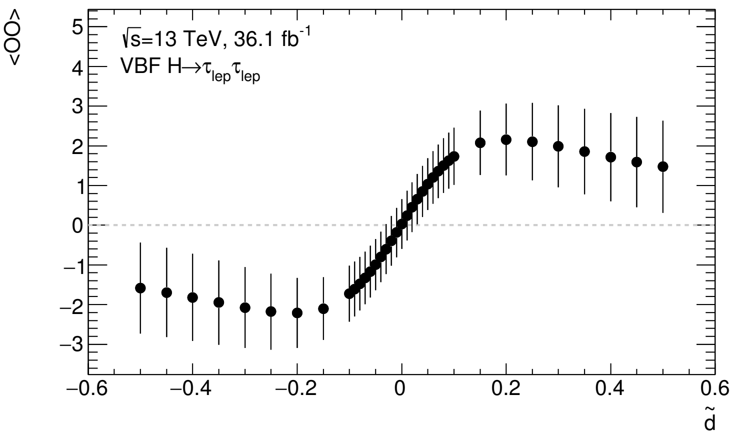

Figure 2.12.: Expectation value of the Optimal Observable as a function of $\tilde{d}$ for VBF $H \to \tau\tau$ events in the fully-leptonic final state. The uncertainties on the expectation value include statistical uncertainties assuming an integrated luminosity of $36.1\,\mathrm{fb}^{-1}$.

3 The ATLAS Experiment

The ATLAS experiment is a multi-purpose detector operating at the Large Hadron Collider (LHC) at CERN near Geneva. It allows to study the outcome of proton and heavy ion collisions, where the particles have been accelerated to center-of-mass energies of up to $\sqrt{s} = 13\,\text{TeV}$ by the LHC. The ATLAS experiment allows to search for new physics phenomena and to probe the predictions of the SM with precision measurements at the highest energies.

The first part of this chapter gives an overview of the LHC and the ATLAS detector based on Refs. [122, 123]. The recorded dataset from the data taking periods in 2015 and 2016, which is analyzed in this thesis, is described in the last section.

3.1. The Large Hadron Collider

The LHC at CERN is a superconducting particle accelerator and collider with a circumference of 27 km. It is located in a tunnel about 100 m below groundlevel, which hosted the former Electron-Positron collider (LEP) from 1989 to 2000. The LHC is able to accelerate protons and large ions with a design center-of-mass energy of $\sqrt{s} = 14\,\text{TeV}$ for proton-proton (pp) collisions. The particles are brought to collision at four points of the ring, where the main experiments are located: The two multi-purpose detectors ATLAS and CMS, the LHCb (Large Hadron Collider beauty) detector [124] with a focus on physics related to bottom-quarks and the heavy-ion experiment ALICE (A Large Ion Collider Experiment), which is dedicated to study quark-gluon plasma states [125]. The ATLAS detector is decribed in detail in Section 3.2.

A schematic view of the LHC ring and its pre-accelerator complex is shown in Figure 3.1. In the first step, protons are extracted from a hydrogen source and injected into the linear accelerator LINAC, where they are accelerated up to an energy of 50 MeV. Next, three circular accelerators are used to further increase the energy: First, the Proton Synchroton Booster allow to accelerate the particles up to 1.4 GeV [126]. It is followed by the Proton Synchroton (PS), which creates 72 particles bunches with a length of 4 ns and time spacing of 25 ns. In the PS, the protons are further accelerated to 25 GeV. Before the particles are injected into the LHC ring, the Super Proton Synchroton (SPS) combines six fillings from the PS into 216 proton bunches and increases the energy to 450 GeV in the last step [127].

The LHC is build of two pipes with beams running in opposite directions. For pp collisions these beams consist of up to 2808 bunches containing 10^{11} particles each. The beams are bent by a magnetic field of up to 8.33 T, which is generated by 1232 superconducting dipol magnets operating at a temperature of 1.9 K. The electric field for the particle acceleration is generated by eight superconducting cavities with a frequency of 500 MHz. In addition, 392 quadrupol magnets are used to focus the beams.

The performance of the LHC can be expressed in terms of its center-of-mass energy and the provided instantanous luminosity [128] with

$$\mathcal{L} = n_b \frac{N^2 \gamma_r f_{ref}}{4\pi\beta^* \epsilon_n} F. \tag{3.1}$$

Here, N is the number of particles per bunch, n_b the number of bunches per beam and f_{rev} refers to the revolution frequency of the protons circulating in the accelerator. The relativistic gamma-factor is given by γ_R and ϵ_n corresponds to the normalized transverse beam emittance. The beta-function generally defines the transverse envelope of the beam for every location in the accelerator, where its value at the interaction point is given by β^*. In addition, the geometric luminosity reduction factor F is applied to account for the crossing angles of the proton beams at the collision point. The design luminosity of the LHC for pp collisions is $\mathcal{L} = 10^{34}\,\mathrm{cm}^{-2}\mathrm{s}^{-1}$ with a beam energy of up to 7 TeV, resulting in a collision center-of-mass energy of $\sqrt{s} = 14\,\mathrm{TeV}$. The integrated luminosity

$$L_{\mathrm{int}} = \int_{t_0}^{t_1} \mathcal{L} dt \tag{3.2}$$

gives the total number of particles passing per unit area and quantifies the amount of data recorded by an experiment for a specific period of time $\Delta t = t_1 - t_0$.

During its first run of pp collisions in 2010 and 2011 the LHC operated at a center-of-mass energy of 7 TeV, which was increased to 8 TeV in 2012. After the first long shutdown of two years the LHC resumed its physics program with Run 2 starting in 2015 at $\sqrt{s} = 13\,\mathrm{TeV}$. The dataset analyzed in this thesis was recorded by the ATLAS experiment in 2015 and 2016. The data taking conditions during this time are discussed in more detail in Section 3.2.6.

3.2. The ATLAS Detector

The ATLAS detector is a multi-purpose experiment, which is designed to explore a wide range of physics processes at high collision energies. It enables the search for new physics phenomena as well as precision measurements of the SM particles and their interactions. The overall structure of the ATLAS detector is illustrated in Figure 3.2. Its cylindrical design covers almost 4π and the high-density detector material enables the precise reconstruction of hard scattering events up to low scattering angles. In addition, a highly efficient trigger system allows for the selection of a wide range of different physics processes. The ATLAS detector is described by a right-handed coordinate system, which originates at the interaction point. The z-axis points in beam direction, the y-axis is defined upwards and the x-axis points in the direction towards the center of the LHC ring. The azimuthal angle ϕ is measured in the $(x-y)$-plane , while the polar angle θ is defined with respect to the z-axis. Transverse observables, such as the transverse momentum p_T

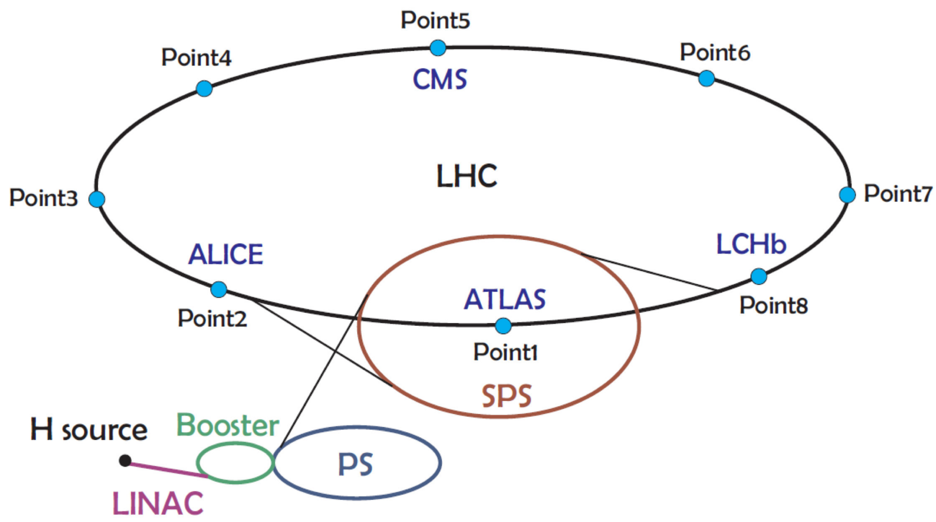

Figure 3.1.: Schematic view of the LHC accelerator ring and the location of the four main experiments ATLAS, CMS, ALICE and LHCb [129].

and transverse energy E_T, are established as their vectorial projection in the $(x-y)$-plane. Furthermore, a widely used observable is the rapidity, defined as

$$y = \frac{1}{2}\ln\left(\frac{E+p_z}{E-p_z}\right), \tag{3.3}$$

where E gives the energy and p_z the projection of the particles momentum in z-direction. The rapidity difference Δy provides a Lorentz-invariant quantity under boost along the z-axis. In case of particles with small masses compared to their energy $m \ll E$, the pseudorapidity is often used instead:

$$\eta = -\ln(\tan(\theta/2)). \tag{3.4}$$

The distance of two objects in the $(\eta-\phi)$-plane can then be measured with

$$\Delta R = \sqrt{\Delta\eta^2 + \Delta\phi^2}. \tag{3.5}$$

The ATLAS experiment consist of several sub-detectors, which are arranged in a cylindrical symmetric way around the beam pipe. The inner detector is build closest to the collision point and is embedded in a solenoid magnetic field with a field strength of up to 2 T. Around the inner detector, the electromagnetic and hadronic calorimeters are installed. The outermost system is given by the muon spectrometer, which is surrounded by three large superconducting toroids with magnetic field strengths between 0.5 T and 1 T.

The sub-detectors of the ATLAS experiment are described in more detail in the following sections. A summary of their resolution goals on the momentum and energy measurements is given in Table 3.1.

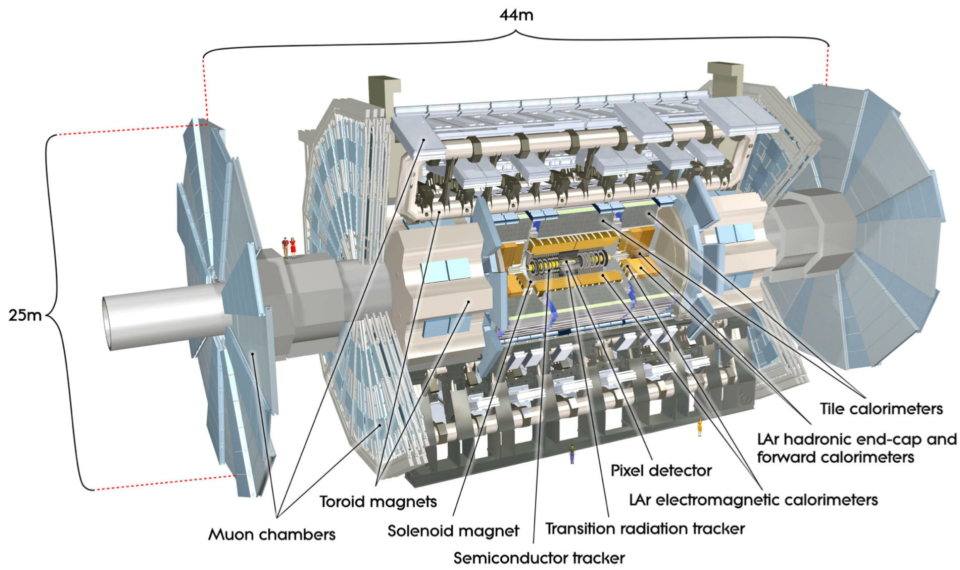

Figure 3.2.: Overview of the ATLAS detector showing the muon system, the toroidal and solenoid magnets, the calorimeters and the inner detector [123].

3.2.1. Inner Detector

The inner detector (ID) of the ATLAS experiment measures the trajectory of charged particles with high precision. It allows for the reconstruction of primary and secondary vertex positions and momenta as well as the identification of the particle charge. For this, the detector has to be constructed to cope with high occupancies and radiation doses and a large data rate.

As shown in Figure 3.3, the ID consists of the pixel detector with the insertable b-Layer (IBL), the semiconducting tracker (SCT) and the transition radiation tracker (TRT) covering a pseudorapidity range of $|\eta| < 2.0$. The ID has a length of 6.2 m with a radius of 2.1 m and is embedded in a solenoid magnetic field with a field strength of 2 T.

The innermost part of the ID is given by the IBL, which was installed during the first long shutdown of the LHC in 2013 at a radius of 33 mm from the beam pipe [130]. It enables the precise reconstruction of secondary vertex positions in the decay of heavy-flavour particles, which is in particular important for the identification of particle jets originating from b-hadrons. Due to its vicinity to the interaction point, the IBL was build to cope with high radiation doses and high temperatures.

Around the IBL, the pixel detector is installed. It consist of three layers of concentric hollow cylinders in the barrel region and three layers of disks arranged radially in the endcap regions [131]. With this arrangement, particles typically traverse three pixel layers on their way through the detector. The pixels vary in their size from $(R - \phi) \times z = 50 \times 400\,\mu\text{m}^2$ to $(R - \phi) \times z = 50 \times 600\,\mu\text{m}^2$ depending on the region. In total, 1744 pixel sensons are installed with about 80.4 million readout channels. With this, the pixel detector has the highest granuality of all sub-detectors in the ATLAS experiment and achieves a single-module accuracy of 10 μm in the $(R - \phi)$-plane and 115 μm along the z-direction.

The pixel detector is surrounded by the semiconductor tracker (SCT) covering a radial region between 30 cm - 52 cm within $|\eta| < 2.5$. It consists of four double-sided layers of silicon strip detectors in the barrel region and nine double layers in each endcap region. In each layer, the strip modules are made of two 6.4 cm long daisy-chained sensors with a strip pitch of 80 μm. Charged particles cross at least eight strip layers when transversing the SCT. Due to the double-layer structure of the strips, this results in the measurement of four space points in the barrel region. In total, 258 active strips and 6.3 million readout channels are used. In the barrel region, the modules are arranged as two layers, which are rotated by 40 mrad against each other. This allows for a precise position measurement along the strip direction. The SCT reaches a nominal hit resolution of 17 μm in the $(R - \phi)$-plane and 580 μm along the z-direction.

The transition radiation tracker (TRT) forms the outermost part of the ID. It covers a rapidity range of $|\eta| < 2.0$ and consists of straw tubes filled with xenon-based gas. The tubes measure 4 mm in diameter and are arranged in the barrel region parallel to the beam axis with a length of 144 cm. In the endcap region, the tubes are installed radially in wheels with 37 mm length. In total, the TRT has 351.000 readout channels. It allows for position measurements in the $(R - \phi)$-plane with a resolution of 130 μm, where on average 36 coordinate measurements are obtained over the radial distance from 55 cm to 108 cm. In addition, the TRT provides important information for particle identification and allows in particular for the discrimination between electrons and charged pions. This is achieved by measuring the transition radiation emitted by particles traversing the interface of materials with different di-electric constants. For this, the gas-filled tubes are stabilised by corban fibres with a diameter of 9 μm, which serve as the transition radiation material.

3.2.2. Calorimeters

The ATLAS calorimeter system measures the energy and direction of charged and neutral particles and allows for the reconstruction of the missing transverse momentum. As shown in Figure 3.4, it consists of the electromagnetic calorimeter (ECal) and the hadronic calorimeter (HCal) covering a pseudorapidity range of $|\eta| < 4.9$ and the full ϕ-range. Both systems are constructed as sampling calorimeters.

The ECal can be divided into the barrel region covering a pseudorapidity range of $|\eta| < 1.375$, the endcap regions with $1.375 < |\eta| < 3.2$ and the forward detectors in the range of $3.1 < |\eta| < 4.9$. The endcap region can be further classified in the central region with $1.375 < |\eta| < 2.5$, where a very fine granulity of at best $\Delta\eta \times \Delta\phi = 0.025 \times 0.025$ is provided, and the forward region in the range of $2.5 < |\eta| < 3.2$ with a coarser granuality. The ECal consists of liquid argon (LAr) as active material, which is combined with lead absorbers in the barrel and endcap regions and copper in the forward detector. In the barrel region, kapton electrodes are installed in an accordian geometry to ensure a detector

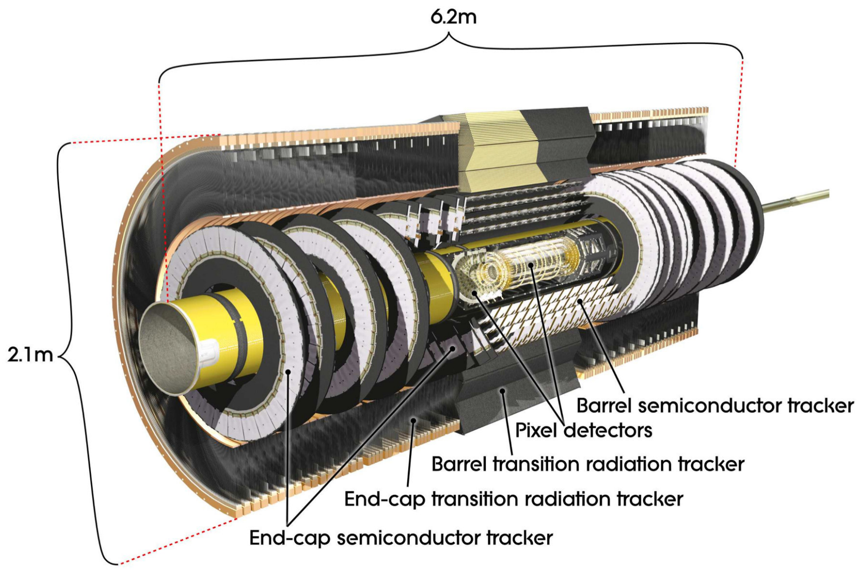

Figure 3.3.: Schematic view of the ATLAS inner detector with the pixel detector, the semiconductor tracker and the transition radiation tracker [123].

coverage in the full ϕ-range. In total, the barrel has a thickness of 47 cm covering more than 22 radiation lengths (X_0)[1] for electrons. The size of the endcaps corresponds to more than $24X_0$. Furthermore, presamplers are installed in front of the ECal for $0 < |\eta| < 1.7$ with a high very high granularity of $\Delta\eta \times \Delta\phi = 0.0031 \times 0.1$. These presamplers allow to distinguish between photons and neutral pions as well as between electrons and charged pions. The high granuality of the ECal enables a precise energy and position measurement of electrons and photons, which can be combined with track information from the ID in the range $|\eta| < 2.5$. The total number of readout channels is approximately 170.000. The outer HCal consists of the tile calorimeter covering $|\eta| < 1.7$, the hadronic endcap calorimeter (HEC) within $1.5 < |\eta| < 3.2$ and the forward calorimeter (FCal) at large pseudorapidities of $3.1 < |\eta| < 4.9$. In the barrel region, the active detector material of the tile calorimeter corresponds to scintillating tiles, while the HEC and FCal use LAr. In the tile calorimeter, they are complemented with steel absorbers, while copper plates are used in the endcap region and tungsten for the forward detector. The HCal enables the energy measurement of the complete hadronic shower, which is crucial for a reliable E_T^{miss} measurement. In addition, the fraction of particles reaching the outermost muon system is limited well below the level of muons from prompt production and decay. For the tile calorimeter, approximately 10.000 readout channels are used, while the total number of readout channels in the HEC and FCal is about 9.000.

[1] Characteristic amount of material traversed by a particle before it looses $1/e$ of its initial energy due to bremsstrahlung

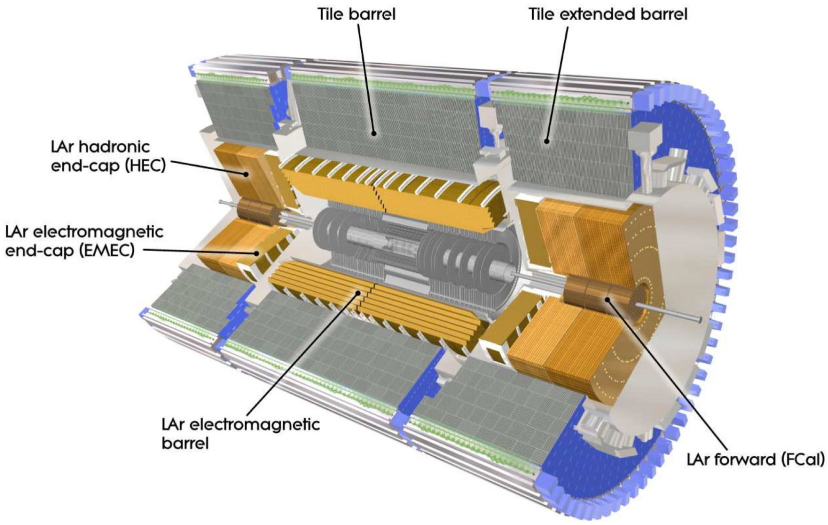

Figure 3.4.: Schematic view of the ATLAS electromagnetic and hadronic calorimeters [123].

3.2.3. Muon System

The muon system (MS) provides the outermost part of the ATLAS detector and is arranged in three concentric cylindrical shells around the beam axis at distances of about 5 m, 7.5 m and 10 m. It enables the detection and momentum measurement of charged particles, which are not absorbered by the preceding detector material. In particular, muons, which are produced in primary collisions or via the decay of heavy-flavor hadrons, only loose a small amount of their energy via bremsstrahlung when traversing the material of the ID and calorimeters. Hence, the MS provides important information for the muon identification and reconstruction in the detector. It can be divided into the barrel region with $|\eta| < 1.4$, the encap region covering a range of $1.6 < |\eta| < 2.7$ and a transition region with $1.5 < |\eta| < 1.6$. As shown in Figure 3.5, the barrel region of the MS consists of three cylindrical layers of muon chambers, which are arranged around the beam axix. Larger η-ranges are covered by four wheels with three layers each, which are installed perpendicular to the beam axis.

The muon chambers are embedded in the magnetic field of three large air-core toroids, which is mostly generated orthogonal to the particle trajectory. These toroids provide field integrals of 1.5 - 55 Tm in the barrel and 1 - 7.5 Tm in the endcap regions. The momentum of the traversing particle is measured from the bending of its trajectory in the magnetic field. For most η-ranges, this is done with monitored drift tubes (MDT) with a spatial resolution of 80 μm per tube and 35 μm per chamber along the z-axis, while cathod strip chambers (CSC) are used at large pseudorapitities. These multi-wire proportional chambers have a high rate capability and good time resolution, which is necessary in particular in the forward regions. The CSCs provide a resolution of 40 μm per chamber in the $(R - z)$-bending plane and about 5 mm per chamber in the transverse plane. To achieve this resolution, a good knowledge of the MS alignment is necessary. For this, 12000 optical sensors are used to measure the relative position and internal deformations of the MDT chambers. The number of readout channels is approximately 800.000.

The MS also serves as a trigger system in the range of $|\eta| < 2.4$, where resistive plate chambers (RPC) are installed in the barrel region and multi-wire proportinal chambers, so called thin gap chambers (TGC), are used in the endcap region. These trigger chambers provide track information within a few nano seconds and allow to additionally determine the muon coordinates perpendicular to the ones measured by the tracking chambers.

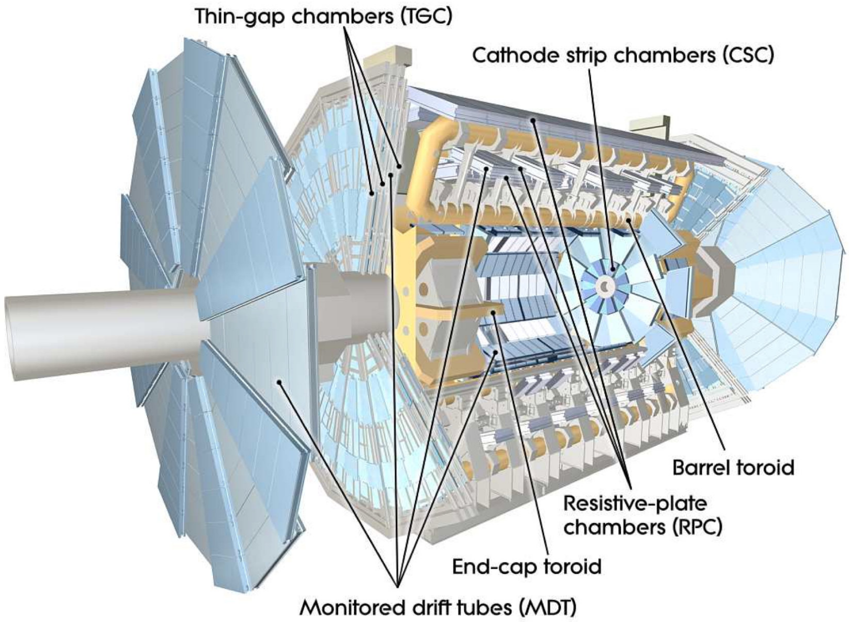

Figure 3.5.: Schematic view of the ATLAS muon system including barrel and endcap toroid [123].

3.2.4. Luminosity Detectors

In addition to the sub-detectors described in the previous section, the ATLAS experiment also hosts two additional detectors, which are dedicated to measure the luminosity provided by the LHC: The Luminosity measurement using Cherenkov Integrating Detector (LUCID) and the Absolute Luminosity For ATLAS Detector (ALFA). These detectors are located in the ATLAS forward regions and are arranged symmetrically with respect to the interaction point.

LUCID is placed at $z = \pm 17\,\mathrm{m}$ from the interaction point and measures the inelastic cross-section in pp collisions σ_{inel} at $\eta \approx 5.8$. The instantaneous luminosity is given by [132]

$$\mathcal{L} = \frac{\mu f_{rev} n_b}{\sigma_{inel}} = \frac{\mu_{vis} f_{rev} n_b}{\sigma_{vis}} \tag{3.6}$$

with the revolution frequency f_{rev} and the number of bunches n_b. The visible average number of inelastic interactions is given by $\mu_{vis} = \epsilon \cdot \mu$ and the visible inelastic cross-section $\sigma_{vis} = \epsilon \cdot \sigma_{inel}$ accounts for the detector efficiency ϵ. As μ_{vis} can be observed in pp collisions, the determination of σ_{vis} allows to extract the luminosity. These luminosity measurements are calibrated during dedicated calibration runs, so called van-der-Meer scans. LUCID also provides input for the online monitoring of the beam conditions.

The ALFA experiment consists of scintillating fibre trackers and is located at $z = \pm 240$ m from the interaction point. It consists of four Roman pots, which allows to place the detector as close as 1 mm away from the beam. With this, the detector is able to measure elastic scattering events at small angles, which allows to determine the luminosity via the optical theorem [133].

3.2.5. Trigger System

At the LHC, pp collisions can occur with instantaneous luminosities of more than $L = 10^{34}\mathrm{cm}^{-2}\mathrm{s}^{-1}$, where the minimum time difference between every bunch crossing is up to 25 ns. This results in an event rate of about 40 MHz, which is impossible to readout and store, but needs to be reduced to a feasible amount. The ATLAS trigger system is constructed to select events, which are found of interest for further physics analysis at a recording rate of approximately 1 kHz. It consists of two stages: the level-1 (L1) and the high-level trigger (HLT) systems. The different stages and the data-flow is illustrated in Figure 3.6.

The hardware-based L1 system searches for objects with high transverse energy by exploiting information from the muon trigger chambers and the full calorimeter system with a coarser granuality. The $(\eta - \phi)$-coordinates of so-called *regions of interest* (RoI) are then forwarded to the HLT. The L1 trigger has an average processing time of 2.5 μs per events and reduces the event rate to 100 kHz.

After L1 acceptance, the events are further processed by the software based HLT system. It uses high-granuality information from the calorimeter, the muon system and the ID to run sophisticated selection algorithms on the RoIs as well as on the full detector. In most cases, a two-stage approach is used. Here, the majority of events is rejected in the first stage based on a fast reconstruction algorithm. In the next step, a more precise reconstruction of the remaining events is performed in order to decide, which events are recorded for further offline analysis. The HLT has an average decision time of 200 ms per event and reduces the output event rate to about 1 kHz. These datasets are then stored at the CERN Tier 0 computing center and distributed for further analysis.

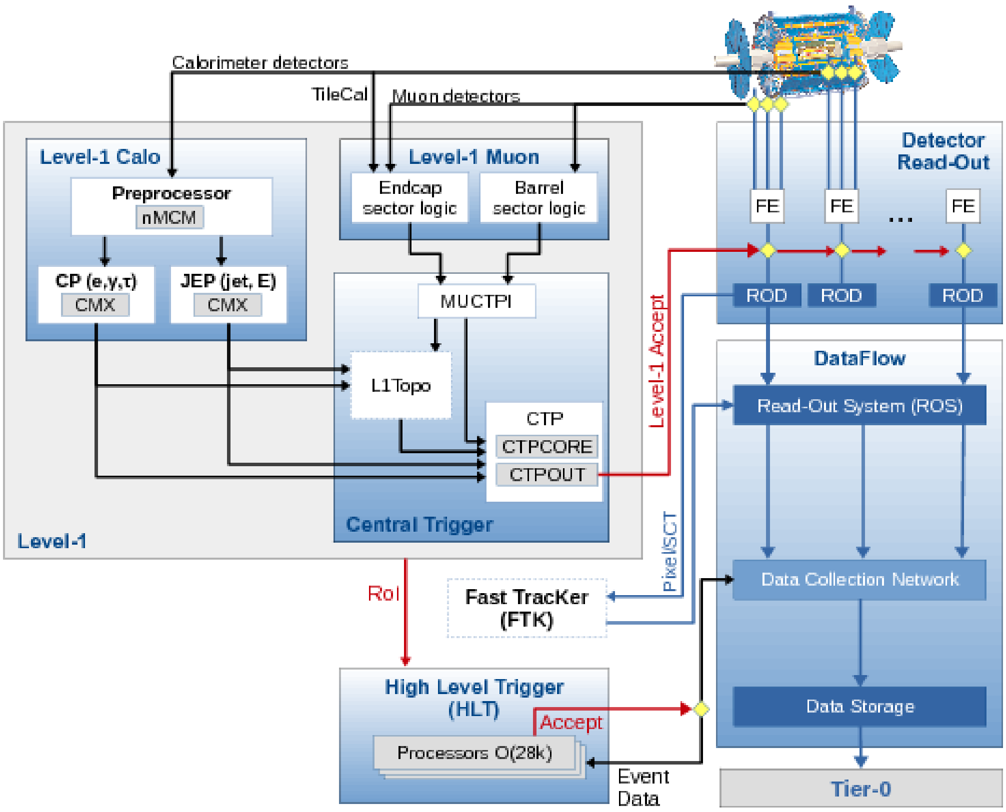

Figure 3.6.: Schemativ view of the ATLAS trigger stages during LHC Run 2 [134].

Subdetector	Required resolution	η-coverage	
		Measurement	Trigger
Inner detector	$\sigma_{p_T}/p_T = 0.05\%\, p_T \oplus 1\%$	± 2.5	
Electromagnetic calorimetry	$\sigma_E/E = 10\%/\sqrt{E} \oplus 0.7\%$	± 3.2	± 2.5
Hadronic calorimetry			
- barrel and endcap	$\sigma_E/E = 50\%/\sqrt{E} \oplus 3\%$	± 3.2	± 3.2
- forward	$\sigma_E/E = 100\%/\sqrt{E} \oplus 10\%$	$3.1 < \lvert\eta\rvert < 4.9$	$3.1 < \lvert\eta\rvert < 4.9$
Muon spectrometer	$\sigma_{p_T}/p_T = 10\%$ at p_T=1 TeV	± 2.7	± 2.4

Table 3.1.: General resolution goals of the sub-detectors of the ATLAS detector. Energy and momentum values are given in units of GeV. The notation a$\oplus$b=$\sqrt{a^2+b^2}$ is used [123].

3.2.6. Data taking in Proton-Proton Collisions in 2015 and 2016

The LHC started operating in 2010 with a first phase of data taking at $\sqrt{s} = 7\,\text{TeV}$. In 2012, the center-of-mass energy was increased to $\sqrt{s} = 8\,\text{TeV}$. During this Run 1 period, the ATLAS experiment collected datasets of $4.5\,\text{fb}^{-1}$ [2] and $20.3\,\text{fb}^{-1}$ at $\sqrt{s} = 7\,\text{TeV}$ and $\sqrt{s} = 8\,\text{TeV}$, respectively.

After the first long shutdown, the LHC resumed data taking with Run 2 at $\sqrt{s} = 13\,\text{TeV}$ in 2015. Figure 3.7 (a) shows the integrated luminosity versus time for the 2016 period. The analysis presented in this thesis is based on the dataset collected in 2015 and 2016 corresponding to an integrated luminosity of $36.1\,\text{fb}^{-1}$. As shown in Figure 3.7 (b), the mean number of interactions per bunch crossing during this period was on average $\langle\mu\rangle = 22.9$ with a minimum time spacing of up to 25 ns between the crossing bunches.

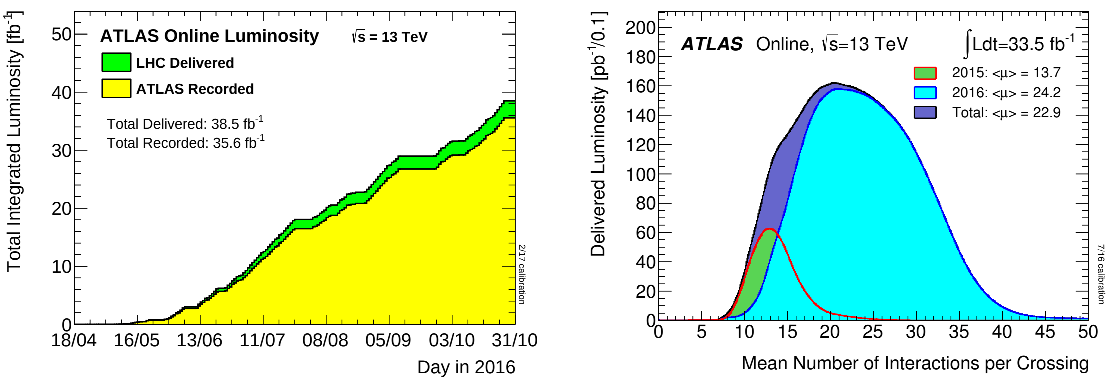

Figure 3.7.: Total integrated luminosity as a function of time for data taken in 2016 (a) and distribution of the mean number of interations per bunch crossing for data taken in 2015 and 2016 (b) [135].

[2] $1\,\text{b(barn)} = 1 \times 10^{-22}\,\text{cm}^2$

4 Signal and Background Processes

This chapter provides an overview of the relevant signal and background processes in the analysis of $H \to \tau_{lep}\tau_{lep}$ decays. As shown in Figure 2.2, the production cross-section for various SM pocesses in pp collisions exceeds the one for Higgs-boson production by several orders of magnitude. Hence, the extraction of $H \to \tau\tau$ signal events in the analysis requires a good theoretical understanding and a precise description of the relevant processes.

The first two sections of this chapter, Section 4.1 and 4.2, give an overview of the experimental signature of the signal and background processes, respectively. The generation of simulated signal and background events is then described in Section 4.3. Last, Section 4.4 introduces the reweighting procedure to derive the signal predictions with CP-violating HVV interactions in the VBF CP analysis.

4.1. Signal Processes

The dominant Higgs-boson production modes at the LHC are introduced in Section 2.2.1, where also the available accuracy for the theoretical cross-section calculations are summarized. Figure 4.1 shows the leading-order Feynman diagrams for the gluon fusion, the vector-boson fusion, the vector-boson associated and the top-quark pair associated production with the subsequent decay of the Higgs boson into a pair of τ-leptons. Other Higgs-boson production modes, such as the associated production with a single top-quark and with bottom-quark pairs, are negligible for the analysis and are not discussed here. While the $H \to \tau\tau$ cross-section measurement exploits all of the main Higgs-boson production modes, the VBF CP analysis aims in investigating the coupling structure of the Higgs boson to vector bosons HVV in the VBF production channel. For all other Higgs-boson production modes, the VBF CP analysis assumes no deviation from the SM and therefore includes these events in the background prediction.

The Higgs-boson production in the gluon-fusion channel (ggF) occurs with a cross-section of 48.5 pb and provides the dominant production mode with a relative contribution of about 87 %. In this channel, the coupling of the Higgs boson to the massless gluons occurs via a heavy-fermion loop, which is dominated by top-quark contributions. At leading order, no additional particles are produced in the final state and hence the Higgs boson does not aquire a transverse momentum. However, higher-order QCD radiations from the incoming partons or quarks in the fermion loop can lead to additional final-state partons, which are then reconstructed as jets in the detector. The recoil against this jet system provides the Higgs boson with a transverse momentum and can be exploited in the analysis.

The second most likely Higgs-boson production channel is given by the vector-boson fusion (VBF) with a cross section of 3.78 pb. Although this cross-section is already one order of magnitude below the ggF production, the VBF channel constitutes an important signal contribution due to its distinct kinematic signature. The incoming partons radiate off vector bosons, which fuse and produce the Higgs boson. These partons then further propagate in opposite directions and are reconstructed in the detector as two well-separated jets with a large invariant mass. In addition, the electroweak coupling of the incoming partons to the vector bosons prohibits additional colour exchange between the final-state particles and therefore results in low hadronic activity in the central part of the detector. This signature allows to efficiently distinguish between signal and background contributions in the analysis.

The production of a vector boson with the radiation of a Higgs boson is referred to as vector-boson associated production (VH), also *Higgsstrahlung*. The associated production with a $W^{\pm}$-boson occurs with a cross section of 1.37 pb, while the Higgs-boson is produced with a Z^0-boson with a cross section of 0.88 pb. The experimental signature of this production mode is characterized by the subsequent decay of the vector bosons into hadrons or leptons. Furthermore, additional final-state jets can appear due to higher order QCD radiation of the incoming partons. This production channel plays a minor role for the analyses described in this thesis due to its small cross section.

The same holds for the Higgs-boson production with top-quark pairs (ttH), which occurs with a cross section of only 0.51 pb. The subsequent decay of the top-quarks into bottom-quarks and $W^{\pm}$-bosons occurs with a branching ratio of almost 100 % and results in final states with jets originating from the hadronic activity of the bottom-quarks. In addition, the leptonic and hadronic decay products of the $W^{\pm}$-bosons can be used to characterize this Higgs-boson production mode.

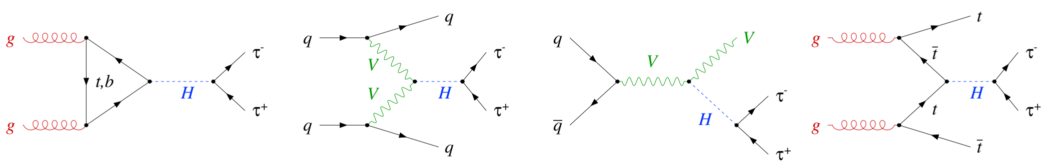

(a) (b) (c) (d)

Figure 4.1.: Example of leading-order Feynman diagrams of the relevant signal processes: Gluon fusion (a), vector-boson fusion (b), vector-boson associated (c) and top-quark pair associated production (d) with the subsequent decay of the Higgs boson into a pair of τ-leptons. The decays of the vector bosons $V = W^{\pm}, Z^0$, the top-quarks and the τ-leptons are omitted.

The analyses presented in this thesis focus on the decay of the Higgs boson into a pair of τ-leptons. In the SM, this decay occurs with a branching ratio of 6.26 % with relative uncertainties of +1.17 % and −1.16 % [85]. The τ-lepton decays further after a mean life-time of $\tau = 2.9 \times 10^{-13}$ s into leptonic or hadronic final states with branching ratios of 35.2 % or 64.8 %, respectively [40]. Figure 4.2 shows the Feynman diagram for the leptonic decay channel $\tau_{lep} \rightarrow \ell 2\nu$ with electrons or muons and the corresponding neutrinos in the final state. On the hadronic side, the τ-lepton dominantly decays into charged and neutral pions with smaller contributions from the decay into kaons. Hence, the $H \to \tau\tau$ decay channel can be classified in three final states depending on the decay of the di-τ system: The fully leptonic channel $\tau_{lep}\tau_{lep}$ with a branching ratio of 12.4 %, the full-hadronic channel $\tau_{had}\tau_{had}$ with a branching ratio of 41.9 % and the semi-leptonic channel $\tau_{lep}\tau_{had}$ with the highest branching ratio of 45.7 %. Although the $\tau_{lep}\tau_{lep}$ final state occurs with the smallest branching ratio, it allows to exploit the highly efficient lepton triggers and also profits from lower background contribution due to QCD multi-jet events compared to the final state including hadronic τ-lepton decays. The analyses presented in this thesis focus on the $\tau_{lep}\tau_{lep}$ channel and therefore select events with two *prompt*[1] leptons of opposite electric charge and missing transverse energy from the neutrinos. This missing transverse energy does not allow for the direct reconstruction of the Higgs-boson mass by combining the four-momenta of the di-τ system, but requires the application of several approximations, which are discussed in detail in Section 6.1.1.

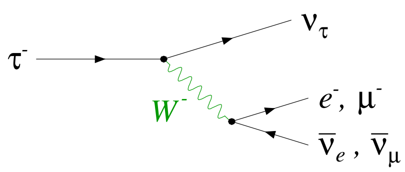

Figure 4.2.: Feynman diagram for the leptonic decay of a τ-lepton into electrons or muons and the corresponding neutrinos.

4.2. Background Processes

In general, most physics analyses are subject to significant contributions of various background processes, which mimic the final-state signature of the signal process. In particular, irreducible background events are provided by processes with the same physical objects in the final state as the signal process, while reducible background contributions arise from insuffiencies in the detection and identification of these objects.

The following section describes the kinematic signatures of the background processes, which are relevant for the $H \to \tau\tau$ cross-section measurement and the VBF CP analysis in the $\tau_{lep}\tau_{lep}$ final state. An overview of the theoretical cross-sections as well as a summary of the event generation is given in Table 4.1.

4.2.1. Production of Z^0/γ^*-Bosons and $W^\pm$-Bosons in Association with Jets

Since the production of a Z^0-boson or a virtual photon γ^* can not be distinguished experimentally, this process is referred to as Z^0-boson production in the following. Figure 4.3 shows the Z^0-boson production in association with jets, which dominantly occurs via QCD interactions, as well as the electroweak production via vector-boson fusion with two

[1] Prompt electrons or muons correspond to the direct decay products of heavy bosons or τ-leptons

final-state jets. While the cross section for the electroweak production scales with the electroweak coupling strength α_{EW}^3, the Z^0-boson production with two additional jets from QCD interactions is governed by a mixture of the electroweak and strong coupling strength with $\alpha_{EW}\alpha_S^2$. In the analysis of the $H \to \tau\tau$ channel, $Z \to \tau\tau$ decays give the dominant background contribution since they provide the same final-state objects as the signal process. The reduction of this irreducible background contribution mainly relies on the reconstructed invariant mass of the di-τ system, which is discussed in Section 6.1.1.

In addition, Z^0-boson decays into prompt electrons or muons, $Z \to \ell\ell$, give an important background contribution as well and correspond to one of the dominant background processes in the $H \to \tau_{lep}\tau_{lep}$ final state with same-flavour (SF) leptons. Here, the missing transverse energy in these $Z \to \ell\ell$ events is mainly caused by deficiencies in the reconstruction of additionally produced jets.

Another background contribution arises from the production of $W^{\pm}$-bosons via electroweak or QCD interactions and exemplary Feynman diagrams are shown in Figure 4.4. In these events, the misidentification of additionally produced jets as electrons or muons as well as the production of *non-prompt* leptons from semi-leptonic decays of heavy-flavour quarks can mimic the final-state signature of the signal process. These kind of events are included in the prediction of the so-called *fake* lepton background, which is described in Section 6.2.3.

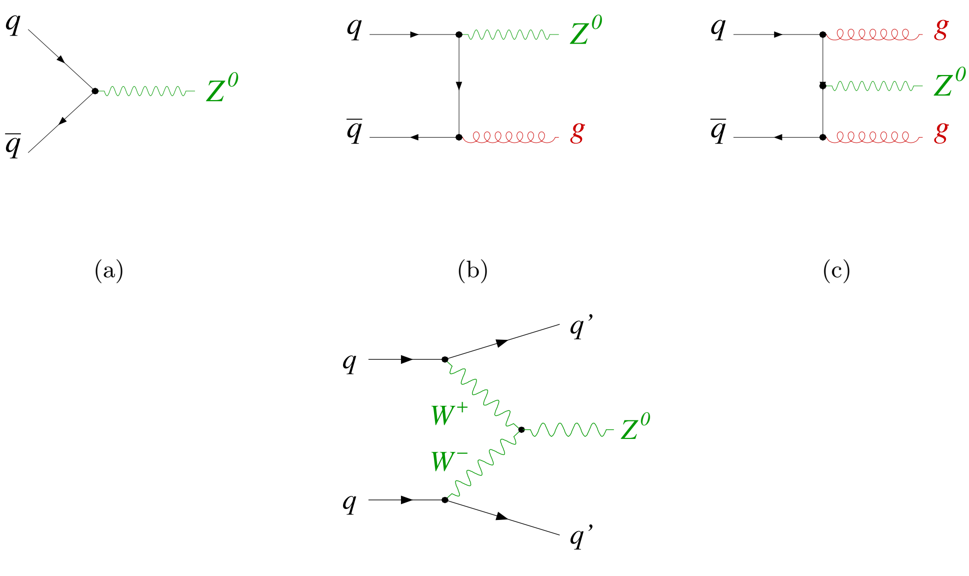

(d)

Figure 4.3.: Examples of Feynman diagrams for Z^0-boson production via QCD interactions in association with no jets (a), one jet (b) and two jets (c) and the electroweak production in association with two jets (d). The decay of the Z^0-boson is omitted.

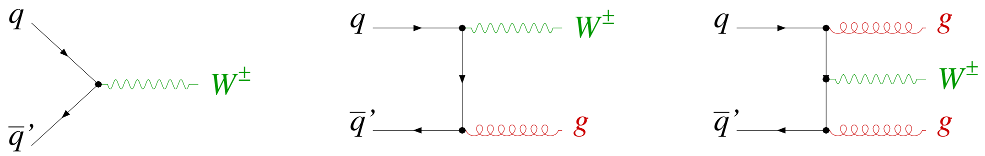

(a) (b) (c)

Figure 4.4.: Examples of Feynman diagrams for $W^{\pm}$-boson production in association with no jets (a), one jet (b) and two jets (c). The decay of the $W^{\pm}$-boson is omitted.

4.2.2. Di-boson Production

Background contributions from di-boson processes occur through the production of WW-, WZ- or ZZ-pairs and are shown in Figure 4.5. In particular, fully leptonic decays of WW- and ZZ-pairs can provide events with two prompt leptons, missing transverse energy and jets in the final state. In addition, di-boson production with subsequent hadronic decays of the vector bosons can also mimic the final state signature of the signal process due to misidentified jets as leptons or insufficiencies in the jet reconstruction.

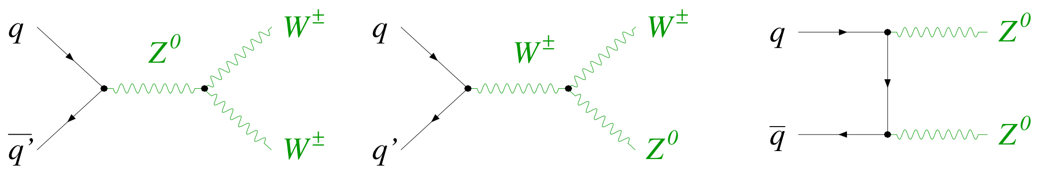

(a) (b) (c)

Figure 4.5.: Example of Feynman diagrams for the production of WW (a), ZZ (b) and WZ (c). The decays of the $W^{\pm}$-bosons and Z^0-bosons are omitted.

4.2.3. Single Top-quark and Top-quark Pair Production

The production of top-quark pairs $t\bar{t}$ is shown in Figure 4.6. Since the top-quark almost exclusively decays into a $W^{\pm}$-boson and a bottom-quark, top-quark pair production is characterized by two final state jets, so called b-jets, which originate from the hadronic decay of the bottom-quarks. In case of further leptonic decays of the $W^{\pm}$-bosons, these events also provide two prompt leptons and missing transverse energy in the final state. Events with non-prompt leptons from semi-leptonic decays of the b-jets are included in the prediction of the fake-lepton background.

The production of single top-quarks needs to be considered as well and is shown in Figure 4.7. Here, background contributions from single top-quark production in the s-channel and t-channel mainly occur through events with subsequent leptonic decays of the $W^{\pm}$ boson and additional non-prompt leptons from semi-leptonic b-jet decays. For the associated production Wt, leptonically decaying $W^{\pm}$-bosons provide final state signatures containing two prompt leptons and missing transverse energy.

Since both the single top-quark and the top-quark pair production are characterized by at least one b-jet in the event, these background contributions can be reduced efficiently in the analysis with so-called *flavour-tagging* techniques, which are described in Section 5.4. In the following, background events from single top-quark and top-quark pair production are commonly referred to as top-quark background.

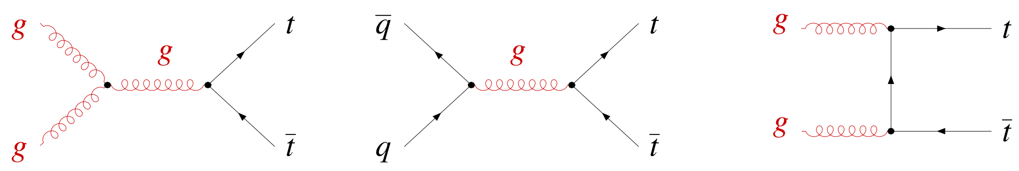

(a) (b) (c)

Figure 4.6.: Example of Feynman diagrams for top-quark pair production. The decay of the top-quarks is omitted.

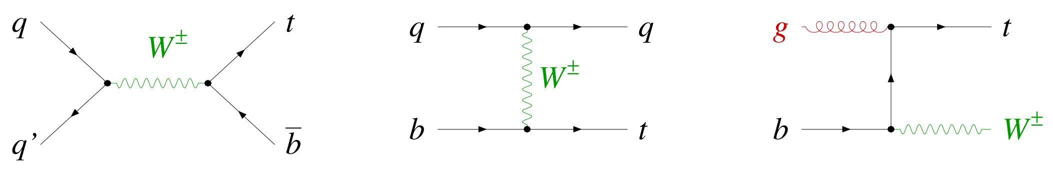

(a) (b) (c)

Figure 4.7.: Feynman diagrams for single top-quark production in the s-channel (a), t-channel (b) and in association with a $W^{\pm}$-boson (c).

4.2.4. QCD Multi-jet Production

In pp collisions, the production cross-section of events with multiple jets exceeds the one for Higgs-boson production by many orders of magnitude. Figure 4.8 shows examples of such QCD multi-jet processes. Here, the misidentification of jets as leptons, non-prompt leptons from semi-leptonic decays of heavy-flavour quarks or deficiencies in the jet reconstruction can result in events with similar final state signatures as the signal processes. This important background contribution is included in the prediction of the fake-lepton background and is estimated based on the data-driven technique described in Section 6.2.3. In the analysis, the suppression of these multi-jet events requires the application of tight lepton identification and isolation criteria as well as a reliable reconstruction of the missing transverse energy.

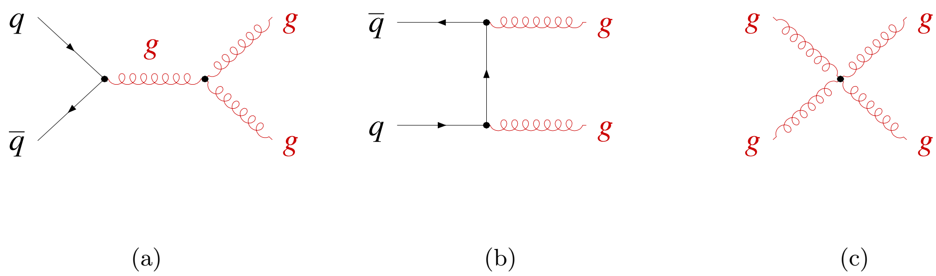

Figure 4.8.: Example of Feynman diagrams for multi-jet production in QCD processes.

4.2.5. Other Higgs-Boson Decays

Events, where the Higgs-boson decays into $W^{\pm}$-bosons $H \to WW$, give a non-negligible background contribution in the search for $H \to \tau\tau$ decays. In particular, further leptonic decays of the $W^{\pm}$-bosons result in final states with two prompt leptons of opposite charge and missing transverse energy and can therefore mimic the signature of the $H \to \tau_{lep}\tau_{lep}$ signal. The cross-section measurement in the $H \to \tau\tau$ channel includes Higgs-bosons production in the VBF and ggF mode with subsequent $H \to WW$ decays in the background prediction, while the VH and ttH production modes for this decay channel are omitted due to their small cross sections.

Since the VBF CP analysis focuses on the investigation of the HVV coupling structure, $H \to WW$ events via VBF production are considered as an additional contribution to the signal prediction. While in principle also events from ggF production with $H \to WW$ decays contain the HVV coupling in the decay vertex, CP-violating effects mainly arise from CP-odd contributions to the SM interaction in the production (see Sec 2.4). The $H \to WW$ decay structure is therefore assumed to follow the SM prediction. Hence, $H \to WW$ events produced in the ggF mode contribute to the background prediction, where no CP violation is expected. More studies on the effect of CP-violating contributions in the $H \to WW$ decay vertex can be found in Ref. [136].

4.3. Generation of Simulated Events

Many physics analyses rely on the theoretical prediction of signal and background processes, which can be compared to the observed data in the experiment. These predictions have to be as precise as possible, while also taking into account experimental effects, such as detector resolution and response. This section gives an overview on the physics of pp collisions and describes the generation of simulated events for the relevant signal and background processes in the analyses.

4.3.1. Phenomenology of Proton-Proton Collisions

In particle physics the outcome of an experiment can often be quantified by the occurance of a particular final state X. Here, the probability for the process $AB \to X$ to take place is quantified by its cross section σ and can be related to the expected number of events N_X with the total integrated luminosity L_{int} as defined in Equation 3.2:

$$N_X = \sigma_{AB\to X} \cdot L_{int}. \tag{4.1}$$

The prediction of N_X for a given experiment therefore requires the theoretical calculation of the corresponding cross section. Since the proton is a composite particle, the interaction in pp collisions takes place between the proton constituents, called *partons*. Here, the main constituents are given by the three valence quarks (uud), while additional partons, so-called sea quarks and sea gluons, arise from quantum fluctuations. The probability to find parton a with momentum fraction x_a of the initial proton momentum p_A in a collision with momentum transfer Q^2 is described by the parton distribution function (PDF) $f_a(x_a, Q^2)$. While the PDF dependency on the momentum fraction x is governed by non-perturbative QCD dynamics, their dependency on Q^2 is calculable and follows the Dokshitzer-Gribov-Lipatov-Altarelli-Parisi (DGLAP) parton evolution equation [137–139] with

$$\frac{\partial}{\partial \ln(Q^2)} f_i(x, Q^2) = \sum_j \int_x^1 \frac{dz}{z} \mathcal{P}_{ij}\left(\frac{x}{z}, \alpha_s(Q^2)\right) f_j(z, Q^2). \tag{4.2}$$

Here, f_i corresponds to the PDF of parton i. The splitting functions $\mathcal{P}_{ij}\left(\frac{x}{z}, \alpha_s(Q^2)\right)$ can be understood as the probability for a parton j with an initial momentum fraction of z to radiate off another parton i with momentum fraction x. They are defined for $q \to qg$, $\bar{q} \to \bar{q}g$, $g \to q\bar{q}$ and $g \to gg$ splittings and can be calculated in perturbative QCD up to $\mathcal{O}(\alpha_s^4)$. The dependency of the PDFs on x is determined from experimental data. Here, a combined fit is performed by using a multitude of experimental measurements with sensitivities to different quark flavours and kinematic regions in Q^2 and x. This global QCD analysis typically includes data from deep inelastic scattering in $e^{\pm}p$ collisions as measured at the HERA collider, as well as data from pp collisions at the Tevatron and the LHC. The sets of PDFs are obtained by parametrizing the dependency on x at a reference scale Q_0^2 of the order of a few GeV^2 and then applying the evolution to the kinematic region of the experimental data. The different data points then provide the input for a global fit. Figure 4.9 shows an example of the PDF set from the NNPDF collaboration [140] at a low and high momentum scale. Here, two clear peaks appear for the valence u-quarks and d-quarks around $x \sim 0.30$, while the contribution from sea quarks and sea gluons is dominant only at lower momentum fractions. In addition, the contribution from the sea quarks and sea gluons becomes even more important for larger momentum transfer, when the proton structure is probed at higher energy scales Q^2.

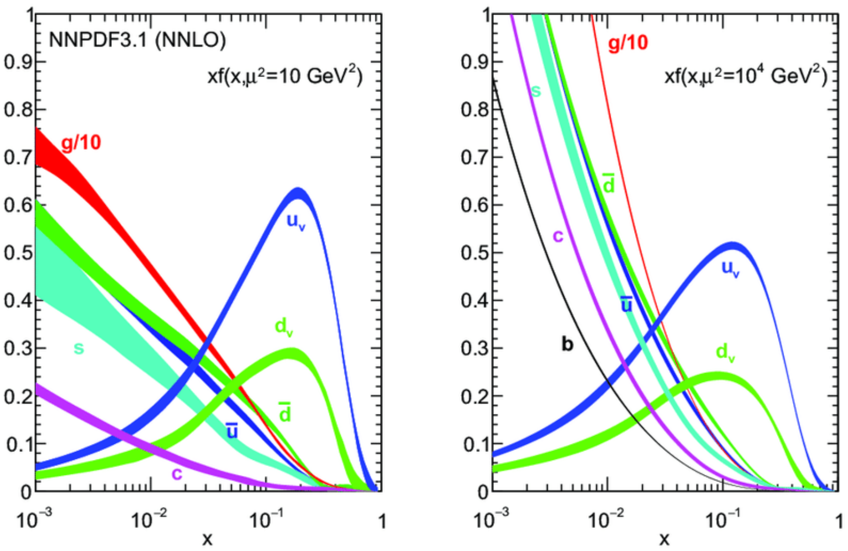

Figure 4.9.: Example of parton distribution functions at momentum scales of $10\,\mathrm{GeV}^2$ (left) and $10^4\,\mathrm{GeV}^2$ (right) from the NNPDF set [140].

In order to calculate the final cross section the factorization theorem [141] allows for the separation of the total pp cross section into a hard scattering process at partonic level, which is governed by short distance interactions (hard interactions) and can be determined by perturbation theory, and the internal non-perturbative dynamics of the proton, which is governed by large distance interactions (soft interactions) and described by the PDFs. This separation is depicted in Figure 4.10 and requires the introduction of a factorization scale μ_F. The total cross section $\sigma(AB \to X)$ can then be expressed in terms of the partonic cross-section $\hat{\sigma}(ab \to X)$ and the PDFs of the interacting partons a and b by integrating over their momenta for all possible parton-flavour combinations:

$$\sigma(AB \to X) = \sum_{a,b} \int dx_a dx_b f_a(x_a, \mu_F^2) f_b(x_b, \mu_F^2) \hat{\sigma}(ab \to X). \tag{4.3}$$

The partonic cross section can be determined with perturbative QCD by calculating the matrix element $\mathcal{M}(ab \to X)$, which contains the dynamical information of the process. This matrix element is obtained by evaluating the transition amplitudes between the initial state ab and the final state X, which can be represented by Feynman diagrams [142]. Depending on the complexity of the interaction, these diagrams describe the process with a defined order in the coupling strength α_s. Here, the lowest order contributing to the cross section $\hat{\sigma}_0$ is also called leading-order (LO) contribution, while higher orders in α_s are refered to as n-next-to-leading order contributions. By integrating the matrix elements over the full phase space, divergencies in the higher-order contributions arise, which result in unphysical predictions for the cross section. This can be solved by introducing the renormalization scale μ_R, which regularizes the finite and divergent parts in the cross-section prediction. With this, the divergencies are absorbed inside the coupling strength, which therefore gains a dependency on μ_R and is said to be running. Since both the factorization and renormalization scales are arbitrary parameters, they are often set to the same value $\mu = \mu_F = \mu_R$. The partonic cross section, evaluated up to a fixed order n in α_s, can then be expressed with the LO cross section $\hat{\sigma}_0$ in terms of a power series in α_s and the center-of-mass energy of the colliding partons $\hat{s}$[2]:

$$\hat{\sigma}(\mu_R^2, \hat{s}) = \hat{\sigma}_0 \left(1 + c_1\alpha_s + c_2\alpha_s^2 + ... + c_n\alpha_s^n\right). \tag{4.4}$$

While the precision of the cross-section prediction clearly increases with higher orders, the computation of these contributions gets significantly complicated. In case of a complete cross-section calculation in terms of pertubation series, the prediction would be independent on the scale choice. However, since only finite-order predictions can be obtained, theoretical uncertainties account for the respective scale choices.

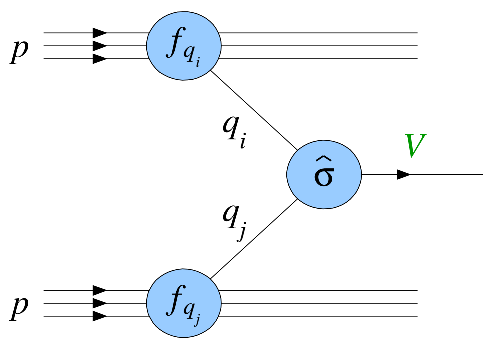

Figure 4.10.: Schematic representation of the factorization approach for the cross-section calculation of a process $pp \to X$ in the partonic cross-section $\hat{\sigma}$ from the hard scattering of the partons q_i, q_j and their parton distribution functions f_q.

The long distance evolution of partons, which participate in the hard scattering, is described by the parton shower. Here, the evolution from higher partonic momenta down to smaller values on the order of the scale Λ_{QCD} is obtained by applying an iterative branching of the type $q \to qg$, $g \to q\bar{q}$ and $g \to gg$ according to the splitting functions in Equation 4.2. Both, initial and final state partons can undergo partonic branching. If an initial state parton radiates off another parton, this is called initial state radiation (ISR), while final state ratiation (FSR) describes the same process, but related to a final-state parton.

[2]Under the assumption of massless partons, $m_a = m_b = 0$, the partonic center-of-mass energy is given by $\hat{s} = x_a x_b p_A p_B$ and can be related to the center-of-mass energy of the colliding protons s by $\hat{s} = x_a x_b s$

At energy scales below $\Lambda_{\mathrm{QCD}} \approx 1\,\mathrm{GeV}$ non-perturbative effects of confinement start to become relevant [143]. Here, the partonic splitting becomes less likely to be resolved and the formation of colour-neutral hadrons takes place, which is called *hadronization*. As in this energy regime large values of the strong coupling appear for small momenta, the hadronization process cannot be calculated with perturbative QCD. Instead, different models, which are tuned to data, are used to describe the hadronization. Common models correspond to the string fragmentation [144] and the parton-cluster fragmentation model [145].

The behaviour of the remaining partons, which do not contribute to the hard scattering, is modelled in the *underlying* event. Here, parton shower and hadronization as well as multi-parton interactions (MPI) of the proton remnants in the highly non-perturbative regime are decribed by phenomenological models tuned to data. This typically results in final states containing large multiplicities of stable particles and hence requires sophisticated experimental techniques to reconstruct and identify the physics objects of interest in the experiment.

4.3.2. Monte-Carlo Simulation

The complex phenomenology of pp collisions with the high multiplicity of final state particles requires the application of sophisticated Monte-Carlo (MC) methods to provide a complete and accurate prediction of the considered process on an event-by-event basis. These MC simulations can be divided into different steps, which are illustrated in Figure 4.11: The matrix-element calculation of the hard interaction, the parton shower, the hadronization and decay of short-living particles and the underlying event. The combination of the fixed-order matrix-element calculation of the hard interaction with the parton shower requires the application of so-called matching and merging algorithms to avoid double counting and ensure that all phase-space regions are populated sufficiently. Here, commonly used methods are the CKKW [146] or MLM [147] matching. Both approaches are based on the phase-space division into soft emission regions of the parton shower and regions with large angles and high energies, where the kinematics of the hard and well separated jets are best described by the matrix-element calculations. Some examples of MC event generators, which are used in this analysis, are the multi-purpose generators Pythia [148] and Sherpa [149]. Both generators are used for LO matrix-element calculations and for simulations of parton shower, hadronization, decay and underlying event and can be interfaced with other generators. A higher precision in the matrix-element calculations at NLO accurancy is achieved with the generators PowHeg [150–153] and MG5_aMc@Nlo [154]. Both generators also allow for the matching between NLO matrix-element calculations and parton shower.

In addition to the steps described above, *in-time* and *out-of-time* pile-up effects need to be simulated. Here, in-time pile-up corresponds to the interaction of multiple partons in one bunch crossing, while the scattering of protons from bunches before or after the one under consideration is referred to as out-of-time pile-up. These pile-up effects are simulated by overlaying events from the hard scattering process with simulated inclusive samples, which have minimum-bias requirements applied. This is done for different numbers of interactions per bunch crossing μ in order to account for the varying luminosity conditions during data taking. For 2015, the mean number of interactions per bunch crossing is $\langle\mu\rangle = 15$, which increased to $\langle\mu\rangle = 21$ for data taken in 2016. Scale factors are applied to the simulated events in order to reweight their μ-distribution to match the observed shape in data. In this analysis, the minimum-bias events are simulated with Pythia 8 by using the MSTW2008LO PDF set [155] with the A2 Tune [156].

In the last step, all simulated events are passed to a detector simulation based on Geant4 [157], where the interaction of the particles produced in the event generation with the detector material is processed. This simulation is based on a detailed description of the ATLAS detector geometry [158]. The reconstruction of the simulated events is then performed identically to the reconstruction of data events and is described in detail in Chapter 5.

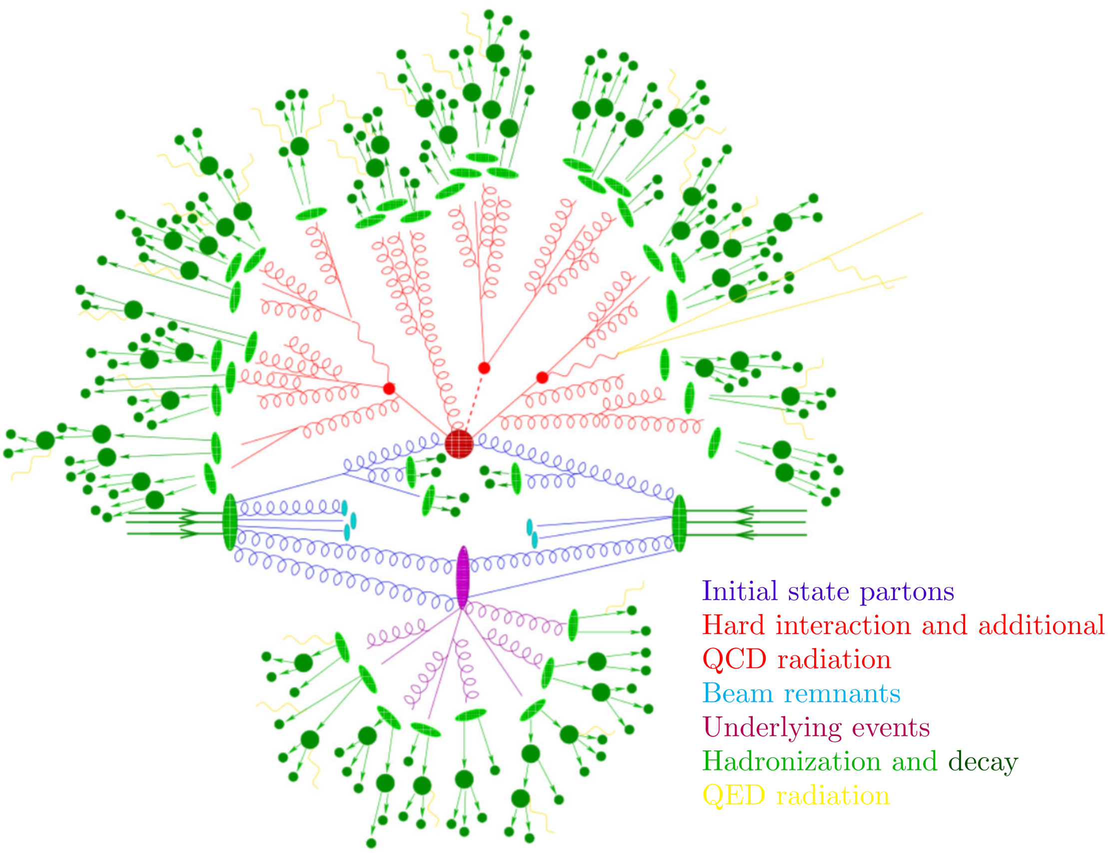

Figure 4.11.: Illustration of an event produced in pp collisions as considered by an event generator [159].

4.3.3. Simulated Signal and Background Processes

The signal and background processes described in Section 4.1 and 4.2 are simulated with various generators as summarized in Table 4.1. For most processes, separate generators are used for the matrix-element (ME) calculation of the hard interactions and for the modelling of parton shower, hadronization and underlying event (PS+UE). The event generation and cross-section predictions for all Higgs-boson processes are obtained for a Higgs-boson mass of $m_H = 125.09\,\mathrm{GeV}$.

The Higgs-boson production in the ggF channel is simulated with the PowHeg-Box v2 [150–153] NNLOPS program [160] using the MiNLO approach [161] at NLO precision in QCD, where the events are reweighted to NNLO in QCD in the Higgs rapidity. The ME is calculated at NNLO precision with the PDF4LHC15 set [162]. The ggF production is normalized to a $\mathrm{N^3LO}$ cross-section calculation in QCD, where NLO electroweak (EW) corrections are applied [70–72].

Signal events from VBF and VH production are generated with PowHeg-Box v2 using the MiNLO approach at NLO accuracy in QCD and the PDF4LHC15 set at NLO precision. The normalization of the VBF production is taken from an approximate-NNLO QCD calculation with NLO EW corrections included [73–75]. For the VH production, a NNLO cross-section calculation in QCD is used, where EW corrections are applied at NLO precision [76–78]. The modelling of PS+UE is done with Pythia 8 [163] using the CTEQ6L1 set [164] for ggF, VBF and VH production. In addition, signal events are generated in the ggF and VBF channel with Herwig 7.0.3 [165, 166] to evaluate the impact of systematic uncertainties from PS+UE modelling.

In the ttH channel, the event generation is done in MG5_aMc@Nlo [154] with the NNPDF30LO set [167], while PS+UE are simulated in Pythia 8 with the NNPDF23LO set [168] and the A14 tune [169] for non-perturbative effects. QED emissions from electroweak vertices and charged leptons are modelled with Photos++ version 3.52 [170]. The ttH production is normalized to a NLO calculation in QCD including NLO EW corrections [79–84].

Background contributions from $W^{\pm}$-boson and Z^0-boson production with additional jets and di-boson production are simulated with Sherpa 2.2.1 [149]. Here, the ME calculation is done with the Comix [171] and OpenLoops [172] generators, where the ME for $W^{\pm}$-boson and Z^0-boson production is calculated at NLO for up to two additional partons and at LO for up to four additional partons. For di-boson production, the matrix elements are calculated for up to one additional parton at NLO and up to three additional partons at LO precision. Events for these background processes are generated with the NNPDF30NNLO set [167], where PS+UE are modelled in Sherpa 2.2.1. [173] and merged to the matrix-element calculation by using the ME+PSNLO prescription [174]. In addition, alternative samples with different generator combinations are used to investigate systematic uncertainties from $W^{\pm}$-boson and Z^0-boson production. Here, events are generated with MG5_aMc@Nlo 2.2.2 at LO interfaced to Pythia 8, where the NNPDF23LO set and the A14 tune is used. These samples allow to evaluate the impact of PS+UE uncertainties in the analysis and provide a comparison of the modelling precision at LO and NLO for leading jets. The normalization of $W^{\pm}$-boson and Z^0-boson production with additional jets is obtained with NNLO calculations from FEWZ [175, 176], while the calculation for EW production is done at LO. For EW Z^0-boson production with two or three jets it was found, that the SHERPA predictions underestimates the cross section with respect to ATLAS Run 2 measurements and also with respect to an alternative NLO sample [177]. Thus, the predicted SHERPA cross section for EW $Z + jj$- and $Z + jjj$-production is corrected with a factor of 1.7, which is derived from a combination of the observed discrepancies in the fiducial regions of Table 17 of Ref. [177]. This correction is only applied in the VBF CP analysis and not in the $H \to \tau\tau$ cross-section measurement. For di-boson production, the inclusive cross section is normalized to the NLO calculation.

The ME generation of top-quark pair production $t\bar{t}$ is done with the POWHEG-Box v2 generator using the CT10 PDF set [121] and interfaced to PYTHIA 6 [178] for the simulation of PS+UE. Here, the CTEQ6L1 PDF set with the corresponding Perugia 2012 tune [156] is used. The predicted cross section is obtained with Top++2.0 at NNLO precision in perturbative QCD with soft gluon resummation at next-to-next-to-leading-log (NNLL) precision [179]. Single top-quark production is simulated with the POWHEG-Box v1 [180, 181] generator, which uses the four-flavour scheme for the ME calculation at NLO precision and the fixed four flavour CT10F4 PDF set. PS+UE are simulated in PYTHIA 6 [178] with the CTEQ6L1 set. For all top-quark processes, a top-quark mass of 172.5 GeV is assumed and the spin correlation is modelled with MadSpin [182]. The EVTGENv1.2.0 program [183] is used to model properties of c-hadron and b-hadron decays.

Background contributions from QCD multi-jet production are not modelled with MC simulation, but estimated in a data-driven way as described in Section 6.2.3.

Process	Generator		PDF set		$\sigma \times \mathcal{BR}$ [pb]	
	ME	PS+UE	ME	PS+UE		
Signal with $m_H = 125.09\,\text{GeV}$						
ggF $H \to \tau\tau$	PowHeg-Box v2	Pythia 8 (Herwig 7)	PDF4LHC15 NNLO	CTEQ6L1	3.04	N^{3}LO QCD + NLO EW
VBF $H \to \tau\tau$	PowHeg-Box v2	Pythia 8 (Herwig 7)	PDF4LHC15 NLO	CTEQ6L1	0.24	NNLO QCD + NLO EW
VH $H \to \tau\tau$	PowHeg-Box v2	Pythia 8	PDF4LHC15 NLO	CTEQ6L1	0.14	NNLO QCD + NLO EW
ttH $H \to \tau\tau$, $W \to \ell\nu$ ($\ell = e, \mu, \tau$)	MG5_aMc@Nlo 2.2.2	Pythia 8	NNPDF30LO	NNPDF23LO	0.05	NLO QCD + NLO EW
ggF $H \to WW \to \ell\nu\ell\nu$ ($\ell = e, \mu, \tau$)	PowHeg-Box v2	Pythia 8	PDF4LHC15 NNLO	CTEQ6L1	1.12	N^{3}LO QCD + NLO EW
VBF $H \to WW \to \ell\nu\ell\nu$ ($\ell = e, \mu, \tau$)	PowHeg-Box v2	Pythia 8	PDF4LHC15 NLO	CTEQ6L1	0.09	NNLO QCD + NLO EW
Background						
$Z \to \ell\ell$ ($\ell = e, \mu, \tau$)	Sherpa 2.2.1 (MG5_aMc@Nlo 2.2.2)	Sherpa 2.2.1 (Pythia 8)	NNPDF30NLO		40400	NNLO
$W \to \ell\nu$ ($\ell = e, \mu, \tau$)	Sherpa 2.2.1	Sherpa 2.2.1	NNPDF30NLO		184500	NNLO
EW $Z \to \ell\ell$ ($\ell = e, \mu, \tau$)	Sherpa 2.2.1	Sherpa 2.2.1	NNPDF30NLO		1.91	LO
EW $W \to \ell\nu$ ($\ell = e, \mu, \tau$)	Sherpa 2.2.1	Sherpa 2.2.1	NNPDF30NLO		20.25	LO
Di-boson	Sherpa 2.2.1	Sherpa 2.2.1	NNPDF30NLO		130	NLO
$t\bar{t}$	PowHeg-Box v2	Pythia 6	CT10	CTEQ6L1	2100	NNLO+NNLL
single top	PowHeg-Box v1	Pythia 6	CT10	CTEQ6L1	140	NLO

Table 4.1.: Overview of MC generators used for the different signal and background processes and their predicted cross sections at $\sqrt{s}$=13 TeV. Alternative event generators, which are used to estimate systematic uncertainties, are shown in parantheses.

4.4. Reweighting Procedure for CP-Violating HVV Couplings

The search for CP violation in HVV interactions requires a variety of signal predictions for different coupling models. As the simulation of signal events for each of these coupling scenarios is very expensive in terms of computing resources, a matrix-element based reweighting method is applied on the existing VBF $H \to \tau\tau$ and $H \to WW$ events with SM-like HVV coupling structures. For this, event weights are calculated as the ratio of the squared matrix-element of the required coupling model, which corresponds to a specific $\tilde{d}$-value, to the squared matrix-element of the SM interaction:

$$w(\tilde{d}) = \frac{|\mathcal{M}(\tilde{d})|^2}{|\mathcal{M}_{\mathrm{SM}}|^2}. \tag{4.5}$$

This reweighting method requires as input the flavour information of the incoming and outgoing partons as well as the four momenta of the outgoing partons and the Higgs boson. The kinematics of the incoming partons are calculated with their Bjorken values $x_{1(2)}$ from the final-state constituents as defined in Equation 2.66. The matrix elements for SM and CP-violating interactions are calculated at LO for two and three final-state partons separately with HAWK [78] and the CT10 PDF set.

In order to validate the reweighting, SM VBF $H \to \tau\tau$ events are generated at NLO with MG5_aMC@NLO and are reweighted to a CP-violating model with $\tilde{d} = 0.1$ [30]. The reweighted sample is then compared to events, which are directly generated with MG5_aMC@NLO for the same $\tilde{d}$-value. The comparison of the Optimal Observable shape between these directly generated and reweighted events are shown in Figure 4.12. Here, a good agreement of the distributions is observed, which allows to validate the reweighting procedure for non-SM processes at approximate NLO precision.

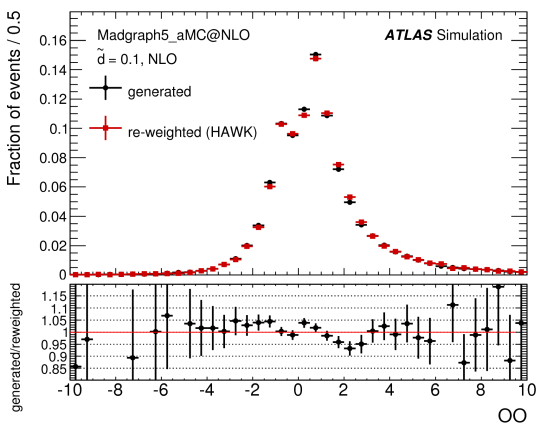

Figure 4.12.: Comparison of the Optimal Observable distribution at generator level between directly generated events with MG5_aMC@NLO at NLO precision with $\tilde{d} = 0.1$ and events, which are obtained by reweighting the SM prediction to $\tilde{d} = 0.1$ [30].

5 Reconstruction and Identification of Physics Objects

This chapter describes the reconstruction and identification techniques to build physics objects from the basic detector signals of hits and energy depositions in the sub-systems of the ATLAS detector. For the analysis of $H \to \tau\tau$ decays in the fully-leptonic final state, the reconstruction of electrons, muons and missing transverse energy is of particular importance. Additionally produced jets are also relevant for the presented analyses to categorize events according to the targeted Higgs-boson production mode. In particular, the VBF CP analysis is based on the distinct kinematic signature of the VBF Higgs-boson production channel by exclusively selecting events, which contain two well separated jets with a large invariant mass. Furthermore, a sufficient background rejection relies on the identification of hadronically decaying τ-leptons as well as on jet-flavour tagging methods, such as *b-tagging*. The reconstruction and identification algorithms can be applied for various operation points, which corresponds to different selection efficiencies and background rejections. Here, simulated events and collision data undergo the same reconstruction and identification procedure to allow for a reasonable comparison in the analysis. In addition, scale factors are applied to simulated events in order to account for differences in reconstruction, identification and trigger selection efficiencies compared to data.

The chapter is organized as follows: The first part gives an overview of the reconstruction of tracks and vertices in the inner detector (ID). This is followed by a description of the reconstruction and identification techniques for electrons, muons and jets along with a brief summary of the exploited b-tagging algorithm. Then, the reconstruction of missing transverse energy and the identification of hadronically decaying τ-leptons is discussed. The procedure for overlap removal between leptons and jets in the analysis is then described in the next section. The chapter closes with an overview of the trigger selection as part of the event selection in the $H \to \tau\tau$ cross-section analysis and the VBF CP analysis, which are discussed in Section 6.1 and Section 7.1, respectively.

5.1. Tracks and Vertices

The reconstruction of tracks and vertices in the ID allows to measure the momentum of charged particles and to identify primary and secondary vertices in the collision event. For this, a combination of different iterative tracking algorithms are used to reconstruct the trajectories of particles traversing the ATLAS detector [184]. The track reconstruction with the *inside-out* algorithm is seeded by clusters of three-dimensional space points corresponding to energy depositions in the IBL and pixel layer. The extrapolation to the outer

ID layers is achieved with a combinatorial Kalman filter [185,186], which successively adds hits to the seed when moving away from the interaction point. Track candidates are then matched to signals from drift-circles around the wires in the TRT. Different combinations of seed and space-point extensions on the same layer lead to track candidate ambiguities. They can be resolved by assigning a track score corresponding to the probablilty that a candidate correctly represents the trajectory of the particle and then processing the collection of tracks in decreasing order of this score. Track candidates are removed from the collection, if they fail additional quality criteria on the the minimum number of associated hits or on the reconstructed transverse momentum. For data taking in Run 2, the track quality cuts require at least seven hits in the pixel and SCT layers and a minimum transverse momentum of 500 MeV. A detailed description of the track finding requirements are given in Ref. [187]. This *inside-out* approach mainly succeeds in finding primary tracks from particles, which are directly produced in the collision. For the reconstruction of particle tracks originating from subsequent decays, where no hits are found in the silicon layers, the *outside-in* algorithm starts from TRT track segments and extrapolates them to the ID layers.

Primary and secondary vertices can be reconstructed by looking for intersections of the extrapolated tracks. Here, the global maximum in the distribution of z-coordinates for reconstructed tracks, which are compatible with the expected bunch-crossing region, serves as seed for the vertex-finding algorithm [188]. The vertex position is then determined by constructing a vertex candidate from a χ^2-fit to the considered tracks and cleaning for outliers, if the calculated χ^2-value between the vertex candidate and the trajectory is less than 8 %. These outliers are then used as seed for a new vertex finding procedure. At least two tracks are required to be associated to a vertex, where the vertex reconstruction efficiency ranges from approximately 85 % for two associated tracks to greater than 95 % for a larger number of associated tracks [189]. If multiple vertices are reconstructed in the event, the primary vertex is chosen as the intersection point with the largest sum of squared transverse track momenta assigned to it. Figure 5.1 shows the primary vertex resolutions for data taken in 2015 and for simulated events as a function of the number of associated tracks.

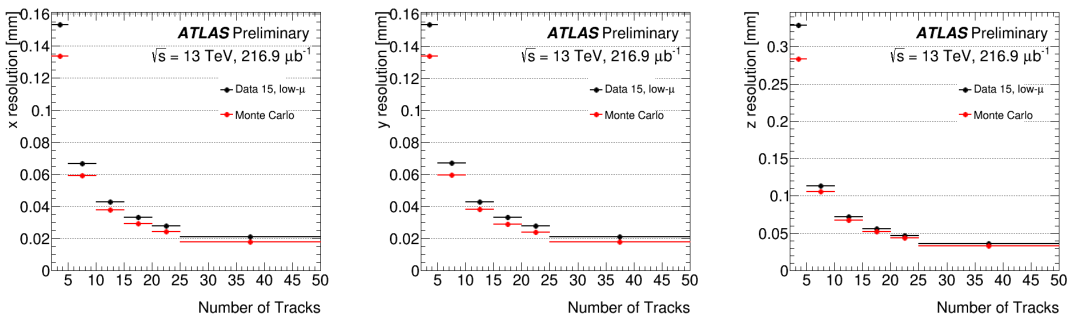

(a) (b) (c)

Figure 5.1.: Primary vertex resolution as a function of the average number of tracks for low-μ data and simulation [189].

5.2. Electrons

Electrons constitute an important signature of $H \to \tau\tau$ decays in the fully-leptonic final state. Thus, high electron reconstruction and identification efficiencies as well as a precise understanding are important for the analysis.

5.2.1. Reconstruction

The reconstruction of electron candidates is based on the cluster localization from energy depositions in the electromagnetic calorimeter (EMCal), the trajectory reconstructed in the ID and the matching of clusters to extrapolated tracks in the (η-ϕ)-space. The energy of the electron candidate is measured from the reconstructed cluster at the electromagnetic scale, while its spatial coordinates correspond to the parameters of the matched track at the interaction point. Electromagnetic energy clusters are seeded from energy depositions by using a *sliding-window* algorithm [190], where electromagnetic towers are build from $(N_\eta \times N_\phi) = (3 \times 4)$ elements with scanning steps of $(\Delta\eta \times \Delta\phi) = (0.025 \times 0.025)$. A cluster is seeded, if the summed transverse energy of localized energy deposits is greater than 2.5 GeV. In case of overlapping clusters, the candidate with the highest E_T is selected. In the next step, the cluster candidates are matched to reconstructed tracks from the ID. Here, only tracks with $p_T > 400\,\text{MeV}$ are considered in the global χ^2-track fitter [191], where the effect of additional energy loss due to bremsstrahlung in the detector material is accounted for by applying an additional Gaussian-sum filter [192] in the track fitting. This filter is only applied to tracks, which are matched to EM clusters and have at least four hits in the silicon layer. The matching criteria take into account the increased curvature of the elecetrons's trajectory due to lower momentum when bremsstrahlung is radiated. A track candidate is considered of good quality, if it has at least one hit in the pixel detector and at least seven hits in the silicon layers associated to it. Finally, the electron candidate is built by applying an additional matching of the track candidate after the Gaussian-sum filter to the calorimeter seed cluster with stricter matching requirements. Here, the distance between cluster-barycenter and the extrapolated track position has to fullfill $|\Delta\eta| < 0.05$ and one of the following conditions: $-0.1 < \Delta\phi < 0.05$ or $-0.2 < \Delta\phi_{res} < 0.05$, where $\Delta\phi$ and $\Delta\phi_{res}$ are calculated as $-q \times (\phi_{cluster} - \phi_{track})$ with the sign of the particle's electric charge q and the momentum of the track rescaled to the cluster energy in case of $\Delta\phi_{res}$. These asymmetric boundaries are chosen in order to include the effect of energy loss due to bremssstrahlung. The final cluster is then constructed in an extended window of size $(N_\eta \times N_\phi) = (3 \times 7)$ in the barrel, while a window size of $(N_\eta \times N_\phi) = (5 \times 5)$ is used in the endcaps region.

After selecting the electron candidates, the calibration of the cluster energy to the energy of the original electron is achieved with multivariate analysis techniques [193, 194] which correct for the expected energy loss in front of and beyond the EMCals as well as the expected energy deposits outside of the reconstructed cluster. For this, $Z \to ee$ decays are selected by imposing tight quality criteria on the electrons, where scale factors are derived from the comparison of data and simulation. The calibration procedure is validated with low-energy electrons from $J/\Psi \to ee$ decays.

The electron reconstruction efficiency corresponds to the number of reconstructed electron candidates divided by the number of electromagnetic cluster candidates and can be measured with a tag-and-probe method in $Z \rightarrow ee$ and $J/\Psi \rightarrow ee$ events. It increases from about 97 % to 99 % in the range of $E_T = 15$ - 50 GeV with an uncertainty of around 1 % for $E_T = 15$ - 20 GeV and reaching the per-mille level at higher E_T-values. Differences in the measured efficiencies between data and simulation are considered by applying scale factors to the simulated events. These corrections range between 1 - 2 % for electrons with $E_T = 15$ - 30 GeV to below 1 % for higher E_T values integrated over the full η-range.

5.2.2. Identification

The identification of electrons is based on a likelihood (LH) score giving the probablilty, that the reconstructed candidate is an electron [195, 196]. This LH score is build from a variety of input variables, which are constructed from information in the ID and the calorimeters. The LH identification of electron candidates is also performed during the online selection at the HLT stage (see Section 3.2.5). By choosing a set of thresholds for the LH discriminant, four operation points with varying signal efficiencies and background rejections are defined: *veryloose*, *loose*, *medium* and *tight*. While the loosest requirement provides the highest signal efficiency, it has to deal with larger contributions from other objects beeing misidentified as electrons compared to the tighter operation points. The analysis of $H \rightarrow \tau\tau$ decays in the fully-leptonic final state requires *medium* electrons with $p_T > 15$ GeV and $|\eta| < 2.4$, excluding the transition region between barrel and endcap calorimeters with $1.37 < |\eta| < 1.52$. Figure 5.2 shows the identification efficiencies for prompt electrons measured in data with $J/\Psi \rightarrow ee$ and $Z \rightarrow ee$ events for the *loose*, *medium* and *tight* operating points as well as the ratio of data to simulation. Here, the identification efficiency is defined as the number of identified and reconstruced electron candidates divided by the total number of reconstructed electron candidates. With the *medium* identification, the efficiency increases from 78 % for electrons with $E_T = 20$ GeV to 94 % for $E_T = 100$ GeV. The corresonding uncertainties vary in the range of 3 % to 0.1 % for $E_T = 4.5$ - 40 GeV integrated over the full η-range. As shown in Figure 5.2 (a) a higher identification efficiency is measured in data compared to simulation for low-E_T electrons. This is caused by a mismodelling of shower shapes in the EMCals, which are used to determine the threshold values in the LH score for the different operation points [196]. The dependency of the identification efficiency on pile-up expressed in terms of the number of primary vertices in the events, is found to be of the size of 5 %. The scale factors for medium electrons, which are applied to simulated events, vary between 2 % to 10 % for electrons in the range of $E_T = 15$ - 40 GeV and decrease to 1 % to 2 % for $E_T > 40$ GeV.

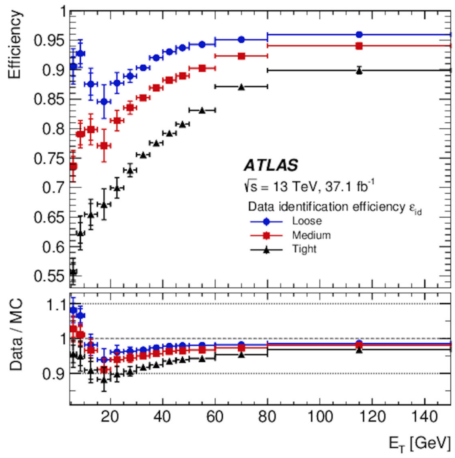

(a)

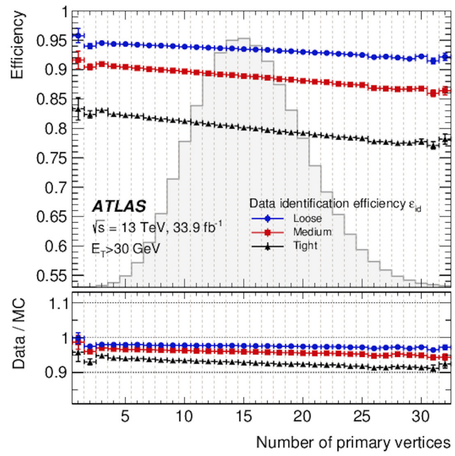

(b)

Figure 5.2.: Electron identification efficiency for *loose*, *medium* and *tight* operation points as a function of the transverse energy of the electron (a) and the number of primary vertices reconstructed in the event (b). The shaded histogram corresponds to the number of primary vertices in 2016 data. The efficiencies are measured in data with $Z \to ee$ events, where the ratios of data to simulation are shown in the lower panels [196].

5.2.3. Isolation

In general, the isolation of a particle quantifies the amount of additional energy or momentum in a cone of radius ΔR around its direction. By imposing strict requirements on the isolation, background contributions from other objects beeing misidentified as electrons can be suppressed significantly as such objects are typically produced in collimated sprays of additional particles. Furthermore, it also allows to separate between directly produced *prompt* electrons and *non-prompt* electrons that originate from the subsequent decay of heavy-flavour hadrons. The isolation criteria can be specified into calorimeter-based and track-based requirements. In the calorimeter, topological clusters [197] are build by selecting cells with energy deposits larger than four times the expected noise level for this cell and iteratively adding neighbouring cells, which have energy deposits of more than twice the noise level. The summed transverse energy of all topological clusters found within a cone of $\Delta R = 0.2$ around the cluster position of the candidate is then corrected for possible energy deposits outside the core cluster. This region is defined as a rectancle of size $(\Delta\eta \times \Delta\phi) = (0.125 \times 0.174)$ around the electron direction. Furthermore, additional energy depositions from pile-up and underlying event are subtracted [196,198]. The track-based isolation corresponds to the sum of transverse momenta of tracks found in a cone around the electron trajectory. The radius ΔR of this cone is variable and depends on p_T of the electron candidate. Only tracks with $p_T > 1\,\text{GeV}$ originating from the primary vertex are considered. Figure 5.3 shows the electron isolation efficiency as a function of E_T and η for different operation points. These efficiencies are calculated as the number of electron candidates satisfying the reconstruction, identification and isolation requirements divided by the number of identified and reconstructed candidates. They are measured in data with $J/\Psi \rightarrow ee$ and $Z \rightarrow ee$ events by imposing tight identification requirements on the electrons.

In the analyses presented in this thesis, electrons are required to satisfy the *gradient* operation point, which corresponds to varying requirements depending on the transverse momentum and target an isolation efficiency of $\epsilon_{iso} = 0.1143 \times p_T + 92.14\,\%$. This results in a rejection[1] of electrons of $10\,\%$ for $p_T = 25\,\text{GeV}$, which decreases to 1% for $p_T > 60\,\text{GeV}$. Correction factors are derived from the comparison of data to simulation and are found to be close to unity over a wide range in η and p_T. The largest difference between data and simulation for low-p_T electrons ranges from relative corrections of $2\,\%$ to $4\,\%$.

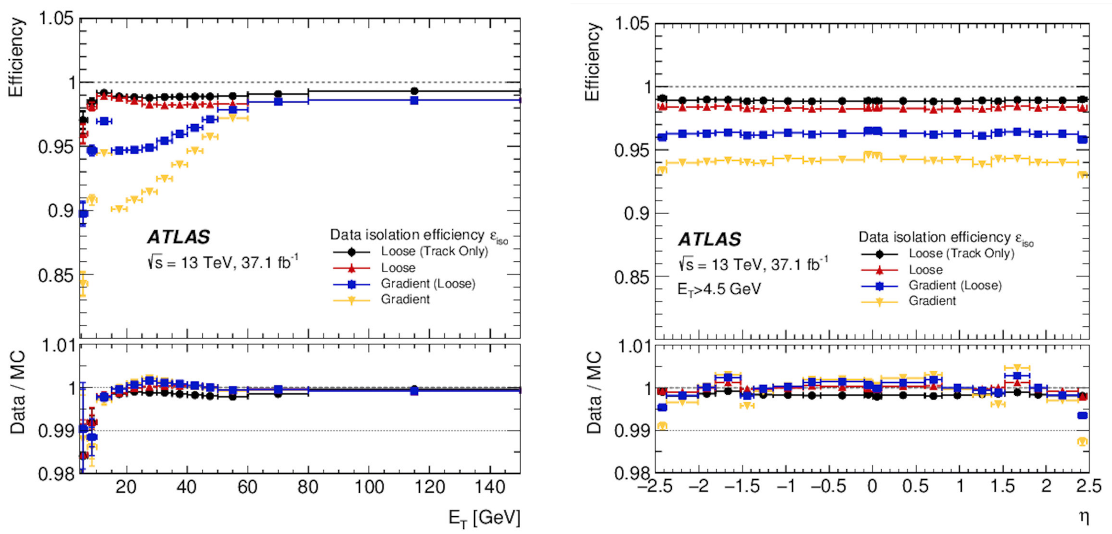

(a) (b)

Figure 5.3.: Electron isolation efficiencies for different isolation criteria as a function of the transverse energy (a) and pseudorapidity (b) measured in $Z \rightarrow ee$ events. The efficiency ratios of data to simulation are shown in the lower panels [196].

5.3. Muons

Since muons only interact very weakly with the detector material, they provide a clear experimental signature by only leaving small energy deposits in the calorimeter and traversing the outermost muon spectrometer (MS). This allows for a good distinction from electrons, photons and jets, where the combined information provided by the ID, the calorimeter and the MS is exploited for the reconstruction and identification of muon candidates.

[1]Rejection is the reciprocal of efficiency

5.3.1. Reconstruction and Isolation

The reconstruction of muon tracks in the ID follows the procedure described in Section 5.1. In the MS, the tracking algorithm is seeded by segments in the middle detectors layers, which are extrapolated to the inner and outer layers. These segments are generated with a straight line fit to hits in the layers of the MDT chambers, while CSC segments are build by searching for hit combinations in the η- and ϕ-direction. Due to the magnetic field in the MS, the muon trajectory is bent in the (R-z)-plane. Thus, the hits found in the RPC and TGC chambers allow to measure the trajectory coordinates orthogonal to this bending plane. A muon track candidate is required to have at least two matched MS segments, which can also be associated to multiple tracks to allow for close-by muons [199]. A global χ^2-fit is performed on the hits of a trajectory candidate and the track is build, if the corresponding χ^2-value satisfies the selection criteria. After building the tracks, the muon reconstruction is done with four different algorithms depending on the available information from the ID, the calorimeters and the MS [200]. For *segment-tagged* (ST) muons, the ID track candiadate has to be associated to at least one segment in the MDT or CSC chambers. *Calorimeter-tagged* (CT) muons are reconstructed by matching the ID track to calorimeter energy depositions consistent with the expected energy loss of a minimum ionizing particle. In addition, muons are labeled as *extrapolated*, if only track information from the MS is available. Here, the muon candidate is required to traverse at least two to three layers depending on the region and its associated track has to originate from the primary vertex to suppress the reconstruction of cosmic muons. The reconstruction of *combined* (CB) muons is based on the combined track information from a global fit to hits in the ID and MS sub-detectors. Here, most muons are reconstructed by extrapolating the MS track towards the detector center to find a matching track candidate in the ID.

Additional identification criteria are applied in order to enhance the fraction of promptly produced muons and to reduce the contribution from objects, which are misidentified as muons, or non-prompt muons. The analysis of the fully-leptonic $H \to \tau\tau$ final state requires combined muons satisfying the *medium* identification criteria with $p_T > 10\,\text{GeV}$ and $|\eta| < 2.5$. For the *medium* operation point, only reconstructed CB tracks are considered in the region $|\eta| < 2.5$, while the acceptance for muons can be extended to $2.5 < |\eta| < 2.7$ by using MS tracks. The CB tracks are required to have at least three hits in at least two MDT or CSC layers. For $|\eta| < 0.1$ this requirement is relaxed to tracks with at least one layer hit. The momentum measurements provided by the ID and MS are expected to differ for non-prompt muons. Thus, the absolute value of the difference between the ratio of the charge and momentum measured in the ID and MS divided by the sum in quadrature of the corresponding uncertainties (q/p significance) is required to be less than seven.

The reconstruction efficiency for muons can be measured with $J/\Psi \to \mu\mu$ and $Z \to \mu\mu$ events and is shown in Figure 5.4. For *medium* ID muons, a constant efficiency of about 99 % is obtained for $p_T > 6\,\text{GeV}$, which is also found to be stable at more than 99 % for $0.1 < |\eta| < 2.5$. The clear drop in efficiency for muons reconstructed within $|\eta| < 0.1$ is caused by an insufficient MS equipment in this region. A reduced efficiency is also observed for $\eta \approx -1.3$ due to a poorly aligned MDT chamber. The relative difference between efficiencies measured in data and simulation is found to be below 2 %.

In this analysis, muons are required to pass the *gradient* isolation requirements based on the track-based isolation $p_T^{varcone30}$ and the calorimeter-based isolation $E_T^{topocone20}$. Here, $p_T^{varcone30}$ is given by the scalar sum of transverse momenta from additional tracks found within a cone of radius $\Delta R = min(10\,\text{GeV}/p_T^{\mu}, 0.3)$ around the muon track, while $E_T^{topocone20}$ corresponds to the transverse energy sum of topological clusters around the muon within a distance of $\Delta R = 0.2$. The *gradient* isolation is tuned to obtain efficiencies of greater than 90 % (99 %) at 25 (60) GeV. Figure 5.5 shows the muon isolation efficiency for this operation point as measured in $Z \to \mu\mu$ events. For the low-E_T range, the isolation efficiency is found to range from 90 % to 93 % and increases up to 99 % for $E_T > 40$ GeV. The scale factors, which are derived from the efficiency differences in data and simulation, are below 1 % for $E_T < 50$ GeV and reach the per-mille level for higher E_T-values.

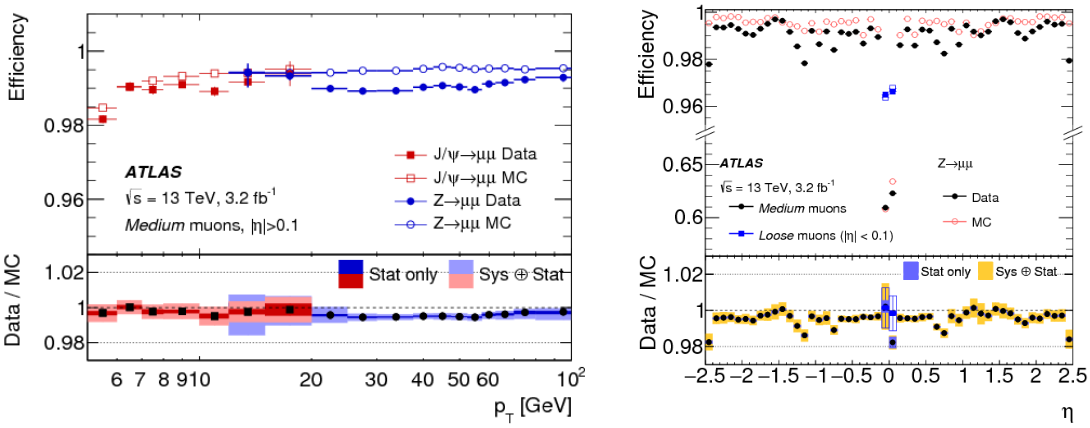

(a) (b)

Figure 5.4.: Muon reconstruction efficiency as a function of the transverse momentum (a) and pseudorapidity (b) for data and simulation. The efficiency ratios of data to simulation are shown in the lower panels [199].

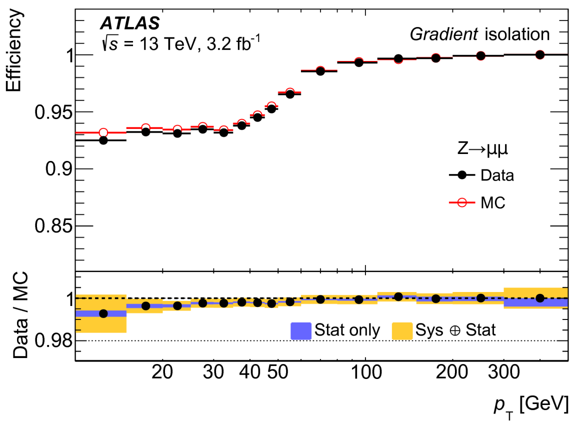

Figure 5.5.: Muon isolation efficiency for gradient isolation as a function of the transverse momentum for data and simulation. The efficiency ratios of data to simulation are shown in the lower panel [199].

5.3.2. Momentum Scale and Resolution

The imperfect description of the material distribution and detector geometry in simulation results in a discrepancy of measured muon momenta compared to data. Therefore, a calibration of the muon momentum scale and resolution is performed by applying correction factors to the simulated events. These correction factors are derived in binned maximum-likelihood fits to the invariant di-muon mass measured in $Z \to \mu\mu$ and $J/\Psi \to \mu\mu$ events, where only CB muons satisfying the *medium* identfication requirement are selected [199]. The corrections are derived separately for muon tracks measured in the ID and MS as a function of p_T, η and ϕ of the reconstructed muon. The combined corrected momentum is then given as the weighted average of corrected ID and MS momenta. The MS momentum smearing factors are found to be in the range of 1.5 % to 2.5 % with uncertainties well below 1 %, while the ID measurement has to be smeared with factors on the order of 0.5 % and 1 % for muons in the central and more forward regions, respectively. The scale correction is less than 0.2 % for the MS and between 0.05 % to 0.1 % for momentum measurements in the ID. The di-muon mass spectrum from Z-boson and J/Ψ decays is shown in Figure 5.6 for data and simulated events. Without corrections, the distribution in simulation is found to be more narrow and slightly shifted compared to the data, while the lineshipe in the corrected samples agrees well with data within the uncertainties.

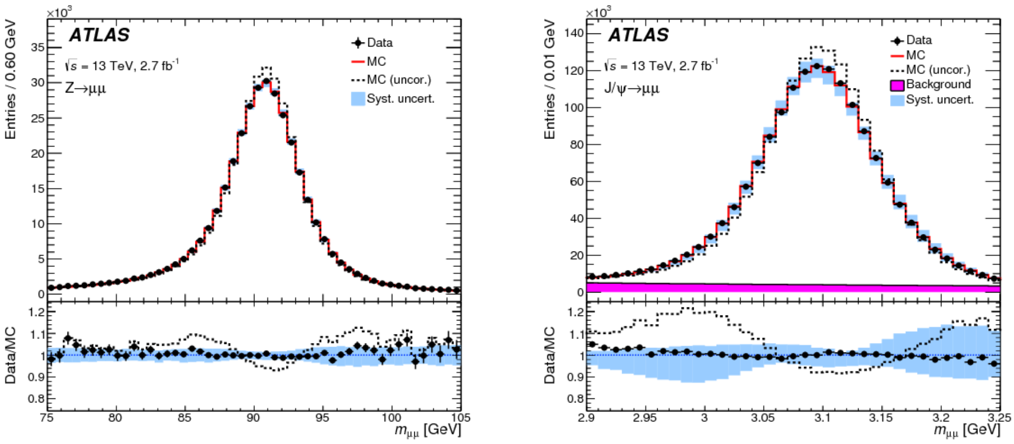

(a) (b)

Figure 5.6.: Invariant mass spectrum of the di-muon mass in $Z \to \mu\mu$ events (a) and $J/\Psi \to \mu\mu$ events (b). The distribution measured in data (black points) is compared to simulation with no corrections applied (black dotted line) and after corrections (red line) [199].

5.4. Jets

As described in Section 4.3.1, partons, which are produced in pp collisions, hadronize and are detected as collimated sprays of color-neutral particles, called *jets*, in the detector. In addition to the contributions from pile-up and underlying event, the very large cross section of QCD interactions results in an abundant production of jets. Thus, the developement of sophisticated reconstruction methods for jets is crucial for many analyses. In this analysis, the kinematics of additionally produced jets are exploited in order to define event categories, which target the topology of the main Higgs-boson production modes. The following sections describe the standard procedure of jet reconstruction with the anti-k_{T} algorithm and the calibration procedure for the jet energy scale. In addition, a brief overview of the *b-tagging* algorithm to identify jets originating from the hadronization of b-quarks is given.

5.4.1. Reconstruction

The reconstruction of jets is based on topological clusters [201] constructed in the electromagnetic and hadronic calorimeters. The cluster finding algorithm [190, 197] is seeded by calorimeter cells having an energy significance of $|E_{cell}|/\sigma_{noise} > 4$, where the cell energy E_{cell} is calculated at the electromagnetic scale and the total cell noise is given by σ_{cell}. The average noise of a calorimeter cell includes contributions from the readout electronic noise as well as pile-up noise estimated from simulation [202]. To suppress the reconstruction of pile-up jets, which are in general produced at low momentum values and do not traverse the full calorimeter, seed cells in the presamplers are excluded. The topological cluster is then built by iteratively adding all neighbouring cells, which satisfy a looser requirement on the energy significance of $|E_{cell}|/\sigma_{noise} > 2$. If one of these cells already served as a seed, the corresponding cluster is merged with the one under construction. In the last step, any neighbouring cell with positive energy contribution, but failing $|E_{cell}|/\sigma_{noise} > 2$, is added to the cluster as well. With this procedure, the final clusters are characterized by local maxima of highly significant cells, which are surrounded by cells with lower significance values. In order to allow for the separation of showers from close-by particles, an attempt is made to split clusters with multiple maxima.

The energy of the reconstructed cluster is measured at the electromagnetic scale and corresponds to the sum of all contributing cells. The cluster direction is determined as the weighted average of the η- and ϕ-coordinates of the affiliated cells. With this, every cluster is assigned a four momentum vector and serves as input for the jet finding algorithm.

In this thesis, the anti-k_{T} algorithm [203] as implemented in the FASTJET package [204] is used for the reconstruction of jets with $p_T > 20\,\mathrm{GeV}$ and $|\eta| < 4.9$. This algorithm starts by calculating a list of distances d_{ij}, d_{iB} for every input cluster i:

$$\begin{aligned} d_{ij} &= \min\left\{\frac{1}{p_{T,i}^2}, \frac{1}{p_{T,j}^2}\right\}\frac{\Delta R_{ij}^2}{R^2} \\ d_{iB} &= \frac{1}{p_{T,i}^2}. \end{aligned} \tag{5.1}$$

The variable d_{ij} gives the minimal distance between two clusters i and j, while d_{iB} corresponds to the distance of cluster i to beam B. These distances are calculated from the transverse momentum of cluster $i(j)$ $p_{T,i(j)}$, the spatial distance between the clusters ΔR_{ij} and the geometrical cone radius for a jet, the so called distance parameter R. In this analysis, a distance parameter of $R = 0.4$ is used. The anti-k_{T} algorithm then iterates over the list of input clusters and compares d_{ij} and d_{iB}. If $d_{ij} < d_{iB}$ holds, cluster i and j are combined by adding their four momentum vector. For $d_{iB} < d_{ij}$, cluster i is called a jet and removed from the list of input clusters. All distances are then recalculated and the procedure is repeated until all input clusters are used for building a jet. This approach results in circular cone shapes for high-p_T jets, while more complex shapes are obtained for jets with lower p_T. In addition, the jet construction is not affected by the additional radiation of low-p_T gluons or gluons with a low emittance angle with respect to the initial parton direction, which is referred to as *soft* and *collinear* safety.

To further suppress jets originating from pile-up events a *Jet Vertex Tagger* (JVT) [202] is employed. This algorithm is based on a multivariate likelihood method to determine the probability, wether a jet originates from the hard scattering process or was produced in a pile-up event. In this analysis, a requirement of $|\mathrm{JVT}| > 0.59$ is imposed on jets with $p_T < 50\,\mathrm{GeV}$ and $|\eta| < 2.4$. With this, the JVT provides an efficiency for hard scattering jets of 95 % with a mistagging rate from pile-up jets of 3 % for $20 < p_T < 50\,\mathrm{GeV}$. In addition, forward jets in the region $|\eta| > 2.5$ have to satisfy a forward JVT requirement [205] of $\mathrm{fJVT} > 0.4$.

5.4.2. Energy-Scale Calibration and Correction

With the reconstruction procedure described above the jet energy and momentum are measured at the electromagnetic scale. In order to account for differences in the detector response to hadronic shower particles the jet four-momentum needs to be calibrated. Additional correction factors are applied to include pile-up effects, detector inefficiencies and the dependency of the measured energy on the shower composition. A detailed description of the jet calibration methods can be found in Ref. [206].

In the first step, the spatial coordinates of the jet four-momentum are corrected to point back to the reconstructed primary vertex, while the energy component remains constant. Pile-up contributions to the measured jet energy are removed by using a jet-area based subtraction approach. This method determines the average energy density in the $(\eta \times \phi)$-plane to derive correction factors depending on the jet area, the number of primary vertices and the mean number of interactions per bunch crossing. These correction factors include contributions from *in-time* pile-up and *out-of time* pile-up effects. In the next step, the jet energy scale (JES) is calibrated with p_T- and η-dependent scale factors derived from simulated di-jet events. Here, isolated jets are reconstructed from topological clusters with the anti-k_{T} algorithm using $R = 0.4$ and are then associated to nearby *truth-level* jets, which are built in simulation from stable particles excluding final state muons and neutrinos. For the geometrical truth-matching, $\Delta R_{jet,truth} < 0.3$ is required. The calorimeter response is then determined by the ratio of measured jet momentum to the truth-level jet momentum p_T^{jet}/p_T^{truth}. A gaussian fit to this ratio allows to extract the average calorimeter response R as well as the energy resolution σ_R. The final jet calibration factor is then calculated as the inverse of the average calorimeter response. In addition, correction factor are applied to account for gaps and transition regions in the calorimeters, which result in a bias for the reconstructed jet η-direction. Furthermore, a global sequential (GS) calibration method is used to account for differences in the particle composition of the shower. In the last step, several in-situ techniques are exploited to further improve the JES calibration. In the η-intercalibration step, di-jet events with back-to-back topologies are used to derive correction factors for the average energy response to forward jets from the measured energy response of central jets. Additional correction factors are applied to simulated events to account for differences in the detector response compared to data. These scale factors are determined by exploiting the p_T balance in $Z+$jets, $\gamma+$jet and multi-jet events.

As shown in Figure 5.7 for data taken in 2015 at $\sqrt{s} = 13\,\text{TeV}$, the JES uncertainty ranges from about 5 % at $p_T = 25\,\text{GeV}$ to 2.6 % for jets with $p_T = 40\,\text{GeV}$. An uncertainty of about 1 % is reached at $p_T = 200\,\text{GeV}$ with a subsequent increase for larger p_T ranges. The JER uncertainty is found to be about 4 % for jets with $p_T = 25\,\text{GeV}$ and decreases further to 2.6 % for $p_T = 40\,\text{GeV}$ and below 1 % for values of $p_T > 200\,\text{GeV}$.

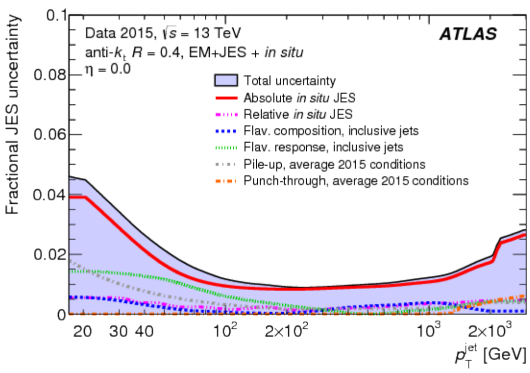

(a)

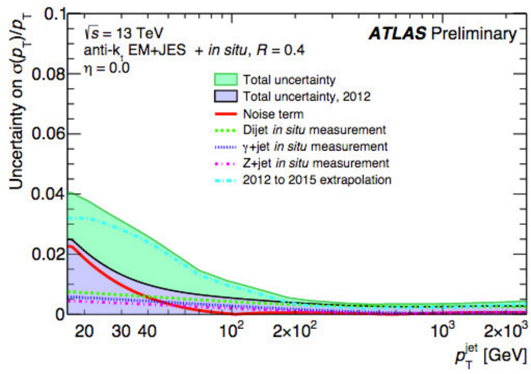

(b)

Figure 5.7.: Uncertainties on the jet energy scale (a) and jet energy resolution (b) as a function of jet p_T for $\eta = 0$ for anti-k_T jets with $\Delta R = 0.40$ [207].

5.4.3. b-Tagging

The identification of jets reconstructed from hadronic showers of b-quarks is achieved with so called *b-tagging* techniques. These algorithms exploit the long lifetime of hadrons containing b-quarks (b-hadrons) by looking for displaced vertices several mm away from the hard interaction point. In this analysis, the *b-tagging* is performed with the MV2 algorithm [208, 209], which provides a multivariate discriminant by combining complimentary information from three algorithms. For this, jets in simulated events are labeled according to the flavour of the parton, which is found within $\Delta R < 0.3$ around the jet. In addition, τ-jets are defined, if they are associated to the hadronic decay of a τ-lepton. If the jet is not matched to a b-quark, c-quark or τ-lepton, it is labeled as a light jet.

The impact parameter tagger (IP2D and IP3D) is based on information from the transverse impact parameter d_0, defined as the minimum distance of tracks to the primary

vertex in the (R-ϕ)-plane, and the longitudinal impact parameter $z_0 \sin\theta$, which gives the distance between track and primary vertex in z-direction at the point of closest approach in the (R-ϕ)-plane. In particular, the combination of impact parameter significiances, d_0/σ_{d_0} and $z_0 \sin\theta/\sigma_{z_0 \sin\theta}$ with the parameter uncertainties σ, are used to built a log-likelihood ratio (LLR) from all tracks associated to a given jet: $\sum_{i=1}^{Ntracks} \log{(p_b/p_u)}$. Here, the probability density functions for b-jets, p_b, and c- and light jets, p_u, is taken from simulations. To increase the discrimination power, these PDFs are derived for different categories depending on the hit pattern of the given track.
The secondary vertex finding (SV1) algorithm enables the explicit reconstruction of secondary decay vertices inside the jet. Inclusive vertex candidates are constructed by selecting tracks, which are significantly displaced from the primary vertex and therefore have a large impact parameter, and then refitting their track parameters using a χ^2-approach. A likelihood ratio is built from the mass of all tracks associated to that vertex, the ratio of the summed track energy from the secondary vertex to all tracks associated to the jet, the number of two track vertices and the ΔR-distance between the jet axis and the line connecting the primary and secondary vertices.
The JetFitter algorithm for multi-vertex reconstruction exploits the decay topology of b-hadron and c-hadrons in the jet and allows to even reconstruct secondary vertices with only one track. Here, a Kalman-Filter technique is used to determine the position of the decay vertices and several variables, which are sensitive to the decay topology, provide the input for a neural network.
The MV2 algorithm finally combines the output of IP2D, IP3D, SV1 and JetFitter into a multivariat-based discriminant by using a Boosted Decision Tree (BDT). The training of this BDT is based on signal samples containing b-jets from $t\bar{t}$-decays. The background sample consists of events with c-jets and light jets, where the sample composition is varied in order to tune the light-jet versus c-jet rejection performance. Figure 5.8 shows the b-tagging efficiency as a function of the rejection of light jets and c-jets for different configurations of the MV2 algorithm. The analysis presented in this thesis uses the MV2c20 2015 configuration corresponding to a training sample composition of 20 % and 80 % for c-jets and light jets, respectively. The operation point is choosen at approximately 85 % b-jet selection efficiency with a rejection factor of 2.6 for c-jets and 27.2 for light jets [210]. Possible differences in tagging efficiencies between data and simulation are corrected with scale factors, which are derived as a function of jet p_T [208, 211]. The determination of these scale factors is based on a combinatorial likelihood approach using di-leptonic $t\bar{t}$-decays for various operation points.

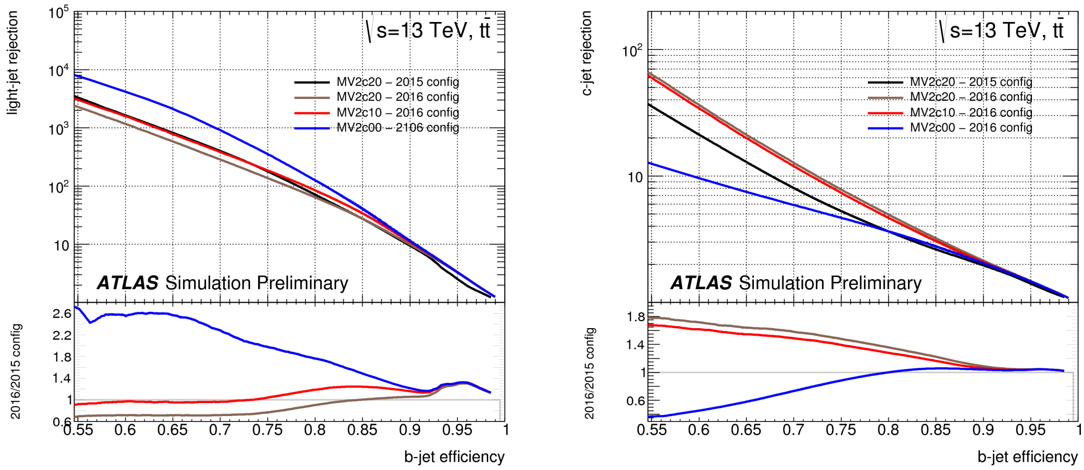

(a) (b)

Figure 5.8.: *b-tagging* efficiencies as a function of the light-jet (a) and c-jet (b) rejection for several configurations of the MV2-algorithm measured in $t\bar{t}$ events. The analysis presented in this thesis uses the MV2c20 algorithm with the 2015 configuration (black curve) [209].

5.5. Missing Transverse Energy

In pp collision, the longitudinal momentum of the interacting partons is not known. Thus, energy and momentum conservation can only by expected in the transverse plane under the assumption, that the transverse momentum of the initial state partons is zero. The imbalance in the vectorial sum of the detected transverse momentum is called missing transverse energy E_T^{miss} and corresponds to the magnitude of the transverse momentum vector, which is missing in order to achieve a total final state momentum of zero:

$$E_T^{miss} = \sqrt{\left(E_x^{miss}\right)^2 + \left(E_y^{miss}\right)^2}. \tag{5.2}$$

In a perfectly reconstructed event, E_T^{miss} only arises from weakly interacting particles, like neutrinos, which leave no signal in the detector. However, low reconstruction efficiencies as well as mismeasurements in the contribution from parton shower and underlying event can result in additional E_T^{miss} contributions in the event. As $H \to \tau\tau$ decays are characterized by a significant amount of E_T^{miss} due to the final state neutrinos from the τ-decays, it provides an important quantity to discriminate the signal from background processes, where no E_T^{miss} is expected. Moreover, the reconstruction of the invariant di-τ mass, as described in Section 6.1.1, depends on a reliable E_T^{miss} measurement as well.

The E_T^{miss} reconstruction is based on the negative sum of all energy depositions corrected with the parametrized energy loss of muons in the calorimeters [212]:

$$E_{x,y}^{miss} = -E_{x,y}^{calo} - E_{x,y}^{muon}. \tag{5.3}$$

Here, the energy depositions in the calorimeter

$$E_{x,y}^{calo} = \sum_{obj} E_{x,y}^{obj} + E_{x,y}^{soft} \tag{5.4}$$

are calculated from fully reconstructed and calibrated objects with the following requirements applied: Electrons and muons have to satisfy the *medium* identification with $p_T > 10$ GeV. For photons, $p_T > 25$ GeV and the *tight* identification are required. Hadronically decaying τ-leptons have to be reconstructed according to the *medium* requirements with $p_T > 25$ GeV. For jets, the anti-k_{T} algorithm with $\Delta R = 0.4$ and a threshold of $p_T > 25$ GeV are used.

The soft term in Equation 5.4 accounts for additional tracks and calorimeter clusters, which are not assigned to any of these objects, and hence reflects the underlying event activity, soft radiations from the hard interaction as well as contributions from pile-up events. This pile-up contribution can be reconstructed either by a calorimeter-based method (CST) or a track-based method (TST) [212]. Although the TST method misses contributions from neutral particles, it was found to be more robust against pile-up effects and is therefore used as the primary method for E_T^{miss} reconstruction in Run 2 [213]. The track soft term is built from unassociated ID tracks with $p_T > 500$ MeV, where tracks found within $\Delta R = 0.05$ of an electron or photon cluster and $\Delta R = 0.2$ around a τ_{had}-candidate are excluded. In order to reject jets originating from pile-up collisions, the TST E_T^{miss} also includes a jet-vertex-tagger requirement of $|\mathrm{JVT}| > 0.64$.

The performance of the E_T^{miss} reconstruction can be studied in $Z \to \mu\mu$ decays, where no significant amount of E_T^{miss} is expected. These studies therefore reveal information about the intrinsic detector resolution and allow to evaluate the performance and reconstruction efficiency. Figure 5.9 shows the E_T^{miss} resolution as a function of the number of primary vertices and the total sum of E_T measured $Z \to \mu\mu$ events with additionally produced jets. While the resolution is found to be relatively robust against the number of reconstructed vertices, a clear increase from 5 GeV to 20 GeV is observed in the range of $\sum E_T = 20$-100 GeV. For larger $\sum E_T$ values, the resolution further increases up to 25 GeV. Information about the E_T^{miss} scale can be obtained from studies of the reconstruction performance in $W \to l\nu$ decays, while $t\bar{t}$ events are used to study the E_T^{miss} robustness against multi-jet production [214].

5.6. Hadronic τ-Lepton Decays

In the analysis of the fully-leptonic $H \to \tau\tau$ final state, events containing hadronically decaying τ-leptons (τ_{had}) are discarded. These hadronic τ-decays take place with a branching ratio of 65 % and can be classified depending on the number of involved charged particles: Hadronic τ-decays with one charged track (*1-prong* decays) occur with a branching ratio of 72 %, while decays with three charged particles (*3-prong* decays) have a branching ratio of 22 %. The remaining decays mostly consist of final states with charged kaons. In 68 % of all cases up to three neutral pions are produced in addition.

The decay products are reconstructed as jets in the detector (see Section 5.4). In order to distinguish between τ_{had}-jets and jets originating from the hadronization of quarks or gluons, the shape of the corresponding energy depositions and the number of associated tracks is investigated. In particular, the consituents of a τ_{had}-jet tend to be highly col-

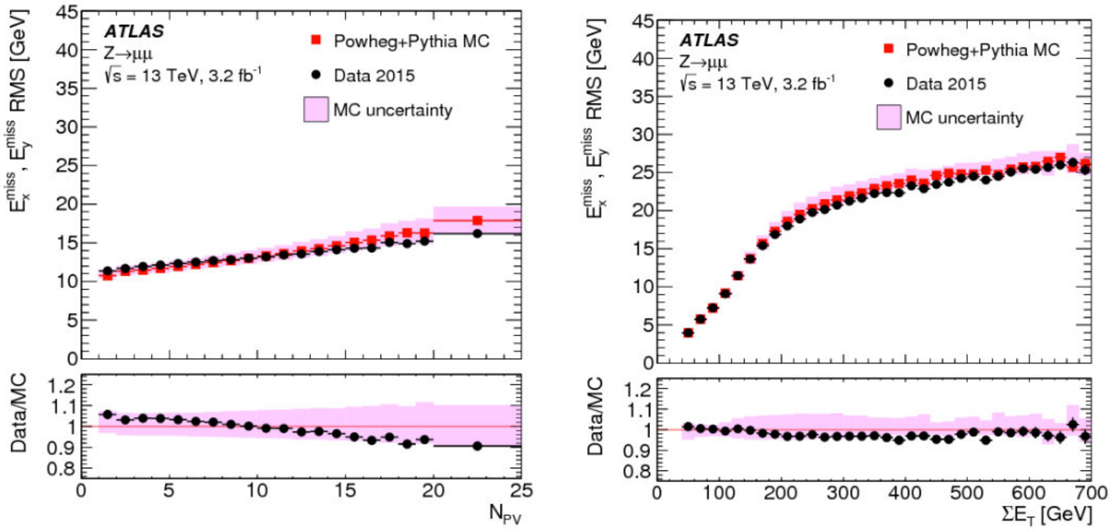

(a) (b)

Figure 5.9.: Resolution of E_T^{miss} as a function of the number of primary vertices (a) and the total sum of E_T (b) measured in inclusive $Z \to \mu\mu$ decays in data and simulation [214].

limated due to the received boost in the decay process and typically consist of a smaller number of charged and neutral pions compared to quark/gluon-jets. The identification and reconstruction algorithms are seeded by reconstructed jets with $p_T > 10$ GeV and $|\eta| < 2.5$ [215]. The decay is then classified as *1-prong* or *3-prong* depending on the number of tracks found within a cone of radius $\Delta R < 0.2$ around the jet direction. This cone is also used for the momentum reconstruction of the τ_{had}-candidate from the sum of all energy depositions. In order to suppress the contribution of quark/gluon-jets, which mimic the signature of hadronic τ-decays, a Boosted Decision Tree (BDT) is used [216]. This BDT is trained separately with signal events containing *1-prong* and *3-prong* decays against di-jet background events by exploiting shower shape and tracking information. The resulting BDT output then provides an identification discriminant and is used to define *loose, medium* and *tight* operation points. These operation points correspond to different identification efficiencies, which are designed in a way to not dependent on the p_T of the τ_{had}-candidate. Another background contribution, especially for *1-prong* τ_{had}-candidates, is given by electrons with similar detector signatures as charged pions. These events can be suppressed with a likelihood-based rejection method, where the discriminator is developed for electron identification [195, 217]. In particular, the τ_{had}-candidate is rejected, if it receives a high likelihood score for being an electron. In the analysis of the $\tau_{lep}\tau_{lep}$ final state, all events containing at least one τ_{had}-candidate with $p_T > 20$ GeV are rejected. Here, the τ_{had}-candidate has to be identified according to the *loose* operation point, which corresponds to an identification efficiency of 60 % (50 %) for *1-prong* (*3-prong*) decays.

5.7. Overlap Removal

The reconstruction algorithms described above are based on the same detector signals corresponding to energy depositions and tracks. In order to avoid duplications in the reconstruction of one particle as multiple objects, an overlap removal between jets, τ_{had}-candidates, electrons and muons is used. For this, a geometrical matching in the $(\eta - \phi)$-plane is applied, where the matched objects are removed from the event according to their misidentification probabilities. The overvlap removal in this thesis corresponds to the following procedure: First, jets are rejected from the event, if they overlap with a τ_{had}-candidate within $\Delta R = 0.2$. If the jet is found within $\Delta R = 0.4$ around an electron or muon, it is removed as well. In the next step, τ_{had}-candidates overlapping with an electron or muon within $\Delta R = 0.2$ are removed. Finally, the overlap between electrons and muons is cleared by discarding any electron within $\Delta R = 0.2$ around a muon.

5.8. Trigger Selection

This section describes the trigger selection, which is applied in an early stage of the event selection in the $H \to \tau\tau$ fully-leptonic final state (see Section 6.1). A description of the ATLAS trigger system can be found in Section 3.2.5.

The analysis uses various combinations of single-lepton and di-lepton triggers depending on the flavour of the final state leptons (ee, $\mu\mu$ or $e\mu$), which are described below. The software-based high-level triggers (HLTs) are configured with hardware-based L1 triggers as seeds and exploit offline-like identification and reconstruction algorithms for the respective trigger objects. The trigger names, which are used in the following, consist of the level (always `HLT` here), the trigger object multiplicities and types (`e` for electrons and `mu` for muons) with their respective p_{T} thresholds at trigger level as well as the imposed identification, isolation and reconstruction requirement. If the HLT trigger is seeded by more than one L1 trigger, the additional trigger name is given as a suffix as well. In the analysis, the reconstructed leptons have to be geometrically matched to the trigger object, which fired the repective trigger chambers. In order to ensure constant trigger efficiencies over the full p_T- and η-range, the p_T thresholds imposed at trigger level are further increased in the analysis. These offline p_{T} thresholds are quoted in the following.

As data taking during 2016 corresponds to a higher instantaneous luminosity and different pile-up conditions compared to the 2015 period, the exploited trigger types and p_T thresholds are adjusted accordingly. The trigger efficiencies are determined with respect to an offline-selected data sample, where the ratio of measured efficiency in data to the one in simulation is used to correct simulated events with scale factors depending on p_T, η and ϕ. In the analysis, single electrons are selected with a trigger efficiency between 90 % and 95 % [134]. For the selection of single muons, the trigger efficiency is found to be about 80 % and 70 % in the barrel region for 2015 and 2016 events, respectively, and 90 % in the endcaps [134]. In order to enable the exclusive selection of events in the analysis, di-muon and di-electron triggers are only considered, if the highest-p_{T} lepton (*leading* lepton) does not pass the requirements of the single-lepton trigger.

$\mu\mu$-Final State

For data taken in 2015, events containing two muons are accepted, if the leading muon with $p_T > 21\,\text{GeV}$ is matched to either the `HLT_mu20_iloose_L1MU15` or the `HLT_mu50` trigger. Otherwise, the di-muon trigger `HLT_mu18_mu8noL1` is exploited, where a leading muon with $p_T > 19\,\text{GeV}$ and a sub-leading muon with $p_T > 10\,\text{GeV}$ are required.

For the 2016 period, the single-muon triggers `HLT_mu26_ivarmedium` or `HLT_mu50` are used with a threshold of $p_T > 28\,\text{GeV}$ for the leading muon. The di-muon trigger is changed to `HLT_mu22_mu8noL1` and the thresholds correspond to $p_T > 24$ GeV and $p_T > 10\,\text{GeV}$ for the leading and sub-leading muon, respectively.

ee-Final State

Events containing two electrons from the 2015 period are selected, if the leading electron with $p_T > 25\,\text{GeV}$ is matched to either `HLT_e24_lhmedium_L1EM20VH`, `HLT_e60_lhmedium` or `HLT_e120_lhloose`. If the selection requirements of these single-electron triggers fail, the di-electron trigger `HLT_2e12_lhloose_L12EM10VH` is used for events containing two electrons with $p_T > 15\,\text{GeV}$.

For 2016 events, the `HLT_e26_lhtight_nod0_ivarloose`, `HLT_e60_lhmedium_nod0` or `HLT_e140_lhloose_nod0` are used instead and the p_T threshold on the leading electron is increased to $p_T > 27\,\text{GeV}$. The di-electron trigger is changed to `HLT_2e17_lhvloose_nod0`, while the p_{T} thresholds remain the same compared to the 2015 selection.

$e\mu$-Final State

In the different flavour final state with one electron and one muon, events are selected based on single-electron and single-muon triggers as well as electron-muon triggers. The first selection is based on the single-lepton trigger for electrons and muons, which corresponds to the single-trigger selection in the ee- and $\mu\mu$-final states described above. Here, the single-electron trigger is given preference due to its higher efficiency compared to the single-muon trigger and the corresponding p_{T} threshold for electrons is applied in case both triggers fired. If none of these single-lepton trigger requirements succeed, the selection of 2015 events exploits the `HLT_e17_loose_mu14` trigger, while for the 2016 data taking period `HLT_e17_lhloose_nod0_mu14` is used. For both triggers, electrons are required to have $p_T > 18\,\text{GeV}$, while a threshold of $p_T > 15\,\text{GeV}$ is applied for muons.

6 Measurement of the $H \to \tau\tau$ Production Cross-Section

This chapter presents the measurement of the cross section times branching ratio for Higgs-boson production with decays into τ-leptons $H \to \tau\tau$ in the fully-leptonic final state $\tau_{lep}\tau_{lep}$. The analysis investigates the dataset collected in 2015 and 2016 at $\sqrt{s} = 13\,\text{TeV}$ corresponding to $36.1\,\text{fb}^{-1}$ and is based on the categorization of events into regions, which target the distinct kinematic signatures of the gluon-fusion (ggF) and vector-boson fusion (VBF) production modes of the Higgs boson. The $H \to \tau\tau$ signal is then extracted by performing a maximum likelihood fit in the reconstructed di-τ mass in these signal categories.

The chapter is organized as follows: First, Section 6.1 gives an overview of the methods to reconstruct the invariant di-τ mass and describes the basic preselection and signal region requirements. The estimation of the relevant background contributions is described in Section 6.2. This is followed by Section 6.3 with a discussion of systematic uncertainties and Section 6.4 describes the statistical model. The last part, Section 6.5, presents the obtained results in the $\tau_{lep}\tau_{lep}$ final state and summarizes the combined measurements with the $\tau_{lep}\tau_{had}$ and $\tau_{had}\tau_{had}$ channels.

6.1. Event Selection

This section describes the selection criteria applied to data and simulated events in order to enhance the relative contribution of $H \to \tau\tau$ events in the signal regions of the $\tau_{lep}\tau_{lep}$ channel. First, the basic preselection looks for events with the final-state objects, that are expected in fully-leptonic di-τ decays, and applies a series of kinematic requirements to reduce the contribution from various background processes. In the second step, the signal regions are defined by categorizing the selected events into regions, which are enriched in signal events from the ggF and VBF Higgs-boson production modes. In order to allow for a reasonable comparison between data and simulation before the statistical analysis, *pre-fit* normalization factors are applied to $Z \to \tau\tau$, $Z \to \ell\ell$ and top-quark background events and can be found in Table 6.3. As discussed in Section 6.2, these normalization factors are determined in dedicated control regions, which are enriched in events from the background process under consideration.

6.1.1. Invariant Mass Reconstruction

The invariant mass of the di-τ system is an important variable in order to discriminate $H \to \tau\tau$ decays from background processes, where no Higgs boson is produced. In particular, it allows to separate signal events from the irreducible $Z \to \tau\tau$ background, which constitutes the dominant contribution in the analysis. However, due to the final-state neutrinos (*invisible* decay products), adding the four momenta of the electrons or muons from the τ-decays (*visible* decay products) does not result in the invariant mass of the Higgs-boson candidate. The following section describes the two approaches, which are exploited in the analysis in order to reconstruct this mass.

Collinear Approximation

The collinear approximation [218] is based on the assumption, that the invisible decay products are emitted in the same direction as the visible system. Furthermore, the missing transverse energy in the event is assumed to only originate from the neutrinos of the τ-decay. By using the measurement of the missing transverse energy $\boldsymbol{E_T^{miss}} = (E_{T,x}^{miss}, E_{T,y}^{miss})$ and transverse momentum of the leptons $\boldsymbol{p_{T,1(2)}^{vis}} = (p_{x,1(2)}^{vis}, p_{y,1(2)}^{vis})$, the fraction of τ-momenta carried by the visible decay products can be expressed as follows:

$$x_{1(2)} = \frac{p_{x,2}^{vis} p_{y,1}^{vis} - p_{y,2}^{vis} p_{x,1}^{vis}}{p_{x,2}^{vis} p_{y,1}^{vis} + (-)E_{T,x}^{miss} p_{x,1(2)}^{vis} - p_{y,2}^{vis} p_{y,1}^{vis} - (+)E_{T,y}^{miss} p_{x,1(2)}^{vis}}. \tag{6.1}$$

Assuming massless leptons, the collinear mass of the di-τ system is then constructed from the invariant mass m_{vis} and the momentum fractions of the visible decay products:

$$m_{\tau\tau}^{coll} = \frac{m_{vis}}{\sqrt{x_1 x_2}}. \tag{6.2}$$

While this method provides a good resolution for events with boosted topologies, it can result in an overestimation of the invariant mass for events, where the collinear assumption for the decay products is not valid. In particular, Equation 6.1 becomes degenerate for events with back-to-back topologies of the decay products. This leads to unphysical values for x_1, x_2 and long tails in the invariant mass distribution, which reduce the separation power between signal and background events. Hence, the basic preselection described in Section 6.1.2 already requires at least one high-p_T jet in the event and also imposes an upper threshold on the spatial separation of the selected leptons.

Figure 6.1 shows the distributions of the collinear mass for $H \to \tau\tau$ and $Z \to \tau\tau$ events in the $\tau_{lep}\tau_{lep}$ VBF and boosted categories, which are defined in Section 6.1.3. Overall, the algorithm is able to reproduce the invariant masses of the respective resonances. In the VBF region, the mean of the invariant mass distributions is 124.7 GeV for $H \to \tau_{lep}\tau_{lep}$ events and 99.7 GeV for $Z \to \tau\tau$ events. These values change only slightly in the boosted region to 126.3 GeV and 100.2 GeV for $H \to \tau_{lep}\tau_{lep}$ and $Z \to \tau\tau$ events, respectively. For $H \to \tau_{lep}\tau_{lep}$ decays, the VBF region provides a better mass resolution with a standard deviation of 18.9 GeV compared to 21.1 GeV in the boosted region. For $Z \to \tau\tau$ decays, the resolution is 20.5 GeV in the VBF region and 19.6 GeV in the boosted region.

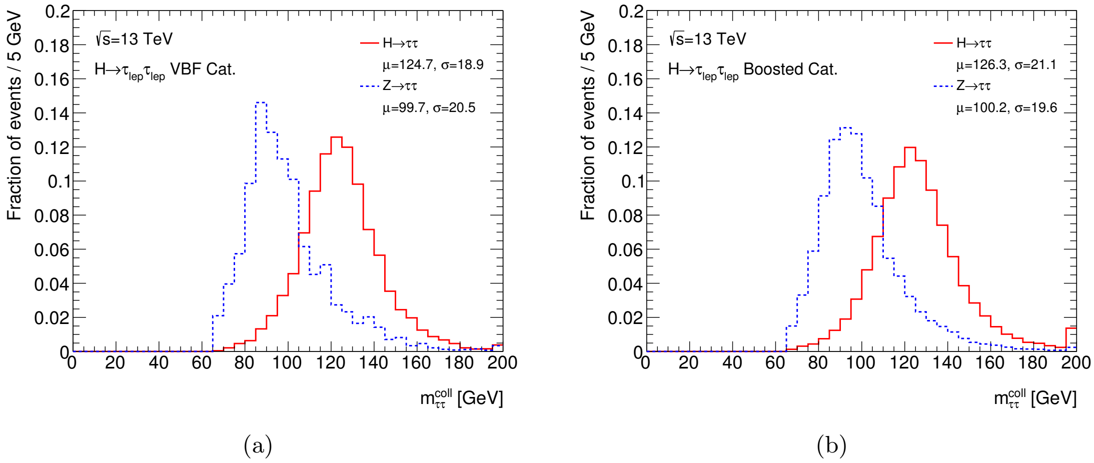

Figure 6.1.: Normalized distributions of the reconstructed di-τ mass in the collinear approximation for $H \to \tau_{lep}\tau_{lep}$ and $Z \to \tau\tau$ events in the VBF category (a) and the boosted category (b) of the $\tau_{lep}\tau_{lep}$ channel.

Missing Mass Calculator

The missing mass calculator (MMC) [219] does not rely on the collinearity assumption, but can be applied for any di-τ decay topology. The algorithm is based on probability density functions for the τ-decay properties and provides an estimate for the most probable kinematic configuration of the neutrino system. For this, a system of equations needs to be solved, where the number of unknown variables depend on the di-τ decay channel. In the fully-leptonic final state the MMC algorithm has to determine eight variables corresponding to the three components of the invisible momentum $p_{1/2}^{miss}$ and the invariant mass $m_{1/2}^{miss}$ of the two-neutrino system from each τ-decay. However, the mass-shell requirements for the τ-leptons only allow to derive the following four equations:

$$\begin{aligned}
E_{T,x}^{miss} &= p_1^{miss}\sin(\theta_1^{miss})\cos(\phi_1^{miss}) + p_2^{miss}\sin(\theta_2^{miss})\cos(\phi_2^{miss})\\
E_{T,y}^{miss} &= p_1^{miss}\sin(\theta_1^{miss})\sin(\phi_1^{miss}) + p_2^{miss}\sin(\theta_2^{miss})\sin(\phi_2^{miss})\\
m_{\tau 1}^2 &= (m_1^{miss})^2 + (m_1^{vis})^2 + 2\sqrt{(p_1^{miss})^2 + (m_1^{miss})^2}\sqrt{(p_1^{vis})^2 + (m_1^{vis})^2}\\
&\quad - 2p_1^{vis}p_1^{miss}\cos(\theta_1^{vis} - \theta_1^{miss})\\
m_{\tau 2}^2 &= (m_2^{miss})^2 + (m_2^{vis})^2 + 2\sqrt{(p_2^{miss})^2 + (m_2^{miss})^2}\sqrt{(p_2^{vis})^2 + (m_2^{vis})^2}\\
&\quad - 2p_2^{vis}p_2^{miss}\cos(\theta_2^{vis} - \theta_2^{miss}).
\end{aligned} \tag{6.3}$$

Since the available information is not sufficient to determine all required variables, the MMC algorithm uses probability density functions (PDFs) depending on the τ-decay kinematics to find the most probable solutions. These PDFs are determined from simulation. The solutions are obtained by performing a scan over the unknown variables of the neutrino system ($\phi_1^{miss}, \phi_2^{miss}, m_1^{miss}, m_2^{miss}$) and solving the set of equations given in Equation 6.3 for each of these scan points. In addition, the solutions are weighted according to the event likelihood calculated for the respective τ-decay kinematics. The most probable value, which corresponds to the maximum of weighted solutions for each scan point, is then used as an estimate for the di-τ mass $m_{\tau\tau}^{\mathrm{MMC}}$. The dependency of the MMC performance on the E_T^{miss} resolution is taken into account by additionally scanning over $(E_{T,x}^{miss}, E_{T,y}^{miss})$ and weighting each scan point with a Gaussian probability depending on the scalar sum of all transverse energy deposits in the calorimeter $\sum_i E_T^i$. The MMC algorithm does not find a solution for events with large fluctuations in the E_T^{miss} measurement, which happens in $< 1\,\%$ of all considered $H \to \tau_{lep}\tau_{lep}$ and $Z \to \tau\tau$ events.

Figure 6.2 shows the $m_{\tau\tau}^{\mathrm{MMC}}$ distributions for $H \to \tau_{lep}\tau_{lep}$ and $Z \to \tau\tau$ events in the VBF and boosted categories of the $\tau_{lep}\tau_{lep}$ channel. For $H \to \tau_{lep}\tau_{lep}$ decays, the MMC algorithm provides an estimated mass of 120.7 GeV in the VBF category and 122.4 GeV in the boosted category. The resolution of the reconstructed mass is 17.4 GeV in the VBF and 19.7 GeV in the boosted region, which corresponds to improvements of about 8 % and 6 %, respectively, compared to the collinear approximation. The Z^0-boson mass is reconstructed as 95.9 GeV and 97.0 GeV in the VBF and boosted category and a resolution of 18.2 GeV and 17.4 GeV is achieved, respectively. This corresponds to an improvement of about 11 % in both categories with respect to the collinear approximation. The reconstucted MMC mass is chosen as the final discriminating variable to extract the $H \to \tau\tau$ signal in the analysis.

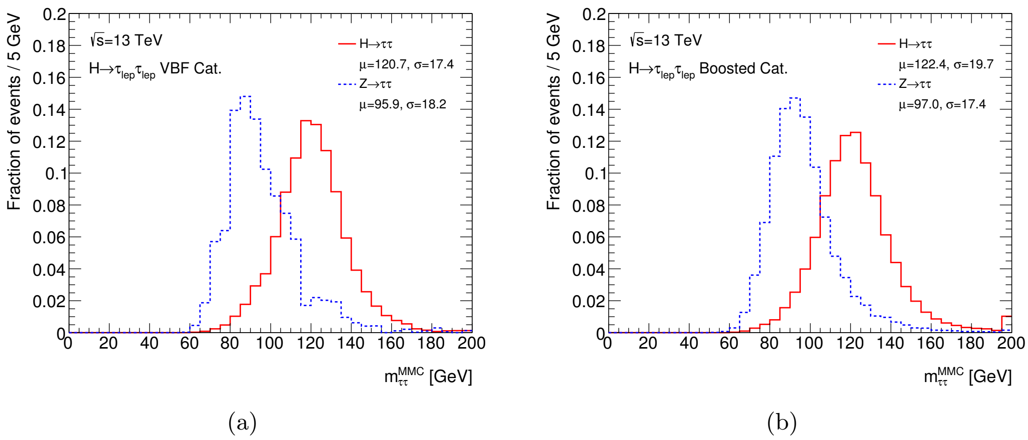

Figure 6.2.: Normalized distributions of the reconstructed di-τ mass with the missing mass calculator (MMC) for $H \to \tau_{lep}\tau_{lep}$ and $Z \to \tau\tau$ events in the VBF category (a) and the boosted category (b) of the $\tau_{lep}\tau_{lep}$ channel.

6.1.2. Preselection

The first part of the preselection consists of requirements, which are applied to data and simulated events in order to ensure sufficient data quality for further analysis.

(1) **Good runs list:**
Data events have to be included in the 2015 and 2016 good runs list (GRL) to reject events from problematic data taking periods, where the ATLAS detector was not fully operational.

(2) **Primary vertex:**
In order to reject events from cosmic radiation and beam induced background effects, at least one primary vertex candidate with a minimum of two associated tracks with $p_T > 0.5$ GeV has to be reconstructed in the event.

(3) **Jet cleaning:**
Events are removed, if any reconstructed jet is associated to suspicious energy depositions in the calorimeters. These depositions can originate from hardware failure, beam halo effects or cosmic rays [220].

In the next step, basic preselection requirements are applied in order to select events with final-state objects expected from fully-leptonic $H \to \tau\tau$ decays:

(4) **Two leptons:**
Exactly two leptons (ee, $\mu\mu$ or $e\mu$) of opposite electric charge are required in the event. These leptons have to fulfill the *medium* identification and *gradient* isolation criteria described in Section 5.2 and 5.3. In the following, the lepton with the highest(second-highest) p_{T} is referred to as the leading (sub-leading) lepton ℓ_0 (ℓ_1).

(5) **τ_{had}-veto:**
Events are removed, if a hadronically decaying τ-candidate passing the *loose* identification requirement is found. This cut removes background contributions from hadronic τ-decays and ensures orthogonality to the $\tau_{lep}\tau_{had}$ and $\tau_{had}\tau_{had}$ analyses.

(6) **Trigger:**
The event has to be triggered following the strategy described in Section 5.8. In addition, the selected leptons in the event are required to match the trigger objects.

(7) **Leading jet:**
At least one jet with $p_T > 40$ GeV is required in the event. This jet is referred to as the *leading* jet j_0 in the following.

In addition, further requirements are applied on kinematic variables related to the visible decay leptons and the missing transverse energy. These requirements improve the suppression of specific background processes and enhance the relative signal contribution further. Figure 6.3 shows as an example the separation power of the invariant di-lepton mass, the missing transverse energy and the distance in ΔR and $\Delta\eta$ between the selected leptons. Here, the variables are shown at selection stages before the respective requirements are applied, while the estimation of the fake-lepton background already includes the requirements described in Section 6.2.3.

(8) **Di-lepton mass:**
Different thresholds are imposed on the reconstructed di-lepton mass depending on the flavour of the final-state leptons: In the different-flavour (DF) channel $30 < m_{\ell\ell} < 100$ GeV is required, which is tightend to $30 < m_{\ell\ell} < 75$ GeV in the same-flavour (SF) final state. As shown in Figure 6.3 (a), this requirement effectively removes events from $Z \to \ell\ell$ decays, which give one of the dominant background contributions in the SF channel.

(9) **Missing transverse energy:**
In the $\tau_{lep}\tau_{lep}$ channel, a significant amount of E_T^{miss} is expected due the four neutrinos from the τ-decays. Hence, $E_T^{miss} > 55\,\text{GeV}$ is required in the SF channel, while for the DF final state a cut of $E_T^{miss} > 20\,\text{GeV}$ is imposed. As shown in Figure 6.3 (c) and (d), this cut significantly reduces the contribution from $Z \to \ell\ell$ decays, where the missing transverse energy only arises due to mismeasured E_T^{miss} contributions. In addition, the minimum threshold also removes events from leptonic di-boson decays without neutrinos. In the SF channel, the background suppression can be improved further by also exploiting the missing transverse energy from high-p_T objects (HPTO), where only the selected leptons and the leading jet are taken into account, and a requirement of $E_T^{miss}(\text{HPTO}) > 55\,\text{GeV}$ is applied.

(10) **Momentum fraction:**
In order to remove events, where the direction of the missing transverse energy is not in agreement with the expected kinematics from di-τ decays, the momentum fractions of the decay leptons as defined in Equation 6.1 are required to be in the range of $0.1 < x_{0,1} < 1$. This allows to reject processes, where the leptonic system does not originate from the decay of a resonance and is therefore not necessarily aligned with the direction of the E_T^{miss}.

(11) **Lepton separation**:
At the LHC, most Z^0-bosons are produced with low transverse momenta, which results in a larger separation of their decay products compared to leptons from di-τ-decays. The distribution of the lepton separation in ΔR and $|\Delta\eta|$ are shown in Figure 6.3 (e) and (f), respectively. In the analysis, upper thresholds of $\Delta R_{\ell\ell} < 2.0$ and $|\Delta\eta_{\ell\ell}| < 1.5$ are applied.

(12) **Collinear mass:**
In the $\tau_{lep}\tau_{lep}$ channel, a lower threshold of $m_{\tau\tau}^{coll} > m_Z - 25 \approx 66\,\text{GeV}$ with m_Z referring to the Z^0-boson mass is required for the collinear mass. This cut ensures orthogonality to analyses investigating $H \to WW$ decays.

(13) **b-jet veto:**
The event is rejected, if any jet with $p_T > 25\,\text{GeV}$ contains the decay products of b-hadrons. For this, the b-tagging technique described in Section 5.4.3 is exploited and the cut effectively removes background events containing b-quarks.

(14) **MMC mass:**
If the MMC algorithm does not converge, the event is not considered for further analysis.

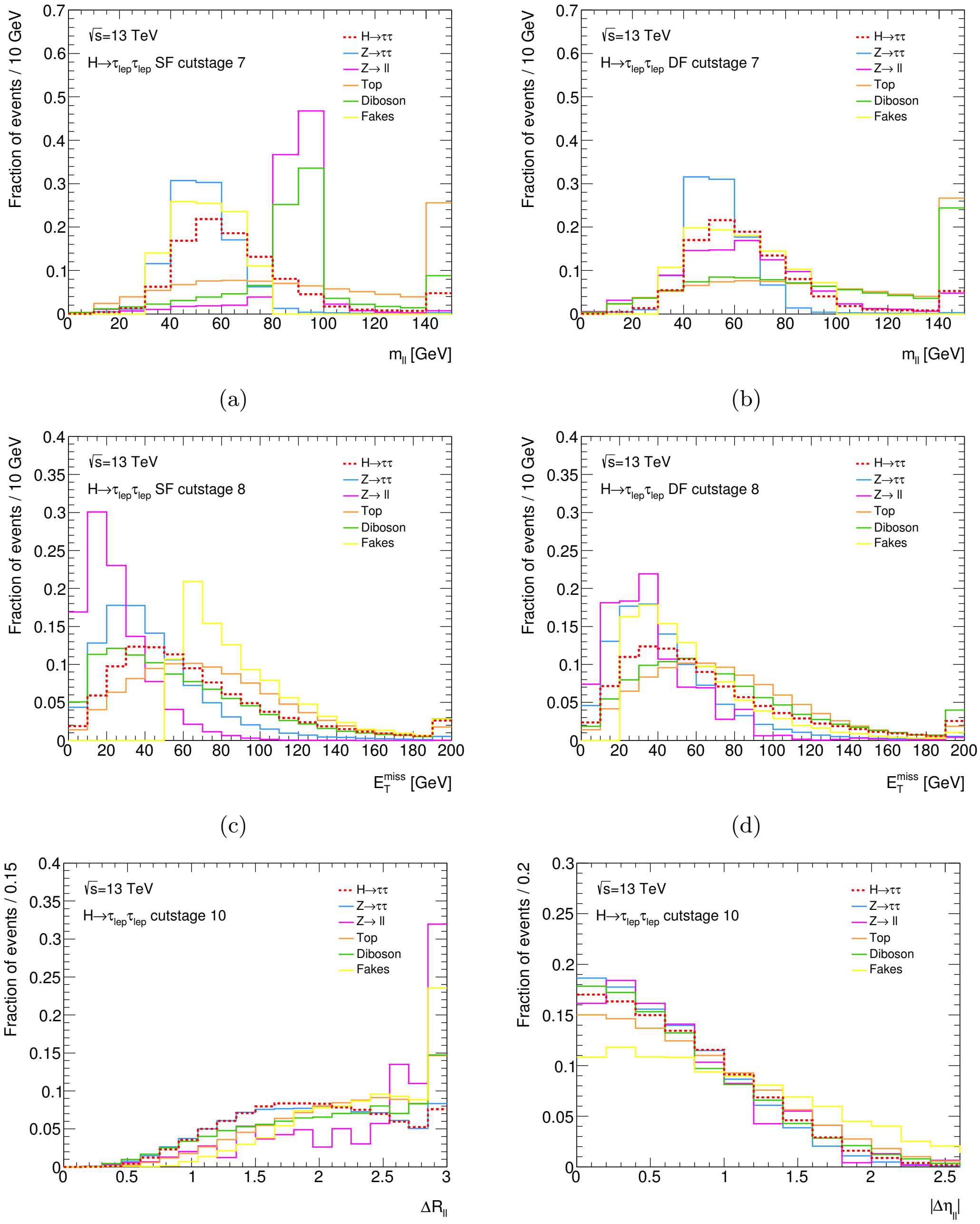

Figure 6.3.: Normalized distributions of the di-lepton mass in the same-flavour (a) and different-flavour channel (b), the missing transverse energy in the same-flavour (c) and different-flavour channel (d), the ΔR separation between the leptons (e) and their $|\Delta\eta|$ separation (f) in the $\tau_{lep}\tau_{lep}$ final state at different stages of the preselection as defined in the text.

Figure 6.4 and 6.5 show various kinematic variables after this preselection, where a good agreement between data and prediction is obtained within the considered uncertainties. The expected event yields for signal and background processes compared to the observed data events are summarized in Table 6.1. The sum of expected signal and background events is found to agree with the observed data yield within statistical uncertainties. The expected $H \to \tau\tau$ signal corresponds to 108.78 ± 0.64 events and is mainly composed of events from Higgs-boson production in the ggF channel with a relative contribution of 67 % and in the VBF channel with a relative contribution of 26 %. The remaining signal events from the associated production with vector-bosons, WH and ZH, as well as the top-quark associated production ttH provide only 7 % of the total expected signal. The total expected background corresponds to 10640 ± 110 events, where the largest fraction arises from $Z \to \tau\tau$ decays with 75 %. The relative contribution from the fake-lepton background is expected to be 8 % and top-quark events constitute 6 % of the total background. Events from $Z \to \ell\ell$ decays correspond to 6 % of the total expected background, where 95 % of these events are expected in the SF final-state. Smaller background contributions arise from di-boson production with 4 % and $H \to WW$ events with less than 1 % of the total expected background.

Process		Preselection
ggF	$H \to \tau\tau$	72.41 ± 0.54
VBF	$H \to \tau\tau$	28.28 ± 0.14
WH	$H \to \tau\tau$	5.35 ± 0.18
ZH	$H \to \tau\tau$	2.54 ± 0.12
ttH	$H \to \tau\tau$	0.20 ± 0.05
$Z \to \tau\tau$		7998 ± 63
$Z \to \ell\ell$		675 ± 84
Top		678 ± 12
Di-Boson		438.6 ± 5.6
Fakes		806 ± 27
$H \to WW$		42.68 ± 0.52
Total bkg.		$10\,640 \pm 110$
$H \to \tau\tau$		108.78 ± 0.64
Data		10630

Table 6.1.: Expected event yields with statistical uncertainties after the preselection in the $\tau_{lep}\tau_{lep}$ channel for signal and background processes compared to the observed data. The normalization factors summarized in Table 6.3 are applied to the $Z \to \tau\tau$, $Z \to \ell\ell$ and top-quark backgrounds.

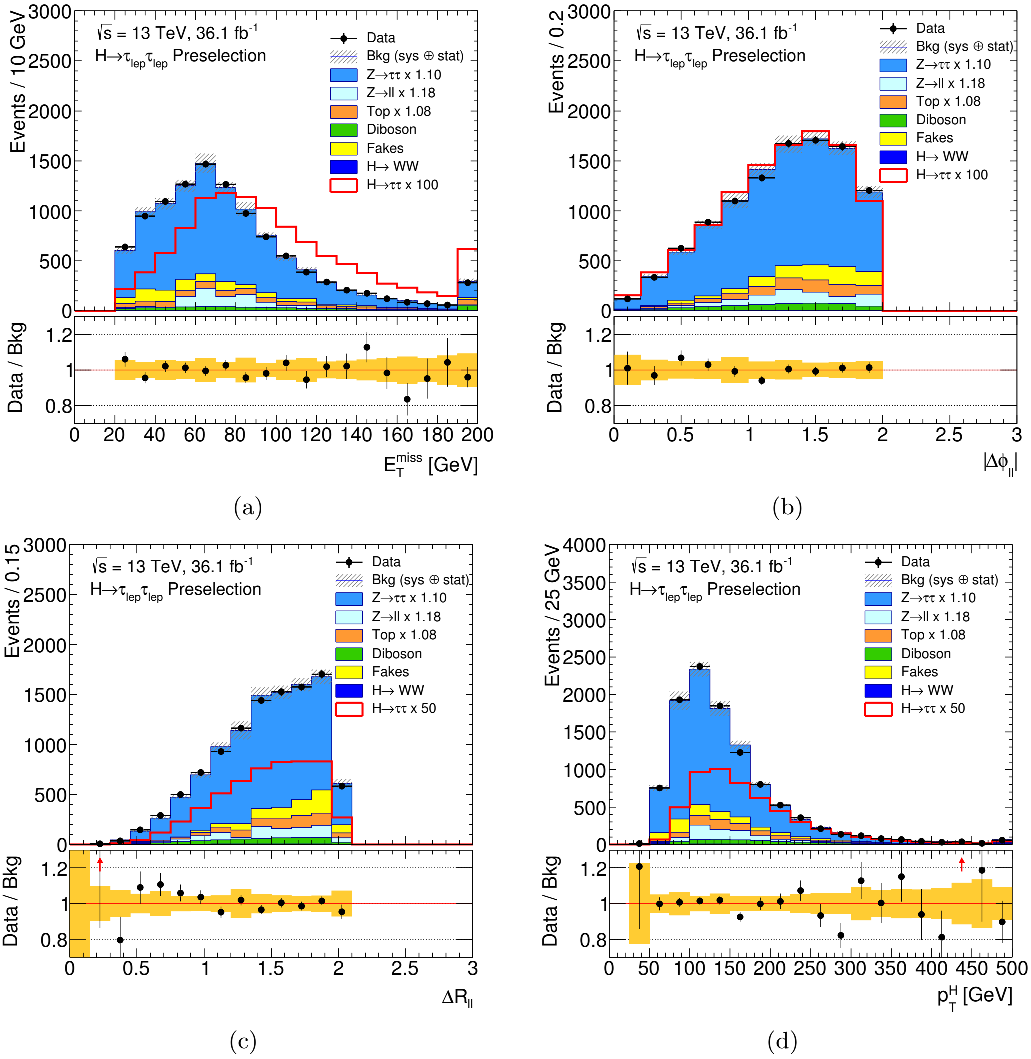

Figure 6.4.: Distributions of the missing transverse energy (a), the separation of the leptons in terms of $|\Delta\phi|$ (b) and ΔR (c) and the transverse momentum of the Higgs-boson candidate (d) after the preselection in the $\tau_{lep}\tau_{lep}$ channel. The Higgs-boson candidate is calculated from the vectorial sum of the visible τ-decay products and the missing transverse energy. The uncertainty band includes statistical uncertainties and those systematic uncertainties, which are applied as event weights.

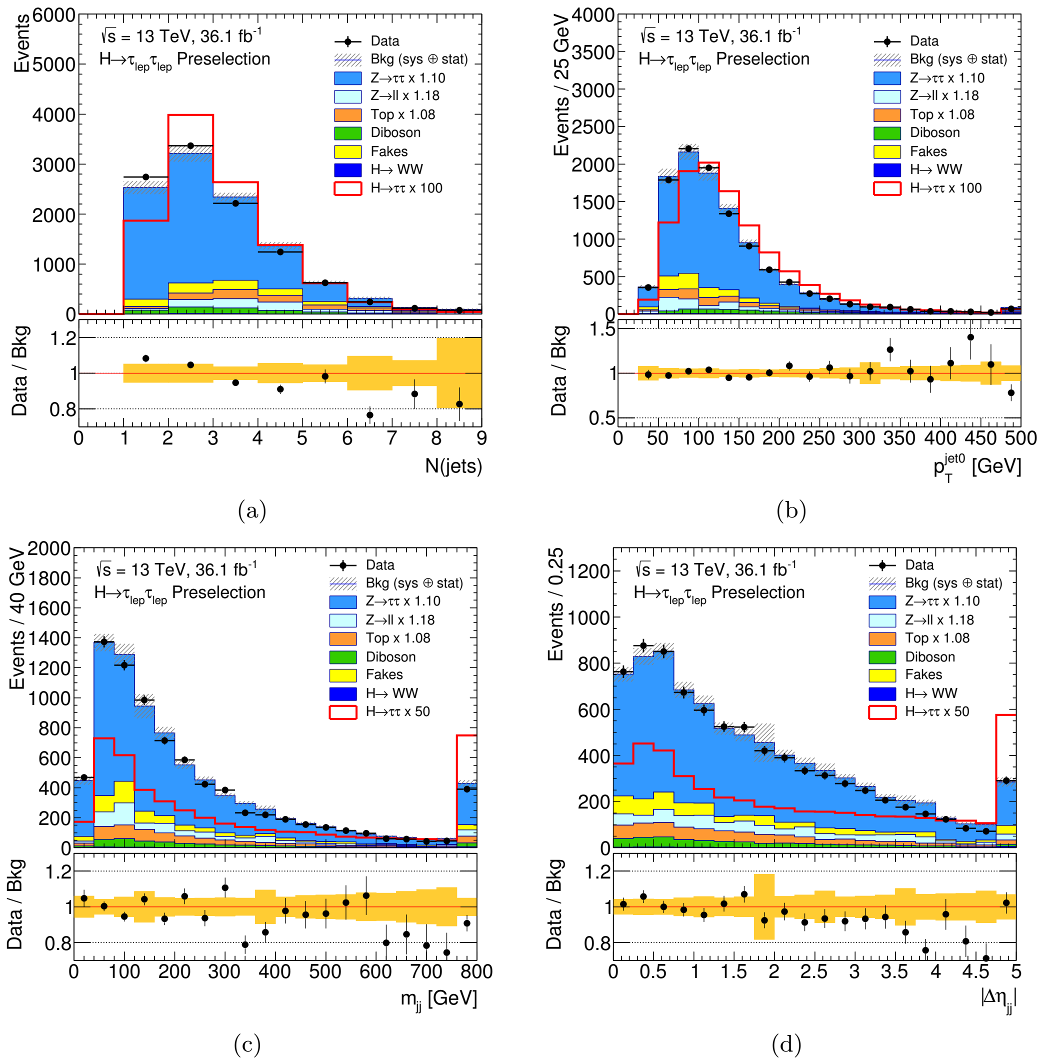

Figure 6.5.: Distribution of the number of jets (a), the p_{T} of the leading jet (b), the invariant di-jet mass m_{jj} and the $\Delta\eta$ separation between the jets (d) after the preselection in the $\tau_{lep}\tau_{lep}$ channel. For the di-jet variables in (c) and (d) a second jet with $p_T > 30\,\mathrm{GeV}$ is required. The uncertainty band includes statistical uncertainties and those systematic uncertainties, which are applied as event weights.

6.1.3. Categorization

The basic preselection described above is followed by a categorization of the selected events into a VBF region and a boosted region by exploiting distinct kinematic features of the Higgs-boson production in the VBF and the ggF channel, respectively. The variables, which are used for this categorization, are shown in Figure 6.6 for the different $H \rightarrow \tau\tau$ signal contributions and the sum of all background processes after the preselection.

VBF category

The event selection in the VBF category aims to enhance the signal contribution from VBF Higgs-boson production, which is characterized by two final-state jets from the scattering of the initial state partons. Hence, it is required that events falling in this category contain a second jet with $p_T > 30\,\text{GeV}$, which is referred to as sub-leading jet j_1 in the following. The two jets are required to have a minimum invariant mass of $m_{jj} > 400\,\text{GeV}$ with a large pseudorapidity separation of $|\Delta\eta_{jj}| > 3.0$. The jets also have to be reconstructed in different detector hemis-spheres corresponding to a requirement of $\eta_{j_0} \times \eta_{j_1} < 0$. In addition, a centrality cut is imposed on the selected leptons by requiring $\min\{\eta_{j_0}, \eta_{j_1}\} < \eta_{l_0(l_1)} < \max\{\eta_{j_0}, \eta_{j_1}\}$. This inclusive VBF region is then further split into a *loose* and *tight* category to exploit different phase-space regions with varying signal-to-background ratios. The VBF tight category selects events with even higher di-jet masses of $m_{jj} > 800\,\text{GeV}$, while the events failing this requirement are assigned to the VBF loose region. The expected signal and background yields as well as the observed number of data events in the VBF loose and tight categories are summarized in Table 6.2. A good agreement between the prediction and the observed data yields is obtained within statistical uncertainties. In the VBF loose category 237 data events are found, while the VBF tight category contains 188 data events. The expected $H \rightarrow \tau\tau$ signal in the VBF loose category is 6.86 ± 0.12 events, which corresponds to a selection efficiency with respect to the preselection of 6 %. In the VBF tight category 11.57 ± 0.12 $H \rightarrow \tau\tau$ events are expected and a signal selection efficicieny of 11 % is achieved. The dominant contribution to the total expected signal arises from VBF $H \rightarrow \tau\tau$ events with relative fractions of 62 % in the VBF loose category and 83 % in the VBF tight category. Both regions also include signal events from the ggF Higgs-boson production, where additionally produced jets mimic the typical VBF signature. In the VBF loose region, the relative signal contribution from ggF $H \rightarrow \tau\tau$ events is 37 %, while the VBF tight region only contains 17 % of ggF $H \rightarrow \tau\tau$ events with respect to the total expected signal due to the stricter VBF-topology requirements. The remaining signal contribution from WH, ZH and ttH production are found to be negligible in both categories. The expected sum of all background processes contribute with 233.3 ± 9.9 events in the VBF loose and 174.8 ± 7.7 events in the VBF tight region. In both categories, the dominant background contributions arise from $Z \rightarrow \tau\tau$ events, which constitute about 58 % of the total expected background. Important background contributions are also given by top-quark and fake-lepton events. Their relative fractions in the total expected background correspond to 15 % in the VBF tight category and 16 % of top-quark events and 9 % of fake-lepton events in the VBF loose category. Events from $Z \rightarrow \ell\ell$ decays constitute 9 % and 8 % of the total expected background in the VBF loose and tight categories, respectively. The relative contributions from di-boson events are 4 % in the VBF loose and 5 % in the VBF tight region, while events from $H \to WW$ decays only provide 1 % and 2 % of the total expected background in the VBF loose and tight categories, respectively. With the tight VBF selection a significance of $\frac{s}{\sqrt{b}} = 0.88$ is achieved, while the loose category contains less signal events and is affected by larger background contributions and hence results in a lower significance of $\frac{s}{\sqrt{b}} = 0.45$. The $m_{\tau\tau}^{\mathrm{MMC}}$ distributions, which are used in the likelihood fit to extract the $H \to \tau\tau$ signal, are shown in Figure 6.7 in the VBF loose and tight categories. Overall, a good agreement between data and prediction within the considered statistical and systematic uncertainties is observed.

Boosted category

The boosted category aims to select signal events from Higgs-boson production in the ggF channel, where the final state contains additionally produced jets via higher-order QCD radiations. These events are characterized by a boosted Higgs-boson candidate, which recoils against the jet system and therefore aquires an additional transverse momentum. The boosted category selects events, which fail the VBF selection described above and contain a Higgs-boson candidate with $p_T^H > 100\,\mathrm{GeV}$. In the $\tau_{lep}\tau_{lep}$ channel, this transverse momentum is calculated from the vectorial sum of the visible decay leptons and the missing transverse momentum. In the next step, the selected events are further split into a boosted *loose* and a boosted *tight* category according to the following criteria: The tight region consists of events with $p_T^H > 140\,\mathrm{GeV}$, while in the loose regions events with lower p_T^H-values are selected if they satisfy the additional requirement $\Delta R_{\ell\ell} < 1.5$. The expected signal and background yields as well as the observed number of data events in the boosted loose and boosted tight categories are summarized in Table 6.2. In both categories a good agreement between the predicted yields and the observed number of data events is obtained within statistical uncertainties. The boosted loose category contains 4124 data events, while 3444 data events are observed in the boosted tight category. The total expected $H \to \tau\tau$ signal corresponds to 39.96 ± 0.38 events in the boosted loose region and 40.18 ± 0.37 events in the boosted tight region. With this, a signal selection efficiency with respect to the preselection of 37 % is achieved in both categories. The contribution from ggF Higgs-boson production is found to be dominant with relative fractions of 75 % and 73 % in the boosted loose and tight category, respectively. Both categories also contain events from VBF Higgs-boson production, which constitute about 16 % of the total expected signal. Events from the WH, ZH and ttH production modes correspond to relative fractions of 8 % in the boosted loose and 10 % in the boosted tight region, where the dominant contribution arises from WH $H \to \tau\tau$ events. The expected sum of all background processes is 4196 ± 90 events in the boosted loose category and 3446 ± 41 events in the boosted tight category. Here, $Z \to \tau\tau$ events give the dominant contribution with relative fractions of 70 % in the boosted loose and 78 % in the boosted tight region. Background events from $Z \to \ell\ell$ decays correspond to 9 % and 7 % of the total expected background in the boosted loose and boosted tight region, respectively. In the boosted loose region, top-quark and fake-lepton events give 8 % of the total expected background, followed by di-boson events with a relative fraction of 4 %. In the boosted tight region, top-quark and di-boson events contribute with 6 % and 5 % of the background yield, respectively, while the relative contribution of the fake-lepton background is 4 %. In both boosted categories, $H \to WW$ events constitute only a minor background with less than 1 % contribution to the total expected background. The boosted loose and tight selections result in a significance of $\frac{s}{\sqrt{b}} = 0.62$ and $\frac{s}{\sqrt{b}} = 0.68$, respectively. Figure 6.8 shows the $m_{\tau\tau}^{\mathrm{MMC}}$ distributions in these regions, where a good agreement between data and prediction is obtained within the considered statistical and systematic uncertainties.

Process		VBF cat.		Boosted cat.	
		loose	tight	loose	tight
ggF	$H \to \tau\tau$	2.49 ± 0.10	1.91 ± 0.09	30.35 ± 0.35	29.47 ± 0.33
VBF	$H \to \tau\tau$	4.30 ± 0.06	9.60 ± 0.08	6.38 ± 0.07	6.62 ± 0.07
WH	$H \to \tau\tau$	0.04 ± 0.01	0.04 ± 0.02	2.13 ± 0.13	2.73 ± 0.14
ZH	$H \to \tau\tau$	0.02 ± 0.01	0.01 ± 0.01	0.88 ± 0.06	1.28 ± 0.08
ttH	$H \to \tau\tau$	<0.01	<0.01	0.13 ± 0.01	0.09 ± 0.01
$Z \to \tau\tau$		133.9 ± 6.3	100.8 ± 5.4	2960 ± 38	2679 ± 35
$Z \to \ell\ell$		20.4 ± 5.0	14.7 ± 3.3	357 ± 79	234 ± 16
Top		34.0 ± 2.6	28.6 ± 2.7	333.7 ± 8.4	202.1 ± 6.3
Di-Boson		9.80 ± 0.71	9.54 ± 0.74	185.9 ± 3.7	184.4 ± 3.1
Fakes		32.4 ± 5.1	16.2 ± 3.4	345 ± 17	131 ± 11
$H \to WW$		2.76 ± 0.12	4.93 ± 0.14	14.21 ± 0.32	15.41 ± 0.32
Total bkg.		233.3 ± 9.9	174.8 ± 7.7	4196 ± 90	3446 ± 41
$H \to \tau\tau$		6.86 ± 0.12	11.57 ± 0.12	39.96 ± 0.38	40.18 ± 0.37
Data		237	188	4124	3444

Table 6.2.: Expected event yields with statistical uncertainties in the signal regions of the $\tau_{lep}\tau_{lep}$ channel for signal and background processes compared to the observed data. The normalization factors summarized in Table 6.3 are applied to the $Z \to \tau\tau$, $Z \to \ell\ell$ and top-quark backgrounds.

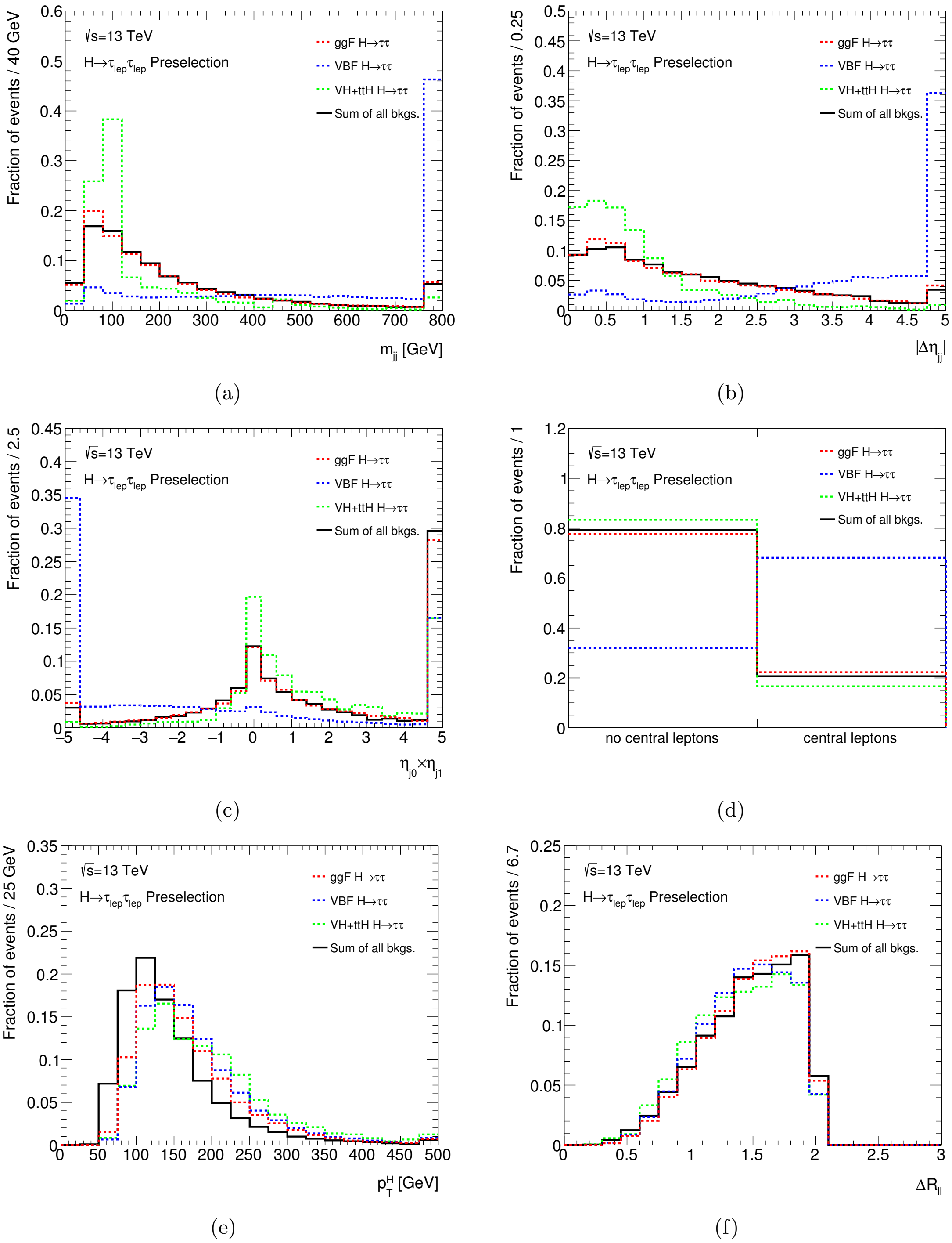

Figure 6.6.: Normalized distributions of the di-jet mass (a), the $\Delta\eta$ separation between the jets (b), the η-product of the jets (c), the centrality of the two leptons (d), the transverse momentum of the Higgs-boson candidate (e) and the ΔR separation of the leptons (f) after the preselection in the $\tau_{lep}\tau_{lep}$ final state.

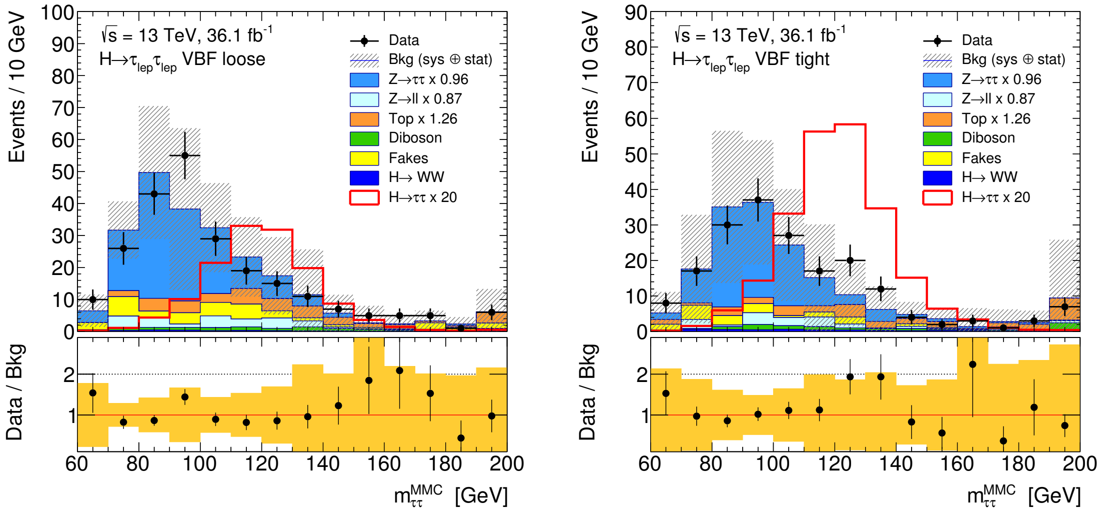

(a) (b)

Figure 6.7.: Distribution of $m_{\tau\tau}^{\mathrm{MMC}}$ in the VBF loose (a) and VBF tight (b) categories of the $\tau_{lep}\tau_{lep}$ channel. The uncertainty band includes statistical uncertainties and systematic uncertainties.

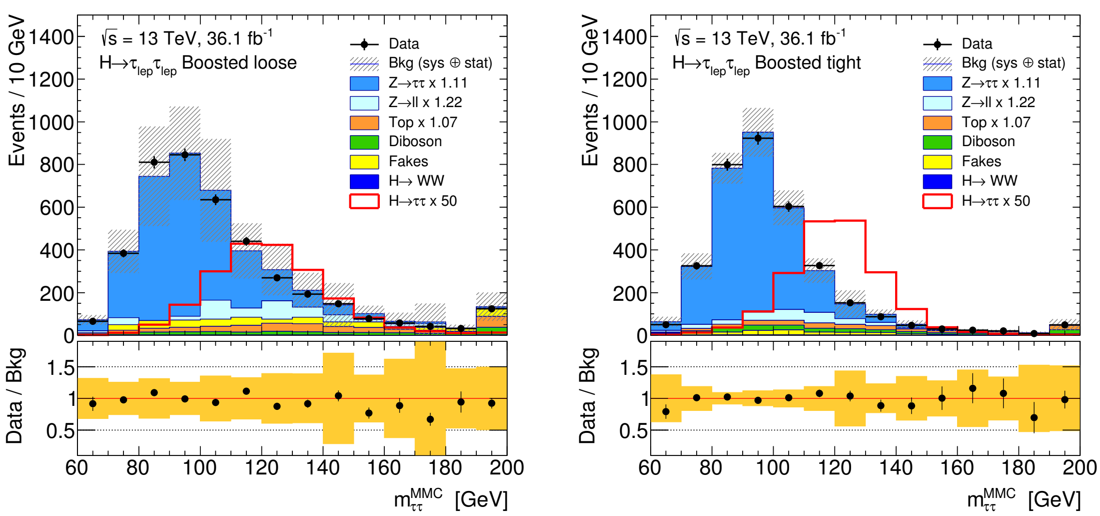

(a) (b)

Figure 6.8.: Distribution of $m_{\tau\tau}^{\mathrm{MMC}}$ in the boosted loose (a) and boosted tight (b) categories of the $\tau_{lep}\tau_{lep}$ channel. The uncertainty band includes statistical uncertainties and systematic uncertainties.

6.2. Background Estimation and Validation

A precise modelling of the various background contributions is crucial in order to extract the $H \to \tau\tau$ signal. In the analysis, background processes including real and prompt leptons are estimated from simulation and the agreement between data and the prediction for the main contributors from $Z \to \tau\tau$, $Z \to \ell\ell$ and top-quark events are validated in dedicated control regions (CRs). These CRs are constructed analogously to the event selection described in Section 6.1, but modifying certain requirements to enhance the phase-space region with events from the background process of interest. The CRs are used to validate the modelling of important kinematic variables and to derive *pre-fit* normalization factors, which are applied to the simulated events in order to match the number of observed data events in these CRs. This allows for a reasonable comparison between data and simulation at an early stage of the analysis, where no likelihood fit is performed yet. The pre-fit normalization factors NF($Z \to \tau\tau$), NF($Z \to \ell\ell$) and NF(Top) are obtained by solving a set of equations with the predicted event yields for the respective processes $\mathrm{N}_{\mathrm{MC}}^{Z\to\tau\tau}$, $\mathrm{N}_{\mathrm{MC}}^{Z\to\ell\ell}$, $\mathrm{N}_{\mathrm{MC}}^{\mathrm{Top}}$, the observed data events $\mathrm{N}_{\mathrm{data}}$ and the prediction for the remaining contributions N_{other} in the different CRs:

$$\mathrm{NF}(Z \to \ell\ell) \cdot \mathrm{N}_{\mathrm{MC}}^{Z\to\ell\ell} + \mathrm{NF}(\mathrm{Top}) \cdot \mathrm{N}_{\mathrm{MC}}^{\mathrm{Top}} + \mathrm{NF}(Z \to \tau\tau) \cdot \mathrm{N}_{\mathrm{MC}}^{Z\to\tau\tau} = \mathrm{N}_{\mathrm{data}} - \mathrm{N}_{\mathrm{other}}. \quad (6.4)$$

The resulting normalization factors with their statistical uncertainties are shown in Table 6.3 for different stages of the event selection. The normalization factor for $Z \to \tau\tau$ events increases the predicted event yield by 10 % at the preselection stage, while the yield prediction for $Z \to \ell\ell$ and top-quark processes is increased by 18 % and 8 %, respectively. In the VBF inclusive region, the normalization factor for $Z \to \tau\tau$ events corresponds to a decrease of 4 % with respect to the predicted yield, while the boosted inclusive selection requires an increase by 11 %. For $Z \to \ell\ell$ events, the normalization in the VBF inclusive region is decreased by 13 % and a correction of 22 % is applied for the boosted inclusive category. The yield predictions for the top-quark background are increased by 26 % and 7 % in the VBF and boosted inclusive category, respectively. The overall event yields for di-boson production and $H \to WW$ events are not corrected as they only represent a small fraction of the total background in the signal regions.

The estimation of background contributions from events with misidentified or non-prompt leptons, which are referred to as fake leptons, is obtained in a data-driven way as described in Section 6.2.3. This data-driven background estimation allows to reduce the impact of simulation on the analysis and hence minimizes the influence of systematic uncertainties.

	$Z \to \tau\tau$	$Z \to \ell\ell$	Top
Preselection	1.103 ± 0.021	1.184 ± 0.044	1.080 ± 0.022
VBF inclusive	0.96 ± 0.11	0.87 ± 0.11	1.256 ± 0.084
Boosted inclusive	1.113 ± 0.030	1.218 ± 0.039	1.065 ± 0.020

Table 6.3.: Pre-fit normalization factors and their statistical uncertainties for the dominant background processes at various stages of the event selection.

6.2.1. $Z \to \tau\tau$ Background

As shown in Table 6.1, the dominant background contribution in the signal regions of the $\tau_{lep}\tau_{lep}$ channel arises from $Z \to \tau\tau$ events with additionally produced jets. Therefore, the validation of the theoretical prediction for this process is an important task. However, it is difficult to select a sufficiently pure $Z \to \tau\tau$ sample in data, since its mass distribution overlaps with the Higgs-boson signal in a wide range. Instead, the kinematic modelling of additionally produced jets, which give the most difficult part in the theoretical prediction but do not depend on the Z^0-boson decay channel, can be validated in a so-called $Z + jets$ validation region (VR), which is enriched in events from $Z \to \ell\ell$ decays. These $Z \to \ell\ell$ events are selected with similar kinematic requirements as the signal region selection described in Section 6.1, but applying a cut of $m_{\ell\ell} > 80\,\text{GeV}$ and dropping the requirements on E_T^{miss} and $m_{\tau\tau}^{\text{MMC}}$. In particular, all requirements on the jet kinematics remain unchanged, while the transverse momentum of the Higgs-boson candidate p_T^H is replaced with the transverse momentum of the reconstructed di-lepton system $p_T^{\ell\ell}$. Table 6.4 shows the expected event yields as well as the observed number of data events in the VBF and boosted categories of this $Z + jets$ VR. The selected samples provide a purity in predicted $Z \to \ell\ell$ events of more than 99 % in both categories. As described in Ref. [31] an overall good agreement is obtained between data and simulation for several variables, which are used in the signal region selection. The distribution of the number of jets, the leading jet p_{T} and the di-jet invariant mass show a slight mismodelling. This was studied by applying a reweighting in these variables to the selected events and the results showed satisfying agreement within the considered theoretical uncertainties. Since no significant change of the final result was obtained, these reweighting methods are not applied to the selected signal region events.

The pre-fit normalization factors for $Z \to \tau\tau$ events as given in Table 6.3 are determined in a low-mass region by selecting events with $60\,\text{GeV} < m_{\tau\tau}^{\text{MMC}} < 100\,\text{GeV}$ to minimize the overlap with $H \to \tau\tau$ signal events.

Process	Z+jets VR	
	VBF cat.	Boosted cat.
$Z \to \ell\ell$	$63\,400 \pm 600$	$398\,610 \pm 910$
Other processes	684.6 ± 8.6	7133 ± 28
Sum of all processes	$64\,120 \pm 600$	$405\,740 \pm 910$
Data	64122	405742

Table 6.4.: Expected event yields with statistical uncertainties and observed data events in the Z+jets validation region (VR) of the $\tau_{lep}\tau_{lep}$ channel. The predicted $Z \to \ell\ell$ yield is scaled by 0.92 in the VBF and 1.11 in the boosted region to match the observed number of data events.

6.2.2. $Z \to \ell\ell$ and Top-Quark Backgrounds

The $Z \to \ell\ell$ CR is constructed by applying all signal region requirements, but only selecting events with SF leptons in the final state and di-lepton masses of $80\,\text{GeV} < m_{\ell\ell} < 100\,\text{GeV}$. As shown in Table 6.5, this selection results in a high purity of $Z \to \ell\ell$ events of 94 % at the preselection stage as well as with the VBF and boosted selections.

The CR for top-quark processes (Top CR) is also defined analogously to the signal region, but removing the b-jet veto and requiring at least one b-jet with $p_T > 25\,\text{GeV}$ instead. Table 6.6 summarizes the expected event yields in the Top CR. At the preselection state, the top-quark background constitutes about 76 % of the total predicted event yield and increases to 81 % in the VBF category and 77 % in the boosted category.

Figure 6.9 and 6.10 show the $m_{\tau\tau}^{\text{MMC}}$-distribution in the $Z \to \ell\ell$ CR and the Top CR, respectively. A good agreement between prediction and data is obtained in the VBF and boosted categories for both CRs.

Process	$Z \to \ell\ell$ CR		
	Preselection	VBF cat.	Boosted cat.
$Z \to \ell\ell$	2847 ± 93	216 ± 24	2637 ± 90
Other processes	179.7 ± 4.2	13.1 ± 1.3	165.9 ± 4.0
Sum of all processes	3027 ± 93	230 ± 24	2803 ± 90
Data	3037	232	2805

Table 6.5.: Expected event yields with statistical uncertainties in the $Z \to \ell\ell$ CR of the $\tau_{lep}\tau_{lep}$ channel compared to the observed data. The normalization factors summarized in Table 6.3 are applied to the $Z \to \tau\tau$, $Z \to \ell\ell$ and top-quark backgrounds.

Process	Top CR		
	Preselection	VBF cat.	Boosted cat.
Top	7991 ± 42	436 ± 11	6585 ± 38
Other processes	2630 ± 44	102.3 ± 6.0	2037 ± 39
Sum of all processes	$10\,621 \pm 61$	538 ± 13	8622 ± 54
Data	10633	538	8622

Table 6.6.: Expected event yields with statistical uncertainties in the Top CR of the $\tau_{lep}\tau_{lep}$ channel compared to the observed data. The normalization factors summarized in Table 6.3 are applied to the $Z \to \tau\tau$, $Z \to \ell\ell$ and top-quark backgrounds.

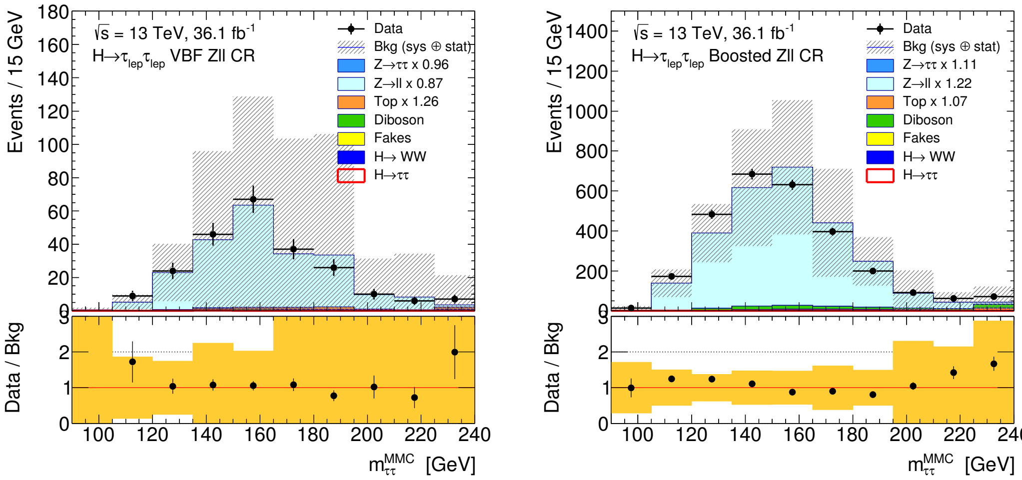

(a) (b)

Figure 6.9.: Distribution of $m_{\tau\tau}^{\mathrm{MMC}}$ in the $Z \to \ell\ell$ CR with the inclusive VBF selection (a) and the inclusive boosted selection (b). The uncertainty band includes statistical and systematic uncertainties. The large variations are caused by systematic uncertainties related to the jet energy scale and resolution measurements.

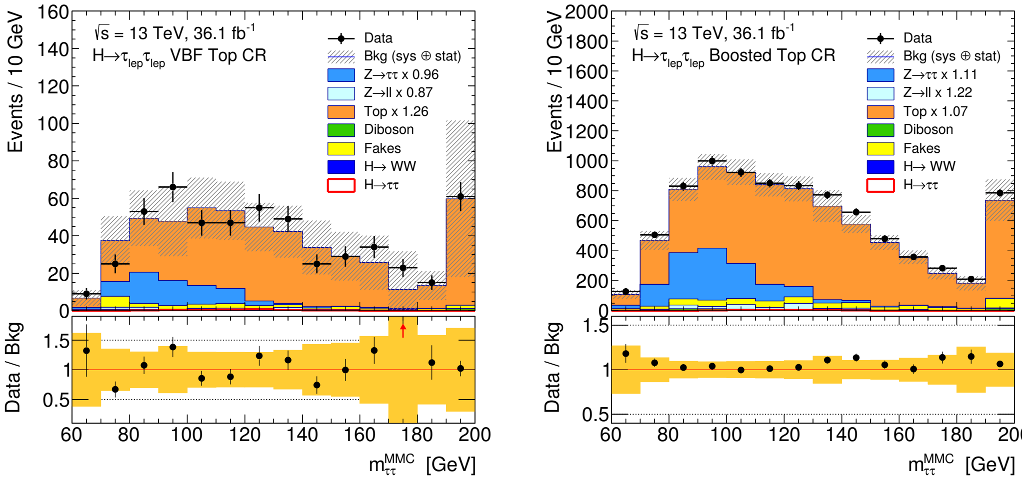

(a) (b)

Figure 6.10.: Distribution of $m_{\tau\tau}^{\mathrm{MMC}}$ in the Top CR with the inclusive VBF selection (a) and the inclusive boosted selection (b). The uncertainty band includes statistical and systematic uncertainties.

6.2.3. Misidentified and Non-Prompt Leptons

Background contributions from events with misidentified or non-prompt leptons, which are referred to as *fake* leptons in the following, mainly originate from multi-jet QCD production, $W^{\pm}$-boson production in association with jets and semi-leptonic decays of top-quarks. In this analysis, background events including fake leptons (fake-lepton background) are estimated with a data-driven method as described in detail in Ref. [31]. This method is based on the definition of various CRs depending on the electric charge $q(\ell_{0,1})$ of the selected leptons and the isolation requirement imposed on the sub-leading lepton. Events with $q(\ell_0) \times q(\ell_1) = -1$ are called opposite-sign (OS), while same-sign (SS) refers to events with $q(\ell_0) \times q(\ell_1) = +1$.

An OS *fake*-region is constructed by applying the signal region selection, but requiring the sub-leading lepton ℓ_1 to fail the *gradient* isolation requirement (*anti-isolated* lepton) and to pass the relaxed electron-identification requirement of *loose* instead of *tight*. In the SF final state, additional anti-isolation requirements are imposed on the sub-leading lepton track to reduce the contribution from events with real and prompt leptons mainly arising from $Z \to \ell\ell$ decays: In the ee-final state, events containing a sub-leading electron, which passes the *medium* ID requirement, but fails the *gradient* isolation working point, is required to have $p_T^{varcone,0.2}/p_T^{e_1} > 0.10$. Here, the variable $p_T^{varcone,0.2}$ corresponds to the track isolation in a cone of radius 0.2 around the electron. In the $\mu\mu$-final state, the sub-leading muon needs to pass the requirement $p_T^{varcone,0.3}/p_T^{\mu_1} > 0.10$ in addition. This OS fake-region is then used to determine the template shape of the fake-lepton background, where the sample of data events is corrected with the predicted contribution from events with two real and prompt leptons, N_{prompt}. The templates are then propagated to the different signal regions by applying transfer factors derived from the following SS CRs: The SS *nominal*-region consists of events with two isolated leptons of same charge, while for the SS *fake*-region the lepton isolation and ID requirements are modified in the same way as in the OS fake-region described above. The transfer factors are then calculated from the number of expected fake-lepton background events in the SS nominal-region $N_{fake}^{SS,nom} = N_{data}^{SS,nom} - N_{prompt}^{SS,nom}$ and the SS fake-region $N_{fake}^{SS,fake} = N_{data}^{SS,fake} - N_{prompt}^{SS,fake}$ as

$$f_{trans} = \frac{N_{fake}^{SS,nom}}{N_{fake}^{SS,fake}}. \tag{6.5}$$

These transfer factors are derived depending on the flavour combination of the final-state leptons and on the lepton trigger, which was exploited to select the event, and are summarized in Table 6.7. Since the fake-lepton background composition also depends on the number of reconstructed b-jets in the event, separate transfer factors are derived for events with at least one b-jet. This allows to estimate the contribution from the fake-lepton background in the Top CR. The corresponding numbers and a detailed description of the validation of this method, like the extrapolation of the transfer factors from the preselection to the signal regions, can be found in Ref. [221]. The systematic uncertainties, which are assigned for this procedure, are discussed in Section 6.3.1.

Trigger region	ee	$\mu\mu$	μe	$e\mu$
Single-e	0.24 ± 0.04	-	0.60 ± 0.02	0.15 ± 0.02
Single-mu	-	0.81 ± 0.04	0.0 ± 0.0	0.21 ± 0.01
Di-lep	0.35 ± 0.08	1.09 ± 0.09	0.50 ± 0.02	0.37 ± 0.04

Table 6.7.: The transfer factors and their uncertainties for the estimation of the fake-lepton background in the single-electron (single-e), single-muon (single-mu) and di-lepton (di-lep) trigger regions for all flavour combinations of the final-state leptons. These factors are derived at the preselection stage [221].

6.3. Systematic Uncertainties

The predictions of signal and background processes from simulation include various sources of systematic uncertainties, which need to be considered in the analysis. These systematic uncertainties can arise from experimental sources related to the limited reconstruction and identification efficiencies of physical objects, trigger efficiencies and uncertainties in the luminosity measurement. In addition, theoretical uncertainties due to the choice of parton distribution functions and the value of the strong coupling constant α_s, the parton shower and underlying event modelling and missing higher-order corrections in the prediction of cross sections and branching ratios need to be considered. The full list of experimental and theoretical uncertainties can be found in Appendix B corresponding to about 160 single uncertainties in the $\tau_{lep}\tau_{lep}$ channel. In order to propagate the effect of these uncertainties to the signal regions, each uncertainty source is varied within ± 1 standard deviation (σ) of its nominal value and the full analysis is repeated. The impacts of the uncertainties are evaluated separately for each signal and background process by applying the *pruning* criteria, that are described in Section 6.4.2. Here, the systematic uncertainties are classified into *acceptance* uncertainties and *shape* uncertainties by investigating their impact on the expected event yield and on the shape of the final discriminant for each signal and background process separately. Acceptance and shape uncertainties from the same systematic source are treated as correlated. Their inclusion in the statistical analysis is described in Section 6.4.2.

This section discusses the *pre-fit* impact of the systematic uncertainties on the predicted signal and background processes. These pre-fit values can be constrained in the likelihood fit by evaluating the agreement between the predictions and their uncertainties with the observed data. For this, the systematic variations are derived separately for each signal and background process and are then correlated across the different regions. If the impact of certain acceptance or shape uncertainties is found to be negligible for the analysis according to the considered pruning criteria, they are not included in the statistical model.

The first part, Section 6.3.1, describes the experimental uncertainties and summarizes the considered uncertainties related to the data-driven method for the fake-lepton background prediction, which is discussed in Section 6.2.3. This is followed by Section 6.3.2 with an overview of the considered theoretical uncertainties for the $H \to \tau\tau$ signal and the dominant $Z \to \tau\tau$ background.

6.3.1. Experimental Uncertainties

This section summarizes the experimental uncertainties on leptons, jets and missing transverse energy as well as uncertainties related to the pile-up reweighting and the luminosity determination. Their impact on the expected signal yield in the signal regions is summarized in Table 6.8-6.9, while the impact on the expected background yields in the signal regions can be found in Table 6.10-6.11. These numbers are derived after applying the symmetrization and smoothing methods described in Section 6.4.2. The uncertainty impact on the expected signal and background yields in the control regions can be found in Appendix C.1.

Lepton Uncertainties

The systematic uncertainties assigned to electron and muons are derived in dedicated tag-and-probe measurements by using Z^0-boson and J/Ψ decays. These uncertainties include variations of the energy and momentum resolution and scale of the leptons as well as uncertainties on the identification and isolation efficiencies. Resolution uncertainties on the ID measurement are included for both electrons and muons, while additional uncertainties are assigned for the muon track reconstruction in the MS. In order to account for differences in the identification and isolation efficiencies between data and simulation, several correction factors are applied to electron and muons. For the likelihood-based electron identification, the determination of the correction factors uses the impact parameter d_0 and its significance. However, as these factors are measured with prompt electrons in Z^0-boson and J/Ψ decays, the different d_0-distribution of electrons originating from τ-decays requires an additional uncertainty, which is applied to $Z \to \tau\tau$ and $H \to \tau\tau$ events. Furthermore, the simulated events are corrected for differences in the trigger efficiencies compared to data.

Since the resolution, scale and efficiency measurements are very precise, their impact in the VBF and boosted signal regions is small with only 1 - 3 % variations of the expected event yields.

Jet Uncertainties

The set of systematic uncertainties, which are assigned to events with reconstructed jets, accounts for uncertainties on the jet energy resolution (JER) and on the jet energy scale (JES) measurements. In this analysis, the JER uncertainties are included as 11 uncorrelated uncertainties, which are constructed from the smearing of data and simulated events with a factor accounting for the uncertainty in the energy resolution measurement. The final variations for the different processes are then taken from the signed difference of the relative variation in data and simulation for each bin of the considered distribution [207]. These JER uncertainties are assumed to be symmetric, such that a two-sided variation is constructed by applying the one-sided deviation from the nominal value in the opposite direction as well. The JER uncertainties constitute one of the dominant uncertainty sources for both signal and background expectations in this analysis. In most cases, their relative impact in the signal regions is on the order of 5 - 30 %, while especially large variations are obtained for the $Z \to \ell\ell$ background in the VBF catgeories. This is mainly caused by limitations in the available sample size for simulated $Z \to \ell\ell$ events in phase-space regions, which require VBF topologies. Figure 6.11 shows the impact of the JER uncertainties, which are found to have the largest impact in the $H \to \tau\tau$ cross-section measurement (see Section 6.5), on the shape of the $m_{\tau\tau}^{\text{MMC}}$ distribution in the signal regions.

Systematic uncertainties on the JES cover several sources [207]: A set of 19 variations are assigned to account for uncertainties related to pile-up effects, the η-intercalibration procedure, differences in the detector response to quark- and gluon-initated jets as well as dependencies on the jet-flavour composition. In addition, uncertainties related to limitations in the JES determination for high-p_{T} jets are included. In the VBF categories, JES uncertainties provide relative variations of the predicted event of with about 10 - 20 %, while their impact in the boosted categories is smaller with about 2 - 4 % relative variations. For the $Z \to \ell\ell$ background, JES uncertainties can lead to relative variations of up to 60 % in the VBF loose signal category, which is caused by limitations in the available sample size in this phase-space region. The impact of the most important JES uncertainties on the $m_{\tau\tau}^{\text{MMC}}$ shape in the signal regions is shown in Figure 6.12.

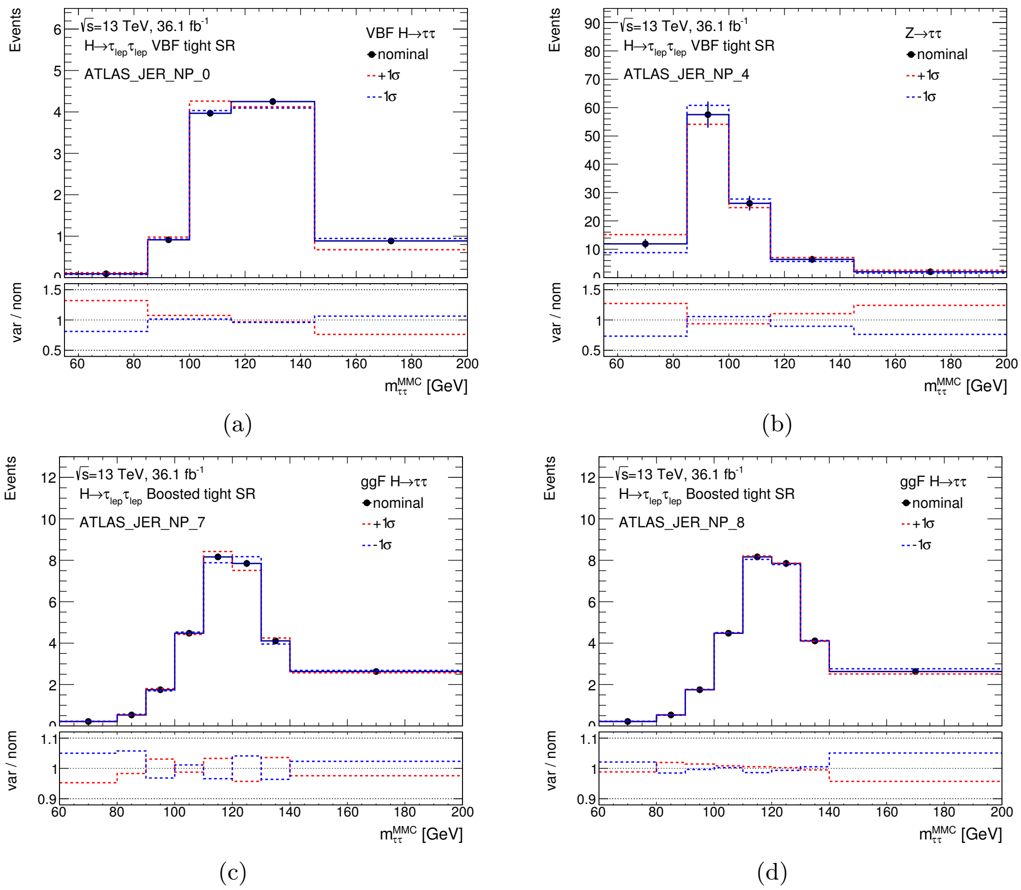

(a) (b) (c) (d)

Figure 6.11.: Impact of jet energy resolution (JER) uncertainties on the shape of the $m_{\tau\tau}^{\text{MMC}}$ distribution in the VBF tight (top) and boosted tight (bottom) signal region of the $\tau_{lep}\tau_{lep}$ channel.

The efficiency of the jet-vertex tagger (JVT), which is used to suppress the contribution from pile-up jets in the central and forward region of the detector, gives another source of systematic uncertainty [205]. Here, the impact in the signal regions is found to be small with only about 1 % variation of the expected signal and background yields.

Since the identification of b-jets is crucial for the suppression of events including top-quark decays in the signal region and the enhancement of top-quark events in the Top CR, systematic uncertainties on the b-tagging efficiency need to be considered as well. Here, uncertainties on the tagging efficiency target events containing b-jets, while events, which pass the b-jet veto requirement of the signal region, are affected by inefficiency uncertainties. These uncertainties also include variations on the identification efficiencies of c-jets, light-jets and jets originating from hadronic τ-decays as well as the extrapolation of the tagging efficiencies to high-p_{T} jets. Systematic uncertainties related to the b-tagging method mainly affect the expected signal yield from the ttH production channel with relative variations on the order of 10 - 20 % and the expected top-quark background yield with relative variations of 10 - 15 %.

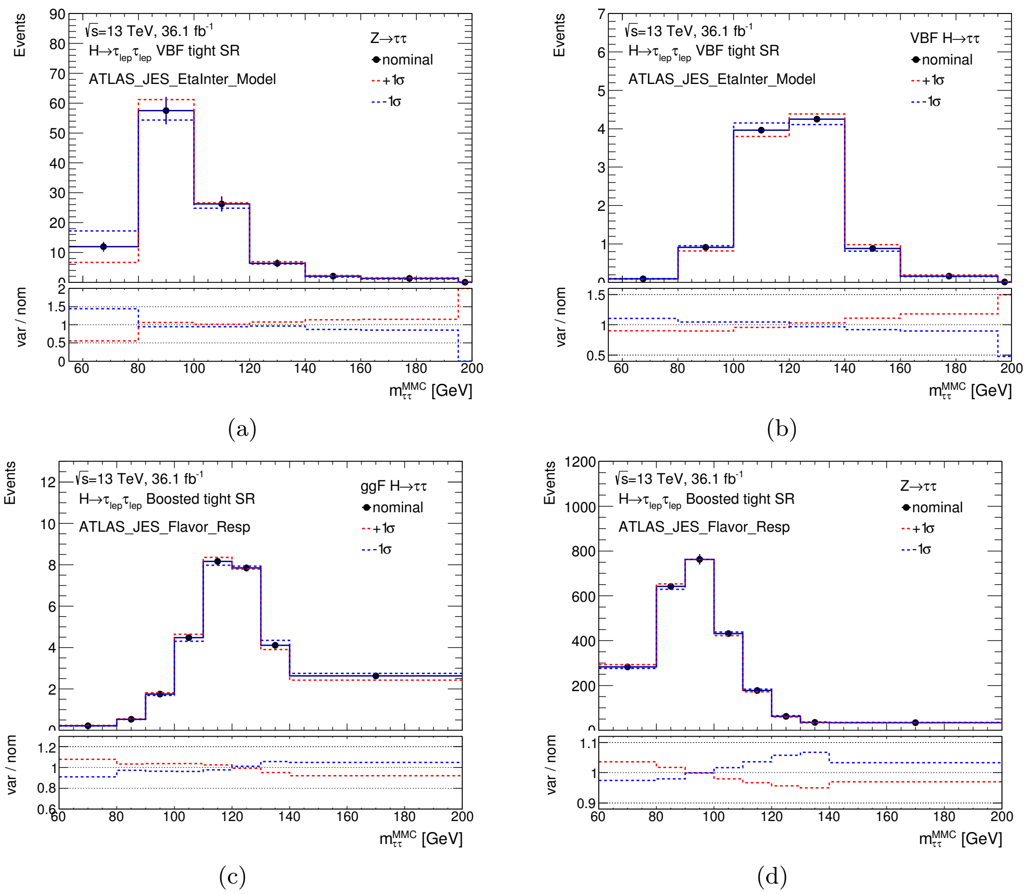

Figure 6.12.: Impact of jet energy scale (JES) uncertainties on the shape of the $m_{\tau\tau}^{\mathrm{MMC}}$ distribution in the VBF tight (top) and boosted tight (bottom) signal region of the $\tau_{lep}\tau_{lep}$ channel.

E_T^{miss} Uncertainties

Since the determination of E_T^{miss} depends on the calibrated energy of electrons, muons and jets, the variation of these calibrations have to be propagated to the E_T^{miss} reconstruction and result in an uncertainty on the soft term defined in Equation 5.4. These variations account for scale and resolution uncertainties depending on the total p_{T} of all objects in the events and are determined in dedicated measurements by comparing data to simulation [207]. Their impact on the expected signal and background yields is small with 2 - 4 % relative variation in the VBF and boosted signal regions. For $Z \to \ell\ell$ events, where E_T^{miss} only occurs due to limited reconstruction and identification efficiencies, the uncertainty on the resolution of the soft term leads to a relative variation of the expected yield of up to 16 % in the VBF loose signal region. Figure 6.13 shows the impact of the most important E_T^{miss} uncertainties on the $m_{\tau\tau}^{\mathrm{MMC}}$ shape in the VBF and boosted signal regions.

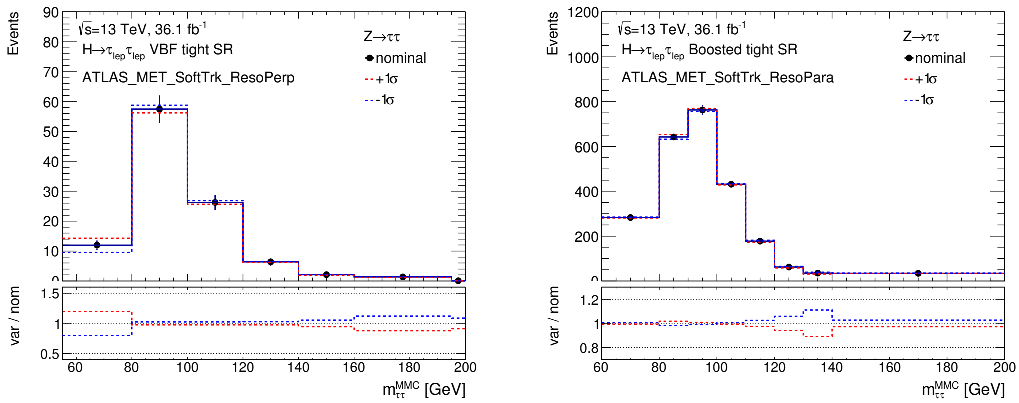

(a) (b)

Figure 6.13.: Impact of E_T^{miss} uncertainties on the shape of the $m_{\tau\tau}^{\mathrm{MMC}}$ distribution for $Z \to \tau\tau$ in the VBF tight (a) and boosted tight (b) signal region of the $\tau_{lep}\tau_{lep}$ channel.

Uncertainties on the Fake-Lepton Background

The data-driven method to estimate the fake-lepton background contribution in the $\tau_{lep}\tau_{lep}$ channel is described in detail in Ref. [31] and summarized in Section 6.2.3 including a description of the various CRs, which are referred to below.

The systematic uncertainties on the estimated shape and normalization of this background are summarized in Table 6.12. These uncertainties depend on the p_{T} of the subleading lepton and are derived separately for the VBF and boosted signal regions. The dominant contributions arise from uncertainties, which account for the extrapolation of the background estimate from the preselection stage to the signal regions (non-closure uncertainty) and from uncertainties related to the heavy-flavour composition of the jets. The non-closure uncertainty is derived by comparing the fake-lepton background estimate to data in a SS fake-region when applying the selection requirement of the signal region. This uncertainty leads to a relative variation of the predicted event yield of up to 65 % in the VBF signal region and 44 % in the boosted signal region. For the uncertainty on the heavy-flavour content, transfer factors are derived in a SS sample, which is enriched in event containing b-jets, and are applied to the OS fake-region, which includes a b-jet veto. The difference in the obtained background estimate compared to the nominal procedure is then assigned as an uncertainty, which corresponds to relative variations between 30 % to 40 % in the VBF regions and 50 % to 60 % in the boosted regions. Additional uncertainties arise from variations of the fractional contribution of top-quark events as well as $W^{\pm}$-boson and QCD multi-jet production in the total fake background estimate. Here, variations of the fractional contribution of top-quark events lead to relative uncertainties on the fake-lepton background yield of 20 %, while variations of the relative contribution from $W^{\pm}$-boson and multi-jet production corresponds to 7 % uncertainty on the yield.

Pile-up Reweighting

The prediction of signal and background processes are reweighted in order to reproduce the pile-up profile of the 2015 and 2016 datasets. For the best agreement between data and simulation, a correction factor of 1/1.16 has to be applied to the simulated number of interactions per bunch crossing with an uncertainty of $+0.07/-0.16$ corresponding to the official ATLAS recommendation. The impact of the pile-up reweighting uncertainty on the shape of the $m_{\tau\tau}^{\mathrm{MMC}}$ distribution in the VBF loose and boosted tight signal region is shown in Figure 6.14.

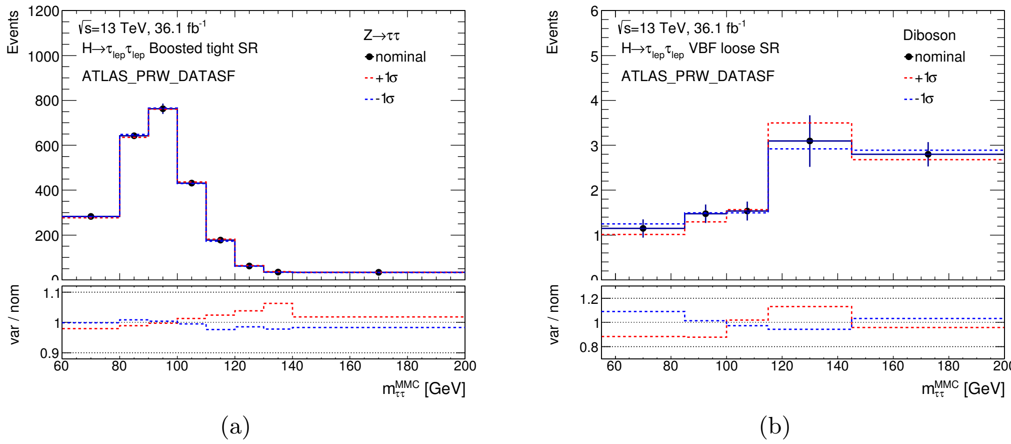

Figure 6.14.: Impact of the pile-up reweighting uncertainty on the shape of the $m_{\tau\tau}^{\mathrm{MMC}}$ distribution in the boosted tight (a) and VBF loose (b) signal region of the $\tau_{lep}\tau_{lep}$ channel.

Luminosity Uncertainties

The uncertainty on the integrated luminosity of the 2015+2016 dataset is measured to be 3.2 % [222, 223] assuming partially correlated uncertainties in 2015 and 2016 and affects the number of predicted signal and background events. Since the prediction for $Z \to \tau\tau$, $Z \to \ell\ell$ and top-quark backgrounds is normalized to the observed data in the corresponding CRs, no luminosity uncertainty is applied to these processes.

	$H \to \tau\tau$				
	ggF	VBF	WH	ZH	$t\bar{t}$H
	VBF loose signal region				
Electrons					
Scale	-	+0.6 / -0.7	-	-	-
Resolution	-	-	-	-	-
Efficiency	+2.1 / -2.1	+2.1 / -2.1	+1.4 / -1.4	+1.7 / -1.7	+1.2 / -1.2
Muons					
Scale	-	+0.7 / -0.7	-	-	-
Resolution	-	-	-	-	+4.3 / -0.0
Efficiency	-	-	-	-	-
Jets					
JER	+21.7 / -22.8	+23.2 / -17.1	+37.9 / -34.7	+77.2 / -72.0	+50.1 / -63.6
JES	+8.6 / -9.4	+5.6 / -8.1	+18.5 / -19.9	-	+66.8 / -66.7
JVT Efficiency	-	-	-	+1.2 / -1.2	+1.4 / -1.4
b-tagging	+1.5 / -1.5	+1.2 / -1.2	+2.8 / -2.7	+2.7 / -2.6	+13.1 / -13.4
E_T^{miss} soft term					
Resolution	+2.2 / -2.2	-	+10.7 / -10.7	+0.0 / -13.2	+9.9 / -9.9
Scale	-	+2.3 / -2.0	+0.0 / -10.7	-	+0.0 / -4.3
Pile-up rew.	-2.4 / +0.7	-3.4 / +2.8	-9.4 / +5.1	+1.0 / -8.1	-9.8 / +11.0
	VBF tight signal region				
Electrons					
Scale	-	-	-	-	+8.8 / -0.1
Resolution	-	-	-	-	-
Efficiency	+2.0 / -2.0	+2.1 / -2.1	-	-	+1.3 / -1.0
Muons					
Scale	-	-	-	-	+13.2 / -0.0
Resolution	+0.4 / -0.3	-	-	-	+8.8 / -0.1
Efficiency	-	-	+1.0 / -1.0	+1.2 / -1.2	-
Jets					
JER	+19.0 / -17.0	+21.3 / -17.2	+48.2 / -41.2	+53.9 / -35.1	+62.8 / -61.9
JES	+9.3 / -7.5	+5.3 / -6.5	+34.1 / -19.3	-	+51.3 / -72.1
JVT Efficiency	-	-	-	-	-
b-tagging	+1.5 / -1.5	-	+1.8 / -1.8	+1.1 / -1.1	+13.1 / -10.9
E_T^{miss} soft term					
Resolution	-	-	-	-	+0.0 / -6.1
Scale	+0.5 / -0.6	+0.4 / -0.7	-	-	+10.4 / -4.5
Pile-up rew.	+2.0 / -2.3	-4.0 / +2.9	-9.8 / +9.3	-15.5 / +23.6	-40.6 / +42.9

Table 6.8.: Relative impact of experimental systematic uncertainties on the total number of expected signal events in the signal regions of the VBF category in the $\tau_{\text{lep}}\tau_{\text{lep}}$ channel. Given is always the up- and downward variation in percent. Variations below 0.1% are ignored.

	$H \to \tau\tau$				
	ggF	VBF	WH	ZH	t$\bar{\text{t}}$H
	Boosted loose signal region				
Electrons					
Scale	-	-	-	-	-
Resolution	-	-	-	-	-
Efficiency	+2.5 / -2.5	+2.5 / -2.5	+1.1 / -1.1	-	-
Muons					
Scale	-	-	-	-	-
Resolution	+0.0 / -0.2	-	-	-	-
Efficiency	-	-	-	-	-
Jets					
JER	+8.0 / -7.1	+7.8 / -5.8	+5.3 / -7.0	+12.5 / -10.6	+16.4 / -13.0
JES	+3.2 / -3.3	+1.3 / -1.6	+3.1 / -2.4	+8.7 / -5.6	+13.4 / -15.9
JVT Efficiency	-	-	-	-	+1.1 / -1.1
b-tagging	+1.2 / -1.2	+1.0 / -1.0	+1.8 / -1.8	+1.5 / -1.5	+12.9 / -12.3
E_T^{miss} soft term					
Resolution	-	+0.6 / -0.6	+3.7 / -3.8	-	+1.4 / -1.4
Scale	+0.4 / -1.3	+0.8 / -0.7	-	-	-
Pile-up rew.	-2.4 / +0.9	-3.2 / +1.6	-1.3 / +2.1	-3.5 / +3.4	-2.7 / +2.3
	Boosted tight signal region				
Electrons					
Scale	-	-	-	+0.5 / -1.1	-
Resolution	-	+0.3 / -0.2	-	+1.0 / -0.6	-
Efficiency	+2.0 / -2.0	+1.9 / -1.9	-	-	-
Muons					
Scale	+0.2 / -0.0	-	-	-	-
Resolution	-	+1.2 / -1.4	-	+0.8 / -0.5	-
Efficiency	-	-	-	-	-
Jets					
JER	+8.2 / -7.6	+9.2 / -9.0	+10.4 / -9.8	+5.5 / -6.4	+14.0 / -12.1
JES	+1.0 / -2.1	+3.0 / -3.5	+6.4 / -7.2	+3.5 / -5.9	+25.5 / -25.9
JVT Efficiency	-	-	-	-	+1.2 / -1.2
b-tagging	+1.6 / -1.6	+1.4 / -1.3	+2.0 / -2.0	+1.9 / -1.9	+21.2 / -18.8
E_T^{miss} soft term					
Resolution	+0.6 / -0.6	-	+1.4 / -1.4	+2.7 / -2.7	+2.0 / -2.0
Scale	+1.6 / -0.2	-	-	+2.9 / -3.9	+0.8 / -0.1
Pile-up rew.	-2.2 / +1.8	-2.0 / +1.1	-3.7 / +2.9	-1.6 / +1.5	+1.6 / -0.5

Table 6.9.: Relative impact of experimental systematic uncertainties on the total number of expected signal events in the signal regions of the boosted category in the $\tau_{\text{lep}}\tau_{\text{lep}}$ channel. Given is the up- and downward variation in percent. Variations below 0.1% are ignored.

	$Z \to \tau\tau$	$Z \to \ell\ell$	Top	Di-boson
	VBF loose signal region			
Electrons				
Scale	-	-	-	-
Resolution	-	-	-	-
Efficiency	+2.5 / -2.5	-	+1.0 / -1.0	-
Muons				
Scale	-	-	-	-
Resolution	-	+3.3 / -1.9	-	-
Scale	-	+1.4 / -2.1	-	-
Jets				
JER	+18.7 / -14.7	+27.4 / -30.0	+27.2 / -25.7	+25.3 / -20.3
JES	+10.2 / -10.8	+64.3 / -55.2	+7.7 / -8.4	+17.8 / -17.9
JVT Efficiency	-	-	-	-
b-tagging	+1.5 / -1.5	+1.1 / -1.1	+15.9 / -14.9	+1.6 / -1.6
E_T^{miss} soft term				
Resolution	+2.3 / -2.3	-	+2.3 / -2.3	-
Scale	+3.4 / -1.6	+12.8 / -16.2	+4.0 / -4.0	-
Pile-up rew.	-6.1 / +4.7	+6.2 / -7.4	-4.4 / +2.5	-
	VBF tight signal region			
Electrons				
Scale	+3.4 / -5.6	-	-	-
Resolution	+3.0 / -3.0	-	-	-
Efficiency	+2.2 / -2.2	-	-	+1.0 / -1.0
Muons				
Scale	-	-	+2.3 / -3.1	+0.9 / -1.3
Resolution	+1.2 / -5.7	-	-	-
Efficiency	-	-	-	-
Jets				
JER	+21.0 / -21.6	+33.7 / -95.5	+23.5 / -17.0	+24.0 / -19.9
JES	+12.8 / -12.7	+52.9 / -42.4	+10.4 / -12.0	+12.8 / -11.1
JVT Efficiency	-	-	-	-
b-tagging	+1.6 / -1.6	+2.0 / -1.9	+10.5 / -9.9	+1.8 / -1.8
E_T^{miss} soft term				
Resolution	+7.5 / -7.5	+12.5 / -12.5	+1.7 / -1.7	+1.4 / -1.8
Scale	-	-	+2.3 / -1.8	-
Pile-up rew.	+5.3 / -4.8	+13.8 / -2.0	-0.8 / -0.7	-4.6 / +1.8

Table 6.10.: Relative impact of experimental systematic uncertainties on the number of expected background events in the signal regions of the VBF category in the $\tau_{\text{lep}}\tau_{\text{lep}}$ channel. Given is the up- and downward variation in percent. Variations below 0.1% are ignored.

	$Z \to \tau\tau$	$Z \to \ell\ell$	Top	Di-boson
	Boosted loose signal region			
Electrons				
Scale	-	+1.2 / -0.8	-	-
Resolution	-	-	-	-
Efficiency	+2.5 / -2.5	-	+1.0 / -1.0	+1.0 / -1.0
Muons				
Scale	-	-	-	-
Resolution	-	-	-	-
Efficiency	-	-	-	-
Jets				
JER	+7.4 / -6.8	+30.6 / -25.3	+7.8 / -7.8	+6.7 / -4.4
JES	+3.1 / -2.9	+26.8 / -26.0	+1.9 / -1.8	+3.0 / -2.3
JVT Efficiency	-	-	-	-
b-tagging	+1.2 / -1.2	+1.4 / -1.4	+15.6 / -14.6	+1.5 / -1.5
E_T^{miss} soft term				
Resolution	-	+11.2 / -11.2	-	-
Scale	+0.4 / -0.0	+7.3 / -11.4	-	-
Pile-up rew.	-2.6 / +1.8	+6.4 / -5.9	-1.3 / +0.8	-1.9 / +0.5
	Boosted tight signal region			
Electrons				
Scale	-	-	-	-
Resolution	-	-	-	-
Efficiency	+2.0 / -2.0	-	-	-
Muons				
Scale	-	-	-	-
Resolution	-	+2.0 / -3.0	-	-
Efficiency	-	+1.1 / -1.1	-	-
Jets				
JER	+4.0 / -4.2	+14.2 / -26.0	+7.5 / -6.6	+7.5 / -4.4
JES	+2.4 / -2.6	+22.7 / -22.1	+2.8 / -2.8	+4.1 / -3.4
JVT Efficiency	-	-	-	-
b-tagging	+1.6 / -1.6	+1.7 / -1.7	+15.1 / -14.1	+1.9 / -1.8
E_T^{miss} soft term				
Resolution	-	+10.5 / -10.5	-	-
Scale	+0.9 / -0.7	+7.0 / -10.9	-	-
Pile-up rew.	-1.4 / +1.4	+4.4 / -2.0	+1.1 / -0.5	-2.7 / +1.6

Table 6.11.: Relative impact of experimental systematic uncertainties on the number of expected background events in the signal regions of the boosted category in the $\tau_{\text{lep}}\tau_{\text{lep}}$ channel. Given is the up- and downward variation in percent. Variations below 0.1% are ignored.

Systematics uncertainties (%)	VBF-inclusive category				Boosted-inclusive category			
Non-closure systematics	p_T (GeV)	10 - 15	15 - 20	>20	p_T (GeV)	10 - 15	15 - 20	>20
	all	39%	65%		all	26%	44%	21%
Top fake fraction	p_T (GeV)	10 - 15	15 - 20	20 -	p_T (GeV)	10 - 15	15 - 20	20 -
	ee	—	20.0%		ee	—	20.2%	
	$\mu\mu$		9.6%		$\mu\mu$		11.1%	
	DF		6.2%		DF		6.1%	
Heavy flavor contents	p_T (GeV)	10 - 15	15 - 20	20 -	p_T (GeV)	10 - 15	15 - 20	20 -
	ee	—	45.0%	38.9%	ee	—	53.5%	52.9%
	$\mu\mu$	50.0%	50%	50%	$\mu\mu$	51.0%	51.4%	50.7%
	DF	38.2	30.5%	36.4%	DF	62.7%	62.4%	59.7%
QCD closure systematics	p_T (GeV)	10 - 15	15 - 20	20 -	p_T (GeV)	10 - 15	15 - 20	20 -
	DF	7.3%	3.2%	4.3%	DF	7.2%	4.7%	4.3%
W + jets closure systematics	p_T (GeV)	10 - 15	15 - 20	20 -	p_T (GeV)	10 - 15	15 - 20	20 -
	all		5.4%		all		6.9%	

Table 6.12.: Systematic uncertainties for the fake lepton background estimation method in $\tau_{lep}\tau_{lep}$ channel [221].

6.3.2. Theoretical Uncertainties

This section describes the systematic uncertainties, which arise from theoretical sources in the prediction and event generation of the signal processes and the dominant $Z \to \tau\tau$ background. The impact of these theoretical uncertainties on the expected event yields in the signal regions are shown in Table 6.13 and 6.14 for signal and $Z \to \tau\tau$ background, respectively. Their impact in the control regions can be found in Appendix C.1. In this analysis, no theoretical uncertainties are included for the $Z \to \ell\ell$, di-boson and top-quark backgrounds.

Signal Modelling

Theoretical uncertainties on the prediction of the $H \to \tau\tau$ signal arise from missing higher-order corrections in the cross-section calculation (QCD-scale uncertainties), the choice of the PDF set, the α_s-value as well as from generator-specific settings in the modelling of the parton shower and non-perturbative effects from underlying events and hadronization (UEPS uncertainties). The impact of these uncertainties are divided into uncertainties on the Higgs-boson production cross-section and uncertainties, that affect the signal acceptance and $m_{\tau\tau}^{\mathrm{MMC}}$ shape in the signal regions. Uncertainties on the total Higgs-boson production cross-section from QCD-scale, PDF and α_s variations are treated as uncorrelated to the acceptance and shape uncertainties related to the same source and are taken from the YellowReport 4 of the LHC Higgs Cross Section Working Group (Lhcxswg) [85].

The impact of QCD-scale uncertainties is evaluated with simulated signal events, where the renormalization and factorization scales, μ_R and μ_F, are varied by a factor of 2 and 1/2 around the nominal value in the range $1/2 \leq \mu_R/\mu_F \leq 2$. Including all possible combinations of these variations, except for $\mu_R = 0.5$, $\mu_F = 2$ and $\mu_R = 2$, $\mu_F = 0.5$, leads to a set of six QCD-scale uncertainties. The largest deviation from the nominal prediction in each bin of the final discriminant (*envelope*) is then used to derive the final uncertainy on the signal acceptance and $m_{\tau\tau}^{\mathrm{MMC}}$ shape. These scale variations, however, are not sufficient to cover the large logarithmic uncertainties, which arise from jet-bin migration effects in the QCD-scale variation for the ggF $H \to \tau\tau$ prediction. Instead, they are evaluated following the prescription of the Lhcxswg, which results in a set of nine uncertainties covering sources related to scale variations, the VBF topology, shape uncertainties on p_T^H and dependencies on the top-quark mass [85, 224]. With this procedure, no additional cross-section uncertainties on the predicted ggF $H \to \tau\tau$ yield have to be applied.

Systematic uncertainties accounting for the choice of the PDF parametrization and α_s-value are obtained by 30 eigenvector variations and two variations of α_s according to the Pdf4lhc recommendations [162].

The estimation of UEPS uncertainties is obtained by comparing the default generator choice of PowHeg+Pythia 8 for the ggF and VBF $H \to \tau\tau$ signal predictions to alternative samples, which are generated with PowHeg+Herwig 7 based on fast simulation [157]. Figure 6.15 shows the impact of these UEPS uncertainties on the $m_{\tau\tau}^{\mathrm{MMC}}$ shape in the signal regions. No UEPS uncertainties are included for the WH, ZH and ttH production modes due to their small contributions.

Furthermore, an uncertainty on the branching ratio of Higgs-boson decays to τ-leptons of $\pm 1.17\,\%$ [225] is applied to $H \rightarrow \tau\tau$ events, while a branching-ratio uncertainty for the decay into $W^{\pm}$-bosons of $\pm 0.99\,\%$ is assigned to $H \rightarrow WW$ events.

As shown in Table 6.13, UEPS uncertainties on the ggF signal are found to have the largest impact on the expected event yield with relative variations of up to 39 % in the VBF tight signal region. QCD-scale uncertainties lead to relative ggF $H \rightarrow \tau\tau$ yield variations of 18 % to 20 % in the VBF signal regions and 16 % to 23 % in the boosted signal regions. The QCD-scale uncertainty also impacts the predicted $H \rightarrow \tau\tau$ yields in the WH and ttH production channels with relative variations of up to 25 % and 24 % in the VBF loose signal region, respectively.

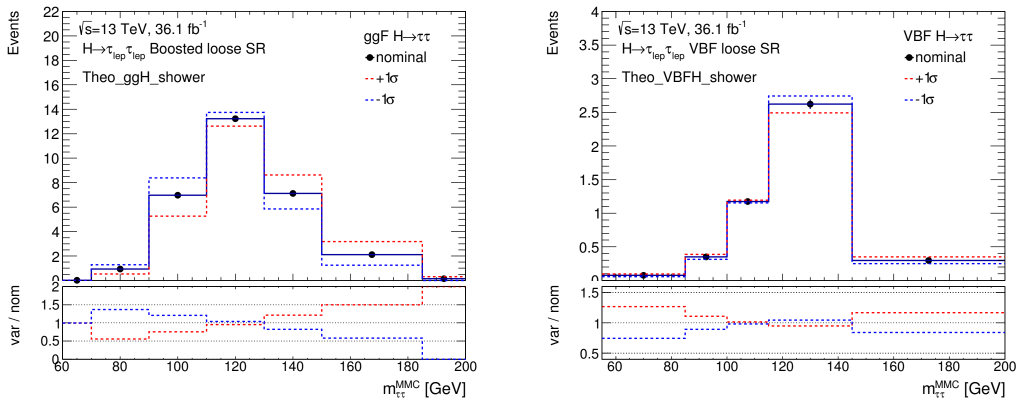

(a) (b)

Figure 6.15.: Impact of UEPS uncertainties on the shape of the $m_{\tau\tau}^{\mathrm{MMC}}$ distribution in the boosted loose (a) and VBF loose (b) signal region of the $\tau_{lep}\tau_{lep}$ channel.

$Z \rightarrow \tau\tau$ Background Modelling

Theoretical uncertainties on the prediction of the dominant $Z \rightarrow \tau\tau$ background from QCD-scale and PDF variations are obtained with the same procedure as described above. Furthermore, variations of the jet-to-parton matching scale (CKKW-scale) and resummation scale (QSF-scale) are included based on a truth-level parametrization, which depends on the jet multiplicity and the Z^0-boson transverse momentum. For the electroweak (EW) production of a Z^0-boson in association with two or three jets, a CKKW-scale uncertainty of 25 % is assigned, which is taken from ATLAS Run 2 measurements of the EW Z^0-boson production cross-section [226]. The impact of uncertainties from non-perturbative effects of the underlying event modelling is evaluated at truth level by comparing the nominal prediction to simulated events from PowHeg+Pythia, where the fractions of multiple parton interactions are varied, and is found to be negligible. Uncertainties related to the UEPS modelling are determined based on the comparison of the nominal $Z \rightarrow \tau\tau$ prediction with Sherpa to an alternative sample, which is generated with MadGraph+Pythia at leading order. Since this alternative sample only includes a limited number of simulated events, the relative variation between the two predictions is derived at the preselection stage and then applied to the default prediction in the signal regions. Figure 6.16 shows the impact of the UEPS, CKKW-scale and QCD-scale uncertainties on the $m_{\tau\tau}^{\mathrm{MMC}}$ shape in the signal regions.

In the statistical analysis, the theoretical uncertainties on the $Z \to \tau\tau$ prediction are treated as uncorrelated between the VBF and boosted regions, while the normalization of the predicted $Z \to \tau\tau$ yields are determined separately in the VBF and boosted regions. These normalization parameters are constructed in a way to account for event migration effects between the signal regions of the $\tau_{lep}\tau_{lep}$, $\tau_{lep}\tau_{had}$ and $\tau_{lep}\tau_{had}$ channels as well as for event migrations within the inclusive VBF and boosted regions for each channel. Here, the *channel-migration* uncertainties are evaluated by comparing the impact of the variation on the total event yield in each channel to the sum of predicted event yields over all channels. This is done for each source of uncertainty (PDF, QCD-scale, CKKW-scale, QSF-scale, UEPS) and results in three variations ($\tau_{lep}\tau_{lep}$, $\tau_{lep}\tau_{had}$, $\tau_{had}\tau_{had}$) per category (VBF and boosted). In the statistical analysis, these variations are treated as correlated between the channels. In addition, the *region-migration* uncertainties account for the impact of the variations on the shape of the final discriminant and for event migration effects between the signal regions of the inclusive VBF and boosted categories. This results in two uncorrelated variations (VBF and boosted) per systematic uncertainty (PDF, QCD-scale, CKKW-scale, QSF-scale, UEPS) for each channel ($\tau_{lep}\tau_{lep}$, $\tau_{lep}\tau_{had}$,$\tau_{had}\tau_{had}$). As shown in Table 6.14, the largest impact on the $Z \to \tau\tau$ prediction arises from channel-migration uncertainties of the CKKW-scale with relative yield variations of 6 % in the VBF loose and 4 % in the boosted tight category. The dominant region-migration uncertainty corresponds to the UEPS variation in the VBF tight region, which is found to vary the predicted $Z \to \tau\tau$ yield by about 5 %.

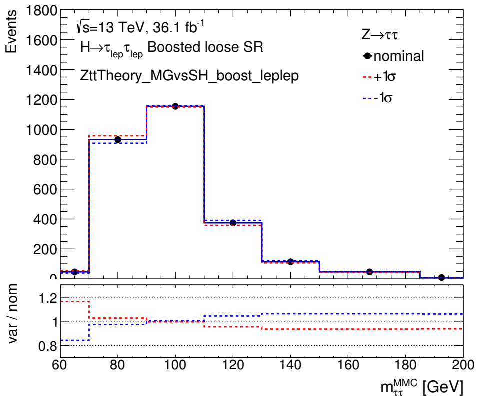

(a)

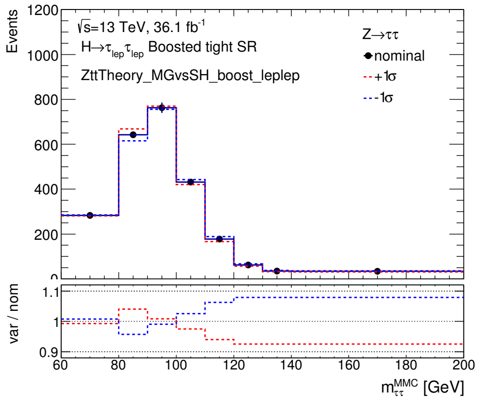

(b)

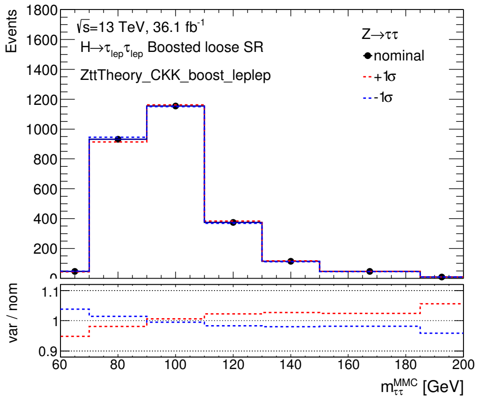

(c)

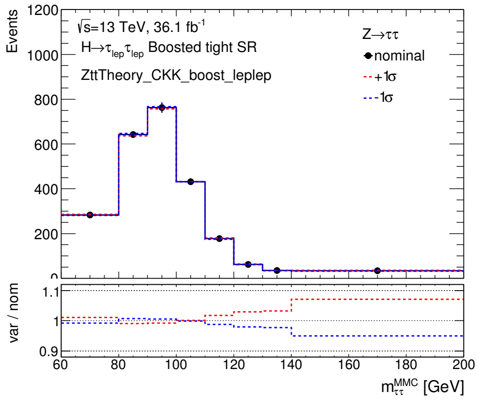

(d)

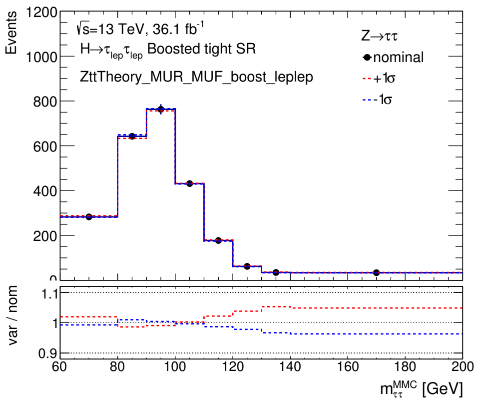

(e)

Figure 6.16.: Impact of UEPS uncertainties (top), CKK-scale uncertainties (middle) and QCD-scale uncertainties (bottom) on the $m_{\tau\tau}^{\mathrm{MMC}}$ shape for the $Z \to \tau\tau$ background in the boosted signal regions of the $\tau_{lep}\tau_{lep}$ channel.

	$H \to \tau\tau$				
	ggF	VBF	WH	ZH	ttH
	Total cross-section uncertainties				
QCD-scale	-	+0.4 / -0.3	+0.5 / -0.7	+3.8 / -3.1	+5.8 / -9.2
α_S	+2.5 / -2.5	+0.5 / -0.5	+0.9 / -0.9		+2.0 / -2.0
PDF	+1.8 / -1.2	+2.1 / -2.1	+1.7 / -1.7	+1.3 / -1.3	+3.0 / -3.0
	VBF loose				
QCD-scale	+18.4 / -18.4	-	+25.1 / -13.4	+23.9 / -13.6	-
α_S	+1.5 / -1.3	-	-	-	-
PDF	+1.3 / -1.3	-	+2.2 / -2.2	+1.6 / -1.6	-
UEPS	+20.5 / -20.5	+3.5 / -3.5	-	-	-
	VBF tight				
QCD-scale	+20.3 / -20.3	+1.2 / -1.6	+9.1 / -6.7	+14.9 / -11.6	-
α_S	+1.6 / -1.4	-	-	-	-
PDF	+2.0 / -2.0	-	-	+1.2 / -1.2	-
UEPS	+39.3 / -38.5	+1.3 / -1.3	-	-	-
	Boosted loose				
QCD-scale	+16.2 / -16.2	-	+3.1 / -2.3	+4.3 / -2.1	-
α_S	+1.5 / -1.4	-	-	-	-
PDF	+1.1 / -1.1	-	-	-	-
UEPS	+9.5 / -9.5	+3.5 / -3.5	-	-	-
	Boosted tight				
QCD-scale	+23.6 / -23.6	+1.4 / -1.0	+4.1 / -3.1	+3.7 / -5.6	-
α_S	+1.5 / -1.3	-	-	-	-
PDF	+2.4 / -2.4	-	-	-	-
UEPS	+5.8 / -5.8	+5.9 / -5.9	-	-	-

Table 6.13.: Relative impact of theoretical uncertainties on the expected number of $H \to \tau\tau$ signal events for the different Higgs-boson production modes in the signal regions of the $\tau_{lep}\tau_{lep}$ channel. Given is the up- and downward variation in percent. Variations below 0.1% are ignored.

	$Z \rightarrow \tau\tau$ Channel-migration	Region-migration
	VBF loose	
QCD-scale	+1.0 / -1.0	-1.4 / +2.3
PDF	-0.1 / +0.2	-
CKKW-scale	+5.9 / -4.1	-
QSF-scale	+1.5 / -1.7	-
UEPS	-1.8 / +1.8	+2.4 / -2.4
EWK $Zjj, Zjjj$	+0.6 / -0.6	
	VBF tight	
QCD-scale	-	-2.5 / +2.6
PDF	-	-
CKKW-scale	-	-
QSF-scale	-	-
UEPS	-	-4.9 / +4.9
EWK $Zjj, Zjjj$	+1.8 / -1.8	
	Boosted loose	
QCD-scale	-	-1.6 / +1.3
PDF	-	-
CKKW-scale	-	-
QSF-scale	-	-
UEPS	-	-1.8 / +1.8
EWK $Zjj, Zjjj$	+0.1 / -0.1	
	Boosted tight	
QCD-scale	+0.8 / -0.6	-
PDF	+0.4 / -0.5	-
CKKW-scale	-4.3 / +3.4	-1.8 / +1.3
QSF-scale	+4.3 / -4.3	-
UEPS	+0.8 / -0.8	+2.6 / -2.6
EWK $Zjj, Zjjj$	+0.1 / -0.1	

Table 6.14.: Relative impact of theoretical uncertainties on the expected number of $Z \rightarrow \tau\tau$ background events in the signal regions of the $\tau_{lep}\tau_{lep}$ channel. Given is the up- and downward variation in percent. Variations below 0.1% are ignored.

6.4. Statistical Data Analysis

This section describes the statistical formalism, which is used in the analysis in order to measure the signal strength and cross-section for Higgs-boson production with $H \to \tau\tau$ decays. In addition, the exploited methods allow to determine significances for a deviation from the *background-only* hypothesis, which does not include any $H \to \tau\tau$ signal, in the observed data. The following descriptions are based on Ref. [227, 228].

The first part of this section gives an introduction to the basic principles of likelihood functions, parameter estimation and hypothesis testing. In addition, the profiled likelihood ratio, which is used in this analysis as the test statistics, is defined. The next section then discusses the inclusion of systematic uncertainties as *nuisance parameters* in the likelihood function. Finally, the fitting procedure and statistical model are described, where an overview of the considered signal and control regions with the respective discriminating variables is given.

The technical implementation and minimization of the likelihood function is done with HistFactory [229] including the RooStats [230] and RooFit [231] packages with Minuit [232].

6.4.1. Likelihood Function and Statistical Testing

The distribution of a set of random variables $\boldsymbol{n} = (n_1, .., n_N)$ is given by the probability density function (PDF) $f(\boldsymbol{n})$ and can depend on a set of unknown parameters $\boldsymbol{\theta} = (\theta_1, .., \theta_m)$ in an underlying model. If $\boldsymbol{n}$ corresponds to an observed dataset of events with contributions from signal and background processes, its PDF is constructed from the combination of PDFs $f_S(\boldsymbol{n}; \theta)$ and $f_B(\boldsymbol{n}; \theta)$ for signal and background, respectively. The underlying model, in which these signal and background PDFs are evaluated, is also referred to as a *hypothesis*. The compatibility of the observed dataset with a specific hypothesis can be evaluated by calculating the likelihood function $\mathcal{L}$

$$\mathcal{L}(\boldsymbol{n}; \boldsymbol{\theta}) = f(\boldsymbol{n}; \boldsymbol{\theta}) = f(n_1; \boldsymbol{\theta}) \cdot ... \cdot f(n_N; \boldsymbol{\theta}), \tag{6.6}$$

where the measurements $(n_1, ..., n_N)$ are assumed to be statistically independent. Here, large values of $\mathcal{L}$ correspond to a high compatibility between measurement and hypothesis.

In case of binned distributions, such as N-bin histograms, the measurement set $(n_1, ..., n_N)$ can be seen as the number of observed data events in each bin i. In each of these bins the predicted number of events $(n_1^{pred}, ..., n_N^{pred})$ from signal s_i and background b_i contribution within the considered model is defined with the signal-strength parameter μ:

$$n_i^{pred}(\mu, \boldsymbol{\theta}) = \mu s_i(\boldsymbol{\theta}) + b_i(\boldsymbol{\theta}). \tag{6.7}$$

The likelihood function is then given as the product of Poisson probabilities to observe n_i events in bin i, when n_i^{pred} events are expected:

$$\mathcal{L}(\boldsymbol{n}; \mu, \boldsymbol{\theta}) = \prod_{i=0}^{N} \mathrm{Pois}(n_i; n_i^{pred}(\mu, \boldsymbol{\theta})) = \prod_{i=0}^{N} \frac{(\mu s_i(\boldsymbol{\theta}) + b_i(\boldsymbol{\theta}))^{n_i}}{(n_i)!} \cdot \mathrm{e}^{-(\mu s_i(\boldsymbol{\theta}) + b_i(\boldsymbol{\theta}))}. \tag{6.8}$$

The maximum likelihood approach (ML) provides a method to determine the best-fit signal strength as the ratio of the measured signal cross-section to the prediction:

$$\hat{\mu} = \frac{\sigma_{meas}}{\sigma_{pred}}. \tag{6.9}$$

The determination of the *parameter of interest* (POI) $\hat{\mu}$ depends on the estimated values of the parameter set $\boldsymbol{\theta}$ for the considered model. In particular, the values $\hat{\mu}$ and $\hat{\boldsymbol{\theta}}$ denote the best-fit parameters, which maximize the likelihood function in Equation 6.8 and are therefore also called maximum likelihood estimators (MLE). With the assumption, that the MLEs are distributed according to Gaussian PDFs, their uncertainties, $\hat{\sigma}^{+}_{\hat{\theta}}$ and $\hat{\sigma}^{-}_{\hat{\theta}}$, can be determined by constructing central confidence intervals (CIs) based on the approximate likelihood method [227]. The Taylor series of the logarithmic likelihood function depending on a generic parameter θ_i around its best-fit value $\hat{\theta}_i$ can be written in the following way:

$$\begin{aligned} \ln(\mathcal{L}(\theta_i)) = \ln(\mathcal{L}(\hat{\theta}_i)) &+ \left[\frac{\partial \ln(\mathcal{L}(\theta_i))}{\partial \theta_i}\right]_{\theta_i=\hat{\theta}_i} (\theta_i - \hat{\theta}_i) \\ &+ \frac{1}{2}\left[\frac{\partial^2 \ln(\mathcal{L}(\theta_i))}{\partial^2 \theta_i}\right]_{\theta_i=\hat{\theta}_i} (\theta - \hat{\theta}_i)^2 + ... \end{aligned} \tag{6.10}$$

By construction the best-fit parameter $\hat{\theta}_i$ maximizes the likelihood function and hence the second term in Equation 6.10 vanishes. Furthermore, the variance of the distribution of $\hat{\theta}_i$ approximated in the large sample limit [227] is given by:

$$\hat{\sigma}^2_{\hat{\theta}_i} = -\left[\frac{\partial^2 \ln(\mathcal{L}(\theta_i))}{\partial^2 \theta_i}\right]^{-1}_{\theta_i=\hat{\theta}_i}. \tag{6.11}$$

With this, Equation 6.10 can be evaluated at $\theta_i = \hat{\theta}_i \pm N\hat{\sigma}^{\pm}_{\hat{\theta}_i}$ and takes the following form, when higher order terms are neglected:

$$\frac{N^2}{2} = \ln(\mathcal{L}(\hat{\theta}_i)) - \ln(\mathcal{L}(\hat{\theta}_i \pm N\hat{\sigma}^{\pm}_{\hat{\theta}_i})). \tag{6.12}$$

Due to technical reasons, the best-fit parameters are usually determined by minimizing the negative logarithm of the likelihood function $\mathrm{NLL}(\theta_i) = -\ln(\mathcal{L}(\theta_i))$ instead of maximizing the likelihood function itself. Then, Equation 6.12 can also be written as

$$\frac{N^2}{2} = \mathrm{NLL}(\hat{\theta}_i \pm N\hat{\sigma}^{\pm}_{\hat{\theta}_i}) - \mathrm{NLL}(\hat{\theta}_i). \tag{6.13}$$

Hence, the CIs at the 68.3 % ($N = 1$) and 95 % ($N = 1.96$) confidence level (CL) $[\hat{\theta}_i - N\hat{\sigma}^{-}_{\hat{\theta}_i}, \hat{\theta}_i + N\hat{\sigma}^{+}_{\hat{\theta}_i}]$ can be determined by calculating the values of θ_i, which lead to a change of the likelihood value $\Delta\mathrm{NLL} = \mathrm{NLL}(\hat{\theta}_i \pm N\hat{\sigma}^{\pm}_{\hat{\theta}_i}) - \mathrm{NLL}(\hat{\theta}_i)$ of 0.50 and 1.92, respectively. This procedure is also illustrated in Figure 6.17 and is used in order to determine the uncertainties on the best-fit signal strength and on the nuisance parameters in the analysis.

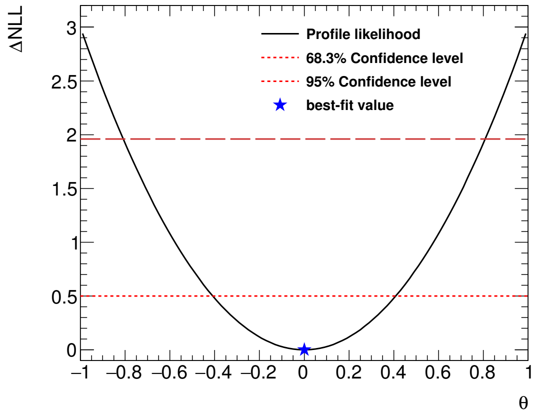

Figure 6.17.: Illustration of a negative log-likelihood (NLL) curve for the parameter θ and the construction of approximate central confidence intervals. The decrease of the NLL-curve of $\Delta\text{NLL} = 0.5\,(1.96)$ with respect to the best-fit value $\hat{\theta}$ (blue star) corresponds to the 68.3 % (95 %) confidence level.

Hypothesis Testing

In order to test a *null* hypothesis H_0 against an *alternative* hypothesis H_1, a test statistics t is used. This test statistic is distributed under H_0 and H_1 according to the probability densities $f(t; H_0)$ and $f(t; H_1)$, respectively, and allows to quantify the level of (dis-)agreement between a hypothesis and the observed data. In particular, the probability, that the test statistics is less or equally compatible with the data than the observed value t_{obs} under H_0 can be determined with

$$p = \int_{t_{obs}}^{\infty} f(t; H_0)dt. \tag{6.14}$$

This p-value is often translated into a significance Z in units of Gaussian standard deviations

$$Z = \Phi^{-1}(1 - p) \tag{6.15}$$

with the cumulative Gaussian distribution Φ^{-1}. The null hpothesis H_0 is rejected, if the observed value of the test statistic t_{obs} is found in a predefined critical region with $t_{obs} > t_{cut}$. Otherwise H_0 is accepted. Here, the choice of t_{cut} can be identified with a specific significance level α:

$$\alpha = \int_{t_{cut}}^{\infty} f(t; H_0)dt. \tag{6.16}$$

Since α corresponds to the probability to reject H_0, when it is true, it is also referred to as *error of first kind*. On the other hand, the probability to not reject H_0, when the alternative hypothesis H_1 is true, corresponds to the *error of second kind*:

$$\beta = \int_{-\infty}^{t_{cut}} f(t; H_1)dt. \tag{6.17}$$

The statistical power of a test statistics is then given by $1 - \beta$ and can therefore be defined as the probability to accept H_1, when H_1 is true. According to the Neyman-Pearson Lemma [227], the test statistics, which provides the highest statistical power for a given significance level for two simple[1] hypotheses H_0 and H_1, corresponds to the ratio of likelihood functions evaluated for the observed dataset $\boldsymbol{n}$ under the hypotheses to be tested:

$$t = \frac{\mathcal{L}(\boldsymbol{n}; H_0)}{\mathcal{L}(\boldsymbol{n}; H_1)}. \tag{6.18}$$

In this analysis, a *profiled likelihood ratio* t_0 is used to quantify the level of disagreement between the null-hypothesis H_0, which corresponds to the absence of any signal contribution with $\mu = 0$ (background-only hypothesis), and the observed data:

$$t_0 = \frac{\mathcal{L}(0, \hat{\hat{\boldsymbol{\theta}}}_0)}{\mathcal{L}(\hat{\mu}, \hat{\boldsymbol{\theta}}_{\hat{\mu}})}. \tag{6.19}$$

In this notation, the *unconditional* estimators $\hat{\mu}$ and $\hat{\boldsymbol{\theta}}$ maximize the likelihood function, while $\hat{\hat{\boldsymbol{\theta}}}_0$ correspond to the *conditional* MLEs for a fixed value of $\mu = 0$. The determination of these conditional MLEs is also called *profiling*. As the analysis is based on the measurement of positive signal rates, $\hat{\mu}$ is forced to be positive and the best level of agreement between data and prediction is assumed to correspond to $\hat{\mu} = 0$ in case of downward fluctuations:

$$t_0 = \begin{cases} \frac{\mathcal{L}(0, \hat{\hat{\boldsymbol{\theta}}}_0)}{\mathcal{L}(\hat{\mu}, \hat{\boldsymbol{\theta}}_{\hat{\mu}})}, & \text{for } \hat{\mu} \geq 0 \\ \frac{\mathcal{L}(0, \hat{\hat{\boldsymbol{\theta}}}_0)}{\mathcal{L}(0, \hat{\hat{\boldsymbol{\theta}}}_0)}, & \text{for } \hat{\mu} < 0 \end{cases} \tag{6.20}$$

Furthermore, it is convenient to express the test statistics in terms of its logarithm in the following form:

$$q_0 = -2\ln(t_0). \tag{6.21}$$

While in general, the probability densities for the test statistic can be determined with toy experiments according to the MC sampling method [233], this procedure is computationally expensive and often not feasible. Instead, the results obtained by Wald [234] allow to approximate the test statistics PDF $f(q_0; H_1)$ in the large sample limit with a non-central χ^2-distribution for one degree of freedom, while the PDF under the background-only hypothesis $f(q_0; H_0)$ asymptotically approaches a χ^2-distribution [235].

Discovery of a new process

In general, the discovery of a new process corresponds to the rejection of the background-only hypothesis $H_0(\mu = 0, \boldsymbol{\theta})$ with a high significance. This means, that the observed p-value p_0^{obs} is found to be below a certain threshold α, which corresponds to a low probability to reject H_0, if it is true. H_0 can then be considered as excluded at a specific confidence level (CL) of $1 - \alpha$. In particle physics, discovery is claimed if

$$p_0^{obs} = \int_{q_0^{obs}}^{\infty} f(q_0; 0, \hat{\hat{\boldsymbol{\theta}}}_0) dq_0 \leq 2.87 \times 10^{-7}, \tag{6.22}$$

[1] A simple hypothesis contains no free parameters.

where q_0 gives the test statistics for the background-only hypothesis $H_0(\mu = 0, \boldsymbol{\theta})$ according to Equation 6.19 and 6.21. In the large sample limit the significance given in Equation 6.15 can then be approximated as

$$Z_0 = \sqrt{q_0}. \tag{6.23}$$

The upper threshold on the observed p-value in order to claim discovery of a new process corresponds to a deviation from the background-only hypothesis with a signficance of $Z_0 \geq 5\,\sigma$.

It is often useful to quantify the sensitivity of an experiment by also giving the expected significance Z^{exp}. Here, the expected p-value is calculated with the PDF for the test statistics in a specific signal model for an assumed signal strength of μ'

$$p_0^{exp} = \int_{q_0^{exp}}^{\infty} f(q_0; \mu', \hat{\hat{\boldsymbol{\theta}}}_{\mu'}) dq_0, \tag{6.24}$$

where q_0^{exp} corresponds to the median value under the hypothesis of μ'. As described above, the test statistics PDF under this hypothesis with $\mu' \neq 0$ can be approximated in the large sample limit with a non-central χ^2-distribution for one degree of freedom. In the analysis, the expected significance is usually derived by constructing a pseudo dataset (*Asimov* dataset) from the signal and background expectation with $\mu' = 1$.

6.4.2. Inclusion of Nuisance Parameters

The systematic uncertainties described in Section 6.3 are included in the likelihood function as a set of *nuisance parameters* (NPs) $\boldsymbol{\theta} = (\theta_1, ..., \theta_{N_{sys}})$, which affect the predicted signal and background yields, $s_i(\boldsymbol{\theta})$ and $b_i(\boldsymbol{\theta})$, in each histogram bin i. These NPs arise from the uncertainty on various quantities, such as scale factors or efficiencies, which are determined in auxiliary measurements (see Chapter 5). Their impact on the signal and background prediction is then evaluated by varying the corresponding quantities within their $\pm 1\sigma$ uncertainties and repeating the full analysis. This additional information is incorporated in the fit model by augmenting the likelihood function in Equation 6.8 with terms of the form

$$\mathcal{L}_{sys}(\boldsymbol{\theta}) = \prod_{t=0}^{N_{sys}} \text{Gaus}(0; \theta_t, 1) = \prod_{t=0}^{N_{sys}} \frac{1}{2\pi} \mathrm{e}^{-\frac{1}{2}\theta_t^2}. \tag{6.25}$$

Here, each NP θ is parametrized by a Gaussian distribution with a mean of 0 representing the measured NP value and a width of 1, which corresponds to the measurement uncertainty. Since the histograms are only provided for the $\pm 1\sigma$ NP variations, the functional form of θ_t is obtained by using a piecewise exponential and linear inter- and extrapolation scheme [236]. Hence, the information on the systematic uncertainties as obtained from auxiliary measurements are taken into account and the terms in Equation 6.25 act as additional constraints in the maximization of the likelihood function.

Statistical uncertainties on the background prediction from simulation are included as γ-parameters, which modify the total background yield in each bin $i = (0, ..., N_{bins})$. These γ-parameters describe the fluctuation of the number of *raw*[2] background events m_i around

[2]For each generated event per bin an average weight is assigned, where the sum of these event weights correspond to the total expected event yield.

the true value $\gamma_i m_i$ in each bin i based on a Poisson distribution:

$$\mathcal{L}_{stat} = \prod_{i=0}^{N_{bins}} \mathrm{Pois}(m_i; \gamma_i m_i) = \prod_{i=0}^{N_{bins}} \frac{(\gamma_i m_i)^{m_i}}{m_i!} \mathrm{e}^{-\gamma_i m_i}. \tag{6.26}$$

Here, the values of m_i in each bin i can be estimated according to $m_i = (\delta_i / b_i)^2$ with the expected background yield b_i and the total statistical uncertainty δ_i [229].

The overall predicted yield for the main background processes are derived from data in the likelihood fit by including additional CRs, which are enriched in events from the considered process. These CRs allow to determine the *free-floating* normalization factors $\phi_{p,c}$, which scale the predicted event yield for process p in category c, but do not contribute with additional constraining terms in the likelihood function. In particular, these normalization factors are correlated across the signal and control regions of each category. As described in the next section, the analysis presented here applies separate normalization factors to the background predictions of $Z \to \tau\tau$, $Z \to \ell\ell$ and top-quark events in the VBF category={VBF loose SR, VBF tight SR, VBF Top CR, VBF $Z \to \ell\ell$ CR} and the boosted category={boosted loose SR, boosted tight SR, boosted Top CR, boosted $Z \to \ell\ell$ CR}. This results in six normalization factors. Hence, the number of predicted events in each region r gain an additional dependency on the set of considered normalization factors $\boldsymbol{\phi}_r = \{\phi_{p,r\in\text{VBF cat./boosted cat.}}\}$ with

$$n_{i,r}^{pred}(\mu, \boldsymbol{\theta}, \boldsymbol{\phi}_r) = \mu s_{i,r}(\boldsymbol{\theta}) + b_{i,r}(\boldsymbol{\theta}, \boldsymbol{\phi}_r). \tag{6.27}$$

The likelihood function including systematic and statistical uncertainties as well as background normalization factors can then be written as

$$\begin{aligned} \mathcal{L}(\mu, \boldsymbol{\theta}, \boldsymbol{\gamma}, \boldsymbol{\phi}) = & \prod_{r\in\text{regions}} \prod_{i\in\text{bins}} \mathrm{Pois}(n_{i,r}; \mu s_{i,r}(\boldsymbol{\theta}) + b_{i,r}(\boldsymbol{\theta}, \boldsymbol{\phi}_r)) \mathrm{Pois}(m_{i,r}; \gamma_{i,r} m_{i,r}) \\ & \cdot \prod_{t\in\text{sys}} \mathrm{Gaus}(0; \theta_t, 1), \end{aligned} \tag{6.28}$$

where r runs over all signal and control regions, i gives the index for each histogram bin and t runs over the set of systematic uncertainties.

6.4.3. Determination of Acceptance and Shape Uncertainties

The $\pm 1\sigma$ variations for each source of systematic uncertainty are included as histograms of the discriminating variable and are compared to the nominal sample, which does not contain any systematic variations. The uncertainties are then grouped into acceptance and shape NPs by evaluating their impact on the expected event yield and on the shape of the discriminating variable for each signal and background process separately. The impact of acceptance NPs is derived from the relative variation of the histogram integral between variation and nominal sample, while for shape NPs the distribution is normalized to the expected nominal yield in order to extract their impact on the histogram shape. As the fit stability improves by reducing the number of parameters in the likelihood function, different *pruning* criteria are applied in order to determine, which NPs are found to have a negligible impact in terms of acceptance and shape variations: Uncertainties on the acceptance are only included, if the relative impact on the expected event yield from either the upward or downward variation is found to be greater than 0.5 %. For uncertainties acting on the shape, more specific pruning criteria are applied: In order to remove variations, which are dominated by statistical noise, shape uncertainties are not included, if the relative statistical uncertainty on the total predicted yield for either the upward or downward variation exceeds 10 %. In addition, the compatibility between the nominal distribution and the variations is estimated by performing a $\mathcal{X}^2$-test from $\mathcal{X}^2_{up,down} = \sum_{i=0}^{N_{bins}} (n_i^{nom} - n_i^{up,down})^2 / \max(\sigma_i^{nom}, \sigma_i^{up,down})$ with the expected yields $n_i^{nom,up,down}$ and statistical uncertainties $\sigma_i^{nom/up/down}$ of the nominal, upward or downward varied sample in each bin i. The shape uncertainty is only retained, if a $\mathcal{X}^2$-value of greater than 0.1 is obtained for either the upward or downward variation. Last, shape uncertainties are required to have a variation significance $S_i = |n_i^{up} - n_i^{down}|/\sigma_i^{nom}$ of greater than 0.1 for at least one histogram bin i.

Table 6.15 - 6.22 summarize the NPs, which are retained after the pruning procedure as shape or acceptance uncertainties in the signal regions of the $\tau_{lep}\tau_{lep}$ channel. An explanation of the NP names can be found in Appendix B. In total, 68 NPs are included to describe experimental uncertainties, while 52 NPs describe theoretical uncertainties. In particular, the VBF loose (tight) category contains 55 (51) experimental NPs and 40 theoretical NPs. For the boosted loose (tight) region, 52 (40) experimental NPs and 37 (42) theoretical NPs are considered. The list of acceptance uncertainties in the $Z \to \ell\ell$ CR and the Top CR can be found in Appendix D.1.

In order to further reduce the impact of statistical noise on the remaining shape uncertainties, additional *symmetrization* and *smoothing* procedures are applied. If both the upward and downward variations of a shape uncertainty result in a deviation from the nominal sample in the same direction (both increasing or decreasing the expected event yields), this bin is symmetrized by applying the largest deviation from the nominal distribution in the opposite direction as well. If this *local* symmetrization predicts a negative yield in any bin, the content of this bin is set to 10^{-6} instead. This is also done for all bins of the nominal and variation histograms, where negative yields can appear due to limitations in the available sample sizes. Furthermore, a smoothing algorithm, as implemented in the ROOT framework [237], is applied to the ratio of variation and nominal histogram This ratio is then multiplied to the nominal histogram in order to derive the smoothed shape of the final variation.

6.4.4. Fitting Procedure

An overview of the different signal and control regions, which are included in the maximum-likelihood fit in the $\tau_{lep}\tau_{lep}$ channel, is given in Table 6.23. In total, four signal regions corresponding to the VBF tight, VBF loose, boosted tight and boosted loose categories as defined in Section 6.1.3 are considered. In these signal regions, the reconstructed di-τ mass $m_{\tau\tau}^{\mathrm{MMC}}$ is used as the discriminating variable, where the binning is chosen in order to account for the available sample sizes in the different regions.

The normalization of background contributions from $Z \to \tau\tau$, $Z \to \ell\ell$ and top-quark events are determined by including free-floating normalization factors, which are applied

Systematic	ggF $H \to \tau\tau$	ggF $H \to WW$	VBF $H \to \tau\tau$	VBF $H \to WW$	WH $H \to \tau\tau$	ZH $H \to \tau\tau$	ttH $H \to \tau\tau$	$Z \to \tau\tau$	$Z \to \ell\ell$	Top	Di-boson	Fakes
EG_SCALE_LARCALIB_2015PRE			• ×									
EL_EFF_ID_NONPROMPT_D0	×		×					×				
EL_EFF_ID_TOTAL					×	×	×	×		×		
FT_EFF_Eigen_b_0							×			×		
FT_EFF_Eigen_b_1										×		
FT_EFF_Eigen_b_2										×		
FT_EFF_Eigen_c_0					×	×	×					
FT_EFF_Eigen_light_0	×	×	×	×	×	×	×	×	×	×	×	
FT_EFF_extrapolation_from_charm					×		×					
JER_CROSSCALIBFWD	• ×		• ×		×	×		• ×			×	
JER_NOISEFWD	• ×	×	• ×		×	×		×	×		×	
JER_NP_0	• ×	×	• ×	×	×	×	×	×	×	×	• ×	
JER_NP_1	×	×	• ×	• ×		×	×	• ×			×	
JER_NP_2	• ×		• ×	• ×	×	×	×	• ×	×	×	• ×	
JER_NP_3	• ×	×	• ×	• ×	×	×	×	• ×	×	• ×	• ×	
JER_NP_4	• ×		• ×	• ×		×	×	• ×		• ×	• ×	
JER_NP_5	• ×	×	• ×	• ×		×	×	• ×		• ×	×	
JER_NP_6	• ×	×	• ×				×			• ×		
JER_NP_7	• ×		• ×	• ×			×	• ×	×	• ×	×	
JER_NP_8	• ×	×	• ×	• ×		×	×	×		×	×	
JES_EffectiveNP_1	• ×	×	• ×	• ×			×	×	×	×	×	
JES_EffectiveNP_2	• ×		• ×	• ×	×		×		×			
JES_EffectiveNP_3		×	• ×				×		×	×		
JES_EffectiveNP_4	• ×		•				×		×	×		
JES_EffectiveNP_5			• ×						×			
JES_EffectiveNP_6			• ×						×			
JES_EffectiveNP_7			• ×							• ×		
JES_EffectiveNP_8			• ×						×			
JES_EtaInter_Model	• ×		• ×	• ×	×		×	• ×	×		• ×	
JES_EtaInter_NonClosure	• ×	×	•	• ×			×		×	×		
JES_EtaInter_Stat	×		• ×		×			×	×		×	
JES_Flavor_Comp	• ×	×	• ×		×		×	×			• ×	
JES_Flavor_Comp_leplepzll									×			
JES_Flavor_Resp	• ×	×	• ×	• ×	×		×	• ×			×	
JES_Flavor_Resp_leplepzll									×			
JES_HighPt												
JES_PU_OffsetMu	• ×	×	• ×	×	×			×	×	• ×		
JES_PU_OffsetNPV	• ×		• ×	• ×	×		×	×		×	• ×	
JES_PU_PtTerm	×		• ×	×	×		×	• ×	×	×	• ×	
JES_PU_Rho	• ×	×	• ×	• ×			×	• ×	×	×	• ×	
JVT						×	×					
MET_SoftTrk_ResoPara	• ×	×	•		×		×	•	×	×		
MET_SoftTrk_ResoPerp	×	×	•	• ×		×	×	• ×	×		•	
MET_SoftTrk_Scale		×	• ×		×		×	×	×	• ×		
MUONS_ID							×					
MUONS_MS									×			
MUONS_SAGITTA_RESBIAS									×			
MUONS_SAGITTA_RHO			• ×									
MUONS_SCALE			• ×						×			
MUON_EFF_SYS		×										
PRW_DATASF	• ×	×	×	• ×	×	×	×	×	×	×	•	
ll_fake_nonclosure												×
ll_fake_stat												×

Table 6.15.: Summary of shape (•) and acceptance (×) uncertainties from experimental sources in the VBF loose signal region of the $\tau_{lep}\tau_{lep}$ channel.

Systematic	ggF $H \to \tau\tau$	ggF $H \to WW$	VBF $H \to \tau\tau$	VBF $H \to WW$	WH $H \to \tau\tau$	ZH $H \to \tau\tau$	ttH $H \to \tau\tau$	$Z \to \tau\tau$	$Z \to \ell\ell$	Top	Di-boson	Fakes
Theo_NLO_EW_Higgs_total			×	×								
Theo_QCDscale_VBF_total			×	×								
Theo_QCDscale_VH_total					×	×						
Theo_QCDscale_ttH_total							×					
Theo_VBFH_shower			• ×									
Theo_VH_MUR_MUF					×	×						
Theo_alphas_Higgs_VBF_total			×	×								
Theo_alphas_Higgs_VH_total					×	×						
Theo_alphas_Higgs_ggH_total	×	×										
Theo_alphas_Higgs_ttH_total							×					
Theo_ggH_shower	• ×											
Theo_ggH_sig_qcd_0	×											
Theo_ggH_sig_qcd_1	×											
Theo_ggH_sig_qcd_2	×											
Theo_ggH_sig_qcd_3	×											
Theo_ggH_sig_qcd_4	×											
Theo_ggH_sig_qcd_6	×											
Theo_ggH_sig_qcd_7	×											
Theo_ggH_sig_qcd_8	×											
Theo_ll_VH_PSUE					×	×						
Theo_ll_vbf_VBFH_PSUE			×	×								
Theo_ll_vbf_ggH_PSUE	×	×										
Theo_pdf_Higgs_VBF_total			×	×								
Theo_pdf_Higgs_VH_total					×	×						
Theo_pdf_Higgs_ggH_total	×	×										
Theo_pdf_Higgs_ttH_total							×					
Theo_sig_alphaS	×											
Theo_sig_pdf_0					×							
Theo_sig_pdf_20						×						
Theo_sig_pdf_3					×							
Theo_sig_pdf_4	×											
Z_EWK_proportion								×				
ZttTheory_CKK_Relative_VBF								×				
ZttTheory_MGvsSH_Relative_VBF								×				
ZttTheory_MGvsSH_vbf_leplep								×				
ZttTheory_MUR_MUF_Relative_VBF								×				
ZttTheory_MUR_MUF_vbf_leplep								×				
ZttTheory_PDF_Relative_VBF								×				
ZttTheory_QSF_Relative_VBF								×				

Table 6.16.: Summary of shape (•) and acceptance (×) uncertainties from theoretical sources in the VBF loose signal region of the $\tau_{lep}\tau_{lep}$ channel.

Systematic	ggF $H \to \tau\tau$	ggF $H \to WW$	VBF $H \to \tau\tau$	VBF $H \to WW$	WH $H \to \tau\tau$	ZH $H \to \tau\tau$	ttH $H \to \tau\tau$	$Z \to \tau\tau$	$Z \to \ell\ell$	Top	Di-boson	Fakes
EG_RESOLUTION_ALL								• ×				
EG_SCALE_ALLCORR								• ×				
EG_SCALE_LARCALIB_2015PRE							×	• ×				
EL_EFF_ID_NONPROMPT_D0	×		×					×				
EL_EFF_ID_TOTAL							×	×			×	
FT_EFF_Eigen_b_0							×			×		
FT_EFF_Eigen_b_1							×			×		
FT_EFF_Eigen_b_2							×					
FT_EFF_Eigen_c_0					×		×					
FT_EFF_Eigen_light_0	×	×			×	×	×	×	×	×	×	
JER_CROSSCALIBFWD	•	×	•	• ×	×		×	• ×	×	×	• ×	
JER_NOISEFWD	• ×	×	•	• ×	×		×	• ×	×	×	• ×	
JER_NP_0	• ×		• ×	• ×	×	×		• ×	×	• ×	• ×	
JER_NP_1	• ×		• ×	• ×	×	×	×	• ×	×	• ×	• ×	
JER_NP_2	• ×		• ×	• ×	×	×	×	• ×	×	• ×	• ×	
JER_NP_3	• ×	×	• ×	• ×		×	×	• ×	×	×	• ×	
JER_NP_4	• ×		• ×	• ×	×	×	×	• ×	×	• ×	• ×	
JER_NP_5	• ×	×	• ×	• ×				• ×	×	• ×	• ×	
JER_NP_6	• ×	×	• ×	• ×	×	×	×	• ×	×	• ×	• ×	
JER_NP_7	• ×	×	• ×	×	×		×	• ×	×	• ×	×	
JER_NP_8	• ×		• ×	×		×	×	×		• ×	• ×	
JES_EffectiveNP_1	• ×	×	• ×	• ×	×		×	×			• ×	
JES_EffectiveNP_2			• ×		×		×	• ×	×	• ×		
JES_EffectiveNP_3	• ×						×	• ×		×		
JES_EffectiveNP_4	• ×						×					
JES_EffectiveNP_5								• ×				
JES_EffectiveNP_6							×			• ×		
JES_EffectiveNP_7	• ×							• ×				
JES_EffectiveNP_8	• ×									• ×		
JES_EtaInter_Model	• ×	×	• ×	• ×	×		×	• ×	×	• ×	×	
JES_EtaInter_NonClosure	• ×	×	• ×	×			×		×		• ×	
JES_EtaInter_Stat	×		• ×	• ×				• ×	×	• ×		
JES_Flavor_Comp	• ×	×	• ×	×	×		×	• ×			• ×	
JES_Flavor_Comp_leplepzll									×			
JES_Flavor_Resp	• ×	×	• ×	×			×	• ×		×	×	
JES_Flavor_Resp_leplepzll									×			
JES_PU_OffsetMu		×	• ×		×				×		×	
JES_PU_OffsetNPV	×		• ×	• ×			×		×		×	
JES_PU_PtTerm	• ×	×	• ×	• ×	×		×	• ×		• ×	×	
JES_PU_Rho	• ×	×	• ×	• ×	×		×	• ×	×	×	• ×	
MET_SoftTrk_ResoPara	•		•	•			×	• ×	×	×	• ×	
MET_SoftTrk_ResoPerp	•		•				×	•	×		×	
MET_SoftTrk_Scale	• ×		• ×				×			• ×		
MUONS_ID							×	• ×				
MUONS_MS	• ×											
MUONS_SAGITTA_RESBIAS							×			• ×		
MUONS_SAGITTA_RHO							×					
MUONS_SCALE							×			• ×	×	
MUON_EFF_SYS					×	×						
PRW_DATASF	• ×	• ×	• ×	• ×	×	×	• ×	• ×	• ×	• ×	• ×	
ll_fake_nonclosure												• ×
ll_fake_stat												×

Table 6.17.: Summary of shape (•) and acceptance (×) uncertainties from experimental sources in the VBF tight signal region of the $\tau_{lep}\tau_{lep}$ channel.

Systematic	ggF $H \to \tau\tau$	ggF $H \to WW$	VBF $H \to \tau\tau$	VBF $H \to WW$	WH $H \to \tau\tau$	ZH $H \to \tau\tau$	ttH $H \to \tau\tau$	$Z \to \tau\tau$	$Z \to \ell\ell$	Top	Di-boson	Fakes
Theo_NLO_EW_Higgs_total			×	×								
Theo_QCDscale_VBF_total			×	×								
Theo_QCDscale_VH_total					×	×						
Theo_QCDscale_ttH_total							×					
Theo_VBFH_MUR_MUF			×									
Theo_VBFH_shower			•									
Theo_VH_MUR_MUF					×	×						
Theo_alphas_Higgs_VBF_total			×	×								
Theo_alphas_Higgs_VH_total					×	×						
Theo_alphas_Higgs_ggH_total	×	×										
Theo_alphas_Higgs_ttH_total							×					
Theo_ggH_shower	• ×											
Theo_ggH_sig_qcd_0	×											
Theo_ggH_sig_qcd_1	×											
Theo_ggH_sig_qcd_2	×											
Theo_ggH_sig_qcd_3	×											
Theo_ggH_sig_qcd_4	×											
Theo_ggH_sig_qcd_6	×											
Theo_ggH_sig_qcd_7	×											
Theo_ggH_sig_qcd_8	×											
Theo_ll_VH_PSUE					×	×						
Theo_ll_vbf_VBFH_PSUE			×	×								
Theo_ll_vbf_ggH_PSUE	×	×										
Theo_pdf_Higgs_VBF_total			×	×								
Theo_pdf_Higgs_VH_total					×	×						
Theo_pdf_Higgs_ggH_total	×	×										
Theo_pdf_Higgs_ttH_total							×					
Theo_sig_alphaS	×											
Theo_sig_pdf_1						×						
Theo_sig_pdf_4	×											
Z_EWK_proportion								×				
ZttTheory_CKK_Relative_VBF								×				
ZttTheory_MGvsSH_Relative_VBF								×				
ZttTheory_MGvsSH_vbf_leplep								×				
ZttTheory_MUR_MUF_Relative_VBF								×				
ZttTheory_MUR_MUF_vbf_leplep								×				
ZttTheory_PDF_Relative_VBF								×				
ZttTheory_PDF_vbf_leplep								•				
ZttTheory_QSF_Relative_VBF								×				

Table 6.18.: Summary of shape (•) and acceptance (×) uncertainties from theoretical sources in the VBF tight signal region of the $\tau_{lep}\tau_{lep}$ channel.

Systematic	ggF $H \to \tau\tau$	ggF $H \to WW$	VBF $H \to \tau\tau$	VBF $H \to WW$	WH $H \to \tau\tau$	ZH $H \to \tau\tau$	ttH $H \to \tau\tau$	$Z \to \tau\tau$	$Z \to \ell\ell$	Top	Di-boson	Fakes
EG_RESOLUTION_ALL		● ×										
EG_SCALE_ALLCORR		● ×							×			
EG_SCALE_LARCALIB_2015PRE		● ×										
EL_EFF_ID_NONPROMPT_D0	×		×					×				
EL_EFF_ID_TOTAL	×	×	×	×	×			×		×	×	
FT_EFF_Eigen_b_0							×			×		
FT_EFF_Eigen_b_1							×			×		
FT_EFF_Eigen_b_2							×			×		
FT_EFF_Eigen_c_0					×		×					
FT_EFF_Eigen_light_0	×	×	×	×	×	×	×	×	×	×	×	
JER_CROSSCALIBFWD	●	×	●	● ×	×		×	●	×	● ×		
JER_NOISEFWD	●		●	● ×	×	● ×		●	×	×		
JER_NP_0	● ×	● ×	● ×	● ×	×	● ×	×	● ×	×	● ×	● ×	
JER_NP_1	● ×	● ×	×	● ×	● ×	×	● ×	● ×	×	×	×	
JER_NP_2	● ×	● ×	● ×	● ×	● ×	● ×		×	×	×	● ×	
JER_NP_3	● ×	● ×	● ×	● ×	● ×	● ×	×	● ×		● ×	● ×	
JER_NP_4	● ×		×	×		● ×	● ×	×		● ×	×	
JER_NP_5	● ×		×	×	×	● ×	● ×	● ×		×		
JER_NP_6	● ×	● ×	×			×	● ×	● ×		● ×	×	
JER_NP_7		● ×	×	×			● ×	● ×			×	
JER_NP_8	● ×	×	×	×	● ×	×	×	● ×		×	×	
JES_EffectiveNP_1	● ×	● ×	● ×	×	×	● ×	×	● ×				
JES_EffectiveNP_2	● ×	● ×					×		×	×		
JES_EffectiveNP_3		● ×				×	×		×			
JES_EffectiveNP_4		● ×							×			
JES_EffectiveNP_5							● ×		×			
JES_EffectiveNP_6		● ×										
JES_EffectiveNP_7	● ×	● ×					×					
JES_EffectiveNP_8	● ×	● ×										
JES_EtaInter_Model	● ×	● ×	● ×	×	×			● ×	×		● ×	
JES_EtaInter_NonClosure		● ×	● ×	×	×				×			
JES_EtaInter_Stat	● ×	● ×				● ×	×					
JES_Flavor_Comp	● ×	● ×	● ×			×	● ×				×	
JES_Flavor_Comp_leplepzll									×			
JES_Flavor_Resp	● ×	×	● ×	● ×		● ×		● ×			● ×	
JES_Flavor_Resp_leplepzll									×			
JES_PU_OffsetMu	● ×								×		● ×	
JES_PU_OffsetNPV		● ×		×			×		×		● ×	
JES_PU_PtTerm	● ×	● ×	● ×	×		● ×	● ×	×	×	×		
JES_PU_Rho	● ×	×	● ×	● ×	● ×	● ×	×	● ×				
JVT							×					
MET_SoftTrk_ResoPara	●	● ×	● ×	● ×				●	×			
MET_SoftTrk_ResoPerp	●	×	●	●	● ×		● ×	●	×			
MET_SoftTrk_Scale	● ×	● ×	● ×					● ×	×			
MUONS_ID	● ×											
MUONS_SAGITTA_RESBIAS		● ×										
MUONS_SCALE		● ×										
PRW_DATASF	● ×	● ×	● ×	● ×	● ×	● ×	×	● ×	● ×	● ×	● ×	
ll_fake_nonclosure												×
ll_fake_stat												×

Table 6.19.: Summary of shape (●) and acceptance (×) uncertainties from experimental sources in the boosted loose signal region of the $\tau_{lep}\tau_{lep}$ channel.

Systematic	ggF $H \to \tau\tau$	ggF $H \to WW$	VBF $H \to \tau\tau$	VBF $H \to WW$	WH $H \to \tau\tau$	ZH $H \to \tau\tau$	ttH $H \to \tau\tau$	$Z \to \tau\tau$	$Z \to \ell\ell$	Top	Di-boson	Fakes
Theo_NLO_EW_Higgs_total			×	×								
Theo_QCDscale_VBF_total			×	×								
Theo_QCDscale_VH_total					×	×						
Theo_QCDscale_ttH_total							×					
Theo_VBFH_shower			• ×									
Theo_VH_MUR_MUF					×	• ×						
Theo_alphas_Higgs_VBF_total			×	×								
Theo_alphas_Higgs_VH_total					×	×						
Theo_alphas_Higgs_ggH_total	×	×										
Theo_alphas_Higgs_ttH_total							×					
Theo_ggH_shower	• ×											
Theo_ggH_sig_qcd_0	×											
Theo_ggH_sig_qcd_1	×											
Theo_ggH_sig_qcd_2	×											
Theo_ggH_sig_qcd_3	×											
Theo_ggH_sig_qcd_6	×											
Theo_ggH_sig_qcd_7	• ×											
Theo_ll_VH_PSUE					×	×						
Theo_ll_boost_VBFH_PSUE			×	×								
Theo_ll_boost_ggH_PSUE	×	×										
Theo_pdf_Higgs_VBF_total			×	×								
Theo_pdf_Higgs_VH_total					×	×						
Theo_pdf_Higgs_ggH_total	×	×										
Theo_pdf_Higgs_ttH_total							×					
Theo_sig_alphaS	×											
Theo_sig_pdf_4	×											
Z_EWK_proportion								×				
ZttTheory_CKK_Relative_Bst								×				
ZttTheory_CKK_boost_leplep								•				
ZttTheory_MGvsSH_Relative_Bst								×				
ZttTheory_MGvsSH_boost_leplep								• ×				
ZttTheory_MUR_MUF_Relative_Bst								×				
ZttTheory_MUR_MUF_boost_leplep								×				
ZttTheory_PDF_Relative_Bst								×				
ZttTheory_QSF_Relative_Bst								×				

Table 6.20.: Summary of shape (•) and acceptance (×) uncertainties from theoretical sources in the boosted loose signal region of the $\tau_{lep}\tau_{lep}$ channel.

Systematic	ggF $H \to \tau\tau$	ggF $H \to WW$	VBF $H \to \tau\tau$	VBF $H \to WW$	WH $H \to \tau\tau$	ZH $H \to \tau\tau$	ttH $H \to \tau\tau$	$Z \to \tau\tau$	$Z \to \ell\ell$	Top	Di-boson	Fakes
EG_RESOLUTION_ALL			• ×			• ×						
EG_SCALE_ALLCORR						• ×						
EL_EFF_ID_NONPROMPT_D0	×		×					×				
EL_EFF_ID_TOTAL				×								
FT_EFF_Eigen_b_0							×			×		
FT_EFF_Eigen_b_1							×			×		
FT_EFF_Eigen_b_2							×			×		
FT_EFF_Eigen_c_0					×		×					
FT_EFF_Eigen_light_0	×	×	×	×	×	×	×	×	×	×	×	
JER_CROSSCALIBFWD				• ×		×		•	• ×	×		
JER_NOISEFWD				• ×		×	×	•	•			
JER_NP_0	• ×	• ×	• ×	• ×	• ×	• ×	×	• ×	• ×	• ×	• ×	
JER_NP_1	• ×	• ×		• ×	• ×		×	• ×	• ×	• ×	×	
JER_NP_2	• ×	• ×	• ×	• ×	• ×			• ×	×	• ×	• ×	
JER_NP_3	• ×	• ×	• ×	• ×	• ×	×	×	• ×	• ×	• ×	×	
JER_NP_4	• ×	• ×	• ×	×	• ×			• ×	• ×	• ×	• ×	
JER_NP_5	• ×	• ×	• ×		×	×		• ×	• ×	×	• ×	
JER_NP_6	• ×	• ×	×	×	• ×	×			×	×	• ×	
JER_NP_7	×	• ×	• ×	×			×	• ×	• ×	• ×	×	
JER_NP_8	• ×	• ×	• ×	×	×	×		• ×	×	×	• ×	
JES_EffectiveNP_1	• ×	×	• ×	• ×			×	• ×	• ×	• ×	×	
JES_EffectiveNP_2		• ×		×			×		×		• ×	
JES_EffectiveNP_3			• ×		• ×		×	• ×	×			
JES_EffectiveNP_4					• ×							
JES_EffectiveNP_5									• ×			
JES_EffectiveNP_6		• ×	• ×	• ×	• ×							
JES_EtaInter_Model	• ×	• ×	• ×	• ×				• ×	• ×		• ×	
JES_EtaInter_NonClosure	•	• ×	•	×		×			• ×			
JES_EtaInter_Stat	• ×	• ×	• ×		• ×				• ×			
JES_Flavor_Comp	• ×	• ×	• ×				×			• ×	×	
JES_Flavor_Comp_leplepzll									• ×			
JES_Flavor_Resp	• ×	• ×						• ×			• ×	
JES_Flavor_Resp_leplepzll									×			
JES_PU_OffsetMu							×	• ×				
JES_PU_OffsetNPV	• ×			×			×	• ×	• ×			
JES_PU_PtTerm	• ×	• ×	•	×		• ×		• ×	×	×	×	
JES_PU_Rho	• ×	×	• ×	• ×	• ×	• ×	×	• ×	• ×	• ×	• ×	
JVT							×					
MET_SoftTrk_ResoPara	• ×				• ×	×	×	•	• ×		•	
MET_SoftTrk_ResoPerp	•	•	•	×	•	×	×	•	×	•		
MET_SoftTrk_Scale	• ×	• ×		• ×		×	×	• ×	• ×			
MUONS_ID									×			
MUONS_MS			• ×			• ×			×			
MUONS_SAGITTA_RHO	• ×											
MUON_EFF_SYS									×			
PRW_DATASF	• ×	• ×	• ×	• ×	• ×	• ×	• ×	• ×	• ×	• ×	• ×	
ll_fake_nonclosure												×
ll_fake_stat												×

Table 6.21.: Summary of shape (•) and acceptance (×) uncertainties from experimental sources in the boosted tight signal region of the $\tau_{lep}\tau_{lep}$ channel.

Systematic	ggF $H \to \tau\tau$	ggF $H \to WW$	VBF $H \to \tau\tau$	VBF $H \to WW$	WH $H \to \tau\tau$	ZH $H \to \tau\tau$	ttH $H \to \tau\tau$	$Z \to \tau\tau$	$Z \to \ell\ell$	Top	Di-boson	Fakes
Theo_NLO_EW_Higgs_total			×	×								
Theo_QCDscale_VBF_total			×	×								
Theo_QCDscale_VH_total					×	×						
Theo_QCDscale_ttH_total							×					
Theo_VBFH_MUR_MUF			×									
Theo_VBFH_shower			• ×									
Theo_VH_MUR_MUF					×	×						
Theo_alphas_Higgs_VBF_total			×	×								
Theo_alphas_Higgs_VH_total					×	×						
Theo_alphas_Higgs_ggH_total	×	×										
Theo_alphas_Higgs_ttH_total							×					
Theo_ggH_shower	• ×											
Theo_ggH_sig_qcd_0	×											
Theo_ggH_sig_qcd_1	×											
Theo_ggH_sig_qcd_2	×											
Theo_ggH_sig_qcd_3	×											
Theo_ggH_sig_qcd_6	×											
Theo_ggH_sig_qcd_7	×											
Theo_ggH_sig_qcd_8	×											
Theo_ll_VH_PSUE					×	×						
Theo_ll_boost_VBFH_PSUE			×	×								
Theo_ll_boost_ggH_PSUE	×	×										
Theo_pdf_Higgs_VBF_total			×	×								
Theo_pdf_Higgs_VH_total					×	×						
Theo_pdf_Higgs_ggH_total	×	×										
Theo_pdf_Higgs_ttH_total							×					
Theo_sig_alphaS	×											
Theo_sig_pdf_16	×											
Theo_sig_pdf_3	×											
Theo_sig_pdf_4	×											
Z_EWK_proportion								×				
ZttTheory_CKK_Relative_Bst								×				
ZttTheory_CKK_boost_leplep								• ×				
ZttTheory_MGvsSH_Relative_Bst								×				
ZttTheory_MGvsSH_boost_leplep								• ×				
ZttTheory_MUR_MUF_Relative_Bst								×				
ZttTheory_MUR_MUF_boost_leplep								•				
ZttTheory_PDF_Relative_Bst								×				
ZttTheory_PDF_boost_leplep								•				
ZttTheory_QSF_Relative_Bst								×				

Table 6.22.: Summary of shape (•) and acceptance (×) uncertainties from theoretical sources in the boosted tight signal region of the $\tau_{lep}\tau_{lep}$ channel.

to the respective processes. In particular, separate normalization factors are used for the VBF and boosted categories, which are correlated across the respective loose and tight regions. Hence, the statistical model in the $\tau_{lep}\tau_{lep}$ final state includes six background normalization factors in total. For the combination with the $\tau_{lep}\tau_{had}$ and $\tau_{had}\tau_{had}$ final states, the normalization factors of the $Z \to \tau\tau$ background are correlated across the channels. While the $Z \to \tau\tau$ normalization is mainly constrained in the lower range of the $m_{\tau\tau}^{\mathrm{MMC}}$ distribution in the signal regions, additional CRs are included to exploit information on the normalization of the $Z \to \ell\ell$ and top-quark backgrounds. In the likelihood fit, these CRs only provide information on the expected event yields in terms of one-bin histograms. The normalization of the remaining background predictions are fixed to their SM prediction.

Region	Variable	Bins
VBF loose signal region	$m_{\tau\tau}^{\mathrm{MMC}}$	5
VBF tight signal region		7
Boosted loose signal region		7
Boosted tight signal region		8
VBF Top control region	Event yield	1
VBF $Z \to \ell\ell$ control region		
Boosted Top control region		
Boosted $Z \to \ell\ell$ cotrol region		

Table 6.23.: Overview of the signal and control regions, discriminating variables and their number of bins for the likelihood fit in the $\tau_{lep}\tau_{lep}$ channel.

The parameter of interest (POI) in the maximum likelihood fit corresponds to the signal strength $\mu_{H\to\tau\tau} = \sigma_{H\to\tau\tau}^{meas}/\sigma_{H\to\tau\tau}^{pred}$. Hence, a signal strenth of one implies the SM prediction, while a signal strength of zero corresponds to the absence of any $H \to \tau\tau$ signal. In order to measure the cross-section of Higgs-boson production with $H \to \tau\tau$ decays, $\sigma_{H\to\tau\tau}^{meas}$, the signal strength $\mu_{H\to\tau\tau}$ is extracted without systematic uncertainties on the theoretical prediction of the signal cross-sections and then multiplied by the SM prediction $\sigma_{H\to\tau\tau}^{pred}$. The measurement of this inclusive Higgs-boson production cross-section is obtained by performing a maximum-likelihood fit with one POI, which is applied to signal events from all considered Higgs-boson production modes (ggF, VBF, VH and ttH). The relative contributions of these production modes to the total signal are assumed to follow the SM prediction. In addition, the analysis also measures the individual Higgs-boson production cross-sections in the ggF channel, $\sigma_{H\to\tau\tau}^{ggF}$, and in the VBF channel, $\sigma_{H\to\tau\tau}^{VBF}$. For this, the likelihood fit is performed with two POIs. One POI scales the $H \to \tau\tau$ signal prediction from ggF production, while the other POI is applied to signal events from the VBF production. The remaining signal contributions from the VH and ttH production modes are fixed to their SM prediction. The results of these cross-section measurements are presented in the next section.

6.5. Results

This section presents the results of the cross-section and signal-strength measurements for Higgs-boson production with $H \to \tau\tau$ decays based on the 2015 and 2016 dataset. The results are obtained with a maximum-likelihood fit in the reconstructed di-τ-mass $m_{\tau\tau}^{\mathrm{MMC}}$ in the VBF and boosted signal regions (SR). Additional control regions (CRs) are included in order to determine the predicted event yields for the dominant background processes and to constrain systematic uncertainties. The observed results from the likelihood fit including collision data are also compared to the expected results by using a pseudo-dataset [228]. This so-called Asimov dataset is constructed from the sum of SM signal and background expectations with a signal strength of $\mu = 1$.

The first part of this section presents the results of the standalone fit in the SRs and CRs of the $\tau_{lep}\tau_{lep}$ channel and discusses the impact of statistical and systematic uncertainties on the measurement. In addition, a combined fit is performed in the SRs and CRs of the $\tau_{lep}\tau_{lep}$, $\tau_{lep}\tau_{had}$ and $\tau_{had}\tau_{had}$ channels and the results are presented in the second part of this section.

6.5.1. $H \to \tau_{lep}\tau_{lep}$

The observed and expected results of the likelihood fit in the $\tau_{lep}\tau_{lep}$ channel are summarized in Table 6.24. The fit in the VBF and boosted categories results in an excess of $H \to \tau\tau$ signal events with respect to the background-only hypothesis with an observed significiance of $2.2\,\sigma$, while $1.2\,\sigma$ are expected. The measured signal strength is

$$\hat{\mu}_{H\to\tau\tau} = 1.96^{+0.83}_{-0.81} = 1.96^{+0.42}_{-0.41}\,(\text{stat.})^{+0.71}_{-0.70}\,(\text{sys.}). \tag{6.29}$$

The following cross-section times branching ratio is obtained:

$$\hat{\sigma}_{H\to\tau\tau} = 6.76^{+2.80}_{-2.78}\,\text{pb} = 6.76^{+1.45}_{-1.41}\,(\text{stat.})^{+2.39}_{-2.40}\,(\text{sys.})\,\text{pb}. \tag{6.30}$$

These results correspond to an upward fluctuation of $H \to \tau\tau$ events with respect to the SM prediction of $\mu_{SM} = 1$ and $\sigma_{SM,H\to\tau\tau} = 3.46 \pm 0.13\,\text{pb}$ [225]. The measurements are in good agreement with the predicted values within two standard deviations, where the dominant contribution to the total uncertainty arises from systematic sources.

In order to investigate the contribution of the VBF and boosted categories to the combined sensitivity, separate likelihood fits are performed by including only the signal and control regions of the respective categories. As shown in Table 6.24, these likelihood fits result in an upward fluctuation of $H \to \tau\tau$ events with respect to the SM prediction for both categories. The measured signal strengths are $\hat{\mu}_{H\to\tau\tau} = 1.62^{+1.22}_{-1.23}$ in the VBF category and $\hat{\mu}_{H\to\tau\tau} = 2.35^{+1.81}_{-1.60}$ in the boosted category. These results agree within their uncertainties and are compatible with the SM expectation. In addition, the separate measurements are also in agreement with the obtained results including both categories. The observed (expected) significance with respect to the background-only hypothesis is found to be $1.49\,\sigma$ $(0.67\,\sigma)$ in the boosted category and $1.29\,\sigma$ $(0.83\,\sigma)$ in the VBF category.

$\tau_{lep}\tau_{lep}$		VBF+Boosted cat.	VBF cat.	Boosted cat.
Signal strength	Exp.	1.00 ± 0.81	1.00 ± 1.10	1.00 ± 1.50
	Obs.	$1.96^{+0.83}_{-0.81}$	$1.62^{+1.22}_{-1.23}$	$2.35^{+1.81}_{-1.60}$
Significance	Exp.	$1.20\,\sigma$	$0.83\,\sigma$	$0.67\,\sigma$
	Obs.	$2.20\,\sigma$	$1.29\,\sigma$	$1.49\,\sigma$

Table 6.24.: Expected and observed signal strengths and significances for the combination of VBF and boosted categories and their separate contributions in the standalone fit in the $\tau_{lep}\tau_{lep}$ channel.

The *post-fit* signal and background yields are derived by evaluating the impact of the best-fit nuisance parameters (NPs) and the signal strength on the predicted event yields. In addition, background contributions from $Z \to \tau\tau$, $Z \to \ell\ell$ and top-quark events are scaled with the respective normalization factors (NFs) as constrained in the likelihood fit. These NFs are summarized in Table 6.25 and show no significant deviation from the pre-fit expectation. The normalization of the $Z \to \tau\tau$ background is constrained to $+17/-15\,\%$ in the VBF and $+6/-5\,\%$ in the boosted regions. For the $Z \to \ell\ell$ background, looser constraints of $+55/-44\,\%$ and $+45/-37\,\%$ are obtained in the VBF and boosted regions, respectively. The normalization of the top-quark background is constrained to $+11/-10\,\%$ in the VBF and $+5/-5\,\%$ in the boosted regions. Table 6.26 shows the post-fit event yields in the SRs for signal and background processes including statistical and systematic uncertainties. The post-fit yields in the $Z \to \ell\ell$ and Top CRs can be found in Appendix F.1. In all regions, the post-fit yields are in good agreement with the pre-fit expectations within uncertainties. The post-fit $m_{\tau\tau}^{\mathrm{MMC}}$ distribution in the SRs are shown in Figure 6.18. Here, the post-fit uncertainties in the $m_{\tau\tau}^{\mathrm{MMC}}$ bins range from about 5 % in the boosted loose region up to 20 % in the VBF tight category. Overall, a good agreement between data and the signal and background prediction is observed.

Background	VBF cat.	Boosted cat.
$Z \to \tau\tau$	$0.88^{+0.17}_{-0.15}$	$1.07^{+0.06}_{-0.05}$
$Z \to \ell\ell$	$1.11^{+0.55}_{-0.44}$	$1.49^{+0.45}_{-0.37}$
Top	$1.25^{+0.11}_{-0.10}$	$1.08^{+0.05}_{-0.05}$

Table 6.25.: Background normalization factors from the standalone likelihood fit in the $\tau_{lep}\tau_{lep}$ channel including statistical and systematic uncertainties.

The breakdown of uncertainties on the measured cross-section $\Delta\hat{\sigma}_{H\to\tau\tau}$ allows to investigate, which source of uncertainty constitutes the dominant contribution and therefore limits the measurement precision. For this, additional likelihood fits are performed, where the values of all NPs, which arise from the respective uncertainty source, are fixed to their best-fit values $\theta_{fix} = \hat{\theta}$. With this, the resulting cross-section uncertainty $\Delta\sigma_{H\to\tau\tau}(\theta_{fix})$ is calculated. The absolute contribution of this source of uncertainty to the measured cross-section uncertainty is then determined by taking the squared difference between the measured uncertainty and the uncertainty from the likelihood fit with the fixed NPs:

$\Delta\sigma'_{H\rightarrow\tau\tau} = \sqrt{(\Delta\hat{\sigma}_{H\rightarrow\tau\tau})^2 - (\Delta\sigma_{H\rightarrow\tau\tau}(\theta_{fix}))^2}$. This procedure is applied in order to retain the correlation of the remaining NPs, which are not fixed, in the likelihood fit. As shown in Table 6.27, the dominant contribution to the measured cross-section uncertainty in the $\tau_{lep}\tau_{lep}$ channel arises from systematic uncertainties related to jets and E_T^{miss}. In addition, uncertainties on the MC statistics of the total background prediction and theoretical uncertainties on the signal and $Z \rightarrow \tau\tau$ background give an important contribution.

The impact of single NPs on the value of the measured cross-section is investigated by performing likelihood fits, where the NP value is fixed to its best-fit value shifted by one standard deviation upwards and downwards: $\theta_{fix} = \hat{\theta} \pm \Delta\hat{\theta}$. The relative change of the resulting cross-sections with respect to $\hat{\sigma}_{H\rightarrow\tau\tau}$ are then determined and the NPs are ranked according to their impact on $\hat{\sigma}_{H\rightarrow\tau\tau}$. The results are shown in Figure 6.19 for the 15 NPs, which are found to have the largest impact on the measured cross-section. The meaning of the NP names and their systematic source are explained in Appendix B. In the $\tau_{lep}\tau_{lep}$ channel, the highest ranked parameters correspond to the normalization of the $Z \rightarrow \tau\tau$ background in the VBF category (Normalization_vbf_Ztt) and various components of JER-related uncertainties (JER_NP). The NP accounting for the UEPS uncertainty of the $Z \rightarrow \tau\tau$ background in the boosted region (ZttTheory_Shower_boost_LL) is ranked high as well. Additional important contributions arise from JES-related NPs (JES_Flavor_Resp, JES_EtaInter_Model, JES_EffectiveNP, JES_PU_OffsetMu) and from the normalization factors of the $Z \rightarrow \tau\tau$ and top-quark backgrounds in the boosted category (Normalization_boost_Ztt, Normalization_LL_boost_Top).

Figure 6.19 also shows the deviations of the best-fit values of the highest ranked NPs $\hat{\theta}$ from their pre-fit value θ_0 normalized to the uncertainty $\Delta\theta$, which are referred to as *pulls*. Hence, a pull in positive (negative) direction corresponds to a shift of the post-fit NP value in the $+1\,\sigma\,(-1\,\sigma)$ direction. All observed pulls are covered by the pre-fit $\pm 1\,\sigma$ uncertainty band and the best-fit NPs are therefore in agreement with their pre-fit values within uncertainties. The largest pull of 64 % is obtained for JER_NP_6, followed by JER_NP_8 with a pull of −57 %.

Figure 6.19 also shows the relative changes of the NP post-fit uncertainties with respect to their pre-fit uncertainties, which are referred to as *constraints*. Several of the highest ranked NPs are constrained in the likelihood fit, while the largest constraints appear for JER-related NPs. In particular, the uncertainty on JER_NP_0 is constrained to $+44/-78\,\%$ of its pre-fit uncertainty, while constraints of $+73/-76\,\%$ and $+82/-80\,\%$ are obtained for JER_NP_4 and JER_NP_6, respectively. These constraints are related to the position of the $Z \rightarrow \tau\tau$ mass peak in the $m_{\tau\tau}^{\mathrm{MMC}}$ distribution. In particular, the impact of JER and JES uncertainties lead to a shift of the mean p_{T} of the jets, which are selected in the VBF and boosted categories. Since these jets recoil against the di-τ system, the effect is propagated to the calculation of the missing transverse energy in the event and in turn also to the $m_{\tau\tau}^{\mathrm{MMC}}$. This results in a shift of the $Z \rightarrow \tau\tau$ mass peak in the $m_{\tau\tau}^{\mathrm{MMC}}$ distribution, which can be constrained by data in the likelihood fit.

Process	$\tau_{lep}\tau_{lep}$ Signal regions			
	VBF loose	VBF tight	Boosted loose	Boosted tight
ggF $H \to \tau\tau$	4.9 ± 2.4	3.6 ± 2.1	61 ± 26	60 ± 26
VBF $H \to \tau\tau$	8.9 ± 3.8	22.0 ± 9.6	13.6 ± 5.6	14.6 ± 6.1
WH $H \to \tau\tau$	0.10 ± 0.06	0.06 ± 0.03	4.2 ± 1.8	5.4 ± 2.2
ZH $H \to \tau\tau$	0.04 ± 0.02	0.03 ± 0.02	2.31 ± 0.95	3.0 ± 1.3
ttH $H \to \tau\tau$	0.19 ± 0.17	0.15 ± 0.13	2.72 ± 1.26	2.3 ± 1.1
$Z \to \tau\tau$	136 ± 16	94 ± 15	2920 ± 110	2630 ± 80
$Z \to \ell\ell$	17.8 ± 7.7	16.5 ± 5.3	378 ± 72	255 ± 48
Top	37.6 ± 8.6	27.8 ± 5.7	333 ± 56	193 ± 32
Di-Boson	10.7 ± 2.2	9.4 ± 1.8	188.2 ± 8.7	188.7 ± 9.1
Fake	18 ± 10	9.6 ± 5.1	209 ± 98	81 ± 37
ggF $H \to WW$	1.21 ± 0.24	1.26 ± 0.37	12.4 ± 3.1	14.7 ± 2.2
VBF $H \to WW$	1.70 ± 0.29	4.37 ± 0.64	2.84 ± 0.30	2.72 ± 0.36
Total bkg.	229 ± 15	167 ± 14	4111 ± 65	3435 ± 56
Total signal	14.1 ± 4.5	25.8 ± 9.8	83 ± 27	85 ± 27
Data	237	188	4124	3444

Table 6.26.: Post-fit event yields for the signal and background predictions from the standalone likelihood fit in the $\tau_{lep}\tau_{lep}$ channel compared to the observed data yields. The uncertainties include statistical and systematic components.

Source of uncertainty	$(\Delta\sigma'_{H\to\tau\tau}/\Delta\hat{\sigma}_{H\to\tau\tau})^2$
Data statistics	$+0.26/-0.25$
Total systematic unc.	$+0.74/-0.75$
Background normalizations	$+0.11/-0.16$
$Z \to \tau\tau$ normalization	$+0.09/-0.13$
Jets, E_T^{miss}	$+0.31/-0.37$
b-tagging	$+0.01/-0.01$
Electrons, Muons	$+0.01/-0.01$
Pileup reweighting	< 0.01
Fake estimation	$+0.01/-0.01$
Luminosity	$+0.01/-0.00$
Signal theory unc.	$+0.06/-0.02$
$Z \to \tau\tau$ theory unc.	$+0.05/-0.04$
Background statistics	$+0.13/-0.19$

Table 6.27.: Fractional contribution of grouped sources of statistical and systematic uncertainties on the measured cross-section uncertainty $\Delta\hat{\sigma}_{H\to\tau\tau}$ from the standalone likelihood fit in the $\tau_{lep}\tau_{lep}$ channel. The variation $\Delta\hat{\sigma}'_{H\to\tau\tau}$ is defined for each source of uncertainty as the squared difference between $\Delta\hat{\sigma}_{H\to\tau\tau}$ and the obtained cross-section uncertainty when fixing the corresponding NPs to their best-fit values.

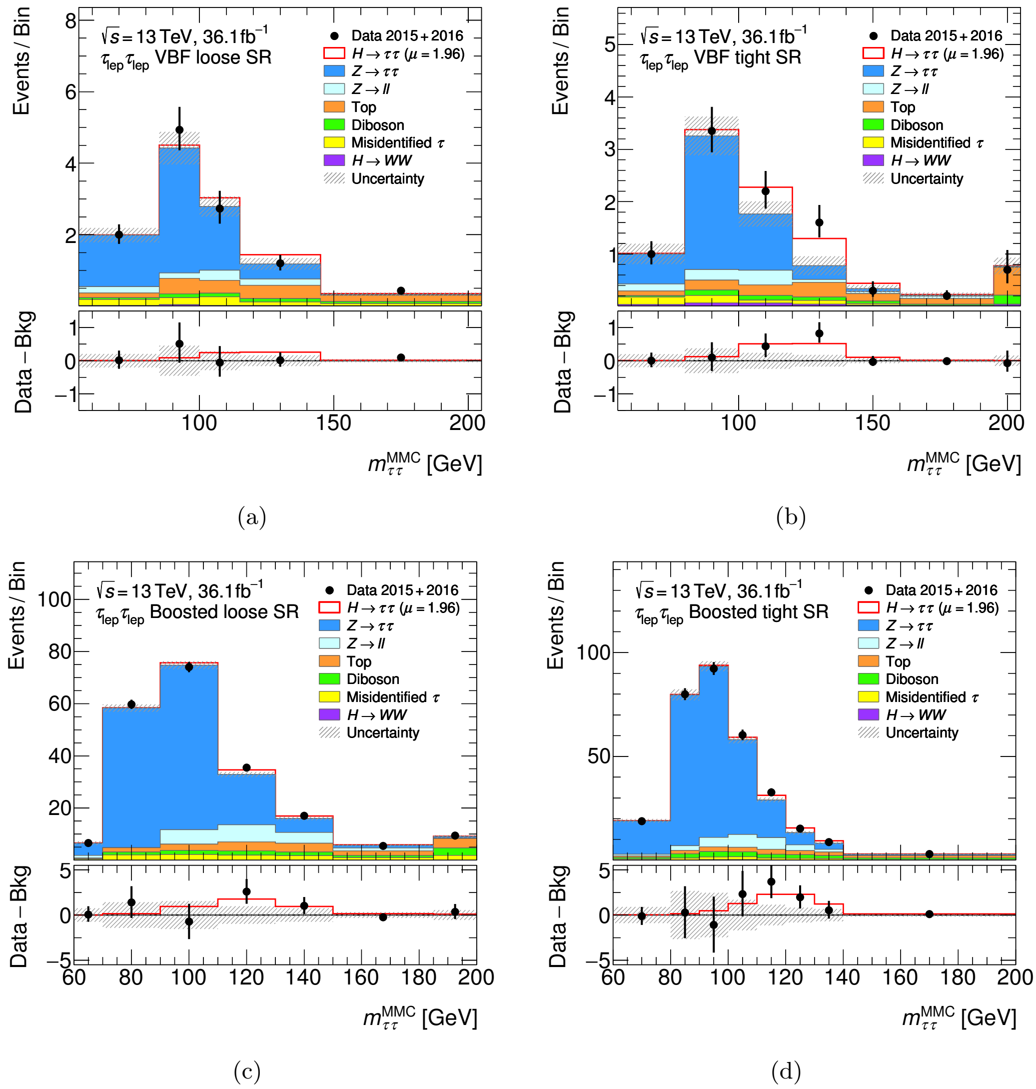

Figure 6.18.: Post-fit distributions of $m_{\tau\tau}^{\mathrm{MMC}}$ in the VBF loose (a), VBF tight (b), boosted loose (c) and boosted tight (d) signal regions of the $\tau_{lep}\tau_{lep}$ channel from the standalone $\tau_{lep}\tau_{lep}$ likelihood fit. In each bin, the observed and predicted events are normalized to the respective bin width. The observed Higgs-boson signal ($\mu = 1.96$) is shown with the solid red line. The uncertainty band includes statistical, experimental and theoretical uncertainties on the background prediction (hatched band). The bottom panels show the difference between the observed data events and the expected background events (black points).

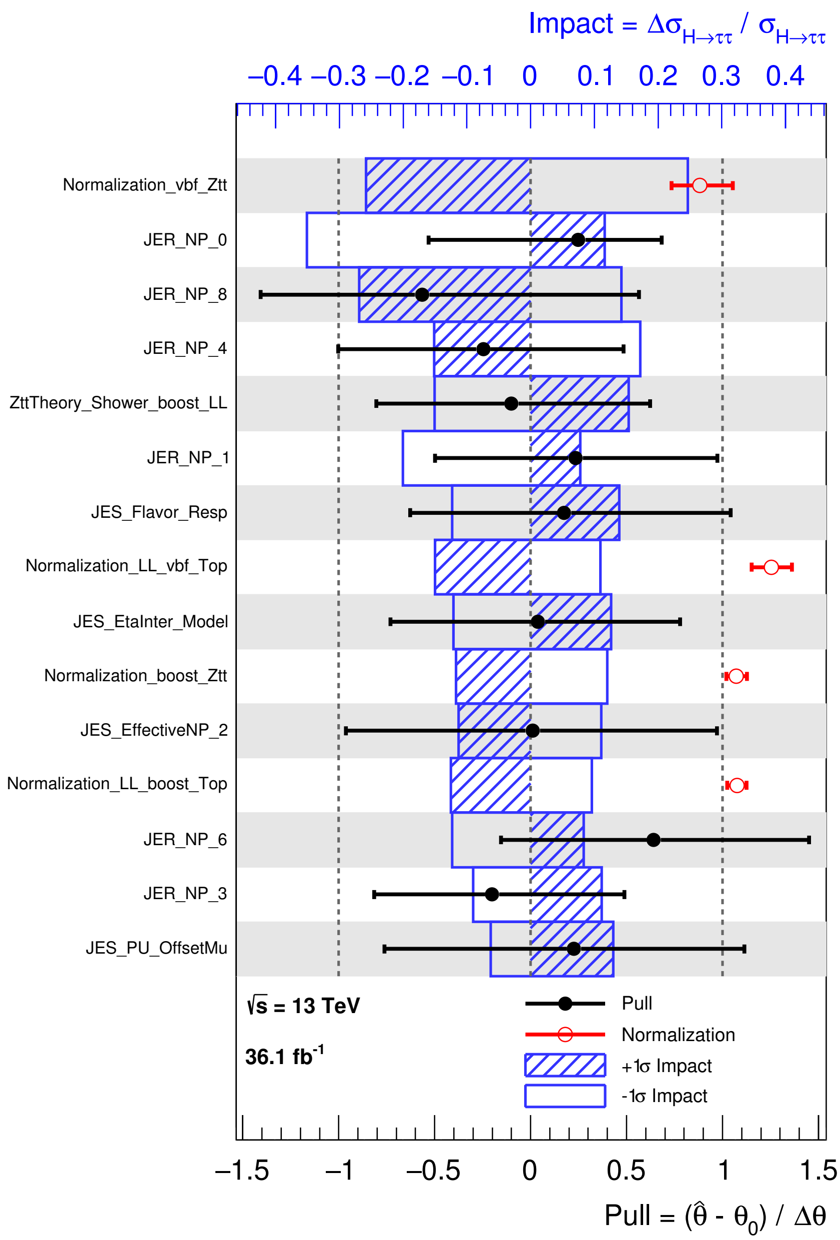

Figure 6.19.: Fractional impact of systematic uncertainties on the measured cross-section (top axis) from the standalone likelihood fit in the $\tau_{lep}\tau_{lep}$ channel. The systematic uncertainties are listed in descreasing order of their impact on the left. The blue boxes show the variation $\Delta\sigma_{H\to\tau\tau}$ with respect to the measured value $\hat{\sigma}_{H\to\tau\tau}$, when the corresponding nuisance paramter is fixed to its post-fit value shifted by one standard deviation upwards or downwards. In addition, the nuisance parameter post-fit values and uncertainties with respect to their pre-fit values are shown in black (referring to the bottom axis). The value of the background normalization factors and their uncertainties are shown in red and refer to the bottom axis. Only the 15 highest ranked parameters are listed.

6.5.2. Combination with Other Decay Channels

The sensitivity of the measurements obtained in the $\tau_{lep}\tau_{lep}$ channel can be improved by also including the signal and control regions of the $\tau_{lep}\tau_{had}$ and $\tau_{had}\tau_{had}$ channels in the likelihood fit. A detailed description of these analyses can be found in Ref. [31]. Table 6.28 summarizes the observed and expected results for the combined significance and signal strength as well as the standalone measurements in the three analysis channels. The combined likelihood fit allows to extract the $H \to \tau\tau$ signal with a significance of $4.4\,\sigma$, while $4.14\,\sigma$ are expected, and the signal strength is

$$\hat{\mu}_{H\to\tau\tau} = 1.09^{+0.32}_{-0.28} = 1.09^{+0.18}_{-0.17}\,(\text{stat.})^{+0.26}_{-0.22}\,(\text{sys.}). \tag{6.31}$$

The following cross-section times branching ratio is obtained:

$$\hat{\sigma}_{H\to\tau\tau} = 3.77^{+1.06}_{-0.95}\,\text{pb} = 3.77^{+0.60}_{-0.59}\,(\text{stat.})^{+0.87}_{-0.74}\,(\text{sys.})\,\text{pb}. \tag{6.32}$$

These results are consistent with the SM prediction of a signal strength of one and a cross-section for Higgs-boson production with $H \to \tau\tau$ decays of 3.46 ± 0.13 pb [225] within uncertainties. The dominant contribution to the measurement precision arises from systematic uncertainties.

Figure 6.20 (a) shows a comparison of the combined and standalone cross-section results. All measurements are in good agreement with the SM prediction and no deviation between the results obtained in the individual analysis channels are observed. The $\tau_{lep}\tau_{lep}$ channel results in a higher than predicted cross-section, while the measurements in the $\tau_{lep}\tau_{had}$ and $\tau_{had}\tau_{had}$ channel are found to be smaller compared to the SM prediction.

	Significance		Signal strength	
	Expected [σ]	Observed [σ]	Expected	Observed
Combination	4.14	4.40	1.00 ± 0.28	$1.09^{+0.32}_{-0.28}$
VBF cat.	2.75	2.57	1.00 ± 0.40	$0.97^{+0.47}_{-0.41}$
Boosted cat.	2.85	3.21	1.00 ± 0.40	$1.16^{+0.46}_{-0.39}$
$\tau_{lep}\tau_{lep}$	1.20	2.20	1.00 ± 0.81	$1.96^{+0.83}_{-0.81}$
VBF cat.	0.83	1.29	1.00 ± 1.10	$1.62^{+1.22}_{-1.23}$
Boosted cat.	0.68	1.48	1.00 ± 1.50	$2.35^{+1.81}_{-1.60}$
$\tau_{lep}\tau_{had}$	2.63	2.44	1.00 ± 0.43	$0.90^{+0.44}_{-0.38}$
VBF cat.	1.68	1.64	1.00 ± 0.64	$0.96^{+0.70}_{-0.59}$
Boosted cat.	1.86	1.91	1.00 ± 0.60	$1.02^{+0.68}_{-0.56}$
$\tau_{had}\tau_{had}$	2.88	2.21	1.00 ± 0.43	$0.73^{+0.41}_{-0.34}$
VBF cat.	1.78	1.39	1.00 ± 0.71	$0.75^{+0.80}_{-0.56}$
Boosted cat.	1.83	1.25	1.00 ± 0.61	$0.63^{+0.59}_{-0.51}$

Table 6.28.: Summary of expected and observed results from the combined likelihood fit as well as the standalone results for the significance and the signal strength. In addition, the results of separate likelihood fits in the corresponding signal and control regions of the VBF category and the boosted category are given.

Separate likelihood fits are also performed in the signal and control regions of the VBF category (VBF-only fit) and the boosted category (boosted-only fit). These results are summarized in Table 6.28 and are compared to the SM prediction in Figure 6.20 (b) for the combination of all analysis channels. The cross sections obtained in the VBF-only fit and the boosted-only fit are in good agreement with each other and also with the combined result, when all VBF and boosted regions are included. In the VBF-only fit, a larger relative uncertainty of $+48/-42\,\%$ on the measured cross-section is obtained compared to the boosted-only result with a relative uncertainty of $+38/-33\,\%$. Both results are dominated by systematic uncertainties.

The background normalization factors from the combined likelihood fit are summarized in Table 6.29. Besides the $Z \to \tau\tau$ normalization factor, which is correlated across the channels, and the normalization of the $Z \to \ell\ell$ and top-quark background in the $\tau_{lep}\tau_{lep}$ channel, the $\tau_{lep}\tau_{had}$ channel applies one normalization factor to the top-quark background, while in the $\tau_{had}\tau_{had}$ channel the normalization of the data-driven background estimate for misidentified τ_{had}-leptons is determined from the likelihood fit. All normalization factors are close to unity and therefore show no significant deviation from their pre-fit expectation. The obtained results for the normalization of the $Z \to \tau\tau$, $Z \to \ell\ell$ and top-quark backgrounds in the $\tau_{lep}\tau_{lep}$ channel agree well with the results from the $\tau_{lep}\tau_{lep}$ standalone fit (see Table 6.25). Since the combined likelihood fit contains more information and therefore allows to further constrain systematic uncertainties, the uncertainty on the background normalization factors in the $\tau_{lep}\tau_{lep}$ channel are reduced compared to the standalone fit. In particular, the normalization of the $Z \to \tau\tau$ background is constrained to $+10/-9\,\%$ in the VBF region and $\pm 5\,\%$ in the boosted region, while the $Z \to \ell\ell$ normalization is constraint to $+34/-30\,\%$ in the VBF region and $+30/-25\,\%$ in the boosted region. The uncertainty on the top-quark background normalization also decreases to $\pm 9\,\%$ in the VBF region and $\pm 5\,\%$ in the boosted region.

	Normalization factors	
Background	VBF cat.	Boosted cat.
$Z \to \tau\tau$ ($\tau_{lep}\tau_{lep}$, $\tau_{lep}\tau_{had}$, $\tau_{had}\tau_{had}$)	$1.04^{+0.10}_{-0.09}$	$1.11^{+0.05}_{-0.05}$
$Z \to \ell\ell$ ($\tau_{lep}\tau_{lep}$)	$0.88^{+0.34}_{-0.30}$	$1.27^{+0.30}_{-0.25}$
Top ($\tau_{lep}\tau_{lep}$)	$1.19^{+0.09}_{-0.09}$	$1.07^{+0.05}_{-0.05}$
Top ($\tau_{lep}\tau_{had}$)	$1.53^{+0.30}_{-0.27}$	$1.13^{+0.07}_{-0.07}$
Fake ($\tau_{had}\tau_{had}$)	$1.12^{+0.12}_{-0.12}$	

Table 6.29.: Background normalization factors from the combined likelihood fit including statistical and systematic uncertainties.

Figure 6.21(a) and (b) show the post-fit $m_{\tau\tau}^{\mathrm{MMC}}$ distributions for the sum of all VBF signal regions and all boosted signal regions from the combined fit in the three analysis channels, respectively. Overall, a good agreement between the signal and background prediction and the observed data is obtained.

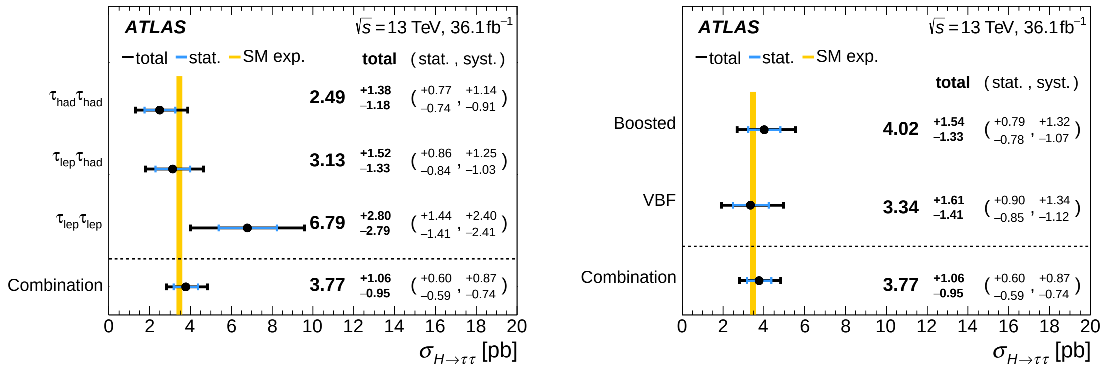

(a) (b)

Figure 6.20.: Overview of the measured cross-section for Higgs-boson production with $H \to \tau\tau$ decays $\sigma_{H\to\tau\tau}$ from the standalone likelihood fits (a) and the combined likelihood fit in the VBF and boosted categories separately (b) compared to the combined result. The total $\pm 1\sigma$ uncertainty in the measurement is indicated by the black error bars with the individual contribution from the statistical uncertainty in blue. The theory uncertainty in the predicted signal cross-section is shown by the yellow band [31].

The breakdown of uncertainties on the measured cross-section from the combined fit is shown in Table 6.30. Here, the main contribution arises from systematic uncertainties related to jets and E_T^{miss} as well as from theoretical uncertainties on the signal prediction. This can also be seen in Figure 6.22, which shows the 15 highest ranked NPs with respect to their impact on the measured cross-section value. Here, the highest ranked NP, Theo_sig_ggH_qcd_7, corresponds to the uncertainty on the ggF cross-section calculation for $H \to \tau\tau$ events with $p_T^H > 120$ GeV. Further important NPs from the same source are given by Theo_sig_ggH_qcd_6 for the ggF cross-section calculation with $p_T^H > 60$ GeV, Theo_sig_ggH_qcd_3 for jet-migration uncertainties and Theo_sig_ggH_qcd_8 for uncertainties from the top-quark mass (see Section 6.3.2). The impact of these NPs on the measured cross-section in the combined likelihood fit mainly arises from the contributions of the $\tau_{lep}\tau_{had}$ and $\tau_{had}\tau_{had}$ channels. From the experimental side, NPs related to the JER uncertainty (JER_NP_0), the JES uncertainty (JES_EffectiveNP_7, JES_EtaInter_NonClosure, JES_PU_PtTerm) and the mis-tagging rate for b-jet identification (FT_EFF_Eigen_light_0) are found to have an important impact on the measured cross-section as well. The normalization of the $Z \to \tau\tau$ and $Z \to \ell\ell$ backgrounds in the boosted categories are also among the highest ranked NPs. In addition, NPs related to the background estimate of misidentified τ_{had}-leptons in the $\tau_{lep}\tau_{had}$ channel (lh_fake_stat_vbf, lh_fake_stat_boost) and the uncertainty on the τ_{had}-identification efficiency (TAU_EFF_ID_TOTAL) are found to have a large impact.

As shown in Figure 6.22, the combined likelihood fit results in pulls and constraints for some of the highest ranked NPs. Here, the largest constraint is obtained for JER_NP_0, where the uncertainty is reduced to $+34/-29\,\%$ with respect to its pre-fit value. The largest pull appears for TAU_EFF_ID_TOTAL, which is found to deviate from its pre-fit value by more than 1σ in the direction of the downward variation. This was studied in detail in the $\tau_{lep}\tau_{had}$ and $\tau_{had}\tau_{had}$ channels and the pull was found to be related to differences in the $Z \to \tau\tau$ background normalization between the three analysis channels [221].

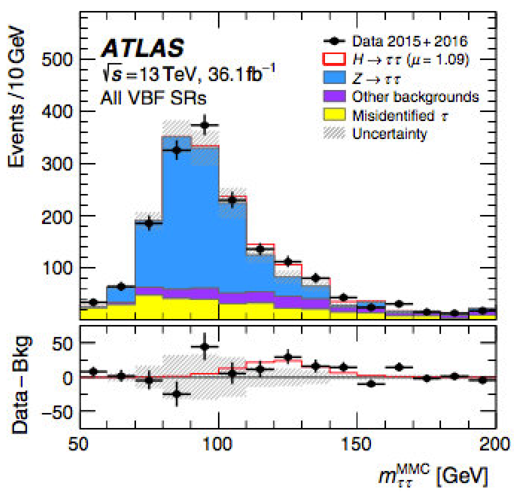

(a)

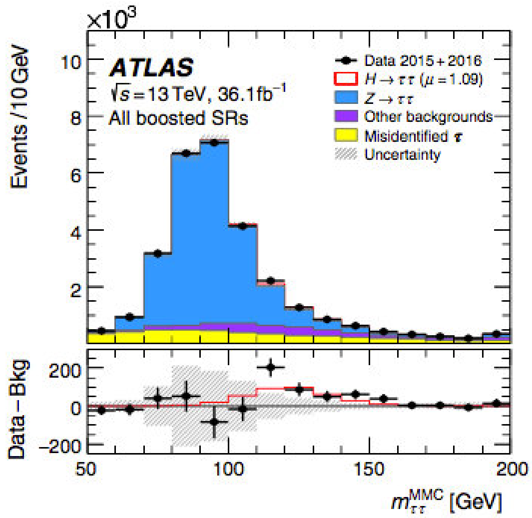

(b)

Figure 6.21.: Distribution of $m_{\tau\tau}^{\mathrm{MMC}}$ for the sum of all VBF signal regions (a) and all boosted signal regions (b). The signal and background predictions are determined in the combined likelihood fit. The uncertainty band included statistical, experimental and theoretical uncertainties in the background prediction. The bottom panel gives the observed difference between data and the expected background events (black points), while the observed Higgs-boson signal with $\mu = 1.09$ is shown with the red line [31].

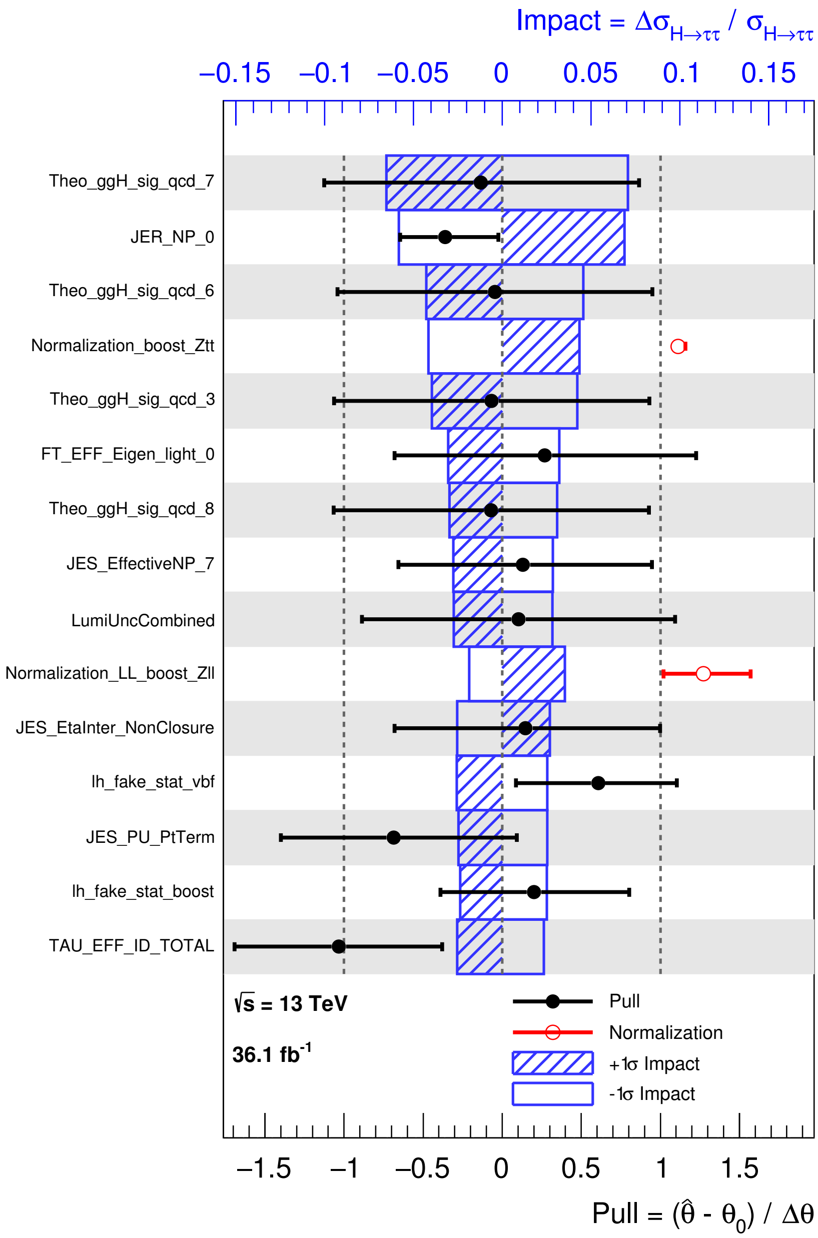

Figure 6.22.: Fractional impact of systematic uncertainties on the measured cross-section (top axis) from the combined likelihood fit. The systematic uncertainties are listed in descreasing order of their impact on the left. The blue boxes show the variation $\Delta\sigma_{H\to\tau\tau}$ with respect to the measured value $\hat{\sigma}_{H\to\tau\tau}$, when the corresponding nuisance paramter is fixed to its post-fit value shifted by one standard deviation upwards or downwards. In addition, the nuisance parameter post-fit values and uncertainties with respect to the pre-fit values are shown in black (referring to the bottom axis). The value of the background normalization factors and their uncertainties are shown in red and refer to the bottom axis. Only the 15 highest ranked parameters are listed.

Source of uncertainty	$(\Delta\sigma'_{H\to\tau\tau}/\Delta\hat{\sigma}_{H\to\tau\tau})^2$
Data statistics	$+0.32/-0.39$
Total systematic unc.	$+0.68/-0.61$
Background normalizations	$+0.05/-0.03$
$Z\to\tau\tau$ normalization	$+0.03/-0.01$
Jets, E_T^{miss}	$+0.16/-0.13$
b-tagging	$+0.01/-0.01$
Electrons, Muons	<0.01
τ_{had}	$+0.02/-0.01$
Pileup reweighting	<0.01
Fake estimation	$+0.02/-0.02$
Luminosity	$+0.01/-0.01$
Signal theory unc.	$+0.22/-0.12$
$Z\to\tau\tau$ theory unc.	$+0.02/-0.02$
Background statistics	$+0.15/-0.16$

Table 6.30.: Fractional contribution of the grouped sources of statistical and systematic uncertainties on the measured cross-section uncertainty $\Delta\hat{\sigma}_{H\to\tau\tau}$ from the combined likelihood fit. The variation $\Delta\hat{\sigma}'_{H\to\tau\tau}$ is defined for each source of uncertainty as the squared difference between $\Delta\hat{\sigma}_{H\to\tau\tau}$ and the obtained cross-section uncertainty when fixing the corresponding nuisance parameters to their best-fit values.

Measurement of the Higgs-Boson Production Cross-Sections in ggF and VBF

The cross-section measurement of Higgs-boson production with $H\to\tau\tau$ decays described in the previous section is further extended by exploiting the sensitivity of the analysis to the different Higgs-boson production modes. In particular, the event categorization in the VBF and boosted regions enables the cross-section measurement of the two main Higgs-boson production modes, $\sigma^{VBF}_{H\to\tau\tau}$ and $\sigma^{ggF}_{H\to\tau\tau}$. For this, a likelihood fit is performed with the same fit model as described above, but including two POIs, which scale the signal predictions for Higgs-boson production in the VBF and ggF channel separately. The remaining signal contributions from the ttH and VH production channels are fixed to their SM prediction. The combined likelihood fit in the $\tau_{lep}\tau_{lep}$, $\tau_{lep}\tau_{had}$ and $\tau_{had}\tau_{had}$ final states results in

$$\hat{\sigma}^{ggF}_{H\to\tau\tau} = 3.1 \;\;\pm 1.0\,(\text{stat.})^{+1.6}_{-1.3}\,(\text{sys.})\,\text{pb} \tag{6.33}$$
$$\hat{\sigma}^{VBF}_{H\to\tau\tau} = 0.28 \pm 0.09\,(\text{stat.})^{+0.11}_{-0.09}\,(\text{sys.})\,\text{pb}. \tag{6.34}$$

The measurement of the Higgs-boson production cross-section in ggF is dominated by systematic uncertainties, while the cross-section measurement of the VBF production is affected by statistical and systematic uncertainties of similar size. Figure 6.23 shows the best-fit values and the two-dimensional contours at the 68 % CL and the 95 % CL compared to the SM prediction. The results are in good agreement with the SM prediction of $\sigma^{SM}_{ggF,H\to\tau\tau} = 3.05 \pm 0.13\,\text{pb}$ and $\sigma^{SM}_{ggF,H\to\tau\tau} = 0.237 \pm 0.006\,\text{pb}$ [225] within the 68 % CL interval. Furthermore, a clear anti-correlation is observed between $\hat{\sigma}^{ggF}_{H\to\tau\tau}$ and $\hat{\sigma}^{VBF}_{H\to\tau\tau}$ with a correlation coefficient of $-52\,\%$. This is expected, since the VBF and boosted categories both contain $H \to \tau\tau$ signal contributions from the VBF and ggF production modes.

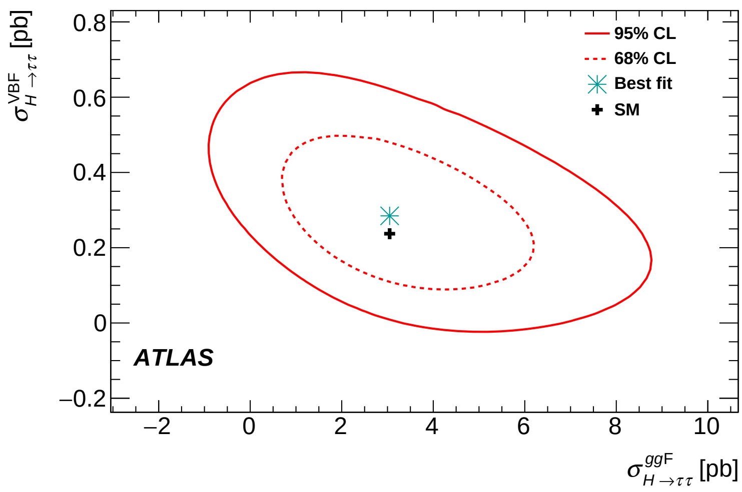

Figure 6.23.: Likelihood contours for the combination of all analysis channels in the ($\sigma^{ggF}_{H\to\tau\tau}$, $\sigma^{VBF}_{H\to\tau\tau}$) plane. The 68 % and 95 % confidence level contours are shown as dashed and solid lines, respectively. The SM expectation is indicated by a plus symbol and the best-fit value from the combination of all channels is shown as a star [31].

Combination with the Run 1 Dataset

The measurement based on the Run 2 dataset of $36.1\,\mathrm{fb}^{-1}$ is combined with the measurement in Run 1 by the ATLAS experiment at $\sqrt{s} = 7\,\mathrm{TeV}$ and $\sqrt{s} = 8\,\mathrm{TeV}$ with datasets of $4.5\,\mathrm{fb}^{-1}$ and $20.3\,\mathrm{fb}^{-1}$, respectively [17]. This combination does not measure the cross-section for Higgs-boson production with $H \to \tau\tau$ decays, but determines the significance of the extracted $H \to \tau\tau$ signal with respect to the background-only hypothesis. The nuisance parameters of the two analyses are treated as uncorrelated and the Run 1 analysis is updated with the most recent cross-section values of Higgs-boson production at 7 TeV and 8 TeV. An important difference between the analyses arises from the estimation of the $Z \to \tau\tau$ background. While the Run 1 analysis uses the data-driven embedding technique [238], the $Z \to \tau\tau$ background estimation in the Run 2 analysis is based on simulation.

The combination of the Run 1 and Run 2 analyses results in a measurement of the $H \to \tau\tau$ signal with a significance of $6.4\,\sigma$ with respect to the background-only hypothesis, while $5.4\,\sigma$ are expected [31], and constitutes the observation of $H \to \tau\tau$ decays with the ATLAS experiment.

7 Test of CP Invariance in VBF Higgs-Boson Production with $H \to \tau\tau$ Decays

This chapter presents a test of CP invariance in the Higgs-boson interaction with weak gauge-bosons in the vector-boson fusion (VBF) production mode. In this analysis, additional CP-odd contributions to the CP-even HVV coupling structure as predicted in the SM are described by a single parameter $\tilde{d}$ within the framework of an effective field theory (see Section 2.3). Here, any non-vanishing value of $\tilde{d}$ directly corresponds to the violation of CP invariance in HVV interactions and would be a sign of new physics beyond the SM. Confidence intervals on the $\tilde{d}$ parameter are determined by performing a likelihood fit in the CP-odd Optimal Observable, which is introduced in Section 2.4.2, for various HVV coupling hypotheses. The analysis focuses on the $H \to \tau\tau$ decay mode in the fully-leptonic final and follows the $H \to \tau\tau$ cross-section measurement described in Chapter 6 to a large extent.

The chapter is organized as follows: The first section Section 7.1 describes the event selection and gives an introduction to the multivariate analysis technique of Boosted Decision Trees. The modelling of the dominant background processes in dedicated control regions is discussed in Section 7.2, followed by an overview of the systematic uncertainties in Section 7.3. Then, Section 7.4 discusses the statistical model and the procedure to derive confidence intervals. The results of the analysis in the fully-leptonic $H \to \tau\tau$ final state and the combination with the $\tau_{lep}\tau_{had}$ and $\tau_{had}\tau_{had}$ channels are presented in Section 7.5.

7.1. Event Selection

This section describes the selection criteria applied to data and simulated samples in order to select VBF $H \to \tau\tau$ signal events. In contrast to the $H \to \tau\tau$ cross-section measurement presented in the previous chapter, events from Higgs-boson production modes, where no HVV interaction occurs (ggF and ttH) contribute to the overall background processes and no CP violation is expected. These processes are referred to as non-VBF Higgs-boson events in the following. Furthermore, $H \to \tau\tau$ events from the VH production mode are also included in the background prediction due to their small overall contribution. In contrast to the $H \to \tau\tau$ cross-section measurement, VBF $H \to WW$ events give an additional contribution to the signal prediction since HVV interactions occur in both the production and decay vertex. However, as shown in Ref. [136], CP violating effects in the $H \to WW$ decay vertex are found to have a negligible impact on the shape of the Optimal Observable distribution. The HVV coupling structure in the $H \to WW$ decay is therefore not investigated, but assumed to follow the SM prediction.

7.1.1. Preselection

The preselection in the VBF CP $H \to \tau\tau$ analysis follows very closely the preselection and VBF categorization described in Section 6.1. In particular, the same event cleaning, lepton selection and trigger requirements are used (up to cut 9 in Section 6.1.2). The events are also required to fulfill the cuts on $m_{\tau\tau}^{\mathrm{MMC}}$, $m_{\tau\tau}^{coll}$ and the b-jet veto (cut 12-14 in Section 6.1.2). The requirements on the lepton momentum fraction and separation (cut 10 and cut 11 in Section 6.1.2) are dropped in order to retain a reasonable event statistic for the following BDT training. Furthermore, at least two tagging jets with $p_T^{j0(j1)} > 40\,(30)$ GeV and a separation of $|\eta_{jj}| > 3$ are required. Compared to the event selection in the VBF category (see Section 6.1.3), the cut on the invariant di-jet mass is relaxed to $m_{jj} > 300$ GeV and no requirements are imposed on the product of the jet pseudorapidities or the lepton centralities. This set of preselection cuts is also referred to as the MVA VBF inclusive region in the following. As described in Section 7.2 pre-fit normalization factors are derived in dedicated control regions for the $Z \to \tau\tau$, $Z \to \ell\ell$ and top-quark background prediction. Furthermore, a reweighting in m_{jj} is applied to $Z \to \tau\tau$ and $Z \to \ell\ell$ events, which is discussed in Section 7.2.1. The distribution of the Optimal Observable in the MVA VBF inclusive region is shown in Figure 7.1 for the same-flavour (SF) and different-flavour (DF) final states. Overall, a good modelling between data and prediction is observed. In the SF channel, the predicted event yields in the central bins of the Optimal Observable are found to be smaller compared to the observed data yields, but still in good agreement within the considered uncertainties.

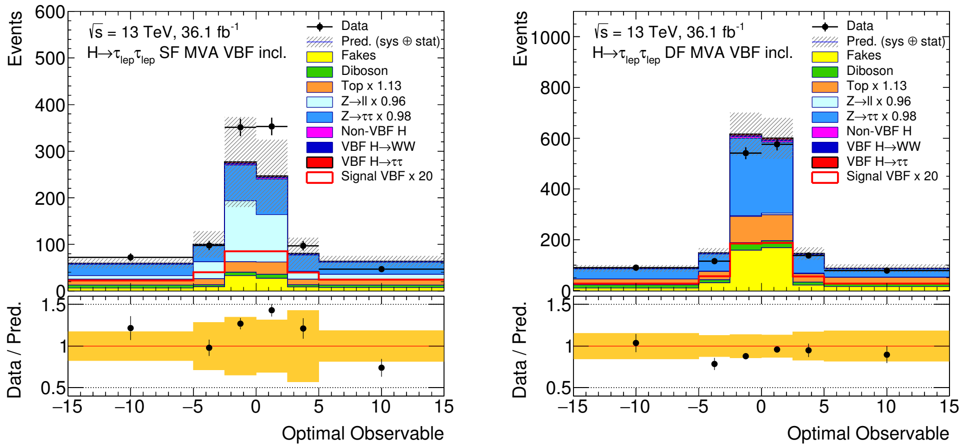

Figure 7.1.: Distribution of the Optimal Observable in the MVA VBF inclusive region for the same-flavour (a) and different-flavour (c) final states. The uncertainty band includes statistical uncertainties and systematic uncertainties related to jets, E_T^{miss} and the fake-lepton background estimate.

The expected event yields for signal and background processes with their statistical uncertainties and the observed number of data events are summarized in Table 7.1. The SF final state contains 1018 data events, while 1539 data events are observed in the DF final state. In the SF final state, about 14.9 ± 0.1 VBF signal events are expected, where $H \to \tau\tau$ decays provide the dominant contribution with a relative fraction of 63 %. The expected sum of all background processes in the SF final state corresponds to 812 ± 99 events. Here, the dominant contributions arise from $Z \to \ell\ell$ decays with 37 % and $Z \to \tau\tau$ decays with 34 % of the total expected background. The contribution of top-quark and fake-lepton events is of similar size with 12 % and 11 %, respectively. Di-processes contribute with 5 %, while events from non-VBF Higgs-boson production only constitute less than 1 % of the expected background. In the DF final state, 26.9 ± 01 VBF $H \to \tau\tau$ signal events are expected with a relative contribution of 65 % from $H \to \tau\tau$ decays. The expected sum of all background processes in the DF final state corresponds to 1658 ± 26 events. Here, $Z \to \tau\tau$ decays provide the dominant contribution with 48 % of the total background, followed by the fake-lepton and top-quark background with relative contributions of 24 % and 19 %, respectively. The relative fraction of di-boson events is 7 %, while events from $Z \to \ell\ell$ decays and non-VBF production modes each constitute only 1 % of the total expected background. In both the SF and DF final states, the MVA VBF inclusive selection provides a signal-to-background ratio of about $\frac{s}{b} = 0.02$. This ratio is further improved with the multivariate analysis technique of BDTs, which is explained in the following section.

Process	MVA VBF inclusive SF	MVA VBF inclusive DF
VBF $H \to \tau\tau$	9.4 ± 0.1	17.6 ± 0.1
VBF $H \to WW$	5.5 ± 0.1	9.3 ± 0.1
$Z \to \tau\tau$	273 ± 10	797 ± 18
$Z \to \ell\ell$	303 ± 95	15 ± 4
Top	99 ± 4	319 ± 8
Di-Boson	37.5 ± 1.4	105.2 ± 3.1
Fake	92 ± 11	405 ± 17
Non-VBF $H \to \tau\tau, WW$	7.8 ± 0.2	17.1 ± 0.3
Total bkg.	812 ± 99	1658 ± 26
Total signal	14.9 ± 0.1	26.9 ± 0.1
Data	1018	1539

Table 7.1.: Expected event yields with statistical uncertainties in the MVA VBF inclusive region in the same-flavour and different-flavour final states for signal and background processes compared to the observed data. The normalization factors summarized in Table 7.6 are applied to the $Z \to \tau\tau$, $Z \to \ell\ell$ and top-quark backgrounds.

7.1.2. Multivariate Analysis

After the preselection presented in Section 7.1.1, further discrimination between the signal and background processes is needed in order to maximize the sensitivity to any CP-violating effects in the HVV coupling structure. This can be achieved by either selecting events based on additional kinematic cuts or by exploiting multivariate analysis (MVA) techniques. These MVA methods allow to not only include multiple variables in the classification of events as being signal- or background-like, but also exploit the variables correlation with each other. With this, an optimal separation between signal and background processes is achieved. In the VBF CP analysis, the separation between VBF $H \to \tau\tau$ signal and background events is obtained with boosted decision trees (BDTs), which are implemented in the Toolkit for MultiVariate Data Analysis(TMVA) package [236]. The following section gives a brief overview of the general concept of BDTs and describes the training and validation prodecure. The BDT application in the analysis to define the signal region is then discussed in the last part.

BDT Construction and Configuration

In general, a decision tree allows to categorize events as signal- or background-like by determining cuts on input variables, for which a maximum separation power between signal and background events is achieved. This decision tree consists of a root node, which contains the full sample of signal events S and background events B, and several additional nodes, which represent a binary decision. For each input variable x_i a separation index is defined as

$$g(c_i) = p(c_i) \cdot (p(c_i) - 1), \tag{7.1}$$

where $p(c_i) = S(c_i)/(S(c_i) + B(c_i))$ corresponds to the purity of the sample when the cut $x_i < c_i$ is applied. This so called *Gini-Index* is evaluated for each variable at a number of equidistand points in order to find the maximum $g^{max}(c_i)$. The successive splitting into signal-like and background-like sub-samples is then based on the variable, which yields the largest separation index for $x_i^{max} < c_i^{max}$. By repeating this procedure recursively for each sub-sample, decision nodes are added to the tree until a stopping criterion is reached. The optimizing of this splitting procedure is also called *training*. After the stopping criterion is reached, each of the final *leaf* notes is assigned a label according to the achieved purity. Hence, leaf notes, which dominantly contain signal events, receive a label of $+1$, while -1 is assigned to leaf notes with a majority of background events. Figure 7.2 shows a sketch of a decision tree with three decision nodes.

The performance of the decision tree can be evaluated in terms of its probability to falsely classify signal events as background-like and vice versa (*misclassification rate*). In principle, a perfect separation between signal and background events would be obtained by adding decision nodes to the tree until each sub-sample contains exactly one event. However, such a decision tree would respond to statistical fluctuations in the training sample and its separation power on an independent test sample would be significantly worse. This effect of *overtraining* can be reduced in several ways: Requiring a minimum number of events for each sub-sample (*nEventsMin*), limiting the size of the decision tree in terms of the number of decision nodes (*MaxDepth*) or by combining nodes with a low number of events after the training (*pruning*). The optimization of these *hyperparameters* is an important task for the decision tree contruction in order to maximize its separation power. Furthermore, the performance and robustness against overtraining can be improved by combining multiple trees with specific *boosting* techniques. Such a combination of single decision trees is also called a Boosted Decision Tree (BDT). For this, the training sample of a specific decision tree is constructed from the initial sample, but applying event weights based on the decision of the preciding tree. As previously misclassified events receive a larger event weight, they have a higher impact on the current training step than correctly classified events. This procedure is repeated for a predefined number of decision trees (*NTrees*). The final event classification then corresponds to the combined event weights of the individual trees, which is also called *BDT score*. In general, the boosting procedure is based on the minimization of a so-called *loss function*, which quantifies the decision tree's misclassification rate. The minimization of this loss function corresponds to finding the set of parameters, for which the decision tree achieves the best separation power. In this analysis, the BDTs are constructed with the *Gradient boosting* method [239]. This algorithm uses a binomial log-likelihood loss function and the minimzation is based on the gradient of this function. This allows to determine the *boost* weights w_i for each decision tree, which are used to construct the combined output $F(\vec{x})$ depending on the full list of variables $\vec{x}$:

$$F(\vec{x}) = \sum_{i=0}^{Ntrees} w_i h_i(\vec{x}). \tag{7.2}$$

Here, the individual classifications $h_i(\vec{x})$ correspond to values of $+1$ for signal-like and -1 for background-like events. This results in a continuous output of the final BDT, where BDT scores between -1 and $+1$ are obtained. The final classification can be further stabilized against statistical fluctuations by applying an additional parameter β with $0 < \beta < 1$ to the boost weights. This learning procedure is also called *shrinkage*.

BDT Training

The BDT performance depends on the available statistics of simulated events for the signal and background samples, which are used in the BDT training. However, these training events can not be used further in the actual analysis in order to avoid a possible bias due to overtraining. In addition, another sample is usually required to select the set of input variables, determine the choice of hyperparameters and validate the BDT performance. This typically results into splitting schemes, where 50 % of the events are used for the training set, 25 % for the validation set and 25 % for the test set. This analysis uses a k-fold cross-validation method [241] instead, which allows to improve the amount of available statistics for the BDT training. Here, the full set of simulated events is split into k slices of equal size and k different BDTs are trained, where each of them uses a different combination of $k-2$ slices for training, one slice for validation and one slice for the testing. With this, the fraction of events, which is used for the training, is always larger than 50 %. By combining all k BDTs, the validation and testing can then be performed with the full available statistics. In this analysis, $k = 10$ is used and the splitting of simulated signal and background events into the different slices is based on a random

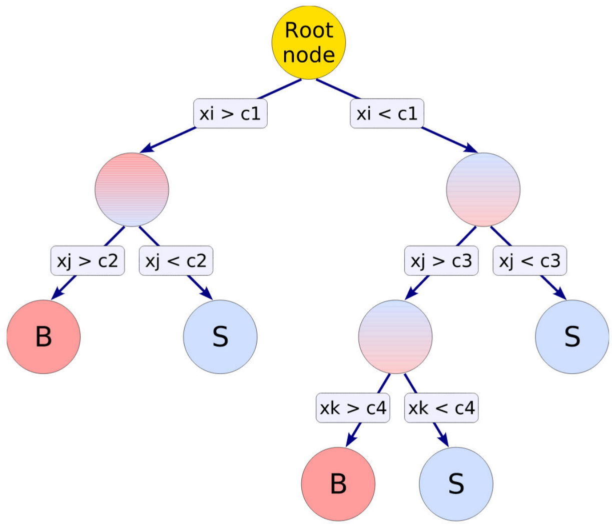

Figure 7.2.: Schematic view of a single decision tree with a depth of three. Starting from the root note with the first decision based on variable x_i the events are grouped into a signal-like and background-like sub-samples (S and B) for a specific cut value c_1 [240]. Each node then splits the classified events further into so called leaf-nodes based on cut-values c_i until a stopping criterion is reached.

number, which is generated once for each event. The splitting of data events is done by using a *modulo-splitting* approach based on EVENT NUMBER MODULO k.

The BDTs are trained in the MVA VBF inclusive region, which allows to exploit as much statistics as possible while reducing the dominant background contributions in a first step. As seen in Table 7.1, the background composition in the $\tau_{lep}\tau_{lep}$ channel depends on the flavour of the final-state leptons. In particular, the contribution of $Z \to \ell\ell$ events differ significantly between the SF and DF final states. Therefore, two separate BDTs are trained in the SF and DF final states to account for possible differences in the importance of kinematic variables and hence to improve the separation power. The signal sample corresponds to VBF $H \to \tau\tau$ and $H \to WW$ events, while the various background processes described in Section 4.2 are included in the background sample. Additional normalization factors for the $Z \to \tau\tau$, $Z \to \ell\ell$ and top-quark backgrounds are applied before the training. Contributions from events with Higgs-boson production in the ggF, VH or ttH modes are not included in the training.

The optimal set of hyperparameters are chosen by training multiple BDTs with a large number of different hyperparameter settings and then comparing their expected sensitivity, which is obtained in a likelihood fit with statistical uncertainties only [242]. An overview of the final hyperparameters, which are used for constructing the BDTs in the SF and DF channel, is given in Table 7.2.

The input variables are selected from a large set of kinematic variables by starting with a BDT trained on the full set of variables, which are listed in Ref. [242], and then iteratively removing the one with the lowest impact on the classification. The remaining variables

Parameter	SF	DF
Boost algorithm	Gradient	
Number of trees	250	
MaxDepth	7	2
MinNodeSize (% of training events)	10	5
Shrinkage	0.1	
Pruning	No pruning	

Table 7.2.: Overview of the hyperparameters for the BDT configuration in the SF and DF final states of the $\tau_{lep}\tau_{lep}$ channel.

are then used for retraining a new BDT and the expected significance of the resulting classifier is calculated in a likelihood fit. This procedure is repeated until only one variable is left and the final set of input variables then corresponds to the setup, which provides the highest significance with the lowest number of variables [242]. As shown in Table 7.3, 10 input variables are used in the SF channel, while the BDT in the DF channel is based on 11 input variables. These variables are exploited by the BDTs since they either allow to efficiently distinguish the $H \to \tau\tau$ decay mode from the final states of the background processes or correspond distinct kinematic features of the VBF Higgs-boson production mode. Both BDTs use the invariant masses of the di-τ, di-lepton and di-jet system as well as the transverse mass between the leading lepton and the missing transverse energy. Furthermore, angular separation variables between the selected leptons and the transverse momentum of the final state system ($\ell_0, \ell_1, j_0, j_1, E_T^{miss}$) are used. Both BDTs also exploit information from the transverse momentum of a possible third jet $p_T(j_2)$ in the event. If no third jet is found, the value of this variable is set to 0 and acts as a third-jet veto in the event classification. In addition, both BDTs take the centrality of the selected lepton as inputs, while in the DF channel the ratio of missing transverse energy to the transverse momentum of the leading and sub-leading leptons are used in addition. Figure 7.3 and 7.4 show the input variable modelling in the MVA VBF inclusive region of the SF and DF final states, respectively. Overall, a good agreement between simulation and data is obtained, while the SF final state is especially affected by low MC statistics for the prediction of the dominant $Z \to \ell\ell$ background.

Figure 7.5 shows a comparison of the BDT scores between training and validation events, combined for all folds of the cross validation, where a good agreement for both signal and background processes is obtained. This agreement is also confirmed by the *Kolmogorov-Smirnoff* test [243], which provides an agreement probablity of 1 for the signal and only slightly below 1 for the background dstributions. Hence, the performance of the BDTs on the training and validation events are found to be similar, which gives confidence, that the classifiers are not significantly affected by overtraining. The modelling of the BDT score is shown in Figure 7.6 for the SF and DF channel. Here, a good agreement is observed between data and prediction within the considered statistical and systematic uncertainties.

Table 7.4 shows a ranking of the input variables with respect to their importance in

[1] $C_{jj}(\ell) = \exp\left(\frac{-4}{(\eta_{j0}-\eta_{j1})^2}\left(\eta_\ell - \frac{\eta_{j0}+\eta_{j1}}{2}\right)^2\right)$ with the (sub-)leading jet $j_{0(1)}$.

Variable	SF	DF
$m_{\tau\tau}^{\mathrm{MMC}}$	•	•
$m_{\ell\ell}$	•	•
m_{jj}	•	•
$m_T(\ell_0, E_T^{miss})$	•	•
$\Delta R_{\ell\ell}$	•	•
$\Delta\phi_{\ell\ell}$	•	
$p_T(\ell_0, \ell_1, j_0, j_1, E_T^{miss})$	•	•
$p_T(j_2)$	•	•
$C_{jj}(\ell_0)^1$	•	•
$C_{jj}(\ell_1)$	•	•
$E_T^{miss}/p_T(\ell_0)$		•
$E_T^{miss}/p_T(\ell_1)$		•

Table 7.3.: Summary of input variables for the BDT training in the SF and DF final states of the $\tau_{lep}\tau_{lep}$ channel.

the training. In particular, this ranking score indicates the number of node splittings, which are based on this variable, averaged over all individual BDTs. In the SF final state, the highest ranked variable is given by the ΔR-separation between the selected leptons, followed by the leading lepton centrality and the reconstructed di-τ mass from the MMC algorithm. The BDT training in the DF final state mainly relies on the invariant mass of the selected leptons, the ratio of missing transverse energy to leading lepton p_{T} and the invariant di-jet mass.

Variable	Importance
$\Delta R_{\ell\ell}$	0.200
$C_{jj}(\ell_0)$	0.127
$m_{\tau\tau}^{\mathrm{MMC}}$	0.122
$m_T(\ell_0, E_T^{miss})$	0.110
$\Delta\Phi_{\ell\ell}$	0.104
$C_{jj}(\ell_1)$	0.099
m_{jj}	0.096
$p_T(j_2)$	0.056
$p_T(\ell_0, \ell_1, j_0, j_1, E_T^{miss})$	0.046
$m_{\ell\ell}$	0.040

Variable	Importance
$m_{\ell\ell}$	0.122
$E_T^{miss}/p_T(\ell_1)$	0.117
m_{jj}	0.098
$C_{jj}(\ell_0)$	0.096
$\Delta R_{\ell\ell}$	0.092
$p_T(\ell_0, \ell_1, j_0, j_1, E_T^{miss})$	0.091
$C_{jj}(\ell_1)$	0.091
$E_T^{miss}/p_T(\ell_0)$	0.086
$m_T(\ell_0, E_T^{miss})$	0.071
$p_T(j_2)$	0.071
$m_{\tau\tau}^{\mathrm{MMC}}$	0.064

Table 7.4.: Ranking of the input variables used in the SF BDT (left) and DF BDT (right) in the $\tau_{lep}\tau_{lep}$ channel.

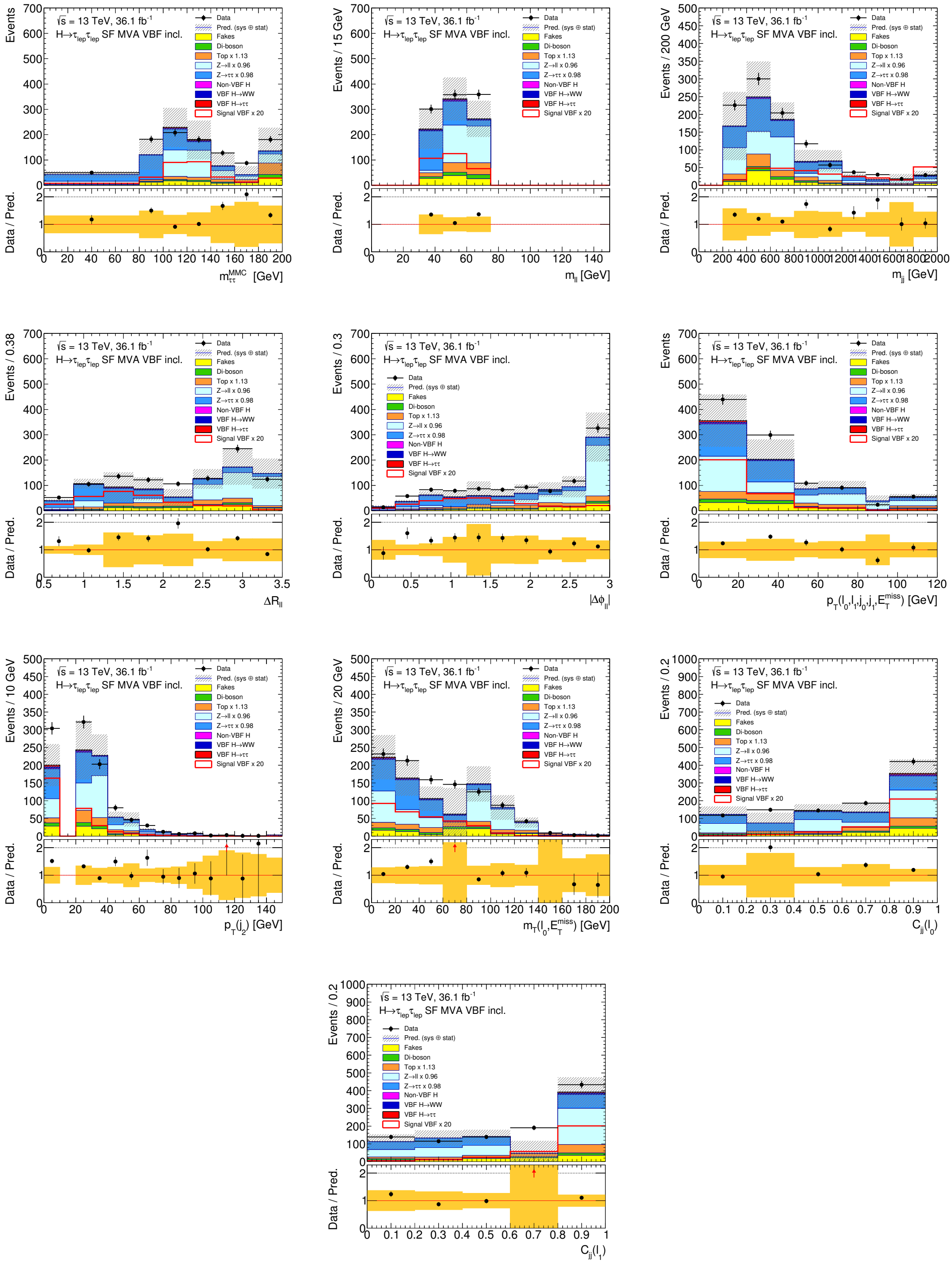

Figure 7.3.: Distributions of the input variables, which are used in the SF BDT. The uncertainty band includes statistical uncertainties and systematic uncertainties related to jets, E_T^{miss} and the fake-lepton background.

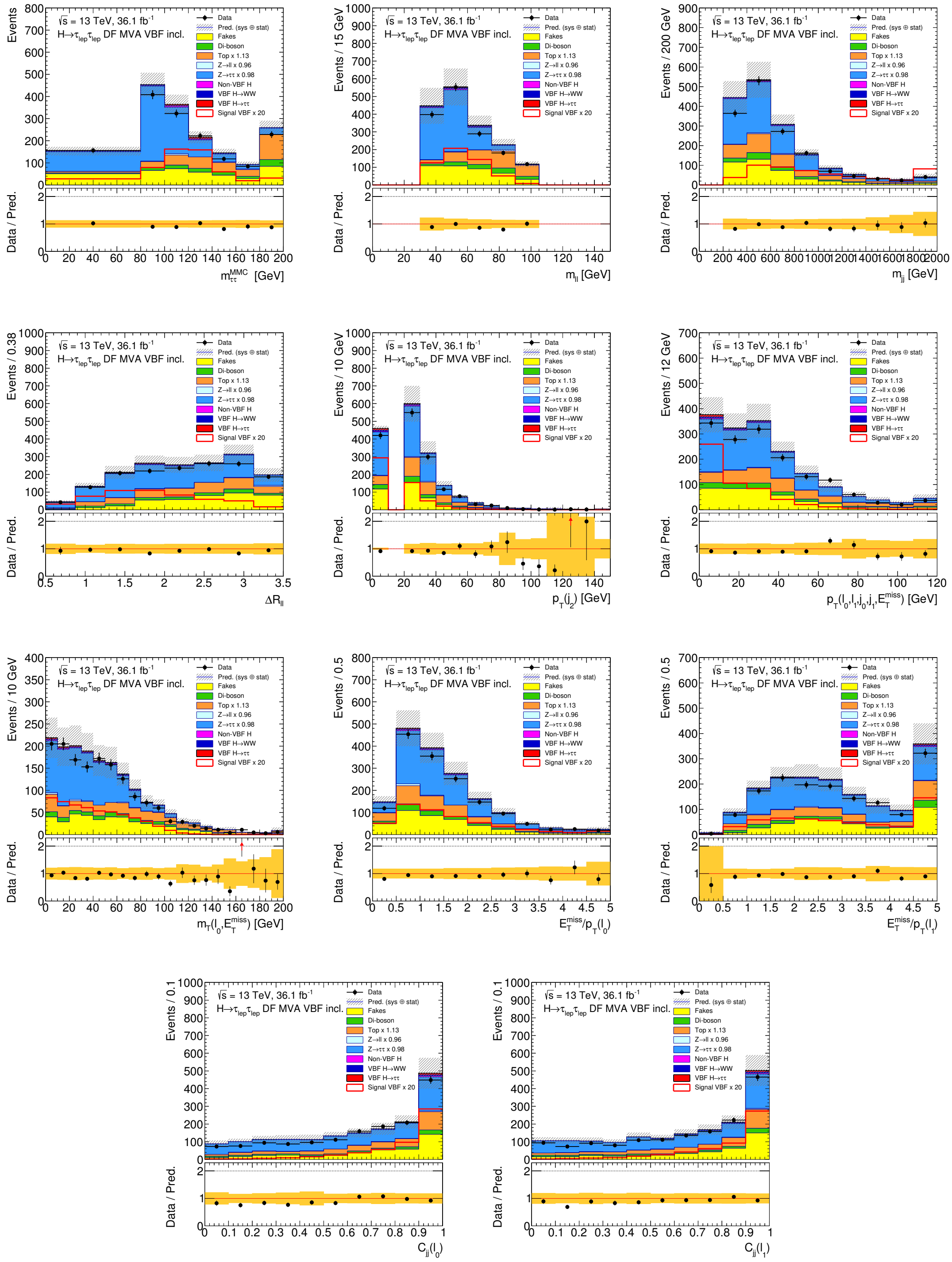

Figure 7.4.: Distributions of the input variables, which are used in the DF BDT. The uncertainty band includes statistical uncertainties and systematic uncertaintiesrelated to jets, E_T^{miss} and the fake-lepton background.

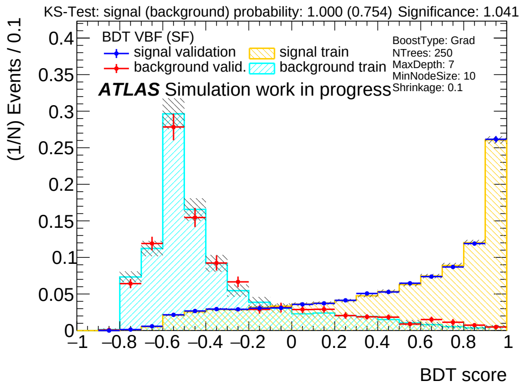

(a)

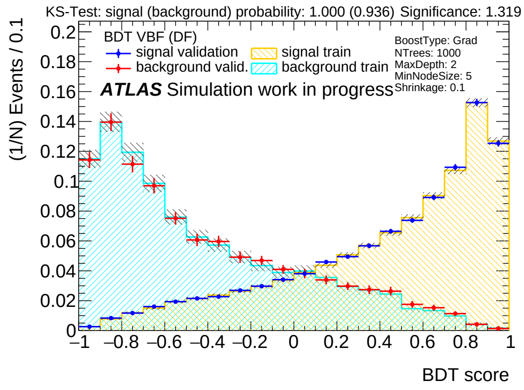

(b)

Figure 7.5.: Comparison of the shapes of the BDT score distributions for training and validation events for the SF BDT (a) and the DF BDT (b) in the $\tau_{lep}\tau_{lep}$ channel. The comparison is shown for background (cyan/red) and signal (yellow/blue) events.

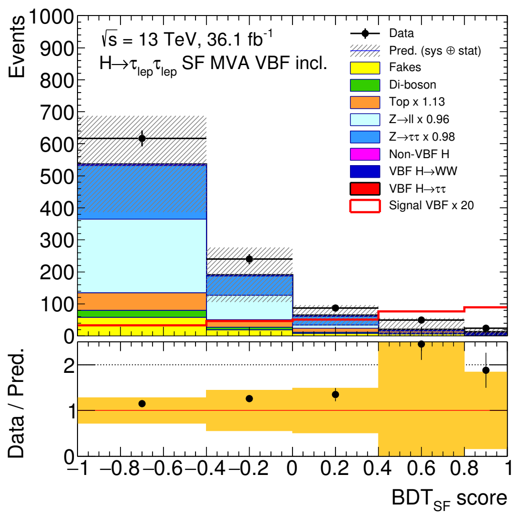

(a)

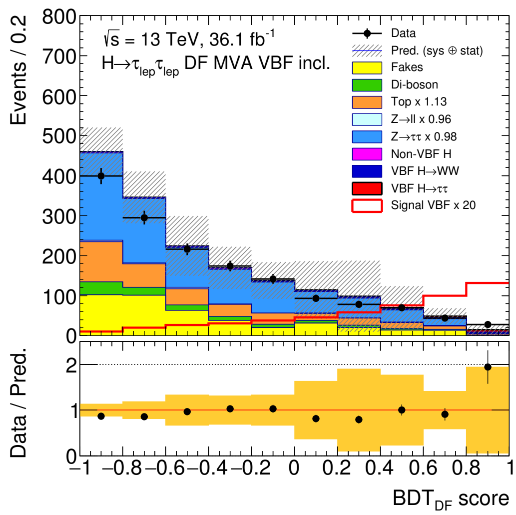

(b)

Figure 7.6.: Distributions of the SF BDT score (a) and the DF BDT score (b) in the MVA VBF inclusive region. The uncertainty band includes statistical uncertainties and systematic uncertainties related to jets, E_T^{miss} and the fake-lepton background.

As mentioned above, the BDT performance is improved by exploiting differences in the variable correlations between signal and background events. Figure 7.7 and 7.8 shows the correlation coefficients of all input variables for signal events and the sum of all background processes in the SF and DF channel, respectively. In general, the correlation of the di-lepton variables $\Delta R_{\ell\ell}, \Delta\Phi_{\ell\ell}, m_{\ell\ell}$ as well as $p_T(j_2)$ and $m_T(\ell_0, E_T^{miss})$ are found to vary between signal and background events. In the DF final state, the BDT can also exploit different correlations between $E_T^{miss}/p_T(\ell_{0(1)}), m_{\ell\ell}$ and $\Delta R_{\ell\ell}$. A comparison of the correlations between all input variables and the BDT score for data and the sum of all background events can be found in Appendix A.

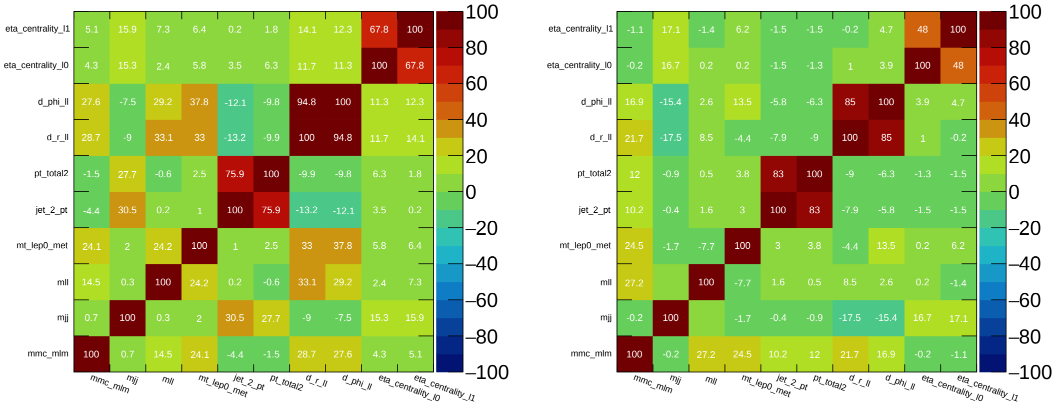

(a) (b)

Figure 7.7.: Correlation coefficient between all input variables used for the SF BDT training for the sum of all backgrounds (a) and the signal (b).

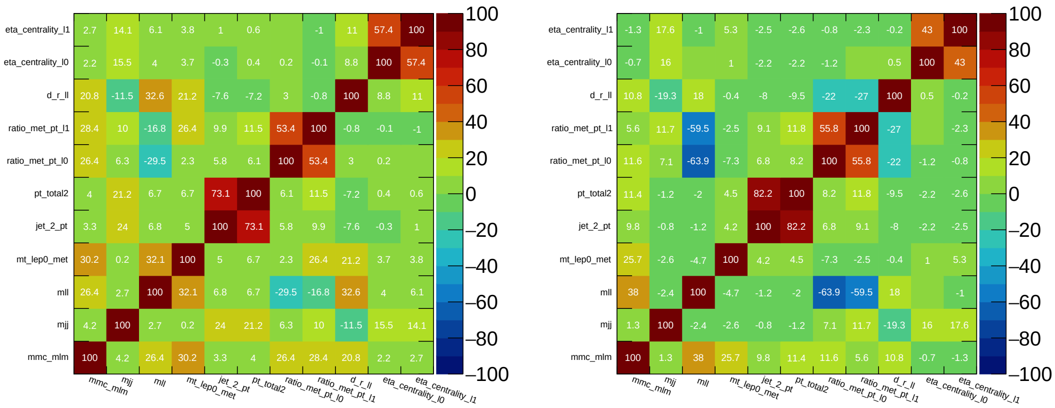

(a) (b)

Figure 7.8.: Correlation coefficient between all input variables used for the DF BDT training for the sum of all backgrounds (a) and the signal (b).

Definition of Signal Region and low-BDT Control Region

The sensitivity to additional CP-odd contributions in the SM HVV coupling structure strongly depends on the suppression of background processes, where no CP violation is expected. In this analysis, the high-BDT signal region is defined by only selecting signal-like events according to the BDT classification with BDT score > 0.78. This lower threshold is determined by maximizing the significance $\frac{s_x}{\sqrt{s_x+b_x+\sigma^2_{b,x}}}$, where $s_x(b_x)$ are the number of signal (background) events with BDT score $> x$ for a given cut value x. The corresponding statistical uncertainty on the background prediction is given by $\sigma_{b,x}$. In order to limit the impact of statistical fluctuations in the background predictions, each background process is required to have a positive event yield when applying the cut. This significance optimization is done separately for the SF and DF BDTs and the results are shown in Figure 7.9. For both BDTs, the maximum significance is reached for a cut of BDT score > 0.80. However, with this threshold, the limited number of simulated events in the $Z \to \ell\ell$ background prediction does not allow for a reasonable binning of the Optimal Observable distribution. Therefore, the signal regions in the SF and DF channels are defined by loosening this cut to BDT score > 0.78.

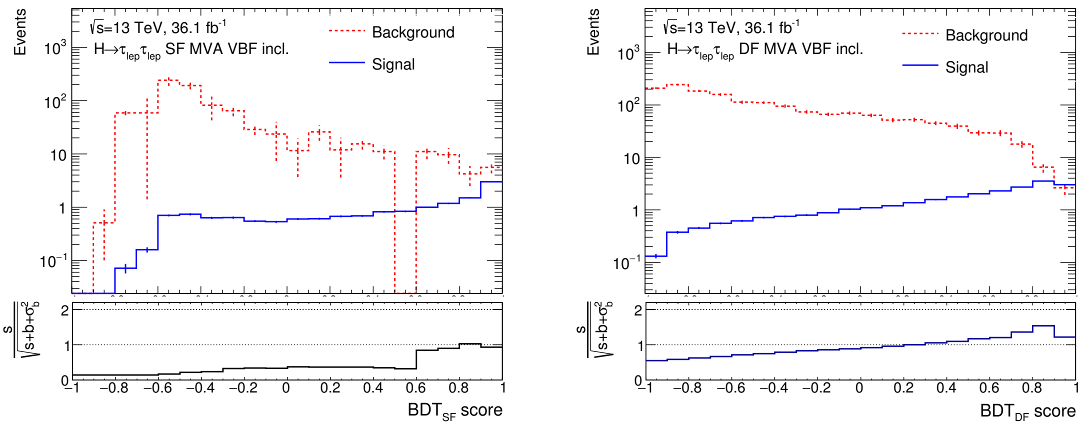

(a) (b)

Figure 7.9.: Optimization of the cut on the BDT score for the definition of the high-BDT signal region in the SF (a) and DF (b) final state. 'Background' (red) corresponds to the sum of all considered background processes, while 'Signal' (blue) refers to the sum of VBF $H \to \tau\tau$ and $H \to WW$ events. Only statistical uncertainties are considered.

The expected event yields with their statistical uncertainties in the high-BDT signal regions and the observed number of data events are shown in Table 7.5. In the SF channel 26 data events are observed, while the DF channel contains 30 data events. In the SF channel the total VBF signal corresponds to 4.7 ± 0.1 expected events and is mainly composed of $H \to \tau\tau$ decays with a relative contribution of 79 %. The total expected background yields 11 ± 4 events with dominant contributions from $Z \to \ell\ell$ decays with 38 % and $Z \to \tau\tau$ decays with 26 %. Top-quark events constitute 20 % of the total expected background. The background contribution from di-boson production and fake-lepton events is expected to be smaller with only 4 % and 3 %, respectively. Events from the non-VBF Higgs-boson production mode provide 5 % of the total expected background. In the DF channel the total VBF signal corresponds to 7.2 ± 0.1 expected events and is mainly composed of $H \to \tau\tau$ decays with a relative contribution of 76 %. The total expected background yields 12 ± 2 events, where the dominant contributions arise from top-quark events with 29 %, $Z \to \tau\tau$ decays with 27 % and fake-lepton events with 24 %. The sum of expected events from $Z \to \ell\ell$ and di-boson production constitute 10 % of the total expected background, while the contribution from non-VBF Higgs-boson production is 6 %. The cut on the BDT score results in a significant improvement of the signal-to-background ratio by factors of 23 in the SF channel and 37 in the DF channel with respect to the MVA VBF inclusive region. In both channels, the expected sum of all signal and background events in the signal region is found to be smaller compared to the observed number of events and does not agree within statistical uncertainties. However, as shown in Table 7.12 and 7.13, this discrepancy is well covered by the large systematic uncertainties, which mainly occur due to the limited number of simulated background events in the signal regions. In particular, the prediction of the $Z \to \ell\ell$ background suffers from limited statistics, which especially affects the SF channel.

Process	High-BDT SR		Low-BDT CR	
	SF	DF	SF	DF
VBF $H \to \tau\tau$	3.7 ± 0.1	5.5 ± 0.1	5.7 ± 0.1	12.1 ± 0.1
VBF $H \to WW$	1.0 ± 0.0	1.7 ± 0.0	4.4 ± 0.1	7.6 ± 0.1
$Z \to \tau\tau$	3.1 ± 1.2	3.3 ± 1.1	270 ± 10	793 ± 18
$Z \to \ell\ell$	4.5 ± 3.1	0.1 ± 0.2	298 ± 95	14 ± 4
Top	2.4 ± 0.7	3.5 ± 0.8	97 ± 4	315 ± 8
Di-Boson	0.5 ± 0.1	1.1 ± 0.2	36 ± 1	103 ± 3
Fakes	0.3 ± 0.4	2.9 ± 1.2	91 ± 11	402 ± 17
Non-VBF $H \to \tau\tau, WW$	0.6 ± 0.1	0.7 ± 0.1	7.2 ± 0.2	16.4 ± 0.3
Total bkg.	11 ± 4	12 ± 2	800 ± 100	1645 ± 27
Total signal	4.7 ± 0.1	7.2 ± 0.1	10.1 ± 0.1	19.7 ± 0.1
Data	26	30	992	1509

Table 7.5.: Expected event yields with statistical uncertainties in the high-BDT signal region and the low-BDT control region in the SF and DF final states for signal and background processes compared to the observed data. The size of the systematic uncertainties on the signal and background components can be found in Table 7.12 and 7.13. The normalization factors summarized in Table 7.6 are applied to the $Z \to \tau\tau$, $Z \to \ell\ell$ and top-quark backgrounds.

While it is in principle desirable to choose a fine binning for the distribution of the Optimal Observable in order to retain as much information as possible about the underlying HVV coupling structure, statistical fluctuations in the predicted background contributions per bin can cause instabilities in the statistical analysis. In particular, the unphysical prediction of negative event yields per bin due to statistical fluctuations in the simulated sample

requires a special treatment and should be avoided. Therefore, a non-equidistant binning with 4 bins in the range $[-15, -5, 0, 5, 15]$ is used and the resulting Optimal Observable distributon is shown in Figure 7.10. Here, only statistical uncertainties are included on the signal and background predictions due to the large size of the systematic components, which are summarized in Table 7.12 and 7.13.
In order to investigate, if the inclusion of VBF $H \to WW$ events in the signal prediction introduces any artifical distortion in the shape of the Optimal Observable, Figure 7.11 shows a comparison between VBF $H \to \tau\tau$ and VBF $H \to WW$ decays for different HVV coupling models. Overall, no significant deviations in the Optimal Observable distributions between the $H \to \tau\tau$ and $H \to WW$ signal events are observed.

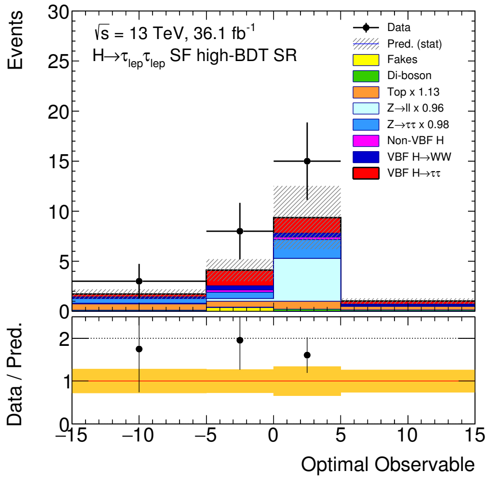

(a)

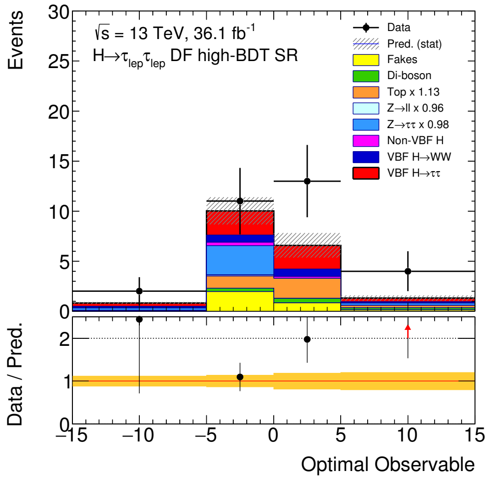

(b)

Figure 7.10.: Distribution of the Optimal Observable in the high-BDT signal region for the SF (a) and DF (c) final states. Only statistical uncertainties are included in the error band. The size of the systematic uncertainties on the signal and background components can be found in Table 7.12 and 7.13.

In addition, it is important to check that the cut on the BDT score does not introduce any bias on the Optimal Observable, which could mimic the presence of CP-violating effects. In particular, the shape of the Optimal Observable has to remain symmetric as expected for all SM processes preserving CP invariance. For this, the mean of the Optimal Observable is calculated depending on the bins of the BDT score for background and signal events. This is shown in Figure 7.12 and Figure 7.13 for the SF and DF BDT scores, respectively. Here, no significant deviation of the mean value from the expectation of 0 is observed for the SM signal and background predictions. For CP-violating scenarios corresponding to $\tilde{d} = 0.30$ and $\tilde{d} = -0.10$, the Optimal Observable mean value for VBF $H \to \tau\tau$ and $H \to WW$ events fluctuates around a constant deviation from 0, as expected.

The modelling of the Optimal Observable can also be studied in a *low-BDT* CR, which is constructed orthogonal to the signal region by requiring BDT score < 0.78. The expected event yields for all processes with their statistical uncertainties and the observed number of data events in this CR are summarized in Table 7.5. In the SF channel the dominant contribution to the total expected yield arises from $Z \to \ell\ell$ events with 36 % and $Z \to \tau\tau$ events with 33 %. The expected event yield in the DF channel is dominated by $Z \to \tau\tau$ events with a relative contribution of 47 %, fake-lepton events with 25 % and top-quark events with 19 %. In both channels the signal contribution is found to be negligible with a signal-to-background ratio of only 1 %. Figure 7.14 shows the modelling of the Optimal Observable distribution in the low-BDT regions of the SF and DF channels. Overall, a good agreement between prediction and data is observed. This low-BDT CR is also included in the likelihood fit to constrain systematic uncertainties and to measure the normalization of the $Z \to \tau\tau$ background (see Section 7.4). For this, the distribution of the reconstructed di-τ mass $m_{\tau\tau}^{\mathrm{MMC}}$ is used as the discriminating variable. The $m_{\tau\tau}^{\mathrm{MMC}}$ distributions in the SF and DF low-BDT CRs are shown in Figure 7.15, where a good agreement between prediction and data is observed. The modelling of the BDT score as well as the Optimal Observable in the $Z \to \ell\ell$ CR and the Top CR are discussed in Section 7.2.2.

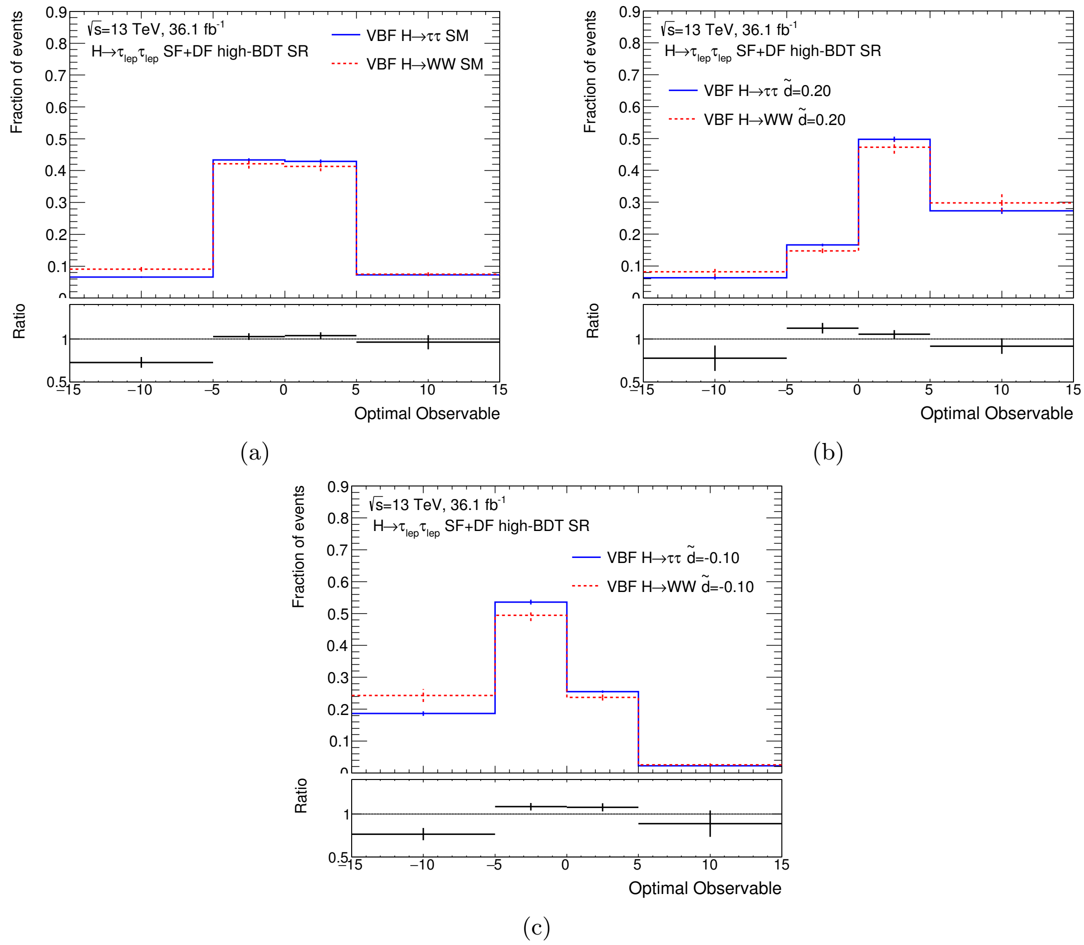

Figure 7.11.: Comparison of the shape of the Optimal Observable distribution for VBF $H \to \tau\tau$ and $H \to WW$ signal events for different $\tilde{d}$-hypotheses in the high-BDT signal region. Only statistical uncertainties are included.

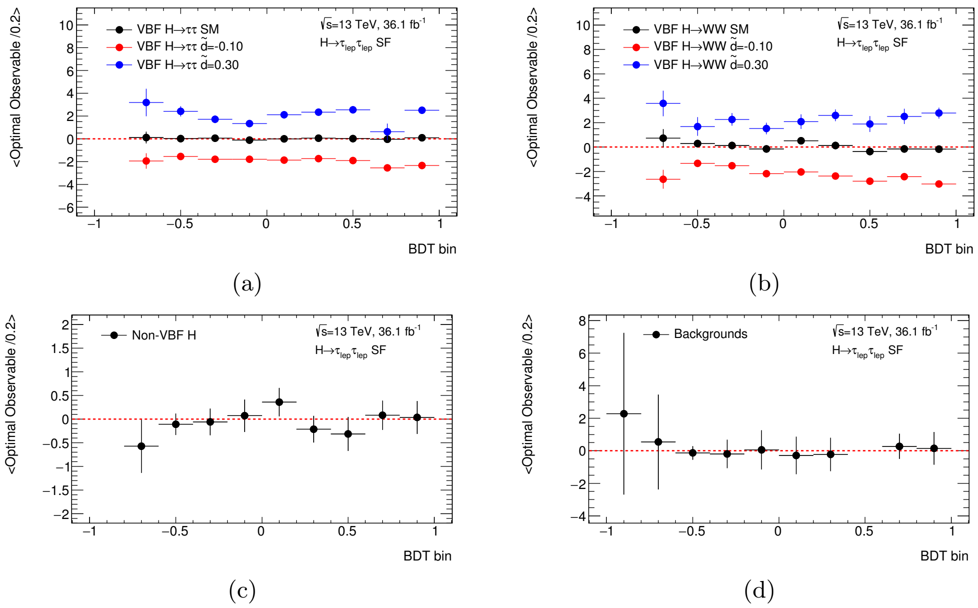

Figure 7.12.: Mean of the Optimal Observable in bins of the SF BDT score for different $\tilde{d}$-values for the $H \to \tau\tau$ signal (a) and the $H \to WW$ signal (b), non-VBF background events (c) and the sum of the remaining background processes (d). Only statistical uncertainties are included.

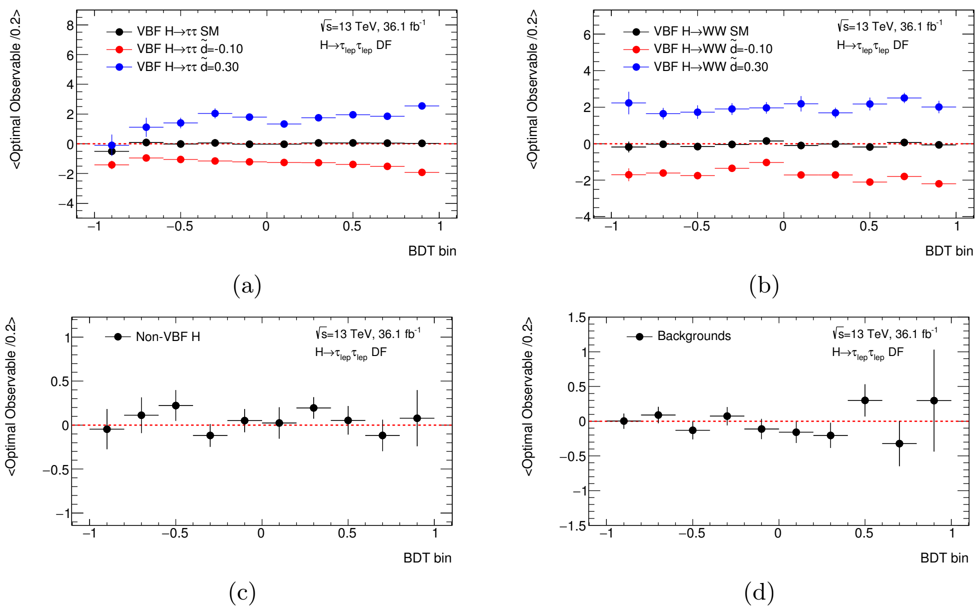

Figure 7.13.: Mean of the Optimal Observable in bins of the DF BDT score for different $\tilde{d}$-values for the $H \to \tau\tau$ signal (a) and the $H \to WW$ signal (b), non-VBF background events (c) and the sum of the remaining background processes (d). Only statistical uncertainties are included.

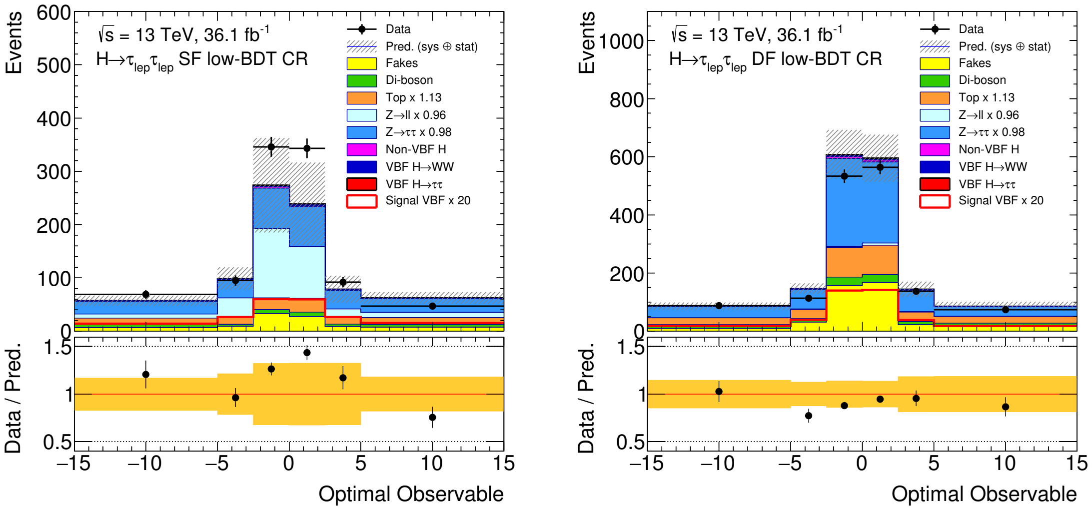

(a) (b)

Figure 7.14.: Distribution of the Optimal Obervable in the low-BDT control region in the SF (a) and DF (b) final state. The error band includes statistical and systematic uncertainties related to jet, E_T^{miss} and the fake-lepton background estimation.

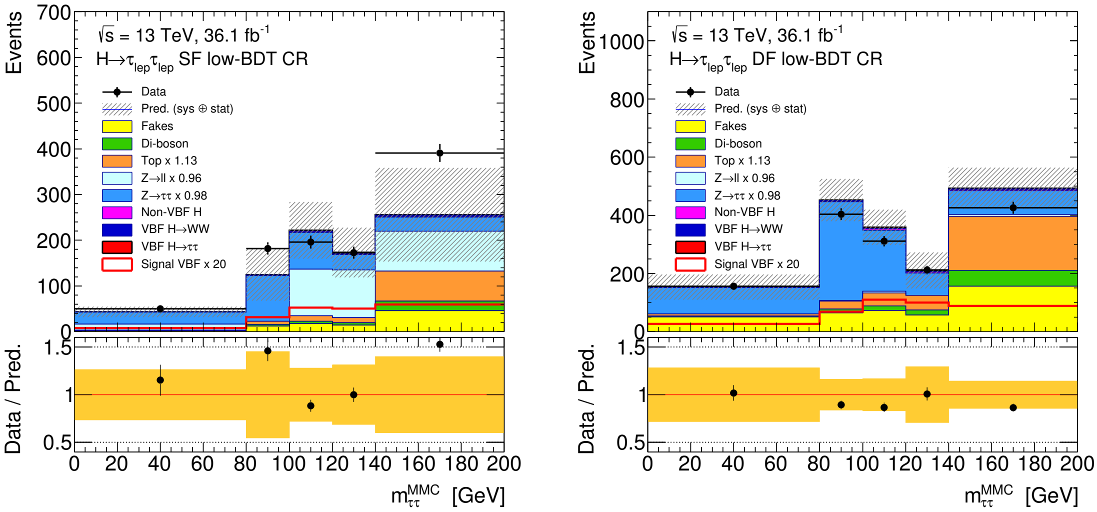

(a) (b)

Figure 7.15.: Distribution of $m_{\tau\tau}^{\mathrm{MMC}}$ in the low-BDT control region in the SF (a) and DF (b) final state. The error band includes statistical and systematic uncertainties related to jet, E_T^{miss} and the fake-lepton background estimation.

7.2. Background Estimation and Validation

The VBF CP analysis exploits the same procedure to validate the predictions of simulated events from $Z \to \tau\tau$, $Z \to \ell\ell$ and top-quark backgrounds as the $H \to \tau\tau$ cross-section measurement (see Section 6.2). For this, the normalization and modelling of important variables, such as $m_{\tau\tau}^{\mathrm{MMC}}$ and the Optimal Observable, are studied in dedicated control regions and are discussed in the following section. These control regions are constructed orthogonal to the MVA VBF inclusive selection described in Section 7.1.1 by inverting specific kinematic requirements to enhance the phase space with events from the process of interest. The estimation of background events including fake leptons is explained in Section 6.2.3 and no correction factors are applied to di-boson and non-VBF Higgs-boson background events.

Table 7.6 summarizes the pre-fit normalization factors for the $Z \to \tau\tau$, $Z \to \ell\ell$ and top-quark background. These factors are derived with the same procedure as described in Section 6.2, where the MVA VBF inclusive region is used to determine the normalization of $Z \to \tau\tau$ events, and are found to be in good agreement with the obtained normalization factors in the VBF inclusive region of the $H \to \tau\tau$ cross-section measurement.

	$Z \to \tau\tau$	$Z \to \ell\ell$	Top
MVA VBF inclusive	0.98 ± 0.03	0.96 ± 0.04	1.13 ± 0.03

Table 7.6.: Pre-fit normalization factors and their statistical uncertainties for the dominant background processes in the MVA VBF inclusive region.

7.2.1. $Z \to \tau\tau$ Background

In the VBF CP analysis, background processes from $Z \to \tau\tau$ decays give one of the main contributions in the high-BDT signal regions. As described in Section 7.4.2, the normalization of this background is determined in data by the inclusion of low-BDT control regions in the likelihood fit. In order to verify, that this normalization factor can be propagated to the signal regions, it is important to validate the modelling of the $Z \to \tau\tau$ kinematics and in particular of the BDT score. However, the low-BDT control regions also contain large contributions from other background processes and therefore not allow for a sufficient validation of the $Z \to \tau\tau$ prediction. Instead, the VBF CP analysis uses a similar approach as the $H \to \tau\tau$ cross-section measurement described in Section 6.2.1 by constructing a $Z + jets$ validation region (VR), which is enriched in events from $Z \to \ell\ell$ decays. In particular, this region allows to validate the modelling of the BDT input variables related to the Z^0-boson and additionally produced jets. Since input variables, which are constructed from the kinematics of the decay constituents clearly differ for $Z \to \tau\tau$ and $Z \to \ell\ell$ decays, this aspect of the BDT classification can not be studied in the VR, but a modified BDT is trained as discussed below. In the context of this thesis, the studies in the $Z + jets$ VR are performed for all three di-τ decay channels, where a description of the VBF CP analysis in the $\tau_{lep}\tau_{had}$ and $\tau_{had}\tau_{had}$ final states can be found in Ref. [32].

The aim of the $Z+jets$ VR is to select a large sample of $Z \to \ell\ell$ events, while staying as close as possible to the signal region selection. Here, a common $Z+jets$ VR is constructed for the $\tau_{lep}\tau_{lep}$ and $\tau_{lep}\tau_{had}$ channels ($\tau_{lep}\tau_{lep}$+$\tau_{lep}\tau_{had}$ $Z+jets$ VR), while slightly different criteria are imposed in the $\tau_{had}\tau_{had}$ channel ($\tau_{had}\tau_{had}$ $Z+jets$ VR):

- two leptons with same flavor and opposite charge (ee or $\mu\mu$)
- leading and sub-leading lepton with $p_T > 40$ GeV for the $\tau_{lep}\tau_{lep}$+$\tau_{lep}\tau_{had}$ VR
  leading lepton with $p_T > 40$ GeV and sub-leading lepton with $p_T > 30$ GeV for the $\tau_{had}\tau_{had}$ VR
- $0.8 < |\Delta R_{\ell\ell}| < 2.5$ for the $\tau_{lep}\tau_{lep}$+$\tau_{lep}\tau_{had}$ VR
  $0.8 < |\Delta R_{\ell\ell}| < 2.5$ and $|\Delta\eta_{\ell\ell}| < 1.5$ for the $\tau_{had}\tau_{had}$ VR
- $m_{\ell\ell} > 80$ GeV and $E_T^{miss} < 55$ GeV
- at least two jets with $p_T^{j0} > 40$ GeV and $p_T^{j1} > 30$ GeV for the $\tau_{lep}\tau_{lep}$+$\tau_{lep}\tau_{had}$ VR
  at least two jets with $p_T^{j0} > 70$ GeV and $p_T^{j1} > 30$ GeV for the $\tau_{had}\tau_{had}$ VR
- $|\Delta\eta_{jj}| > 3$ and $m_{jj} > 300$ GeV
- no b-tagged jet with $p_T > 25$ GeV

Here, the requirement on $m_{\ell\ell}$ ensures orthogonality to the signal selection in the $\tau_{lep}\tau_{lep}$ channel, while the upper threshold on E_T^{miss} is imposed in order to reject events with a large fraction of mismeasured E_T^{miss}. As shown in Table 7.7, the fractional contribution of $Z \to \ell\ell$ events is found to be 99 % in the $\tau_{lep}\tau_{lep}$+$\tau_{lep}\tau_{had}$ VR and 98 % in the $\tau_{had}\tau_{had}$ VR. In the $\tau_{lep}\tau_{lep}$+$\tau_{lep}\tau_{had}$ VR, the predicted event yield is larger compared to the observed number of data events. This is accounted for by scaling the $Z \to \ell\ell$ events with a factor of 0.97. In the $\tau_{had}\tau_{had}$ VR, a good agreement between data yield and predicted yield is found and no additional correction is applied. As discussed in Section 4.3.3 the cross-section for EW Z^0-boson production is scaled with a factor of 1.7 in order to account for the disagreement between the Sherpa prediction and the measured production cross-section.

13 TeV, 36.1 fb^{-1}	$\tau_{lep}\tau_{lep}$+$\tau_{lep}\tau_{had}$ VR	$\tau_{had}\tau_{had}$ VR
$Z \to \ell\ell$	199700 ± 1400	47430 ± 380
Other processes	1907 ± 14	492 ± 6
Sum of all processes	201607 ± 1400	47922 ± 380
Data	193570	47390

Table 7.7.: Event yields with statistical uncertainties for $Z \to \ell\ell$ events and the remaining signal and background processes compared to the observed data yield in the $\tau_{lep}\tau_{lep}$+$\tau_{lep}\tau_{had}$ and $\tau_{had}\tau_{had}$ $Z+jets$ validation regions.

The input variables, which are used in the BDT training (see Table 7.3 and Ref. [32] for the $\tau_{lep}\tau_{had}$ and $\tau_{had}\tau_{had}$ channels), are related to the final-state leptons or the hadronically decaying τ-lepton, additionally produced jets and the missing transverse energy in the event. While the jet-related variables do not depend on the decay channel of the Z^0-boson, a clear difference between $Z \to \ell\ell$ and $Z \to \tau\tau$ events is expected for variables, which are constructed from the kinematics of the Z-boson decay products. This can be seen in Figure 7.16 and 7.17, which show a comparison of the input variables between $Z \to \ell\ell$ events selected in the $Z + jets$ VR and $Z \to \tau\tau$ events in the MVA VBF inclusive regions of the three analysis channels. As expected, a good agreement is observed between the jet-related input variables in Figure 7.16, while the distributions in Figure 7.17 demonstrate the different kinematic configurations of the $Z \to \ell\ell$ and $Z \to \tau\tau$ decay products.

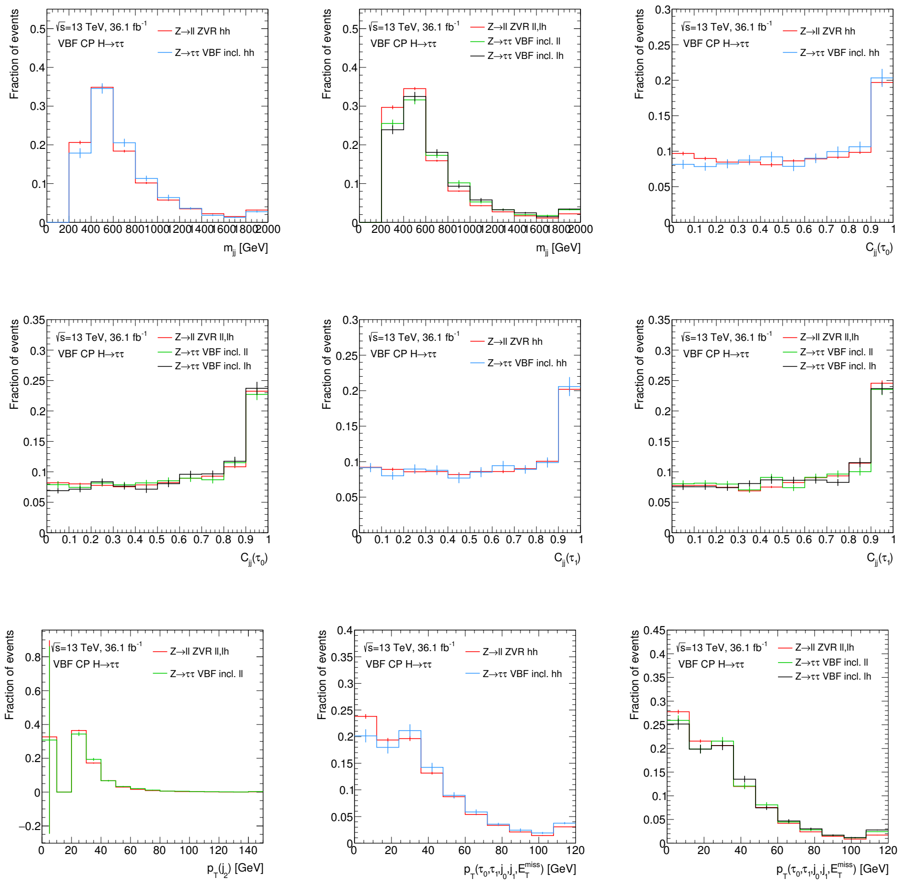

Figure 7.16.: Normalized distributions of the BDT input variables related to the jet kinematics and $p_T^{\text{Total}} = p_T(\tau_0, \tau_1, j_0, j_1, E_T^{miss})$ comparing $Z \to \tau\tau$ events in the MVA VBF inclusive regions of the $\tau_{lep}\tau_{lep}$ (green), $\tau_{lep}\tau_{had}$ (black) and $\tau_{had}\tau_{had}$ (blue) channels to $Z \to \ell\ell$ events in the corresponding $Z + jets$ validation regions (red). For $\tau_{lep}\tau_{lep}$ events, the label τ corresponds to the decay leptons $\ell = e, \mu$. In the $\tau_{lep}\tau_{had}$ channel, τ_0 refers to the hadronically decaying τ-lepton, while τ_1 refers to the final-state leptons $\ell = e, \mu$ from the leptonic τ-decay. In the $\tau_{had}\tau_{had}$ channel, τ always corresponds to the hadronically decaying τ-lepton.

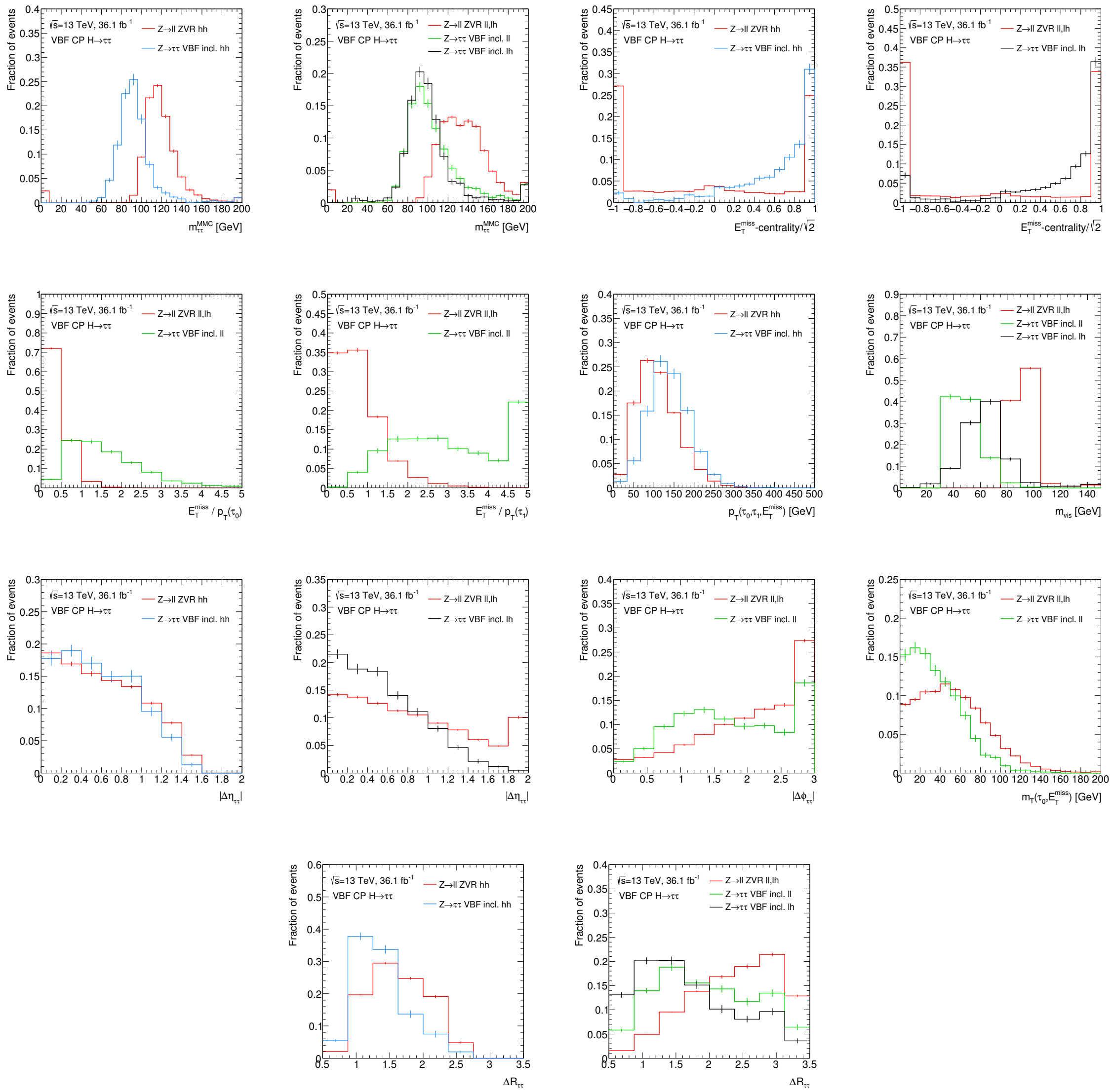

Figure 7.17.: Normalized distributions of the BDT input variables related to the τ-lepton decay comparing $Z \to \tau\tau$ events in the MVA VBF inclusive regions of the $\tau_{lep}\tau_{lep}$ (green), $\tau_{lep}\tau_{had}$ (black) and $\tau_{had}\tau_{had}$ (blue) channels to $Z \to \ell\ell$ events in the corresponding $Z+jets$ validation regions (red). For $\tau_{lep}\tau_{lep}$ events, the label τ corresponds to the decay leptons $\ell = e, \mu$. In the $\tau_{lep}\tau_{had}$ channel, τ_0 refers to the hadronically decaying τ-lepton, while τ_1 refers to the final-state leptons $\ell = e, \mu$ from the leptonic τ-decay. In the $\tau_{had}\tau_{had}$ channel, τ always corresponds to the hadronically decaying τ-lepton.

Therefore, this validation region is only used to study the modelling of the following input variables:

$$m_{jj},\ p_T(j_2),\ C_{jj}(\tau_0),\ C_{jj}(\tau_1),\ p_T(\tau_0,\tau_1,j_0,j_1,E_T^{miss})$$
$$\text{with } \tau_0,\tau_1 = \begin{cases} \ell_0,\ell_1 & \text{, for } \tau_{lep}\tau_{lep} \\ \tau_{had},\ell & \text{, for } \tau_{lep}\tau_{had} \\ \tau_{had,0},\tau_{had,1} & \text{, for } \tau_{had}\tau_{had} \end{cases} \tag{7.3}$$

In the $Z+jets$ VR, the τ-related variables are constructed from the $Z\to\ell\ell$ decay leptons and are therefore labeled with $\tau=\ell$ in the following. The input variable modelling can be seen in Figure 7.18 and 7.19 for the $\tau_{lep}\tau_{lep}+\tau_{lep}\tau_{had}$ VR and $\tau_{had}\tau_{had}$ VR, respectively. Overall, a good agreement between simulation and data is observed. However, an over-estimation of the $Z\to\ell\ell$ prediction with respect to the observed data is found for high values of m_{jj} and $p_T(j_2)$. This is accounted for by deriving a reweighting histogram based on the observed m_{jj} slope from the ratio of data to $Z\to\ell\ell$ prediction in the $Z+jets$ VR. Here, the simulated events are scaled to match the observed data yield in order to only include shape differences. The resulting reweighting histograms, which are shown in Figure 7.20, are then used to derive event weights depending on m_{jj}, which are applied to simulated $Z\to\ell\ell$ events in the $Z+jets$ VR. As shown in Figure 7.21 and 7.22 for the $\tau_{lep}\tau_{lep}+\tau_{lep}\tau_{had}$ and $\tau_{had}\tau_{had}$ VR, respectively, the reweighting impact on the other input variables is found to be small.

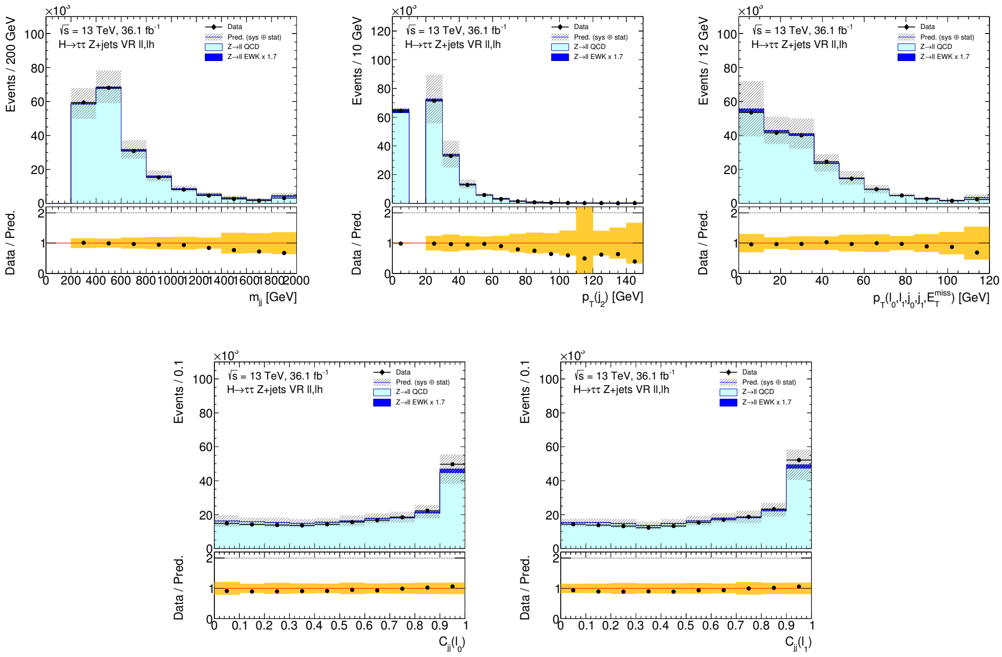

Figure 7.18.: Distributions of jet-related BDT input variables in the $\tau_{lep}\tau_{lep}$ and $\tau_{lep}\tau_{had}$ $Z+jets$ validation region including statistical and systematic uncertainties.

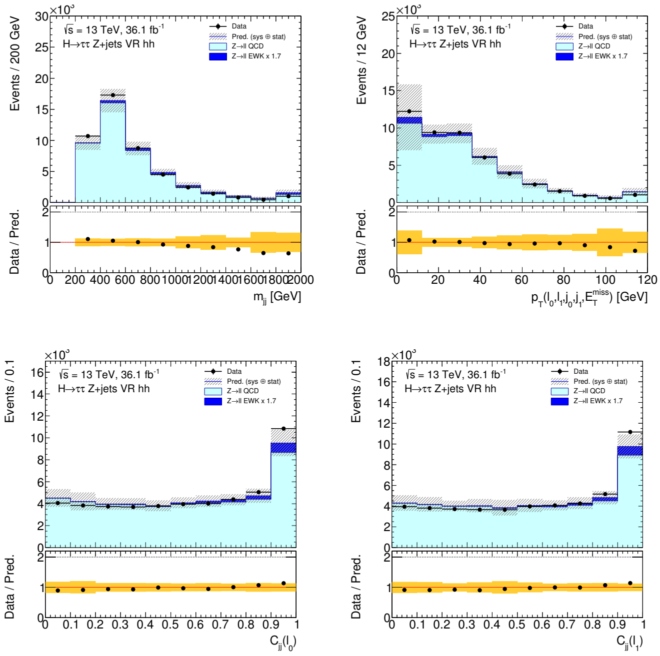

Figure 7.19.: Distributions of jet-related BDT input variables in the $\tau_{had}\tau_{had}$ $Z + jets$ validation region including statistical and systematic uncertainties.

This procedure is propagated to the MVA VBF inclusive and high-BDT regions, where simulated $Z \to \tau\tau$ and $Z \to \ell\ell$ events are reweighted according to the histograms in Figure 7.20 and an additional systematic uncertainty is assigned for these processes (see Section 7.3).

In the VBF CP analysis, the signal region corresponds to a high-BDT region, where the BDT score is used to select events with typical VBF-like kinematics. The validation of the input variable modelling in such a VBF-enhanced phase space is achieved by constructing a similar high-BDT validation region from a BDT, which is trained with the set of input variables given in Equation 7.3. In order to enhance the signal contribution and therefore improve the BDT training an additional cut of $90 < m_{\tau\tau}^{\mathrm{MMC}} < 150\,\mathrm{GeV}$ is applied. Figure 7.23 shows the output of these BDTs in the $\tau_{lep}\tau_{lep}$+$\tau_{lep}\tau_{had}$ and $\tau_{had}\tau_{had}$ VRs. Here, a good agreement between the prediction and the observed data is obtained within the uncertainties. The high-BDT VR is then constructed by requiring a BDT score > 0.7 in the $\tau_{lep}\tau_{lep}$+$\tau_{lep}\tau_{had}$ and a BDT score > 0.6 in the $\tau_{had}\tau_{had}$ VR. These thresholds correspond to a similar selection efficiency for $Z \to \tau\tau$ events in the MVA VBF inclusive region compared to $Z \to \ell\ell$ events in the VR for the corresponding channels. Table 7.8 summarizes the event yields, where a good agreement between prediction and observed number of data events is obtained. The input variables in these high-BDT regions are shown in Figure 7.24 and 7.25 for the $\tau_{lep}\tau_{lep}$+$\tau_{lep}\tau_{had}$ and $\tau_{had}\tau_{had}$ VRs, respectively. Here, a good modelling between prediction and data events within statistical and systematic uncertainties is found as well.

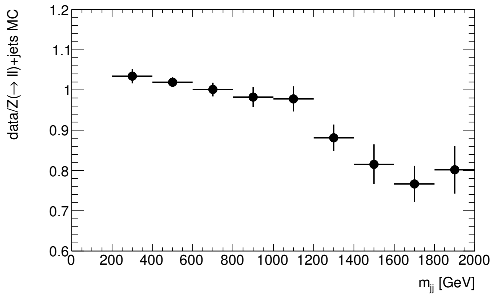

(a)

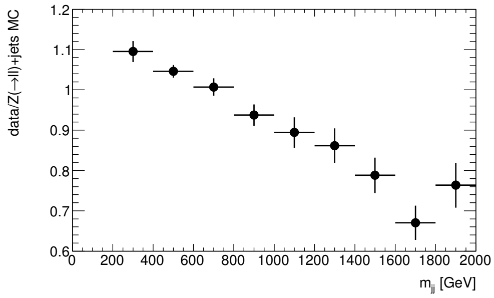

(b)

Figure 7.20.: Ratio of data to simulated $Z \rightarrow \ell\ell$ events for the m_{jj} distribution in the $\tau_{lep}\tau_{lep}$+$\tau_{lep}\tau_{had}$ (a) and $\tau_{had}\tau_{had}$ (b) $Z + jets$ validation regions. Only statistical uncertainties are included.

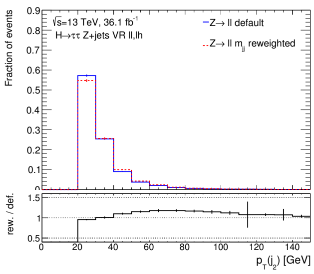

(a)

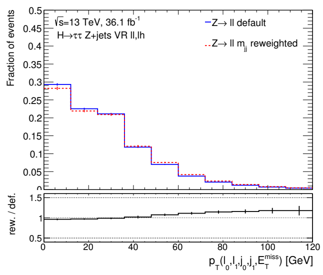

(b)

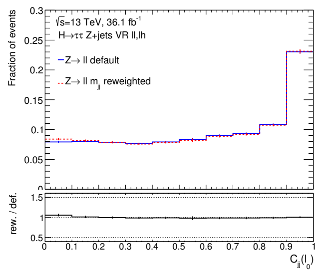

(c)

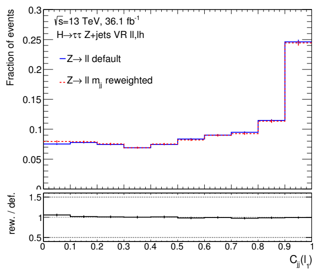

(d)

Figure 7.21.: Impact of m_{jj} reweighting on the shape of the BDT input variables in the $\tau_{lep}\tau_{lep}$+$\tau_{lep}\tau_{had}$ Z+$jets$ validation region for $Z \rightarrow \ell\ell$ events. Only statistical uncertainties are shown.

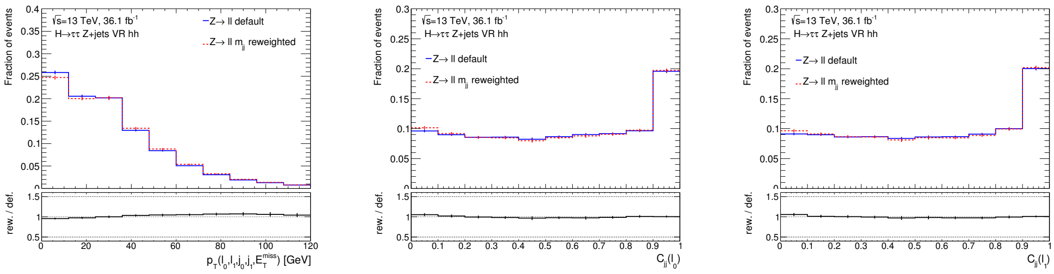

(a) (b) (c)

Figure 7.22.: Impact of m_{jj} reweighting on the shape of the BDT input variables in the $\tau_{had}\tau_{had}$ $Z + jets$ validation region for $Z \to \ell\ell$ events. Only statistical uncertainties are shown.

13 TeV, 36.1 fb^{-1}	$\tau_{lep}\tau_{lep}$+$\tau_{lep}\tau_{had}$ high-BDT VR	$\tau_{had}\tau_{had}$ high-BDT VR
$Z \to \ell\ell$	6932 ± 253	2942 ± 93
Data	6520	3154

Table 7.8.: Event yields for data and simulated $Z \to \ell\ell$ events in the high-BDT $Z + jets$ validation regions with statistical uncertainties.

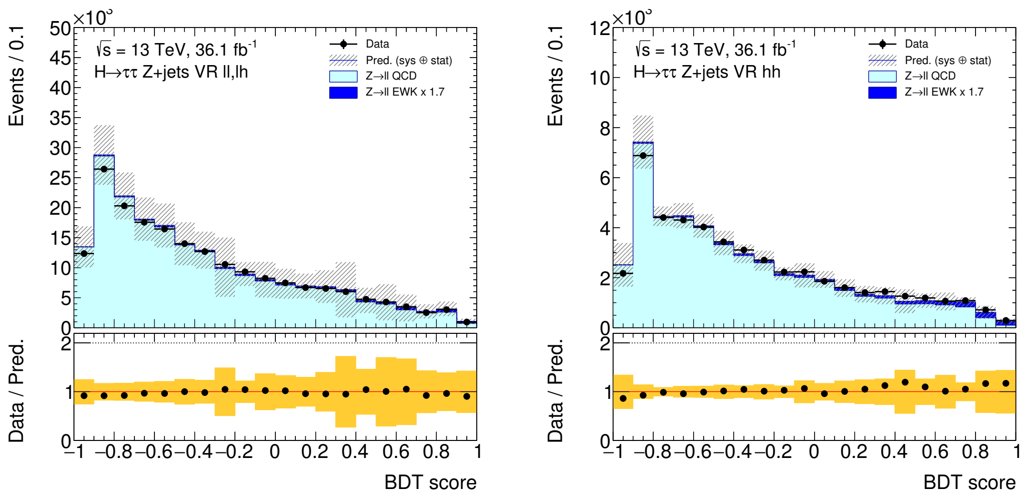

(a) (b)

Figure 7.23.: Distributions of BDT scores in the $\tau_{lep}\tau_{lep}$+$\tau_{lep}\tau_{had}$ (a) and $\tau_{had}\tau_{had}$ (b) $Z + jets$ validation regions including statistical and systematic uncertainties. This BDT classifier was trained with a reduced set of input variables as described in the text.

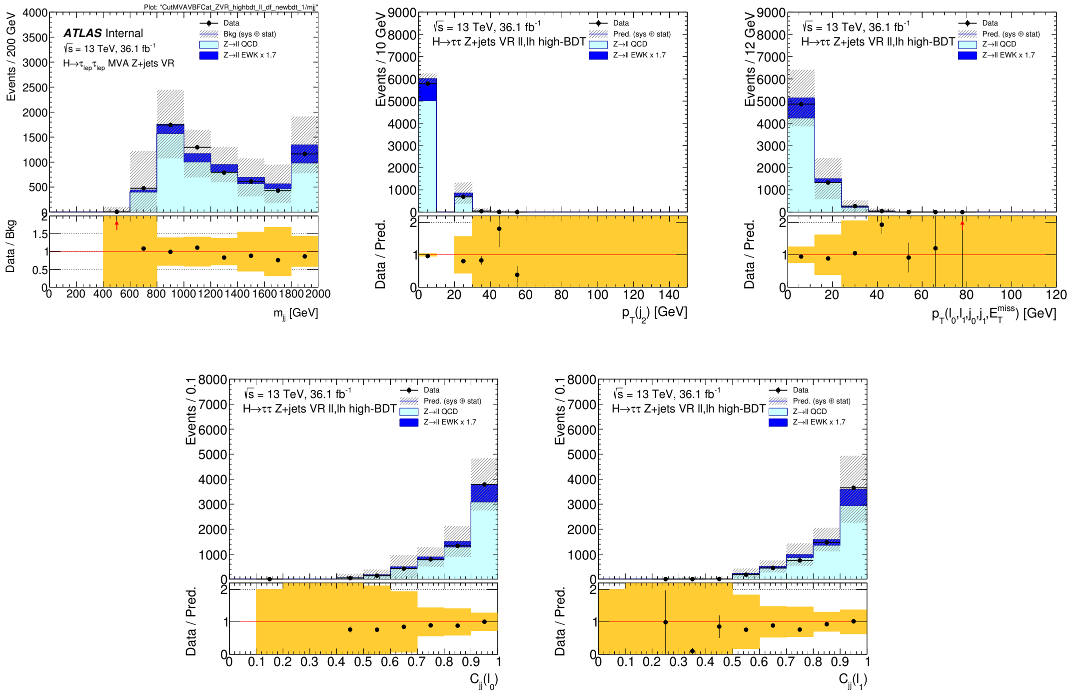

Figure 7.24.: Distributions of jet-related BDT input variables in the high-BDT region of the $\tau_{lep}\tau_{lep}$+$\tau_{lep}\tau_{had}$ $Z + jets$ validation region including statistical and systematic uncertainties.

7.2.2. $Z \to \ell\ell$ and Top-Quark Backgrounds

The control regions to validate the modelling of $Z \to \ell\ell$ and top-quark background events are based on the event selection of the MVA VBF inclusive region, which is given in Section 7.1.1. The $Z \to \ell\ell$ CR then requires two SF leptons in the final state with an inverted cut on their invariant mass of $80 < m_{\ell\ell} < 100$ GeV. Since the contribution from $Z \to \ell\ell$ events with DF leptons is negligible in the analysis, no $Z \to \ell\ell$ CR is used for the DF final state. The Top CR contains events with at least one b-jet with $p_T > 25$ GeV and is splitted into SF and DF final states. Table 7.9 summarizes the expected and observed event yields. In the $Z \to \ell\ell$ CR a purity of 98 % is obtained, while top-quark events constitute 76 % and 86 % of the total background yields in the SF and DF Top CR, respectively. As the signal region definition is based on the separation power of the BDT classifier, Figure 7.26 shows the BDT score distributions in the $Z \to \ell\ell$ and Top CRs. The distributions of the Optimal Observable are shown in Figure 7.27. An overall good agreement between data and prediction within the considered statistical and systematic uncertainties is observed. In both CRs, large uncertainties are obtained in the first and last bins of the BDT score distributions, which are mainly caused by limited event statistics for the background prediction in this regions.

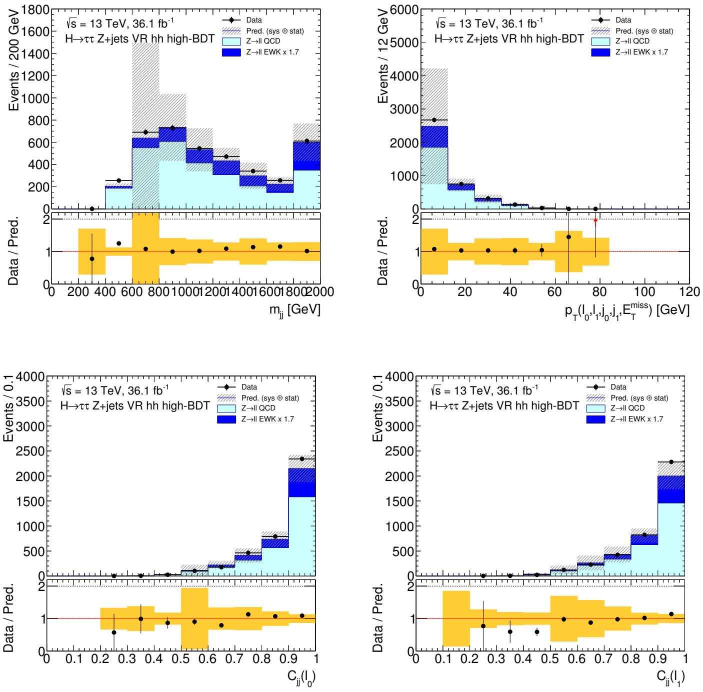

Figure 7.25.: Distributions of jet-related BDT input variables in the high-BDT region of the $\tau_{had}\tau_{had}$ $Z + jets$ validation region including statistical and systematic uncertainties.

Process	$Z \to \ell\ell$ CR	Top CR	
		SF	DF
$Z \to \ell\ell$/ Top	6490 ± 270	736 ± 13	2457 ± 23
Other processes	145.1 ± 3.2	226 ± 16	404 ± 15
Sum of all processes	6635 ± 270	962 ± 21	2861 ± 27
Data	6632	968	2864

Table 7.9.: Expected event yields with statistical uncertainties in the $Z \to \ell\ell$ control region and in the SF and DF final states of the Top CR compared to the observed data yields. The normalization factors summarized in Table 7.6 are applied to the $Z \to \tau\tau$, $Z \to \ell\ell$ and top-quark backgrounds.

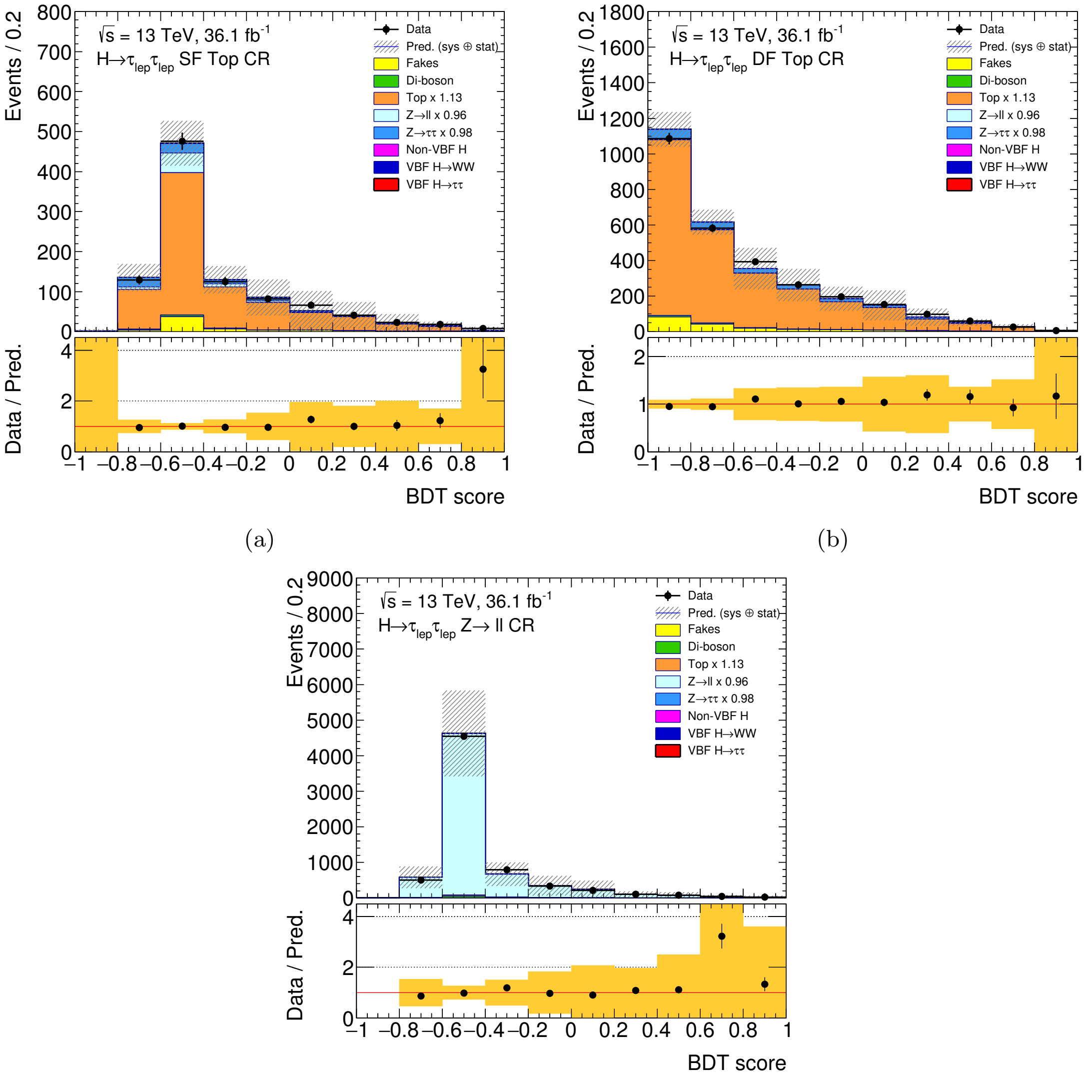

(a) (b) (c)

Figure 7.26.: Distribution of the BDT score in the SF Top CR (a), the DF Top CR (b) and the $Z \to \ell\ell$ CR (c). The uncertainty band includes statistical uncertainties and systematic uncertainties related to jets, E_T^{miss} and the fake-lepton background estimate.

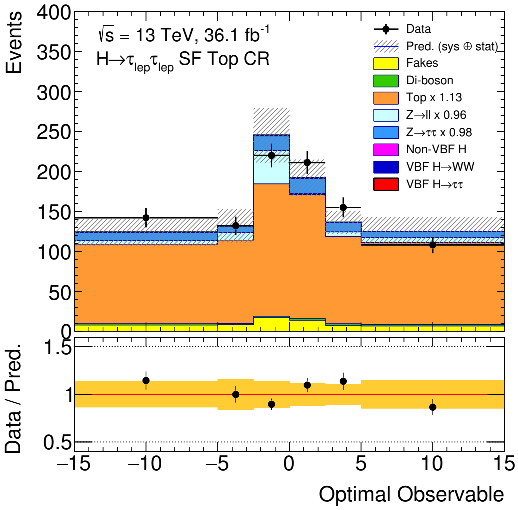

(a)

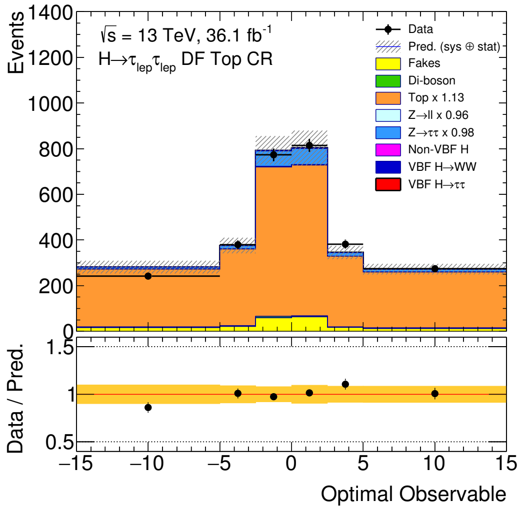

(b)

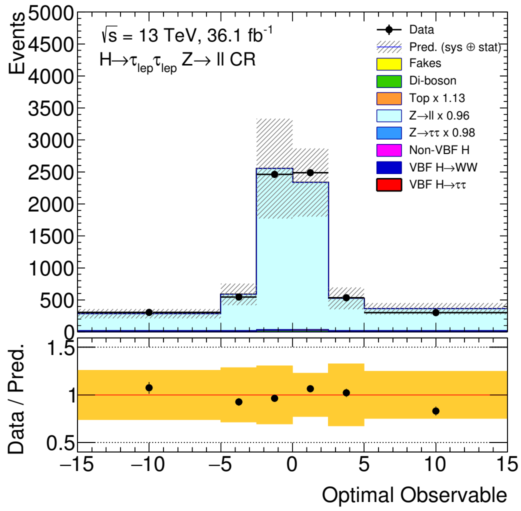

(c)

Figure 7.27.: Distribution of the Optimal Observable in the SF Top CR (a), the DF Top CR (b) and the $Z \to \ell\ell$ CR (c). The error band includes statistical and systematic uncertainties related to jets, E_T^{miss} and the fake-lepton background estimate.

7.3. Systematic Uncertainties

The systematic uncertainties, which are included in the VBF CP analysis, are based on the same uncertainties as considered in the $H \to \tau\tau$ cross-section measurement and are described in Section 6.3. Their impact on the expected event yields (acceptance uncertainties) and on the shape of the final discriminants (shape uncertainties) is re-evaluated in the signal and control regions of the VBF CP analysis. The differences in the exploited pruning and symmetrization techniques compared to the $H \to \tau\tau$ cross-section measurement are summarized in Section 7.4.2.

The first part of this section discusses the slightly different approach for deriving the impact of uncertainties related to the jet energy resolution and the re-evaluation of systematic uncertainties on the fake-lepton background estimation in the MVA VBF inclusive region. Furthermore, the inclusion of additional uncertainties due to the BDT-based approach is described. This is followed by an overview of the theoretical uncertainties on the VBF signal, non-VBF Higgs-boson and $Z \to \tau\tau$ background events. In addition, the differences in the $Z \to \tau\tau$ theory uncertainty scheme compared to the $H \to \tau\tau$ cross-section measurement is described.

7.3.1. Experimental Uncertainties

The relative impact of systematic uncertainties from experimental sources on the predicted signal and background yields in the high-BDT signal regions are summarized in Table 7.12 and Table 7.13, respectively. Their impact on the predicted yields in the low-BDT, Top and $Z \to \ell\ell$ control regions can be found in Appendix C.2.

Jet Energy Resolution

As described in Section 6.3.1, systematic uncertainties related to the jet energy resolution (JER) are included with a set of 11 uncorrelated nuisance parameters (NPs). As the VBF CP analysis particulary suffers from limited statistics for data events and the background predictions in the high-BDT signal regions, the default procedure to derive the final JER variations results in a large number of Optimal Observable bins with negative yields. These unphysical predictions can cause instabilities in the likelihood fit and need to be avoided. In respond to this problem, the JER uncertainties are derived from the variation in simulated events only and the smearing of data events is not used. Their impact on the predicted event yields is obtained by applying the largest relative deviation of the upward or downward variation in the opposite direction. This results in symmetric acceptance uncertainties for each JER component. The impact of the JER uncertainties on the shape of the Optimal Observable and $m_{\tau\tau}^{\mathrm{MMC}}$ distribution is shown in Figure 7.28 for VBF $H \to \tau\tau$ and $Z \to \tau\tau$ events. These shape variations are shown for two JER NPs, which are found to have a large impact on the signal strength measurement in the $\tau_{lep}\tau_{lep}$ channel (see Section 7.5).

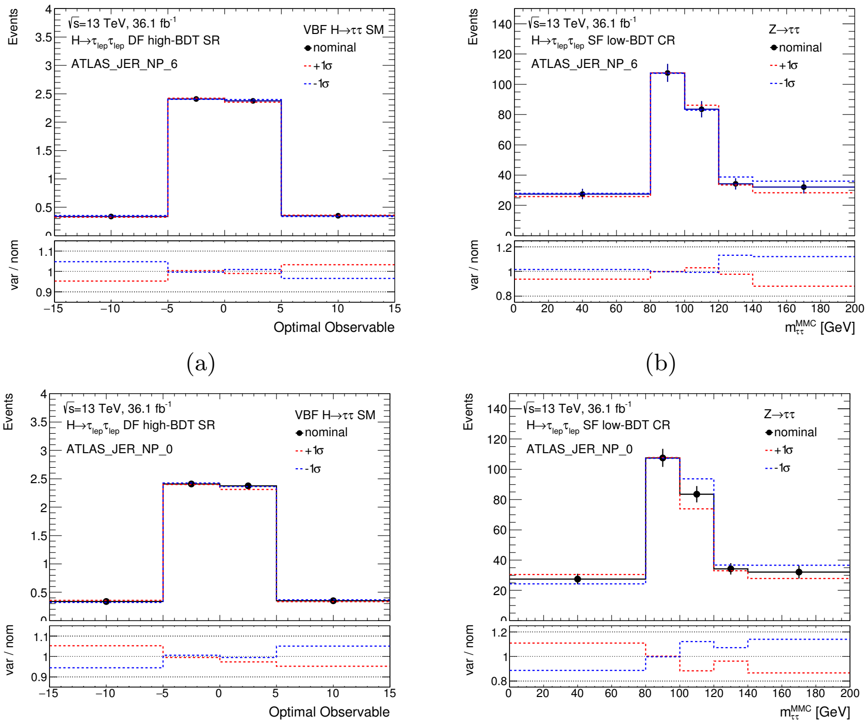

(a) (b)

(c) (d)

Figure 7.28.: Impact of jet energy resolution (JER) uncertainties on the shape of the discriminating variables in the signal and control regions.

In addition, the procedure to evaluate the impact of the JER uncertainty on the predicted $Z \to \ell\ell$ yield in the high-BDT signal region is updated in order to reduce the impact from statistical fluctuations in the analysis. These acceptance uncertainties are derived by performing a fit in the trend of the relative differences between the nominal yield and the variation yield when scanning the lower threshold on the BDT score. Here, the fits are based polynomial functions of first, second and third order. These fit functions are then evaluated at the signal region threshold of BDT score > 0.78 and the final acceptance uncertainty is taken as the largest variation. As an example, Figure 7.29 shows the trend of relative variations depending on the scanned BDT score threshold for two JER NPs with the corresponding fit results. Here, the relative variation in each bin i is calculated as

$$\text{relative variation}(i) = 100 \cdot \left(\frac{N^{nom}(i) - N^{var}(i)}{N^{nom}(i)} \right) \tag{7.4}$$

with $N^{nom(var)}(i)$ corresponding to the predicted $Z \to \ell\ell$ yields in the nominal (varied) sample when integrating from bin i to the last bin in the BDT-score distribution. The results of this fitting procedure are summarized in Table 7.10 and can be compared to the direct calculation of acceptance variations in the SF high-BDT signal region. Although both approaches provide similar values, the acceptance uncertainties obtained with the fitting method are used in the statistical analysis as they accounts for the limited event size in the $Z \to \ell\ell$ background prediction.

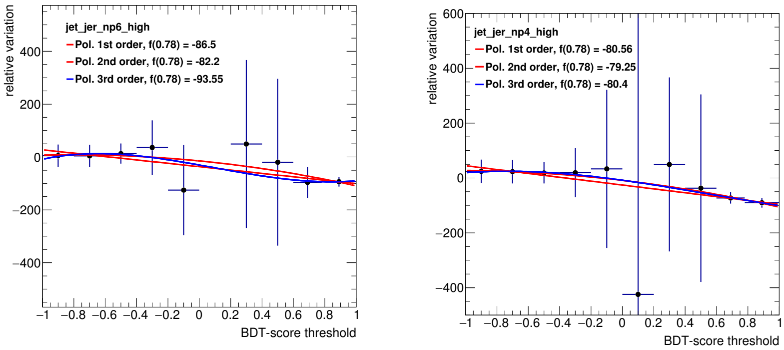

(a) (b)

Figure 7.29.: Results of the fitting method to determine acceptance uncertainties on the $Z \to \ell\ell$ background. for the down variation of two jet energy resolution (JER) nuisance parameters: JER_NP_6 (a) and JER_NP_4 (b).

Systematic	$Z \to \ell\ell$	
	SR	fit method
MC stat (nominal) in SR	$+61.2/-61.2$	
ATLAS_JER_CROSSCALIBFWD	$+79.2/-79.2$	$+78.4/-78.4$
ATLAS_JER_NOISEFWD	$+67.0/-67.0$	$+57.5/-57.5$
ATLAS_JER_NP_0	$+83.4/-82.4$	$+85.2/-85.2$
ATLAS_JER_NP_1	$+85.3/-85.3$	$+70.9/-70.9$
ATLAS_JER_NP_2	$+83.0/-83.0$	$+69.7/-69.7$
ATLAS_JER_NP_3	$+82.1/-82.1$	$+75.0/-75.0$
ATLAS_JER_NP_4	$+94.6/-94.6$	$+85.1/-85.1$
ATLAS_JER_NP_5	$+74.3/-74.3$	$+76.3/-76.3$
ATLAS_JER_NP_6	$+89.9/-89.9$	$+94.4/-94.4$
ATLAS_JER_NP_7	$+85.4/-85.4$	$+71.2/-71.2$
ATLAS_JER_NP_8	$+84.8/-84.8$	$+77.7/-77.7$

Table 7.10.: Comparison of JER acceptance uncertainties (in %) evaluated in the high-BDT signal region and with the fit method for the $Z \to \ell\ell$ background. The statistical uncertainty on the simulated event size is given as well.

Fake-Lepton Background

In the VBF CP analysis, the non-closure systematic uncertainty on the data-driven estimate of the fake-lepton background (see Section 6.3.1) is re-derived in the MVA VBF inclusive region in order to account for the different kinematic selection. Table 7.11 summarizes this uncertainty for the different final states and p_T regions of the sub-leading lepton and Figure 7.30 shows the impact on the $m_{\tau\tau}^{\mathrm{MMC}}$ distribution in the SF low-BDT CR. Additional systematic uncertainties as listed in Table 6.12 are adopted from the $H \to \tau\tau$ cross-section measurement.

Systematic uncertainties	MVA VBF inclusive		
	$p_T(\ell_1)$	$10 - 15\,\mathrm{GeV}$	$> 15\,\mathrm{GeV}$
Non-closure	ee	-	100.0%
	$\mu\mu$	31.1%	33.9%
	DF	26.7%	30.6%

Table 7.11.: Non-closure systematic uncertainties for the estimation of the fake-lepton background in the MVA VBF inclusive region.

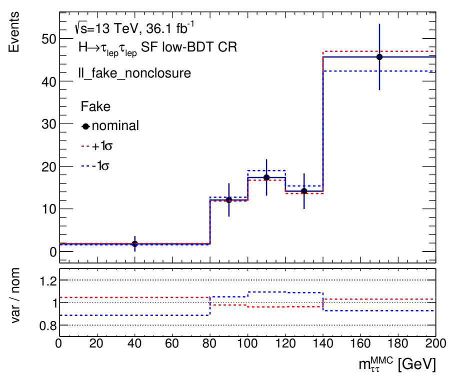

Figure 7.30.: Impact of the non-closure uncertainty for the estimation of the fake-lepton background on the shape $m_{\tau\tau}^{\mathrm{MMC}}$ distribution in the SF low-BDT CR.

Reweighting of $Z + jets$ Events

As described in Section 7.2.1, simulated $Z \to \tau\tau$ and $Z \to \ell\ell$ events are reweighted in m_{jj} in order to account for the observed discrepancy between data and simulation in the $Z + jets$ validation region. This reweighting procedure requires an additional systematic uncertainty, which is determined by comparing the expected yields and shapes of the discriminating variables in the signal and control regions between the reweighted and the non-reweighted samples. The impact of the reweighting procedure on the shape of the Optimal Observable and $m_{\tau\tau}^{\mathrm{MMC}}$ distributions is shown in Figure 7.31 and 7.32, respectively, and is found to be negligible. Therefore, the analysis only consideres acceptance uncertainties related to the reweighting procedure, which are given in Table 7.13.

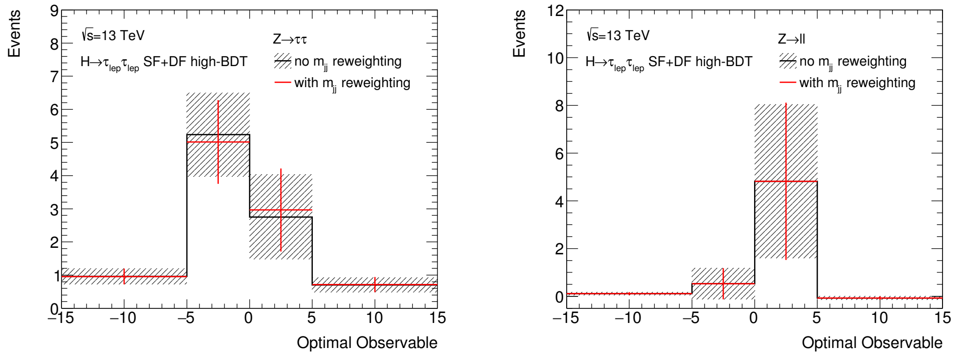

(a) (b)

Figure 7.31.: Impact of m_{jj} reweighting on the shape of the Optimal Observable in the high-BDT signal region for $Z \to \tau\tau$ (a) and $Z \to \ell\ell$ (b) events.

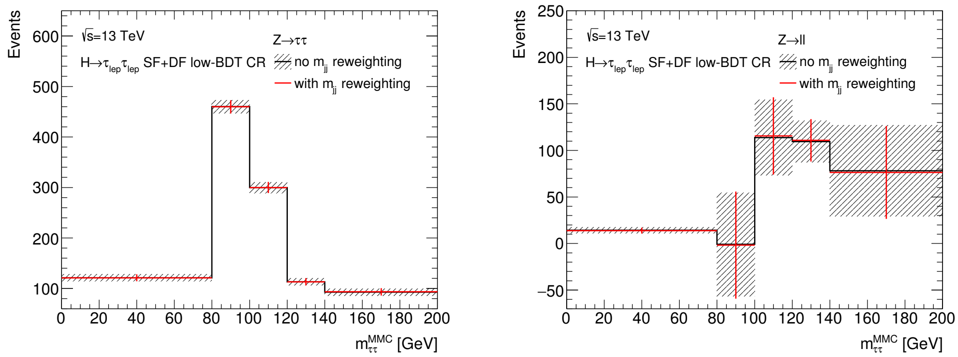

(a) (b)

Figure 7.32.: Impact of m_{jj} reweighting on the shape of $m_{\tau\tau}^{\mathrm{MMC}}$ in the low-BDT control region for $Z \to \tau\tau$ (a) and $Z \to \ell\ell$ (b) events.

Impact of Other Experimental Uncertainties

As shown in Figure 7.40, various experimental uncertainties are found to have an important impact on the measurement of the VBF $H \to \tau\tau$ signal in the $\tau_{lep}\tau_{lep}$ channel. The impact of these systematic uncertainties on the shape of the Optimal Observable and $m_{\tau\tau}^{\mathrm{MMC}}$ distributions are shown in Figure 7.33 for various signal and background components.

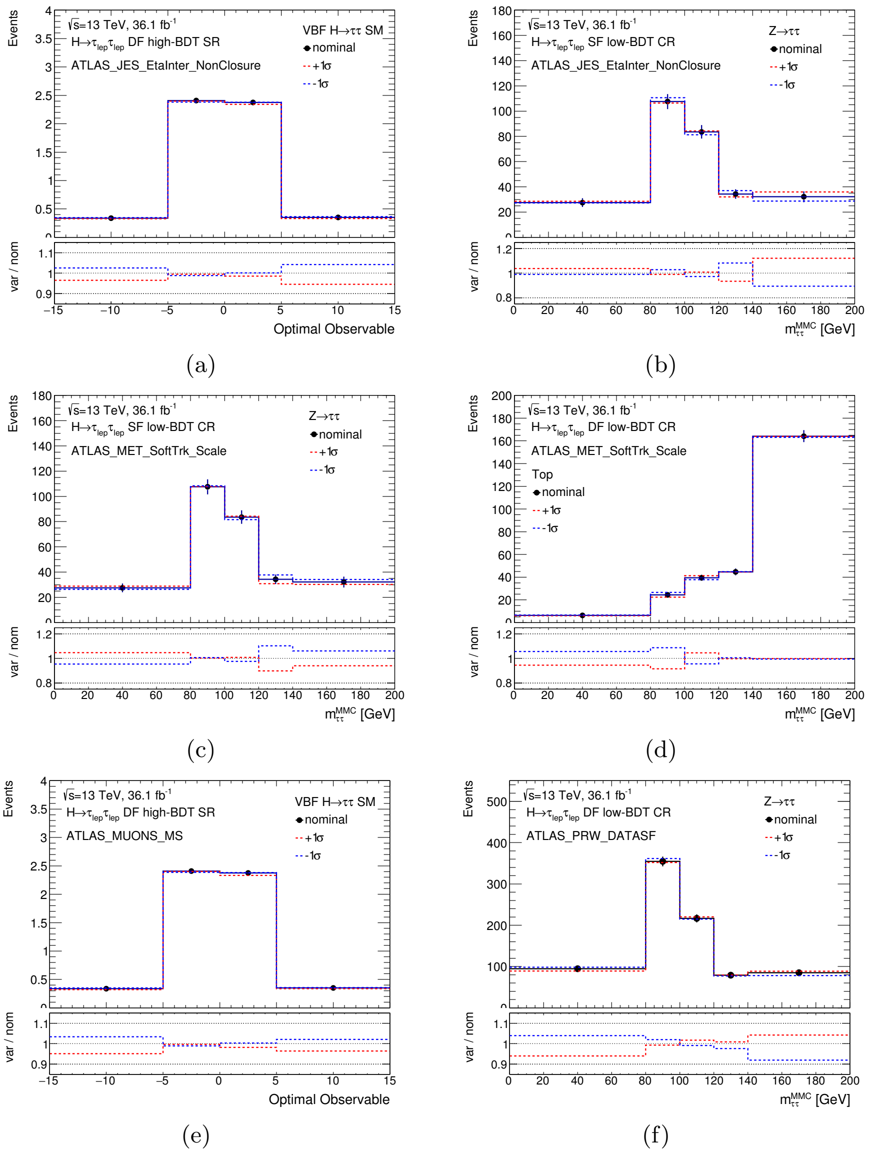

Figure 7.33.: Impact of the most important experimental uncertainties on the shape of the Optimal Observable and $m_{\tau\tau}^{\text{MMC}}$ distributions in the $\tau_{lep}\tau_{lep}$ channel.

	VBF $H \to \tau\tau$	VBF $H \to WW$	non-VBF H
		high-BDT SF	
Electrons			
Scale	+0.4 / -0.4	+1.5 / -1.5	+12.7 / -10.5
Resolution	-	+1.5 / -3.2	+4.0 / -4.0
Efficiency	-	-	-
Muons			
Scale	+0.1 / -1.2	+1.1 / -1.1	+2.4 / -2.4
Resolution	-	+2.6 / -3.1	+1.5 / -1.5
Efficiency	-	-	-
Jets			
JER	+2.2 / -2.2	+10.2 / -10.2	+29.9 / -29.9
JES	+3.9 / -4.8	+10.1 / -7.7	+10.6 / -14.2
JVT Efficiency	-	-	-
b-tagging	-	-	+1.0 / -1.0
E_T^{miss} soft term			
Resolution	+1.3 / -1.3	+1.9 / -1.9	+13.5 / -13.5
Scale	+1.7 / -0.9	+1.1 / -0.4	+2.3 / -1.7
Jet veto	-	-	+30.8 / -25.6
Pile-up rew.	-4.2 / +3.4	-4.6 / +4.0	-1.1 / +1.3
		high-BDT DF	
Electrons			
Scale	-	+1.0 / -1.0	+3.7 / -5.1
Resolution	-	+0.3 / -1.2	+2.5 / -2.5
Efficiency	+1.0 / -1.0	-	+1.1 / -1.1
Muons			
Scale	-	-	-
Resolution	+0.4 / -0.4	+1.2 / -0.0	+3.4 / -3.0
Efficiency	-	-	-
Jets			
JER	+3.6 / -3.6	+3.3 / -3.3	+19.6 / -19.6
JES	+4.2 / -3.3	+6.3 / -6.2	+11.4 / -14.7
JVT Efficiency	-	-	-
b-tagging	-	-	-
E_T^{miss} soft term			
Resolution	-	-	+5.1 / -5.1
Scale	-	+1.3 / -1.3	+4.5 / -2.1
Jet veto	-	-	+26.6 / -22.1
Pile-up rew.	-4.8 / +3.6	-5.6 / +2.9	-5.0 / +2.4

Table 7.12.: Relative impact of experimental systematic uncertainties on the number of expected VBF $H \to \tau\tau$ and $H \to WW$ signal events and on the expected background events from the ggF, VH and ttH production modes (non-VBF) in the SF and DF high-BDT signal regions in percent. Variations below 0.1 % are ignored.

	$Z \to \tau\tau$	Top	$Z \to \ell\ell$	Di-Boson
	high-BDT SF			
Electrons				
Scale	+13.4 / -13.4	+9.3 / -9.3	+392.9 / -101.8	+20.2 / -20.2
Resolution	+5.1 / -5.1 -		+9.0 / -9.0	+6.4 / -23.5
Efficiency	-	-	+1.0 / -1.0	+1.0 / -1.0
Muons				
Scale	+8.4 / -3.0	+12.0 / -12.0	-	+22.8 / -17.2
Resolution	+14.2 / -14.2	+15.4 / -15.4	+94.7 / -113.8	+13.1 / -13.1
Efficiency	-	+1.1 / -1.1	-	-
Jets				
JER	+74.6 / -74.6	+77.3 / -77.3	+254.6 / -254.6	+81.3 / -81.3
JES	+42.5 / -41.4	+52.6 / -66.9	+171.2 / -322.5	+76.4 / -50.9
JVT Efficiency	-	-	-	-
b-Tagging	-	+4.3 / -4.3	-	+1.4 / -1.3
E_T^{miss} soft term				
Resolution	+10.7 / -10.7	+14.9 / -14.9	+129.4 / -130.5	+50.8 / -39.5
Scale	-	+6.0 / -6.0	+129.8 / -100.0	+14.0 / -10.9
m_{jj} rew.	+8.5 / -8.5	-	+4.9 / -4.9	-
Pile-up rew.	-5.6 / +10.5	-2.4 / +2.9	+18.2 / -30.8	+4.5 / -4.5
	high-BDT DF			
Electrons				
Scale	+11.4 / -17.5	+17.1 / -69.8	+18.6 / -18.6	
Resolution	-	+1.2 / -17.4	+11.0 / -11.0	
Efficiency	-	-	-	
Muons				
Scale	+15.8 / -7.7	+13.0 / -13.0	+5.9 / -5.9	
Resolution	+14.2 / -14.2	+26.5 / -26.5	+7.3 / -7.3	
Efficiency	-	-	-	
Jets				
JER	+59.6 / -59.6	+112.7 / -112.7	+61.5 / -61.5	
JES	+22.4 / -26.5	+45.1 / -59.9	+38.7 / -36.1	
JVT Efficiency	-	-	-	
b-tagging	-	+5.3 / -5.2	+1.2 / -1.2	
E_T^{miss} soft term				
Resolution	+46.6 / -16.1	+5.4 / -5.4	+30.9 / -30.9	
Scale	+8.9 / -41.2	+0.5 / -68.4	+18.4 / -3.6	
m_{jj} rew.	+8.5 / -8.5	-	-	
Pile-up rew.	-6.6 / +0.2	-6.2 / +0.6	-	

Table 7.13.: Relative impact of experimental systematic uncertainties on the number of expected background events in the SF and DF high-BDT signal regions in percent. In the DF channel, events from $Z \to \ell\ell$ and di-boson production are combined. Variations below 0.1 % are ignored.

7.3.2. Theoretical Uncertainties

The relativ impact of systematic uncertainties from theoretical sources in the high-BDT signal regions are summarized in Table 7.15 for the $H \to \tau\tau$ and $H \to WW$ predictions and in Table 7.15 for the $Z \to \tau\tau$ prediction. Their impact in the low-BDT, Top and $Z \to \ell\ell$ control regions can be found in Appendix C.2. No theoretical uncertainties are applied for the $Z \to \ell\ell$, top-quark and di-boson backgrounds.

Modelling of Higgs-boson Events

As the VBF CP analysis focuses on the measurement of the $\tilde{d}$-parameter, no theoretical uncertainties are applied on the total predicted cross-section for VBF $H \to \tau\tau$ and $H \to WW$ events. For background contributions from the ggF, VH and ttH production modes, the full set of theoretical uncertainties are included (see Section 6.3.2).

Uncertainties related to hadronization, underlying event and parton shower (UEPS) are evaluated with the same approach as described in Section 6.3.2 for $H \to \tau\tau$ decays from the VBF and ggF production modes. Here, the ratio of two alternative samples, which are generated with POWHEG+HERWIG 7 by using fast simulation [157], is determined in the MVA VBF inclusive region and then applied to the nominal prediction inthe signal and control regions. These UEPS uncertainties are also included for VBF $H \to WW$ signal events by using the alternative VBF $H \to \tau\tau$ samples. Figure 7.34 shows the impact of the UEPS uncertainties on the shape of the Optimal Observable for VBF $H \to \tau\tau$ and non-VBF Higgs-boson events.

Furthermore, a branching ratio uncertainty of 1.17 % and 0.99 % [225] is included for $H \to \tau\tau$ and $H \to WW$ events, respectively.

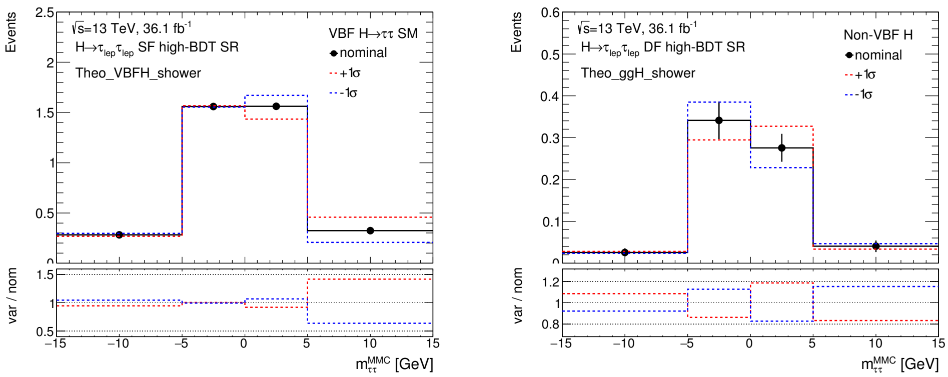

(a) (b)

Figure 7.34.: Impact of UEPS uncertainties on the shape of the Optimal Observable distribution for VBF $H \to \tau\tau$ (a) and non-VBF Higgs-boson (b) events.

	VBF $H \to \tau\tau$	VBF $H \to WW$	non-VBF $H \to \tau\tau, WW$
	high-BDT SF		
QCD scale	+1.3 / -1.7	+1.6 / -2.1	+17.4 / -17.4
α_s	-	-	+2.9 / -3.0
PDF	-	-	+2.7 / -2.3
UEPS	+7.2 / -7.2	-	+61.4 / -45.6
	high-BDT DF		
QCD scale	+1.6 / -2.2	+1.3 / -1.7	+13.1 / -13.1
α_s	-	-	+2.9 / -2.9
PDF	-	-	+2.4 / -2.0
UEPS	+12.8 / -12.8	-	+11.7 / -11.7

Table 7.14.: Relative impact of theoretical uncertainties on the expected number of Higgs-boson signal and background events in the SF and DF high-BDT signal regions in percent. Variations below 0.1 % are ignored.

Jet-Veto Uncertainty

The training of the BDT classifier in the SF final state exploits the transverse momentum of a possible third jet in the event p_T^{j2}, which is shown in Figure 7.3. By selecting events with a high BDT score, the signal region definition effectively imposes a veto on events, where a third jet is found. Since the considered theory uncertainties for the ggF $H \to \tau\tau$ background do not include uncertainties on the exclusive Higgs-boson production with two jets, the corresponding scale uncertainty is evaluated with the Stewart-Tackmann method [244]. This leads to an additional acceptance uncertainty of $+36.6\,\%/-30.4\,\%$ [245], which is applied to the ggF $H \to \tau\tau$ prediction in the high-BDT signal regions.

$Z \to \tau\tau$ Background Modelling

The VBF CP analysis uses the same scheme to consider $Z \to \tau\tau$ theory uncertainties from QCD scale, PDF, CKKW matching scale, QSF resummation scale and UEPS variations as described in Section 6.3.2. Here, the *region-migration* uncertainties are evaluated between the high-BDT signal regions and the low-BDT control regions and are treated as uncorrelated between the three analysis channels. Uncertanties from UEPS are obtained by comparing the nominal Sherpa sample to an alternative sample generated in MadGraph+Pythia. Due limitations in the available event number for the $Z \to \tau\tau$ prediction, shape uncertainties from QCD-scale, PDF, CKKW-scale and UEPS variations are estimated in the MVA inclusive region and then applied to the nominal Optimal Observable distribution in the high-BDT signal regions. Figure 7.35 shows the impact of the QCD-scale variations on the shape of the Optimal Observable and $m_{\tau\tau}^{\mathrm{MMC}}$ distributions.

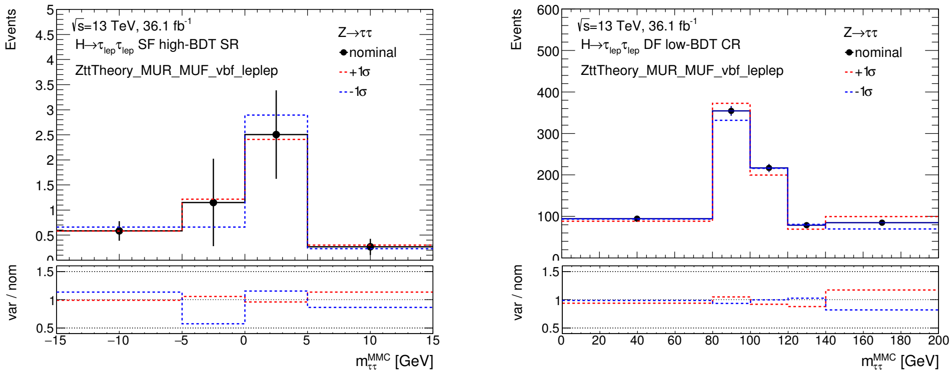

(a) (b)

Figure 7.35.: Impact of QCD-scale uncertainties on the shape of the Optimal Observable in the SF high-BDT signal region (a) and on the shape of the $m_{\tau\tau}^{\text{MMC}}$ distribution in the DF low-BDT control region (b) for $Z \to \tau\tau$ background events.

	$Z \to \tau\tau$	
	high-BDT SF	
	channel-migration	region-migration
QCD scale	-	+0.3 / -0.3
PDF	-	+4.4 / -5.2
CKKW	+8.8 / -7.0	-
QSF	-1.2 / +1.2	-
UEPS	-4.5 / +4.5	-
EW Zjj, $Zjjj$	+7.3 / -7.3	
	high-BDT DF	
QCD scale	-	+1.7 / -1.7
PDF	-	+4.9 / -5.7
CKKW	+7.4 / -5.9	-
QSF	-1.0 / +1.0	-
UEPS	-3.8 / +3.8	-
EW Zjj, $Zjjj$	+10.1 / -10.1	

Table 7.15.: Relative impact of theoretical uncertainties on the expected number of $Z \to \tau\tau$ background events in the SF and DF high-BDT signal regions in percent. Variations below 0.1 % are ignored.

7.4. Statistical Data Analysis

In this analysis, the parameter $\tilde{d}$ describes the additional CP-odd contributions to the CP-even HVV coupling structure as predicted in the SM. This section describes the statistical methods, which are exploited in order to measure the $\tilde{d}$-parameter and to derive central confidence intervals based on maximum likelihood fits in the Optimal Observable. The general concept of the maximum likelihood approach is introduced in Section 6.4.1, while the inclusion of systematic and statistical uncertainties as nuisance parameters can be found in Section 6.4.2.

7.4.1. Measurement of $\tilde{d}$ and Determination of Central Confidence Intervals

The statistical analysis is based on a maximum likelihood approach with a binned likelihood function $\mathcal{L}$ as given in Equation 6.28. This likelihood function depends on the measured dataset $\boldsymbol{n}$, the signal strength μ and a set of nuisance parameters (NPs), which consist of systematic uncertainties $\boldsymbol{\theta}$, statistical uncertainties on the background prediction $\boldsymbol{\gamma}$ and normalization factors $\boldsymbol{\phi}$ for the $Z \to \tau\tau$, $Z \to \ell\ell$ and top-quark backgrounds. In the VBF CP analysis, the likelihood function is constructed with an underlying model of signal plus SM background expectation, where the signal prediction corresponds to a specific HVV coupling hypothesis. The likelihood function therefore gains an additional dependency on $\tilde{d}$:

$$\begin{aligned}\mathcal{L}(\boldsymbol{n};\tilde{d},\mu,\boldsymbol{\theta},\boldsymbol{\gamma},\boldsymbol{\phi}) = &\prod_{r\in\text{reg}}\prod_{i\in\text{bins}} \text{Pois}(n_{i,r};\mu s_{i,r}(\tilde{d},\boldsymbol{\theta}) + b_{i,r}(\boldsymbol{\theta},\boldsymbol{\phi}))\text{Pois}(m_{i,r};\gamma_{i,r}m_{i,r}) \\ &\cdot \prod_{t\in\text{sys}} \text{Gaus}(0;\theta_t,1).\end{aligned} \tag{7.5}$$

Here, r runs over all signal and control regions, i gives the index for each histogram bin and t runs over the set of systematic uncertainties. While the background normalization factors in the $H \to \tau\tau$ cross-section measurement are decorrelated between the VBF and the boosted categories, this analysis clearly only applies these normalization factors in the signal and control regions of the VBF category $\boldsymbol{\phi} = \boldsymbol{\phi}_{\text{VBF}}$. The CP-violating signal predictions ($\tilde{d} \neq 0$) are obtained by reweighting the SM signal events ($\tilde{d} = 0$) according to the procedure described in Section 4.4. In addition, the overall event yields of the CP-violating hypotheses are normalized to the expected SM signal yield. This allows to reduce the impact of possible contributions from higher-order CP-even operators, which can affect the signal rate, but do not lead to CP-violating HVV interactions. For a given signal hypothesis, the best-fit signal strength and NPs are determined by minimizing the negative logarithm of the likelihood function (NLL) in Equation 7.5. These likelihood fits are performed for 53 signal hypotheses in the range of $-0.5 \leq \tilde{d} \leq 0.5$. Here, the $\tilde{d}$-values are varied in steps of 0.01 for $0 < |\tilde{d}| < 0.2$ and in steps of 0.05 for larger $\tilde{d}$-values of $0.2 < |\tilde{d}| < 0.5$. The resulting NLL-values from these likelihood fits are then used to construct a so-called ΔNLL-curve depending on the tested $\tilde{d}$-values. As illustrated in Figure 6.17, the best-fit value $\hat{\tilde{d}}$ then corresponds to the signal model, for which the minimum NLL-value with respect to all other tested signal hypotheses is obtained. This ΔNLL-curve is also used to determine the central confidence intervals (CIs) for $\tilde{d}$: $[\hat{\tilde{d}} - N\hat{\sigma}^{-}_{\hat{\tilde{d}}}, \hat{\tilde{d}} + N\hat{\sigma}^{+}_{\hat{\tilde{d}}}]$. As described in Section 6.4.1, the CIs corresponding to the 68.3 % ($N = 1$) and 95 % ($N = 2$) confidence level (CL) are given by the $\tilde{d}$-values, which lead to a change in the ΔNLL-curve of 0.5 and 1.96, respectively. With this procedure, the observed results for $\tilde{d}$ and the CIs are obtained from likelihood fits to collision data in all signal and control regions. In addition, expected CIs are determined by using so-called *pseudo* datasets (Asimov datasets) based on the following approaches: First, the *pre-fit* expected ΔNLL-curve is constructed with the same fitting procedure as described above, but replacing the measured dataset $\boldsymbol{n}$ in each histogram bin i by the pre-fit SM signal plus background expectation:

$$n_i^{\text{exp,pre-fit}} = s_i(\tilde{d} = 0, \boldsymbol{\theta}) + b_i(\boldsymbol{\theta}, \boldsymbol{\phi}). \tag{7.6}$$

In addition, a *post-fit* expected ΔNLL-curve is constructed. Here, the best-fit NPs $\hat{\boldsymbol{\theta}}_{SM}$ and background normalization factors $\hat{\boldsymbol{\phi}}_{SM}$ are determined in a likelihood fit for the SM signal plus background prediction, where only control regions are included. These results are then used to construct the *post-fit* Asimov dataset by evaluating the SM signal and background predictions depending on the best-fit values:

$$n_i^{\text{exp,post-fit}} = \mu \cdot s_i(\tilde{d} = 0, \hat{\boldsymbol{\theta}}_{SM}) + b_i(\hat{\boldsymbol{\theta}}_{SM}, \hat{\boldsymbol{\phi}}_{SM}). \tag{7.7}$$

This approach allows to investigate the impact of the best-fit NP and background normalization factors on the CIs for $\mu = 1$. In addition, the post-fit Asimov dataset is also constructed with the observed signal strength $\mu = \hat{\mu}$ as obtained from the likelihood fit to collision data in all signal and control regions under the best-fit signal hypothesis.

7.4.2. Fitting Procedure

The likelihood fits described above are based on the Optimal Observable distribution with events selected in the high-BDT signal regions. Figure 7.10 shows these distributions for the SF and DF final states. While it is in general desirable to exploit a large number of bins in the Optimal Observable distribution in order to be sensitive to shape variations caused by possible CP-violating effects, the limited MC statistics for the background predictions only allows for a maximum number of four bins. However, statistical fluctuations in the variation histograms from systematic uncertainties can still cause negative or empty bins in the background prediction for the Optimal Observable distribution. In order to account for these unphysical predictions and to stabilize the fitting procedure, bins with negative yields are set to a constant value of 10^{-6}. Furthermore, the content of empty bins is set to the histogram integral divided by the number of simulated events. In order to reduce the impact from statistical fluctuations in the tails of the Optimal Observable, the distribution range is limited to $[-15, 15]$, while the content of overflow and underflow bins are added to the content of the first and last bin, respectively.

In this analysis, the overall predicted event yields of $Z \to \tau\tau$, $Z \to \ell\ell$ and top-quark events are derived from data, which results in three background normalization factors in total. These normalization factors are determined in the likelihood fit in dedicated control regions. The $Z \to \tau\tau$ normalization is measured in two low-BDT control regions (SF and DF), which are constructed by inverting the signal region cut to BDT score < 0.78. Here, the $m_{\tau\tau}^{\text{MMC}}$ distribution as shown in Figure 7.15 is used as the discriminating variable. Besides the measurement of the $Z \to \tau\tau$ background normalization, these low-BDT control regions also allow to constrain systematic uncertainties. Furthermore, two Top control regions (SF and DF) and one $Z \to \ell\ell$ control region (SF) are included. The Top control regions are constructed by inverting the veto on b-tagged jets, while for the $Z \to \ell\ell$ control region a cut on the invariant di-lepton mass around the Z^0-boson mass peak is applied. These control regions only exploit event yield information in order to constrain the normalization of the respective background processes. In the DF final state, the background predictions for $Z \to \ell\ell$ events and di-boson production are combined due to their small overall contribution. The combination of these processes is also referred to as *other backgrounds* in the following. An overview of the signal and control regions with information on the corresponding discriminants is given in Table 7.16.

Region		Variable	Bins
high-BDT signal region	SF DF	Optimal Observable	$[-15, -5, 0, 5, 15]$
low-BDT control region	SF DF	$m_{\tau\tau}^{\mathrm{MMC}}$	$[0, 80, 100, 120, 140, 200]$
Top control region	SF DF	Event yield	1
$Z \to \ell\ell$ control region	SF	Event yield	1

Table 7.16.: Overview of the signal and control regions, discriminating variables and their number of bins as considered in the fitmodel of the $\tau_{lep}\tau_{lep}$ channel. Under- and overflow bins are included in the first and last bins, respectively.

The impact of systematic uncertainties, which are described in Section 7.3, is evaluated in the signal and control regions for each signal and background process separately. For this, the same pruning, symmetrization and smoothing techniques as described in Section 6.4.3 are applied. An overview of all systematic uncertainties, which are included as acceptance uncertainties on the predicted event yield or shape uncertainties on the considered distributions, is given in Table 7.18-7.25 for the signal regions and the low-BDT control regions. The NP names are explained in Appendix B. In total, 107 nuisance parameters from experimental sources and 24 nuisance parameters from theoretical sources are included. The list of acceptance uncertainties in the $Z \to \ell\ell$ and Top control regions can be found in Appendix D.2. Besides the symmetrization of shape uncertainties for bins, where the upward and downward variation results in a deviation from the nominal prediction in the same direction, the VBF CP analysis also applies a symmetrization of acceptance uncertainties in the following way: If both the upward and downward variation of a systematic uncertainty results in the deviation from the nominal predicted yield in the same direction, the final variations are taken as 50 % of the difference between the original variations applied to the nominal prediction in the upward and downward direction each. This approach is used in order to avoid the artificial increase of pre-fit uncertainties due to large statistical fluctuations.

The limited statistics in the prediction of the $Z \to \ell\ell$ background also results in large differences between the pre-fit and post-fit values (*pulls*) of nuisance parameters related to JER, JES and pile-up reweighting. The relative impact of these NPs on the expected $Z \to \ell\ell$ yield in the SF signal and control regions can be found in Table 7.17. In addition, the pile-up reweighting NP also acts as a shape uncertainty in the likelihood fit. Its impact on the shape of the Optimal Observable and $m_{\tau\tau}^{\mathrm{MMC}}$ distribution is shown in Figure 7.36. In order to avoid propagating these artificial pulls from the limited statistics to other signal and background predictions, the JER_NP_0, JES_EtaInterModel, JES_FlavorComp, JES_FlavorResp and PRW_DATASF NPs are decorrelared between $Z \to \ell\ell$ events and the remaining processes.

	$Z \to \ell\ell$			
	high-BDT SR	low-BDT CR	$Z \to \ell\ell$ CR	Top CR
JER_NP_0	+85.2 / -85.2	<0.1	+17.4 / -17.4	+19.7 / -19.7
JES_EtaInter_Model	+9.5 / -9.5	+42.6 / -15.1	+12.7 / -9.6	+6.3 / -50.6
JES_Flavor_Comp	-80.8 / +172.6	+59.3 / -22.2	+22.4 / -20.6	+39.1 / -15.1
JES_Flavor_Resp	+18.1 / -18.1	-9.5 / +34.6	-6.2 / +8.2	-13.1 / +11.4
PRW_DATASF	+18.2 / -30.8	-9.5 / +9.6	+8.8 / -7.5	+3.1 / -4.1

Table 7.17.: Relative impact of nuisance parameters on the number of expected $Z \to \ell\ell$ events in percent. These nuisance parameters are decorrelated between the $Z \to \ell\ell$ background and the remaining processes in the likelihood fit.

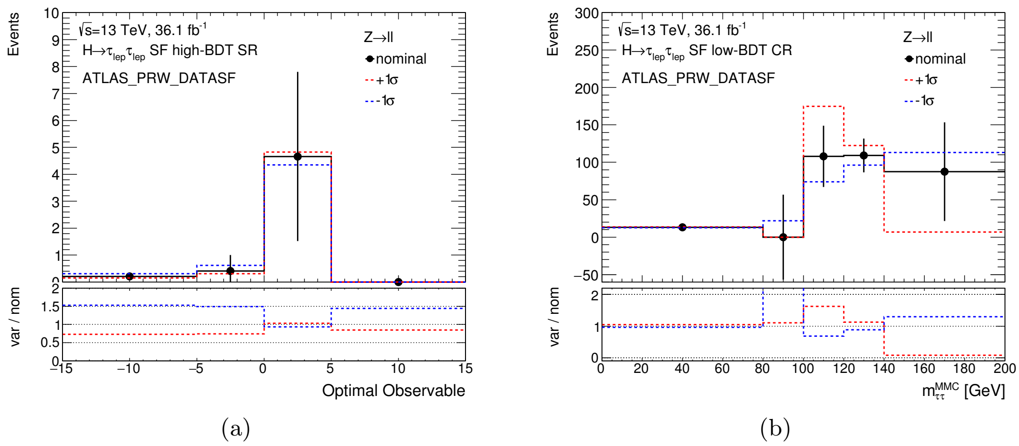

Figure 7.36.: Impact of the pile-up reweighting uncertainty on the shape of the Optimal Observable distribution in the SF high-BDT signal region (a) and on the shape of the $m_{\tau\tau}^{\mathrm{MMC}}$ distribution in the SF low-BDT control region (b) for $Z \to \ell\ell$ events. These nuisance parameter is decorrelated between the $Z \to \ell\ell$ background and the other processes in the likelihood fit.

Systematic	VBF $H \to \tau\tau$	VBF $H \to WW$	Non-VBF H	Top	Di-boson	Fake	$Z \to \tau\tau$	$Z \to \ell\ell$
EG_RESOLUTION_ALL		• ×	• ×		×		×	×
EG_SCALE_ALLCORR	• ×	•	×	×	×		×	×
EG_SCALE_E4SCINTILLATOR	•	• ×	• ×	×			×	×
EG_SCALE_LARCALIB_2015PRE	•	•	• ×		×		×	×
EG_SCALE_LARTEMP_2015PRE	×	• ×	• ×	×			×	×
EG_SCALE_LARTEMP_2016PRE		• ×	• ×					×
EL_EFF_ID_TOTAL					×			×
FT_EFF_Eigen_b_0				×				
FT_EFF_Eigen_b_1				×				
FT_EFF_Eigen_light_0			×	×	×			
JER_CROSSCALIBFWD	•	•	• ×	×	×		×	×
JER_NOISEFWD	•	• ×	• ×	×	×		×	×
JER_NP_0	• ×	• ×	• ×	×	×		×	
JER_NP_0_zll_leplep								×
JER_NP_1	•	• ×	• ×	×	×		×	×
JER_NP_2		• ×	• ×	×	×		×	×
JER_NP_3	• ×	• ×	• ×	×	×		×	×
JER_NP_4		• ×	• ×	×	×		×	×
JER_NP_5	•	• ×	• ×	×	×		×	×
JER_NP_6	•	• ×	• ×	×	×		×	×
JER_NP_7	•	• ×	• ×	×	×		×	×
JER_NP_8	• ×	•	• ×	×	×		×	×
JES_BJES		•	• ×	×	×		×	×
JES_EffectiveNP_1		• ×	• ×		×			×
JES_EffectiveNP_2	•	• ×	•		×		×	×
JES_EffectiveNP_3		• ×	•		×		×	
JES_EffectiveNP_4	•	•	• ×				×	×
JES_EffectiveNP_5		• ×	• ×	×	×		×	×
JES_EffectiveNP_6		• ×	• ×	×	×		×	×
JES_EffectiveNP_7		×	• ×	×	×		×	×
JES_EffectiveNP_8		• ×	•		×		×	
JES_EtaInter_Model	×	• ×	• ×	×			×	
JES_EtaInter_Model_zll_leplep								×
JES_EtaInter_NonClosure	• ×	• ×	• ×	×	×			×
JES_EtaInter_Stat	•	• ×	• ×	×				×
JES_Flavor_Comp	×	• ×	• ×	×	×		×	
JES_Flavor_Comp_leplepzll								×
JES_Flavor_Resp		• ×	• ×	×	×		×	
JES_Flavor_Resp_leplepzll								×
JES_HighPt	•	• ×	•	×	×		×	×
JES_PU_OffsetMu		• ×	• ×	×			×	×
JES_PU_OffsetNPV		×	• ×	×	×			×
JES_PU_PtTerm	• ×	• ×	• ×	×	×		×	
JES_PU_Rho	• ×	• ×	• ×	×	×		×	×
JES_PunchThrough		•	• ×	×	×		×	×
MET_SoftTrk_ResoPara		×	• ×	×	×		×	×
MET_SoftTrk_ResoPerp	×		•	×	×		×	×
MET_SoftTrk_Scale	×	×	• ×	×	×			×
MUONS_ID	•	• ×	•	×	×		×	×
MUONS_MS		• ×	• ×	×	×		×	×
MUONS_SAGITTA_RESBIAS	•	• ×	•	×	×			×
MUONS_SAGITTA_RHO	×	•	• ×	×	×			×
MUONS_SCALE		×	• ×	×	×		×	×
MUON_EFF_SYS				×				
PRW_DATASF	×	×	• ×	• ×	• ×		×	
PRW_DATASF_zll_leplep								• ×
Zttrew_mjj							×	
Zllrew_mjj								×
ll_fake_nonclosure						• ×		
ll_fake_stat						×		

Table 7.18.: Summary of shape (•) and acceptance (×) uncertainties from experimental sources in the SF high BDT signal region of the $\tau_{lep}\tau_{lep}$ channel.

Systematic	VBF $H \to \tau\tau$	VBF $H \to WW$	Non-VBF H	Top	Fake	$Z \to \tau\tau$	$Z \to \ell\ell$ +Di-boson	Systematic	VBF $H \to \tau\tau$	VBF $H \to WW$	Non-VBF H	Top	Fake	$Z \to \tau\tau$	$Z \to \ell\ell$ +Di-boson
EG_RESOLUTION_ALL	•	• ×	• ×	×			×	JES_EffectiveNP_4		•	• ×				
EG_SCALE_ALLCORR		•	•	×			×	JES_EffectiveNP_5		•				×	×
EG_SCALE_E4SCINTILLATOR		• ×	• ×	×		×		JES_EffectiveNP_6		• ×		×		×	×
EG_SCALE_LARCALIB_2015PRE	•	•	•	×		×	×	JES_EffectiveNP_7		• ×	•	×		×	×
EG_SCALE_LARTEMP_2015PRE		• ×	• ×	×		×	×	JES_EffectiveNP_8		•		×		×	×
EG_SCALE_LARTEMP_2016PRE		•	• ×	×		×		JES_EtaInter_Model	• ×	• ×	• ×			×	×
EL_EFF_ID_TOTAL	×		×	•				JES_EtaInter_NonClosure	• ×	• ×	• ×	×		×	×
EL_EFF_ISO_TOTAL				•				JES_EtaInter_Stat	•	• ×	×	×		×	×
EL_EFF_RECO_TOTAL				•				JES_Flavor_Comp		• ×	• ×				×
EL_EFF_TRIG2015_TOTAL				•				JES_Flavor_Resp		• ×	• ×	×		×	×
EL_EFF_TRIG2016_TOTAL				•				JES_HighPt	•	•	×			×	×
FT_EFF_Eigen_b_0				• ×				JES_PU_OffsetMu	• ×	•	×	×		×	
FT_EFF_Eigen_b_1				•				JES_PU_OffsetNPV	• ×	• ×	•				×
FT_EFF_Eigen_b_2				•				JES_PU_PtTerm	×	• ×	×	×		×	×
FT_EFF_Eigen_c_0				•				JES_PU_Rho		• ×	• ×	×		×	×
FT_EFF_Eigen_c_1				•				JES_PunchThrough		• ×	• ×			×	×
FT_EFF_Eigen_c_2				•				JVT				•			
FT_EFF_Eigen_light_0				•			×	MET_SoftTrk_ResoPara		•	• ×	×		×	×
FT_EFF_Eigen_light_1				•				MET_SoftTrk_ResoPerp		•	×	×		×	×
FT_EFF_Eigen_light_2				•				MET_SoftTrk_Scale		• ×	• ×	×		×	×
FT_EFF_Eigen_light_3				•				MUONS_ID	×	• ×	×	×			×
FT_EFF_Eigen_light_4				•				MUONS_MS	•	•	• ×	×		×	×
FT_EFF_extrapolation				•				MUONS_SAGITTA_RESBIAS		• ×	•	×		×	×
FT_EFF_extrapolation_from_charm				•				MUONS_SAGITTA_RHO	×	•	• ×	×		×	
Forward_JVT				•				MUONS_SCALE		• ×	• ×			×	×
JER_CROSSCALIBFWD	•	• ×	• ×	×		×	×	MUON_EFF_LOWPT_STAT				•			
JER_NOISEFWD	• ×	•	• ×	×		×	×	MUON_EFF_LOWPT_SYST				•			
JER_NP_0	• ×	•	• ×	×		×	×	MUON_EFF_STAT				•			
JER_NP_1	•	•	• ×	×		×	×	MUON_EFF_SYS				•			
JER_NP_2	• ×	• ×	• ×	×		×	×	MUON_EFF_TrigStat2015				•			
JER_NP_3	•	•	• ×	×		×	×	MUON_EFF_TrigStat2016				•			
JER_NP_4	•	• ×	• ×	×		×	×	MUON_EFF_TrigSyst2015				•			
JER_NP_5	•	•	• ×	×		×	×	MUON_EFF_TrigSyst2016				•			
JER_NP_6	•	•	• ×	×		×	×	MUON_ISO_STAT				•			
JER_NP_7	•	• ×	• ×	×		×	×	MUON_ISO_SYS				•			
JER_NP_8	•	•	• ×	×		×	×	PRW_DATASF	• ×	• ×	• ×	• ×		×	•
JES_EffectiveNP_1		•	• ×	×		×	×	Zttrew_mjj						×	
JES_EffectiveNP_2	•	•	×	×		×	×	ll_fake_nonclosure					×		
JES_EffectiveNP_3	×	• ×	• ×	×			×	ll_fake_stat					×		

Table 7.19.: Summary of shape (•) and acceptance (×) uncertainties from experimental sources in the DF high BDT signal region of the $\tau_{lep}\tau_{lep}$ channel.

Systematic	VBF $H \to \tau\tau$	VBF $H \to WW$	Non-VBF H	Top	Di-boson	Fake	$Z \to \tau\tau$	$Z \to \ell\ell$
EG_SCALE_ALLCORR	$\times$						$\times$	
EG_SCALE_E4SCINTILLATOR								$\times$
EG_SCALE_LARTEMP_2015PRE	$\bullet$							
EG_SCALE_LARTEMP_2016PRE	$\bullet$							
EL_EFF_ID_TOTAL				$\times$	$\times$			
FT_EFF_Eigen_b_0				$\times$				
FT_EFF_Eigen_b_1				$\times$				
FT_EFF_Eigen_b_2				$\times$				
FT_EFF_Eigen_light_0	$\times$	$\times$	$\times$	$\times$	$\times$		$\times$	$\times$
JER_CROSSCALIBFWD	$\bullet$	$\bullet$	$\bullet$	$\times$			$\bullet\times$	$\times$
JER_NOISEFWD	$\bullet$	$\bullet\times$	$\bullet\times$	$\bullet\times$	$\times$		$\times$	$\times$
JER_NP_0	$\bullet$	$\bullet\times$	$\bullet\times$	$\bullet\times$	$\bullet\times$		$\bullet\times$	
JER_NP_1	$\bullet$				$\bullet\times$			$\times$
JER_NP_2	$\bullet$	$\bullet\times$	$\bullet$	$\bullet\times$	$\bullet\times$		$\times$	$\times$
JER_NP_3	$\bullet$		$\times$	$\bullet\times$	$\bullet\times$		$\bullet\times$	$\times$
JER_NP_4	$\bullet$		$\bullet\times$	$\bullet\times$	$\bullet\times$		$\bullet\times$	$\times$
JER_NP_5	$\bullet$	$\bullet$	$\bullet\times$	$\bullet$	$\bullet\times$		$\bullet\times$	$\times$
JER_NP_6	$\bullet$	$\bullet\times$		$\bullet\times$	$\times$		$\bullet$	$\times$
JER_NP_7	$\bullet$	$\bullet$	$\bullet\times$	$\bullet\times$	$\bullet\times$		$\times$	$\times$
JER_NP_8	$\bullet\times$			$\times$	$\bullet\times$		$\bullet\times$	$\times$
JES_EffectiveNP_1	$\bullet\times$		$\bullet\times$		$\times$		$\bullet\times$	$\times$
JES_EffectiveNP_2	$\bullet$			$\bullet\times$			$\bullet$	$\times$
JES_EffectiveNP_3	$\bullet$		$\bullet$	$\times$			$\times$	$\times$
JES_EffectiveNP_4		$\bullet$		$\times$			$\bullet$	
JES_EffectiveNP_5	$\bullet$						$\bullet$	
JES_EffectiveNP_6	$\bullet$	$\times$					$\bullet$	
JES_EffectiveNP_7				$\times$			$\bullet$	
JES_EffectiveNP_8	$\bullet$	$\bullet\times$	$\bullet$				$\bullet$	
JES_EtaInter_Model	$\bullet\times$	$\bullet\times$	$\bullet\times$	$\times$	$\bullet\times$		$\bullet\times$	
JES_EtaInter_Model_zll_leplep								$\times$
JES_EtaInter_NonClosure	$\bullet$	$\bullet$	$\bullet$	$\bullet$	$\bullet\times$		$\bullet\times$	$\times$
JES_EtaInter_Stat	$\bullet$	$\times$	$\times$	$\bullet\times$	$\times$		$\times$	$\times$
JES_Flavor_Comp	$\bullet\times$	$\bullet\times$	$\bullet\times$	$\bullet\times$	$\bullet\times$		$\bullet\times$	
JES_Flavor_Comp_leplepzll								$\times$
JES_Flavor_Resp	$\bullet\times$	$\times$	$\bullet\times$	$\times$	$\bullet\times$		$\bullet\times$	
JES_Flavor_Resp_leplepzll								$\times$
JES_PU_OffsetMu	$\bullet$	$\bullet\times$	$\bullet\times$	$\bullet\times$	$\bullet\times$		$\bullet$	$\times$
JES_PU_OffsetNPV	$\bullet$		$\bullet\times$	$\bullet$	$\times$		$\bullet\times$	$\times$
JES_PU_PtTerm	$\bullet\times$	$\times$	$\bullet\times$	$\bullet\times$	$\times$		$\times$	
JES_PU_Rho	$\bullet\times$	$\bullet\times$	$\bullet\times$	$\bullet\times$	$\bullet\times$		$\bullet\times$	$\times$
MET_SoftTrk_ResoPara	$\bullet$	$\bullet$	$\bullet\times$	$\bullet$	$\bullet$		$\bullet$	$\times$
MET_SoftTrk_ResoPerp	$\bullet$			$\bullet$	$\bullet\times$		$\bullet\times$	$\times$
MET_SoftTrk_Scale	$\bullet$	$\bullet$					$\bullet$	$\times$
MUONS_ID	$\bullet$							$\times$
PRW_DATASF	$\bullet\times$	$\bullet\times$	$\bullet\times$	$\bullet\times$	$\times$		$\times$	
PRW_DATASF_zll_leplep								$\bullet\times$
Zllrew_mjj								$\times$
ll_fake_nonclosure						$\times$		
ll_fake_stat						$\times$		

Table 7.20.: Summary of shape ($\bullet$) and acceptance ($\times$) uncertainties from experimental sources in the SF low-BDT control region of the $\tau_{lep}\tau_{lep}$ channel.

Systematic	VBF $H \to \tau\tau$	VBF $H \to WW$	Non-VBF H	Top	Fake	$Z \to \tau\tau$	$Z \to \ell\ell$ +Di-boson
EG_SCALE_ALLCORR							•
EG_SCALE_LARCALIB_2015PRE							•
EL_EFF_ID_TOTAL	×	×	×	×		×	×
FT_EFF_Eigen_b_0				×			
FT_EFF_Eigen_b_1				×			
FT_EFF_Eigen_b_2				×			
FT_EFF_Eigen_light_0	×		×	×		×	×
JER_CROSSCALIBFWD	•	•	• ×	• ×		• ×	• ×
JER_NOISEFWD	•	•	• ×	• ×		• ×	• ×
JER_NP_0	•	•	• ×	• ×		• ×	• ×
JER_NP_1		•		•		• ×	•
JER_NP_2	•	•		•		•	•
JER_NP_3	•	•	•	• ×		•	• ×
JER_NP_4		•	•	•		•	•
JER_NP_5	•	•	• ×	•		•	• ×
JER_NP_6	•	•	•			•	•
JER_NP_7	•		• ×			•	•
JER_NP_8			×	•		•	•
JES_EffectiveNP_1	• ×	• ×	• ×	•		• ×	• ×
JES_EffectiveNP_2			•			•	•
JES_EffectiveNP_3				•		•	
JES_EffectiveNP_4	•					•	•
JES_EffectiveNP_6							•
JES_EffectiveNP_7	•			•		•	
JES_EffectiveNP_8			•			•	
JES_EtaInter_Model	• ×	×	• ×	• ×		• ×	• ×
JES_EtaInter_NonClosure	• ×	•	×	×		• ×	• ×
JES_EtaInter_Stat	•	×	×			• ×	• ×
JES_Flavor_Comp	•	×	• ×	• ×		• ×	• ×
JES_Flavor_Resp	• ×	×	• ×	×		• ×	• ×
JES_PU_OffsetMu	• ×	×	•	×		• ×	• ×
JES_PU_OffsetNPV			•			• ×	• ×
JES_PU_PtTerm	•	×	×	×		• ×	• ×
JES_PU_Rho	• ×	×	• ×	• ×		• ×	• ×
MET_SoftTrk_ResoPara	•		•				
MET_SoftTrk_ResoPerp	•						•
MET_SoftTrk_Scale	•			•		•	
MUONS_ID			•			•	•
MUONS_SAGITTA_RESBIAS	•						
MUONS_SAGITTA_RHO	•						
MUONS_SCALE	•					•	
PRW_DATASF	• ×	• ×	•	×		• ×	• ×
ll_fake_nonclosure					×		
ll_fake_stat					×		

Table 7.21.: Summary of shape (•) and acceptance (×) uncertainties from experimental sources in the DF low-BDT control region of the $\tau_{lep}\tau_{lep}$ channel.

Systematic	VBF $H \to \tau\tau$	VBF $H \to WW$	Non VBF H	Top	Di-boson	Fake	$Z \to \tau\tau$	$Z \to \ell\ell$
Theo_VBFH_MUR_MUF	×							
Theo_VBFH_shower	• ×							
Theo_alphas_Higgs_ggH_total			×					
Theo_ggH_shower			• ×					
Theo_ggH_sig_qcd_1			×					
Theo_ggH_sig_qcd_2			×					
Theo_ggH_sig_qcd_3			×					
Theo_ggH_sig_qcd_4			×					
Theo_ggH_sig_qcd_5			×					
Theo_ggH_sig_qcd_6			×					
Theo_ggH_sig_qcd_7			×					
Theo_ggH_sig_qcd_8			×					
Theo_ll_vbf_ggH_PSUE			×					
Theo_ll_vbf_ggH_jetveto			×					
Theo_pdf_Higgs_ggH_total			×					
Theo_sig_alphaS			×					
Theo_sig_pdf_4			×					
Z_EWK_proportion							×	×
ZttTheory_MUR_MUF_vbf_leplep							×	
ZttTheory_MUR_MUF_vbf_leplep_oo_shape							•	
ZttTheory_PDF_vbf_leplep							×	

Table 7.22.: Summary of shape (•) and acceptance (×) uncertainties from theoretical sources in the SF high-BDT signal region of the $\tau_{lep}\tau_{lep}$ channel.

Systematic	VBF $H \to \tau\tau$	VBF $H \to WW$	Non-VBF H	Top	Fake	$Z \to \tau\tau$	$Z \to \ell\ell$ +Di-boson
Theo_VBFH_MUR_MUF	×						
Theo_VBFH_shower	• ×						
Theo_alphas_Higgs_ggH_total			×				
Theo_ggH_shower			• ×				
Theo_ggH_sig_qcd_2			×				
Theo_ggH_sig_qcd_3			×				
Theo_ggH_sig_qcd_4			×				
Theo_ggH_sig_qcd_5			×				
Theo_ggH_sig_qcd_6			×				
Theo_ggH_sig_qcd_7			×				
Theo_ggH_sig_qcd_8			×				
Theo_ll_vbf_ggH_PSUE			×				
Theo_ll_vbf_ggH_jetveto			×				
Theo_pdf_Higgs_ggH_total			×				
Theo_sig_alphaS			×				
Theo_sig_pdf_4			×				
Z_EWK_proportion						×	
ZttTheory_MUR_MUF_vbf_leplep						×	
ZttTheory_MUR_MUF_vbf_leplep_oo_shape						•	
ZttTheory_PDF_vbf_leplep						×	

Table 7.23.: Summary of shape (•) and acceptance (×) uncertainties from theoretical sources in the DF high-BDT signal region of the $\tau_{lep}\tau_{lep}$ channel.

Systematic	VBF $H \to \tau\tau$	VBF $H \to WW$	Non-VBF H	Top	Di-boson	Fake	$Z \to \tau\tau$	$Z \to \ell\ell$
Theo_VBFH_shower	• ×							
Theo_alphas_Higgs_ggH_total			×					
Theo_ggH_shower			• ×					
Theo_ggH_sig_qcd_1			×					
Theo_ggH_sig_qcd_2			×					
Theo_ggH_sig_qcd_3			×					
Theo_ggH_sig_qcd_4			×					
Theo_ggH_sig_qcd_6			×					
Theo_ggH_sig_qcd_7			• ×					
Theo_ggH_sig_qcd_8			×					
Theo_ll_vbf_ggH_PSUE			×					
Theo_pdf_Higgs_ggH_total			×					
Theo_sig_alphaS			×					
Theo_sig_pdf_4			×					
ZttTheory_MUR_MUF_vbf_leplep							• ×	
ZttTheory_PDF_vbf_leplep							×	

Table 7.24.: Summary of shape (•) and acceptance (×) uncertainties from theoretical sources in the SF low-BDT control region of the $\tau_{lep}\tau_{lep}$ channel.

Systematic	VBF $H \to \tau\tau$	VBF $H \to WW$	Non-VBF H	Top	Fake	$Z \to \tau\tau$	$Z \to \ell\ell$ +Di-boson
Theo_VBFH_shower	• ×						
Theo_alphas_Higgs_ggH_total			×				
Theo_alphas_Higgs_ttH_total							
Theo_ggH_shower			• ×				
Theo_ggH_sig_qcd_2			×				
Theo_ggH_sig_qcd_3			×				
Theo_ggH_sig_qcd_4			×				
Theo_ggH_sig_qcd_6			×				
Theo_ggH_sig_qcd_7			×				
Theo_ll_vbf_ggH_PSUE			×				
Theo_pdf_Higgs_ggH_total			×				
Theo_sig_alphaS			×				
ZttTheory_MUR_MUF_vbf_leplep						• ×	

Table 7.25.: Summary of shape (•) and acceptance (×) uncertainties from theoretical sources in the DF low-BDT control region of the $\tau_{lep}\tau_{lep}$ channel.

7.5. Results

This section presents the results of the search for CP-violating HVV interactions by measuring the $\tilde{d}$-parameter and deriving central confidence intervals (CIs). These results are based on the negative-logarithmic-likelihood curve (ΔNLL-curve), which is constructed from maximum likelihood fits to collision data in all signal and control regions under various HVV coupling hypotheses. The CIs are determined by interpolating between the tested $\tilde{d}$-values with a spline function as implemented in ROOT [237]. In order to derive expected CIs, the ΔNLL-curve is also derived for pre-fit and post-fit pseudo datasets according to the procedure described in Section 7.4.1. Here, the pseudo datasets are constructed with the SM signal hypothesis ($\tilde{d} = 0$).

In the following, the first part discusses the obtained results from the standalone fit in the $\tau_{lep}\tau_{lep}$ channel. The combined measurement with the $\tau_{lep}\tau_{had}$ and $\tau_{had}\tau_{had}$ channels is then presented in the second part.

7.5.1. $H \to \tau_{lep}\tau_{lep}$

The observed ΔNLL-curve as a function of $\tilde{d}$ is shown in Figure 7.37(a) and results in a best-fit signal hypothesis of $\hat{\tilde{d}} = -0.03$. Since the curve only reaches a maximum of $\Delta\text{NLL}_{\text{max}} = 0.23$, the standalone fit in the $\tau_{lep}\tau_{lep}$ channel does not allow to derive CIs on $\tilde{d}$. The observed ΔNLL-curve can be compared to the expected pre-fit and post-fit results, which are shown in Figure 7.37 as well. The results of the control-region only fit, which is used in order to derive the expected post-fit sensitivity, can be found in Appendix E.1. Both expected ΔNLL-curves provide a higher sensitivity to CP-violating interactions compared to the observed result. However, no expected CIs on $\tilde{d}$ are obtained. While the expected pre-fit ΔNLL-curve reaches a maximum of $\Delta\text{NLL}_{\text{max}} = 0.39$, the impact of the best-fit NPs and background normalization factors, which are determined in the control-region only fit, further reduce the sensitivity of the expected curve to $\Delta\text{NLL}_{\text{max}} = 0.30$.

Figure 7.37(a) shows the expected and observed best-fit values for the signal strength as a function of $\tilde{d}$. For the SM hypothesis, the signal strength is measured to be $\hat{\mu} = 1.32^{+1.43}_{-1.32}$, while the likelihood fit with the best-fit signal hypothesis of $\hat{\tilde{d}} = -0.03$ results in in a lower value of $\hat{\mu} = 1.00^{+1.33}_{-1.00}$. These results agree with the SM expectation of $\mu_{SM} = 1$ within uncertainties. For $\tilde{d}$-values in the range of $0.04 < \tilde{d} < 0.5$, a best-fit signal strength of zero is obtained. This is caused by requiring positive values for the signal strength in the likelihood function. In particular, best-fit values of zero are obtained for coupling hypotheses, where statistical fluctuations in bins with large signal contributions lead to predicted background yields, which are equal or larger compared to the observed number of data events. Therefore, the best agreement between data and prediction corresponds to the absence of any signal contribution. This is also reflected in the observed ΔNLL-curve, where no distinction between signal hypotheses in the range of $0.04 < \tilde{d} < 0.5$ is achieved.

The post-fit normalization factors for the $Z \to \tau\tau$, $Z \to \ell\ell$ and top-quark background are summarized in Table 7.26. Here, the obtained results under the SM and the best-fit signal hypothesis are very similar and the background normalization factors are in good agreement with the pre-fit expectations and also with the results from the control-region only fit.

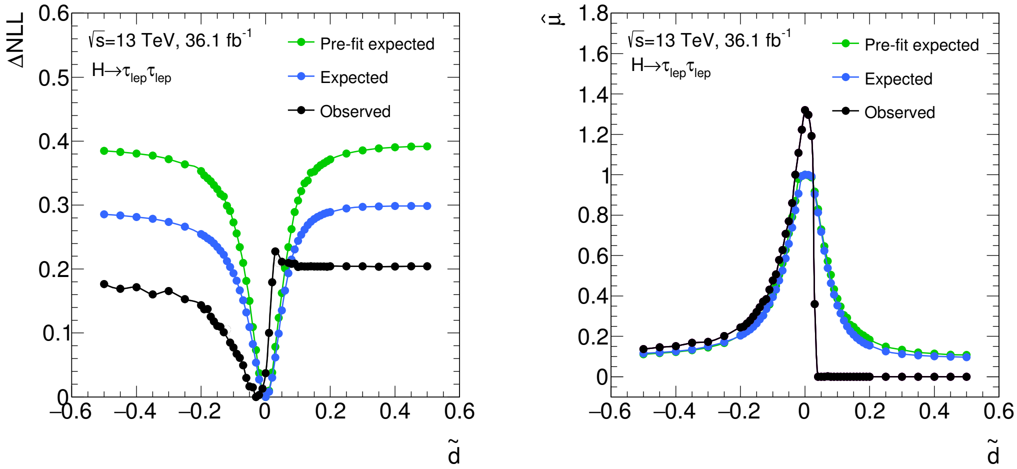

(a) (b)

Figure 7.37.: Observed ΔNLL-curve (a) and best-fit signal strength (b) as a function of $\tilde{d}$ from the standalone fit in the $\tau_{lep}\tau_{lep}$ channel (black). For comparison, the expected curves are also shown. For the expected pre-fit results (green), the pseudo dataset is constructed from the pre-fit SM signal and background prediction with $\mu = 1$. The expected post-fit curves (blue) are obtained by evaluating the SM signal and background predictions with the best-fit nuisance parameters and background normalization factors as obtained in a control-region only fit with $\mu = 1$.

Parameter	$\tilde{d} = 0$	$\tilde{d} = -0.03$	CR-only
Signal strength	$1.32^{+1.43}_{-1.32}$	$1.00^{+1.33}_{-1.00}$	-
NF $Z \to \tau\tau$	$0.94^{+0.15}_{-0.12}$	$0.94^{+0.15}_{-0.12}$	$0.95^{+0.16}_{-0.13}$
NF $Z \to \ell\ell$	$0.98^{+0.43}_{-0.26}$	$0.98^{+0.43}_{-0.26}$	$0.93^{+0.26}_{-0.42}$
NF Top	$1.14^{+0.07}_{-0.06}$	$1.14^{+0.07}_{-0.06}$	$1.12^{+0.09}_{-0.07}$

Table 7.26.: Post-fit values for the signal strength and background normalization factors from the standalone fit in the $\tau_{lep}\tau_{lep}$ channel with the SM ($\tilde{d} = 0$) and the best-fit hypothesis of $\hat{\tilde{d}} = -0.03$ including statistical and systematic uncertainties. In addition, the background normalization factors from the control-region only fit are given.

Figure 7.38 shows the post-fit distribution of the Optimal Observable in the high-BDT signal regions with the best-fit signal hypothesis. The corresponding $m_{\tau\tau}^{\mathrm{MMC}}$ distributions in the low-BDT control regions are shown in Figure 7.39. In the SF final state, no data events are found in the last bin of the Optimal Observable distribution, which results in a measured signal strength of zero for coupling hypotheses with $0.04 < \tilde{d} < 0.5$ as discussed above. Overall, a good agreement between signal and background prediction and the observed data is obtained. The relative uncertaninty per bin ranges from about 24 % in the DF channels up to about 65 % in the SF channel. The observed post-fit yields in the high-BDT signal regions from the fit with the best-fit signal hypothesis are given in Table 7.27. The corresponding numbers in the control regions can be found in Appendix F.2. In both the SF and DF signal regions, the sum of signal and background events is in good agreement with the observed data yield within the uncertainties. Compared to the pre-fit expectation, which is given in Table 7.5, the total background yield increases by a factor of 2 in both the SF and DF channel due to the enhanced contributions from $Z \to \tau\tau$, $Z \to \ell\ell$ and top-quark events. For the $Z \to \tau\tau$ and $Z \to \ell\ell$ processes, this increase is mainly caused by the observed pulls and correlations of NPs related to the JER uncertainty, which is discussed below. Furthermore, these pulls result in a large uncertainty on the predicted $Z \to \ell\ell$ yield in the SF channel and also enhanced the contribution from top-quark events, where in addition the pre-fit expectation is scaled up by 14 % due to the post-fit normalization factor. The obtained event yields for the VBF $H \to \tau\tau$ and $H \to WW$ signal are close to their respective pre-fit expectations.

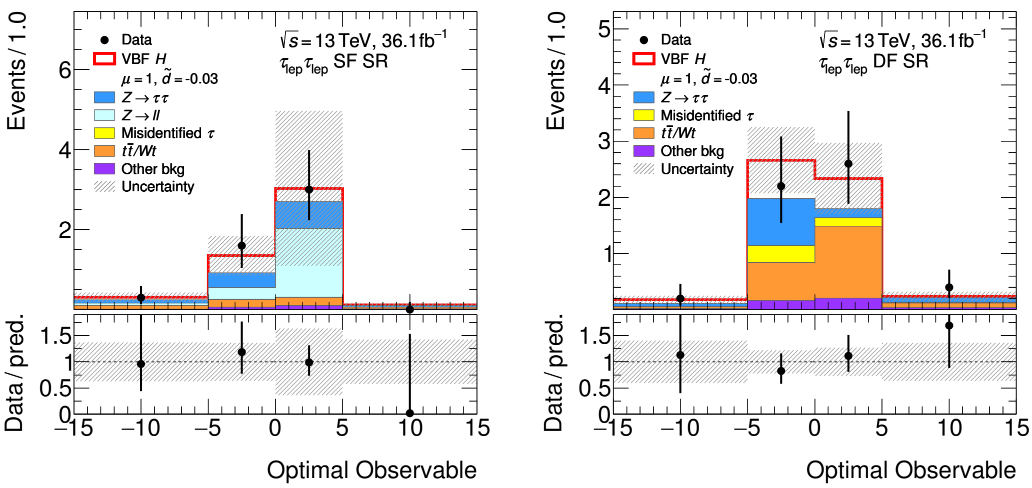

(a) (b)

Figure 7.38.: Post-fit distributions of the Optimal Observable in the signal regions of the $\tau_{lep}\tau_{lep}$ SF (a) and DF (b) channel. The signal and background predictions in each bin are determined in the standalone $\tau_{lep}\tau_{lep}$ fit with the best-fit signal hypothesis of $\hat{\tilde{d}} = -0.03$ and are normalized to the bin width. The uncertainty band includes statistical, experimental and theoretical uncertainties. The lower panel shows the number of data events divided by the signal plus background prediction.

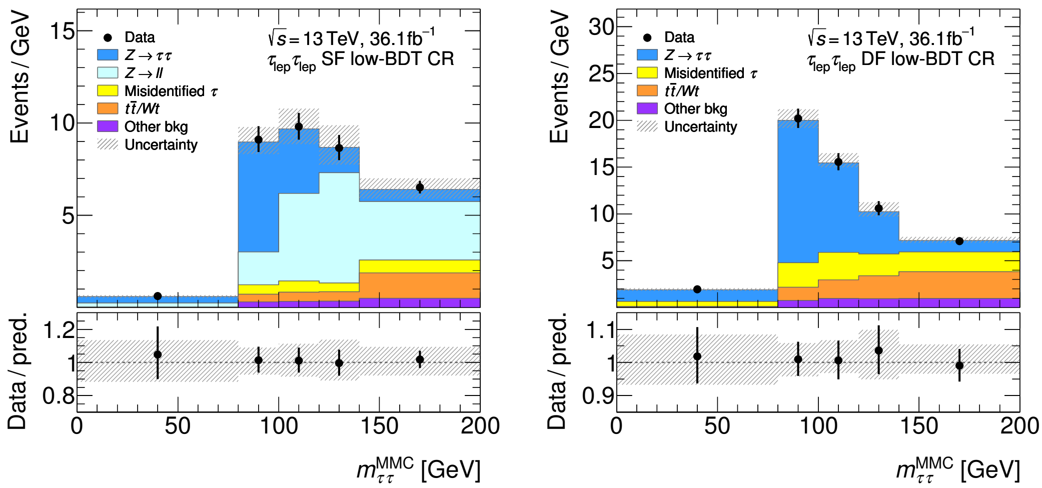

(a) (b)

Figure 7.39.: Post-Fit distributions of $m_{\tau\tau}^{\mathrm{MMC}}$ in the low-BDT control regions of the $\tau_{lep}\tau_{lep}$ SF (a) and DF (b) channel. The background predictions in each bin are determined in the standalone $\tau_{lep}\tau_{lep}$ fit with the best-fit signal hypothesis of $\hat{\tilde{d}} = -0.03$ and are normalized to the bin width. The signal contribution in these control regions is negligible. The uncertainty band includes statistical, experimental and theoretical uncertainties. The lower panel shows the number of data events divided by the signal plus background prediction.

Figure 7.40 shows the impact of the 15 most important NPs on the measured signal strength under the best-fit signal hypothesis according to the procedure described in Section 6.5.1. Here, the highest ranked parameter corresponds to the MC uncertainty on the background prediction in the first bin of the Optimal Observable distribution in the SF high-BDT region (Stat_ll_SF_regsig_bin1). This is followed by several components of the JER uncertainty (JER_NP_[6,0,5,4,7]). Further statistical uncertainties on the background prediction in the SF signal and control region are ranked high as well (Stat_ll_SF_reglowbdt_bin1, Stat_ll_SF_regsig_bin2). The NPs related to the uncertainty on the resolution of the muon momentun (MUONS_MS), the estimation of the fake-lepton background (ll_fake_nonclsoure), the JES uncertainty (JES_EtaInter) and the E_T^{miss} scale uncertainty (MET_SoftTrk_Scale) are found to have a high impact as well. The highest ranked NP from theoretical sources is given by the QCD-scale uncertainty on the $Z \to \tau\tau$ background prediction (ZttTheory_MUR_MUF_ll). Furthermore, the normalization of the $Z \to \tau\tau$ background is also found to have an important impact on the measured signal strength. As shown in Figure 7.40, no large pulls or constraints are observed for the highest ranked NPs, where all post-fit values are found within the pre-fit $\pm 1\sigma$ uncertainty band and hence are in agreement with their respective pre-fit values within uncertainties. The largest pulls and constraints appear for NPs related to the JER uncertainty, which is consistent with the observation in the $H \to \tau\tau$ cross-section measurement. In particular, the largest pull of 51 % with respect to the pre-fit value is obtained for JER_NP_4, where the uncertainty is constrained to +89/71 %. The largest constrain of +87/ − 68 % corresponds to JER_NP_, while the remaining JER NPs are constraint between 94 % and 71 % with respect to their pre-fit uncertainty.

The relative breakdown of the NP contribution to the measured signal-strength uncertainty is summarized in Table 7.28. These numbers are obtained with the same procedure as described in Section 6.5.1. Here, the largest contributions arise from uncertainties related to jets and E_T^{miss}, followed by the statistical uncertainty on the background prediction.

Process	High-BDT SR	
	SF	DF
VBF $H \to \tau\tau$ ($\hat{\tilde{d}} = -0.03$, $\hat{\mu} = 1.00$)	3.7 ± 5.4	5.5 ± 7.9
VBF $H \to WW$ ($\hat{\tilde{d}} = -0.03$, $\hat{\mu} = 1.00$)	1.0 ± 1.4	1.6 ± 2.3
$Z \to \tau\tau$	6.3 ± 4.5	6.4 ± 3.5
Top	3.2 ± 2.2	11 ± 8
$Z \to \ell\ell$	11 ± 13	
Di-Boson	0.6 ± 0.6	1.7 ± 1.2
Fake	0.1 ± 0.2	2.4 ± 0.7
non-VBF $H \to \tau\tau$,WW	0.5 ± 0.4	0.7 ± 0.3
Total bkg.	22 ± 14	22 ± 11
Total signal ($\hat{\tilde{d}} = -0.03$, $\hat{\mu} = 1.00$)	4.7 ± 6.8	7.1 ± 10.1
Total signal ($\tilde{d} = 0$, $\mu = 1$)	4.7 ± 6.5	7.2 ± 9.9
Data	26	30

Table 7.27.: Post-fit event yields for signal and background predictions from the standalone fit in the $\tau_{lep}\tau_{lep}$ channel with the best-fit signal hypothesis of $\hat{\tilde{d}} = -0.03$ compared to the observed data. In addition, the expected pre-fit signal yields for the SM hypothesis ($\tilde{d} = 0$, $\mu = 1$) are given. The $Z \to \ell\ell$ and di-boson background are combined in the DF channel. The uncertainty includes statistical, experimental and theoretical uncertainties.

In order to evaluate the impact of systematic uncertainties on the sensitivity to CP-violating interactions, the expected pre-fit ΔNLL-curve is also constructed from likelihood fits without systematic uncertainties, but only considering the statistical uncertainties on the dataset. The resulting ΔNLL-curve is shown in Figure 7.41 and can be compared to the expected pre-fit sensitivity. Without systematic uncertainties, the curve provides a maximum of $\Delta\text{NLL}_{\text{max}} = 1.54$, which corresponds to an increase by a factor of 3.9 compared to the expected pre-fit ΔNLL-curve including statistical and systematic uncertainties. In particular, the 68 % CL interval is determined to be $[-0.09, 0.09]$, while no 68 % CL intervals can be derived from the expected pre-fit ΔNLL-curve. Hence, systematic uncertainties clearly have an important impact on the sensitivity to $\tilde{d}$ in the analysis. In order to identify, which source of uncertainty primarily impacts the sensitivity, the expected pre-fit ΔNLL-curve is also determined by removing all NPs related to a specific uncertainty group from the likelihood function. Here it is found, that NPs, which arise from jet uncertainties and the statistical uncertainty on the background prediction, have the largest impact on the expected ΔNLL-curve. The impact from uncertainties related to leptons, the estimation of the fake-lepton background and theoretical uncertainties are found to be negligible. As shown in Figure 7.41, excluding jet related uncertainties results in a maximum of $\Delta\text{NLL}_{\text{max}} = 0.88$ and therefore provides an increase of $\Delta\text{NLL}_{\text{max}}$ by a factor of 2.3 with respect to the expected pre-fit curve. In addition, the 68 % CL interval is determined to be $[-0.11, 0.12]$. This interval is only a factor of 1.2 larger compared to the result, when all systematic uncertainties are removed. In addition, the impact of statistical uncertainties from simulated background events on the expected ΔNLL-curve is shown in Figure 7.41. Here, a maximum of $\Delta\text{NLL}_{\text{max}} = 0.50$ is reached, which corresponds to an improvement by a factor of 1.3 compared to the expected pre-fit curve. Hence, systematic uncertainties related to jets clearly have the largest impact on the expected ΔNLL-curve and are found to be the dominant cause for the limited sensitivity in the $\tau_{lep}\tau_{lep}$ channel.

Source of uncertainty	$(\Delta\mu'/\Delta\hat{\mu})^2$
Data statistics	$+0.19/-0.10$
Total systematic unc.	$+0.81/-0.90$
Background normalizations	$+0.09/-0.17$
$Z \to \tau\tau$ normalization	$+0.02/-0.08$
Jets, E_T^{miss}	$+0.56/-0.73$
b-tagging	$+0.02/-0.02$
Electrons, Muons	$+0.09/-0.05$
Pileup reweighting	< 0.01
Fake estimation	$+0.02/-0.03$
Luminosity	< 0.01
$H \to \tau\tau$ theory unc.	$+0.01/-0.05$
$Z \to \tau\tau$ theory unc.	$+0.03/-0.04$
Background statistics	$+0.18/-0.44$

Table 7.28.: Fractional contribution of grouped sources of statistical and systematic uncertainties on the measured signal strength uncertainty $\Delta\hat{\mu}$ in the standalone fit in the $\tau_{lep}\tau_{lep}$ channel with the best-fit signal hypothesis of $\hat{\tilde{d}} = -0.03$. The variation $\Delta\hat{\mu}'$ is defined for each source of uncertainty as the squared difference between $\Delta\hat{\mu}$ and the obtained cross-section uncertainty when fixing the corresponding nuisance parameters to their best-fit values.

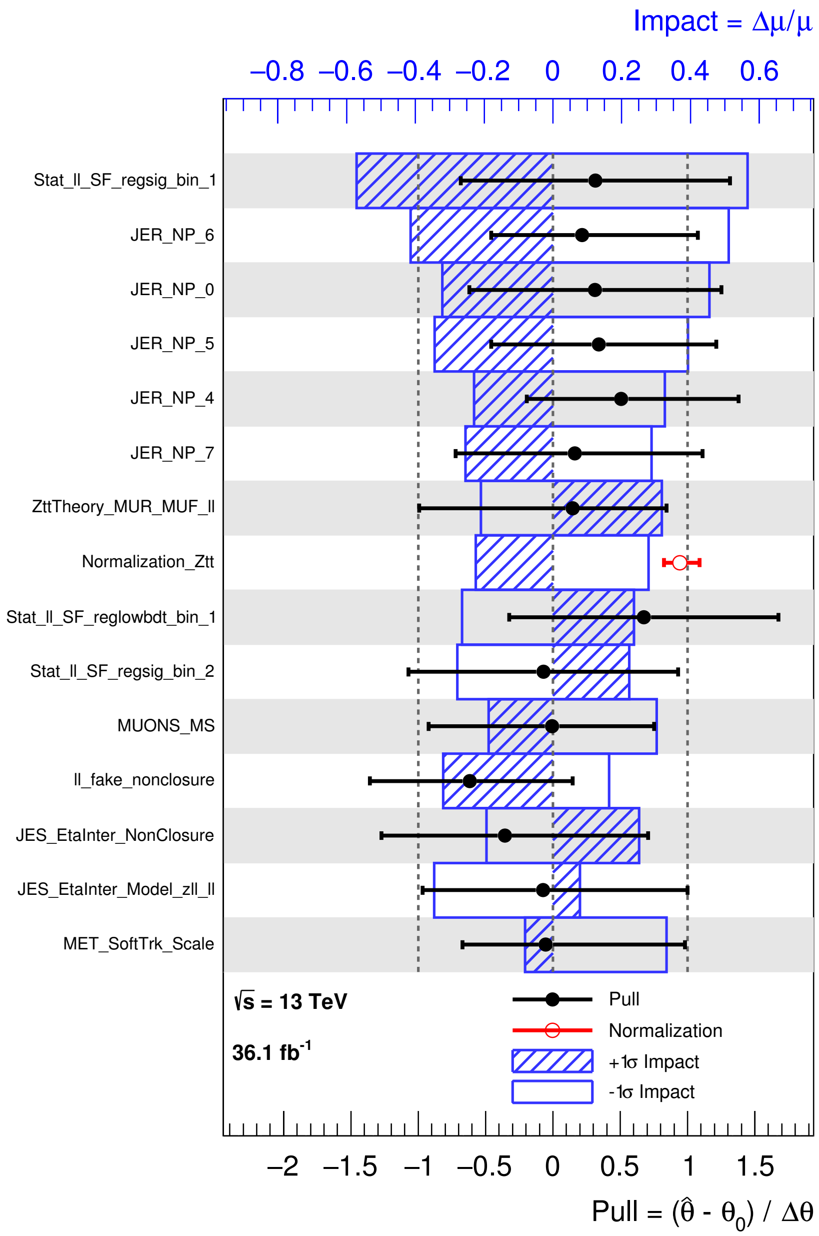

Figure 7.40.: Fractional impact of systematic uncertainties on the measured signal strength (top axis) in the standalone likelihood fit in the $\tau_{lep}\tau_{lep}$ channel with the best-fit signal hypothesis of $\hat{\hat{d}} = -0.03$. The blue boxes show the variation $\Delta\mu$ with respect to the measured value $\hat{\mu}$, when the corresponding nuisance parameter is fixed to its post-fit value shifted by one standard deviation upwards or downwards. In addition, the nuisance parameter post-fit values and uncertainties with respect to the pre-fit values are shown in black (referring to the bottom axis). The value of the background normalization factors and their uncertainties are shown in red and refer to the bottom axis. Only the 15 highest ranked parameters are listed.

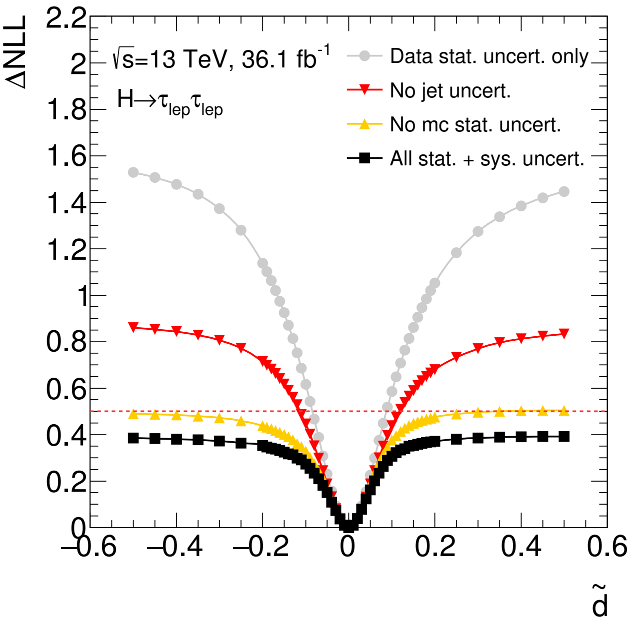

(a)

Figure 7.41.: Pre-fit expected ΔNLL-curves comparing the sensitivity of the fit with and without systematic uncertainties in the $\tau_{lep}\tau_{lep}$ channel. In addition, pre-fit expected curves are shown, where systematic uncertainties related to jets and the statistics of the background prediction are removed from the likelihood function.

7.5.2. Combination with Other Decay Channels

The sensitivity to CP-violating HVV interactions in the $\tau_{lep}\tau_{lep}$ channel can be improved by also including the signal and control regions of the $\tau_{lep}\tau_{had}$ and $\tau_{had}\tau_{had}$ channels in the likelihood fit. A detailed description of these analyses can be found in Ref. [32].

The observed and expected ΔNLL-curves from the combined fit in the $\tau_{lep}\tau_{lep}$, $\tau_{lep}\tau_{had}$ and $\tau_{had}\tau_{had}$ channels are shown in Figure 7.42. The minimum NLL-value is obtained for a best-fit hypothesis of $\hat{\tilde{d}} = -0.01$ and the observed 68 % CL interval for $\tilde{d}$ is measured to be

$$[-0.090, 0.035]. \tag{7.8}$$

From the observed ΔNLL-curve no exclusion interval at the 95 % CL can be derived. The obtained results are consistent with the SM expectation of $\tilde{d} = 0$ and hence no sign of CP violation is observed. For the best-fit signal hypothesis of $\hat{\tilde{d}} = -0.01$ the signal strength is measured to be $\hat{\mu} = 0.73^{+0.48}_{-0.47}$, which is also in agreement with the SM prediction of one within the uncertainties.

The expected exclusion intervals for $\tilde{d}$ are determined based on the expected pre-fit and post-fit ΔNLL-curves and are summarized in Table 7.29. Here, the expected pre-fit ΔNLL-curve provides a 68 % CL interval for $\tilde{d}$ of $[-0.033, 0.032]$ and also allows to derive a 95 % CL interval of $[-0.12, 0.10]$. For the expected post-fit curve, the pseudo dataset is constructed based on the best-fit NPs and background normalization factors as determined in a control-region only fit. These results can be found in Appendix E.2. The post-fit pseudo dataset is build according to the SM signal prediction with $\mu = 1$ and also with the observed signal strength of $\mu = 0.73$. With the SM signal strength, the expected intervals for $\tilde{d}$ are found to be $[-0.035, 0.033]$ at the 68 % CL and $[-0.21, 0.15]$ at the 95 % CL. Hence, the impact of the best-fit NPs and background normalization factors results in an increase of the 68 % CL interval by a factor of 1.05 compared to the corresponding pre-fit interval, while the 95 % CL interval is increased by a factor of 1.64. From the expected post-fit ΔNLL-curve with $\mu = 0.73$ the 68 % CL interval for $\tilde{d}$ is found to be $[-0.050, 0.048]$, while no 95 % CL is reached. Hence, the impact of the measured signal strength results in an increase of the 68 % CL interval by a factor of 1.44 compared to the post-fit expectation with $\mu = 1$. In particular, the downward fluctuation of the measured signal strength with respect to the SM expectation limits the sensitivity and is the main reason why no 95 % CL interval for $\tilde{d}$ can be derived. The asymmetry in the expected intervals are caused by limited statistics in the background predictions, which lead to slightly asymmetric Optimal Observable distributions in the signal regions.

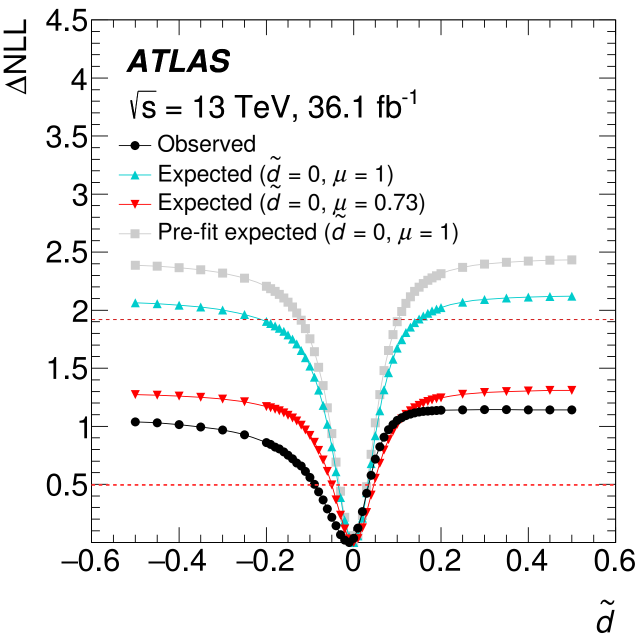

Figure 7.42.: Observed ΔNLL-curve as a function of $\tilde{d}$ from the combined fit in the $\tau_{lep}\tau_{lep}$, $\tau_{lep}\tau_{had}$ and $\tau_{had}\tau_{had}$ channels (black). For comparison, expected ΔNLL-curves are also shown. For the expected pre-fit ΔNLL-curve (grey), the pseudo dataset is constructed from the pre-fit SM signal and background prediction with $\mu = 1$. The expected post-fit ΔNLL-curves are obtained by evaluating the SM signal and background predictions with the best-fit nuisance parameters and background normalization factors as obtained in a control-region only fit with $\mu = 1$ (cyan) and $\mu = 0.73$ (red) [32].

	observed	expected ($\tilde{d} = 0$)		
		pre-fit ($\mu = 1$)	post-fit ($\mu = 1$)	post-fit ($\mu = 0.73$)
68 % CL interval	$[-0.090, 0.035]$	$[-0.033, 0.032]$	$[-0.035, 0.033]$	$[-0.050, 0.048]$
95 % CL interval	-	$[-0.12, 0.10]$	$[-0.21, 0.15]$	-

Table 7.29.: Comparison of observed and expected exclusion intervals for $\tilde{d}$ at the 68 % and 95 % confidence level (CL). For the expected pre-fit result, the pseudo dataset is constructed from the pre-fit SM signal and background prediction with $\mu = 1$. The expected post-fit results are obtained by evaluating the SM signal and background predictions with the best-fit nuisance parameters and background normalization factors as obtained in a control-region only fit with $\mu = 1$ and $\mu = 0.73$.

The measured signal strength and background normalization factors from the combined likelihood fit with the SM and the best-fit hypothesis of $\hat{\tilde{d}} = -0.01$ are summarized in Table 7.30. Here, in addition to the normalization factors of the $Z \to \tau\tau$ background, which is correlated across the analysis channels, and the normalization of the $Z \to \ell\ell$ and top-quark backgrounds in the $\tau_{lep}\tau_{lep}$ channel, the $\tau_{had}\tau_{had}$ channel also includes a normalization factor for background events from misidentified τ_{had}-leptons. Overall, the measured values for the signal strength and the background normalization factors are consistent between the SM and the best-fit signal hypothesis and also agree with the results from the control-region only fit within the uncertainties. Furthermore, a good agreement between the pre-fit expectation and the post-fit background normalization factors is obtained, where the measured $Z \to \tau\tau$ normalization is also consistent with the result from the standalone $\tau_{lep}\tau_{lep}$ fit. Figure 7.43 shows the post-fit distributions of the Optimal Observable in all signal regions for the best-fit signal hypothesis, where a good agreement between data and prediction is obtained. The corresponding post-fit yields for all signal and background processes are summarized in Appendix F.2.

Parameter	$\tilde{d} = 0$	$\tilde{d} = -0.01$	CR-only
Signal strength	$0.73^{+0.49}_{-0.48}$	$0.73^{+0.48}_{-0.47}$	-
NF $Z \to \tau\tau$	$0.93^{+0.09}_{-0.07}$	$0.93^{+0.09}_{-0.07}$	$0.91^{+0.09}_{-0.08}$
NF $Z \to \ell\ell$ ($\tau_{lep}\tau_{lep}$)	$0.99^{+0.42}_{-0.26}$	$0.99^{+0.42}_{-0.26}$	$0.96^{+0.44}_{-0.27}$
NF Top ($\tau_{lep}\tau_{lep}$)	$1.16^{+0.06}_{-0.06}$	$1.15^{+0.06}_{-0.06}$	$1.14^{+0.07}_{-0.06}$
NF Fake ($\tau_{had}\tau_{had}$)	$0.99^{+0.10}_{-0.09}$	$0.99^{+0.10}_{-0.09}$	$0.96^{+0.44}_{-0.27}$

Table 7.30.: Post-fit values for the signal strength and background normalization factors from the combined fit with the SM $\tilde{d} = 0$ and the best-fit signal hypothesis of $\tilde{d} = -0.01$ with statistical and systematic uncertainties. In addition, the background normalization factors from the control-region only fit are also given. The normalization of the $Z \to \tau\tau$ background is correlated across the analysis channels.

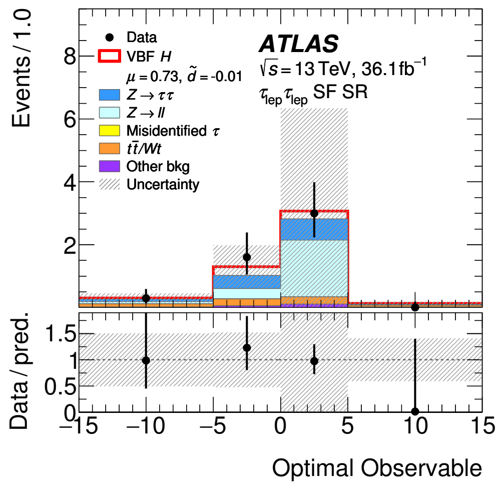

(a)

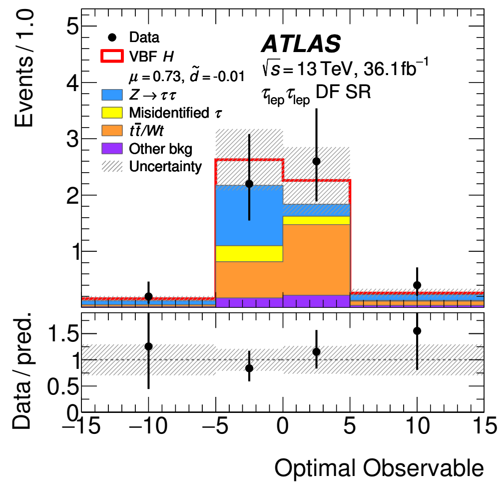

(b)

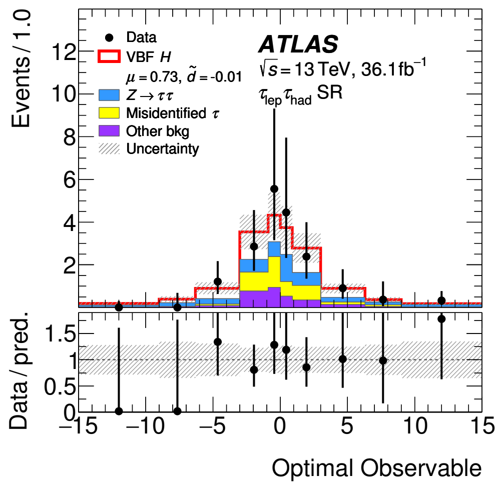

(c)

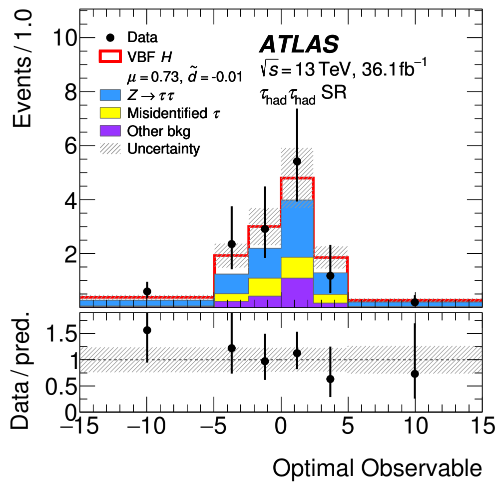

(d)

Figure 7.43.: Post-fit distributions of the Optimal Observable in the signal regions of the $\tau_{lep}\tau_{lep}$ SF (a), $\tau_{lep}\tau_{lep}$ DF (b), $\tau_{lep}\tau_{had}$ (c) and $\tau_{had}\tau_{had}$ (d) channel. The signal and background predictions in each bin are determined in the combined fit with the best-fit signal hypothesis of $\hat{\tilde{d}} = -0.01$ and are normalized to the bin width. The uncertainty band includes statistical, experimental and theoretical uncertainties. The lower panel shows the number of data events divided by the signal plus background prediction [32].

In addition to the measurement of the best-fit signal hypothesis and of the CL intervals for $\tilde{d}$, the mean value of the Optimal Observable allows to test for CP invariance in a more model-independent way (see Section 2.4). Table 7.31 summarizes the Optimal Observable mean values measured in data in the signal regions of the three analysis channels. All results are consistent with the SM expectation of a mean value of zero within statistical uncertainties and hence no sign of CP violation is observed.

Channel	$\langle$Optimal Observable$\rangle$
$\tau_{lep}\tau_{lep}$ SF	-0.54 $\pm$ 0.72
$\tau_{lep}\tau_{lep}$ DF	0.71 $\pm$ 0.81
$\tau_{lep}\tau_{had}$	0.74 $\pm$ 0.78
$\tau_{had}\tau_{had}$	-1.13 ± 0.65

Table 7.31.: Mean values of the Optimal Observable with statistical uncertainties that are observed in data in the signal regions [32].

In order to investigate the contributions of the different analysis channels to the preferred signal hypothesis, the observed ΔNLL-curves are also determined for each channel separately. Here, the likelihood fits for a specific channel are performed in all signal and control regions of the combined analysis, but only including event yield information in the signal regions of the other channels. This allows to retain the best-fit NP values and background normalization factors as observed in the combination, while only the senstivity to $\tilde{d}$ from the analysis channel under consideration is exploited. The resulting ΔNLL-curves are shown in Figure 7.44. In the $\tau_{lep}\tau_{lep}$ SF and $\tau_{had}\tau_{had}$ channels, the mimimum NLL-value is obtained for signal hypotheses with negative $\tilde{d}$-values of $\hat{\tilde{d}} = -0.07$ and $\hat{\tilde{d}} = -0.13$, respectively. The $\tau_{lep}\tau_{lep}$ DF and $\tau_{lep}\tau_{had}$ channels provide best-fit hypothesis corresponding to positive $\tilde{d}$-values of $\hat{\tilde{d}} = 0.25$ and $\hat{\tilde{d}} = 0.03$, respectively. These results are consistent with the Optimal Observable mean in data (see Table 7.31), where the $\tau_{lep}\tau_{lep}$ SF and $\tau_{lep}\tau_{had}$ measure a negative value, while postive values are obtained in the $\tau_{lep}\tau_{lep}$ DF and $\tau_{lep}\tau_{had}$ channels.

The relative breakdown of the NP contribution to the measured signal-strength uncertainty is summarized in Table 7.32. These numbers are obtained with the same procedure as described in Section 6.5.1. In the combined fit, the largest contributions arise from uncertainties related to jets and E_T^{miss}, followed by statistical uncertainties on the background prediction. In addition, systematic uncertainties from the identification of τ_{had}-leptons and theoretical uncertainties on the prediction of the Higgs-boson processes give an important contribution.

Figure 7.45 shows the impact of the 15 most important NPs on the measured signal strength. Here, the NP ranking is determined according to the procedure described in Section 6.5.1. The highest ranked parameter corresponds to one component of the JER uncertainty (JER_NP_0), followed by the τ_{had}-energy scale uncertainty(TAU_TES_INSITU) and the statistical uncertainty on the background prediction in the signal region of the $\tau_{lep}\tau_{had}$ channel (Stat_chanlh_regsig_bin2). An important impact on the measured signal strength is also found to arise from additional components of the JER uncertainty

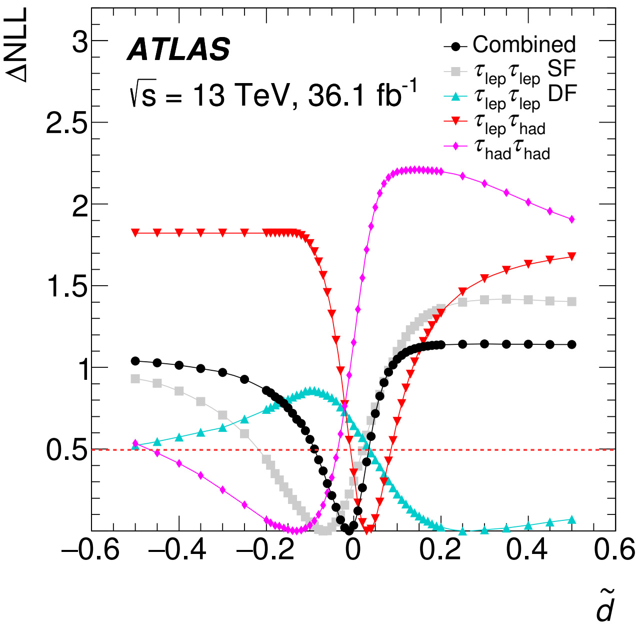

Figure 7.44.: Observed ΔNLL-curves for each channel as a function of $\tilde{d}$ compared to the combination. The ΔNLL-curves for the individual channels are determined by only including event yield information in the other signal regions [32].

(JER_NP_[6,8]), the electron scale uncertainty (EG_SCALE_E4SCINTILLATOR), two components of the JES uncertainty (JES_EtaInter_NonClosure, JES_EffectiveNP_8) and the E_T^{miss}-scale uncertainty (MET_SoftTrk_ResoPerp). Further statistical uncertainties on the background prediction in the signal and control regions of the $\tau_{had}\tau_{had}$ channel have an important impact on the signal strength as well. The normalization of the top-quark background in the $\tau_{lep}\tau_{lep}$ channel and theoretical uncertainties on the UEPS-modelling of the VBF $H \to \tau\tau$ signal (Theo_VBFH_shower) and ggF $H \to \tau\tau$ background (Theo_ggH_shower) are also among the highest ranked NPs. Overall, no large pulls or constraints are observed for these NPs, where all post-fit values are found to agree with their pre-fit values within the $\pm 1\sigma$ uncertainty. The largest pulls and constraints are obtained for NPs related to the JER uncertainty and the τ_{had}-energy scale uncertainty, which is consistent with the observation in the $H \to \tau\tau$ cross-section measurement. In particular, the largest pull of 59 % appears for TAU_TES_INSITU, which is also constrained to $+64/-75$ % of its pre-fit uncertainty, followed by JER_NP_8 with a pull of 49 % and MET_SoftTrk_ResoPerp with a pull of -39 %. The largest constraints are obtained for JER_NP_0 with $+57/-56$ % and JER_NP_6, which is constrained to $+78/-59$ % of its pre-fit uncertaintiy.

Source of uncertainty	$(\Delta\mu'/\Delta\hat{\mu})^2$
Data statistics	$+0.27/-0.24$
Total systematic unc.	$+0.73/-0.76$
Background normalizations	$+0.03/-0.01$
$Z \to \tau\tau$ normalization	$+0.02/-0.00$
Jets, E_T^{miss}	$+0.34/-0.42$
b-tagging	< 0.01
Electrons, Muons	$+0.07/-0.16$
τ_{had}	$+0.12/-0.10$
Pileup reweighting	$+0.02/-0.03$
Fake estimation	$+0.01/-0.01$
Luminosity	< 0.01
$H \to \tau\tau$ theory unc.	$+0.14/-0.05$
$Z \to \tau\tau$ theory unc.	$+0.05/-0.03$
Background statistics	$+0.14/-0.24$

Table 7.32.: Fractional contribution of grouped sources of statistical and systematic uncertainties on the measured signal strength uncertainty $\Delta\hat{\mu}$ in the combined fit with the best-fit signal hypothesis of $\hat{\tilde{d}} = -0.01$. The variation $\Delta\hat{\mu}'$ is defined for each source of uncertainty as the squared difference between $\Delta\hat{\mu}$ and the obtained cross-section uncertainty when fixing the corresponding nuisance parameters to their best-fit values.

In order to evaluate the impact of systematic uncertainties on the sensitivity to CP-violating interactions, the expected pre-fit ΔNLL-curve from the combined analysis is also constructed without systematic uncertainties. Furthermore, the impact of specific uncertainty sources is investigated by excluding all NPs, which arise from the considered uncertainty source. Here it is found, that systematic uncertainties related to jets, the τ_{had}-lepton identification and the statistical uncertainty on the background prediction have the largest impact on the expected sensitivity, while the impact of systematic uncertainties from theoretical sources, the estimation of the fake background and the lepton reconstruction and identification are small. Figure 7.46 shows a comparison of the resulting ΔNLL-curves and the expected pre-fit curve, while the corresponding 68 % and 95 % CL intervals for $\tilde{d}$ are summarized in Table 7.33. It is found, that by excluding all systematic uncertainties, the 68 % (95 %) CL interval is improved by 13 % (42 %) with respect to the expected pre-fit result including all statistical and systematic uncertainties. In particular, the largest impact on the sensitivity to $\tilde{d}$ appears for jet-related uncertainties, where the ΔNLL-curve without these NPs provides an improvement of 7 % (28 %) for the 68 % (95 %) CL interval. A smaller impact is found for statistical uncertainties on the background prediction. Here, the 68 % (95 %) CL interval improves by 5 % (14 %), when the corresponding NPs are not considered. Furthermore, excluding all systematic uncertainties related to the τ_{had}-lepton identification results in a improvement of the 68 % (95 %) CL interval by 3 % (6 %). These results show, that systematic uncertainties clearly impact the sensitivity to CP-violating couplings in the analysis, where the largest decrease in sensitivity appears for the 95 % CL interval for $\tilde{d}$.

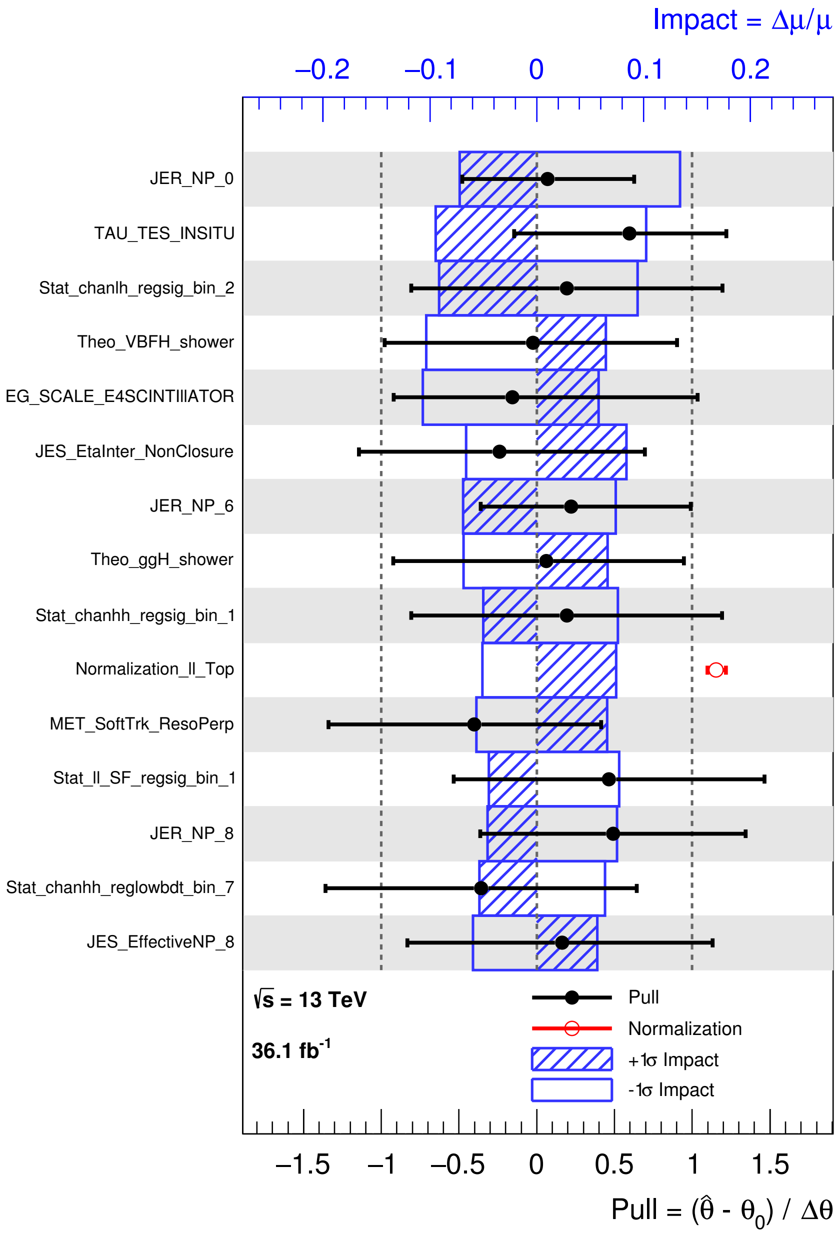

Figure 7.45.: Fractional impact of systematic uncertainties on the measured signal strength (top axis) in the combined fit with the best-fit signal hypothesis of $\hat{\tilde{d}} = -0.01$. The blue boxes show the variation $\Delta\mu$ with respect to the measured value $\hat{\mu}$, when the corresponding nuisance parameter is fixed to its post-fit value shifted by one standard deviation upwards or downwards. In addition, the nuisance parameter post-fit values and uncertainties with respect to the pre-fit values are shown in black (referring to the bottom axis). The value of the background normalization factors and their uncertainties are shown in red and refer to the bottom axis. Only the 15 highest ranked parameters are listed.

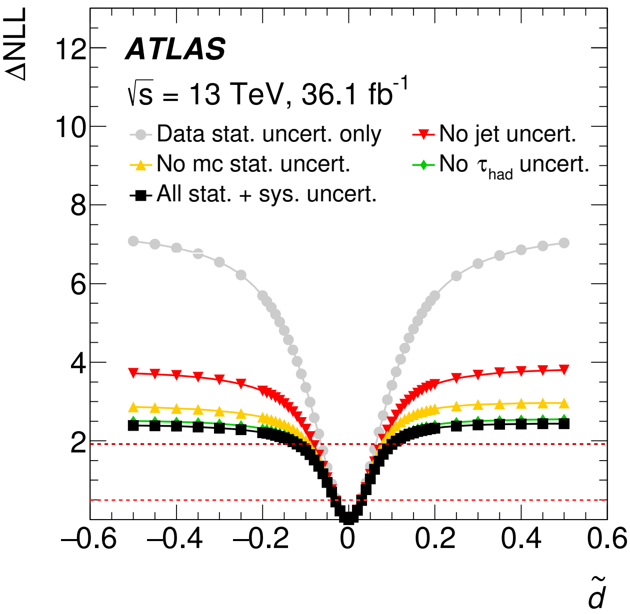

Figure 7.46.: Pre-fit expected ΔNLL-curves comparing the sensitivity of the combined fit with and without systematic uncertainties. In addition, pre-fit expected curves are shown, where systematic uncertainties related to jets, τ_{had}-lepton identification and background statistics are removed from the likelihood function [32].

	68 % CL interval	95 % CL interval
Pre-fit expected	$[-0.033, 0.032]$	$[-0.12, 0.10]$
No systematic uncert.	$[-0.029, 0.028]$	$[-0.06, 0.06]$
No jet uncert.	$[-0.031, 0.030]$	$[-0.08, 0.07]$
No bkg. stat. uncert.	$[-0.032, 0.030]$	$[-0.10, 0.08]$
No τ_{had} uncert.	$[-0.032, 0.031]$	$[-0.11, 0.09]$

Table 7.33.: Comparison of the expected pre-fit exclusion intervals on $\tilde{d}$ and the expected intervals, when all systematic uncertainties are removed from the likelihood function. In addition, the expected intervals are also given, when systematic uncertainties related to jets, the statistical uncertainty on the background prediction and uncertainties on the τ_{had}-lepton identification are removed from the likelihood function.

7.5.3. Comparison to Other Results for CP-Violating HVV Interactions

The results obtained in this analysis can be compared to already existing constraints for CP-violating HVV interactions. While several analysis are based on the measurement of inclusive, simplified and CP-even cross-sections, these results do not yield a direct test of CP invariance and are therefore not considered here. Table 7.34 gives an overview of the results obtained in analyses of the $H \to VV$ decay channel as well as the VBF Higgs-boson production with $H \to \tau\tau$ decays based on data taken in Run 1 and Run 2 with the ATLAS and CMS experiments. Since these measurements differ in their parametrizations of the CP-odd coupling contributions, the results are translated into exclusion limits on $\tilde{d}$ with the relations given in Appendix G.

Analysis			68% CL interval		95% CL interval	
			expected	observed	expected	observed
CMS	H→ VV	R1 (24.8 fb^{-1})	[-1.45, 1.45]	[-0.78, 0.78]	[-2.81, 2.81]	[-1.61, 1.65]
CMS	H→ VV	R1 + R2 (80.2 fb^{-1})	[-0.11, 0.11]	[-0.10, 0.05]	[-0.76, 0.76]	[-1.12, 0.80]
CMS	H→ $\tau\tau$	R2 (35.9 fb^{-1})	[-0.043, 0.043]	[-0.053, 0.078]	[-0.154, 0.154]	N.A.
CMS		combination	[-0.039, 0.039]	[-0.042, 0.042]	[-0.086, 0.086]	[-0.81, 0.30]
ATLAS	H→ VV	R1 (24.8 fb^{-1})	[-1.2, 1.2]*	[-0.1, 1.4]*	[-2.34, 2.34]	[-0.83, 2.20]
ATLAS	H → $\tau\tau$	R1 (20.3 fb^{-1})	[-0.16, 0.16]	[-0.11, 0.05]	N.A.	N.A.
ATLAS	H → $\tau\tau$	R2 (36.1 fb^{-1})	[-0.035, 0.033]	[-0.09, 0.035]	[-0.21, 0.15]	N.A.

Table 7.34.: Comparison of the observed and expected exclusion intervals for $\tilde{d}$ at the 68% and 95% confidence level (CL) based on data taken in Run 1 (R1) and Run 2 (R2). 'N.A.' denotes that the results are not published or no sensitvity was reached. The results for [ ]* are taken from Ref. [246].

The analysis of the $H \to VV$ decay channel based on data taken in Run 1 with the ATLAS experiment exploits a set of one CP-odd and three CP-even observables [28]. Here, the obtained results are comparable to the sensitivity obtained in the same decay channel with the Run 1 dataset of the CMS experiment, where four CP-even and one CP-odd observables are used [247]. In Run 1, the ATLAS experiment also searched for CP violation in the VBF Higgs-boson production mode with subsequent $H \to \tau\tau$ decays [30]. This analysis is based on the CP-odd Optimal Observable and improves the expected 68 % CL interval by factors of 8 and 9 compared to the Run 1 $H \to VV$ results by the ATLAS and CMS experiment, respectively. The sensitivity to CP-violating HVV interactions is further increased by the analysis presented in this thesis, which is based on the Run 2 dataset and also exploits the CP-odd Optimal Observable in the VBF $H \to \tau\tau$ channel [32]. Here, the expected 68 % CL interval is improved by a factor of 4.6 compared to the VBF $H \to \tau\tau$ result based on the Run 1 dataset. In addition, the analysis presented in this thesis improves the sensitivity further by also deriving an expected 95 % CL interval for $\tilde{d}$. The VBF $H \to \tau\tau$ channel is also investigated by the CMS experiment with the Run 2 dataset, where one CP-odd and three CP-even observables are used [248]. The expected 68 % CL interval obtained in this thesis is found to be a factor of 1.3 better compared to the CMS result, while the expected 95 % CL interval of the CMS analysis exceeds the corresponding interval of the ATLAS analysis by a factor of 1.2. The CMS experiment also performs a combination of the results obtained in the VBF $H \rightarrow \tau\tau$ channel and the analysis of $H \rightarrow VV$ decays, which is based on the Run 1 and Run 2 datasets and uses three CP-odd and six CP-even observables [249]. While the analysis presented in this thesis still provides the highest expected sensitivity at the 68 % CL by a factor of 1.15 compared to the CMS combination, this combination improves the expected 95 % CL interval by a factor of 2.1 and results in the most stringent observed constraints on $\tilde{d}$ at both the 68 % CL and 95 % CL. However, while all of these results are based on information from CP-even and CP-odd observables, the analysis presented in this thesis allows to test CP invariance in HVV interactions in a more model-independent way, as it only relies on the CP-odd Optimal Observable.

8 Sensitivity to Different CP-odd Operators

The analysis presented in this chapter investigates the sensitivity of CP-odd observables to different CP-odd operators in the VBF Higgs-boson production mode. For this, the Fisher information matrix is used in order to determine the expected sensitivity to the parameters

$$\begin{aligned} \theta_{B\widetilde{B}} &= \frac{f_{B\widetilde{B}}}{\Lambda^2} \\ \theta_{W\widetilde{W}} &= \frac{f_{W\widetilde{W}}}{\Lambda^2} \end{aligned} \tag{8.1}$$

with the Wilson coefficients $f_{B\widetilde{B}}$ and $f_{W\widetilde{W}}$. As described in Section 2.3, these coefficients allow to parametrize the contribution of additional CP-odd dimension-six operators, $\mathcal{O}_{B\widetilde{B}}$ and $\mathcal{O}_{W\widetilde{W}}$, to the CP-even HVV coupling structure. Hence, non-vanishing values of $\theta_{B\widetilde{B}}$ or $\theta_{W\widetilde{W}}$ correspond to a violation of CP invariance in these interactions. While the maximum sensitivity to the values of $\theta_{B\widetilde{B}}$ or $\theta_{W\widetilde{W}}$ is clearly obtained by exploiting the full phase-space information, this analysis also investigates the information, which is contained in the distribution of the Optimal Observable as defined in Equation 2.63. Since the Optimal Observable includes the full phase-space information for small deviations from the SM, its reach on $\theta_{B\widetilde{B}}$ and $\theta_{W\widetilde{W}}$ is expected to be comparable to the sensitivity provided by the full phase-space information.

The analysis presented here is performed within the MadMiner framework [250]. In total, 500 000 events are generated at leading order for Higgs-boson production in the VBF channel with the SM HVV coupling with MG5_aMC@NLO at $\sqrt{s} = 13\,\text{TeV}$. For this, hadronization is not simulated and the analysis is performed at *parton level* without considering particle reconstruction or detector effects. The predictions for CP-violating HVV interactions ($\theta_{B\widetilde{B}} \neq 0, \theta_{W\widetilde{W}} \neq 0$) are determined by reweighting the SM events based on the operator morphing technique described in Ref. [251]. The events are generated with the NNPDF23LO1 PDF set [167] in a four quark-flavour scheme and the Higgs boson is assumed to be stable since the analysis does not depend on the Higgs-boson decay channel. The kinematic cuts, which are imposed on the final-state partons during the event generation, are summarized in Table 8.1.

In the SM, the VBF production mode of the Higgs boson can be classified at leading order into HWW and HZZ interactions with dominant contributions from $W^{\pm}$-boson mediated diagrams (74 %), while $H\gamma\gamma$ and $HZ\gamma$ interactions can only occur via additional CP-odd contributions.

Variable	Threshold
$p_{T,j_{0,1}}$	$> 20\,\mathrm{GeV}$
$\lvert\eta_{j_{0,1}}\rvert$	< 5.0
$\Delta R_{j_0 j_1}$	> 0.4
$m_{j_0 j_1}$	$> 500\,\mathrm{GeV}$

Table 8.1.: Overview of kinematic cuts, which are applied to the two final-state partons $j_{0,1}$ in the leading-order generation of VBF Higgs-boson production with MG5_aMC@NLO.

As shown in Equation 2.52, additional CP-odd contributions to the SM HWW coupling structure are driven by $\theta_{W\widetilde{W}}$, while $\theta_{B\widetilde{B}}$ only affects Z^0/γ-mediated diagrams. According to Equation 2.55, the relation between $\theta_{B\widetilde{B}}$, $\theta_{W\widetilde{W}}$ and the parameters used in the VBF CP analysis $\tilde{d}$, $\tilde{d}_B$, is given by

$$\begin{aligned} \tilde{d} &= -\frac{m_W^2}{\Lambda^2} f_{W\widetilde{W}} \\ \tilde{d}_B &= -\frac{m_W^2}{\Lambda^2} \tan^2(\theta_W) f_{B\widetilde{B}} \ . \end{aligned} \tag{8.2}$$

Hence, the assumption in the VBF CP analysis of $\tilde{d} = \tilde{d}_B$ corresponds to the choice $\theta_{W\widetilde{W}} = \tan^2(\theta_W)\theta_{B\widetilde{B}}$ with the weak mixing angle θ_W. In this analysis, the impact of $\theta_{B\widetilde{B}}$ and $\theta_{W\widetilde{W}}$ is investigated for parameter values in the range of $[-200, 200]$ and $[-20, 20]$, respectively. These ranges approximately correspond to the measured 68 % confidence level intervals for $\tilde{d}$, which are obtained in the VBF CP analysis (see Section 7.5).

The first part of this chapter gives a brief introduction into the theoretical concept of the Fisher information matrix and describes the procedure to derive optimal exclusion intervals. This is followed by the investigation of the impact of $\theta_{B\widetilde{B}}$ and $\theta_{W\widetilde{W}}$ on the distribution of the Optimal Observable, where also the assumption of $\tilde{d} = \tilde{d}_B$ in the Optimal Observable construction is studied. The last part then presents the expected sensitivity of the VBF Higgs-boson production mode to $\theta_{B\widetilde{B}}$ and $\theta_{W\widetilde{W}}$ from the Fisher information matrix based on the full phase-space information and gives a comparison of the results obtained with the Optimal Observable distribution.

8.1. Fisher Information Matrix

The sensitivity of an experiment to the parameters of the underlying model $\boldsymbol{\theta} = (\theta_0, ..., \theta_N)^T$ can be evaluated with the Fisher information matrix [111,252]. In general, the estimation of the model parameters $\hat{\boldsymbol{\theta}}$ is based on the measurement of an observable set $\boldsymbol{x}$ with probability density functions (PDF) $f(\boldsymbol{x};\boldsymbol{\theta})$. Here, the estimators are distributed around the true parameters according to $g(\hat{\theta}_i;\boldsymbol{\theta})$ with expectation values $\bar{\theta}_i \equiv E[\hat{\theta}_i;\boldsymbol{\theta}]$. The expected precision of the measurement for a combination of parameters (θ_i, θ_j) is then given by the covariance matrix [227] with

$$C_{ij}(\boldsymbol{\theta}) = E[(\hat{\theta}_i - \bar{\theta}_i)(\hat{\theta}_j - \bar{\theta}_j);\boldsymbol{\theta}]. \tag{8.3}$$

The Fisher information matrix allows to determine the experimental reach of the measurement to these model parameters and is given by

$$\mathcal{F}_{ij}(\boldsymbol{\theta}) = -E\Big[\frac{\partial^2 \ln(f(\boldsymbol{x};\boldsymbol{\theta}))}{\partial\theta_i \partial\theta_j};\boldsymbol{\theta}\Big]. \tag{8.4}$$

Large entries in this matrix correspond to directions in the parameter space, where the measurement provides a high sensitivity, while eigenvectors with zero eigenvalues indicate blind directions, where no information is contained. According to the Cramér-Rao-Fréchet bound [227], the inverse of the Fisher information matrix under the assumption of non-biased estimators $E[\hat{\theta}_i] - \theta_i = 0$ corresponds to the smallest achievable uncertainty of a measurement

$$(\mathcal{F}^{-1})_{ij}(\boldsymbol{\theta}) \leq C_{ij}(\boldsymbol{\theta}) \tag{8.5}$$

and therefore allows to determine the maximum amount of provided information on the model parameters. The functional form of $f(\boldsymbol{x};\boldsymbol{\theta})$ can be determined with MC simulation and represents the probability for a single event to populate the phase-space point $\boldsymbol{x}$. Integrating over the entire phase space then results in the minimum covariance matrix, which is achievable with this measurement. In addition, $\boldsymbol{x}$ can be replaced by a set of kinematic variables, which allows to compare the information contained in a specific observable to the maximum sensitivity from the full phase-space information.

In order to determine the probability of measuring $\hat{\boldsymbol{\theta}} = \boldsymbol{\theta}_b$ given the true values $\boldsymbol{\theta}$, the Fisher information matrix is used to define a local distance in the model parameter space of

$$d(\boldsymbol{\theta}_b;\boldsymbol{\theta}) = \sqrt{(\boldsymbol{\theta}-\boldsymbol{\theta}_b)_i \mathcal{F}_{ij}(\boldsymbol{\theta})(\boldsymbol{\theta}-\boldsymbol{\theta}_b)_j}. \tag{8.6}$$

For small differences $\Delta\boldsymbol{\theta} = \boldsymbol{\theta} - \boldsymbol{\theta}_b$, this local distance approximates the expected log-likelihood ratio between $\boldsymbol{\theta}_b$ and $\boldsymbol{\theta}$ assuming non-biased estimators and can be translated into an expected p-value for excluding $\boldsymbol{\theta}_b$ if $\boldsymbol{\theta}$ is true. In this analysis, the local distance is used to calculate expected confidence intervals (CIs) on the combined measurement of $\theta_{B\widetilde{B}}$ and $\theta_{W\widetilde{W}}$ in the VBF Higgs-boson production mode for the assumption, that the true values correspond to the SM: $\boldsymbol{\theta}_{SM} = (0,0)^T$. Here, the expected 68 % confidence level (CL) contours for two parameters are obtained with local distances of $d(\boldsymbol{\theta}_b;\boldsymbol{\theta}) = 1.509$.

8.2. Impact of $\mathcal{O}_{B\widetilde{B}}$ and $\mathcal{O}_{W\widetilde{W}}$ on CP-odd Observables

The distribution of the Optimal Observable is shown in Figure 8.1 for the SM coupling ($\theta_{B\widetilde{B}} = 0,\ \theta_{W\widetilde{W}} = 0$) and for different CP-violating scenarios. Here, the CP-odd contributions only arise either from $\theta_{B\widetilde{B}}$ or $\theta_{W\widetilde{W}}$, while the other parameter is fixed to zero. As expected, non-vanishing values for $\theta_{B\widetilde{B}}$ or $\theta_{W\widetilde{W}}$ result in an asymmetric distribution, which is shifted to positive (negative) values for negative (positive) $\theta_{B\widetilde{B}}$ and $\theta_{W\widetilde{W}}$ values. This asymmetry can also be quantified in terms of the expectation value of the Optimal Observable distribution depending on the parameter values, which is shown in Figure 8.2. As expected, the symmetric distribution for the SM coupling provides an expectation value, which is consistent with zero, while CP-violating scenarios correspond to deviations of the expectation values from zero. In addition, small deviations from the SM show a linear dependency of the expectation value on $\theta_{B\widetilde{B}}$ and $\theta_{W\widetilde{W}}$, while for larger parameter values the sensitivity to the CP-odd contribution decreases and the expectation value will eventually approach zero again. In order to compare the sensitivity of the Optimal Observable to $\theta_{B\widetilde{B}}$ and $\theta_{W\widetilde{W}}$, a linear fit is performed in the distribution of the expectation values shown in Figure 8.2. In particular, the slope of the linear function provides a measure of the sensitivity to CP-violating effects for small deviations from the SM. For this, the respective fits are performed in ranges of $\theta_{B\widetilde{B}} \in [-80, 80]$ and $\theta_{W\widetilde{W}} \in [-8, 8]$. As shown in Table 8.2, non-vanishing values of $\theta_{B\widetilde{B}}$ result in a slope of the expectation values, which is a factor of 0.05 smaller compared to $\theta_{W\widetilde{W}}$. Therefore, the Optimal Observable is clearly found to be more sensitive to CP-violating effects originating from $\theta_{W\widetilde{W}}$ under the assumption of similar uncertainties on the expectation values for both cases.

The sensitivity of the Optimal Observable can also be compared to the widely used CP-odd observable $\Delta\Phi_{jj}^{sign}$ [103], which is defined as the signed azimuthal-angle difference between the outgoing partons found in the positive (+) and in the negative (−) detector hemis-sphere:

$$\Delta\Phi_{jj}^{sign} = \Phi^{+} - \Phi^{-} \tag{8.7}$$

Figure 8.3 shows the $\Delta\Phi_{jj}^{sign}$ distribution for the SM coupling and different CP-violating scenarios. While the SM coupling provides a symmetric distribution, non-vanishing values of $\theta_{B\widetilde{B}}$ and $\theta_{W\widetilde{W}}$ result in a clear asymmetry towards positive (negative) values for negative (positive) $\theta_{B\widetilde{B}}$ and $\theta_{W\widetilde{W}}$ values. The dependency of the $\Delta\Phi_{jj}^{sign}$ expectation value on $\theta_{B\widetilde{B}}$ and $\theta_{W\widetilde{W}}$ is shown in Figure 8.4 and the resulting slopes from the linear fit are summarized in Table 8.2. Compared to the Optimal Observable, the $\Delta\Phi_{jj}^{sign}$ distribution provides a lower sensitivity for both parameters. This is expected, since the information contained in $\Delta\Phi_{jj}^{sign}$ is restrict to the outgoing partons, while the Optimal Observable includes information about the full multi-dimensional phase-space for small deviations from the SM. In particular, the slopes of the $\Delta\Phi_{jj}^{sign}$ expectation values depending on the values of $\theta_{B\widetilde{B}}$ and $\theta_{W\widetilde{W}}$ are found to be smaller by factors of 0.21 and 0.25, respectively, compared to the results obtained with the Optimal Observable. The sensitivity of $\Delta\Phi_{jj}^{sign}$ on $\theta_{B\widetilde{B}}$ is also found to be lower compared to $\theta_{W\widetilde{W}}$, where the corresponding slopes differ by a factor of 0.05.

As described in Section 2.4.2, the default construction of the Optimal Observable corresponds to the assumption $\tilde{d} = \tilde{d}_B$ in order to account for the indistinguishability of the different HVV contributions in the VBF Higgs-boson production mode. In order to study the impact of this assumption, the Optimal Observable is also calculated with $\tilde{d} = 1, \tilde{d}_B = 0$ ($OO_{\tilde{d}}$) and $\tilde{d} = 0, \tilde{d}_B = 1$ ($OO_{\tilde{d}_B}$) and the distributions are shown in Figure 8.5 and 8.6, respectively. In general, the distributions of $OO_{\tilde{d}}$ are found to be similar compared to the default Optimal Observable construction with $\tilde{d} = \tilde{d}_B = 1$. On the other hand, larger differences are observed for $OO_{\tilde{d}_B}$, where the distributions appear to be more narrow compared to the default Optimal Observable construction. The deviations of the expectation values of $OO_{\tilde{d}}$ and $OO_{\tilde{d}_B}$ depending on $\theta_{B\widetilde{B}}$ and $\theta_{W\widetilde{W}}$ are shown in Figure 8.7 and 8.8, respectively. The results of the linear fit for the corresponding slopes are given in Table 8.2. Compared to the default Optimal Observable construction, both $OO_{\tilde{d}}$ and $OO_{\tilde{d}_B}$ provide a lower sensitivity to $\theta_{B\widetilde{B}}$ and $\theta_{W\widetilde{W}}$. However, this sensitivity decrease is clearly driven by the underlying choice of $\tilde{d}$ and $\tilde{d}_B$. In particular, the slope of the expectations values from the $OO_{\tilde{d}}$ distribution for $\theta_{B\widetilde{B}}$ is found to be smaller by a factor of 0.38 compared to the default choice, while the slope depending on $\theta_{W\widetilde{W}}$ only decreases by a factor of 0.90. On the other hand, the sensitivity of $OO_{\tilde{d}_B}$ on $\theta_{B\widetilde{B}}$ is similar compared to the information contained in the default Optimal Observable, where the slope only decreases by a factor of 0.91. Depending on $\theta_{W\widetilde{W}}$, the slope of the expectation values for $OO_{\tilde{d}_B}$ is smaller by a factor of 0.10 compared to the default Optimal Observable construction.

	$a \cdot 10^{-3}$	
Variable	Parameter = $\theta_{B\widetilde{B}}$	Parameter = $\theta_{W\widetilde{W}}$
Optimal Observable	-7.98 ± 0.08	-148.4 ± 0.8
Optimal Observable ($\tilde{d} = 1, \tilde{d}_B = 0$)	-2.78 ± 0.03	-133.6 ± 0.7
OptimalObservable ($\tilde{d} = 0, \tilde{d}_B = 1$)	-7.31 ± 0.01	-14.8 ± 0.1
$\Delta\Phi_{jj}^{sign}$	-1.69 ± 0.02	-37.4 ± 0.2

Table 8.2.: Comparison of slopes a from a linear fit of ($a\cdot$parameter$+b$) to the distribution of the variable expectation values as a function of $\theta_{B\widetilde{B}}$ and $\theta_{W\widetilde{W}}$. The linear fits are performed for small deviations from the SM corresponding to ranges of $\theta_{B\widetilde{B}} \in [-80, 80]$ and $\theta_{W\widetilde{W}} \in [-8, 8]$. Only statistical uncertainties arising from the limited number of simulated events are considered.

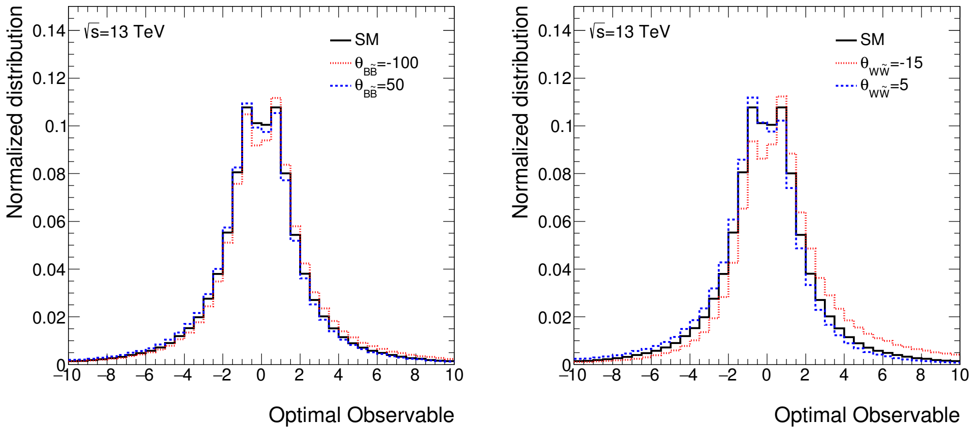

(a) (b)

Figure 8.1.: Impact of the CP-odd model parameters $\theta_{B\widetilde{B}}$ (a) and $\theta_{W\widetilde{W}}$ (b) on the Optimal Observable distribution for Higgs-boson production in the VBF channel at leading order. Only one parameter is varied, while the other one is fixed to zero. The distributions are normalized to unit area and only statistical uncertainties arising from the limited number of simulated events are shown.

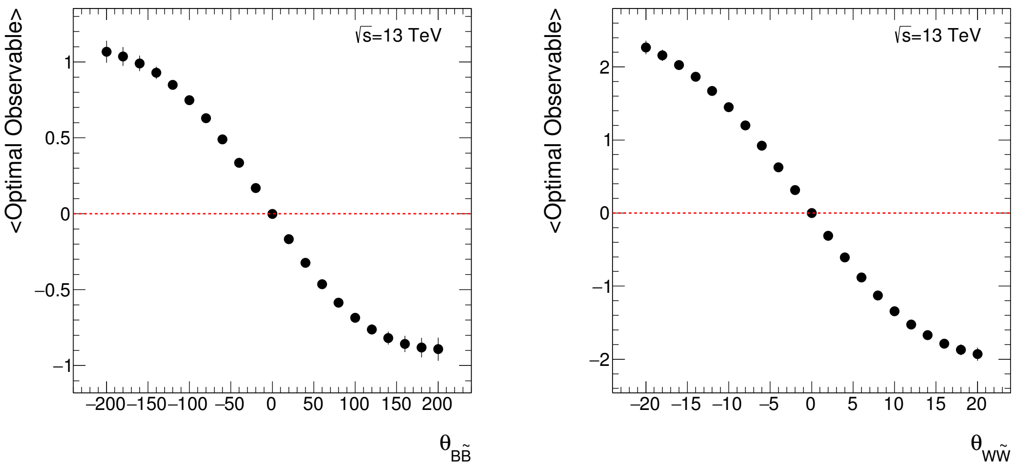

(a) (b)

Figure 8.2.: Expectation values of the Optimal Observable depending on $\theta_{B\widetilde{B}}$ (a) and $\theta_{W\widetilde{W}}$ (b) for Higgs-boson production in the VBF channel at leading order. Only statistical uncertainties arising from the limited number of simulated events are considered.

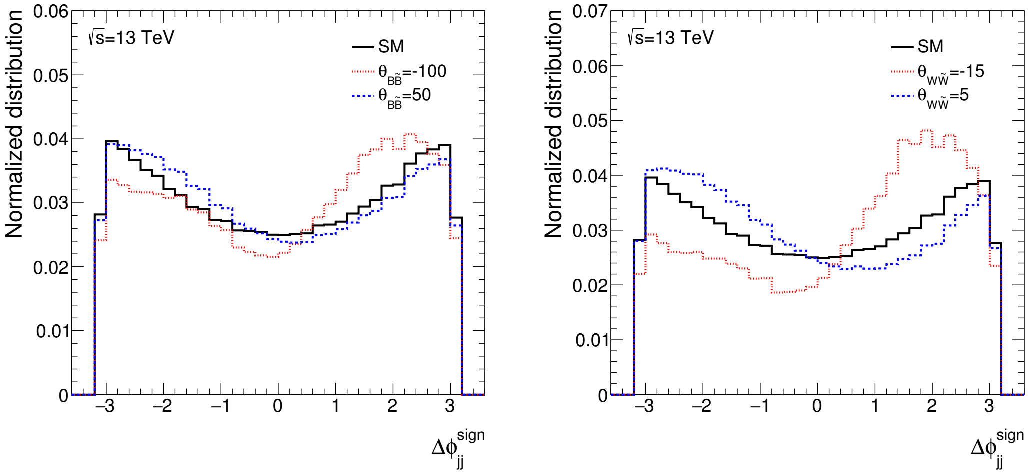

(a) (b)

Figure 8.3.: Impact of the CP-odd parameters $\theta_{B\widetilde{B}}$ (a) and $\theta_{W\widetilde{W}}$ (b) on the $\Delta\Phi_{jj}^{sign}$ distribution for Higgs-boson production in the VBF channel at leading order. Only one parameter is varied, while the other one is fixed to zero. The distributions are normalized to unit area and only statistical uncertainties arising from the limited number of simulated events are shown.

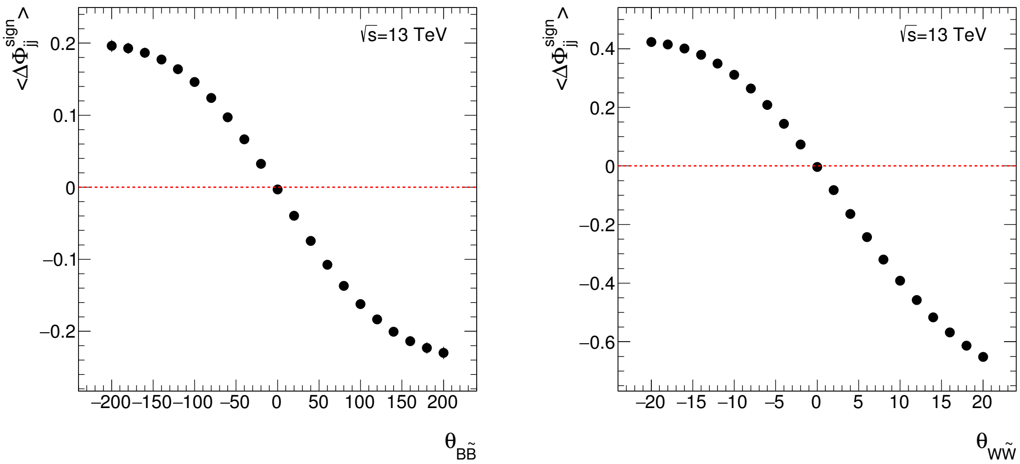

(a) (b)

Figure 8.4.: Expectation values of $\Delta\Phi_{jj}^{sign}$ depending on $\theta_{B\widetilde{B}}$ (a) and $\theta_{W\widetilde{W}}$ (b) on parton level for Higgs-boson production in the VBF channel at leading order. Only statistical uncertainties arising from the limited number of simulated events are considered.

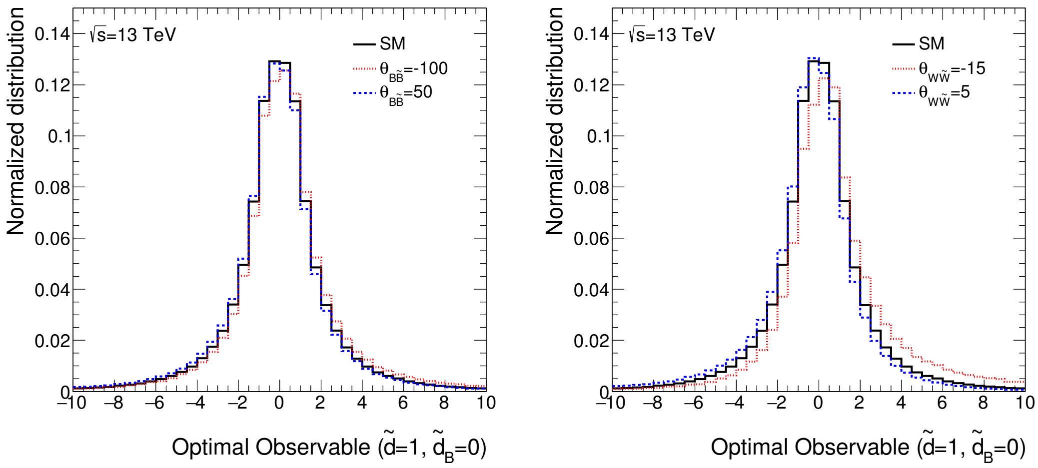

(a) (b)

Figure 8.5.: Impact of the CP-odd parameters $\theta_{B\widetilde{B}}$ (a) and $\theta_{W\widetilde{W}}$ (b) on the Optimal Observable distribution constructed with $\tilde{d} = 1$ and $\tilde{d}_B = 0$ for Higgs-boson production in the VBF channel at leading order. Only one parameter is varied, while the other one is fixed to zero. The distributions are normalized to unit area and only statistical uncertainties arising from the limited number of simulated events are shown.

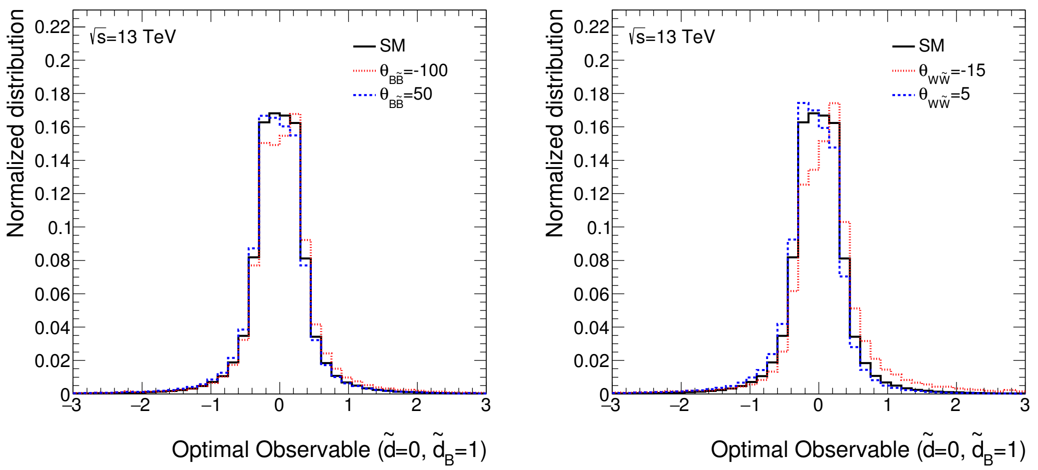

(a) (b)

Figure 8.6.: Impact of the CP-odd parameters $\theta_{B\widetilde{B}}$ (a) and $\theta_{W\widetilde{W}}$ (b) on the Optimal Observable distribution onstructed with $\tilde{d} = 0$ and $\tilde{d}_B = 1$ for Higgs-boson production in the VBF channel at leading order. Only one parameter is varied, while the other one is fixed to zero. The distributions are normalized to unit area and only statistical uncertainties arising from the limited number of simulated events are considered.

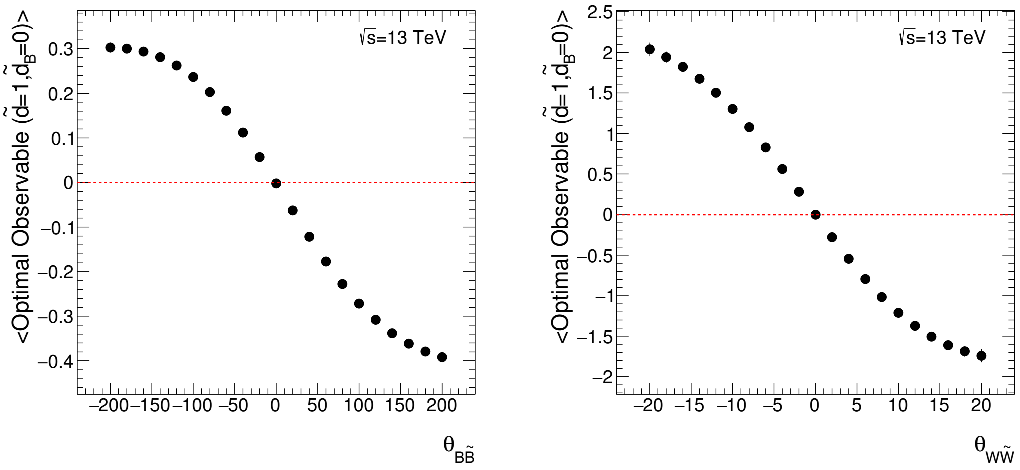

(a) (b)

Figure 8.7.: Expectation values of the Optimal Observable constructed with $\tilde{d} = 1$, $\tilde{d}_B = 0$ depending on $\theta_{B\widetilde{B}}$ (a) and $\theta_{W\widetilde{W}}$ (b) on parton level for Higgs-boson production in the VBF channel at leading order. Only statistical uncertainties arising from the limited number of simulated events are considered.

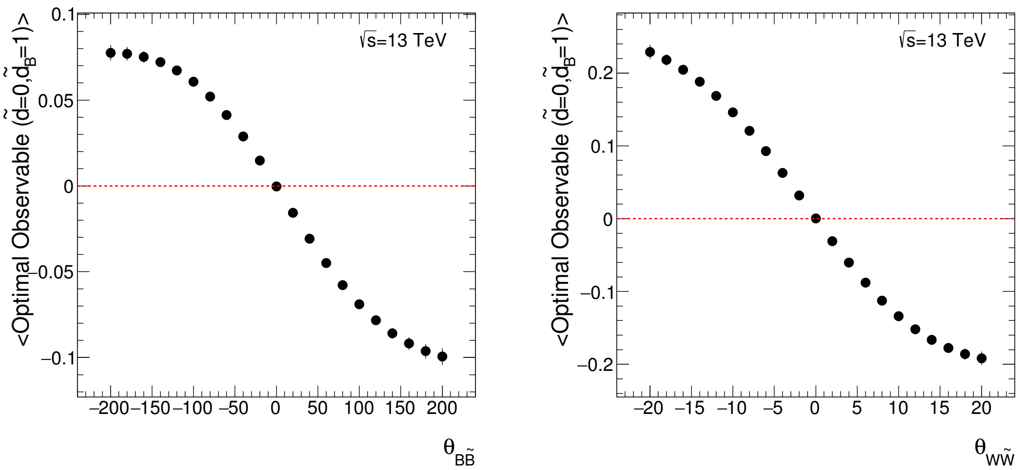

(a) (b)

Figure 8.8.: Expectation values of the Optimal Observable constructed with $\tilde{d} = 0$, $\tilde{d}_B = 1$ depending on $\theta_{B\widetilde{B}}$ (a) and $\theta_{W\widetilde{W}}$ (b) on parton level for Higgs-boson production in the VBF channel at leading order. Only statistical uncertainties arising from the limited number of simulated events are considered.

8.3. Expected Sensitivity on $\mathcal{O}_{B\widetilde{B}}$ and $\mathcal{O}_{W\widetilde{W}}$

In order to investigate the sensitivity of the VBF Higgs-boson production channel to CP-violating contributions from the CP-odd operators $\mathcal{O}_{B\widetilde{B}}$ and $\mathcal{O}_{W\widetilde{W}}$, the Fisher information matrix is evaluated for the SM prediction of $\boldsymbol{\theta}_{SM} = (0,0)^T$ assuming an integrated luminosity of $100\,\text{fb}^{-1}$. The standard deviations of $\theta_{B\widetilde{B}}$ and $\theta_{W\widetilde{W}}$ are then determined from the inverse Fisher information matrix, which corresponds to the covariance matrix according to Equation 8.5. Exploiting the full phase-space information allows to determine the maximum reach on $\theta_{B\widetilde{B}}$ and $\theta_{W\widetilde{W}}$ and corresponds to the following inverse of the Fisher information matrix:

$$\mathcal{F}^{-1}_{full}(\boldsymbol{\theta}_{SM}) = \begin{pmatrix} 23.3 & -0.021 \\ -0.021 & 0.0034 \end{pmatrix} \tag{8.8}$$

The standard deviations of $\theta_{B\widetilde{B}}$ and $\theta_{W\widetilde{W}}$ are summarized in Table 8.3 and Figure 8.9 shows the expected 68 % CL contours. It is found, that the VBF Higgs-boson production channel is most sensitive to $\theta_{W\widetilde{W}}$, while the information on $\theta_{B\widetilde{B}}$ from the Z^0/γ-mediated diagrams appears to be smaller. In particular, the standard deviation of $\theta_{B\widetilde{B}}$ is about two orders of magnitude larger compared to $\theta_{W\widetilde{W}}$.

Furthermore, this maximum achievable sensitivity is compared to the information provided by the one-dimensional distributions of the Optimal Observable and $\Delta\Phi_{jj}^{sign}$. For the Optimal Observable, 100 bins in the range of $[-10, 10]$ are used and the $\Delta\Phi_{jj}^{sign}$ distribution is based on 100 bins in the range of $[-\pi, \pi]$. This binning choice allows to retain as much information as possible on the shape of the distributions, while avoiding large statistical fluctuations per bin due to the limited number of simulated events. The inverse of the Fisher information matrix for the Optimal Observable is found to be

$$\mathcal{F}^{-1}_{OO}(\boldsymbol{\theta}_{SM}) = \begin{pmatrix} 592.6 & -0.34 \\ -0.34 & 0.0044 \end{pmatrix} \tag{8.9}$$

and the $\Delta\Phi_{jj}^{sign}$ distribution leads to the following inverse of the Fisher information matrix:

$$\mathcal{F}^{-1}_{\Delta\Phi_{jj}^{sign}}(\boldsymbol{\theta}_{SM}) = \begin{pmatrix} 3323.8 & -6.7 \\ -6.7 & 0.023 \end{pmatrix}. \tag{8.10}$$

The expected 68 % CL contours for both the Optimal Observable and $\Delta\Phi_{jj}^{sign}$ are shown in Figure 8.9 and Table 8.3 summarizes the corresponding standard deviations. As expected, the Optimal Observable is found to provide more information on both $\theta_{B\widetilde{B}}$ and $\theta_{W\widetilde{W}}$ compared to $\Delta\Phi_{jj}^{sign}$, where the corresponding standard deviations are smaller by factors of 2.4 and 2.3, respectively. However, compared to the full phase-space information, the sensitivity of the Optimal Observable to $\theta_{B\widetilde{B}}$ is decreased by a factor of 5, while the sensitivity to $\theta_{W\widetilde{W}}$ only decreases by a factor of 1.1.

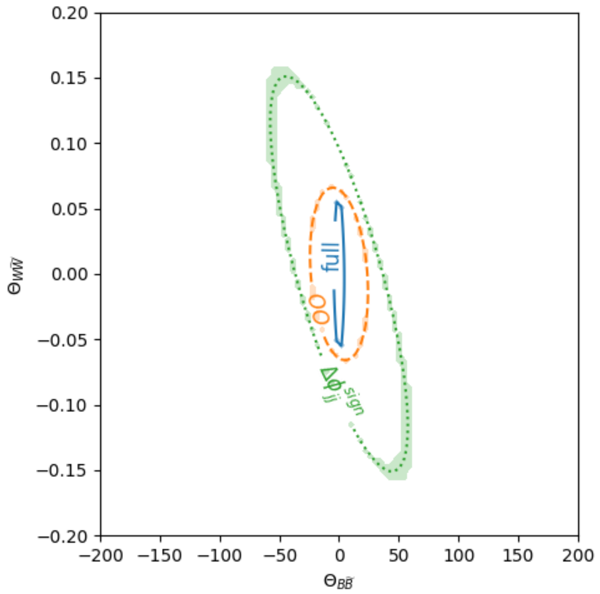

Figure 8.9.: Expected 68 % CL contours for $\theta_{B\widetilde{B}}$ and $\theta_{W\widetilde{W}}$ assuming an integrated luminosity of 100 fb^{-1}. The Fisher information matrix is evaluated with the full phase-space information (blue), the Optimal Observable distribution (orange) and the $\Delta\Phi_{jj}^{sign}$ distribution (green) for the SM expectation ($\theta_{B\widetilde{B}} = \theta_{W\widetilde{W}} = 0$). Only statistical uncertainties arising from the limited number of simulated events are considered.

In order to investigate the impact of the assumption $\tilde{d} = \tilde{d}_B$ in the Optimal Observable construction, the observable is also calculated with two alternative settings of $\tilde{d} = 1, \tilde{d}_B = 0$ ($OO_{\tilde{d}}$) and $\tilde{d} = 0, \tilde{d}_B = 1$ ($OO_{\tilde{d}_B}$). While for the $OO_{\tilde{d}}$ distribution the same binning as the default Optimal Observable is used, the distribution of $OO_{\tilde{d}_B}$ is based on 100 bins with a restricted range of $[-1, 1]$ and the following results are obtained:

$$\mathcal{F}^{-1}_{OO_{\tilde{d}}}(\boldsymbol{\theta}_{SM}) = \begin{pmatrix} 510.3 & -0.31 \\ -0.31 & 0.0042 \end{pmatrix} \tag{8.11}$$

$$\mathcal{F}^{-1}_{OO_{\tilde{d}_B}}(\boldsymbol{\theta}_{SM}) = \begin{pmatrix} 1718.9 & -1.3 \\ -1.3 & 0.0077 \end{pmatrix} \tag{8.12}$$

The corresponding standard deviations on $\theta_{B\widetilde{B}}$ and $\theta_{W\widetilde{W}}$ are summarized in Table 8.3 and Figure 8.10 shows a comparison of the expected 68 % CL contours for $OO_{\tilde{d}}$, $OO_{\tilde{d}_B}$ and the default Optimal Observable. Here, the sensitivity provided by $OO_{\tilde{d}}$ is found to be slightly enhanced compared to the results obtained with the default Optimal Observable, where the standard deviations on $\theta_{B\widetilde{B}}$ and $\theta_{W\widetilde{W}}$ only decrease by factors of 1.1 and 1.04, respectively. On the other hand, the sensitivity provided by $OO_{\tilde{d}_B}$ appears to be limited for both parameters. Here, the standard deviations on $\theta_{B\widetilde{B}}$ and $\theta_{W\widetilde{W}}$ are larger by factors of 1.7 and 1.3, respectively, compared to the default Optimal Observable.

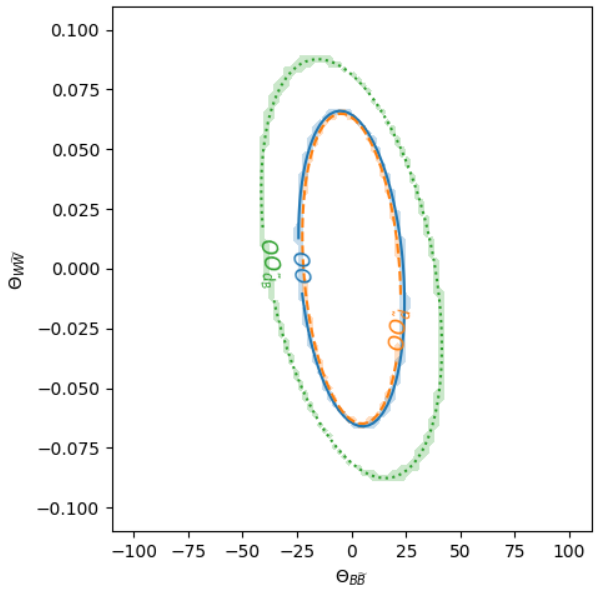

Figure 8.10.: Expected 68 % CL contours for $\theta_{B\widetilde{B}}$ and $\theta_{W\widetilde{W}}$ assuming an integrated luminosity of $100\,\mathrm{fb}^{-1}$. The Fisher information matrix is evaluated with the Optimal Observable distribution constructed with the default choice of $\tilde{d} = \tilde{d}_B = 1$ (blue) and two alternative choices of $\tilde{d} = 1, \tilde{d}_B = 0$ (orange) and $\tilde{d} = 0, \tilde{d}_B = 1$ (green) for the SM expectation ($\theta_{B\widetilde{B}} = \theta_{W\widetilde{W}} = 0$). Only statistical uncertainties arising from the limited number of simulated events are considered.

In addition to these one-dimensional distributions, the Fisher information matrix is also evaluated with two-dimensional histograms of $OO_{\tilde{d}}$ and $OO_{\tilde{d}_B}$. Based on the same binning choices as described above, the following result is obtained:

$$\mathcal{F}^{-1}_{OO_{\tilde{d}},OO_{\tilde{d}_B}}(\boldsymbol{\theta}_{SM}) = \begin{pmatrix} 59.63 & -0.033 \\ -0.033 & 0.0039 \end{pmatrix} \tag{8.13}$$

The corresponding standard deviations on $\theta_{B\widetilde{B}}$ and $\theta_{W\widetilde{W}}$ are summarized in Table 8.3 and Figure 8.11 shows a comparison of the expected 68 % CL contours from the two-dimensional distribution, the default one-dimensional Optimal Observable distribution and the full phase-space information. It is found, that the combination of $OO_{\tilde{d}}$ and $OO_{\tilde{d}_B}$ clearly improves the sensitivity on $\theta_{B\widetilde{B}}$, where the corresponding standard deviation decreases by a factor of 3.2 compared to the result obtained with the default Optimal Observable distribution. On the other hand, the reach on $\theta_{W\widetilde{W}}$ is only slightly enhanced. However, this sensitivity is still limited compared to the reach obtained with the full phase-space information. In particular, the standard deviations of $\theta_{B\widetilde{B}}$ and $\theta_{W\widetilde{W}}$ from the two-dimensional distribution are larger by factors of 1.5 and 1.04, respectively, compared to the results with the full phase-space information. In order to investigate, if this difference is caused by the limited number of bins in the Optimal Observable distributions, this number is increased to 500 bins for both $OO_{\tilde{d}}$ and $OO_{\tilde{d}_B}$. With this, the following inverse

Fisher information matrix is obtained:

$$\mathcal{F}^{-1}_{OO_{\tilde{d}},OO_{\tilde{d}_B}\text{fine}}(\boldsymbol{\theta}_{SM}) = \begin{pmatrix} 45.5 & -0.025 \\ -0.025 & 0.0039 \end{pmatrix} \tag{8.14}$$

As shown in Table 8.3, increasing the number of bins improves the sensitivity to $\theta_{B\widetilde{B}}$ by a factor of 1.15 compared to the coarser binning choice, while the impact on the sensitivity to $\theta_{W\widetilde{W}}$ appears to be negligible. With this binning choice, the sensitivity provided by the two-dimensional distribution of $OO_{\tilde{d}}$ and $OO_{\tilde{d}_B}$ is similar compared to the results obtained with the full phase-space information, where the standard devations of $\theta_{B\widetilde{B}}$ and $\theta_{W\widetilde{W}}$ are larger by factors of 1.3 and 1.04, respectively. However, increasing the number of bins also enhances the statistical uncertainty on the predicted event yield in each bin, which can limit the sensitivity to the parameters as well. This assesement is in particular challenging for analyses, which suffer from limited statistics for signal or background processes in certain phase-space regions, as discussed in Chapter 7 for the VBF CP $H \to \tau\tau$ analysis in the $\tau_{lep}\tau_{lep}$ final state.

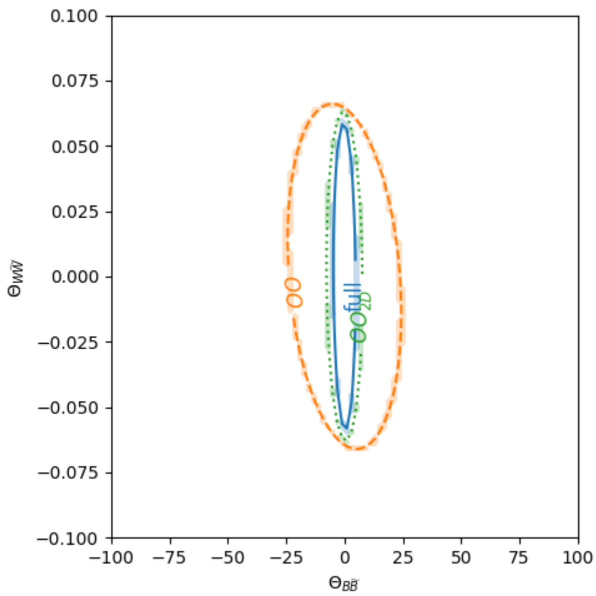

Figure 8.11.: Expected 68 % CL contours for $\theta_{B\widetilde{B}}$ and $\theta_{W\widetilde{W}}$ assuming an integrated luminosity of 100 fb^{-1}. The Fisher information matrix is evaluated with the full phase-space information (blue), the one-dimensional Optimal Observable distribution with the default choice of $\tilde{d} = \tilde{d}_B = 1$ (blue) and the two-dimensional distribution combining the Optimal Observables constructed with $\tilde{d} = 1, \tilde{d}_B = 0$ and $\tilde{d} = 0, \tilde{d}_B = 1$ (green) for the SM expectation ($\theta_{B\widetilde{B}} = \theta_{W\widetilde{W}} = 0$). Only statistical uncertainties arising from the limited number of simulated events are considered.

In summary, this analysis indicates, that the VBF Higgs-boson production mode is mostly sensitive to CP-violating effects arising from non-vanishing values of $\theta_{W\widetilde{W}}$, while the reach on $\theta_{B\widetilde{B}}$ is found to be smaller by about two orders of magnitute. In addition, the assumption $\tilde{d} = \tilde{d}_B = 1$ in the Optimal Observable construction only slightly decreases the sensitivity to $\theta_{W\widetilde{W}}$ and $\theta_{B\widetilde{B}}$ compared to the results obtained with the Optimal Observable with $\tilde{d} = 1, \tilde{d}_B = 0$. On the other hand, choosing $\tilde{d} = 0, \tilde{d}_B = 1$ results in a clearly lower sensitivity of the Optimal Observable to both parameters. Compared to the maximum achievable sensitivity provided by the full phase-space information, the two-dimensional distribution of the Optimal Observables constructed with $\tilde{d} = 1, \tilde{d}_B = 0$ and $\tilde{d} = 0, \tilde{d}_B = 1$ is found to yield a similar reach on $\theta_{W\widetilde{W}}$, while the sensitivity on $\theta_{B\widetilde{B}}$ is slightly reduced. This is mainly caused by limitations in the number of Optimal Observable bins in order to reduce the impact from statistical fluctuations due to the limited number of simulated events.

$100\,\text{fb}^{-1}$	$\sigma_{\theta_{B\widetilde{B}}}$	$\sigma_{\theta_{W\widetilde{W}}}$
Full phase-space	4.8	0.058
One-dimensional distributions		
OO ($\tilde{d} = \tilde{d}_B = 1$)	24.3	0.066
$\Delta\Phi_{jj}^{sign}$	57.7	0.151
$OO_{\tilde{d}}$ ($\tilde{d} = 1,\ \tilde{d}_B = 0$)	22.6	0.065
$OO_{\tilde{d}_B}$ ($\tilde{d} = 0,\ \tilde{d}_B = 1$)	41.5	0.088
Two-dimensional distributions		
$OO_{\tilde{d}}$ vs. $OO_{\tilde{d}_B}$	7.7	0.063
$OO_{\tilde{d}}$ vs. $OO_{\tilde{d}_B}$ fine binning	6.7	0.063

Table 8.3.: Expected sensitivity on the CP-odd parameters $\theta_{B\widetilde{B}}$ and $\theta_{W\widetilde{W}}$ in terms of their standard deviation σ from the Fisher information matrix for the SM expectation of $\theta_{B\widetilde{B}} = 0$ and $\theta_{W\widetilde{W}} = 0$. The Fisher information matrix is evaluated with the full phase-space information as well as with one-dimensional and two-dimensional distributions of the Optimal Observable (OO) and $\Delta\Phi_{jj}^{sign}$.

9 Conclusion

This thesis presents the results of the cross-section measurement for Higgs-boson production in the $H \to \tau\tau$ decay channel and provides a test of CP invariance in the vector-boson-fusion production mode of the Higgs boson with subsequent $H \to \tau\tau$ decays. The analyzed dataset corresponds to an integrated luminosity of $36.1\,\mathrm{fb}^{-1}$ and was taken with the ATLAS detector in 2015 and 2016 at a center-of-mass energy of $\sqrt{s} = 13\,\mathrm{TeV}$. The leptonic and hadronic decays of the individual τ-leptons result in three $H \to \tau\tau$ final-state signatures and the work presented in this thesis focuses on the fully-leptonic channel $H \to \tau\tau \to 2\ell 4\nu$. Although this final state occurs with the smallest branching ratio, it profits from highly efficient lepton triggers and lower background contributions from QCD multi-jet production compared to final states with hadronically decaying τ-leptons. The dominant background process corresponds to $Z \to \tau\tau$ decays, which lead to the same final-state signature as the $H \to \tau\tau$ signal and therefore give an irreducible background contribution. In the fully-leptonic final state, additional background contributions arise from $Z \to \ell\ell$ decays, events containing single top-quarks and top-quark pairs and di-boson production. Moreover, QCD multi-jet production and non-prompt leptons from the decay of heavy-flavour quarks, called *fake* leptons, can result in similar final-state signatures as the signal process as well. The predictions of the $H \to \tau\tau$ signal and the $Z \to \tau\tau$, $Z \to \ell\ell$, top-quark and di-boson backgrounds are obtained from simulation, while the fake-lepton background is estimated in a data-driven way. In addition, the total expected yields of the main background contributions from $Z \to \tau\tau$, $Z \to \ell\ell$ and top-quark events are determined directly from data.

The measurement of the Higgs-boson production cross-section in the $H \to \tau\tau$ decay channel is based on the classification of events into categories, which specifically target the dominant Higgs-boson production modes in gluon-fusion (ggF) and vector-boson fusion (VBF) and the $H \to \tau\tau$ signal is extracted with a maximum-likelihood fit in the reconstructed di-τ mass. The analysis of the fully-leptonic $H \to \tau\tau$ final state results in a measured Higgs-boson production cross-section times branching ratio of

$$\hat{\sigma}_{H\to\tau\tau} = 6.76^{+1.45}_{-1.41}\,(\mathrm{stat.})\,^{+2.39}_{-2.40}\,(\mathrm{sys.})\,\mathrm{pb}, \tag{9.1}$$

which is consistent with the SM prediction of $\sigma_{H\to\tau\tau} = 3.56 \pm 0.13\,\mathrm{pb}$ [225] within two standard deviations. The precision of this measurement is limited by systematic uncertainties, where uncertainties related to jets and E_T^{miss} give the dominant contribution. Systematic uncertainties arising from the limited number of simulated background events, particularly in the VBF-enhanced categories, are found to have an important impact on the measurement as well. In the fully-leptonic final state, the $H \to \tau\tau$ signal is observed with a significance of $2.2\,\sigma$ with respect to the background-only hypothesis, while $1.2\,\sigma$ are expected. The combination with the semi-leptonic and fully-hadronic final states results in a measured Higgs-boson production cross-section times branching ratio of

$$\hat{\sigma}_{H\to\tau\tau} = 3.77^{+0.60}_{-0.59}\,(\text{stat.})\,^{+0.87}_{-0.74}\,(\text{sys.})\,\text{pb}. \tag{9.2}$$

This result is consistent with the SM predicition within uncertainties, where systematic uncertainties related to jets, E_T^{miss} and the limited number of simulated background events dominate. The $H \to \tau\tau$ signal is measured with a significance of $4.4\,\sigma$ with respect to the background-only hypothesis, while $4.14\,\sigma$ are expected. This result is combined with the search for $H \to \tau\tau$ decays at $\sqrt{s} = 7\,\text{TeV}$ and $8\,\text{TeV}$ based on datasets of $4.5\,\text{fb}^{-1}$ of $20.3\,\text{fb}^{-1}$, respectively. The combination results in a signal significance of $6.4\,\sigma$, while $5.4\,\sigma$ are expected, and leads to the observation of $H \to \tau\tau$ decays with the ATLAS experiment. Furthermore, the analysis presented in this thesis also measures the individual cross-sections for Higgs-boson production in the dominant ggF and VBF production modes:

$$\begin{aligned}\hat{\sigma}^{ggF}_{H\to\tau\tau} &= 3.1 \pm 1.0\,(\text{stat.})\,^{+1.6}_{-1.3}\,(\text{sys.})\,\text{pb}\\ \hat{\sigma}^{VBF}_{H\to\tau\tau} &= 0.28 \pm 0.09\,(\text{stat.})\,^{+0.11}_{-0.09}\,(\text{sys.})\,\text{pb}.\end{aligned} \tag{9.3}$$

These measurements are consistent with the SM prediction of $\sigma^{ggF}_{H\to\tau\tau} = 3.05 \pm 0.13\,\text{pb}$ and $\sigma^{VBF}_{H\to\tau\tau} = 0.237 \pm 0.006\,\text{pb}$ [225] within uncertainties. While the measurement precision of the ggF production cross-section is limited by systematic uncertainties, the contributions of systematic and statistical uncertainties to the VBF production cross-section are of similar size.

The test of CP invariance in the Higgs-boson interaction with weak gauge-bosons HVV is performed in the VBF production channel with subsequent $H \to \tau\tau$ decays. Here, small CP-odd contributions in addition to the CP-even HVV coupling structure as predicted in the SM correspond to the violation of CP invariance and would imply the presence of new physics beyond the SM. These CP-odd contributions are described by the parameter $\tilde{d}$ in the framework of an effective field theory, where $\tilde{d} = 0$ corresponds to the SM prediction. The $\tilde{d}$-parameter is measured by exploiting the CP-odd Optimal Observable, which combines the information of the multi-dimensional phase space and provides the highest sensitivity for small deviations from the SM. While the analysis follows the cross-section measurement described above to a large extent, the event selection is based on a multivariate approach by using Boosted Decision Trees (BDTs). Events, which are classified as VBF-like, are selected in the signal regions by imposing a lower threshold on the BDT score. This allows to efficiently reject background events, where no Higgs boson is produced, and also reduces the contribution from non-VBF Higgs-boson production, where no CP-violation is expected. In the fully-leptonic final state with two same-flavour (SF) leptons, a signal selection efficiency of 33 % with respect to the inclusive selection is achieved, while only 2 % of the background events satisfy the signal region requirement. In the fully-leptonic final state with two different-flavour (DF) leptons, 26 % of the signal and 1 % of the background processes are accepted for the signal region. The $\tilde{d}$-parameter and its confidence intervals are determined in these signal regions with a negative-logarithmic likelihood curve, which is constructed based on a set of maximum likelihood fits for various HVV coupling scenarios. These likelihood fits only include information on the observable shape and do not exploit the cross-section dependency on $\tilde{d}$ in order to stay as model independent as possible. In the fully-leptonic final state, the measured $\tilde{d}$-value is $\hat{\tilde{d}} = -0.03$ and no confidence intervals on $\tilde{d}$ can be derived. The limited sensitivity is mainly caused by the impact from systematic uncertainties related to jets as well as statistical uncertainties on the limited number of simulated background events. The combination with the semi-leptonic and fully-hadronic final states results in a $\tilde{d}$-value of $\hat{\tilde{d}} = -0.01$ and the following 68 % CL interval for $\tilde{d}$ is obtained:

$$[-0.090, 0.035]. \tag{9.4}$$

This result is consistent with the SM prediction of $\tilde{d} = 0$ and hence no sign of CP violation is observed. The expected sensitivity with respect to the SM hypothesis corresponds to a 68 % CL interval for $\tilde{d}$ of $[-0.035, 0.033]$ and a 95 % CL interval of $[0.21, 0.15]$. No observed 95 % CL interval for $\tilde{d}$ can be quoted, which is mainly caused by an observed downward fluctuation of VBF $H \to \tau\tau$ events with respect to the SM prediction. Moreover, systematic uncertainties related to jets are found to have a significant impact on the sensitivity as well. The analysis also calculates the expectation value of the Optimal Observable to test for CP invariance in a more mode-independent way. The following expectation values are measured in data in the signal regions of all analysis channels:

Channel	⟨Optimal Observable⟩
Fully-leptonic SF	-0.54 $\pm$ 0.72
Fully-leptonic DF	0.71 $\pm$ 0.81
Semi-leptonic	0.74 $\pm$ 0.78
Fully-hadronic	-1.13 ± 0.65

(9.5)

These results are consistent with the SM prediction of an expectation value of zero within statistical uncertainties and hence show no sign of CP-violating HVV interactions.

This thesis also investigates the sensitivity of the VBF Higgs-boson production mode to CP-violating contributions arising from the higher-dimensional CP-odd operators $\mathcal{O}_{B\widetilde{B}}$ and $\mathcal{O}_{W\widetilde{W}}$. Here, the Optimal Observable sensitivity to the Wilson coefficients $f_{B\widetilde{B}}$ and $f_{W\widetilde{W}}$ is investigated based on the Fisher information matrix and compared to the maximum achievable sensitivity provided by the full phase-space information. This analysis is performed on parton level and no background processes or systematic uncertainties are considered. It is found, that the VBF Higgs-boson production mode is mainly sensitive to $f_{W\widetilde{W}}$, which describes CP-violating contributions from $W^{\pm}$-mediated diagrams, while the sensitivity to $f_{B\widetilde{B}}$ is smaller by about two orders of magnitude due to the minor contribution from Z^0/γ^*-mediated diagrams. Furthermore, the Optimal Observable provides a better reach on both $f_{B\widetilde{B}}$ and $f_{W\widetilde{W}}$ by about a factor of two compared to the observable $\Delta\Phi_{jj}^{sign}$, which only contains information on the azimuthal-angle difference between the outgoing jets. It is also shown that by using the Optimal Observable, the analysis can achieve a comparable sensitivity to both $f_{B\widetilde{B}}$ and $f_{W\widetilde{W}}$ as the full-phase space information.

While the work presented in this thesis only exploits a fraction of the total dataset recorded by the ATLAS experiment at $\sqrt{s} = 13$ TeV, the analysis of the full Run 2 dataset with an integrated luminosity of 139 fb^{-1} will further improve the cross-section measurement of Higgs-boson production in the $H \to \tau\tau$ decay channel, as well as the sensitivity to possible CP-violating effects in HVV interactions. However, as both analyses are limited by systematic uncertainties, the improvement of this component is an important task for future studies. In particular, the impact of systematic uncertainties arising from additionally produced jets can be reduced significantly by exploiting data-driven techniques for the estimation of the dominant $Z \to \tau\tau$ background, such as τ-embedding [238]. Furthermore, the statistical uncertainty on the overall background prediction can be improved with advanced filtering techniques in the process of the event generation. This would allow to particularly improve the statistical uncertainty on the $Z \to \ell\ell$ background in the VBF-enriched phase-space. The increased precision of the measurements presented in this thesis will allow to study the SM predictions in more detail and might be a key to search for physics beyond the SM.

A Correlation of BDT Input Variables

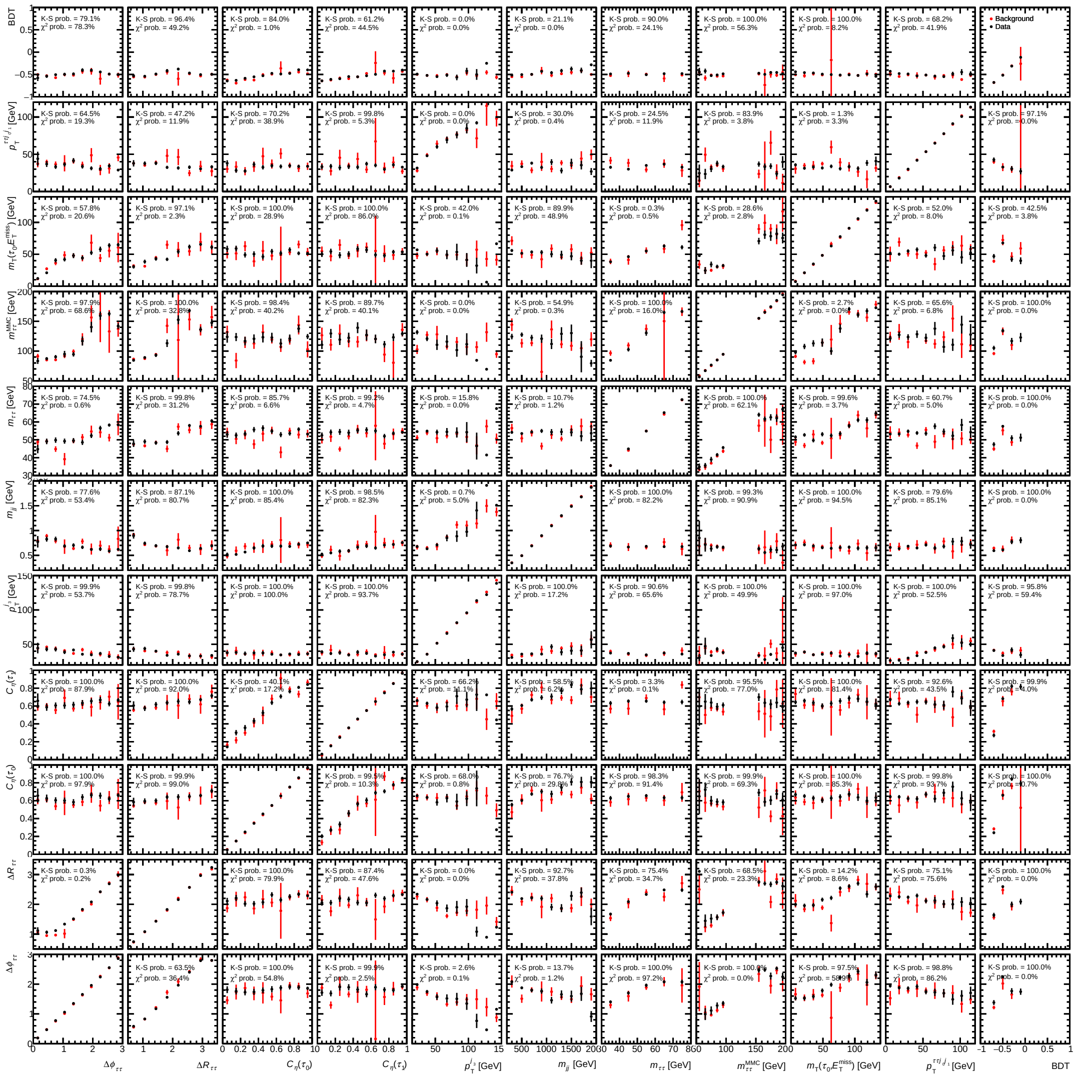

Figure A.1.: Correlation between all input variables used in the $\tau_{lep}\tau_{lep}$ VBF SF BDT and the BDT output for the sum of all backgrounds (red) and data (black). The uncertainties only indicate statistical uncertainties. The blinded bins in the $m_{\tau\tau}^{\mathrm{MMC}}$ and the BDT score distributions are excluded in the calculation of the Kolmogorov-Smirnov (KS) probability.

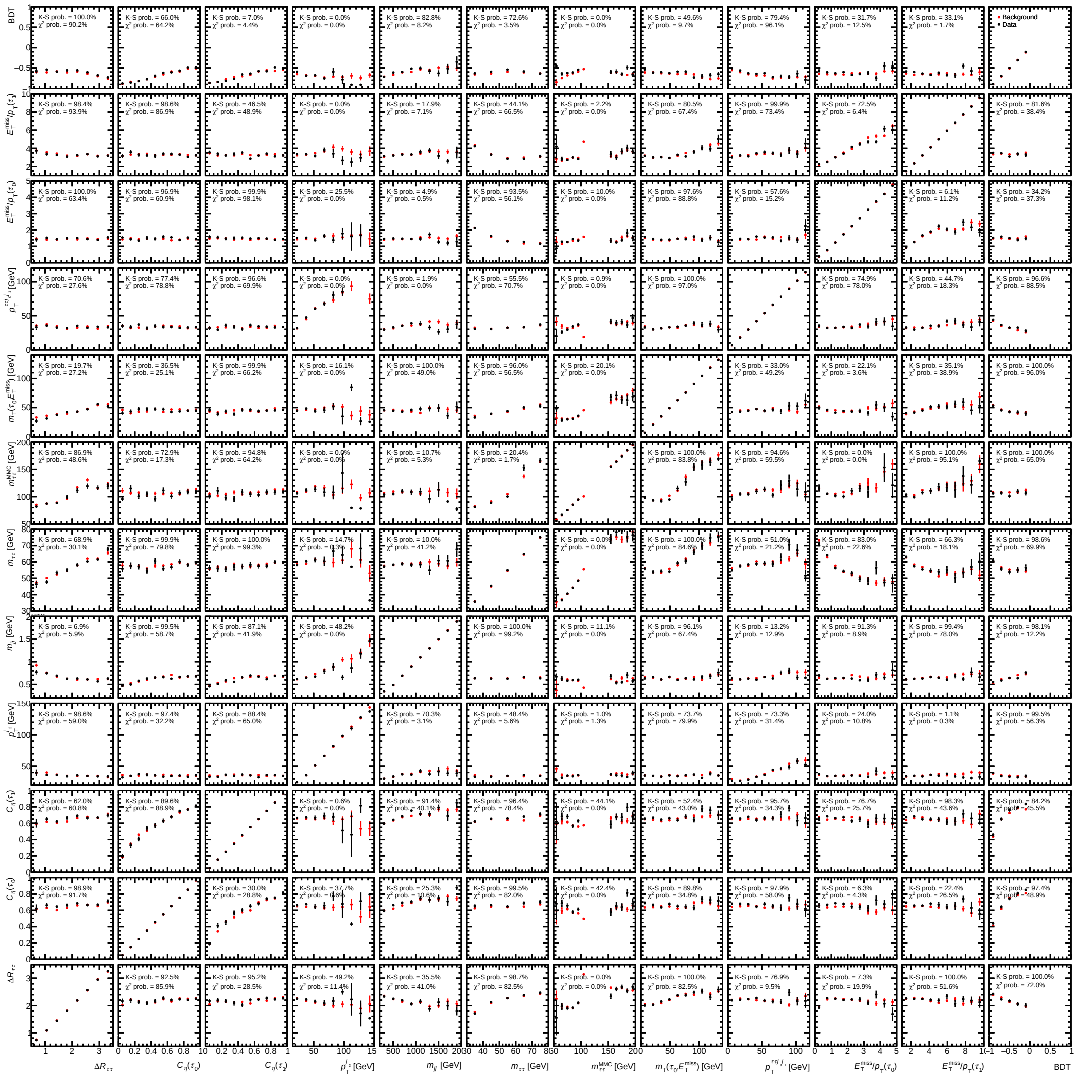

Figure A.2.: Correlation between all input variables used in the $\tau_{lep}\tau_{lep}$ VBF DF BDT and the BDT output for the sum of all backgrounds (red) and data (black). The uncertainties only indicate statistical uncertainties. The blinded bins in the $m_{\tau\tau}^{\mathrm{MMC}}$ and the BDT score distributions are excluded in the calculation of the Kolmogorov-Smirnov (KS) probability.

B Explanation of Nuisance Parameter Names

The following tables give an overview of the nuisance parameters and their corresponding source of uncertainty in the $H \to \tau\tau$ cross-section measurement and the VBF CP analysis.

Theory systematic uncertainty	Short description
Theo_NLO_EW_total	uncertainty on total integrated luminosity
Theo_QCDscale_VBF_total	QCD scale uncertainty on the total VBF production cross section
Theo_QCDscale_VH_total	QCD scale uncertainty on the total VH production cross section
Theo_alphas_Higgs_VBF_total	α_S uncertainty on the total VBF production cross section
Theo_alphas_Higgs_VH_total	α_S uncertainty on the total VH production cross section
Theo_alphas_Higgs_ggH_total	α_S uncertainty on the total ggH production cross section
Theo_pdf_Higgs_VBF_total	PDF uncertainty on the total VBF production cross section
Theo_pdf_Higgs_VH_total	PDF uncertainty on the total VH production cross section
Theo_pdf_Higgs_ggH_total	PDF uncertainty on the total ggH production cross section
Theo_ggH_sig_qcd_[0-8]	LHCHXSWG scheme for perturbative uncertainties on ggH (cross section and acceptance)
Theo_ll_vbf_ggH_jetveto	Jet veto uncertainty for ggH evaluated using the Stewart Tackmann method.
Theo_VBFH_MUR_MUF	QCD scale acceptance uncertainty for VBF
Theo_VH_MUR_MUF	QCD scale acceptance uncertainty for VH
Theo_[ll/lh/hh]_vbf_VBFH_PSUE	Comparison of Pythia8 and Herwig7 for VBF production
Theo_[ll/lh/hh]_vbf_ggH_PSUE	Comparison of Pythia8 and Herwig7 for ggH production
Theo_sig_alphaS	α_S acceptance uncertainty for the signal
Theo_sig_pdf_[0-30]	PDF acceptance uncertainties for the signal (PDF4LHC)
ATLAS_BR_tautau	Branching ratio uncertainty for $H \to \tau\tau$
ATLAS_BR_WW	Branching ratio uncertainty for $H \to WW^*$
ZttTheory_CKK_Relative_VBF ZttTheory_CKK_vbf_[leplep/lephad/hadhad]	jet-to-parton matching uncertainty
ZttTheory_MUR_MUF_Relative_VBF ZttTheory_MUR_MUF_vbf_[leplep/lephad/hadhad]	QCD scale uncertainties
ZttTheory_PDF_Relative_VBF ZttTheory_PDF_vbf_[leplep/lephad/hadhad]	PDF uncertainties
ZttTheory_QSF_Relative_VBF ZttTheory_QSF_vbf_[leplep/lephad/hadhad]	Resummation scale uncertainty
ZttTheory_PS_Relative_VBF ZttTheory_PS_vbf_[leplep/lephad/hadhad]	Parton shower uncertainty, comparison between Sherpa and Madgraph+Pythia8
Z_EWK_proportion	Uncertainty on the EW Z production cross section

Table B.1.: Summary of the theoretical sytematic uncertainties.

Experimental systematic uncertainty	Short description
Luminosity	uncertainty on total integrated luminosity
PRW_DATASF	uncertainty on pileup reweighting
Electrons	
EL_EFF_Trigger_Total_1NPCOR_PLUS_UNCOR	trigger efficiency uncertainty
EL_EFF_Reco_Total_1NPCOR_PLUS_UNCOR	reconstruction efficiency uncertainty
EL_EFF_ID_CorrUncertaintyNP (0 to 14)	ID efficiency uncertainty splits in 15 components
EL_EFF_ID_SIMPLIFIED_UncorrUncertaintyNP (0 to 15)	ID efficiency uncertainty splits in 16 components
EL_EFF_Iso_Total_1NPCOR_PLUS_UNCOR	isolation efficiency uncertainty
EG_SCALE_ALLCORR EG_SCALE_E4SCINTILLATOR EG_SCALE_LARTEMPERATURE_EXTRA[2015—2016]PRE EG_SCALE_LARCALIB_EXTRA[2015—2016]PRE	energy scale uncertainties
EG_RESOLUTION_ALL	energy resolution uncertainty
Muons	
MUON_EFF_Trig[Stat—Syst]Uncertainty	trigger efficiency uncertainty
MUON_EFF_[STAT—SYS]	reconstruction and ID efficiency uncertainty for muons with p_T ¿ 15 GeV
MUON_ISO_[STAT—SYS]	isolation efficiency uncertainty
MUON_TTVA_[STAT—SYS]	track-to-vertex association efficiency uncertainty
MUON_ID	momentum resolution uncertainty from inner detector
MUON_MS	momentum resolution uncertainty from muon system
MUON_SCALE	momentum scale uncertainty
MUON_SAGITTA_RHO MUON_SAGITTA_RESBIAS	charge dependent momentum scale uncertainty
Taus	
TAU_EFF_TRIG_[STATDATA—STATMC—SYST]2015	2015 trigger efficiency uncertainty
TAU_EFF_TRIG_TOTAL2016	2016 trigger efficiency uncertainty
TAU_EFF_ID_[TOTAL—HIGHPT]	ID efficiency uncertainty
TAU_EFF_RECO_[TOTAL—HIGHPT]	reconstruction efficiency uncertainty
TAU_EFF_ELEORL_[TRUEELE—TRUEHADTAU]	overlap removal uncertainty
TAU_TES_DETECTOR	energy scale uncertainty due to modeling of detector geometry
TAU_TES_INSITU	energy scale uncertainty on the measurement in the tag-and-probe analysis
TAU_TES_MODEL	energy scale uncertainty due to the GEANT4 physics list
Jets	
JES_EffectiveNP_[1-8]	energy scale uncertainty from the in situ analyses splits into 8 components
JES_EtaIntercalibration_Modeling	energy scale uncertainty on eta-intercalibration (modeling)
JES_EtaIntercalibration_TotalStat	energy scale uncertainty on eta-intercalibrations (statistics/method)
JES_EtaIntercalibration_NonClosure	energy scale uncertainty on eta-intercalibrations (non-closure)
JES_Pileup_OffsetMu	energy scale uncertainty on pile-up (mu dependent)
JES_Pileup_OffsetNPV	energy scale uncertainty on pile-up (NPV dependent)
JES_Pileup_PtTerm	energy scale uncertainty on pile-up (pt term)
JES_Pileup_RhoTopology	energy scale uncertainty on pile-up (density ρ)
JES_Flavor_Composition	energy scale uncertainty on flavour composition
JES_Flavor_Response	energy scale uncertainty on samples' flavour response
JES_BJES_Response	energy scale uncertainty on b-jets
JES_PunchThrough_MC15	energy scale uncertainty for punch-through jets
JES_SingleParticle_HighPt	energy scale uncertainty from the behaviour of high-p_T jets
JET_JER	11NP energy resolution uncertainty
JET_JVT	JVT efficiency uncertainty
btag_b_[0-2] btag_c_[0-3] btag_light_[0-4]	b-tagging efficiency uncertainties ("BTAG_MEDIUM"): 3 components for b jets, 4 for c jets and 5 for light jets
btag_extrapolation	b-tagging efficiency uncertainty on the extrapolation to high-p_T jets
btag_extrapolation_from_charm	b-tagging efficiency uncertainty on tau jets
MET	
MET_SoftTrk_ResoPara	track-based soft term related longitudinal resolution uncertainty
MET_SoftTrk_ResoPerp	track-based soft term related transverse resolution uncertainty
MET_SoftTrk_Scale	track-based soft term related longitudinal scale uncertainty

Table B.2.: Summary of the experimental systematic uncertainties.

C Impact of Nuisance Parameters in the Control Regions

The following tables summarize the impact of the nuisance parameters on the expected background yields in the control regions of the $H \to \tau\tau$ cross-section measurement and the VBF CP analysis.

C.1. $H \to \tau\tau$ Cross-section Measurement

	$Z \to \tau\tau$	$Z \to \ell\ell$	Top	Di-boson
	VBF $Z \to \ell\ell$ control region			
Electrons				
Scale	–	$+1.5$ / -1.6	$+0.0$ / -2.2	$+0.7$ / -2.2
Resolution	$+8.5$ / -0.0	–	–	–
Efficiency	–	–	–	–
Muons				
Scale	–	–	–	–
Resolution	–	–	$+0.0$ / -2.2	$+0.2$ / -1.0
Efficiency	–	–	–	–
Jets				
JER	$+50.6$ / -57.1	$+25.9$ / -30.2	$+20.4$ / -9.7	$+19.6$ / -13.4
JES	$+47.5$ / -49.0	$+49.2$ / -28.5	$+8.1$ / -5.5	$+19.0$ / -15.6
JVT Efficiency	$+1.0$ / -1.0	–	–	–
b-tagging	$+3.0$ / -2.9	$+1.5$ / -1.5	$+7.6$ / -7.1	$+2.0$ / -2.0
E_T^{miss} soft term				
Resolution	$+13.0$ / -13.0	$+13.9$ / -13.9	$+2.8$ / -2.8	$+2.8$ / -2.8
Scale	$+9.2$ / -0.0	$+6.9$ / -7.1	$+2.5$ / -0.0	$+1.5$ / -0.4
Pile-up rew.	$+38.8$ / -24.7	$+7.3$ / -7.1	$+9.0$ / -0.7	-0.0 / $+2.1$

Table C.1.: Relative impact of experimental systematic uncertainties on the total number of expected background events in the $Z \to \ell\ell$ control region of the VBF category in the $\tau_{\rm lep}\tau_{\rm lep}$ channel. Given is always the up- and downward fluctuation in percent. Variations below 0.1% are ignored.

	$Z \to \tau\tau$	$Z \to \ell\ell$	Top	Di-boson
	Boosted $Z \to \ell\ell$ control region			
Electrons				
Scale	–	+1.2 / −1.7	–	+0.6 / −1.1
Resolution	–	–	–	–
Efficiency	–	–	–	–
Muons				
Scale	+3.3 / −2.5	–	–	–
Resolution	+4.3 / −6.5	–	–	–
Efficiency	–	–	–	–
Jets				
JER	+17.8 / −18.7	+17.3 / −25.8	+15.6 / −3.4	+16.0 / −10.6
JES	+11.8 / −10.9	+23.4 / −20.5	+2.7 / −4.8	+9.3 / −7.2
JVT Efficiency	–	–	–	–
b-tagging	+1.8 / −1.7	+1.8 / −1.8	+14.6 / −13.7	+2.0 / −1.9
E_T^{miss} soft term				
Resolution	+4.1 / −4.1	+12.0 / −12.0	–	+4.1 / −4.1
Scale	–	+8.0 / −8.6	–	+2.3 / −2.8
Pile-up rew.	−4.0 / +3.0	+6.5 / −6.7	−1.3 / +0.4	+1.5 / −1.6

Table C.2.: Relative impact of experimental systematic uncertainties on the total number of expected background events in the $Z \to \ell\ell$ control region of the boosted category in the $\tau_{\mathrm{lep}}\tau_{\mathrm{lep}}$ channel. Given is always the up- and downward fluctuation in percent. Variations below 0.1% are ignored.

	$Z \to \tau\tau$ channel-migration	$Z \to \tau\tau$ region-migration
	VBF $Z \to \ell\ell$ control region	
QCD scale	+0.8 / −0.8	+6.3 / −6.2
PDF	−0.1 / +0.1	−1.8 / +2.1
CKKW	+4.9 / −3.4	+13.5 / −10.5
QSF	+1.3 / −1.4	−4.1 / +4.5
UEPS	−1.5 / +1.5	–
EWK $Zjj, Zjjj$	+4.9 / −4.9	
	Boosted $Z \to \ell\ell$ control region	
QCD scale	+0.8 / −0.6	+5.9 / −5.3
PDF	+0.4 / −0.5	–
CKKW	−4.3 / +3.4	+2.7 / −2.0
QSF	+4.3 / −4.3	−1.1 / +1.2
UEPS	+0.8 / −0.8	–
EWK $Zjj, Zjjj$	+0.3 / −0.3	

Table C.3.: Relative impact of theoretical uncertainties on the expected number of $Z \to \tau\tau$ background events in the $Z \to \ell\ell$ control region of the VBF and boosted category in the $\tau_{lep}\tau_{lep}$ channel. Given is always the up- and downward fluctuation in percent. Variations below 0.1% are ignored.

	$Z \to \tau\tau$	$Z \to \ell\ell$	Top	Di-boson
	VBF Top control region			
Electrons				
Scale	–	–	–	–
Resolution	–	–	–	–
Efficiency	+1.1 / −1.1	–	–	–
Muons				
Scale	–	–	–	–
Resolution	–	+18.1 / −1.5	–	–
Efficiency	–	–	–	–
Jets				
JER	+11.3 / −10.8	+80.0 / −72.6	+4.5 / −4.2	+16.0 / −15.7
JES	+10.1 / −6.7	+59.6 / −51.8	+5.0 / −4.6	+3.8 / −5.9
JVT Efficiency	–	–	–	–
b-tagging	+7.2 / −7.1	+6.6 / −6.4	+1.8 / −1.8	+8.3 / −8.2
E_T^{miss} soft term				
Resolution	+3.0 / −3.0	+12.1 / −12.1	–	+1.1 / −1.1
Scale	–	+6.4 / −18.8	–	–
Pile-up rew.	−8.5 / +3.4	+6.3 / −9.1	−2.3 / +1.2	–

Table C.4.: Relative impact of experimental systematic uncertainties on the total number of expected background events in the Top control region of the VBF boosted category in the $\tau_{\text{lep}}\tau_{\text{lep}}$ channel. Given is always the up- and downward fluctuation in percent. Variations below 0.1% are ignored.

	$Z \to \tau\tau$	$Z \to \ell\ell$	Top	Di-boson
	Boosted Top control region			
Electrons				
Scale	–	+1.1 / −0.4	–	–
Resolution	–	–	–	–
Efficiency	+1.0 / −1.0	–	–	–
Muons				
Scale	–	+1.4 / −0.2	–	–
Resolution	–	+2.0 / −0.7	–	–
Efficiency	–	–	–	–
Jets				
JER	+1.4 / −2.1	+39.1 / −46.1	+1.3 / −0.8	+3.6 / −3.1
JES	+3.9 / −3.5	+25.6 / −20.1	+3.7 / −3.6	+6.3 / −8.2
JVT Efficiency	–	–	–	–
b-tagging	+6.9 / −6.9	+5.8 / −5.7	+1.4 / −1.3	+7.6 / −7.5
E_T^{miss} soft term				
Resolution	+2.0 / −2.0	+4.3 / −4.3	–	–
Scale	–	+4.2 / −8.8	–	–
Pile-up rew.	−1.4 / +0.7	+7.6 / −7.0	−1.8 / +0.9	−1.6 / +0.8

Table C.5.: Relative impact of experimental systematic uncertainties on the total number of expected background events in the Top control region of the boosted category in the $\tau_{\text{lep}}\tau_{\text{lep}}$ channel. Given is always the up- and downward fluctuation in percent. Variations below 0.1% are ignored.

	$Z \to \tau\tau$	
	channel-migration	region-migration
	VBF Top control region	
QCD scale	+1.0 / −1.0	+6.4 / −3.5
PDF	−0.1 / +0.2	−1.1 / +1.2
CKKW	+5.9 / −4.1	+1.8 / −1.4
QSF	+1.5 / −1.6	–
UEPS	−1.8 / +1.8	–
EWK $Zjj, Zjjj$	+0.7 / −0.7	
	Boosted Top control region	
QCD scale	+0.8 / −0.6	+3.2 / −2.4
PDF	+0.4 / −0.5	−1.4 / +1.6
CKKW	−4.3 / +3.4	+1.9 / −1.4
QSF	+4.3 / −4.3	–
UEPS	+0.8 / −0.8	–
EWK $Zjj, Zjjj$	+0.1 / −0.1	

Table C.6.: Relative impact of theoretical uncertainties on the expected number of $Z \to \tau\tau$ background events in the Top control region of the VBF and boosted category in the $\tau_{lep}\tau_{lep}$ channel. Given is always the up- and downward fluctuation in percent. Variations below 0.1% are ignored.

C.2. VBF CP $H \to \tau\tau$ Analysis

	VBF $H \to \tau\tau$	VBF $H \to WW$	non-VBF H
		low-BDT SF	
Electrons			
Scale	+0.3 / −0.3	–	–
Resolution	–	–	–
Efficiency	–	–	–
Muons			
Scale	–	–	–
Resolution	–	–	–
Efficiency	–	–	–
Jets			
JER	+1.2 / −1.2	+2.8 / −2.8	+4.3 / −4.3
JES	+4.4 / −4.2	+6.4 / −7.7	+10.1 / −9.1
JVT Efficiency	–	–	–
b-tagging	+1.1 / −1.1	+1.0 / −1.0	+1.4 / −1.4
E_T^{miss} soft term			
Resolution	–	–	+1.1 / −1.1
Scale	–	–	–
Pile-up rew.	−1.4 / +1.0	−2.3 / +1.4	−1.4 / +1.0
		low-BDT DF	
Electrons			
Scale	–	–	–
Resolution	–	–	–
Efficiency	+1.2 / −1.2	+1.2 / −1.2	+1.2 / −1.2
Muons			
Scale	–	–	–
Resolution	–	–	–
Efficiency	–	–	–
Jets			
JER	–	–	+4.4 / −4.4
JES	+3.8 / −4.2	+7.2 / −9.0	+10.1 / −9.6
JVT Efficiency	–	–	–
b-tagging	+1.0 / −1.0	–	+1.2 / −1.2
E_T^{miss} soft term			
Resolution	–	–	–
Scale	–	–	–
Pile-up rew.	−2.1 / +1.1	−2.9 / +2.0	–

Table C.7.: Relative impact of experimental systematic uncertainties on the number of expected VBF $H \to \tau\tau$ and $H \to WW$ signal events and on the expected background events fromthe ggF, VH and ttH production modes (non-VBF) in the SF and DF low-BDT signal regions in percent. Variations below 0.1 % are ignored.

	$Z \to \tau\tau$	Top	$Z \to \ell\ell$	Di-Boson
	low-BDT SF			
Electrons				
Scale	+0.5 / −0.5	–	+1.0 / −0.4	–
Resolution	–	–	–	–
Efficiency	–	+1.1 / −1.1	–	+1.1 / −1.1
Muons				
Scale	–	–	–	–
Resolution	–	–	+0.5 / −3.2	–
Efficiency	–	–	–	–
Jets				
JER	+5.6 / −5.6	+7.4 / −7.4	+97.1 / −97.1	+10.7 / −10.7
JES	+7.8 / −11.3	+4.9 / −7.2	+96.2 / −68.4	+10.0 / −6.1
JVT Efficiency	–	–	–	–
b-tagging	+1.4 / −1.4	+12.9 / −12.3	+1.3 / −1.2	+1.6 / −1.6
E_T^{miss} soft term				
Resolution	+1.9 / −1.9	–	+12.7 / −18.7	+1.7 / −1.7
Scale	–	–	+19.0 / −11.1	–
m_{jj} rew.	–	–	+1.8 / −1.8	–
Pile-up rew.	−3.1 / +1.8	−3.0 / +0.9	−9.5 / +9.6	−3.3 / +1.2
	low-BDT DF			
Electrons				
Scale	–	–	–	
Resolution	–	–	–	
Efficiency	+1.4 / −1.4	+1.0 / −1.0	+1.1 / −1.1	
Muons				
Scale	–	–	–	
Resolution	–	–	–	
Efficiency	–	–	–	
Jets				
JER	+4.5 / −4.5	+3.9 / −3.9	+6.4 / −6.4	
JES	+10.4 / −10.9	+4.6 / −4.9	+10.5 / −11.6	
JVT Efficiency	–	–	–	
b-tagging	+1.2 / −1.2	+13.2 / −12.5	+1.5 / −1.4	
E_T^{miss} soft term				
Resolution	–	–	–	
Scale	–	–	–	
m_{jj} rew.	–	–	–	
Pile-up rew.	+0.1 / −1.1	+0.6 / −0.6	+0.4 / −0.4	

Table C.8.: Relative impact of experimental systematic uncertainties on the number of expected background events in the SF and DF low-BDT control regions in percent. In the DF channel, events from $Z \to \ell\ell$ and di-boson production are combined. Variations below 0.1 % are ignored.

	VBF $H \to \tau\tau$	VBF $H \to WW$	non-VBF H
	low-BDT SF		
QCD scale	–	–	+7.9 / −7.9
α_S	–	–	+2.8 / −2.8
PDF	–	–	+2.1 / −1.6
UEPS	+2.6 / −2.1	–	+13.3 / −13.3
	low-BDT DF		
QCD scale	–	–	+7.1 / −7.1
α_S	–	–	+2.7 / −2.8
PDF	–	–	+1.8 / −1.2
UEPS	+2.2 / −2.2	–	+14.5 / −14.5

Table C.9.: Relative impact of theoretical systematic uncertainties on the number of expected VBF $H \to \tau\tau$ and $H \to WW$ signal events and on the expected background events from the ggF, VH and ttH production modes (non-VBF) in the SF and DF low-BDT signal regions in percent. Variations below 0.1 % are ignored.

	$Z \to \tau\tau$	
	low-BDT SF	
	channel-migration	region-migration
QCD scale	+2.4 / −2.4	–
PDF	–	+0.8 / −1.1
CKKW	+12.0 / −9.6	–
QSF	−1.6 / +1.7	–
UEPS	−6.2 / +6.2	+1.1 / −1.1
	low-BDT DF	
QCD scale	+2.4 / −2.4	−2.5 / +2.5
PDF	–	–
CKKW	+12.2 / −9.7	–
QSF	−1.6 / +1.7	–
UEPS	−6.3 / +6.3	–

Table C.10.: Relative impact of theoretical uncertainties on the expected number of $Z \to \tau\tau$ background events in the SF and DF low-BDT control regions in percent. Variations below 0.1 % are ignored.

	VBF $H \to \tau\tau$	VBF $H \to WW$	non-VBF H
		Top CR SF	
Electrons			
Scale	–	–	–
Resolution	–	–	–
Efficiency	+1.0 / −1.0	+1.2 / −1.2	+1.1 / −1.1
Muons			
Scale	–	–	–
Resolution	–	–	–
Efficiency	–	–	–
Jets			
JER	+3.8 / −3.8	+6.6 / −6.6	+4.5 / −4.5
JES	+5.9 / −3.8	+5.6 / −8.3	+16.6 / −10.9
JVT Efficiency	–	–	–
b-tagging	+7.1 / −7.1	+7.2 / −7.1	+6.9 / −6.8
E_T^{miss} soft term			
Resolution	–	–	+1.6 / −1.6
Scale	–	–	–
Pile-up rew.	−3.0 / +1.6	−2.7 / +3.2	−4.7 / +6.6
		Top CR DF	
Electrons			
Scale	–	–	–
Resolution	–	–	–
Efficiency	+1.1 / −1.1	+1.1 / −1.1	+1.1 / −1.1
Muons			
Scale	–	–	–
Resolution	–	–	–
Efficiency	–	–	–
Jets			
JER	+1.3 / −1.3	+5.2 / −5.2	+2.3 / −2.3
JES	+3.0 / −2.8	+13.2 / −7.5	+9.1 / −9.2
JVT Efficiency	–	–	–
b-tagging	+7.0 / −7.0	+6.6 / −6.6	+5.9 / −5.8
E_T^{miss} soft term			
Resolution	–	+1.5 / −1.5	–
Scale	–	–	–
Pile-up rew.	–	−4.7 / +2.7	−3.9 / +0.6

Table C.11.: Relative impact of experimental systematic uncertainties on the number of expected VBF $H \to \tau\tau$ and $H \to WW$ signal events and on the expected background events fromthe ggF, VH and ttH production modes (non-VBF) in the SF and DF Top control regions in percent. Variations below 0.1 % are ignored.

	$Z \to \tau\tau$	Top	$Z \to \ell\ell$	Di-Boson
	Top CR SF			
Electrons				
Scale	–	–	–	–
Resolution	–	–	+4.4 / −0.5	–
Efficiency	–	+1.1 / −1.0	–	–
Muons				
Scale	–	–	–	–
Resolution	–	–	+0.2 / −1.1	–
Efficiency	–	–	+1.0 / −1.0	–
Jets				
JER	+13.9 / −13.9	+3.3 / −3.3	+84.5 / −84.5	+15.3 / −15.3
JES	+11.8 / −9.3	+5.4 / −4.6	+49.8 / −59.1	+5.7 / −11.7
JVT Efficiency	–	–	–	–
b-tagging	+7.8 / −7.7	+1.6 / −1.5	+10.5 / −10.4	+8.3 / −8.2
E_T^{miss} soft term				
Resolution	+3.2 / −3.2	–	+6.7 / −6.7	+1.0 / −1.0
Scale	+1.7 / −1.7	–	+5.1 / −3.2	–
m_{jj} rew	–	–	+1.0 / −1.0	–
Pile-up rew.	+1.0 / −3.0	−2.4 / +1.8	+3.1 / −4.1	−4.1 / +3.6
	Top CR DF			
Electrons				
Scale	–	–	+0.2 / −3.5	
Resolution	–	–	–	
Efficiency	+1.4 / −1.4	–	+1.3 / −1.3	
Muons				
Scale	–	–	–	
Resolution	–	–	+1.1 / −0.3	
Efficiency	–	–	–	
Jets				
JER	+5.6 / −5.6	+1.7 / −1.7	+5.4 / −5.4	
JES	+10.4 / −11.0	+4.7 / −4.7	+14.6 / −8.9	
JVT Efficiency	–	–	–	
b-tagging	+7.2 / −7.1	+1.8 / −1.7	+8.4 / −8.3	
E_T^{miss} soft term				
Resolution	–	–	+1.3 / −1.3	
Scale	–	–	–	
m_{jj} rew.	–	–	–	
Pile-up rew.	+0.8 / −0.8	−2.2 / +0.8	+3.3 / −4.5	

Table C.12.: Relative impact of experimental systematic uncertainties on the number of expected background events in the SF and DF Top control regions in percent. In the DF channel, events from $Z \to \ell\ell$ and di-boson production are combined. Variations below 0.1 % are ignored.

	VBF $H \to \tau\tau$	VBF $H \to WW$	non-VBF H
		Top CR SF	
QCD scale	–	–	$+8.1$ / -8.1
α_S	–	–	$+2.4$ / -2.5
PDF	$+1.5$ / -1.5	$+1.8$ / -1.8	$+1.9$ / -1.5
UEPS	$+12.0$ / -12.0	–	$+18.8$ / -18.8
		Top CR DF	
QCD scale	–	–	$+7.1$ / -7.1
α_S	–	–	$+2.2$ / -2.2
PDF	$+1.7$ / -1.7	$+1.5$ / -1.5	$+1.4$ / -0.9
UEPS	$+10.6$ / -10.6	–	$+9.0$ / -9.0

Table C.13.: Relative impact of theoretical systematic uncertainties on the number of expected VBF $H \to \tau\tau$ and $H \to WW$ signal events and on the expected background events from the ggF, VH and ttH production modes (non-VBF) in the SF and DF Top control regions in percent. Variations below 0.1 % are ignored.

	$Z \to \tau\tau$	
	Top CR SF	
	channel-migration	region-migration
QCD scale	2.4 / -2.4	$+13.7$ / -13.7
PDF	–	-1.1 / $+1.3$
CKKW	$+12.2$ / -9.7	–
QSF	-1.6 / $+1.7$	–
UEPS	-6.3 / $+6.3$	–
	Top CR DF	
QCD scale	$+2.5$ / -2.5	$+2.4$ / -2.4
PDF	–	-1.0 / $+1.2$
CKKW	$+12.2$ / -9.8	–
QSF	-1.6 / $+1.7$	–
UEPS	-6.3 / $+6.3$	–

Table C.14.: Relative impact of theoretical uncertainties on the expected number of $Z \to \tau\tau$ background events in the SF and DF Top control regions in percent. Variations below 0.1 % are ignored.

	VBF $H \to \tau\tau$	VBF $H \to WW$	non-VBF H
	$Z \to \ell\ell$ CR SF		
Electrons			
Scale	–	+0.1 / −1.8	+0.5 / −1.9
Resolution	–	–	+1.2 / −2.6
Efficiency	–	–	–
Muons			
Scale	–	+8.0 / −0.0	–
Resolution	–	+8.9 / −4.5	+1.0 / −3.3
Efficiency	–	–	–
Jets			
JER	+6.9 / −6.9	+29.8 / −29.8	+21.9 / −21.9
JES	+8.7 / −9.1	+21.3 / −16.4	+11.0 / −13.1
JVT Efficiency	–	–	–
b-tagging	+1.1 / −1.1	+1.3 / −1.3	+1.9 / −1.8
E_T^{miss} soft term			
Resolution	+1.3 / −1.3	+2.1 / −2.1	+7.4 / −7.4
Scale	–	+0.0 / −2.2	+1.9 / −1.9
Pile-up rew.	−1.3 / +0.6	−1.9 / +1.2	−6.2 / +2.2

Table C.15.: Relative impact of experimental systematic uncertainties on the number of expected VBF $H \to \tau\tau$ and $H \to WW$ signal events and on the expected background events fromthe ggF, VH and ttH production modes (non-VBF) in the SF $Z \to \ell\ell$ control region in percent. Variations below 0.1 % are ignored.

	VBF $H \to \tau\tau$	VBF $H \to WW$	non-VBF H
	$Z \to \ell\ell$ CR SF		
QCD scale	+1.0 / −0.7	+1.2 / −0.5	+10.9 / −10.8
α_S	–	–	+2.2 / −2.3
PDF	–	–	+1.4 / −0.9
UEPS	+1.8 / −1.8	–	+35.3 / −35.3

Table C.16.: Relative impact of theoretical systematic uncertainties on the number of expected VBF $H \to \tau\tau$ and $H \to WW$ signal events and on the expected background events from the ggF, VH and ttH production modes (non-VBF) in the SF $Z \to \ell\ell$ control region in percent. Variations below 0.1 % are ignored.

	$Z \to \tau\tau$	Top	$Z \to \ell\ell$	Di-Boson
	$Z \to \ell\ell$ CR SF			
Electrons				
Scale	–	–	–	–
Resolution	–	–	–	–
Efficiency	–	–	–	–
Muons				
Scale	–	–	–	–
Resolution	+2.8 / −0.0	+1.1 / −0.2	–	–
Efficiency	–	–	–	–
Jets				
JER	+27.0 / −27.0	+11.1 / −11.1	+24.3 / −24.3	+14.4 / −14.4
JES	+20.9 / −14.6	+6.6 / −5.3	+30.1 / −26.7	+17.1 / −12.7
JVT Efficiency	–	–	–	–
b-tagging	+1.5 / −1.5	+14.7 / −13.6	+1.0 / −1.0	+1.5 / −1.5
E_T^{miss} soft term				
Resolution	+6.5 / −6.5	–	+11.6 / −11.6	+3.0 / −3.0
Scale	+2.8 / −0.0	–	+7.5 / −4.3	+2.0 / −3.1
m_{jj} rew.	–	–	+1.5 / −1.5	–
Pile-up rew.	+2.5 / −5.2	−3.8 / +1.6	+8.8 / −7.5	+2.7 / −2.5

Table C.17.: Relative impact of experimental systematic uncertainties on the number of expected background events in the SF $Z \to \ell\ell$ control regions in percent. In the DF channel, events from $Z \to \ell\ell$ and di-boson production are combined. Variations below 0.1 % are ignored.

	$Z \to \tau\tau$	
	$Z \to \ell\ell$ CR SF	
	channel-migration	region-migration
QCD scale	+2.4 / −2.4	−2.2 / +2.2
PDF	–	−3.0 / +3.6
CKKW	+12.0 / −9.6	–
QSF	−1.6 / +1.7	–
UEPS	−6.2 / +6.2	–

Table C.18.: Relative impact of theoretical uncertainties on the expected number of $Z \to \tau\tau$ background events in the SF $Z \to \ell\ell$ control regions in percent. Variations below 0.1 % are ignored.

D List of Acceptance Uncertainties in the Control Regions

D.1. $H \to \tau\tau$ Cross-Section Measurement

Systematic	ggF $H \to \tau\tau$	ggF $H \to WW$	VBF $H \to \tau\tau$	VBF $H \to WW$	WH $H \to \tau\tau$	ZH $H \to \tau\tau$	ttH $H \to \tau\tau$	$Z \to \tau\tau$	$Z \to \ell\ell$	Top	Di-boson	Fakes
EG_RESOLUTION_ALL					×							
EG_SCALE_ALLCORR							×					
EL_EFF_ID_TOTAL		×	×		×	×		×				
FT_EFF_Eigen_b_0							×		×	×		
FT_EFF_Eigen_c_0			×	×	×	×		×			×	
FT_EFF_Eigen_light_0	×	×	×	×	×	×		×	×		×	
FT_EFF_Eigen_light_1	×	×	×	×	×	×		×	×		×	
FT_EFF_Eigen_light_2						×						
FT_EFF_Eigen_light_3	×	×			×			×	×		×	
FT_EFF_Eigen_light_4					×	×						
JER_CROSSCALIBFWD		×				×	×		×	×	×	
JER_NOISEFWD		×	×	×		×	×		×	×	×	
JER_NP_0	×	×			×	×	×	×	×		×	
JER_NP_1	×	×						×	×	×	×	
JER_NP_2	×			×	×			×	×	×	×	
JER_NP_3	×		×						×			
JER_NP_4			×	×			×	×	×	×	×	
JER_NP_5	×	×	×	×	×	×	×		×	×	×	
JER_NP_6		×				×	×		×			
JER_NP_7	×	×	×	×		×		×	×		×	
JER_NP_8	×							×	×		×	
JES_EffectiveNP_1	×	×	×	×		×		×	×	×	×	
JES_EffectiveNP_2		×					×		×		×	
JES_EffectiveNP_3									×		×	
JES_EffectiveNP_4									×		×	
JES_EffectiveNP_5		×										
JES_EffectiveNP_6		×										
JES_EffectiveNP_8		×									×	
JES_EtaInter_Model	×	×	×	×		×	×	×	×	×	×	
JES_EtaInter_NonClosure	×	×		×		×	×		×			
JES_EtaInter_Stat		×		×				×	×			
JES_Flavor_Comp	×	×	×	×		×	×	×		×	×	
JES_Flavor_Comp_leplepzll									×			
JES_Flavor_Resp	×	×	×	×		×		×		×	×	
JES_Flavor_Resp_leplepzll									×			
JES_PU_OffsetMu	×	×		×			×	×	×			
JES_PU_OffsetNPV		×					×		×		×	
JES_PU_PtTerm	×	×	×	×				×	×	×		
JES_PU_Rho	×	×	×	×			×	×	×	×	×	
JVT							×					
MET_SoftTrk_ResoPara	×			×			×		×			
MET_SoftTrk_ResoPerp	×			×		×	×	×	×		×	
MET_SoftTrk_Scale	×	×		×			×		×			
MUONS_ID									×			
MUONS_MS				×								
MUONS_SAGITTA_RESBIAS				×								
PRW_DATASF	×	×	×	×	×	×	×	×	×	×		
ll_fake_nonclosure												×
ll_fake_stat												×

Table D.1.: Summary of shape (•) and acceptance (×) uncertainties from experimental sources in the VBF Top control region of the $\tau_{lep}\tau_{lep}$ channel.

Systematic	ggF $H \to \tau\tau$	ggF $H \to WW$	VBF $H \to \tau\tau$	VBF $H \to WW$	WH $H \to \tau\tau$	ZH $H \to \tau\tau$	ttH $H \to \tau\tau$	$Z \to \tau\tau$	$Z \to \ell\ell$	Top	Di-boson	Fakes
Theo_NLO_EW_Higgs_total			×	×								
Theo_QCDscale_VBF_total			×	×								
Theo_QCDscale_VH_total					×	×						
Theo_QCDscale_ttH_total							×					
Theo_VH_MUR_MUF					×	×						
Theo_alphas_Higgs_VBF_total			×	×								
Theo_alphas_Higgs_VH_total					×	×						
Theo_alphas_Higgs_ggH_total	×	×										
Theo_alphas_Higgs_ttH_total							×					
Theo_ggH_sig_qcd_0	×											
Theo_ggH_sig_qcd_1	×											
Theo_ggH_sig_qcd_2	×											
Theo_ggH_sig_qcd_3	×											
Theo_ggH_sig_qcd_4	×											
Theo_ggH_sig_qcd_5	×											
Theo_ggH_sig_qcd_6	×											
Theo_ggH_sig_qcd_7	×											
Theo_ggH_sig_qcd_8	×											
Theo_ll_VH_PSUE					×	×						
Theo_ll_vbf_VBFH_PSUE			×	×								
Theo_ll_vbf_ggH_PSUE	×	×										
Theo_pdf_Higgs_VBF_total			×	×								
Theo_pdf_Higgs_VH_total					×	×						
Theo_pdf_Higgs_ggH_total	×	×										
Theo_pdf_Higgs_ttH_total							×					
Theo_sig_alphaS	×											
Theo_sig_pdf_0					×	×						
Theo_sig_pdf_1			×			×						
Theo_sig_pdf_14					×							
Theo_sig_pdf_16	×											
Theo_sig_pdf_3	×											
Theo_sig_pdf_4	×											
Z_EWK_proportion								×				
ZttTheory_CKK_Relative_VBF								×				
ZttTheory_CKK_vbf_leplep								×				
ZttTheory_MGvsSH_Relative_VBF								×				
ZttTheory_MUR_MUF_Relative_VBF								×				
ZttTheory_MUR_MUF_vbf_leplep								×				
ZttTheory_PDF_Relative_VBF								×				
ZttTheory_PDF_vbf_leplep								×				
ZttTheory_QSF_Relative_VBF								×				

Table D.2.: Summary of shape (•) and acceptance (×) uncertainties from theoretical sources in the VBF Top control region of the $\tau_{lep}\tau_{lep}$ channel.

Systematic	ggF $H \to \tau\tau$	ggF $H \to WW$	VBF $H \to \tau\tau$	VBF $H \to WW$	WH $H \to \tau\tau$	ZH $H \to \tau\tau$	ttH $H \to \tau\tau$	$Z \to \tau\tau$	$Z \to \ell\ell$	Top	Di-boson	Fakes
EG_SCALE_ALLCORR									×			
EL_EFF_ID_TOTAL			×			×		×				
FT_EFF_Eigen_b_0										×		
FT_EFF_Eigen_c_0	×	×	×	×	×	×		×	×		×	
FT_EFF_Eigen_c_1				×	×							
FT_EFF_Eigen_light_0	×	×	×	×	×	×		×	×		×	
FT_EFF_Eigen_light_1	×	×	×	×				×	×		×	
FT_EFF_Eigen_light_3	×			×					×			
JER_CROSSCALIBFWD				×					×			
JER_NOISEFWD				×		×			×			
JER_NP_0		×	×	×			×	×	×	×	×	
JER_NP_1		×		×		×			×			
JER_NP_2		×	×			×		×	×		×	
JER_NP_3		×	×			×			×		×	
JER_NP_4			×	×							×	
JER_NP_5											×	
JER_NP_6		×		×	×				×			
JER_NP_7									×		×	
JER_NP_8		×		×	×	×		×	×		×	
JES_EffectiveNP_1	×	×		×	×	×	×	×	×	×	×	
JES_EffectiveNP_2				×								
JES_EffectiveNP_3				×					×			
JES_EffectiveNP_5				×								
JES_EffectiveNP_6									×			
JES_EffectiveNP_7									×			
JES_EffectiveNP_8				×					×			
JES_EtaInter_Model				×			×	×	×	×	×	
JES_EtaInter_NonClosure				×								
JES_EtaInter_Stat				×					×			
JES_Flavor_Comp	×	×	×	×			×			×	×	
JES_Flavor_Comp_leplepzll									×			
JES_Flavor_Resp	×	×		×			×	×		×	×	
JES_Flavor_Resp_leplepzll									×			
JES_PU_OffsetMu									×			
JES_PU_OffsetNPV		×			×				×			
JES_PU_PtTerm		×		×		×			×			
JES_PU_Rho	×	×		×	×	×	×	×	×	×	×	
JVT							×					
MET_SoftTrk_ResoPara	×			×				×				
MET_SoftTrk_ResoPerp	×	×		×				×	×			
MET_SoftTrk_Scale		×				×			×			
MUONS_MS									×			
MUONS_SCALE									×			
PRW_DATASF	×	×	×				×	×	×	×	×	
ll_fake_nonclosure												×
ll_fake_stat												×

Table D.3.: Summary of shape (•) and acceptance (×) uncertainties from experimental sources in the boosted Top control region of the $\tau_{lep}\tau_{lep}$ channel.

Systematic	ggF $H \to \tau\tau$	ggF $H \to WW$	VBF $H \to \tau\tau$	VBF $H \to WW$	WH $H \to \tau\tau$	ZH $H \to \tau\tau$	ttH $H \to \tau\tau$	$Z \to \tau\tau$	$Z \to \ell\ell$	Top	Di-boson	Fakes
Theo_NLO_EW_Higgs_total			×	×								
Theo_QCDscale_VBF_total			×	×								
Theo_QCDscale_VH_total					×	×						
Theo_QCDscale_ttH_total							×					
Theo_VBFH_MUR_MUF			×									
Theo_VH_MUR_MUF					×	×						
Theo_alphas_Higgs_VBF_total			×	×								
Theo_alphas_Higgs_VH_total					×	×						
Theo_alphas_Higgs_ggH_total	×	×										
Theo_alphas_Higgs_ttH_total							×					
Theo_ggH_sig_qcd_0	×											
Theo_ggH_sig_qcd_1	×											
Theo_ggH_sig_qcd_2	×											
Theo_ggH_sig_qcd_3	×											
Theo_ggH_sig_qcd_6	×											
Theo_ggH_sig_qcd_7	×											
Theo_ggH_sig_qcd_8	×											
Theo_ll_VH_PSUE					×	×						
Theo_ll_boost_VBFH_PSUE			×	×								
Theo_ll_boost_ggH_PSUE	×	×										
Theo_pdf_Higgs_VBF_total			×	×								
Theo_pdf_Higgs_VH_total					×	×						
Theo_pdf_Higgs_ggH_total	×	×										
Theo_pdf_Higgs_ttH_total							×					
Theo_sig_alphaS	×											
Theo_sig_pdf_1			×									
Theo_sig_pdf_16	×											
Theo_sig_pdf_3	×											
Theo_sig_pdf_4	×											
Z_EWK_proportion								×				
ZttTheory_CKK_Relative_Bst								×				
ZttTheory_CKK_boost_leplep								×				
ZttTheory_MGvsSH_Relative_Bst								×				
ZttTheory_MUR_MUF_Relative_Bst								×				
ZttTheory_MUR_MUF_boost_leplep								×				
ZttTheory_PDF_Relative_Bst								×				
ZttTheory_PDF_boost_leplep								×				
ZttTheory_QSF_Relative_Bst								×				

Table D.4.: Summary of shape (•) and acceptance (×) uncertainties from theoretical sources in the boosted Top control region of the $\tau_{lep}\tau_{lep}$ channel.

Systematic	ggF $H \to \tau\tau$	ggF $H \to WW$	VBF $H \to \tau\tau$	VBF $H \to WW$	WH $H \to \tau\tau$	ZH $H \to \tau\tau$	ttH $H \to \tau\tau$	$Z \to \tau\tau$	$Z \to \ell\ell$	Top	Di-boson	Fakes
EG_RESOLUTION_ALL	×			×				×				
EG_SCALE_ALLCORR	×			×					×	×	×	
EL_EFF_ID_TOTAL				×			×					
EL_EFF_ISO_TOTAL				×								
FT_EFF_Eigen_b_0							×			×		
FT_EFF_Eigen_b_1										×		
FT_EFF_Eigen_b_2										×		
FT_EFF_Eigen_c_0							×					
FT_EFF_Eigen_light_0	×		×	×			×	×	×	×	×	
FT_EFF_Eigen_light_3								×				
JER_CROSSCALIBFWD	×		×	×			×	×	×	×	×	
JER_NOISEFWD	×		×	×			×	×	×		×	
JER_NP_0	×		×	×			×	×	×	×	×	
JER_NP_1	×			×				×	×	×	×	
JER_NP_2			×	×			×	×	×		×	
JER_NP_3			×	×				×	×		×	
JER_NP_4				×			×	×	×		×	
JER_NP_5	×			×					×	×	×	
JER_NP_6			×	×			×		×	×	×	
JER_NP_7	×								×	×	×	
JER_NP_8			×	×				×			×	
JES_EffectiveNP_1				×				×	×		×	
JES_EffectiveNP_2	×			×				×	×	×	×	
JES_EffectiveNP_3	×			×					×	×	×	
JES_EffectiveNP_4				×					×			
JES_EtaInter_Model	×		×	×					×		×	
JES_EtaInter_NonClosure	×		×	×					×	×	×	
JES_EtaInter_Stat			×	×				×	×			
JES_Flavor_Comp			×	×			×	×		×	×	
JES_Flavor_Comp_leplepzll									×			
JES_Flavor_Resp	×		×	×				×			×	
JES_Flavor_Resp_leplepzll									×			
JES_PU_OffsetMu	×							×	×		×	
JES_PU_OffsetNPV				×				×	×		×	
JES_PU_PtTerm			×	×			×		×	×	×	
JES_PU_Rho	×		×	×			×	×	×		×	
JVT								×				
MET_SoftTrk_ResoPara								×	×	×	×	
MET_SoftTrk_ResoPerp								×	×	×	×	
MET_SoftTrk_Scale	×			×				×	×	×	×	
MUONS_MS	×									×	×	
MUONS_SAGITTA_RESBIAS			×	×								
PRW_DATASF			×	×			×	×	×	×	×	

Table D.5.: Summary of shape (•) and acceptance (×) uncertainties from experimental sources in the VBF $Z \to \ell\ell$ control region of the $\tau_{lep}\tau_{lep}$ channel.

Systematic	ggF $H \to \tau\tau$	ggF $H \to WW$	VBF $H \to \tau\tau$	VBF $H \to WW$	WH $H \to \tau\tau$	ZH $H \to \tau\tau$	ttH $H \to \tau\tau$	$Z \to \tau\tau$	$Z \to \ell\ell$	Top	Di-boson	Fakes
Theo_NLO_EW_Higgs_total			×	×								
Theo_QCDscale_VBF_total			×	×								
Theo_QCDscale_VH_total					×	×						
Theo_QCDscale_ttH_total							×					
Theo_VBFH_MUR_MUF			×									
Theo_alphas_Higgs_VBF_total			×	×								
Theo_alphas_Higgs_VH_total					×	×						
Theo_alphas_Higgs_ggH_total	×	×										
Theo_alphas_Higgs_ttH_total							×					
Theo_ggH_sig_qcd_0	×											
Theo_ggH_sig_qcd_1	×											
Theo_ggH_sig_qcd_2	×											
Theo_ggH_sig_qcd_3	×											
Theo_ggH_sig_qcd_4	×											
Theo_ggH_sig_qcd_5	×											
Theo_ggH_sig_qcd_6	×											
Theo_ggH_sig_qcd_7	×											
Theo_ggH_sig_qcd_8	×											
Theo_ll_VH_PSUE					×	×						
Theo_ll_vbf_VBFH_PSUE			×	×								
Theo_ll_vbf_ggH_PSUE	×	×										
Theo_pdf_Higgs_VBF_total			×	×								
Theo_pdf_Higgs_VH_total					×	×						
Theo_pdf_Higgs_ggH_total	×	×										
Theo_pdf_Higgs_ttH_total							×					
Theo_sig_alphaS	×											
Theo_sig_pdf_29			×									
Theo_sig_pdf_4	×											
Z_EWK_proportion								×				
ZttTheory_CKK_Relative_VBF								×				
ZttTheory_CKK_vbf_leplep								×				
ZttTheory_MGvsSH_Relative_VBF								×				
ZttTheory_MUR_MUF_Relative_VBF								×				
ZttTheory_MUR_MUF_vbf_leplep								×				
ZttTheory_PDF_Relative_VBF								×				
ZttTheory_PDF_vbf_leplep								×				
ZttTheory_QSF_Relative_VBF								×				
ZttTheory_QSF_vbf_leplep								×				

Table D.6.: Summary of shape (•) and acceptance (×) uncertainties from theoretical sources in the VBF $Z \to \ell\ell$ control region of the $\tau_{lep}\tau_{lep}$ channel.

Systematic	ggF $H \to \tau\tau$	ggF $H \to WW$	VBF $H \to \tau\tau$	VBF $H \to WW$	WH $H \to \tau\tau$	ZH $H \to \tau\tau$	ttH $H \to \tau\tau$	$Z \to \tau\tau$	$Z \to \ell\ell$	Top	Di-boson	Fakes
EG_RESOLUTION_ALL	×					×						
EG_SCALE_ALLCORR						×	×		×		×	
EG_SCALE_E4SCINTILLATOR						×						
EG_SCALE_LARCALIB_2015PRE	×					×	×					
EL_EFF_ID_TOTAL			×		×							
FT_EFF_Eigen_b_0							×			×		
FT_EFF_Eigen_b_1							×			×		
FT_EFF_Eigen_b_2							×			×		
FT_EFF_Eigen_c_0					×	×	×					
FT_EFF_Eigen_light_0	×	×	×	×	×	×	×	×	×	×	×	
JER_CROSSCALIBFWD			×			×		×	×		×	
JER_NOISEFWD			×			×	×		×		×	
JER_NP_0	×	×	×		×	×		×	×	×	×	
JER_NP_1			×		×	×	×	×	×		×	
JER_NP_2					×				×		×	
JER_NP_3	×		×		×	×	×	×		×		
JER_NP_4		×						×			×	
JER_NP_5	×		×		×	×	×	×			×	
JER_NP_6			×		×		×			×		
JER_NP_7	×		×		×			×	×			
JER_NP_8	×		×		×	×		×	×	×	×	
JES_EffectiveNP_1					×	×	×		×	×	×	
JES_EffectiveNP_2	×		×			×		×	×	×	×	
JES_EffectiveNP_3	×		×			×	×		×	×	×	
JES_EffectiveNP_6							×					
JES_EffectiveNP_8								×				
JES_EtaInter_Model	×		×		×			×	×		×	
JES_EtaInter_NonClosure	×		×						×		×	
JES_EtaInter_Stat									×			
JES_Flavor_Comp	×		×			×	×				×	
JES_Flavor_Comp_leplepzll									×			
JES_Flavor_Resp	×		×					×			×	
JES_Flavor_Resp_leplepzll									×			
JES_PU_OffsetMu					×			×				
JES_PU_OffsetNPV	×					×		×	×	×		
JES_PU_PtTerm	×		×					×	×	×	×	
JES_PU_Rho			×			×	×		×	×	×	
JVT							×					
MET_SoftTrk_ResoPara	×				×			×	×		×	
MET_SoftTrk_ResoPerp	×		×				×	×	×		×	
MET_SoftTrk_Scale	×					×	×		×		×	
MUONS_ID	×							×				
MUONS_MS						×	×	×				
MUONS_SAGITTA_RESBIAS					×	×		×				
MUONS_SCALE			×									
PRW_DATASF	×	×	×	×	×	×	×	×	×	×	×	

Table D.7.: Summary of shape (•) and acceptance (×) uncertainties from experimental sources in the boosted $Z \to \ell\ell$ control region of the $\tau_{lep}\tau_{lep}$ channel.

Systematic	ggF $H \to \tau\tau$	ggF $H \to WW$	VBF $H \to \tau\tau$	VBF $H \to WW$	WH $H \to \tau\tau$	ZH $H \to \tau\tau$	ttH $H \to \tau\tau$	$Z \to \tau\tau$	$Z \to \ell\ell$	Top	Di-boson	Fakes
Theo_NLO_EW_Higgs_total			×	×								
Theo_QCDscale_VBF_total			×	×								
Theo_QCDscale_VH_total					×	×						
Theo_QCDscale_ttH_total							×					
Theo_VBFH_MUR_MUF			×									
Theo_VH_MUR_MUF					×	×						
Theo_alphas_Higgs_VBF_total			×	×								
Theo_alphas_Higgs_VH_total					×	×						
Theo_alphas_Higgs_ggH_total	×	×										
Theo_alphas_Higgs_ttH_total							×					
Theo_ggH_sig_qcd_0	×											
Theo_ggH_sig_qcd_1	×											
Theo_ggH_sig_qcd_2	×											
Theo_ggH_sig_qcd_3	×											
Theo_ggH_sig_qcd_6	×											
Theo_ggH_sig_qcd_7	×											
Theo_ggH_sig_qcd_8	×											
Theo_ll_VH_PSUE					×	×						
Theo_ll_boost_VBFH_PSUE			×	×								
Theo_ll_boost_ggH_PSUE	×	×										
Theo_pdf_Higgs_VBF_total			×	×								
Theo_pdf_Higgs_VH_total					×	×						
Theo_pdf_Higgs_ggH_total	×	×										
Theo_pdf_Higgs_ttH_total							×					
Theo_sig_alphaS	×											
Theo_sig_pdf_1						×						
Theo_sig_pdf_16	×											
Theo_sig_pdf_18						×						
Theo_sig_pdf_4	×					×						
Z_EWK_proportion								×				
ZttTheory_CKK_Relative_Bst								×				
ZttTheory_CKK_boost_leplep								×				
ZttTheory_MGvsSH_Relative_Bst								×				
ZttTheory_MUR_MUF_Relative_Bst								×				
ZttTheory_MUR_MUF_boost_leplep								×				
ZttTheory_PDF_Relative_Bst								×				
ZttTheory_PDF_boost_leplep												
ZttTheory_QSF_Relative_Bst								×				
ZttTheory_QSF_boost_leplep								×				

Table D.8.: Summary of shape (•) and acceptance (×) uncertainties from theoretical sources in the boosted $Z \to \ell\ell$ control region of the $\tau_{lep}\tau_{lep}$ channel.

D.2. VBF CP $H \to \tau\tau$ Analysis

Systematic	VBF $H \to \tau\tau$	VBF $H \to WW$	Non-VBF H	Top	Di-boson	Fake	$Z \to \tau\tau$	$Z \to \ell\ell$
EG_RESOLUTION_ALL								×
EL_EFF_ID_TOTAL	×	×	×	×				
FT_EFF_Eigen_b_0				×				×
FT_EFF_Eigen_c_0	×	×			×			
FT_EFF_Eigen_light_0	×	×	×		×		×	×
FT_EFF_Eigen_light_1	×	×	×		×		×	×
FT_EFF_Eigen_light_2								×
FT_EFF_Eigen_light_3			×		×		×	
FT_EFF_Eigen_light_4								×
JER_CROSSCALIBFWD		×		×	×		×	×
JER_NOISEFWD		×		×	×		×	×
JER_NP_0	×	×	×	×			×	
JER_NP_0_zll_leplep								×
JER_NP_1		×		×	×		×	×
JER_NP_2	×	×	×		×		×	×
JER_NP_3	×		×		×		×	×
JER_NP_4			×		×		×	×
JER_NP_5					×		×	×
JER_NP_6		×	×		×		×	×
JER_NP_7		×	×		×			×
JER_NP_8	×	×		×	×		×	×
JES_EffectiveNP_1	×	×	×	×	×		×	×
JES_EffectiveNP_2					×			
JES_EffectiveNP_3					×		×	×
JES_EffectiveNP_4					×			×
JES_EtaInter_Model	×	×	×	×	×		×	
JES_EtaInter_Model_zll_leplep								×
JES_EtaInter_NonClosure					×		×	×
JES_EtaInter_Stat			×		×		×	×
JES_Flavor_Comp	×	×	×	×	×		×	
JES_Flavor_Comp_leplepzll								×
JES_Flavor_Resp	×	×	×	×	×		×	
JES_Flavor_Resp_leplepzll								×
JES_HighPt								
JES_PU_OffsetMu	×	×	×	×			×	×
JES_PU_OffsetNPV		×	×		×			×
JES_PU_PtTerm	×	×	×	×	×		×	×
JES_PU_Rho	×	×	×	×	×		×	×
MET_SoftTrk_ResoPara							×	×
MET_SoftTrk_ResoPerp			×		×		×	×
MET_SoftTrk_Scale							×	×
MUONS_MS								×
MUON_EFF_SYS								×
PRW_DATASF	×	×	×	×	×		×	
PRW_DATASF_zll_leplep								×
Zllrew_mjj								×
ll_fake_nonclosure						×		
ll_fake_stat						×		

Table D.9.: Summary of shape (•) and acceptance (×) uncertainties from experimental sources in the SF Top control region of the $\tau_{lep}\tau_{lep}$ channel.

Systematic	VBF $H \to \tau\tau$	VBF $H \to WW$	Non-VBF H	Top	Fake	$Z \to \tau\tau$	$Z \to \ell\ell$ +Di-boson
EG_SCALE_ALLCORR							×
EL_EFF_ID_TOTAL	×	×	×			×	×
FT_EFF_Eigen_b_0				×			
FT_EFF_Eigen_c_0	×	×					×
FT_EFF_Eigen_light_0	×	×	×			×	×
FT_EFF_Eigen_light_1	×	×	×			×	×
FT_EFF_Eigen_light_3	×		×			×	×
JER_CROSSCALIBFWD						×	
JER_NOISEFWD							×
JER_NP_0	×	×	×	×			×
JER_NP_1		×	×			×	×
JER_NP_2		×				×	
JER_NP_3		×	×				×
JER_NP_4		×				×	×
JER_NP_5						×	×
JER_NP_6						×	×
JER_NP_7			×			×	×
JER_NP_8		×					
JES_EffectiveNP_1	×	×	×	×		×	×
JES_EffectiveNP_2		×					
JES_EffectiveNP_3		×					
JES_EffectiveNP_4		×					
JES_EffectiveNP_5		×					
JES_EffectiveNP_7		×					
JES_EtaInter_Model	×	×	×	×		×	×
JES_EtaInter_NonClosure		×				×	
JES_EtaInter_Stat						×	×
JES_Flavor_Comp	×	×	×	×		×	×
JES_Flavor_Resp	×	×	×	×		×	×
JES_PU_OffsetMu		×	×			×	×
JES_PU_OffsetNPV		×	×				
JES_PU_PtTerm		×	×	×		×	×
JES_PU_Rho	×	×	×	×		×	×
MET_SoftTrk_ResoPerp		×					×
MUONS_ID							×
PRW_DATASF		×	×	×		×	×
ll_fake_nonclosure					×		
ll_fake_stat					×		

Table D.10.: Summary of shape (•) and acceptance (×) uncertainties from experimental sources in the DF Top control region of the $\tau_{lep}\tau_{lep}$ channel.

Systematic	VBF $H \to \tau\tau$	VBF $H \to WW$	Non-VBF H	Top	Di-boson	Fake	$Z \to \tau\tau$	$Z \to \ell\ell$
Theo_QCDscale_ttH_total			$\times$					
Theo_VBFH_shower	$\times$							
Theo_alphas_Higgs_ggH_total			$\times$					
Theo_ggH_shower			$\times$					
Theo_ggH_sig_qcd_1			$\times$					
Theo_ggH_sig_qcd_2			$\times$					
Theo_ggH_sig_qcd_3			$\times$					
Theo_ggH_sig_qcd_4			$\times$					
Theo_ggH_sig_qcd_6			$\times$					
Theo_ggH_sig_qcd_7			$\times$					
Theo_ggH_sig_qcd_8			$\times$					
Theo_ll_vbf_ggH_PSUE			$\times$					
Theo_pdf_Higgs_ggH_total			$\times$					
Theo_sig_alphaS			$\times$					
Theo_sig_pdf_1	$\times$							
Theo_sig_pdf_4			$\times$					
ZttTheory_MUR_MUF_vbf_leplep							$\times$	
ZttTheory_PDF_vbf_leplep							$\times$	

Table D.11.: Summary of shape ($\bullet$) and acceptance ($\times$) uncertainties from theoretical sources in the SF Top control region of the $\tau_{lep}\tau_{lep}$ channel.

Systematic	VBF $H \to \tau\tau$	VBF $H \to WW$	Non-VBF H	Top	Fake	$Z \to \tau\tau$	$Z \to \ell\ell$ +Di-boson
Theo_QCDscale_ttH_total			$\times$				
Theo_VBFH_shower	$\times$						
Theo_alphas_Higgs_ggH_total			$\times$				
Theo_ggH_shower			$\times$				
Theo_ggH_sig_qcd_2			$\times$				
Theo_ggH_sig_qcd_3			$\times$				
Theo_ggH_sig_qcd_4			$\times$				
Theo_ggH_sig_qcd_5			$\times$				
Theo_ggH_sig_qcd_6			$\times$				
Theo_ggH_sig_qcd_7			$\times$				
Theo_ggH_sig_qcd_8			$\times$				
Theo_ll_vbf_ggH_PSUE			$\times$				
Theo_pdf_Higgs_ggH_total			$\times$				
Theo_sig_alphaS			$\times$				
Theo_sig_pdf_1	$\times$						
ZttTheory_MUR_MUF_vbf_leplep						$\times$	
ZttTheory_PDF_vbf_leplep						$\times$	

Table D.12.: Summary of shape ($\bullet$) and acceptance ($\times$) uncertainties from theoretical sources in the DF Top control region of the $\tau_{lep}\tau_{lep}$ channel.

Systematic	VBF $H \to \tau\tau$	VBF $H \to WW$	Non-VBF H	Top	Di-boson	Fake	$Z \to \tau\tau$	$Z \to \ell\ell$
EG_RESOLUTION_ALL			×					
EG_SCALE_ALLCORR		×	×					
FT_EFF_Eigen_b_0			×	×				
FT_EFF_Eigen_b_1				×				
FT_EFF_Eigen_b_2				×				
FT_EFF_Eigen_light_0	×	×	×	×	×	×	×	
JER_CROSSCALIBFWD	×	×	×	×	×	×	×	
JER_NOISEFWD	×	×	×	×	×		×	
JER_NP_0	×	×	×	×	×	×		
JER_NP_0_zll_leplep							×	
JER_NP_1	×	×	×	×	×	×	×	
JER_NP_2		×	×	×	×	×		
JER_NP_3	×	×	×	×		×	×	
JER_NP_4	×	×	×	×	×	×		
JER_NP_5		×	×	×		×	×	
JER_NP_6		×	×	×		×	×	
JER_NP_7		×	×			×	×	
JER_NP_8	×	×	×	×		×	×	
JES_EffectiveNP_1	×	×	×	×	×	×	×	
JES_EffectiveNP_2	×	×		×	×	×		
JES_EffectiveNP_3			×			×	×	
JES_EffectiveNP_4		×					×	
JES_EffectiveNP_5			×				×	
JES_EffectiveNP_6		×					×	
JES_EffectiveNP_7			×					
JES_EffectiveNP_8		×						
JES_EtaInter_Model	×	×	×	×	×	×		
JES_EtaInter_Model_zll_leplep							×	
JES_EtaInter_NonClosure	×	×	×		×		×	
JES_EtaInter_Stat	×	×	×	×	×		×	
JES_Flavor_Comp	×	×	×	×	×			
JES_Flavor_Comp_leplepzll							×	
JES_Flavor_Resp	×	×	×	×	×	×		
JES_Flavor_Resp_leplepzll							×	
JES_PU_OffsetMu			×	×		×	×	
JES_PU_OffsetNPV	×	×	×	×	×	×	×	
JES_PU_PtTerm	×	×	×	×	×		×	
JES_PU_Rho	×	×	×	×	×	×	×	
MET_SoftTrk_ResoPara	×	×	×		×	×	×	
MET_SoftTrk_ResoPerp			×		×	×	×	
MET_SoftTrk_Scale		×	×		×	×	×	
MUONS_ID		×	×	×				
MUONS_MS		×	×			×		
MUONS_SAGITTA_RESBIAS		×						
MUONS_SCALE		×						
PRW_DATASF	×	×	×	×	×	×		
PRW_DATASF_zll_leplep							×	
Zllrew_mjj							×	

Table D.13.: Summary of shape (•) and acceptance (×) uncertainties from experimental sources in the SF $Z \to \ell\ell$ control region of the $\tau_{lep}\tau_{lep}$ channel.

Systematic	VBF $H \to \tau\tau$	VBF $H \to WW$	Non-VBF H	Top	Di-boson	Fake	$Z \to \tau\tau$	$Z \to \ell\ell$
Theo_VBFH_MUR_MUF	×							
Theo_VBFH_shower	×							
Theo_VH_MUR_MUF			×					
Theo_alphas_Higgs_ggH_total			×					
Theo_ggH_shower			×					
Theo_ggH_sig_qcd_1			×					
Theo_ggH_sig_qcd_2			×					
Theo_ggH_sig_qcd_3			×					
Theo_ggH_sig_qcd_4			×					
Theo_ggH_sig_qcd_6			×					
Theo_ggH_sig_qcd_7			×					
Theo_ggH_sig_qcd_8			×					
Theo_ll_vbf_ggH_PSUE			×					
Theo_pdf_Higgs_ggH_total			×					
Theo_sig_alphaS			×					
ZttTheory_MUR_MUF_vbf_leplep						×		
ZttTheory_PDF_vbf_leplep						×		

Table D.14.: Summary of shape (•) and acceptance (×) uncertainties from theoretical sources in the SF $Z \to \ell\ell$ control region of the $\tau_{lep}\tau_{lep}$ channel.

E Control-Region Fit

This chapter summarizes the nuisance parameter pulls and constraints as obtained from a likelihood fit in the control regions of the VBF CP analysis. In addition, the obtained pulls and constraints from the default fit in all signal and control regions are shown.

E.1. $H \rightarrow \tau_{lep}\tau_{lep}$ Standalone

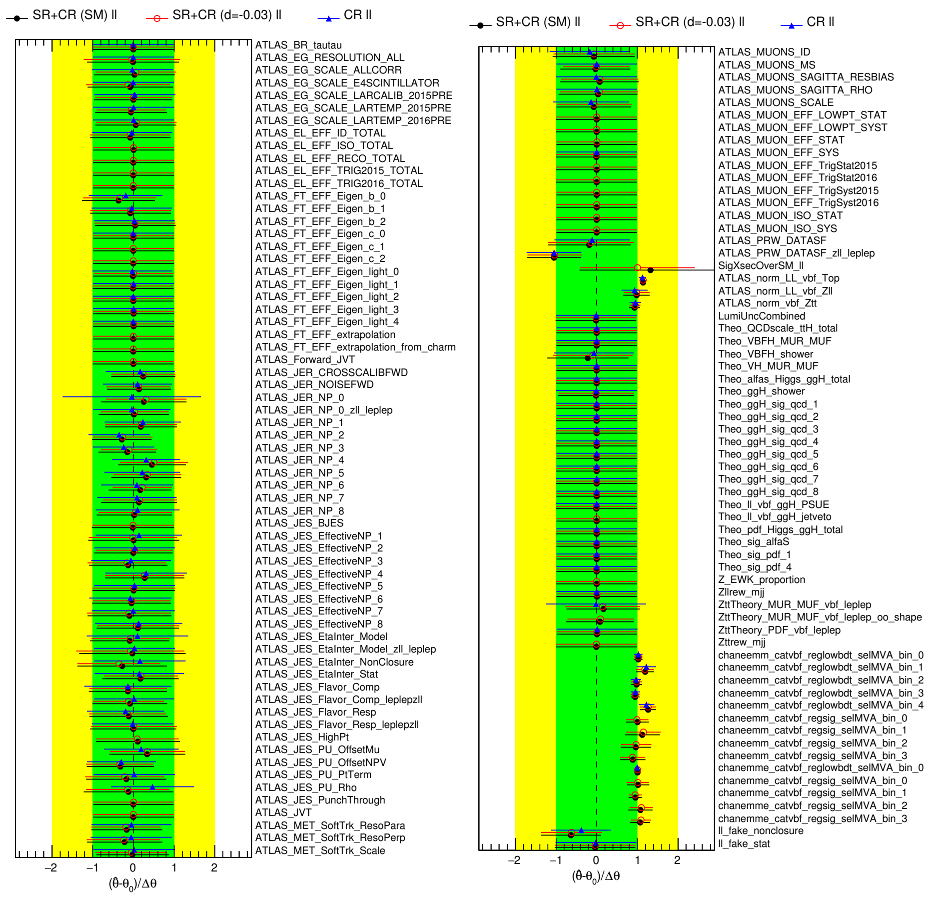

Figure E.1.: Observed pulls and constraints for nuisance parameters and background normalization factors from the likelihood fit in all $\tau_{lep}\tau_{lep}$ signal and control regions with the SM hypothesis (black) and the best-fit hypothesis of $\hat{\tilde{d}} = -0.03$ (red) compared to the results from the control-region only fit (blue).

E.2. Combination

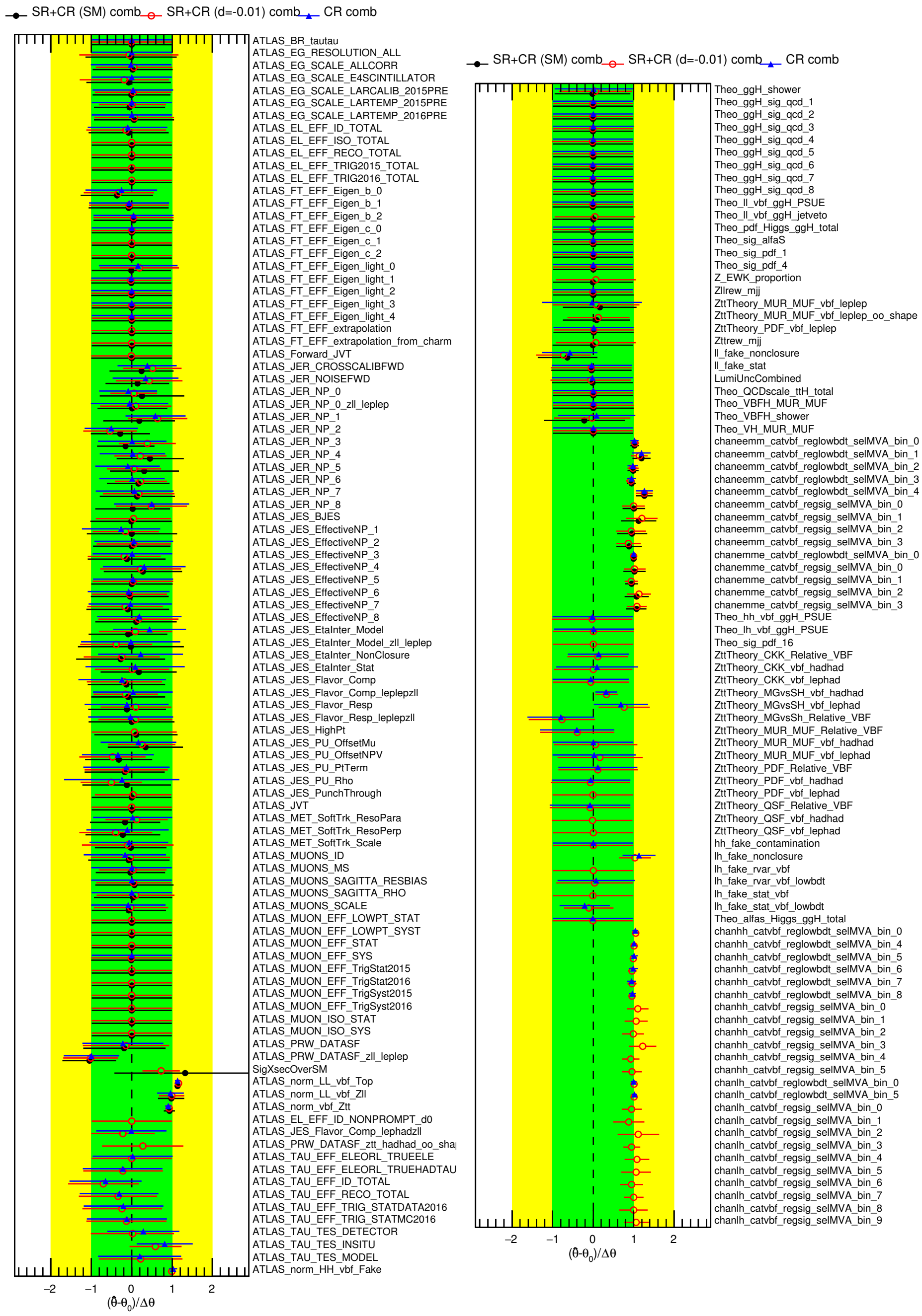

Figure E.2.: Observed pulls and constraints for nuisance parameters and background normalization factors from the likelihood fit in all $\tau_{lep}\tau_{lep}$, $\tau_{lep}\tau_{had}$ and $\tau_{had}\tau_{had}$ signal and control regions with the SM hypothesis (black) and the best-fit hypothesis of $\hat{\hat{d}} = -0.01$ (red) compared to the results from the control-region only fit (blue).

F Post-fit Event Yields

Section F.1 and F.2 summarize the post-fit yields in the $\tau_{lep}\tau_{lep}$ control regions of the $H \to \tau\tau$ cross-section measurement and the VBF CP analysis as obtained from the likelihood fit in all signal and control regions of the $\tau_{lep}\tau_{lep}$ channel. In addition, the post-fit yields in the signal and control regions of the $\tau_{lep}\tau_{lep}$ channels from the combined likelihood fit in the VBF CP analysis are given in Table F.4 and F.5. The post-fit yields in the signal and control regions of the $\tau_{lep}\tau_{had}$ and $\tau_{had}\tau_{had}$ channels from the combined likelihood fit in the VBF CP analysis are given in Table F.6 and F.7, respectively.

F.1. $H \to \tau\tau$ Cross-Section Measurement

Process	$\tau_{lep}\tau_{lep}$			
	Boosted Top CR	Boosted $Z \to \ell\ell$ CR	VBF Top CR	VBF $Z \to \ell\ell$ CR
ggF $H \to \tau\tau$	25 ± 11	1.13 ± 0.49	1.98 ± 0.91	0.11 ± 0.05
VBF $H \to \tau\tau$	5.4 ± 2.3	0.55 ± 0.26	4.2 ± 1.8	0.41 ± 0.17
WH $H \to \tau\tau$	3.7 ± 1.6	0.36 ± 0.17	0.05 ± 0.02	<0.01
ZH $H \to \tau\tau$	3.2 ± 1.3	0.13 ± 0.06	0.05 ± 0.03	<0.01
ttH $H \to \tau\tau$	116 ± 49	0.39 ± 0.19	4.4 ± 1.9	0.02 ± 0.03
$Z \to \tau\tau$	1310 ± 130	9.8 ± 1.6	59 ± 12	0.37 ± 0.23
$Z \to \ell\ell$	221 ± 63	2641 ± 66	5.6 ± 3.2	218 ± 18
Top	6550 ± 250	44.8 ± 7.6	441 ± 28	5.8 ± 1.1
Diboson	99.2 ± 9.9	107 ± 13	5.87 ± 0.83	6.0 ± 1.3
Fake	280 ± 130	-	14.5 ± 7.3	-
ggF $H \to WW$	5.88 ± 0.59	0.10 ± 0.02	0.38 ± 0.21	<0.01
VBF $H \to WW$	1.03 ± 0.11	0.03 ± 0.01	0.78 ± 0.10	<0.01
Total bkg.	8614 ± 96	2804 ± 66	534 ± 23	230 ± 18
Total signal	153 ± 50	2.56 ± 0.71	10.7 ± 2.8	0.54 ± 0.18
Data	8622	2805	538	232

Table F.1.: Post-fit event yields for signal and background predictions from the standalone likelihood fit in the $\tau_{lep}\tau_{lep}$ channel compared to the observed data yield in the Top and $Z \to \ell\ell$ control regions (CR). The uncertainties include statistical and systematic components.

F.2. VBF CP $H \to \tau\tau$ Analysis

Process	$\tau_{lep}\tau_{lep}$ SF Low-BDT CR	Top CR	$Z \to \ell\ell$ CR
VBF $H \to \tau\tau$ ($\tilde{d} = -0.03$, $\mu = 1.00$)	5.6 ± 8.0	1.3 ± 1.9	0.35 ± 0.49
VBF $H \to WW$ ($\tilde{d} = -0.03$, $\mu = 1.00$)	4.4 ± 6.3	0.8 ± 1.2	0.06 ± 0.09
$Z \to \tau\tau$	284 ± 47	81 ± 18	6.1 ± 1.5
$Z \to \ell\ell$	457 ± 95	81 ± 28	6470 ± 110
Top	112 ± 21	750 ± 30	61 ± 11
Di-Boson	42.8 ± 6.4	10.9 ± 1.6	89 ± 17
Fake	75 ± 31	45 ± 17	-
non-VBF $H \to \tau\tau$,WW	7.7 ± 1.6	1.58 ± 0.40	0.28 ± 0.11
Total bkg.	979 ± 71	970 ± 30	6631 ± 113
Total signal ($\tilde{d} = -0.03$, $\mu = 1.00$)	10 ± 14	2.1 ± 3.0	0.41 ± 0.57
Data	992	968	6632

Table F.2.: Post-fit event yields for signal and background predictions from the standalone fit in the $\tau_{lep}\tau_{lep}$ channel with the best-fit signal hypothesis of $\tilde{d} = -0.03$ compared to the observed data in the same-flavour (SF) control regions (CR). The uncertainty includes statistical, experimental and theoretical uncertainties.

Process	$\tau_{lep}\tau_{lep}$ DF Low-BDT CR	Top CR
VBF $H \to \tau\tau$ ($\hat{\tilde{d}} = -0.03$, $\hat{\mu} = 1.00$)	12 ± 17	2.5 ± 3.6
VBF $H \to WW$ ($\hat{\tilde{d}} = -0.03$, $\hat{\mu} = 1.00$)	7 ± 11	1.2 ± 1.8
$Z \to \tau\tau$	760 ± 73	184 ± 28
$Z \to \ell\ell$ +Di-Boson	100 ± 12	23.7 ± 3.5
Top	235 ± 42	2490 ± 69
Fake	326 ± 83	152 ± 39
non-VBF $H \to \tau\tau$,WW	16.1 ± 3.1	3.92 ± 0.64
Total bkg.	1497 ± 47	2854 ± 53
Total signal ($\hat{\tilde{d}} = -0.03$, $\hat{\mu} = 1.00$)	19 ± 28	3.7 ± 5.4
Data	1509	2864

Table F.3.: Post-fit event yields for signal and background predictions from the standalone fit in the $\tau_{lep}\tau_{lep}$ channel with the best-fit signal hypothesis of $\hat{\tilde{d}} = -0.03$ compared to the observed data in the different-flavour (DF) control regions (CR). The uncertainty includes statistical, experimental and theoretical uncertainties.

Process	$\tau_{lep}\tau_{lep}$ SF			
	Low-BDT CR	High-BDT SR	Top CR	$Z \to \ell\ell$ CR
VBF $H \to \tau\tau$ ($\hat{\tilde{d}} = -0.01$, $\hat{\mu} = 0.73$)	4.1 ± 2.6	2.6 ± 1.6	0.94 ± 0.63	0.25 ± 0.16
VBF $H \to WW$ ($\hat{\tilde{d}} = -0.01$, $\hat{\mu} = 0.73$)	3.2 ± 2.0	0.67 ± 0.45	0.60 ± 0.37	0.05 ± 0.03
$Z \to \tau\tau$	293 ± 48	6.6 ± 3.7	84 ± 19	6.3 ± 1.2
$Z \to \ell\ell$	452 ± 99	11 ± 18	69 ± 23	6470 ± 120
Top	118 ± 22	3.8 ± 2.3	766 ± 26	623 ± 10
Di-Boson	43 ± 6.2	0.70 ± 0.59	11.1 ± 1.5	87 ± 14
Fake	70 ± 27	0.02 ± 0.20	42 ± 15	-
non-VBF $H \to \tau\tau$,WW	7.6 ± 1.5	0.49 ± 0.48	1.51 ± 0.36	0.29 ± 0.11
Total bkg.	983 ± 77	23 ± 16	974 ± 26	6630 ± 120
Total signal ($\hat{\tilde{d}} = -0.01$, $\hat{\mu} = 0.73$)	7.3 ± 4.6	3.3 ± 2.1	1.5 ± 1.0	0.30 ± 0.19
Total signal ($\tilde{d} = 0$, $\mu = 1$)	10.0 ± 6.3	4.5 ± 2.9	2.1 ± 1.4	0.42 ± 0.26
Data	992	26	968	6632

Table F.4.: Post-fit event yields for signal and background predictions from the combined fit with the best-fit signal hypothesis of $\hat{\tilde{d}} = -0.01$ compared to the observed data in the signal regions (SR) and control regions (CR) of the $\tau_{lep}\tau_{lep}$ same-flavour (SF) channel. In addition, the expected pre-fit signal yields for the SM hypothesis ($\tilde{d} = 0$, $\mu = 1$) are given. The uncertainty includes statistical, experimental and theoretical uncertainties.

Process	$\tau_{lep}\tau_{lep}$ DF		
	Low-BDT CR	High-BDT SR	Top CR
VBF $H \to \tau\tau$ ($\hat{\tilde{d}} = -0.01$, $\hat{\mu} = 0.73$)	8.7 ± 5.5	3.9 ± 2.4	1.8 ± 1.1
VBF $H \to WW$ ($\hat{\tilde{d}} = -0.01$, $\hat{\mu} = 0.73$)	5.3 ± 3.4	1.1 ± 0.7	0.88 ± 0.55
$Z \to \tau\tau$	773 ± 63	8.2 ± 3.8	182 ± 24
Top	306 ± 42	10.6 ± 5.5	2498 ± 66
$Z \to \ell\ell$ +Di-Boson	97 ± 11	1.8 ± 1.1	23 ± 3
Fake	313 ± 73	2.29 ± 0.65	145 ± 35
non-VBF $H \to \tau\tau$,WW	15.9 ± 2.9	0.70 ± 0.30	3.83 ± 0.59
Total bkg.	1505 ± 39	23.6 ± 6.1	2852 ± 52
Total signal ($\hat{\tilde{d}} = -0.01$, $\hat{\mu} = 0.73$)	14 ± 9	5.1 ± 3.1	2.6 ± 1.6
Total signal ($\tilde{d} = 0$, $\mu = 1$)	19 ± 12	6.9 ± 4.4	3.6 ± 2.3
Data	1509	30	2864

Table F.5.: Post-fit event yields for signal and background predictions from the combined fit with the best-fit signal hypothesis of $\tilde{d} = -0.01$ compared to the observed data in the signal regions (SR) and control regions (CR) of the $\tau_{lep}\tau_{lep}$ different-flavour (DF) channel. In addition, the expected pre-fit signal yields for the SM hypothesis ($\tilde{d} = 0$, $\mu = 1$) are given. The uncertainty includes statistical, experimental and theoretical uncertainties.

Process	$\tau_{lep}\tau_{had}$ Low-BDT CR	$\tau_{lep}\tau_{had}$ High-BDT SR
VBF $H \to \tau\tau$ ($\hat{\tilde{d}} = -0.01$, $\hat{\mu} = 0.73$)	28 ± 17	11.8 ± 7.4
$Z \to \tau\tau$	1769 ± 91	7.8 ± 3.5
$Z \to \ell\ell$ +Top+Di-Boson	534 ± 74	2.8 ± 3.1
Fake	3000 ± 110	6.2 ± 1.0
non-VBF $H \to \tau\tau$	32.0 ± 8.0	2.1 ± 1.5
Total bkg.	5336 ± 76	19.0 ± 5.5
Total signal ($\hat{\tilde{d}} = -0.01$, $\hat{\mu} = 0.73$)	28 ± 17	11.8 ± 7.4
Total signal ($\tilde{d} = 0$, $\mu = 1$)	38 ± 23	16 ± 10
Data	5375	30

Table F.6.: Post-fit event yields for signal and background predictions from the combined fit with the best-fit signal hypothesis of $\tilde{d} = -0.01$ compared to the observed data in the signal regions (SR) and control regions (CR) of the $\tau_{lep}\tau_{had}$ channel. In addition, the expected pre-fit signal yields for the SM hypothesis ($\tilde{d} = 0$, $\mu = 1$) are given. The uncertainty includes statistical, experimental and theoretical uncertainties.

Process	$\tau_{had}\tau_{had}$ Low-BDT CR	$\tau_{had}\tau_{had}$ High-BDT SR
VBF $H \to \tau\tau$ ($\hat{\tilde{d}} = -0.01$, $\hat{\mu} = 0.73$)	9.2 ± 6.1	8.9 ± 5.6
$Z \to \tau\tau$	805 ± 49	15.5 ± 5.2
$Z \to \ell\ell$ +Top+Di-Boson+$W \to \tau\nu$	62.2 ± 7.9	2.3 ± 0.8
Fake	603 ± 53	5.4 ± 2.7
non-VBF $H \to \tau\tau$	13.1 ± 5.5	2.8 ± 1.4
Total bkg.	1483 ± 39	26.0 ± 6.6
Total signal ($\hat{\tilde{d}} = -0.01$, $\hat{\mu} = 0.73$)	9.2 ± 6.1	8.9 ± 5.6
Total signal ($\tilde{d} = 0$, $\mu = 1$)	12.6 ± 8.3	12.3 ± 7.7
Data	1479	37

Table F.7.: Post-fit event yields for signal and background predictions from the combined fit with the best-fit signal hypothesis of $\tilde{d} = -0.01$ compared to the observed data in the signal regions (SR) and control regions (CR) of the $\tau_{had}\tau_{had}$ channel. In addition, the expected pre-fit signal yields for the SM hypothesis ($\tilde{d} = 0$, $\mu = 1$) are given. The uncertainty includes statistical, experimental and theoretical uncertainties.

G Translation between Parametrizations for CP-Violating HVV Interactions

In the following, the parametrizations used by the ATLAS and CMS experiments to derive limits on anomalous contributions to the HVV coupling structure [109, 249] are put into relation to the $\tilde{d}$-parameter, which is used in the analysis presented in this thesis. The derivation of these relations are based on Ref. [253].

The following relations between the parameters $\tilde{d} = -\tilde{\kappa}_{AVV}/\kappa_{SM}\tan\alpha$ and f_3 hold and are used to convert the confidence intervals obtained for one parameter into the corresponding one for the other parameter:

$$\tilde{d} = \frac{f_3}{|f_3|}\sqrt{\frac{|f_3|}{|1-f_3|}\frac{\sigma_{SM}}{\sigma_{CP}}} = -\tilde{\kappa}_{AVV}/\kappa_{SM}\tan\alpha \tag{G.1}$$

and

$$f_3 = \frac{\tilde{d}}{|\tilde{d}|}\frac{r_\sigma^2}{1+r_\sigma^2} \quad \text{where} \quad r_\sigma^2 = \tilde{d}^2\frac{\sigma_{CP}}{\sigma_{SM}}. \tag{G.2}$$

The source and numerical values for the cross-section ratios $\frac{\sigma_{CP}}{\sigma_{SM}} = \frac{\sigma_4}{\sigma_1}$ are given below.
As explained in Section 2.3 the following Lagrangian is considered in the analysis presented in this note:

$$\mathcal{L}_{eff} = \mathcal{L}_{SM} + \tilde{g}_{HAA}H\tilde{A}_{\mu\nu}A^{\mu\nu} + \tilde{g}_{HAZ}H\tilde{A}_{\mu\nu}Z^{\mu\nu} + \tilde{g}_{HZZ}H\tilde{Z}_{\mu\nu}Z^{\mu\nu} + \tilde{g}_{HWW}H\tilde{W}^{+}_{\mu\nu}W^{\mu\nu}_{-} \tag{G.3}$$

where the couplings expressed in dependence on $\tilde{d}$ are given by

$$\tilde{g}_{HAA} = \tilde{g}_{HZZ} = \frac{1}{2}\tilde{g}_{HWW} = \frac{g}{2M_W}\tilde{d} \quad \text{and} \qquad \tilde{g}_{HAZ} = 0\,. \tag{G.4}$$

This effective Lagrangian yields the following Lorentz structure for each vertex of the Higgs boson and two electroweak gauge bosons (VV = W^+ W^-, ZZ, $\gamma\gamma$) with $p_{1,2}$ denoting the momenta of the gauge bosons:

$$T^{\mu\nu}(p_1,p_2) = \frac{2M_V^2}{v}g^{\mu\nu} + \frac{2\tilde{d}}{v}\,\varepsilon^{\mu\nu\alpha\beta}p_{1\alpha}p_{2\beta}\,, \tag{G.5}$$

where the relation $M_W = 1/2gv$ has been inserted.
The CMS collaboration uses the following Ansatz for the amplitude $A(H \to VV)$, when

only considering a SM like contribution and an anomalous CP-odd contribution:

$$A(H \to VV) = \frac{1}{v}(g_1 M_V^2 \epsilon_1^* \epsilon_2^* + g_4 f_{\mu\nu}^{(1)*} \tilde{f}^{(2)*,\mu\nu}) \tag{G.6}$$

with $f^{(i)*\mu\nu} = \epsilon_i^{*\mu} q_i^\nu - \epsilon_i^{*\nu} q_i^\mu$ and $\tilde{f}_{\mu\nu}^{(i)*} = 1/2\epsilon_{\mu\nu\alpha\beta} f^{(i)\alpha\beta}$, where ϵ_i^* denote the polarisation vectors and p_i (i=1,2) the four-momenta of the outgoing gauge bosons. The amplitude can be rewritten in the following form

$$A(H \to VV) = \frac{1}{v}\epsilon_1^{*\mu}\epsilon_2^{*\nu}(g_1 M_V^2 g_{\mu\nu} - 2g_4 \epsilon_{\mu\nu\alpha\beta} p_1^\alpha p_2^\beta)\,. \tag{G.7}$$

Comparing this with the vertex structure $T^{\mu\nu}(p_1, p_2)$ shows that $\tilde{d}$ is proportional to the ratio g_4 over g_1 assuming all parameters are real.
Let $\sigma_{SM} = \sigma_1$ be the cross section for $g_1 = 1$ and $g_4 = 0$ and $\sigma_{CP} = \sigma_4$ be the crossection for $g_1 = 0$ and $g_4 = 1$ the CMS collaboration defines the cross section ratio $f_3 = f_{g_4}$ as:

$$f_3 = f_{g4} = \frac{|g_4|^2\sigma_4}{|g_1|^2\sigma_1 + |g_4|^2\sigma_4} = \frac{r_{41}^2}{1 + r_{41}^2} \tag{G.8}$$

with

$$r_{41} = \frac{|g_4|}{|g_1|}\sqrt{\frac{\sigma_4}{\sigma_1}} \tag{G.9}$$

and $f_3 \cos(\phi_3)$ with $\phi_3 = 0$ and $\phi_3 = \pi$ is used as the fit parameter of interest. The numerical values for the ratio σ_4/σ_1 correspond to 0.143 (0.153) at center-of-mass energies of 8 (13 TeV), respectively. The ratio $\frac{|g_4|}{|g_1|}$ is equal to $\tilde{d}$ at the Lagrangian level.

Bibliography

[1] UA1 Collaboration, *Experimental Observation of Lepton Pairs of Invariant Mass around* $95\,\mathrm{GeV}/c^2$ *at the CERN SPS Collider*, Phys. Lett. **B126** (1983) 398.

[2] UA2 Collaboration, *Observation of Single Isolated Electrons of High Transverse Momentum in Events with Missing Transverse Energy at the CERN* $\bar{p}p$ *Collider*, Phys. Lett. **B122** (1983) 476.

[3] UA2 Collaboration, *Evidence for* $Z^0 \to e^+e^-$ *at the CERN* $\bar{p}p$ *Collider*, Phys. Lett. **B129** (1983) 130.

[4] P. W. Higgs, *Broken Symmetries and the Masses of Gauge Bosons*, Phys. Rev. **13** (1964) 508.

[5] P. W. Higgs, *Spontaneous Symmetry Breakdown without Massless Bosons*, Phys. Rev. **145** (1966) 1156.

[6] F. Englert and R. Brout, *Broken Symmetry and the Mass of Gauge Vector Mesons*, Phys. Rev. **13** (1964) 321.

[7] G. Guralnik, C. Hagen, and T. Kibble, *Global Conservation Laws and Massless Particles*, Phys. Rev. **13** (1964) 585.

[8] T. Kibble, *Symmetry breaking in nonAbelian gauge theories*, Phys. Rev. **155** (1967) 1554.

[9] ATLAS Collaboration, *Observation of a new particle in the search for the Standard Model Higgs boson with the ATLAS detector at the LHC*, Phys. Lett. **B716** (2012) 1–29.

[10] CMS Collaboration, *Observation of a new boson at a mass of 125 GeV with the CMS experiment at the LHC*, Phys. Lett. **B716** (2012) 30–61.

[11] ATLAS Collaboration, *Observation of Higgs boson production in association with a top quark pair at the LHC with the ATLAS detector*, Phys. Lett. **B784** (2018) 173–191.

[12] CMS Collaboration, *Observation of* $\mathrm{t\bar{t}}H$ *production*, Phys. Rev. Lett. **120** no. 23, (2018) 231801, `arXiv:1804.02610 [hep-ex]`.

[13] ATLAS Collaboration, *Observation of* $H \to b\bar{b}$ *decays and VH production with the ATLAS detector*, Phys. Lett. **B786** (2018) 59 – 86.

[14] CMS Collaboration, *Observation of Higgs boson decay to bottom quarks*, Phys. Rev. Lett. **121** no. 12, (2018) 121801, `arXiv:1808.08242 [hep-ex]`.

[15] ATLAS Collaboration, *Search for the Dimuon Decay of the Higgs Boson in pp Collisions at* $\sqrt{s} = 13$ TeV *with the ATLAS Detector*, Phys. Rev. Lett. **119** (2017) 051802.

[16] CMS Collaboration, *Search for the Higgs boson decaying to two muons in proton-proton collisions at* $\sqrt{s} = 13$ *TeV*, Phys. Rev. Lett. **122** (2019) 021801.

[17] ATLAS Collaboration, *Evidence for the Higgs-boson Yukawa coupling to tau leptons with the ATLAS detector*, JHEP **04** (2015) 117, `arXiv:1501.04943 [hep-ex]`.

[18] ATLAS and CMS Collaborations, *Measurements of the Higgs boson production and decay rates and constraints on its couplings from a combined ATLAS and CMS analysis of the LHC pp collision data at* $\sqrt{s} = 7$ *and* 8 *TeV*, JHEP **08** (2016) 45.

[19] A. D. Sakharov, *Violation of CP Invariance, c Asymmetry, and Baryon Asymmetry of the Universe*, Pisma Zh. Eksp. Teor. Fiz. **5** (1967) 32–35.

[20] N. Cabibbo, *Unitary Symmetry and Leptonic Decays*, Phys. Rev. Lett. **10** (1963) 531–533.

[21] M. Kobayashi and T. Maskawa, *CP-Violation in the Renormalizable Theory of Weak Interaction*, Progress of Theoretical Physics **49** .

[22] P. Huet and E. Sather, *Electroweak baryogenesis and standard model CP violation*, Phys. Rev. **D51** (1995) 379–394, `arXiv:hep-ph/9404302 [hep-ph]`.

[23] M. B. Gavela, P. Hernandez, J. Orloff, and O. Pene, *Standard model CP violation and baryon asymmetry*, Mod. Phys. Lett. **A9** (1994) 795–810, `arXiv:hep-ph/9312215 [hep-ph]`.

[24] A. G. Cohen, D. B. Kaplan, and A. E. Nelson, *Progress in electroweak baryogenesis*, Ann. Rev. Nucl. Part. Sci. **43** (1993) 27–70, `arXiv:hep-ph/9302210 [hep-ph]`.

[25] A. Riotto and M. Trodden, *Recent progress in baryogenesis*, Ann. Rev. Nucl. Part. Sci. **49** (1999) 35–75, `arXiv:hep-ph/9901362 [hep-ph]`.

[26] W.-S. Hou, *Source of CP Violation for the Baryon Asymmetry of the Universe*, Chin. J. Phys. **47** (2009) 134, `arXiv:0803.1234 [hep-ph]`.

[27] ATLAS Collaboration, *Evidence for the spin-0 nature of the Higgs boson using ATLAS data*, Phys. Lett. **B726** (2013) 120–144, `arXiv:1307.1432 [hep-ex]`.

[28] ATLAS Collaboration, *Study of the spin and parity of the Higgs boson in diboson decays with the ATLAS detector*, Eur. Phys. J. C **75** no. 10, (2015) 476, `arXiv:1506.05669 [hep-ex]`, [Erratum: Eur.Phys.J.C 76, 152 (2016)].

[29] CMS Collaboration, *Study of the Mass and Spin-Parity of the Higgs Boson Candidate Via Its Decays to Z Boson Pairs*, Phys. Rev. Lett. **110** no. 8, (2013) 081803, `arXiv:1212.6639 [hep-ex]`.

[30] ATLAS Collaboration, *Test of CP Invariance in vector-boson fusion production of the Higgs boson using the Optimal Observable method in the ditau decay channel with the ATLAS detector*, Eur. Phys. J. C **76** no. 12, (2016) 658, `arXiv:1602.04516 [hep-ex]`.

[31] ATLAS Collaboration, *Cross-section measurements of the Higgs boson decaying into a pair of τ-leptons in proton-proton collisions at $\sqrt{s} = 13$ TeV with the ATLAS detector*, Phys. Rev. D **99** (2019) 072001, `arXiv:1811.08856 [hep-ex]`.

[32] ATLAS Collaboration, *Test of CP invariance in vector-boson fusion production of the Higgs boson in the $H \to \tau\tau$ channel in proton–proton collisions at $\sqrt{s} = 13$ TeV with the ATLAS detector*, Phys. Lett. B **805** (2020) 135426, `arXiv:2002.05315 [hep-ex]`.

[33] CDF Collaboration, *Observation of top quark production in $\bar{p}p$ collisions*, Phys. Rev. Lett. **74** (1995) 2626–2631, `arXiv:hep-ex/9503002`.

[34] F. Halzen and A. D. Martin, *Quarks and Leptons: An Introductory Course in Modern Particle Physics*. Wiley, 2008.

[35] M. E. Peskin and D. V. Schroeder, *An Introduction to Quantum Field Theory*. Westview Press, 1995.

[36] D. Griffith, *Introduction to Elementary Particles*. Wiley, 1984.

[37] Super-Kamiokande Collaboration, *Evidence for oscillation of atmospheric neutrinos*, Phys. Rev. Lett. **81** (1998) 1562–1567, `arXiv:hep-ex/9807003`.

[38] SNO Collaboration, *Measurement of the rate of $\nu_e + d \to p + p + e^-$ interactions produced by ^8B solar neutrinos at the Sudbury Neutrino Observatory*, Phys. Rev. Lett. **87** (2001) 071301, `arXiv:nucl-ex/0106015`.

[39] SNO Collaboration, *Direct evidence for neutrino flavor transformation from neutral current interactions in the Sudbury Neutrino Observatory*, Phys. Rev. Lett. **89** (2002) 011301, `arXiv:nucl-ex/0204008`.

[40] Particle Data Group, *Review of Particle Physics*, Phys. Rev. D **98** (2018) 030001.

[41] G. V. Chibisov, *Astrophysical upper limits on the photon rest mass*, Soviet Physics Uspekhi **19** no. 7, (1976) 624–626.

[42] V. V. Ezhela, S. B. Lugovsky, and O. V. Zenin, *Hadronic part of the muon g-2 estimated on the sigma**2003(tot)(e+ e- —> hadrons) evaluated data compilation*, `arXiv:hep-ph/0312114 [hep-ph]`.

[43] P. Schmuser, *Feynman-Graphen und Eichtheorien fuer Experimentalphysiker*. Springer Berlin Heidelberg, 1995.

[44] D. J. Gross and F. Wilczek, *Ultraviolet Behavior of Nonabelian Gauge Theories*, Phys. Rev. Lett. **30** (1973) 1343–1346.

[45] H. Politzer, *Reliable Perturbative Results for Strong Interactions?*, Phys. Rev. Lett. **30** (1973) 1346–1349.

[46] LHCb Collaboration, *Observation of the resonant character of the $Z(4430)^-$ state*, Phys. Rev. Lett. **112** no. 22, (2014) 222002, `arXiv:1404.1903 [hep-ex]`.

[47] LHCb Collaboration, *Observation of $J/\psi p$ Resonances Consistent with Pentaquark States in $\Lambda_b^0 \to J/\psi K^- p$ Decays*, Phys. Rev. Lett. **115** (2015) 072001, `arXiv:1507.03414 [hep-ex]`.

[48] S. L. Glashow, *Partial Symmetries of Weak Interactions*, Nucl. Phys. **22** (1961) 579–588.

[49] S. Weinberg, *A Model of Leptons*, Phys. Rev. Lett. **19** (1967) 1264–1266.

[50] A. Salam, *Weak and Electromagnetic Interactions*, Conf. Proc. C **680519** (1968) 367–377.

[51] K. Nishijima, *Charge Independence Theory of V Particles*, Prog. Theor. Phys. **13** no. 3, (1955) 285–304.

[52] M. Gell-Mann, *The interpretation of the new particles as displaced charge multiplets*, Nuovo Cim. **4** no. S2, (1956) 848–866.

[53] T. Lee and C.-N. Yang, *Question of Parity Conservation in Weak Interactions*, Phys. Rev. **104** (1956) 254–258.

[54] C. Wu, E. Ambler, R. Hayward, D. Hoppes, and R. Hudson, *Experimental Test of Parity Conservation in β Decay*, Phys. Rev. **105** (1957) 1413–1414.

[55] Y. Nambu, *Quasiparticles and Gauge Invariance in the Theory of Superconductivity*, Phys. Rev. **117** (1960) 648–663.

[56] J. Goldstone, *Field Theories with Superconductor Solutions*, Nuovo Cim. **19** (1961) 154–164.

[57] T. Han and Y. Li, *Genuine CP-odd Observables at the LHC*, Phys. Lett. B **683** (2010) 278–281, `arXiv:0911.2933 [hep-ph]`.

[58] G. Valencia, *Constructing CP odd observables* pp. 0235–270. 1994. `arXiv:hep-ph/9411441`. Theoretical Advanced Study Institute in Elementary Particle Physics (TASI 94): CP Violation and the limits of the Standard Model.

[59] D. Choudhury and Mamta, *Anomalous Higgs Couplings at an e gamma Collider*, Phys. Rev. D **74** (2006) 115019, `arXiv:hep-ph/0608293`.

[60] Planck Collaboration, *Planck 2015 results - XIII. Cosmological parameters*, A&A **594** (2016) A13.

[61] J. Christenson, J. Cronin, V. Fitch, and R. Turlay, *Evidence for the* 2π *Decay of the* K_2^0 *Meson*, Phys. Rev. Lett. **13** (1964) 138–140.

[62] CDF Collaboration, *Observation of* $B_s^0 - \bar{B}_s^0$ *Oscillations*, Phys. Rev. Lett. **97** (2006) 242003, `arXiv:hep-ex/0609040 [hep-ex]`.

[63] BaBar Collaboration, *Observation of CP violation in the* B^0 *meson system*, Phys. Rev. Lett. **87** (2001) 091801, `arXiv:hep-ex/0107013 [hep-ex]`.

[64] Belle Collaboration, *Observation of large CP violation in the neutral B meson system*, Phys. Rev. Lett. **87** (2001) 091802, `arXiv:hep-ex/0107061 [hep-ex]`.

[65] LHCb Collaboration, *First observation of* CP *violation in the decays of* B_s^0 *mesons*, Phys. Rev. Lett. **110** no. 22, (2013) 221601, `arXiv:1304.6173 [hep-ex]`.

[66] LHCb Collaboration, *Observation of* $D^0 - \overline{D}^0$ *oscillations*, Phys. Rev. Lett. **110** no. 10, (2013) 101802, `arXiv:1211.1230 [hep-ex]`.

[67] J. M. Cline, *Baryogenesis* in *Les Houches Summer School - Session 86: Particle Physics and Cosmology: The Fabric of Spacetime Les Houches, France, July 31-August 25, 2006*. 2006. `arXiv:hep-ph/0609145 [hep-ph]`.

[68] W. Bernreuther, *CP violation and baryogenesis*, Lect. Notes Phys. **591** (2002) 237–293, `arXiv:hep-ph/0205279 [hep-ph]`.

[69] ATLAS Collaboration, `https://twiki.cern.ch/twiki/bin/view/AtlasPublic/StandardModelPublicResults`.

[70] C. Anastasiou, C. Duhr, F. Dulat, F. Herzog, and B. Mistlberger, *Higgs Boson Gluon-Fusion Production in QCD at Three Loops*, Phys. Rev. Lett. **114** (2015) 212001, `arXiv:1503.06056 [hep-ph]`.

[71] C. Anastasiou, C. Duhr, F. Dulat, E. Furlan, T. Gehrmann, F. Herzog, A. Lazopoulos, and B. Mistlberger, *High precision determination of the gluon fusion Higgs boson cross-section at the LHC*, JHEP **05** (2016) 058, `arXiv:1602.00695 [hep-ph]`.

[72] S. Actis, G. Passarino, C. Sturm, and S. Uccirati, *NLO Electroweak Corrections to Higgs Boson Production at Hadron Colliders*, Phys. Lett. **B670** (2008) 12–17, `arXiv:0809.1301 [hep-ph]`.

[73] M. Ciccolini, A. Denner, and S. Dittmaier, *Strong and electroweak corrections to the production of Higgs + 2jets via weak interactions at the LHC*, Phys. Rev. Lett. **99** (2007) 161803, `arXiv:0707.0381 [hep-ph]`.

[74] M. Ciccolini, A. Denner, and S. Dittmaier, *Electroweak and QCD corrections to Higgs production via vector-boson fusion at the LHC*, Phys. Rev. **D77** (2008) 013002, `arXiv:0710.4749 [hep-ph]`.

[75] P. Bolzoni, F. Maltoni, S.-O. Moch, and M. Zaro, *Higgs production via vector-boson fusion at NNLO in QCD*, Phys. Rev. Lett. **105** (2010) 011801, `arXiv:1003.4451 [hep-ph]`.

[76] O. Brein, A. Djouadi, and R. Harlander, *NNLO QCD corrections to the Higgs-strahlung processes at hadron colliders*, Phys. Lett. **B579** (2004) 149–156, `arXiv:hep-ph/0307206 [hep-ph]`.

[77] L. Altenkamp, S. Dittmaier, R. V. Harlander, H. Rzehak, and T. J. E. Zirke, *Gluon-induced Higgs-strahlung at next-to-leading order QCD*, JHEP **02** (2013) 078, `arXiv:1211.5015 [hep-ph]`.

[78] A. Denner, S. Dittmaier, S. Kallweit, and A. Muck, *Electroweak corrections to Higgs-strahlung off W/Z bosons at the Tevatron and the LHC with HAWK*, JHEP **03** (2012) 075, `arXiv:1112.5142 [hep-ph]`.

[79] W. Beenakker, S. Dittmaier, M. Kramer, B. Plumper, M. Spira, and P. M. Zerwas, *Higgs radiation off top quarks at the Tevatron and the LHC*, Phys. Rev. Lett. **87** (2001) 201805, `arXiv:hep-ph/0107081 [hep-ph]`.

[80] W. Beenakker, S. Dittmaier, M. Kramer, B. Plumper, M. Spira, and P. M. Zerwas, *NLO QCD corrections to t anti-t H production in hadron collisions*, Nucl. Phys. **B653** (2003) 151–203, `arXiv:hep-ph/0211352 [hep-ph]`.

[81] S. Dawson, L. H. Orr, L. Reina, and D. Wackeroth, *Associated top quark Higgs boson production at the LHC*, Phys. Rev. **D67** (2003) 071503, `arXiv:hep-ph/0211438 [hep-ph]`.

[82] S. Dawson, C. Jackson, L. H. Orr, L. Reina, and D. Wackeroth, *Associated Higgs production with top quarks at the large hadron collider: NLO QCD corrections*, Phys. Rev. **D68** (2003) 034022, `arXiv:hep-ph/0305087 [hep-ph]`.

[83] Y. Zhang, W.-G. Ma, R.-Y. Zhang, C. Chen, and L. Guo, *QCD NLO and EW NLO corrections to $t\bar{t}H$ production with top quark decays at hadron collider*, Phys. Lett. **B738** (2014) 1–5, `arXiv:1407.1110 [hep-ph]`.

[84] S. Frixione, V. Hirschi, D. Pagani, H. S. Shao, and M. Zaro, *Electroweak and QCD corrections to top-pair hadroproduction in association with heavy bosons*, JHEP **06** (2015) 184, `arXiv:1504.03446 [hep-ph]`.

[85] LHC Higgs Cross Section Working Group, *Handbook of LHC Higgs Cross Sections: 4. Deciphering the Nature of the Higgs Sector*, `arXiv:1610.07922 [hep-ph]`.

[86] B. W. Lee, C. Quigg, and H. Thacker, *Weak Interactions at Very High-Energies: The Role of the Higgs Boson Mass*, Phys. Rev. D **16** (1977) 1519.

[87] M. Spira and P. M. Zerwas, *Electroweak symmetry breaking and Higgs physics*, Lect. Notes Phys. **512** (1998) 161–225, `arXiv:hep-ph/9803257`.

[88] J. Ellis, *Outstanding questions: Physics beyond the Standard Model*, Phil. Trans. Roy. Soc. Lond. A **370** 818–830.

[89] T. Hambye and K. Riesselmann, *Matching conditions and Higgs mass upper bounds revisited*, Phys. Rev. **D55** (1997) 7255–7262, `arXiv:hep-ph/9610272 [hep-ph]`.

[90] A. Djouadi, *The Anatomy of electro-weak symmetry breaking. I: The Higgs boson in the standard model*, Phys. Rept. **457** (2008) 1–216, `arXiv:hep-ph/0503172 [hep-ph]`.

[91] G. Degrassi, S. Di Vita, J. Elias-Miro, J. R. Espinosa, G. F. Giudice, G. Isidori, and A. Strumia, *Higgs mass and vacuum stability in the Standard Model at NNLO*, JHEP **08** (2012) 098, `arXiv:1205.6497 [hep-ph]`.

[92] LEP Working Group for Higgs boson searches, ALEPH, DELPHI, L3, OPAL, *Search for the standard model Higgs boson at LEP*, Phys. Lett. B **565** (2003) 61–75, `arXiv:hep-ex/0306033`.

[93] TEVNPH (Tevatron New Phenomina and Higgs Working Group), CDF, D0, *Combined CDF and D0 Search for Standard Model Higgs Boson Production with up to 10.0 fb^{-1} of Data* 2012. `arXiv:1203.3774 [hep-ex]`. `http://lss.fnal.gov/archive/2012/conf/fermilab-conf-12-065-e.pdf`.

[94] Tevatron New Physics Higgs Working Group, *Updated Combination of CDF and D0 Searches for Standard Model Higgs Boson Production with up to 10.0 fb^{-1} of Data* 2012. `arXiv:1207.0449 [hep-ex]`. `http://lss.fnal.gov/cgi-bin/find_paper.pl?conf-12-318`.

[95] ALEPH, DELPHI, L3, OPAL, LEP Electroweak Collaborations, *Electroweak Measurements in Electron-Positron Collisions at W-Boson-Pair Energies at LEP*, Phys. Rept. **532** 119–244, `arXiv:1302.3415 [hep-ex]`.

[96] ATLAS and CMS Collaborations, *Combined Measurement of the Higgs Boson Mass in pp Collisions at $\sqrt{s} = 7$ and 8 TeV with the ATLAS and CMS Experiments*, Phys. Rev. Lett. **114** (2015) 191803, `arXiv:1503.07589 [hep-ex]`.

[97] ATLAS Collaboration, *Measurement of the Higgs boson mass in the $H \to ZZ^* \to 4\ell$ and $H \to \gamma\gamma$ channels with $\sqrt{s} = 13$ TeV pp collisions using the ATLAS detector*, Phys. Lett. B **784** (2018) 345–366, `arXiv:1806.00242 [hep-ex]`.

[98] L. Landau, *On the angular momentum of a system of two photons*, Dokl. Akad. Nauk SSSR **60** no. 2, (1948) 207–209.

[99] C.-N. Yang, *Selection Rules for the Dematerialization of a Particle Into Two Photons*, Phys. Rev. **77** (1950) 242–245.

[100] ATLAS Collaboration, *Combined measurements of Higgs boson production and decay using up to 80 fb^{-1} of proton-proton collision data at $\sqrt{s}$ = 13 TeV collected with the ATLAS experiment*, Phys. Rev. D **101** no. 1, (2020) 012002, `arXiv:1909.02845 [hep-ex]`.

[101] W. Buchmuller and D. Wyler, *Effective lagrangian analysis of new interactions and flavour conservation*, Nuclear Physics B **268** no. 3, (1986) 621 – 653.

[102] B. Grzadkowski, M. Iskrzynski, M. Misiak, and J. Rosiek, *Dimension-Six Terms in the Standard Model Lagrangian*, JHEP **10** (2010) 085, `arXiv:1008.4884 [hep-ph]`.

[103] V. Hankele, G. Klamke, D. Zeppenfeld, and T. Figy, *Anomalous Higgs boson couplings in vector boson fusion at the CERN LHC*, Phys. Rev. **D74** (2006) 095001, `arXiv:hep-ph/0609075 [hep-ph]`.

[104] ALEPH Collaboration, *Improved measurement of the triple gauge-boson couplings γWW and ZWW in e^+e^- collisions*, Phys. Lett. **B614** (2005) 7–26.

[105] OPAL Collaboration, *Measurement of W boson polarizations and CP violating triple gauge couplings from W^+W^- production at LEP*, Eur. Phys. J. **C19** (2001) 229–240, `arXiv:hep-ex/0009021 [hep-ex]`.

[106] DELPHI Collaboration, *Study of W boson polarisations and Triple Gauge boson Couplings in the reaction $e^+e^- \to W^+W^-$ at LEP 2*, Eur. Phys. J. **C54** (2008) 345–364, `arXiv:0801.1235 [hep-ex]`.

[107] L3 Collaboration, *Search for anomalous couplings in the Higgs sector at LEP*, Phys. Lett. **B589** (2004) 89–102, `arXiv:hep-ex/0403037 [hep-ex]`.

[108] ATLAS Collaboration, *Measurements of Higgs boson properties in the diphoton decay channel with 36 fb^{-1} of pp collision data at $\sqrt{s} = 13$ TeV with the ATLAS detector*, Phys. Rev. **D98** (2018) 052005, `arXiv:1802.04146 [hep-ex]`.

[109] ATLAS Collaboration, *Measurement of the Higgs boson coupling properties in the $H \to ZZ^* \to 4\ell$ decay channel at $\sqrt{s}$ = 13 TeV with the ATLAS detector*, JHEP **03** (2018) 095, `arXiv:1712.02304 [hep-ex]`.

[110] CMS Collaboration, *Combined search for anomalous pseudoscalar HVV couplings in VH($H \to b\bar{b}$) production and $H \to VV$ decay*, Phys. Lett. **B759** (2016) 672–696, `arXiv:1602.04305 [hep-ex]`.

[111] J. Brehmer, F. Kling, T. Plehn, and T. M. P. Tait, *Better Higgs-CP Tests Through Information Geometry*, Phys. Rev. D **97** no. 9, (2018) 095017, `arXiv:1712.02350 [hep-ph]`.

[112] D. Atwood, S. Bar-Shalom, G. Eilam, and A. Soni, *CP violation in top physics*, Phys. Rept. **347** (2001) 1–222, `arXiv:hep-ph/0006032`.

[113] D. Atwood and A. Soni, *Analysis for magnetic moment and electric dipole moment form-factors of the top quark via $e^+e^- \to t\bar{t}$*, Phys. Rev. **D45** (1992) 2405–2413.

[114] M. Diehl and O. Nachtmann, *Optimal observables for the measurement of three gauge boson couplings in* $e^-e^+ \to W^-W^+$, Z. Phys. **C62** (1994) 397–412.

[115] M. Diehl, O. Nachtmann, and F. Nagel, *Triple gauge couplings in polarized* $e^-e^+ \to W^-W^+$ *and their measurement using optimal observables*, Eur. Phys. J. **C27** (2003) 375–397, `arXiv:hep-ph/0209229 [hep-ph]`.

[116] M. Davier, L. Duflot, F. Le Diberder, and A. Rouge, *The Optimal method for the measurement of tau polarization*, Phys. Lett. B **306** (1993) 411–417.

[117] OPAL Collaboration, *Search for CP violation in* $Z^0 \to \tau^+\tau^-$ *and an Upper Limit on the Weak Dipole Moment of the* τ *Lepton*, Zeitschrift fuer Physik C Particles and Fields **74** no. 3, (1997) 403–413.

[118] M. Schumacher, *Determination of the cp quantum numbers of the Higgs boson and test of cp invariance in the higgs-strahlung process at a future e+ e- linear collider*, LC-PHSM-2001-003, 1403–1417, 2001.

[119] M. Ciccolini, A. Denner, and S. Dittmaier, *Strong and electroweak corrections to the production of Higgs + 2jets via weak interactions at the LHC*, Phys. Rev. Lett. **99** (2007) 161803, `arXiv:0707.0381 [hep-ph]`.

[120] M. Ciccolini, A. Denner, and S. Dittmaier, *Electroweak and QCD corrections to Higgs production via vector-boson fusion at the LHC*, Phys. Rev. D **77** (2008) 013002, `arXiv:0710.4749 [hep-ph]`.

[121] H.-L. Lai, M. Guzzi, J. Huston, Z. Li, P. M. Nadolsky, J. Pumplin, and C. P. Yuan, *New parton distributions for collider physics*, Phys. Rev. **D82** (2010) 074024, `arXiv:1007.2241 [hep-ph]`.

[122] L. Evans and P. Bryant, *LHC Machine*, JINST **3** (2008) S08001.

[123] ATLAS Collaboration, *The ATLAS Experiment at the CERN Large Hadron Collider*, JINST **3** (2008) S08003.

[124] LHCb Collaboration, *The LHCb Detector at the LHC*, JINST **3** (2008) S08005.

[125] ALICE Collaboration, *The ALICE experiment at the CERN LHC*, JINST **3** (2008) S08002.

[126] M. Barnes *et al.*, *The PS complex as proton pre-injector for the LHC: design and implementation report*. CERN Yellow Reports: Monographs. CERN, Geneva, 2000. `https://cds.cern.ch/record/449242`.

[127] P. Collier *et al.*, *The SPS as Injector for LHC: Conceptual Design*, https://cds.cern.ch/record/322782, CERN-SL-97-007-DI, 1997.

[128] M. Hostettler and G. Papotti, *Luminosity Lifetime at the LHC in 2012 Proton Physics Operation* in *Proceedings, 4th International Particle Accelerator Conference (IPAC 2013): Shanghai, China, May 12-17, 2013*, p. TUPFI029. 2013.

[129] O. S. Bruning and P. Collier, *Building a behemoth*, Nature **448** (2007) 285–289.

[130] ATLAS Collaboration, *ATLAS Insertable B-Layer Technical Design Report*, https://cds.cern.ch/record/1291633, CERN-LHCC-2010-013, 2010.

[131] ATLAS Collaboration, *ATLAS pixel detector electronics and sensors*, JINST **3** (2008) P07007.

[132] ATLAS Collaboration, *Improved luminosity determination in pp collisions at sqrt(s) = 7 TeV using the ATLAS detector at the LHC*, Eur. Phys. J. C **73** no. 8, (2013) 2518, `arXiv:1302.4393 [hep-ex]`.

[133] U. Amaldi *et al.*, *The Real Part of the Forward Proton Proton Scattering Amplitude Measured at the CERN Intersecting Storage Rings*, Phys. Lett. **66B** (1977) 390–394.

[134] ATLAS Collaboration, *Performance of the ATLAS Trigger System in 2015*, Eur. Phys. J. **C77** (2017) 317.

[135] ATLAS Collaboration, `https://twiki.cern.ch/twiki/bin/view/AtlasPublic/LuminosityPublicResultsRun2`.

[136] C. Schillo, *Search for the Standard Model Higgs Boson and Test of CP Invariance in Vector-Boson Fusion Production of the Higgs Boson in the Fully Leptonic $H \to \tau\tau \to \ell\ell 4\nu$ Final State in Proton-Proton Collisions with the ATLAS Detector at the LHC*, https://cds.cern.ch/record/2239966, CERN-THESIS-2016-216, 2016.

[137] Y. L. Dokshitzer, *Calculation of the Structure Functions for Deep Inelastic Scattering and e+ e- Annihilation by Perturbation Theory in Quantum Chromodynamics.*, Sov. Phys. JETP **46** (1977) 641–653.

[138] V. Gribov and L. Lipatov, *Deep inelastic electron scattering in perturbation theory*, Physics Letters B **37** no. 1, (1971) 78 – 80.

[139] G. Altarelli and G. Parisi, *Asymptotic freedom in parton language*, Nuclear Physics B **126** no. 2, (1977) 298 – 318.

[140] NNPDF Collaboration, *Parton distributions from high-precision collider data*, Eur. Phys. J. C **77** no. 10, (2017) 663, `arXiv:1706.00428 [hep-ph]`.

[141] J. C. Collins, D. E. Soper, and G. F. Sterman, *Factorization of Hard Processes in QCD*, Adv. Ser. Direct. High Energy Phys. **5** (1988) 1, `arXiv:hep-ph/0409313`.

[142] R. P. Feynman, *Space-Time Approach to Quantum Electrodynamics*, Phys. Rev. **76** (Sep, 1949) 769–789.

[143] A. Buckley *et al.*, *General-purpose event generators for LHC physics*, Phys. Rept. **504** (2011) 145–233, `arXiv:1101.2599 [hep-ph]`.

[144] B. Andersson, G. Gustafson, G. Ingelman, and T. Sjstrand, *Parton fragmentation and string dynamics*, Physics Reports **97** no. 2, (1983) 31 – 145.

[145] B. Webber, *A QCD model for jet fragmentation including soft gluon interference*, Nuclear Physics B **238** no. 3, (1984) 492 – 528.

[146] S. Catani, F. Krauss, R. Kuhn, and B. R. Webber, *QCD matrix elements + parton showers*, JHEP **11** (2001) 063, `arXiv:hep-ph/0109231 [hep-ph]`.

[147] J. Alwall *et al.*, *Comparative study of various algorithms for the merging of parton showers and matrix elements in hadronic collisions*, Eur. Phys. J. **C53** (2008) 473–500, `arXiv:0706.2569 [hep-ph]`.

[148] T. Sjostrand, S. Mrenna, and P. Skands, *A brief introduction to PYTHIA 8.1*, Computer Physics Communications **178** no. 11, (2008) 852 – 867.

[149] T. Gleisberg, S. Hoeche, F. Krauss, M. Schonherr, S. Schumann, F. Siegert, and J. Winter, *Event generation with SHERPA 1.1*, JHEP **02** (2009) 007, `arXiv:0811.4622 [hep-ph]`.

[150] P. Nason, *A New method for combining NLO QCD with shower Monte Carlo algorithms*, JHEP **11** (2004) 040, `arXiv:hep-ph/0409146`.

[151] S. Frixione, P. Nason, and C. Oleari, *Matching NLO QCD computations with Parton Shower simulations: the POWHEG method*, JHEP **11** (2007) 070, `arXiv:0709.2092 [hep-ph]`.

[152] S. Alioli, P. Nason, C. Oleari, and E. Re, *A general framework for implementing NLO calculations in shower Monte Carlo programs: the POWHEG BOX*, JHEP **06** (2010) 043, `arXiv:1002.2581 [hep-ph]`.

[153] E. Bagnaschi, G. Degrassi, P. Slavich, and A. Vicini, *Higgs production via gluon fusion in the POWHEG approach in the SM and in the MSSM*, JHEP **02** (2012) 088, `arXiv:1111.2854 [hep-ph]`.

[154] J. Alwall, R. Frederix, S. Frixione, V. Hirschi, F. Maltoni, O. Mattelaer, H. S. Shao, T. Stelzer, P. Torrielli, and M. Zaro, *The automated computation of tree-level and next-to-leading order differential cross sections, and their matching to parton shower simulations*, JHEP **07** (2014) 079, `arXiv:1405.0301 [hep-ph]`.

[155] A. D. Martin, W. J. Stirling, R. S. Thorne, and G. Watt, *Parton distributions for the LHC*, Eur. Phys. J. **C63** (2009) 189–285, `arXiv:0901.0002 [hep-ph]`.

[156] ATLAS Collaboration, *Summary of ATLAS Pythia 8 tunes*, ATL-PHYS-PUB-2012-003, 8, 2012.

[157] The GEANT4 Collaboration, *Geant4: A simulation toolkit*, Nuclear Instruments and Methods in Physics Research Section A: Accelerators, Spectrometers, Detectors and Associated Equipment **506** no. 3, (2003) 250 – 303.

[158] ATLAS Collaboration, *The ATLAS Simulation Infrastructure*, Eur. Phys. J. **C70** (2010) 823–874, `arXiv:1005.4568 [physics.ins-det]`.

[159] F. Siegert, *Monte-Carlo event generation for the LHC.* PhD thesis, 2010. `http://etheses.dur.ac.uk/484/`.

[160] K. Hamilton, P. Nason, E. Re, and G. Zanderighi, *NNLOPS simulation of Higgs boson production*, JHEP **10** (2013) 222, `arXiv:1309.0017 [hep-ph]`.

[161] K. Hamilton, P. Nason, and G. Zanderighi, *Finite quark-mass effects in the NNLOPS POWHEG+MiNLO Higgs generator*, JHEP **05** (2015) 140, `arXiv:1501.04637 [hep-ph]`.

[162] J. Butterworth *et al.*, *PDF4LHC recommendations for LHC Run II*, J. Phys. **G43** (2016) 023001, `arXiv:1510.03865 [hep-ph]`.

[163] T. Sjostrand, S. Mrenna, and P. Z. Skands, *A Brief Introduction to PYTHIA 8.1*, Comput. Phys. Commun. **178** (2008) 852–867, `arXiv:0710.3820 [hep-ph]`.

[164] J. Pumplin, D. R. Stump, J. Huston, H. L. Lai, P. M. Nadolsky, and W. K. Tung, *New generation of parton distributions with uncertainties from global QCD analysis*, JHEP **07** (2002) 012, `arXiv:hep-ph/0201195 [hep-ph]`.

[165] M. Bahr *et al.*, *Herwig++ Physics and Manual*, Eur. Phys. J. C **58** (2008) 639–707, `arXiv:0803.0883 [hep-ph]`.

[166] J. Bellm *et al.*, *Herwig 7.0/Herwig++ 3.0 release note*, Eur. Phys. J. C **76** no. 4, (2016) 196, `arXiv:1512.01178 [hep-ph]`.

[167] NNPDF Collaboration, *Parton distributions for the LHC Run II*, JHEP **04** (2015) 040, `arXiv:1410.8849 [hep-ph]`.

[168] R. D. Ball *et al.*, *Parton distributions with LHC data*, Nucl. Phys. **B867** (2013) 244–289, `arXiv:1207.1303 [hep-ph]`.

[169] ATLAS Collaboration, *ATLAS Pythia 8 tunes to 7 TeV data*, https://cds.cern.ch/record/1966419, ATL-PHYS-PUB-2014-021, 2014.

[170] N. Davidson, T. Przedzinski, and Z. Was, *PHOTOS interface in C++: Technical and Physics Documentation*, Comput. Phys. Commun. **199** (2016) 86–101, `arXiv:1011.0937 [hep-ph]`.

[171] T. Gleisberg and S. Hoeche, *Comix, a new matrix element generator*, JHEP **12** (2008) 039, `arXiv:0808.3674 [hep-ph]`.

[172] F. Cascioli, P. Maierhofer, and S. Pozzorini, *Scattering Amplitudes with Open Loops*, Phys. Rev. Lett. **108** (2012) 111601, `arXiv:1111.5206 [hep-ph]`.

[173] S. Schumann and F. Krauss, *A Parton shower algorithm based on Catani-Seymour dipole factorisation*, JHEP **03** (2008) 038, `arXiv:0709.1027 [hep-ph]`.

[174] S. Hoeche, F. Krauss, M. Schonherr, and F. Siegert, *QCD matrix elements + parton showers: The NLO case*, JHEP **04** (2013) 027, `arXiv:1207.5030 [hep-ph]`.

[175] K. Melnikov and F. Petriello, *Electroweak gauge boson production at hadron colliders through $O(\alpha_s^2)$*, Phys. Rev. **D74** (2006) 114017, `arXiv:hep-ph/0609070 [hep-ph]`.

[176] C. Anastasiou, L. J. Dixon, K. Melnikov, and F. Petriello, *High precision QCD at hadron colliders: Electroweak gauge boson rapidity distributions at NNLO*, Phys. Rev. **D69** (2004) 094008, `arXiv:hep-ph/0312266 [hep-ph]`.

[177] ATLAS Collaboration, *Measurement of electroweak production of dijets in association with a Z boson in pp collisions at $\sqrt{s} = 13$ TeV with the ATLAS detector*, https://cds.cern.ch/record/2151791, ATL-COM-PHYS-2016-460, 2016.

[178] T. Sjostrand, S. Mrenna, and P. Z. Skands, *PYTHIA 6.4 Physics and Manual*, JHEP **05** (2006) 026, `arXiv:hep-ph/0603175 [hep-ph]`.

[179] M. Czakon and A. Mitov, *Top++: A Program for the Calculation of the Top-Pair Cross-Section at Hadron Colliders*, Comput. Phys. Commun. **185** (2014) 2930, `arXiv:1112.5675 [hep-ph]`.

[180] S. Alioli, P. Nason, C. Oleari, and E. Re, *NLO single-top production matched with shower in POWHEG: s- and t-channel contributions*, JHEP **09** (2009) 111, `arXiv:0907.4076 [hep-ph]`, [Erratum: JHEP02,011(2010)].

[181] E. Re, *Single-top Wt-channel production matched with parton showers using the POWHEG method*, Eur. Phys. J. **C71** (2011) 1547, `arXiv:1009.2450 [hep-ph]`.

[182] P. Artoisenet, R. Frederix, O. Mattelaer, and R. Rietkerk, *Automatic spin-entangled decays of heavy resonances in Monte Carlo simulations*, JHEP **03** (2013) 015, `arXiv:1212.3460 [hep-ph]`.

[183] D. J. Lange, *The EvtGen particle decay simulation package*, Nuclear Instruments and Methods in Physics Research Section A: Accelerators, Spectrometers, Detectors and Associated Equipment **462** no. 1, (2001) 152 – 155, BEAUTY2000, Proceedings of the 7th Int. Conf. on B-Physics at Hadron Machines.

[184] T. Cornelissen, M. Elsing, S. Fleischmann, W. Liebig, E. Moyse, and A. Salzburger, *Concepts, Design and Implementation of the ATLAS New Tracking (NEWT)*, https://cds.cern.ch/record/1020106, ATL-SOFT-PUB-2007-007, 2007.

[185] R. Fruhwirth, *Application of Kalman filtering to track and vertex fitting*, Nucl. Instrum. Meth. **A262** (1987) 444–450.

[186] R. E. Kalman, *A New Approach to Linear Filtering and Prediction Problems*, J. Fluids Eng. **82.1** (1960) 35–45.

[187] ATLAS Collaboration, *Performance of the ATLAS Track Reconstruction Algorithms in Dense Environments in LHC Run 2*, Eur. Phys. J. C **77** no. 10, (2017) 673, `arXiv:1704.07983 [hep-ex]`.

[188] G. Piacquadio, K. Prokofiev, and A. Wildauer, *Primary vertex reconstruction in the ATLAS experiment at LHC*, J. Phys. Conf. Ser. **119** (2008) 032033.

[189] ATLAS Collaboration, *Vertex Reconstruction Performance of the ATLAS Detector at $\sqrt{s}$ =13 TeV*, http://cds.cern.ch/record/2037717, ATL-PHYS-PUB-2015-026, 2015.

[190] W. Lampl, S. Laplace, D. Lelas, P. Loch, H. Ma, S. Menke, S. Rajagopalan, D. Rousseau, S. Snyder, and G. Unal, *Calorimeter Clustering Algorithms: Description and Performance*, https://cds.cern.ch/record/1099735, ATL-LARG-PUB-2008-002, 2008.

[191] T. G. Cornelissen, M. Elsing, I. Gavrilenko, J. F. Laporte, W. Liebig, M. Limper, K. Nikolopoulos, A. Poppleton, and A. Salzburger, *The global χ^2 track fitter in ATLAS*, J. Phys. Conf. Ser. **119** (2008) 032013.

[192] ATLAS Collaboration, *Improved electron reconstruction in ATLAS using the Gaussian Sum Filter-based model for bremsstrahlung*, https://cds.cern.ch/record/1449796, ATLAS-CONF-2012-047, 2012.

[193] ATLAS Collaboration, *Electron and photon energy calibration with the ATLAS detector using LHC Run 1 data*, Eur. Phys. J. C **74** no. 10, 3071, `arXiv:1407.5063 [hep-ex]`.

[194] ATLAS Collaboration, *Electron and photon energy calibration with the ATLAS detector using 2015-2016 LHC proton-proton collision data*, JINST **14** no. 03, (2019) P03017, `arXiv:1812.03848 [hep-ex]`.

[195] ATLAS Collaboration, *Electron efficiency measurements with the ATLAS detector using 2012 LHC proton–proton collision data*, Eur. Phys. J. C **77** no. 3, (2017) 195, `arXiv:1612.01456 [hep-ex]`.

[196] ATLAS Collaboration, *Electron reconstruction and identification in the ATLAS experiment using the 2015 and 2016 LHC proton-proton collision data at $\sqrt{s}$ = 13 TeV*, Eur. Phys. J. C **79** no. 8, (2019) 639, `arXiv:1902.04655 [physics.ins-det]`.

[197] ATLAS Collaboration, *Topological cell clustering in the ATLAS calorimeters and its performance in LHC Run 1*, Eur. Phys. J. **C77** (2017) 490, `arXiv:1603.02934 [hep-ex]`.

[198] M. Cacciari and G. P. Salam, *Pileup subtraction using jet areas*, Phys. Lett. **B659** (2008) 119–126, `arXiv:0707.1378 [hep-ph]`.

[199] ATLAS Collaboration, *Muon reconstruction performance of the ATLAS detector in proton-proton collision data at $\sqrt{s}$ =13 TeV*, Eur. Phys. J. C **76** no. 5, (2016) 292, `arXiv:1603.05598 [hep-ex]`.

[200] ATLAS Collaboration, *Measurement of the muon reconstruction performance of the ATLAS detector using 2011 and 2012 LHC proton–proton collision data*, Eur. Phys. J. C **74** no. 11, (2014) 3130, `arXiv:1407.3935 [hep-ex]`.

[201] ATLAS Collaboration, *Properties of Jets and Inputs to Jet Reconstruction and Calibration with the ATLAS Detector Using Proton-Proton Collisions at $\sqrt{s} = 13$ TeV*, https://cds.cern.ch/record/2044564, ATL-PHYS-PUB-2015-036, 2015.

[202] ATLAS Collaboration, *Performance of pile-up mitigation techniques for jets in pp collisions at $\sqrt{s} = 8$ TeV using the ATLAS detector*, Eur. Phys. J. C **76** no. 11, (2016) 581, `arXiv:1510.03823 [hep-ex]`.

[203] M. Cacciari, G. P. Salam, and G. Soyez, *The anti-k_t jet clustering algorithm*, JHEP **04** (2008) 063, `arXiv:0802.1189 [hep-ph]`.

[204] M. Cacciari, G. P. Salam, and G. Soyez, *FastJet User Manual*, Eur. Phys. J. **C72** (2012) 1896, `arXiv:1111.6097 [hep-ph]`.

[205] ATLAS Collaboration, *Identification and rejection of pile-up jets at high pseudorapidity with the ATLAS detector*, Eur. Phys. J. C **77** no. 9, (2017) 580, `arXiv:1705.02211 [hep-ex]`, [Erratum: Eur.Phys.J.C 77, 712 (2017)].

[206] ATLAS Collaboration, *Jet energy scale measurements and their systematic uncertainties in proton-proton collisions at $\sqrt{s} = 13$ TeV with the ATLAS detector*, Phys. Rev. D **96** no. 7, (2017) 072002, `arXiv:1703.09665 [hep-ex]`.

[207] ATLAS Collaboration, *Jet Calibration and Systematic Uncertainties for Jets Reconstructed in the ATLAS Detector at $\sqrt{s} = 13$ TeV*, http://cds.cern.ch/record/2037613, ATL-PHYS-PUB-2015-015, 2015.

[208] ATLAS Collaboration, *Performance of b-Jet Identification in the ATLAS Experiment*, JINST **11** no. 04, (2016) P04008, `arXiv:1512.01094 [hep-ex]`.

[209] ATLAS Collaboration, *Optimisation of the ATLAS b-tagging performance for the 2016 LHC Run*, https://cds.cern.ch/record/2160731, ATL-PHYS-PUB-2016-012, 2016.

[210] ATLAS Collaboration, *ATLAS flavour tagging group recommendation for 2015 data*, `https://twiki.cern.ch/twiki/bin/view/AtlasProtected/BTaggingBenchmarksRelease20`, 2017.

[211] ATLAS Collaboration, *Expected performance of the ATLAS b-tagging algorithms in Run-2*, http://cds.cern.ch/record/2037697, ATL-PHYS-PUB-2015-022, 2015.

[212] ATLAS Collaboration, *Performance of algorithms that reconstruct missing transverse momentum in $\sqrt{s} = 8$ TeV proton-proton collisions in the ATLAS detector*, Eur. Phys. J. C **77** no. 4, (2017) 241, `arXiv:1609.09324 [hep-ex]`.

[213] ATLAS Collaboration, *Expected performance of missing transverse momentum reconstruction for the ATLAS detector at $\sqrt{s} = 13$ TeV*, https://cds.cern.ch/record/2037700, ATL-PHYS-PUB-2015-023, 2015.

[214] ATLAS Collaboration, *Performance of missing transverse momentum reconstruction with the ATLAS detector using proton-proton collisions at $\sqrt{s}$ = 13 TeV*, Eur. Phys. J. C **78** no. 11, (2018) 903, `arXiv:1802.08168 [hep-ex]`.

[215] ATLAS Collaboration, *Measurement of the tau lepton reconstruction and identification performance in the ATLAS experiment using pp collisions at* $\sqrt{s} = 13$ TeV, https://cds.cern.ch/record/2261772, ATLAS-CONF-2017-029, 2017.

[216] ATLAS Collaboration, *Identification and energy calibration of hadronically decaying tau leptons with the ATLAS experiment in pp collisions at $\sqrt{s}$=8 TeV*, Eur. Phys. J. C **75** no. 7, (2015) 303, `arXiv:1412.7086 [hep-ex]`.

[217] ATLAS Collaboration, *Electron efficiency measurements with the ATLAS detector using the 2015 LHC proton-proton collision data*, https://cds.cern.ch/record/2157687, ATLAS-CONF-2016-024, 2016.

[218] R. K. Ellis, I. Hinchliffe, M. Soldate, and J. J. van der Bij, *Higgs Decay to tau+ tau-: A Possible Signature of Intermediate Mass Higgs Bosons at the SSC*, Nucl. Phys. **B297** (1988) 221–243.

[219] A. Elagin, P. Murat, A. Pranko, and A. Safonov, *A New Mass Reconstruction Technique for Resonances Decaying to di-tau*, Nucl. Instrum. Meth. **A654** (2011) 481–489, `arXiv:1012.4686 [hep-ex]`.

[220] ATLAS Collaboration, *Data-Quality Requirements and Event Cleaning for Jets and Missing Transverse Energy Reconstruction with the ATLAS Detector in Proton-Proton Collisions at a Center-of-Mass Energy of sqrts = 7 TeV*, https://cds.cern.ch/record/1277678, ATLAS-CONF-2010-038, 2010.

[221] ATLAS Collaboration, *Measurement of the $H \to \tau^+\tau^-$ cross-section in* 13 *TeV Collisions with the ATLAS Detector*, https://cds.cern.ch/record/2261605, ATL-COM-PHYS-2017-446, 2017.

[222] ATLAS Collaboration, *Luminosity recommendations for physics analyses*, `https://twiki.cern.ch/twiki/bin/viewauth/Atlas/LuminosityForPhysics`, 2017.

[223] ATLAS Collaboration, *Luminosity determination in pp collisions at* $\sqrt{s} = 13$ *TeV using the ATLAS detector at the LHC*, https://cds.cern.ch/record/2677054, ATLAS-CONF-2019-021, 2019.

[224] LHC Higgs Cross Section Working Group, *Handbook of LHC Higgs Cross Sections: 3. Higgs Properties*, `arXiv:1307.1347 [hep-ph]`.

[225] LHC Higgs Cross Section Working Group, *Handbook of LHC Higgs Cross Sections: 1. Inclusive Observables*, `arXiv:1101.0593 [hep-ph]`.

[226] ATLAS Collaboration, *Measurement of the cross-section for electroweak production of dijets in association with a Z boson in pp collisions at $\sqrt{s}$ = 13 TeV with the ATLAS detector*, Phys. Lett. **B775** (2017) 206–228, `arXiv:1709.10264 [hep-ex]`.

[227] G. Cowan, *Statistical Data Analysis.* Oxford University Press, Oxford, 1998.

[228] G. Cowan, K. Cranmer, E. Gross, and O. Vitells, *Asymptotic formulae for likelihood-based tests of new physics*, Eur. Phys. J. **C71** (2011) 1554, `arXiv:1007.1727 [physics.data-an]`, [Erratum: Eur. Phys. J.C73,2501(2013)].

[229] ROOT Collaboration, *HistFactory: A tool for creating statistical models for use with RooFit and RooStats*, https://cds.cern.ch/record/1456844, CERN-OPEN-2012-016, 2012.

[230] L. Moneta, K. Cranmer, G. Schott, and W. Verkerke, *The RooStats project* in *Proceedings of the 13th International Workshop on Advanced Computing and Analysis Techniques in Physics Research*, p. 57. 2010. `arXiv:1009.1003 [physics.data-an]`.

[231] W. Verkerke and D. P. Kirkby, *The RooFit toolkit for data modeling*, eConf **C0303241** (2003) MOLT007, `arXiv:physics/0306116`.

[232] F. James and M. Roos, *Minuit - a system for function minimization and analysis of the parameter errors and correlations*, Computer Physics Communications **10** no. 6, (1975) 343 – 367.

[233] N. Metropolis and S. Ulam, *The Monte Carlo Method*, Journal of the American Statistical Association **44** no. 247, (1949) 335–341.

[234] A. Wald, *Sequential Tests of Statistical Hypotheses*, Ann. Math. Statist. **16** no. 2, (06, 1945) 117–186.

[235] S. Wilks, *The Large-Sample Distribution of the Likelihood Ratio for Testing Composite Hypotheses*, Annals Math. Statist. **9** no. 1, (1938) 60–62.

[236] A. Hocker *et al.*, *TMVA - Toolkit for Multivariate Data Analysis*, `arXiv:physics/0703039`.

[237] R. Brun and F. Rademakers, *ROOT: An object oriented data analysis framework*, Nucl. Instrum. Meth. **A389** (1997) 81–86.

[238] ATLAS Collaboration, *Modelling $Z \to \tau\tau$ processes in ATLAS with τ-embedded $Z \to \mu\mu$ data*, JINST **10** no. 09, (2015) P09018, `arXiv:1506.05623 [hep-ex]`.

[239] J. Friedman, *Greedy Function Approximation: A Gradient Boosting Machine*, The Annals of Statistics **29** (11, 2000) .

[240] *TMVA Users Guide*, `http://tmva.sourceforge.net/docu/TMVAUsersGuide.pdf`.

[241] T. Hastie, R. Tibshirani, and J. Friedman, *The Elements of Statistical Learning: Data mining, Inference and Prediction.* Springer, 2 ed., 2009.

[242] B. Rottler, *Optimizing the measurement of the signal strength for Higgs-boson production in the H to tautau decay using multivariate techniques at 13 TeV with the ATLAS detector*, http://terascale.physik.uni-freiburg.de/Publikationen/abschlussarbeiten/diplom-masterarbeiten/masterBenjaminRottler/view, 2017.

[243] N. Smirnov, *Table for Estimating the Goodness of Fit of Empirical Distributions*, Ann. Math. Statist. **19** no. 2, (06, 1948) 279–281.

[244] I. W. Stewart and F. J. Tackmann, *Theory Uncertainties for Higgs and Other Searches Using Jet Bins*, Phys. Rev. D **85** (2012) 034011, `arXiv:1107.2117 [hep-ph]`.

[245] ATLAS Collaboration, *Measurements of the Higgs boson production cross section via ggF and VBF in $H \to WW^* \to l\nu l\nu$ with 36.1 fb^{-1} of data collected with the ATLAS detector at $\sqrt{s} = 13$ TeV*, https://cds.cern.ch/record/2276143, ATL-COM-PHYS-2017-1094, 2017.

[246] K. M. Ecker, *Measurement of the Higgs boson tensor coupling in $H \to ZZ^* \to 4\ell$ decays with the ATLAS detector - How odd is the Higgs boson?*, https://cds.cern.ch/record/2624277, CERN-THESIS-2018-073, 2018.

[247] CMS Collaboration, *Constraints on the spin-parity and anomalous HVV couplings of the Higgs boson in proton collisions at 7 and 8 TeV*, Phys. Rev. D **92** no. 1, (2015) 012004, `arXiv:1411.3441 [hep-ex]`.

[248] CMS Collaboration, *Constraints on anomalous HVV couplings from the production of Higgs bosons decaying to τ lepton pairs*, Phys. Rev. D **100** no. 11, (2019) 112002, `arXiv:1903.06973 [hep-ex]`.

[249] CMS Collaboration, *Measurements of the Higgs boson width and anomalous HVV couplings from on-shell and off-shell production in the four-lepton final state*, Phys. Rev. D **99** no. 11, (2019) 112003, `arXiv:1901.00174 [hep-ex]`.

[250] J. Brehmer, F. Kling, I. Espejo, and K. Cranmer, *MadMiner: Machine learning-based inference for particle physics*, Comput. Softw. Big Sci. **4** no. 1, (2020) 3, `arXiv:1907.10621 [hep-ph]`.

[251] J. Brehmer, K. Cranmer, G. Louppe, and J. Pavez, *A Guide to Constraining Effective Field Theories with Machine Learning*, Phys. Rev. D **98** no. 5, (2018) 052004, `arXiv:1805.00020 [hep-ph]`.

[252] J. Brehmer, K. Cranmer, F. Kling, and T. Plehn, *Better Higgs boson measurements through information geometry*, Phys. Rev. D **95** no. 7, (2017) 073002, `arXiv:1612.05261 [hep-ph]`.

[253] M. Schumacher, private communication, 2019.

Acknowledgements

The last page of this thesis is dedicated to thank everybody, who supported me and shared their knowledge with me throughout the last years. Everyone, who is mentioned here, contributed in many different ways to my daily work in Freiburg and within the ATLAS collaboration and took a great part in the successful writing of this thesis. I am also most thankful for the help of many other people, who are not mentioned here, since I want to keep this part directly work-related.

An erster Stelle geht mein Dank an dich, Markus, für die Möglichkeit in deiner Arbeitsgruppe zu promovieren und für deine stetige Unterstützung in den letzten Jahren. Auf meinem Weg von der Bachelorarbeit über die Masterarbeit bis hin zur Promotion hast du es mir immer ermöglicht, selbstständig zu arbeiten und warst stets bereit, über physikalische Fragestellungen zu diskutieren. Ich habe sehr von deiner fachlichen Kompetenz aber auch von deiner Offenheit und Hilfsbereitschaft profitiert und bin dankbar für deine Unterstützung, auch in den schwierigeren Zeiten.

Ein großer Dank geht außerdem an meine direkten Betreuer, Elias, Duc, Ulrike und Kathrin, die mir in den letzten Jahren über einen längeren oder auch kürzeren Zeitraum stets mit Rat und Tat zur Seite standen und deren Unterstützung und Ermutigung maßgeblich dazu beigetragen haben, dass ich gelernt habe, eigenständig zu arbeiten und die Qualität meiner Arbeit an erste Stelle zu setzen. Danke Kathrin, für deine Unterstützung, deine beeindruckende Arbeitsbereitschaft und dass ich mich auch besonders in den stressigeren Phasen zu jeder (Uhr-)Zeit an dich wenden konnte.

Thanks to the VBF CP team with Christian, Serhat, Alessia and Dirk. I enjoyed working with all of you and the results presented here would not have been possible without you.

Ich möchte mich auch bei Tilman Plehn und Felix Kling bedanken, für ihre Hilfe bei physikalischen und technischen Fragen zu CP Verletzung und Madminer.

Ein großer Dank geht auch an alle Mitstreiter in der Arbeitsgruppe für die zahlreichen Diskussionen und Hilfestellungen, aber auch fürs Kaffee trinken, Pflanzen gießen und die Organisation von Unterkünften. Liebe Chris, vielen Dank für deine Unterstẗzung bei den alltäglichen bürokratischen Hindernissen und auch für alles andere. Danke an Benjamin, für deine Zeit und Geduld bei meinen großen und kleinen Programmierproblemen. Danke Katharina, für all unsere Diskussionen und Gespräche und für deine Zimmergesellschaft auf den zahlreichen Tagungen und Reisen. Danke Anton, Felix, Stefan und Michael, dass ihr mir den Umgang mit der IT erleichtert und euch nie beschwert habt, wenn ich zum wiederholten Male nachfrage, warum meine Jobs nicht anlaufen. Danke auch an Benoit, Valerie, Diego und Daniel für eure Zeit, diese Arbeit Korrektur zu lesen. Danke David, für deine Hilfsbereitschaft bei technischen und physikalischen Fragen jeglicher Art, das (wiederholte) Lesen und Korrigieren dieser Arbeit und natürlich für die Katzen.